MICROBEAM ANALYSIS SOCIETY

PROCEEDINGS

THIRTEENTH ANNUAL CONFERENCE

JUNE 19-23, 1978

ANN ARBOR, MICHIGAN

Additional copies of these and previous Proceedings
may be obtained from:

MICROBEAM ANALYSIS SOCIETY

PROCEEDINGS

THIRTEENTH ANNUAL CONFERENCE

JUNE 19-23, 1978

ANN ARBOR, MICHIGAN

PREFACE

We welcome you to another Annual Conference of the Microbeam Analysis
Society. This year the Conference is independent from any other meeting
since 1974, and the strong technical program of 109 papers (including
tutorials and workshop abstracts) indicates that microbeam analysis
is still very much alive and healthy. We are particularly pleased with
the contributions made to the sessions on SIMS, Biomedical Sciences,
and Particulate Analysis. These are very contemporary subjects, and
you will find these sessions particularly interesting. The session
on Spectral Analysis covers a wide range of applications, and the
sessions on Quantitative Analysis, Surface Analysis, and SEM also
deserve your interest. The tutorials are designed to be of interest
to "young" and "old" alike, and the workshop on Cryogenic Sample
Preparation is outstanding.

Conferences such as this do not simply organize themselves, but are
the result of much effort by many different people. This conference
is officially sponsored by the Midwest Probe Users Group (affiliated
with the National MAS) and the Department of Materials Engineering,
University of Michigan. We express our deep gratitude to Wilbur
Bigelow and John Bomback for the effort they and their committees
have put into the preparations for this conference. Without their
help there would be no meeting this year. We also thank Donald
Beaman and Gordon Cleaver for their assistance in printing the
Proceedings and Technical Program booklet. I want to publicly thank
my wife, Janell, for her assistance in typing the numerous extra
pages for the Proceedings, and all of the booklet. Lastly, I thank
each of the organizing session chairmen who helped me so much in
arriving at the technical program this year. Their expertise is
obvious in the program.

David F. Kyser
Technical Program Chairman

MICROBEAM ANALYSIS SOCIETY

1978 National Officers

President

James D. Brown
Faculty of Engineering Science
University of Western Ontario
London, Canada N6A-5B9

President-Elect

David F. Kyser
IBM Research Laboratory
5600 Cottle Road
San Jose, CA 95193

Past President

Joseph I. Goldstein
Dept. of Metallurgy & Materials Science
Lehigh University
Bethlehem, PA 18015

Treasurer

Arthur A. Chodos
Division of Geological & Planetary Sciences
California Institute of Technology
Pasadena, CA 91125

Secretary

Robert L. Myklebust
Analytical Chemistry Division
National Bureau of Standards
Washington, D. C. 20234

Members-at-Large

Mary C. Finn
Lincoln Laboratory
244 Wood Street
Lexington, MA 02173

C. Gordon Cleaver
General Electric Company
Vallecitos Nuclear Center
Pleasanton, CA 94566

Noel C. MacDonald
Physical Electronics Industries
6509 Flying Cloud Drive
Eden Prairie, MN 55343

NATIONAL MAS COMMITTEES - 1978

Society Awards:	L. Birks (Chairman)
Presidential Awards:	O. Wells (Chairman)
Membership:	J. Goldstein
Sustaining Membership:	D. Beaman (Chairman) J. Tabock D. Kyser
Legal:	P. Lublin
Standards:	A. Chodos
Employment Services:	W. Fricke, Jr.
Nominations:	G. Cleaver (Chairman) R. Gooley F. Laabs R. Myklebust
Micro News:	P. DeNee (Editor) V. Shull
Future Meeting Sites:	P. Lublin (Chairman)
Section Liaison:	
Speaker's Tour	J. Goldstein
Local Sections	J. Brown
Publications:	K. Heinrich (Chairman)
1979 Meeting:	
Local Arrangements	R. Dobrott (Chairman)
Technical Program	D. Newbury (Chairman)

ORGANIZING COMMITTEES

13th ANNUAL MAS CONFERENCE - 1978

Local Arrangements:

W. Bigelow (Chairman)
P. Hollingsworth
G. Brooks

Commercial Exhibits:

J. Bomback (Chairman)
H. Estry
J. Lenke
J. Russ

Technical Program:

D. Kyser (Chairman)
P. Echlin
A. Saubermann
D. Newbury
J. Coleman
D. Joy
K. Heinrich
O. Wells
D. Beaman
J. Brown

Meeting Facilities:

L. Allard
A. Mardinly
S. Krause
C. Montross

Tours and Special Events:

P. Hollingsworth
J. Tabock
K. Carroll

Publicity and Printing:

V. Shull
G. Cleaver
D. Beaman

14th ANNUAL MAS CONFERENCE - 1979

nual MAS Conference will be a joint meeting with the Electron
Society of America (EMSA) in San Antonio, Texas (August 12–17, 1979 ➤

Local Arrangements:

Robert Dobrott
Texas Instruments, Inc.
P. O. Box 5936
Dallas, Texas 75222

Technical Program:

Dale Newbury
Chemistry A121
National Bureau of Standards
Washington, D. C. 20234

HONORARY MEMBERS

ory and Technology
stitution
C. 20560

I. B. Borovskii
Institute of Solid State Physics
Academy of Sciences
Moscow, U.S.S.R.

ıg
'aris
ences

Peter Duncumb
Tube Investments Research Laboratories
Nor. Saffron Walden
Essex, England

.aboratory
. 20390

Gunji Shinoda
Osaka University
Osaka, Japan

V. E. Cosslett
The Cavendish Laboratory
University of Cambridge
Cambridge, England

ANNUAL AWARDS MADE BY THE MICROBEAM ANALYSIS SOCIETY

MACRES AWARD

This award of $300 was established in 1973 to honor the memory of Dr. Victor Macres, one of the pioneers of electron probe analysis, a dedicated teacher, and a competitive instrument manufacturer. The award is given for the best instrumentation paper presented at the annual meeting. In 1977 the award was made to R. Castaing and G. Blaise, "Analysis of Solid Surfaces by Thermal Ionization of Sputtered Particles" (Univ. of Paris)

JEOL AWARD

The Japan Electron Optics Laboratory Corporation sponsors this award of $300 but it is administered by the Microbeam Analysis Society. The award is given for an outstanding student paper presented at the annual MAS meeting. In 1977 the JEOL Award was given to C. Wu and D. Wittry, "Measurement of Diffusion Lengths of Excess Carriers in Semiconductors" (Univ. of Southern California)

CORNING AWARD

In 1975 the Corning Glass Works established an award of $300 for the most outstanding contributed paper presented at the annual MAS meeting. The award is administered by the Microbeam Analysis Society. The 1977 award was made to E. Lifshin, M. Ciccarelli, and R. Bolon, "New Measurements of the Voltage Dependence of Absolute X-Ray Yields Using EDS" (General Electric Co.)

THE MAS STUDENT SUPPORT PROGRAM

The encouragement of student participation at the annual meeting is an important objective of the Microbeam Analysis Society. The registration fee is reduced for student attendees, of course, but the Student Support Program is specifically pointed towards soliciting the presentation of research papers by students at the annual meeting. In addition to being good experience for the students, such presentations often bring refreshing new views of theoretical, as well as experimental, aspects of microbeam analysis.

The guidelines for the support program are simple:
1. The paper must be co-authored by a bona fide student and his or her professor.
2. It must be of a quality to be accepted by the Technical Program Committee.
3. It must be presented at the meeting by the student.
4. The professor is asked to attest to the kind and amount of contribution made by the student.

Travel support for the student is furnished by MAS to ensure that his or her attendance will not be an undue financial burden to either the student or the university.

In addition to the student travel support, the Microbeam Analysis Society administers the annual JEOL Award for an outstanding student presentation (see description of the MAS awards).

MICROBEAM ANALYSIS SOCIETY

SUSTAINING MEMBERS

UNITED SCIENTIFIC CORPORATION
ANALYTICAL INSTRUMENT DIVISION
Mountain View, California

ORTEC INCORPORATED
Oak Ridge, Tennessee

THE PERKIN-ELMER CORPORATION
Mountain View, California

PHILIPS ELECTRONIC INSTRUMENTS INC.
Mahwah, New Jersey

PHYSICAL ELECTRONICS INDUSTRIES, INC.
Eden Prairie, Minnesota

PRINCETON GAMMA-TECH, INC.
Princeton, New Jersey

QBI INTERNATIONAL
San Francisco, California

CHARLES M. TAYLOR CO.
Stanford, California

TRACOR NORTHERN
Middleton, Wisconsin

VARIAN ASSOCIATES
VACUUM DIVISION
Palo Alto, California

MICRON, INC.
Wilmington, Delaware

INDEX OF AUTHORS

INDEX OF AUTHORS

INDEX OF AUTHORS

INDEX OF AUTHORS

TECHNICAL PROGRAM CALENDAR

Monday - June 19, 1978

(AM) SESSION 1A - Tutorials on SIMS, EDS
(AM) SESSION 2A - Workshop on Cryogenic Sample Preparation
(PM) SESSION 1B - Tutorials on STEM Microanalysis, STEM
                  Microscopy
(PM) SESSION 2B - Workshop on Cryogenic Sample Preparation

Tuesday - June 20, 1978

(AM) SESSION 3A - SIMS: Theory and Quantitative Analysis
(AM) SESSION 4A - Microanalysis in Biomedical Sciences
(PM) SESSION 3B - SIMS: Instrumentation
(PM) SESSION 4B - Microanalysis in Biomedical Sciences

Wednesday - June 21, 1978

(AM) SESSION 5A - SIMS: Applications
(AM) SESSION 6A - Quantitative Analysis: Theory
(PM) SESSION 5B - Spectral Analysis with Computers
(PM) SESSION 6B - EBIC in the SEM

Thursday - June 22, 1978

(AM) SESSION 7A - Particulate Analysis
(AM) SESSION 8A - Surface Analysis
(PM) SESSION 7B - Particulate Analysis
(PM) SESSION 8B - Surface Analysis

Friday - June 23, 1978

(AM) SESSION 9A - Quantitative Analysis: Applications
(AM) SESSION 10A - SEM

All morning sessions will commence at 8:30 AM (except session 8A-
at 8:00 AM)

All afternoon sessions will commence at 1:30 PM (except
session 8B - at 1:00 PM)

SESSION IA - TUTORIALS

Organized by David Kyser
                IBM Research Lab.

T1   8:30AM   PRINCIPLES AND PRACTICE OF SIMS MICROANALYSIS
                    K. Wittmaack
                    IBM Watson Research Center

        10:00   Break

T2   10:30   PRINCIPLES AND PRACTICE OF QUANTITATIVE X-RAY CHEMICAL
                    ANALYSIS WITH E.D.S. SYSTEMS
                    P. Statham
                    Link Systems

MONDAY AFTERNOON - JUNE 19, 1978

SESSION IB - TUTORIALS

T3   1:30PM   PRINCIPLES AND PRACTICE OF STEM MICROANALYSIS
                    J. Goldstein
                    Lehigh University

        3:00   Break

T4   3:30   PRINCIPLES AND PRACTICE OF STEM MICROSCOPY
                    R. Geiss
                    IBM Research Lab.

SESSION IIA - WORKSHOP ON CRYOGENIC SAMPLE PREPARATION FOR MICROSCOPY AND MICROANALYSIS

Organized by Albert Saubermann
Harvard Medical School
and Patrick Echlin
Cambridge University

W1   8:30AM   CONDITIONS FOR AVOIDANCE OF ICE CRYSTALLIZATION IN CELLS
L. Rebhun
University of Virginia

W2   9:00   THE USE OF POLYMERIC CRYOPROTECTANTS IN MORPHOLOGICAL AND
ANALYTICAL STUDIES OF BIOLOGICAL MATERIAL
F. Franks, P. Echlin and H. Skaer
University of Cambridge

W3   9:30   RADIATION DAMAGE IN BIOLOGICAL SPECIMENS AT LOW TEMPERATURES
R. Glaeser
University of California, Berkeley

10:00   Discussion

10:30   Break

W4   10:45   FRACTURING OR CUTTING FROZEN SECTIONS FOR ELECTRON PROBE
MICROANALYSIS?
R. Kirk
Yale University and
G. Dobbs
Washington and Lee University

W5   11:15   CRYOSECTIONING OF BIOLOGICAL SPECIMENS FOR X-RAY MICROANALYSIS
A. Saubermann
Harvard Medical School

11:45   Discussion

12:00   Lunch

SESSION IIB - WORKSHOP ON CRYOGENIC SAMPLE PREPARATION FOR MICROSCOPY AND MICROANALYSIS

W6   1:30PM   LOW TEMPERATURE SCANNING ELECTRON MICROSCOPY AND X-RAY
                    MICROANALYSIS OF BIOLOGICAL MATERIAL
                    P. Echlin
                    Cambridge University

W7   2:00   APPLICABILITY OF THE BIOCHAMBER TO PREPARATION OF COLD
                    BIOLOGICAL SAMPLES FOR X-RAY MICROANALYSIS
                    J. Pawley
                    University of California, Berkeley

        2:30   Discussion

W8   3:00   FROZEN-HYDRATED SECTIONS
                    P. Peters
                    Harvard Medical School

W9   3:30   A NEW PROCEDURE FOR PREPARING BULK FROZEN-HYDRATED
                    BIOLOGICAL SPECIMENS FOR X-RAY MICROANALYSIS
                    P. Burgio, W. Low and M. Lawrence
                    University of Michigan

        4:00   Discussion

        4:30   Round Table

SESSION IIIA - SECONDARY ION MASS SPECTROMETRY: THEORY AND QUANTITATIVE ANALYSIS

Organized by Dale Newbury
National Bureau of Standards

1   8:30AM   *MECHANISM OF OXYGEN ENHANCEMENT OF SPUTTERED ION YIELDS
            P. Williams
            University of Illinois

2   9:15   *A ONE FITTING PARAMETER METHOD FOR QUANTITATIVE SIMS
            A. Morgan and H. Werner
            Phillips Research Laboratories

3   9:55   ENERGY DISTRIBUTION OF POSITIVE IONS OF GROUP III AND
            GROUP V ELEMENTS SPUTTERED FROM SEMICONDUCTORS
            D. Wittry
            University of Southern California and
            T. Whatley
            Applied Research Laboratories

    10:15   Break

4   10:35   SIMS ANALYSIS: THE DETERMINATION OF DETECTION LIMITS -
            SAMPLE VOLUME RELATIONSHIP USING MICRODOT STANDARDS
            R. Dobrott and G. Larrabee
            Texas Instruments

5   11:00   ADVANCES IN QUANTITATIVE STUDIES USING Cs^+ SECONDARY ION
            MASS SPECTROMETRY
            V. Deline, P. Williams, and C. Evans, Jr.
            University of Illinois

6   11:25   ON THE ACCURACY OF QUANTITATIVE ANALYSIS IN SECONDARY ION
            MASS SPECTROMETRY - ROUND ROBIN RESULTS
            D. Newbury
            National Bureau of Standards

    11:45   Discussion

    12:00   Lunch

*Invited Papers

SESSION IIIB - SECONDARY ION MASS SPECTROMETRY: INSTRUMENTATION

7   1:30PM   *SELECTION OF PRIMARY ION SOURCE FOR SIMS
H. Storms
General Electric Co.

8   2:10   A SYSTEM FOR COMBINED SIMS-AES-XPS ANALYSIS OF SOLIDS
M. Frisch, W. Reuter and K. Wittmaack
IBM Watson Research Center

9   2:40   THE SECONDARY ION OPTICS OF A QUADRUPOLE ION MICROPROBE
J. Potosky and D. Wittry
University of Southern California

10   3:05   INSTRUMENTAL DISCRIMINATION EFFECTS IN SIMS
M. Rudat and G. Morrison
Cornell University

    3:30   Break

11   3:45   OPTIMIZATION OF RECORDING SECONDARY ION MASS SPECTRA
D. Wittry
University of Southern California

12   4:10   MULTIFEATURE MASS ANALYSIS UTILIZING DIGITAL IMAGE PROCESSING
OF SECONDARY ION MASS SPECTROMETRIC IMAGES
J. Fassett and G. Morrison
Cornell University

13   4:35   USE OF SPECIMEN CURRENT INTEGRATION IN SIMS
F. Guo and D. Wittry
University of Southern California

14   5:00   APPLICATION USING SECOND GENERATION HIGH RESOLUTION ION
MICROANALYZER
C. Conty
CAMECA

    5:20   Discussion

*Invited Papers

SESSION IVA - MICROANALYSIS IN BIOMEDICAL SCIENCES

Organized by James Coleman
University of Rochester

15 8:30AM *ELECTRON ENERGY-LOSS SPECTROSCOPY (EELS) AND ITS
APPLICATION TO BIOLOGY
D. Joy and D. Maher
Bell Laboratories

16 9:10 *THE LAMMA INSTRUMENT: A NEW LASER MICROPROBE MASS
ANALYZER FOR BIOMEDICAL PURPOSES
R. Kaufmann, R. Nitsche and M. Schurmann
University Dusseldorf
F. Hillenkamp
University Frankfurt
H. Vogt and R. Wechsung
Leybold-Heraeus

17 9:50 ZAF-CORRECTION PROCEDURES IN ELECTRONPROBE X-RAY MICRO-
ANALYSIS OF BIOLOGICAL BULK SPECIMENS
A. Boekestein, G. Roomans, A. Stols and A. Stadhouders
University of Nijmegen

10:30 Break

18 10:40 ENVIRONMENTAL CHAMBERS FOR MICROANALYSIS
D. Parsons
New York State Department of Health

19 11:20 SOME EFFECTS OF ELECTRON IRRADIATION OF BIOLOGICAL SPECIMENS
J. Edie and P. Glick
University of Iowa

12:00 Lunch

*Invited Papers

SESSION IVB - MICROANALYSIS IN BIOMEDICAL SCIENCES

20   1:30PM   *MICROPROBE ANALYSIS IN MINERALIZING TISSUES
              E. Krefting, H. Hohling and R. Barckhaus
              University of Munster

21   2:10   *ELECTRON PROBE ANALYSIS OF SMOOTH AND STRIATED MUSCLE
              A. P. Somlyo, A. V. Somlyo, H. Schuman, B. Sloane and
              A. Scarpa
              Presb.-University of Penn. Medical Center

22   2:50   IMPROVEMENT OF PEAK/BACKGROUND RATIOS FOR ANALYSIS OF
              FROZEN-HYDRATED TISSUE SECTIONS
              P. Peters, A. Saubermann and W. Riley
              Harvard Medical School

      3:30   Break

23   3:40   ELECTRON MICROPROBE LOCALIZATION OF ALUMINUM DEPOSITS IN
              RAT LUNG AFTER INHALATION EXPOSURE TO ALUMINUM CHLORHYDRATE
              W. Hamilton
              Applied Research Laboratories and
              N. Woodside
              Experimental Pathology Laboratories, Inc.

24   4:20   ELECTRON PROBE ANALYSIS IN KIDNEY PHYSIOLOGY
              R. Warner and C. Lechene
              Harvard Medical School

25   5:00   ELECTRON PROBE MICROANALYSIS AND THE CELLULAR BASIS OF
              INTESTINAL CALCIUM ABSORPTION
              J. Coleman
              University of Rochester

26   5:40   APPLICATION OF ELECTRON PROBE MICROANALYSIS IN REPRODUCTIVE
              BIOLOGY
              C. Lechene
              Harvard Medical School

              *Invited Papers

SESSION VA - SECONDARY ION MASS SPECTROMETRY: APPLICATIONS

Organized by Dale Newbury
National Bureau of Standards

27   8:30AM   *ORGANIC SIMS
A. Benninghoven
University of Munster

28   9:15   A REVIEW OF SECONDARY ION MASS SPECTROMETRY IN BIOLOGICAL RESEARCH
M. Burns-Bellhorn
Albert Einstein College of Medicine

29   9:40   ION MICROPROBE ANALYSIS OF Li IN SNAIL EGGS IN EARLY CLEAVAGE STAGES
P. Elbers
University of Utrecht
D. Gras and A. von Rosenstiel
Metaalinstituut TNO and
J. Brown
University of Western Ontario

     10:05   Break

30   10:30   ION MICROPROBE ANALYSIS OF ^{30}Si DIFFUSION IN a-SiC
J. Hong and R. Davis
North Carolina State University and
D. Newbury
National Bureau of Standards

31   10:55   ELEMENTAL IMAGING FACILITIES OF THE ION MICROPROBE APPLIED TO NODULAR CAST IRON
J. Schilling, P. Buger and H. Fidos
National Physical Research Laboratory, South Africa

32   11:20   THE EFFECT OF PREFERENTIAL SPUTTERING ON ION MICROPROBE DEPTH PROFILES IN MINERALS
E. Zinner
Washington University

     11:40   Discussion

     12:00   Lunch

*Invited papers

SESSION VB - ELECTRON BEAM INDUCED CONDUCTION (EBIC) IN THE SEM

Organized by Oliver Wells
IBM Watson Research Center

33   8:30AM   *HISTORICAL COMMENTS ON EBIC METHODS IN THE SEM
T. Everhart
University of California Berkeley

34   8:50   *CHARGE COLLECTION MICROSCOPY
H. Leamy
Bell Laboratories

35   9:20   *STUDY OF DOPANT STRIATIONS FOR HIGHLY DOPED SILICON IN
SOLAR CELL STRUCTURE BY SCANNING ELECTRON MICROSCOPY
J. Chi and H. Gatos
Mass. Institute of Technology

36   9:40   *ELECTRON BEAM INDUCED CURRENTS IN METAL OXIDE SILICON
DEVICES
P. Roitman
National Bureau of Standards

10:10   Break

37   10:30   *ELECTRON BEAM INDUCED CURRENT EXAMINATION OF DEFECTS IN
SOLAR CELLS
C. Rao
Mobil Tyco Solar Energy Corp.

38   11:00   *A CONTAMINATION EFFECT WHEN EXAMINING EITHER SILICON SOLAR
CELLS OR GALLIUM ARSENIDE LASER DIODES BY THE EBIC METHOD
O. Wells
IBM Watson Research Center

11:30   Discussion

12:00   Lunch

*Invited Papers

SESSION VIA - QUANTITATIVE ANALYSIS: THEORY

Organized by James Brown
University of Western Ontario

39   8:30AM   *A NEW CORRECTION PROCEDURE FOR QUANTITATIVE ELECTRON
PROBE MICROANALYSIS
G. Love and V. Scott
University of Bath

40   9:00   *A TRANSPORT EQUATION THEORY OF ELECTRON BACKSCATTERING
AND X-RAY PRODUCTION
D. Fathers
University of Oxford and
P. Rez
University of California, Berkeley

41   9:30   LIMIT SPATIAL DISTRIBUTION OF ELECTRONS IN A HOMOGENEOUS
AND ISOTROPIC TARGET
C. Landron
SFAX, Tunisia

42   9:50   EFFECT OF ELECTRON INCIDENCE ANGLE ON QUANTITATIVE
CORRECTIONS IN ELECTRON PROBE MICROANALYSIS
W. Robinson and J. Brown
University of Western Ontario

        10:10   Break

43   10:30   INFORMATION, PROBABILITY, AND MICROPROBE ANALYSIS
N. Walter
Boeing Vertol Co.

44   10:50   QUANTITATIVE MICROANALYSIS WITH Si DETECTOR AND CAMAC
AUTOMATED MICROPROBE
J. Rucklidge
University of Toronto

45   11:10   AN ENERGY DISPERSIVE TECHNIQUE FOR THE QUANTITATIVE
ANALYSIS OF CLAY MINERALS BY THE ELECTRON MICROPROBE
D. Smith and P. Cavell
University of Alberta

46   11:30   A FAST, SELF-CONTAINED, NO-STANDARDS QUANTITATIVE
PROGRAM FOR EDS
J. Russ
EDAX Laboratories

        11:50   Lunch

*Invited Papers

SESSION VIB - SPECTRAL ANALYSIS WITH COMPUTERS

Organized by Dale Newbury
           National Bureau of Standards
       and David Joy
           Bell Laboratories

47	1:30PM	*COMPUTER TECHNIQUES FOR ANALYSIS OF ENERGY-DISPERSIVE X-RAY SPECTRA P. Statham Link Systems
48	2:10	*SPECTRAL ANALYSIS TECHNIQUES IN AUGER-ELECTRON SPECTROSCOPY C. Powell National Bureau of Standards
49	2:45	*THE ELECTRON ENERGY-LOSS SPECTRUM AND REQUIREMENTS FOR ITS PROCESSING D. Joy, D. Maher and P. Mochel Bell Laboratories
	3:15	Break
50	3:35	AN OVERVIEW OF CURVE FITTING TECHNIQUES F. Schamber Tracor-Northern
51	4:05	SYSTEMATIC ERRORS IN DIGITAL FILTER ANALYSES OF EDS SPECTRA R. Miller and M. Giles Princeton Gamma-Tech, Inc.
52	4:30	OBSERVATIONS ON THE SEQUENTIAL SIMPLEX METHOD AND ITS APPLICATION TO PEAK FITTING IN ENERGY-DISPERSIVE X-RAY SPECTROMETRY C. Fiori and R. Myklebust National Bureau of Standards
53	4:55	A DATA COLLECTION AND REDUCTION SYSTEM FOR ELECTRON ENERGY-LOSS SPECTROSCOPY D. Maher, P. Mochel and D. Joy Bell Laboratories
54	5:20	INTERACTIVE DISPLAYS AND SIMPLE ALGORITHMS AS AN AID TO QUALITATIVE ANALYSIS OF ED SPECTRA J. Russ and V. Chopra EDAX Laboratories
55	5:45	COMPUTER INDEXING OF X-RAY EMISSION SPECTRA N. Spielberg Kent State University

*Invited Papers

SESSION VIIA - MICROANALYSIS OF PARTICULATES

Organized by Kurt Heinrich
National Bureau of Standards

56   8:30AM   *PROGRESS IN QUANTITATION OF SINGLE-PARTICLE ANALYSIS
WITH THE ELECTRON PROBE
J. Small, K. Heinrich, C. Fiori, D. Newbury and R. Myklebust
National Bureau of Standards

57   9:00   ESTIMATING MASS THICKNESS IN SEMI-THIN SECTIONS
M. Giles and N. Barbi
Princeton Gamma-Tech, Inc.

58   9:20   VARIATION IN INTENSITY RATIOS USED TO IDENTIFY ASBESTOS
FIBERS
J. Russ
EDAX Laboratories

59   9:40   CHEMICAL AND PHYSICAL CHARACTERIZATION OF COAL GASIFICATION
PARTICULATES, AND ITS RELEVANCE TO INHALATION TOXICOLOGY
D. Davidson and E. Gause
Southwest Research Center

      10:00   Break

60   10:20   QUANTITATIVE ANALYSIS OF SMALL PARTICLES USING WAVELENGTH
AND ENERGY DISPERSIVE SYSTEMS IN AN ELECTRON BEAM INSTRUMENT
J. Gavrilovic
McCrone Associates, Inc.

61   10:40   MONTE CARLO ELECTRON TRAJECTORY SIMULATION - AN AID FOR
PARTICLE ANALYSIS
R. Myklebust, D. Newbury, K. Heinrich, J. Small and C. Fiori
National Bureau of Standards

      11:00   Late Breaking Paper

      11:30   Discussion

      12:00   Lunch

*Invited Paper

SESSION VIIB - MICROANALYSIS OF PARTICULATES

62   1:30PM   *QUANTITATIVE ANALYSIS OF LYOPHILIZED SOLUTIONS:
EXPERIMENTAL AND THEORETICAL EVALUATION OF THE LIMITS OF
LINEARITY OF THE CALIBRATION CURVES
N. Roinel, M. Champigny, L. Meny and J. Henoc
CEN Saclay, France

63   2:00   *QUANTITATIVE CHARACTERIZATION OF PARTICULATES BY SCANNING
AND HIGH VOLTAGE ELECTRON MICROSCOPY
R. Lee and R. Fisher
U. S. Steel Corp.

64   2:30   *APPLICATION OF AUGER-ELECTRON SPECTROSCOPY AND X-RAY
PHOTOELECTRON SPECTROSCOPY TO THE CHARACTERIZATION OF
PARTICLES
C. Powell
National Bureau of Standards

      3:00   Break

65   3:20   *SECONDARY ION MASS SPECTROMETRY FOR PARTICLE ANALYSIS
D. Newbury
National Bureau of Standards

66   3:40   *PARTICLE ANALYSIS WITH THE LASER-RAMAN MICROPROBE
E. Etz, G. Rosasco, J. Blaha and K. Heinrich
National Bureau of Standards and
W. Cunningham
University of Maryland

      4:10   Discussion

*Invited Papers

SESSION VIIIA - SURFACE ANALYSIS

Organized by Donald Beaman
            Dow Chemical Co.

67   8:00AM   *PARAMETERS OF QUANTITATIVE XPS AND AES
                W. Riggs and L. Davis
                Physical Electronics Industries

68   9:00   *THE ROLE OF THE CASCADE AS A BACKGROUND EFFECT IN
                SECONDARY-ELECTRON EMISSION SPECTROSCOPY
                E. Sickafus
                Ford Motor Co.

      9:30   Discussion

69   10:00   *THE DIGITAL ACQUISITION AND PROCESSING OF AUGER SPECTRA
                Y. Strausser and N. Taylor
                Varian Associates, Inc.

70   10:30   *SCANNING AUGER MICROBEAM ANALYSIS: PAST, PRESENT, AND
                FUTURE
                 N. MacDonald, R. Gerlach, and C. Hovland
                Physical Electronics Industries

71   11:00   *HIGH SPATIAL RESOLUTION SCANNING AUGER ELECTRON
                SPECTROSCOPY
                R. Rowe and C. Briant
                General Electric Co.

      11:30   Discussion

      12:00   Lunch

      *Invited Papers

SESSION VIIIB - SURFACE ANALYSIS

72   1:00PM   *ANALYSIS OF LIFE-TESTED DISPENSER CATHODES
              B. Artz, J. Bomback, E. Sickafus and M. Smith
              Ford Motor Co.

73   1:30   *XPS AND AES STUDIES OF GAS-PHASE AND ELECTROCHEMICAL
              OXIDATION OF TITANIUM AND TITANIUM HYDRIDES
              N. Armstrong, C. Linkous and C. Sayers
              Michigan State University

74   2:00   *THE USE OF COMBINED ION- AND ELECTRON-BEAM TECHNIQUES
              IN METALLURGY RESEARCH
              P. Needham, Jr.
              U. S. Department of Interior

      2:30   Discussion

75   2:45   *SPATIALLY RESOLVED XPS
              C. Hovland
              Physical Electronics Industries

76   3:15   *X-RAY PHOTOELECTRON SPECTROSCOPIC AND PHOTOCURRENT
              STUDIES OF DYE-MODIFIED SEMICONDUCTOR ELECTRODES
              D. Hawn and N. Armstrong
              Michigan State University

77   3:45   *A KALEIDOSCOPIC VIEW OF RECENT ADVANCES IN ESCA-ISS-SIMS
              G. Mateescu
              Case Western Reserve University

      4:15   Discussion

78   4:30   *SURFACE CHARACTERIZATION OF METALS, POLYMERS AND COMPOSITES
              BY COMBINED TECHNIQUES: ISS, SIMS, SEM AND EDX
              G. Sparrow
              3M company

79   5:00   *COMPUTER SIMULATIONS OF ION-SOLID INTERACTIONS: H^+
              AND He^+ ON Au
              H. Helbig, F. Moore and M. Linder
              Clarkson College of Technology and
              B. Popp
              Cornell University

80   5:30   *NON-DESTRUCTIVE, QUANTITATIVE ANALYSIS OF THIN FILMS
              R. Musket
              Kevex Corporation

      6:00   Discussion

              *Invited Papers

SESSION IXA - QUANTITATIVE ANALYSIS: APPLICATIONS

Organized by James Brown
         University of Western Ontario

81   8:20AM   THERMAL BATTERY REACTION PRODUCTS
                P. Hlava
                Sandia Laboratories

82   8:40   ANALYSIS OF PRIMARY DEPOSITION SITES FOR SILICA IN GRASSES
                AND RUSHES BY SEM AND EDS MICROANALYSIS
                P. Kaufman, P. Dayanandan, M. Goldoftas, E. Lau, J. Srinivasan,
                J. Clark, P. Hollingsworth, J. Mardinly and W. Bigelow
                University of Michigan

83   9:00   MICROPROBE AND X-RAY ANALYSIS OF GAS TURBINE MATERIALS
                AFTER HOT CORROSION
                H. van Amerongen, D. Gras, A. von Rosenstiel and J. Visser
                TNO, Holland
                J. Brown
                University of Western Ontario

84   9:20   MICROPROBE AUTOMATION USING A GENERAL PURPOSE MICROCOMPUTER
                SYSTEM
                W. Hatfield and M. McConnell
                General Electric

85   9:40   ELECTRON PROBE ANALYSIS USING COMPUTER AUTOMATED ELECTRON
                BEAM POSITIONING
                W. Hamilton, J. Hinthorne and H. Gille
                Applied Research Laboratories

      10:00   Break

86   10:20   AN EFFICIENT COMBINED ED/WD X-RAY ANALYSIS SYSTEM
                J. Russ and R. Shen
                EDAX Laboratories

87   10:40   COMPUTER CONTROLLED PHOTOGRAPHY ON AN ELECTRON MICROPROBE
                W. Chambers
                Sandia Laboratories

88   11:00   A GRAPHICAL METHOD OF RESOLVING X-RAY INTERFERENCES ON THE
                ELECTRON MICROPROBE
                J. Geissman and E. Essene
                University of Michigan

SESSION IXA (CON'T)

89   11:20   MICROANALYSIS OF SMALL PARTICLES ON COMPLEX SURFACES
D. Brandon and M. Hornstein
Technion, Israel Institute of Technology

90   11:40   A KOSSEL CAMERA DESIGNED FOR THE CAMECA MBX-INSTRUMENT
C. Conty
CAMECA and
F. Maurice
CEA Saclay and
R. Tixier
IRSID, France

12:00   Lunch

SESSION XA - SCANNING ELECTRON MICROSCOPY

Organized by Oliver Wells
IBM Watson Research Center

):00AM CONTRAST MECHANISM OF ELECTRON CHANNELING PATTERNS
T. Yamamoto
Jeol Ltd.
M. Mori and Y. Ishida
University of Tokyo

9:20 SEM TECHNIQUE FOR MEASURING THE LOCAL NITROGEN CONCENTRATI
IN GaP
Ya. Golubev, V. Lejnin, V. Petrov and G. Spivak
Moscow State University
V. Evstropov and B. Kalinin
A. F. Ioffe Physico-Technical Institute, USSR

9:40 COLOR AND VIDEO ENHANCEMENT OF SEM BACKSCATTERED
ELECTRON IMAGES
P. DeNee
National Institute OSH and
R. Frederickson
West Virginia University

94 10:00 SCANNING ELECTRON MICROSCOPY OF ANCIENT GEOLOGICAL
FLUIDS AND THEIR CRYSTALLIZATION PRODUCTS
W. Kelly, B. Nesbitt, F. Metzger and E. Essene
University of Michigan

95 10:20 APPLICATION OF SCANNING ELECTRON MICROSCOPY TO INCLUSIONS
IN CARBONATITES
B. Nesbitt and W. Kelly
University of Michigan

96 10:40 TYPE II MAGNETIC CONTRAST IN PERMALLOY AND AMORPHOUS
MAGNETIC FILMS
H. Tong
IBM Corporation

THIRTEENTH ANNUAL CONFERENCE

OF THE

MICROBEAM ANALYSIS SOCIETY

TUTORIALS

AND

WORKSHOPS

PRINCIPLES AND PRACTICE OF SIMS MICROANALYSIS

K. Wittmaack[*]

IBM Thomas J. Watson Research Center
Yorktown Heights, New York 10598

Secondary ion mass spectrometry (SIMS) is now a well-established technique for microanalysis of solid samples. The basic features of SIMS are rather simple: The sample is bombarded by a 'probing' primary ion beam. The primary ions cause sputter erosion of the sample. Thereby single atoms as well as clusters are emitted from the upper atomic layers. Most of the sputtered species leave as neutral atoms or molecules, but a small fraction is ejected as positive or negative ions. These secondary ions are extracted into a mass spectrometer for mass-to-charge separation to provide an analysis of that part of the sample which is probed by the primary ion beam. In SIMS analysis all elements including hydrogen can be detected. There are, however, pronounced differences in elemental sensitivity which are mainly due to variations in the atomic or molecular properties such as the ionization potential or the electron affinity (see below).

Instrumentation

SIMS microanalysis is achieved either by ion emission microscopy[1-3] or by ion microprobe analysis.[2,3] In ion emission microscopes (or direct imaging mass analyzers) the sample is hit by a static primary ion beam with a diameter of several hundred μm. A magnified secondary ion image of the sample surface is formed by electrostatic lenses and a stigmatically focusing sector magnet. The ion image is converted to an electron image which can be focused on a fluorescent screen or other detection systems. Due to the one-to-one correspondence between the point of origin of a secondary ion emitted from the sample and its location in the mass resolved beam, the final magnified image contains information with respect to the spatial distribution of the selected element or isotope.

In ion microprobe mass spectrometers[1,2] a finely focused primary ion beam bombards the sample. The secondary ions are extracted into a mass spectrometer in which either a sector magnet[4] or a quadrupole filter[5] provide mass analysis. The ion microprobe produces a

---

* On leave from Gesellschaft für Strahlen-und Umweltforschung mbH, D-8042 Neuherberg, FR Germany.

magnified image of the distribution of a given element or isotope in a manner similar to that of the electron probe. The primary ion beam is scanned across the sample surface in a raster pattern. The mass spectrometer is tuned to the desired mass/charge, and the secondary ions are detected by an electron multiplier. The multiplier output is amplified and used to modulate the intensity (z axis) of an oscilloscope whose x, y deflection is synchronized to the primary ion raster. When the primary ions sputter an area containing the element of interest, the oscilloscope intensity increases at a position corresponding to the relative location of that element. By continuing to remove material, one can obtain successive images which provide three-dimensional characterization of one or more elements in the sample.

Liebl[6] has recently discussed the limits of lateral resolution in SIMS microanalysis. As a consequence of the chromatic aberration of the extraction field, the smallest resolvable distance in ion emission microscopy is given approximately by the ratio of the initial volt energy of the secondary ion to the electrical field strength at the sample surface. Accordingly the initial energy distribution of the sputtered ions plays an important role. More specifically this means that improvements in lateral resolution are obtained at the expense of reduced transmission, i.e. reduced sensitivity. With reasonable assumptions concerning the shape of the secondary ion energy distribution Liebl[6] found that in ion emission microscopy a resolution of 1 μm (or better) is achievable only at a maximum transmission in the 10^{-3} range (or less).

In ion microprobe analysis, on the other hand, the lateral resolution is given by the diameter of the primary ion beam at the sample surface. Accordingly brightness and energy spread of the primary ion source as well as aberations of the objective lens are of particular importance in microprobe performance. Current efforts in this direction concentrate on field ionization and field desorption sources.[6] Optimum secondary ion transmission in ion micro-probes is achieved when the acceptance of the mass spectrometer is matched to the emittance of the secondary ion source. Considerably improved transmission in ion microprobes with magnetic sector fields can be achieved by the concept of dynamic emittance matching (DEM)[6]. In this approach the movement of the image point of the secondary ion source across the entrance slit of the mass spectrometer is compensated by a secondary ion beam deflection which is synchronized with the primary beam raster. Thereby the virtual emittance of the secondary ion beam is greatly reduced. This allows a larger fraction of secondary ions to be accepted at the same mass resolution than without DEM. For example, for a 0-50 eV energy band pass and an assumed mass resolution of 2500 the calculated transmission with DEM is about 5 to 15%, depending upon the shape of the secondary ion energy distribution, which is a factor of five better than without DEM.

Similar calculations for quadrupole-type ion microprobes have not been performed as yet. This is due to the fact that the ion transport characteristics are much more complex than in ion microprobes with magnetic sector fields. One particular problem in quadrupole systems is that the acceptance varies with the phase of the rf frequency.[7] Matching of the emittance of the secondary ion source to the acceptance of the quadrupole becomes an elaborate task, therefore. Calculations can be done most adequately by applying phase space dynamics[8] which allow the total ion microprobe system (secondary ion source, lenses, energy filter, fringing fields, quadrupole field, ion exit) to be considered. As to experimental investigations of ion transport in quadrupole-type ion microprobes, available data must be considered rudimentary. Only very recently, the field of view has been determined in such an instrument under certain operation conditions.[9] Because of the outstanding advantages of quadrupoles, in particular the capability for rapid peak switching, it would be very useful to arrive at a more quantitative characterization of ion transport in quadrupole based secondary ion mass spectrometers.

Quantitation

Quantitative SIMS microanalysis has been limited by the difficulty of relating secondary ion signals to elemental concentrations. Secondary ion yields have been found to vary greatly with element, matrix, instrumental design and sampling conditions.[10-12] Therefore, any practical quantitation approach must reduce variables to a minimum and be adaptable to any SIMS instrument. Two general approaches have been proposed for the conversion of secondary ion intensities to elemental concentrations: the use of relative elemental sensitivity factors[10,13,14] and empirical models of the ionization process.[15-17]

The most popular model of ionization is the local thermal equilibrium (LTE) approach of Andersen and Hinthorne.[15] Although this model has achieved some success as a semiquantitative correction procedure, the complete lack of a physical basis for the use of the applied Saha-Eggert ionization equation has caused frequent criticism and extensive testing of the model. In the LTE model the temperature T and the electron density N_e serve as free parameters which are derived for the respective sample and bombardment conditions from two internal standards. The calculation of the optimum pair of (T, N_e)-values is usually done by means of a computer. Depending upon the internal standard pair chose, the temperature T is found to vary by as much as a factor of two[13,17], the electron densities N_e differing sometimes by four orders of magnitude.[13] Such results strongly argue against a physical interpretation of the T and N_e parameters as a true temperature and a true electron density. It is thus not surprising that there have been attempts to reduce the complexity of the LTE model.[16,17] Morgan and Werner[16] have frequently discussed the use of a thermodynamic model which

contains only one fitting parameter, the temperature T. This approach has been found to yield encouraging results. Practically all elemental concentrations can be derived to within a factor of two of their quoted bulk values. Morgan and Werner have also pointed out the importance of well-defined experimental conditions such as the necessity of sample saturation with oxygen.[16]

Comparison of the results obtained by the LTE model with those derived by using relative sensitivy factors (RSF) has shown that the RSF technique yields more accurate results.[13,14] The disadvantage of the RSF method is, however, that each kind of matrix requires a different set of sensitivity factors. Although it might be possible to reduce these matrix effects artifically, e.g. by complete saturation of the sample with oxygen, it is obvious that efforts to arrive at a better physical interpretation of secondary ion emission are highly desirable.

References

1) C. A. Evans, Jr., Anal. Chem. **44** (13), 67A (1972).

2) H. Liebl, J. Phys. E: Sci. Instrum. **8**, 797 (1975).

3) G. H. Morrison and G. Slodzian, Anal. Chem. **47**, 943A (1975).

4) H. Liebl, J. Appl. Phys. **38**, 5277 (1967).

5) K. Wittmaack, Rev. Sci. Instrum. **47**, 157 (1976).

6) H. Liebl, Adv. Mass Spectrom. **7** (1977).

7) P. H. Dawson, Int. J. Mass Spectrom. Ion Phys. **17**, 423 (1975).

8) P. H. Dawson (Ed.), *Quadrupole Mass Spectrometry and Its Applications* (Elsevier, Amsterdam, 1976).

9) K. Wittmaack in Proc. 8th Int. Conf. *X-ray Optics and Microanalysis*, in press.

10) J. A. McHugh in *Methods and Phenomena, Vol. 1: Methods of Surface Analysis*, ed. by A. W. Czanderna (Elsevier, Amsterdam, 1975) p. 223.

11) K. Wittmaack in *Inelastic Ion-Surface Collisions*, ed. by N. H. Tolk, J. C. Tully, W. Heiland and C. W. White (Academic Press, New York, 1977) p. 153.

12) G. Blaise in *Materials Characterization Using Ion Beams*, ed. by J. P. Thomas and A. Cachard (Plenum, New York).

13) D. H. Smith and W. H. Christie, Int. J. Mass Spectrom. Ion Phys. **26**, 61 (1978).

14) J. D. Ganjei, D. P. Leta and G. H. Morrison, Anal. Chem. **50**, 285 (1978).

15) C. A. Andersen and J. R. Hinthorne, Anal. Chem. **45**, 1421 (1973).

16) A. E. Morgan and H. W. Werner, Anal. Chem. **48**, 699 (1976); **49**, 927 (1977).

17) D. S. Simons, J. E. Baker and C. A. Evans, Jr., Anal. Chem. **48**, 1341 (1976).

QUANTITATIVE CHEMICAL ANALYSIS WITH E.D.S. SYSTEMS

Peter J. Statham

LINK SYSTEMS,
Halifax Road,
High Wycombe,
Bucks HP12 3SE
ENGLAND.

A tutorial on Energy Dispersive Spectrometry (EDS) was organised five years ago at the 8th National E.P.A.S.A. Conference (1) and the proceedings still provide a very useful critique of the state of the art. This is not to imply that no improvement has taken place over the last five years but it is probably fair to say that the principle advance has been in a more widespread appreciation of the problems that are peculiar to this technology. Unfortunately, since the controls on a typical EDS system are as easy to operate as a pocket calculator, the user is isolated from the difficulties of x-ray energy measurement and may be easily shocked when paradoxical results from an attempted chemical analysis give the first indication that something has gone wrong. In this tutorial, I will attempt to draw attention to the factors which are not always transparent to the user and also try to define the present state of the art in terms of the accuracy that can be attained with EDS systems for chemical analysis.

X-Ray Fluorescence techniques will not be discussed in this tutorial which will concentrate on electron-beam microanalysis, but the only major difference in the spectrometry required lies in the treatment of the background, so most of the comments herein are also relevant to the XRF application of EDS systems.

RECOMMENDED LITERATURE

The principle features of an Energy Dispersive Spectrometer are perhaps best shown in a comparison with a Crystal Spectrometer. The review by Beaman and Isasi (2), which includes such a comparison, also gives a good overall picture of the microanalysis field and is therefore very useful for the newcomer to the subject. A complete book on microanalysis by Reed (3) contains three chapters specifically devoted to EDS and serves as a comprehensive reference work for all aspects of electron-beam microanalysis. Further reviews, primarily consisting of descriptions of EDS instrumentation are given by Fitzgerald and Gantzel (4) and Gedcke (5) and methods for spectrum processing are reviewed by Statham (6).

DETECTOR ARRANGEMENTS

On an electron-beam instrument, such as a microprobe or SEM, the Si (Li) detector can be mounted very close to the specimen to improve the collection efficiency. However, although this reduces the necessary beam current, it also aggravates a number of problems associated with the large solid angle subtended by the detector. Spurious radiation generated by backscattered electrons and primary x-rays will enter the detector unless it is well-collimated so that the detector can only view the point where the beam strikes the specimen surface. Further collimation is also advisable to restrict incident x-rays to the central region of the detector where charge collection is more efficient and thus "tailing" on spectral peaks is reduced (7).

Backscattered electrons themselves can penetrate the beryllium vacuum window and register in the detector as an additional background component which can be seriously high when a very thin beryllium window is present. Although rough calculations show that only about 0.2% of 20 kv electrons are transmitted through a $7_{\mu m}$ Be window, it should be remembered that there are of the order of 1000 backscattered electrons for every x-ray photon incident on the detector so the transmission has to be reduced to 0.001% to keep the spurious contribution below 1% of total spectrum content. Since Be windows invariably have 'thin spots' which are less than the nominal thickness, a window thicker than $7_{\mu m}$ is advisable if the background is to be minimised. An alternative solution is to deflect the electrons into a trap using a magnetic or electric field before they reach the detector, but this is impractical when the detector is very close to the specimen. A further spurious contribution can arise from "beam tailing" an electron-optical defect which permits primary electrons to strike the specimen in regions far away from the main beam entry point (8).

Knowledge of the x-ray take-off angle (TOA) is most important for quantitative analysis. The geometry in electron microprobes is usually fixed but in an SEM, a wide variety of specimen orientations is possible and rather complex trigonometrical formulae have been devised to calculate an effective take-off angle for a given geometry (e.g. (9)). Although such formulae do make some allowance for variable excitation conditions it should be emphasised that only the case for normal incidence of the electron-beam has been extensively studied to date so if any different geometry is to be used it is virtually essential to use spectra from standards placed in exactly the same geometry when calculating apparent concentration ratios and also to make sure that the absorption correction is not large. When the detector is close to the specimen, TOA is difficult to define because x-rays enter the detector at different places. In situations where the absorption correction is large (say $f_{(\chi)} < 0.5$), there may be some error in assuming that all x-rays come off at the same mean angle. This effect is only likely to reach significant proportions when the change in $f_{(\chi)}$ for x-rays reaching the extremes of the detector window is at least 10% because the second-order dependence of $f_{(\chi)}$ with angle is small (for example, see plots in (10).

It should now be apparent that it is an advantage to position the detector as far from the specimen as can be tolerated, for this reduces many of the problems discussed in this section.

DATA ACQUISITION

Beam Current Stability

The first stage of quantitative analysis normally involves comparing the measured x-ray intensity for a given characteristic x-ray line for the specimen with that for a standard of known composition exposed to the same beam current. This necessitates some method of measuring the beam current with an accuracy much better than 1%. This can be achieved by flipping a "Faraday cup" beneath the beam to collect all the electrons and measuring the current directly, but in fact, all that is required is a measure which is proportional to the beam current and this can be obtained using a double final lens aperture in which a second smaller aperture intercepts a fraction of the beam profile defined by a larger, earthed aperture and passes current to a meter. Another measure which is proportional to beam current is the input count rate obtained from a homogeneous, flat, polished standard which is always placed in the same

geometry relative to detector and incident beam. Instead of attempting to measure the current, it may be considerably simpler to maintain the current at the same constant value for both specimen and standard measurements. Unfortunately, all these techniques are only of use provided the beam current is stable for the duration of the data acquisition period, which is typically about 100 seconds per spectrum. If the current drifts in one direction to a value not more than a few percent different from the starting value, then a mean current can be defined for the spectrum, but if fluctuations are spasmodic, there is no easy correction and some means of stabilisation is required. If fluctuations are slight and a double-aperture monitor is available, then the current can be corrected by adjusting the condenser lens current either manually or electronically. Another method that can be used with EDS systems equipped with an accurate input-rate monitor is to measure the beam current immediately before starting spectrum accumulation, then put the beam on the specimen and manually adjust the condenser lens to keep the input rate constant throughout the accumulation period.

Livetime Correction

Because the pulse processor takes time to measure a charge pulse from the detector, not every photon which arrives can be measured so the number of counts recorded in the spectrum for a given time interval is less than it should be. For this reason, the electronics usually includes "livetime correction" circuitry which corrects for rejected events in such a way that when the spectrum is recorded for a preset livetime, the number of counts in a given energy range divided by the livetime equals the count rate for x-rays in that range. The circuitry may also have to correct for events that are rejected because the ADC is still digitising the pulse height or because the computer which should service the ADC is busy performing another task such as maintaining a T.V display. The circuitry is therefore likely to be system-dependant and probably proprietary, but in any case it is vital to check that the correction works if quantitative analysis is to be performed. One way to test this is to set up a given preset livetime and record a number of spectra at different beam current values and check that the number of counts recorded in a given integration range is exactly proportional to beam current. When beam current cannot be measured accurately, an indirect test can be used. A radioactive source, such as Fe 55 is fixed firmly near the detector to provide a constant count-rate of around 1 kcps, a spectrum is recorded for a given preset livetime and the number of counts in the major peak is measured. If the fast channel discriminator level is lowered, the noise triggering rate will increase (see below) and thus a high input count rate can be simulated. With the source still in position, several spectra are recorded at different (simulated) input rates for the same preset livetime and if the livetime circuitry is working, the count accumulated in the major peak should remain a constant.

Throughput Rate

The maximum accumulation rate is limited by the time taken to measure each pulse but the shorter the time taken, the worse the resolution so a compromise is involved. For quantitative chemical analysis a total of 300 K counts in the spectrum is usually adequate and this can be obtained with an input rate of 3 kcps and a preset livetime of 100 seconds. This throughput rate should be easily attainable with any commercial system, while still maintaining adequate resolution, and implies a total accumulation time of typically 2 to 3 minutes. However, there is one major restriction which may force one to use

inspection channel uses short time constants and is therefore "noisier" but it can separate two closely-spaced pulses and send a rejection signal to the pulse height analyser. The design and adjustment of the pile-up inspector are crucial to the success of pulse-measurement and if not optimised can cripple the performance of an otherwise well-designed system. If the threshold on the fast inspection channel is set too high, small (low-energy) pulses will not be detected, but if it is too low the discriminator will keep triggering on noise excursions and the "noise rate" will be very high, thus swamping the processor. The user should therefore manually adjust the discriminator threshold so that the "noise rate" in the absence of x-rays is as high as can be tolerated (e.g. 500 cps would not significantly alter the required accumulation time when total spectrum input count rates are around 5 kcps). If the time constants in the fast channel are too short, (i.e. too small a "pulse-pair resolution time"), the inspector may be unable to detect low-energy pulses even if the threshold is properly adjusted and the spectrometer will be virtually useless for accurate quantitative work. (A more complete discussion of the implications is given in (13)).

Drift and Resolution Changes

When 2 or more peaks overlap in the spectrum, individual peak areas can be computed if the shapes of the component peaks are accurately known. This process of "peak deconvolution" will give large errors if peaks shift away from their expected position, or if the spectrometer resolution changes (6). Such changes can be due to a variety of causes but the most common one is a change in input count rate so the processor must have a low "count rate sensitivity". In order to fully exploit the statistical accuracy available in a spectrum of 300 K counts and accommodate for a wide range of peak overlap situations, peak position and width must stay constant to within 1eV (1/10 channel at 10 eV/channel) throughout the range of experimental conditions that would normally be encountered (14). If this requirement cannot be met, and it is not possible to predict position and width when the count rate is known, then the accuracy is compromised and spurious results are to be expected when peak overlaps occur.

Speed and Resolution

The speed of pulse-processing is normally limited by the length of the pulse in the measurement channel, T_d (see Fig. 1). Many pulse shaping schemes have been suggested but the parameter which is most important in determining the noise performance is the peaking time, T_p . Thus the shorter the tail following the peak, the faster the speed for a given resolution and in general, the smaller the peak shift for a given count rate. Although, theoretical calculations suggest that a "time-variant" pulse processor, where time constants for the shaping network are switched during the processing of a pulse, can give significantly better noise performance than "passive" shapers (15) and better count rate stability (16), there is no reason for rejecting a particular processor on design principles alone until its performance has been thoroughly checked.

For microprobe analysis, the ADC has to digitise pulse heights, so if the largest pulse corresponds to 10 keV and the spectrum is recorded at 10 eV/channel, the ADC must place such a pulse in channel 1000. If a "run-down" ADC is used, 1000 clock pulses must be generated so if a 100 MHZ clock is used, this will take 10μS whereas a 10 MHZ clock would involve a conversion time of 100μS . If the ADC is too slow, the maximum throughput rate will be limited but there is no point in paying a high price for a fast ADC if the computer cannot store pulses at the same rate or if the pulse-processor itself cannot operate at an equivalent speed.

even lower count rates and that is the pulse pile-up problem which is discussed in more detail below. If the pile-up inspector is not optimised for low-energy x-rays, (i.e. 1 keV), then the practical limit on count rate will be around 1 kcps, irrespective of the choice of pulse-processing time.

Much higher output rates are achievable if the electron beam can be switched on or off in a fraction of a µS under control of the pulse processor (11). For a given pulse processing time the "beam switching" method can increase the maximum throughput rate by up to a factor of 4 and with suitably designed electronics quantitative analysis appear to be feasible at accumulation rates in excess of 12 kcps with no degradation in spectrometer resolution (11). The major limitation to using high rates is still the pile-up problem but nevertheless, beam switching still helps because it reduces the input rate required for a given output rate and can also improve the general performance of the pulse processor (12).

One further limitation to accumulation rate may be the computer itself. If the spectrometer has "Direct Memory Access" (DMA) there is no problem, but if counts are processing by "Interrupt Servicing", the maximum rate may be less than 5 kcps in some systems.

Memory Capacity

The energy range of most interest for quantitative analysis is 1 to 10 keV so a minimum requirement is that the computer or MCA used for spectrum storage should be able to display this region. With commonly-used "16-bit" computers, channel capacity is usually limited to 65535 counts. This is perfectly adequate for quantitative work at 10 eV channel width, for even if all the counts appeared in a single peak, which is highly unlikely, a total spectrum count of around 10^6 could be accommodated. At 20 eV channel width the capacity is halved but 65535 counts per channel is still not a serious restriction for routine quantitative work. The only situation where more capacity is needed is when a trace peak sits on a very high background and very long accumulation times are needed to increase statistical precision after background subtraction.

PULSE-PROCESSOR

Although often referred to disrespectfully as the "amplifier", the EDS electronics has the job of measuring the height of a single pulse to an accuracy of 0.1% or better in a period of around 20 µS and then restoring the status quo in a few tens of µS to be ready for the next pulse. It also must arrange to reject measurements that are "contaminated" by other pulses (pile-up rejection), digitise the measurement for the computer (ADC) and make appropriate corrections for timing (livetime correction). Thus, the pulse processor is so complex that it is ABSOLUTELY ESSENTIAL to test the performance experimentally before attempting any quantitative analysis for even the best designs are subject to component failure and mistakes in assembly of the finished unit. Further-more, the pulse-processor must be tested in conjunction with the detector and pre-amplifier, because the behaviour of all three stages are inter-related.

Pile-up Rejection

Fig. 1 is an idealised representation of a pulse-processor. The measurement channel has to use long-time-constant shaping to reduce noise, so two pulses which arrive close together in time will be unresolved. The auxillary

Testing

The importance of testing the spectrometer performance cannot be over-stated, for a dependable spectrometer is an essential prerequisite for accurate spectrum processing. Peak shifts of less than 1 channel cannot be detected by visual inspection and it is best to fit peaks with a Gaussian function to determine position and width. The following procedure can be used to fit a Gaussian to 15 channels straddling a peak which is centred near to channel i_0. Defining the sums

$$S_1 = \sum_{i=i_0-7}^{i_0+7} \ln(y_i) \quad , \quad S_2 = \sum_{i=i_0-7}^{i_0+7} (i-i_0)\ln(y_i) \quad , \quad S_3 = \sum_{i=i_0-7}^{i_0+7} (i-i_0)^2 \ln(y_i)$$

then,

$$\sigma^2 = -1/(-9.04977\times10^{-3}S_1 + 4.848093\times10^{-4}S_3)$$

$$x_0 = i_0 + \sigma^2 \times 3.571429\times10^{-3}S_2 \tag{1}$$

$$P = \exp(\ 0.1511312S_1 - 0.452489\times10^{-2}S_3 + (x_0-i_0)^2/2\sigma^2)$$

Where x_0 is the centre of the peak, fwhm $= 2.355\sigma$ and P is the fitted peak height. If the peak height is around 10,000 counts and f.w.h.m is around 12 channels, then x_0 will have a statistical error of better than 0.1 channels and f.w.h.m will be accurate to within about 1%.

System performance is commonly specified for the $MnK\alpha$ peak obtained with an Fe^{55} radioactive source. However, such a specification is virtually useless for a system that is going to be used for electron beam microanalysis.

The elements Na, Mg, Al, Si all produce peaks in the low-energy region below 2keV and even when they are not present, the bremsstrahlung continuum provides a significant low-energy component to the spectrum. Because of fundamental limitations set by electronic noise, the performance of most pulse-processing systems is worse when the spectrum contains a large fraction of low-energy x-rays thn when it contains just the Mn K peaks as from an Fe^{55} source. Therefore peak shift, resolution changes and pile-up protection should be tested by using a spectrum from a specimen of Mg, MgO, Al or $Al_2 O_3$ rather than from Mn, or an Fe^{55} source. As mentioned above, shift and resolution changes should ideally be kept down to around 1eV but this is an extremely difficult specification to meet, especially when room temperatures and supply line voltages are apt to vary, and for most purposes a variation within ± 2 eV should be adequate. If count-rate-induced effects are greater than this, the solution is either to only work very low count rates, or else attempt to quantify the count-rate-induced distortion, but this latter route is often impractical because the correction usually depends on spectral content.

Pile-up is most troublesome when the "parent peaks" involved have low energies because then the "sum peak" appears within the range of interest. Thus, for example when the spectrum contains large $SiK\alpha$ and $CaK\alpha$ peaks, unresolved $SiK\alpha$ and $CaK\alpha$ pulses will produce a "sum-peak" which is very close to the $CrK\alpha$ energy and, therefore, the analysis will yield a spurious chromium concentration. Furthermore, combinations of $NaK\alpha$, $MgK\alpha$, $AlK\alpha$, $SiK\alpha$ and L lines from heavy elements give rise to a smeared-out pile-up distribution around 2 to 3 keV which can seriously affect background corrections which rely on the fitting

of a function to peak-free regions of the spectrum. Therefore, pile-up protection should be tested using a source of low-energy x-rays such as a spectrum from Mg. In this case, if the Mg $K\alpha$ peak area is A_{Mg} and the area of the Mg + Mg sum peak is A_{Mg+Mg} then

$$A_{Mg+Mg} = \frac{A_{Mg}^2}{T_L} \cdot \tau_{Mg,Mg} \qquad (2)$$

where T_L is the preset livetime for the spectrum and $\tau_{Mg,Mg}$ is the pulse-pair resolution for 2 MgKα pulses (13). For example, if the pulse-pair resolution is $\tau_{Mg+Mg} = 2\mu S$ and the count rate in the Mg peak (A_{Mg}/T_L) is 1 kcps then the sum peak will be 0.2% of the parent peak area. If the pile-up inspector is ineffective for low energy x-rays, either because the time constants in the fast channel are too short or the discriminator level is set too high, then the spectrum may exhibit a pile-up continuum which appears below the sum-peak energy (fig. 2). If this is the case, then the corresponding peak shift and broadening are likely to be unacceptable for quantitative analysis.

SPECTRUM PROCESSING

Quantitative and Qualitative Analysis

The preceding sections describe tests which one can carry out to see whether the spectrometer is suitable for quantitative microprobe analysis. The guidelines given presume that a relative accuracy of $\pm$ 2% in peak areas (and hence apparent concentration ratios) is required so that the accuracy available in subsequent x-ray correction procedures can be fully exploited. The argument is sometimes given that such precautions and tests are unnecessary if the system is to be used solely for qualitative chemical analysis. A qualitative analysis should reveal the chemical elements which are present in the sample and give some indication of the relative compositions. When peaks are well separated, element markers or x-ray tables can be used to identify the characteristic lines and the only difficulties arise when escape peaks or pile-up peaks are mis-interpreted as true x-ray peaks. However, when significant overlaps occur, the decision as to whether a given peak is present or not cannot be made by visual inspection alone and one has to rely on some sort of computer processing. For example, suppose we wish to determine whether cobalt is present in a specimen which has a high iron content. The FeKβ peak overlaps the CoKα position so one way of revealing a suspected CoKα peak is to subtract the appropriate fraction of a spectrum of pure Fe so as to completely remove the FeKα peak. This "spectrum stripping" procedure should also remove the FeKβ peak (if differential absorption of FeKα and FeKβ x-rays is negligible) and expose any CoKα . However, if the peaks in the pure Fe spectrum are shifted by only a fraction of a channel or the resolution has changed by a few percent relative to the spectrum for the unknown, the stripping procedure will produce large residual "lobes" (see fig. 3) which make it very difficult to detect a small nearby peak. If two overlapping peaks are of comparable size, shift and resolution changes will always introduce errors into a determination of relative peak heights, whatever method is used to correct for the overlap. Thus, even for qualitative analysis, it is important to test the spectrometer and consider carefully the method of spectrum processing.

Spectral Artefacts

Perhaps the best understood spectral artefact is the SiKα escape peak. If the incident x-rays make an angle, θ , with the normal to the detector surface

which is greater than zero degrees, then the escape peak fraction is larger, but it is still an easy matter to remove escape peaks by a channel-by-channel subtraction routine started from the high-energy end of the spectrum. Thus, if $N(I)$ is the count in channel I of the spectrum, IS channels represent 1.74 keV and E is the energy for channel I in keV then (17),

$$N(I - IS) = N(I-IS) - k.N(I) \qquad (3)$$

where
$$k = 0.02 / (1 + (mE + b) E^2)$$
and
$$m = 0.01517 \cos\theta \quad - 0.000803$$
$$b = 0.0455 \cos\theta \quad + 0.01238$$

Another common artefact is a small silicon peak. This may in fact be simply the absorption step in the background, due to the Si dead layer on the detector, which is transformed into a peak-like structure by detector broadening. Another possibility is contamination as a result of using vacuum greases and oils which contain silicon and in some defective detectors, such a peak may be due to fluorescence of a totally-dead layer of silicon on the detector surface. However, with a well-made detector, the contribution from internal silicon fluorescence should be virtually negligible. Sum peaks have already been mentioned. If the parent peaks have energies E_1 and E_2 then the sum peak appears near $E_1 + E_2$ and has an area A_{sum} given by

$$A_{sum} = \frac{A_1 . A_2}{T_L} (\tau_{12} + \tau_{21}) \qquad (4)$$

Here, τ_{12} is the pulse-pair resolution time for a pulse E_1 followed by a pulse E_2, which may in fact differ from the resolution time τ_{21} for a pulse E_2 followed by E_1 (13). Equation 2 shows how the formula is modified when only one parent is involved. Although corrections for pile-up effects are possible in principle (13), in practice the fact that τ_{12} usually depends on the component peak heights makes computer corrections very difficult to perform quickly on a routine basis and it is therefore usually necessary to keep count rates low to avoid such artefacts.

Further artefacts can be due to spurious x-rays generated by electrons or x-rays striking surfaces within the specimen chamber or the detector housing, but such effects are best tackled by establishing the source rather than attempting computer correction of the spectrum.

Peak Deconvolution and Background Subtraction

This topic will be discussed in detail at a special symposium on spectrum processing techniques to be held at this conference, and is also considered in review papers (6) and (18). Since the user often has no control over the program sold by a manufacturer, and since there is some controversy as to which method is best, it is perhaps more relevant in a tutorial to consider how a complete package should be tested for accuracy.

Detection limits for EDS are typically quoted to be around 0.1% concentration by weight for a spectrum of about 300 K counts, but this usually only applies to isolated peaks. The following type of test can be used to find the detection limit in the presence of overlaps and absorption edge steps. For example, several spectra of pure iron can be recorded and the computer told that Fe, Co and Ni are present; the results should of course be 100% Fe, 0% Co and 0% Ni ! Similarly, a spectrum with a well-defined Barium L peak multiplet can be analysed for both Ba and Ti to see how much spurious Ti (positive or negative) is

picked up. The region below 3 keV poses additional problems due to curvature of the background and diagnostic tests here can reveal a great deal about the accuracy of the whole system. A spectrum which does not contain Na, Mg, Al or Si can be analysed to see what values (which should of course be zero) are obtained for these elements, and a spectrum containing large Mg and Si peaks can be analysed for Mg, Al and Si to determine a realistic detection limit for Al in the presence of overlaps. This type of test can reveal weaknesses in a system in a much simpler and more effective way than any theoretical analysis and is more closely related to the real analysis situation.

Standardless Analysis

The efficiency of a well-designed energy-dispersive spectrometer does not change with time and if considerable care is taken with the measurements involved, the absolute x-ray intensity generated for a given incident beam current can be determined (19). This opens up the exciting possibility of performing quantitative analysis without the need for standards, although at present this type of absolute intensity measurement has not been attempted by enough independent investigators to establish whether a repeat accuracy better than 10% relative can be obtained.

If all the elements being analysed have peaks within the spectrum so that the sum of the concentrations can be taken to be 100%, then knowledge of detector efficiency and x-ray production cross sections allows one to obtain a corrected analysis without the need for absolute measurements. However, in practice, a few standards are still required in order to establish fixed points of reference so that an approximate formula for x-ray production and detector efficiency can be used to interpolate in between and thus obtain reasonably accurate values for elements with no available standards (20). A fairly obvious weakness to this method is the fact that the analysis total is assumed to be 100% so the results give no indication when a gross error, such as the omission of an element which is in fact present in the spectrum, has occurred. Therefore, some independent means of normalisation is useful and a single standard can be used for this purpose.

The standardless approach still relies on accurate spectrum processing and the existence of accurate x-ray correction procedures. Normalisation to 100% can effectively conceal errors due to inaccurate knowledge of peak positions, widths and x-ray take-off angle. Moreover, when rough surfaces or small particles are being studied, normalisation will hide the errors which arise because standard "ZAF" correction procedures are only applicable to flat polished samples with a well-defined take-off-angle, so scaling analysis results to give a total of 100% is strongly inadvisable. Alternative methods of normalising the results have been suggested, such as use of the backscattered electron signal (21) or measurement of the peak-to-background ratio (22), but the accuracy of these methods has not yet been well-established. Even though such techniques circumvent the need to determine x-ray intensities from a wide range of well-characterised standards, it is still necessary to measure the peak profile for each element to categorise the spectrometer response accurately so standards of some sort will still be required (18).

QUANTITATIVE ACCURACY

Probably the most successful application of quantitative EDS microanalysis has been in mineralogy and the number of laboratories which are using EDS as a routine tool are too numerous to mention. Reed and Ware's summary report on a quantitative system (23) brings out the practical aspects very well, but is

perhaps most useful in demonstrating how a system, once established, can be tested for accuracy and repeatability. This testing phase is often overlooked but is of vital importance because it reveals weaknesses in the overall system, which may not be understood at first, but which give insight into fundamental problems. The detection limit for elements with atomic numbers 11 to 30 is still around 0.1% concentration by weight in routine analysis (say 300 K counts/ spectrum), but it should be recognised that the realistic detection limit may be more like 1% for elements involved in significant overlap situations. Elements with higher atomic numbers can be analysed through their L and M lines, but the interferences are much worse and even more care has to be taken to avoid spurious results. It is difficult to make a relevant statement about the state of the art which is more specific than this because of the absence of detailed studies such as (23) in the literature. Relative accuracies of $\pm$ 2% can certainly be attained in peak areas, but it is the spurious values for elements in low concentration which are most troublesome for both qualitative and quantitative analysis. Beaman and Solosky (24) suggested that the standard deviation in relative accuracy for EDS analysis for concentrations above 5% improved from 7.2% to 4.3% in the period 1972 to 1974 for analysis of well-characterised alloy and mineral standards. Instrumental improvements and advances in spectrum processing techniques over the last few years are bound to have had some effect in reducing the error still further, but there is still considerable room for improvement in quantitative accuracy for elements below 5% concentration which are subject to peak interferences. Although improved detector resolution will help to a small extent, the major advances in this area will be a result of improved stability of the whole spectrometer which will facilitate spectrum treatment procedures that can fully exploit the statistical accuracy available in the spectrum.

REFERENCES

1. D.R. Beaman, L.F. Solosky and L.A. Settlemeyer, 73 -85 in tutorial proceedings of 8th Nat. Conf. of the Electron Probe Analysis Society of America, New Orleans, 1973.

2. D.R. Beaman and J.A. Isasi, A.S.T.M. special pub. 506, 1972 or Materials Research and Standards Nov/Dec 1971.

3. S.J.B. Reed, "Electron Microprobe Analysis", Cambridge University Press, 1975.

4. R. Fitzgerald and P. Gantzel, A.S.T.M. special technical publication 485, 1971.

5. D.A. Gedcke, x-ray Spectrometry 1, 129 - 141, 1972.

6. P.J. Statham, x-ray Spectrometry, 5, 16 - 28, 1976.

7. D.A. Landis, F.S. Goulding and B.V. Jarrett, Nucl. Instrum. and Meth. 101, 127, 1972.

8. R.B. Bolon and M.D. McConnell, Scanning Electron Microscopy/1976 (Part 1), ed. O. Johari, IITRI, Chicago, Ill. 60616, U.S.A., 1976 pp 163 - 170.

9. S.H. Moll, N. Baumgarten and W. Donnelly, in Proc. 12th Ann. Conf. Microbeam Analysis Society of America (M.A.S.), Boston, Mass., U.S.A., 1977, 33A - 33F.

10. T.R. Sweatman and J.V.P. Long, J. Petrol. 10, 332 - 379, 1969.

11. P.J. Statham, J.V.P. Long, G. White and K. Kandiah, x-ray Spectrom. 3, 153 - 158, 1974.

12. P.J. Statham, in Proc. 11th Ann. Conf. M.A.S., Miami Beach, Forida, U.S.A., 1976, 11A - 11G.

13. P.J. Statham, x-ray Spectrom. 6, 94 - 103, 1977.

14. P.J. Statham, submitted to x-ray Spectrom., Oct. 1977.

15. J. Llacer and D.F. Meier, Nucl. Instr. & Meth. 142, 597 -599, 1977.

16. M.O. Deighton, Nucl. Instr. & Meth. 103, 1 - 12, 1972.

17. P.J. Statham, J. Phys. E: Sci. Instr. 9, 1023, 1976.

18. P.J. Statham, Proc. 12th Ann. Conf. M.A.S., 95A - 95F and Proc. 8th Int. Conf. x-ray Optics and Microanalysis, Boston, Mass., U.S.A., 1977 (to be published).

19. E. Lifshin, M.F. Ciccarelli and R.B. Bolon, ibid. 104A, 104C.

20. J.C. Russ, Proc. 11th Ann. Conf. M.A.S., Miami Beach, Florida, U.S.A., 1976, 19A - 19C.

21. J.C. Russ, Proc. 12th Ann. Conf. M.A.S., Boston, Mass., U.S.A., 1977, 34A - 34I.

22. P.J. Statham & J.B. Pawley, Scanning Electron Microscopy/78, ed. O. Johari, Los Angeles, California, U.S.A., 1978, paper 74.

23. S.J.B. Reed and N.J. Ware, J. Petrol. 16, 499 - 519, 1975.

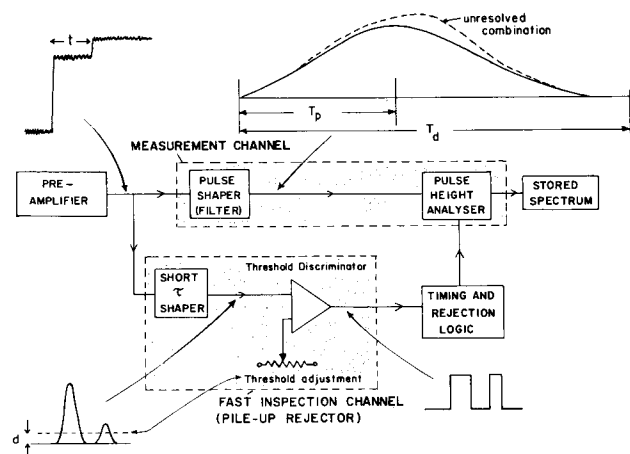24. D.R. Beaman and L.F. Solosky, Proc. 9th Ann. Conf. M.A.S., Ottawa, Canada, 1974, 26A - 26E.

Figure 1. Schematic diagram for a typical pulse-processing system. The waveforms are not exactly to scale: T_d is typically $4 \times T_p$ though with switched-time-constant filtering it can be as low as $2 \times T_p$, and the pulses in the inspection channel are usually less than 1μS in duration which is considerably less than a typical value, 20μS, for T_p.
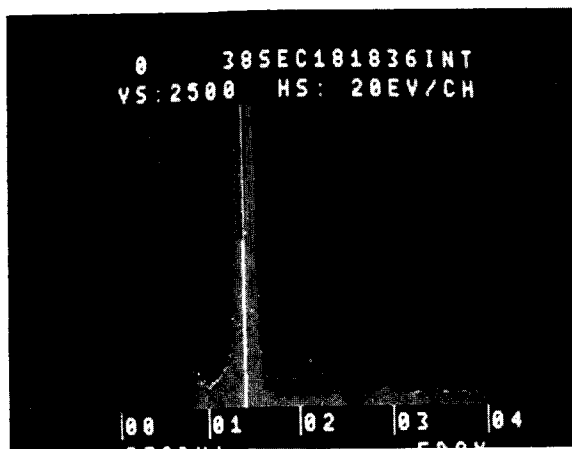

Figure 2. Superimposed spectra from aluminium, both obtained at an input rate of 5kcps and containing the same total number of counts. The bars were obtained with a noise rate of 700cps and the dots with the threshold raised well above noise. The AlKα peak height is 32000 counts. At the higher threshold there is essentially no pile-up protection for AlKα pulses and a significant pile-up
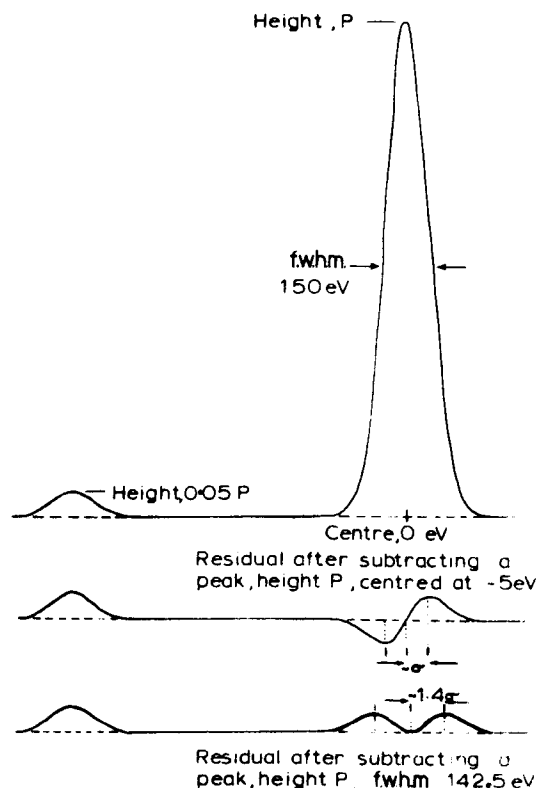

Figure 3. A source of error in stripping & fitting techniques for peak deconvolution. The difference between two peaks of the same height but different shape is shown with a peak, 5% of the height, for comparison.

PRINCIPLES AND PRACTICE OF STEM MICROANALYSIS

J. I. Goldstein

Department of Metallurgy and Materials Engineering

Lehigh University, Bethlehem, PA 18015

Introduction

The scanning electron microscope-electron probe microanalyzer (SEM-EPMA) and transmission electron microscope (TEM) are two established tools for microscopy. The first instrument enables one to obtain high magnification pictures as well as microchemical information from micron sized areas in solid samples. The second instrument enables one to obtain high magnification pictures and diffraction data from electron transmission thin specimens. Over 10 years ago Duncumb mounted a wavelength dispersive X-ray spectrometer on a TEM in order to obtain chemical and structural as well as diffraction data from the same area of a thin specimen. This idea of a combination instrument has developed rapidly in the last few years into the scanning transmission electron microscope (STEM) instrument of today. In the modern version of this instrument a 60 to 200 kV electron beam is focused to < 100 and often to < 10 nm diameter at the specimen surface. Scanning coils move the beam over the specimen and the emitted X-rays are measured with an energy dispersive X-ray spectrometer (EDS). Normal electron probe microanalysis including particle identification, X-ray scanning, and quantitative analysis can be accomplished with this instrument.

Besides obtaining structural, X-ray and diffraction data from the same area of a thin specimen, there are several other advantages of the STEM instrument. Only minimal spreading of the focused electron beam occurs in the thin specimen and hence a very small X-ray source region is obtained. A schematic drawing of the distribution of electrons and the activated volume in a thick and thin specimen is shown in Figure 1.[1] The X-ray source size in STEM microanalysis can equal that of the beam diameter $\leq 10 - 100$ nm for very thin specimens. Another advantage of using a thin foil specimen is that in most cases no absorption or fluorescence correction need be applied to the X-ray data. This allows for the application of relatively simple procedures for obtaining quantitative analyses of samples.
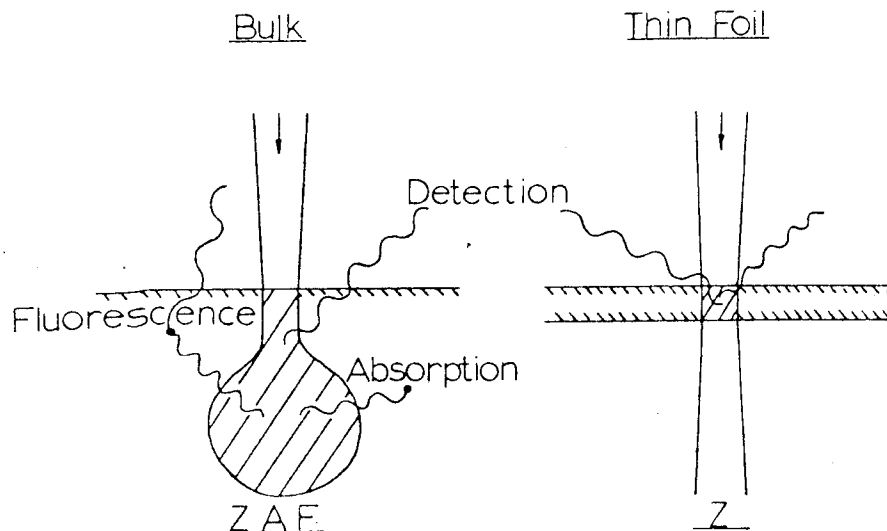
Bulk   Thin Foil

Figure 1 - Schematic distribution of electrons and activated volume in a thick and thin specimen.[1]

There are however several problems which still make STEM microanalysis a challenge. Among these is the presence of spurious X-rays generated in the electron column, specimen holder, and X-ray collimator. These X-rays often make their way in one form or another into the EDS detector. In addition the small currents in the electron beam combined with the small excitation volume in the thin foil, lead to low X-ray count rates. These low count rates limit the detection of small amounts of elements in a specimen as well as the accuracy and precision of an analysis. Lastly the method of specimen preparation may be crucial to an analysis as contamination layers may build up on the surfaces of thin films. In this tutorial the technique for obtaining successful STEM microanalysis will be discussed. The problems inherent in the technique will also be discussed and solutions will be outlined when available. Several comprehensive review papers on STEM X-ray microanalysis have been written to which the serious reader is referred.[2-4] The review paper by Goldstein and Williams[4] has been used extensively for some portions of this tutorial.

Quantitative X-ray Analysis

Basic Theory

The average number of ionizations n per primary beam electron incident on a sample with energy E_o is:[5]

$$n = \frac{N \, C_A \rho}{A_A} \int_{E_o}^{E_c} \frac{Q}{dE/dX} \, dE \qquad (1)$$

where dE/dX is the mean energy change of an electron in traveling a distance X, N is Avogadro's number, ρ is the density of the material, A_A is the atomic weight of A, C_A is the concentration of element A, E_c is the critical excitation energy for K, L, or M characteristic X-rays from element A, and Q is the ionization cross section (the probability per unit path length of an electron of a given energy causing ionization of a particular shell (K, L, or M) of an atom in the specimen) which is a function of E. In solid samples some fraction of electrons, $1 - R$, is backscattered from the target and does not generate ionizations. Multiplying n by the fluorescence yield ω_K or ω_L and the backscatter factor R gives the characteristic X-ray intensity in photons per incident electron generated in the sample:

$$I_A = \frac{const}{A_A} \ C_A \ R\,\omega \int_{E_c}^{E_o} \frac{Q}{dE/dX} \ dE \tag{2}$$

The measured intensity of the characteristic X-ray line must also be corrected for absorption of X-rays within the specimen and fluorescence effects from X-rays generated from other elements in the target. Classical microprobe analysis considers all of the so called ZAF factors in order to obtain accurate local chemical analyses. Methods of quantitative X-ray analysis have been discussed in several recent books.[6,7]

In electron microscope thin films, few electrons are backscattered and the electrons lose only a small fraction of their energy in the film. Therefore Q can be assumed constant in the film. The characteristic X-ray intensity produced along the trajectory of the electron t, which is assumed to be the thickness of the thin film, can then be given by a much more simplified formula namely:

$$I_A = const \ C_A \ \omega\,Q\,t/A_A \tag{3}$$

If one assumes that the analyzed film is infinitely thin, the effects of X-ray absorption and fluorescence can be neglected, and the generated X-ray intensity and the X-ray intensity leaving the film are identical. This assumption is known as the thin film criterion.

A number of techniques have been developed for quantitative thin film analysis. In some techniques bulk standards are used while in others thin film standards or standardless techniques are employed. The various analysis techniques are outlined in the following sections.

Analysis Using Bulk Standards

Several investigators[8-12] have proposed analysis techniques in which the X-ray intensity ratio I_A/I_B of two elements A and B in a foil which is measured simultaneously is related to the mass concentration ratio C_A/C_B by an equation of the form:

$$\frac{I_A}{I_B} = \frac{C_A}{C_B} \frac{I(A)}{I(B)} \frac{P_A}{P_B} \cdot \frac{f(\chi)_{(B)}}{f(\chi)_{(A)}} \tag{4}$$

where P_A and P_B correct the measured X-ray intensities generated by the pure bulk standards $I(A)$, $I(B)$ (measured at the same probe current and beam potential) for atomic number effects and correct the measured X-ray intensities generated by the thin film I_A, I_B for differences in ionization cross section. The terms $f(\chi)_{(B)}$ and $f(\chi)_{(A)}$ correct the measured X-ray intensities generated by the pure bulk standards for absorption. It is also assumed that the foil is thin enough that X-ray absorption and backscattering can be neglected.

Duncumb[8] suggests measuring the standard intensities $I(A)$ and $I(B)$ at lower beam potentials. This procedure is used in order that correction procedures which have been developed for low operating potentials can be employed. Duncumb used the method with good results at E_o 15 - 35 kV while Jacobs and Baborovska[13] and Jacobs[14] used the method successfully on several metal and oxide samples with the EMMA-3 instrument operating at 100 or 40 kV.

Analysis Using Thin Film Standards

Cliff and Lorimer[15] have shown that if the bulk composition of a thin film is known, the specimen can be used as its own standard. If the characteristic X-ray intensities of two elements in the standard I_A and I_B are measured simultaneously as in an energy-dispersive spectrometer (EDS) from the same point, they can be simply related to the composition C_A and C_B by the expression:

$$\frac{I_A}{I_B} = (k_{AB})^{-1} \frac{C_A}{C_B} \tag{5}$$

where k_{AB} is a factor which can be determined experimentally or by calculation. The constant k_{AB} varies with operating voltage but is independent of the sample thickness and composition as long as the thin film criterion is satisfied (that is that the generated X-rays of elements A or B or both are not

preferentially absorbed or fluoresced by the thin film). If k_{AB} scaling factors are available for various combinations of elements, weight fraction ratios can be obtained simply by multiplying the measured intensity ratio by the appropriate k_{AB} factor. This method is often referred to as the standardless method in that pure bulk standards are not needed for the analysis.

Experimental values of k_{AB} using an EMMA-4 instrument at 100 kV have been determined by Cliff and Lorimer[16] for a series of elements A, relative to Si which is then element B. The constant k_{ASi} is commonly called k in the literature and is given by:

$$k = k_{ASi} = (\frac{C_A}{C_{Si}}) \cdot (\frac{I_{Si}}{I_A}) \tag{6}$$

Experimental values of k from Cliff and Lorimer[16] are plotted in Figure 2 as a function of the energy of the measured characteristic line of element A.
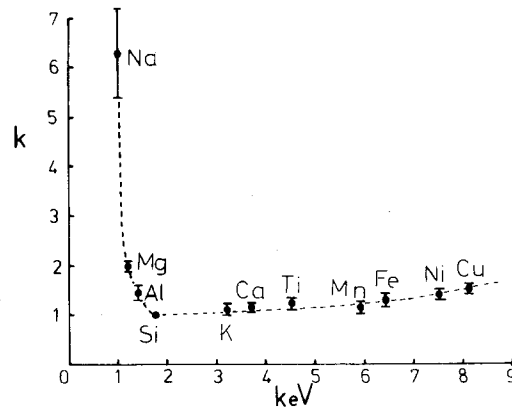

Figure 2 - Experimental k values for 100 kV plotted as a function of X-ray energy (keV) for K_α lines.[16]

Combinations of experimental values of k can be used along with Eq. (6) to factor out the Si and to obtain k_{AB} values for various combinations of elements AB. The k_{AB} values will change with operating conditions and may change from one instrument to another particularly if the EDS detector has different characteristics. Experimental k curves have also recently been reported for a Philips EM 300 instrument by Sprys and Short.[17]

Values of k_{AB} and k can also be calculated using Eq. (3) for the intensity of characteristic radiation of thin films. The equation must be corrected for the proportion "a" of K_α or L_α radiation of the total K or L radiation

produced and for the absorption of characteristic X-ray photons in the Be window of the detector. Hence

$$k = \frac{A_x \, (Q \, \omega \, a)_{Si} \, e^{-\mu/\rho_{Be}^{Si} \, \rho y}}{A_{Si} \, (Q \, \omega \, a)_x \, e^{-\mu/\rho_{Be}^{x} \, \rho y}} \tag{7}$$

where μ/ρ_{Be} is the mass absorption coefficient of the Be window for various characteristic lines, ρ is the density of Be and y is the Be window thickness. The value of k or k_{AB} calculated from Eq. (7) can be considered as the k or k_{AB} ratio obtained in an infinitely thin film, $k_{AB})_{T.F.}$. This equation can be applied to either K or L radiation and has been used by Goldstein, et al.[18] and Russ.[19] Goldstein, et al.[18] found that, by using Green-Cosslett Q values for K lines and either the Mott-Massey or Bethe-Powell Q values for L lines, calculated k values are in close agreement with experimental values at various operating voltages. Figures 3 and 4 show the calculated and measured k values at 100 kV as a function of the energy of the K_α and L_α lines respectively. Except for characteristic line energies below 1.6 keV ($Na_{K\alpha}$, $Mg_{K\alpha}$, $Al_{K\alpha}$), calculation techniques for k values appear to be quite promising.
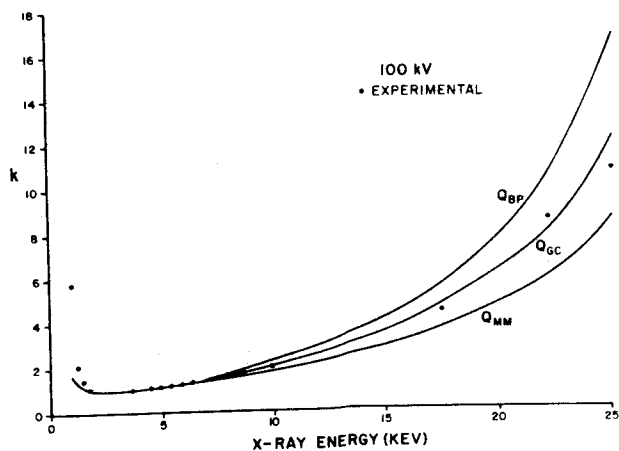

Figure 3 - Calculated and measured k values at 100 kV as a function of the energy of the K_α lines.
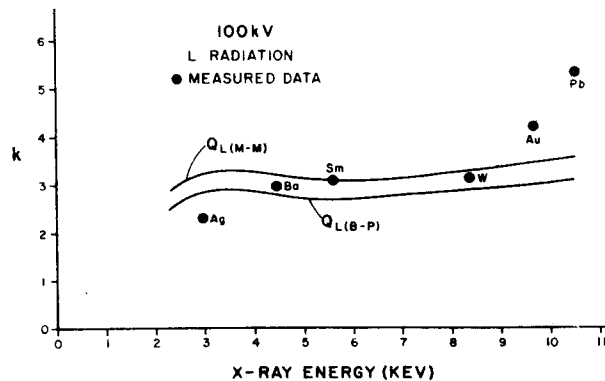
Figure 4 - Calculated and measured k values at 100 kV as a function of the energy of the L_α lines.

Corrections to Thin Film Model

Absorption in Thin Films. Tixier and Philibert[10] and other authors[14,15] have noted that X-ray absorption can occur even in thin films which are transparent to the impinging electron beam. König[20] argues that one must consider

the effects of elastic and inelastic scattering of electrons in thin films. He considers the depth distribution of X-ray production $\phi(\rho z)$ and also the absorption of X-rays in the thin film at a take off angle α, the angle between the detector axis and the specimen surface. Experimental values of $\phi(\rho z)$ have not been measured at high voltages (>50 kV) used for the X-ray analysis technique. Unless the film is transmission thick to the electron beam $\phi(\rho z)$ will approach a value of 1.0 to 1.10 at 100 kV and above. For almost all cases considerations of $\phi(\rho z)$ for high voltage thin film analysis are unnecessary.

Goldstein, et al.[18] have evaluated the effect of absorption assuming $\phi_B(\rho z) \simeq \phi_A(\rho z) \simeq 1.0$ and have observed that it is the difference in mass absorption coefficients between elements B and A in the specimen times csc α which is primarily responsible for the effect of absorption. The α term is the X-ray take off angle. If the value of $(\mu/\rho_{SPEC}^{B} - \mu/\rho_{SPEC}^{A})X$ (csc α) is larger than 200 to 500 cm^2/g, the change in the value of k_{AB} will be greater than 10% of the $k_{AB})_{T.F.}$ value and must therefore be considered in a thin film analysis.[18] The effect of absorption can be calculated assuming $\phi_A(\rho t) = \phi_B(\rho t) = 1.0$, by the equation

$$k_{AB} = k_{AB})_{T.F.} \cdot \left(\mu/\rho_{SPEC}^{A} \Big/ \mu/\rho_{SPEC}^{B} \right) \times \left[\frac{1-e^{-\mu/\rho)_{SPEC}^{B} \, csc \, \alpha(\rho t)}}{1-e^{-\mu/\rho)_{SPEC}^{A} \, csc \, \alpha(\rho t)}} \right] \quad (8)$$

where t is the film thickness.[18]

In order to calculate the effect of absorption using Eq. 8 in a specimen where absorption is significant it is necessary to measure the specimen thickness at each analysis point. Several techniques for measuring specimen thickness have been developed. Lorimer, et al.[21] have a technique of tilting the specimen after analysis to measure the separation between pairs of contamination spots and calculate the corresponding thickness. Joy and Maher[22] have suggested a technique for measuring crystal thickness using a calibration curve developed from the relative transmission of the primary electron beam through the specimen. These techniques are seldom accurate to within $\pm$ 10%. Kelly, et al.[23] have described a method which makes use of measurements of spacing of intensity oscillations in convergent beam diffraction patterns obtained with the STEM. Foil thicknesses to $\pm$ 2% can be determined as shown by Rao.[24] Depending on the specimen distortion, spot analysis position and specimen tilt, it should be possible to use one of these techniques for thickness measurement.

Fluorescence in Thin Films. Philibert and Tixier[12] have found
that continuum fluorescence is negligible and that characteristic
fluorescence will be negligible if μ/ρ_{SPEC}^{B} (t) $\ll 1$. In this case
element B radiation is assumed to be the cause of the fluorescence in
the film. A correction for characteristic fluorescence in thin films
has been developed by Philibert and Tixier.[12] Lorimer[2] has shown
an X-ray fluorescence effect resulting in an apparent increase in chromium
concentration in thin foils of three Fe-Cr alloys.

Instrumental Limitations

As shown in the previous section, quantitative analysis can be
obtained from thin film samples analyzed by STEM techniques. A discussion
of the instrumental setup including the choice of accelerating voltage,
electron gun, and the sample X-ray detector configuration is found in
several papers[4,25] and will not be repeated here. However certain
instrumental factors produce spectra measured in the EDS detector which
contain X-rays originating from regions outside the volume excited by
the primary electron beam. This spurious or extraneous radiation not
only causes errors in the quantitative analysis but may also give rise
to errors in identification. In addition, increased background radiation
raises the detectability limit. The following discussion outlines the
causes of such extraneous or "spurious" X-ray signals and the steps that
can be taken to eliminate this unwanted radiation.

An electron microscope operated at 100 kV is an efficient source of
X-rays from places other than the specimen. It is essential to prevent
these X-rays from entering the detector. Furthermore the electron beam
must be well collimated since stray electrons will similarly excite spurious
X-rays, or may themselves enter the detector. A study of the problem in
the SEM has been made by Bolon and McConnell.[26] Figure 5 shows a corres-
ponding diagram for X-ray generation in the TEM. Possible sources of X-rays
include:

(a) X-rays from the point of interest (desired).

(b) X-rays from around the specimen due to uncollimated electrons.

(c) X-rays from around the specimen due to electron scatter from the
second condenser lens aperture, situated above the upper objective
lens pole piece.

(d) X-rays generated from the upper objective lens pole piece due to
electron backscatter from the specimen.

(e) X-ray fluorescence from the specimen and surrounds due to continuum X-ray production in the C_2 aperture.

(f) X-rays from the specimen chamber (cold finger, upper objective pole piece) due to backscatter of transmitted electrons from the lower objective pole piece.

(g) X-ray fluorescence from the specimen holder on grid and surrounds due to continuum X-ray production in the specimen.
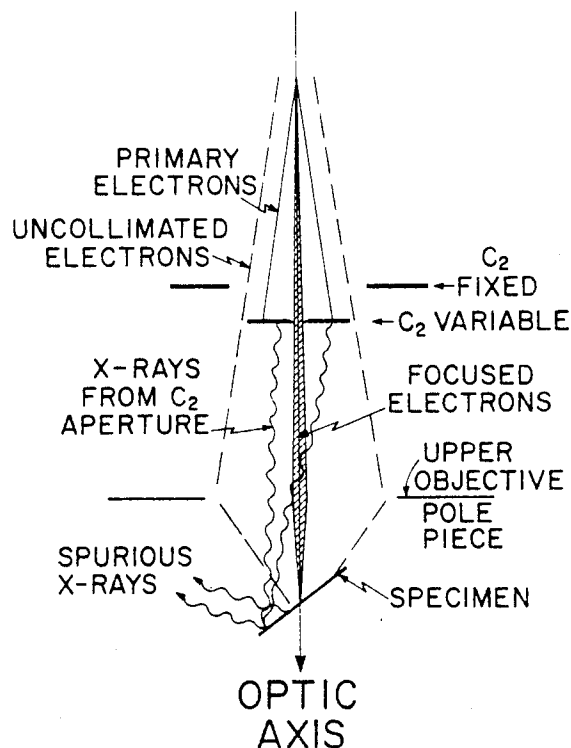

Figure 5 - Diagram of electron optical column showing various sources of spurious X-rays.

There is conflicting evidence in the literature,[4,25,27-31] concerning the primary mechanism responsible for the spurious X-rays. However it appears that these effects may be reduced by taking certain basic precautions. Poor beam collimation (b) may be improved by insertion of a spray aperture of $\sim 1\,mm$ diameter in place of the fixed C_2 aperture[27] or by positioning a suitable insert below the C_2 variable aperture holder.[32] Effect (d) is probably a small factor since the amount of back scattered electrons from thin films is small and it is probable that these electrons will be taken away from the immediate region of the specimen by the strong field of the final prefield objective lens.[33] Effect (f) mainly results in electron interaction with the cold finger which can be shielded with Pb or manufactured

from low Z material.[29] It should be noted that the effect of specimen generated continuum X-rays, effect (g), cannot be avoided at present. These continuum X-rays come from the point of interest and can excite specimen holders and support grids. To minimize this effect (g), it is good practice to use specimen holders made from Be or graphite and to support specimens when necessary on Be grids. This will remove any X-rays produced from the specimen surrounds and result in a substantially cleaner spectrum.

The presence of effects (c) and (e), stray radiation from the illumination system, can be observed by putting the focused electron beam down a hole in a support grid. If an X-ray spectrum is observed, it is referred to as the "hole count." The use of a Be grid does not eliminate the radiation responsible for the "hole count." The stray radiation effects (c) and (e) will still irradiate the bulk of any specimen when placed in the instrument. A "hole count" can also be observed when the electron beam is placed down a hole in a self supported sample since the sample itself is irradiated by the stray radiation. The "hole count" spectrum observed from either the grid or the self supported sample gives rise to a spurious X-ray contribution in addition to the actual X-ray peaks from the specimen. This spurious X-ray spectrum must be minimized if quantitative microanalysis is to be achieved.

Figure 6 shows a typical X-ray spectrum obtained from a Ag disk specimen in the Philips EM 300 TEM/STEM when the electron beam is focused on a thin region. Both the $Ag_{L\alpha}$ and K_{α} peaks are observed.
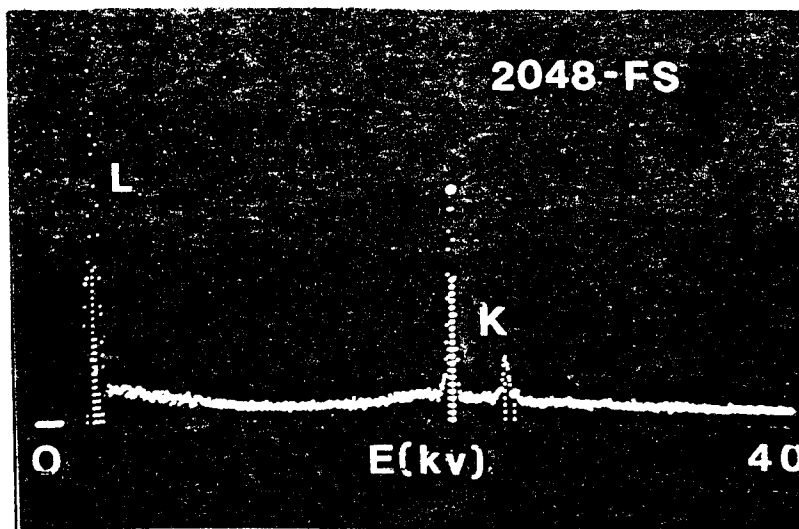

Figure 6 - Typical EDS spectrum from Ag disk specimen.
Full scale is 2048 counts.

Figure 7 shows the Ag hole count from a Ag disk specimen when the beam
is placed in a hole in the Ag disk. A Pb plug has been inserted below
the 100 μm thick Pt C_2 aperture and this eliminates the vast majority
of uncollimated electrons, effect (b).[32] No spectral peaks from the
supporting grid or specimen holder were observed. The intensity of the
$Ag_{L\alpha}$ peak is reduced greatly but is clearly present in the spectrum.
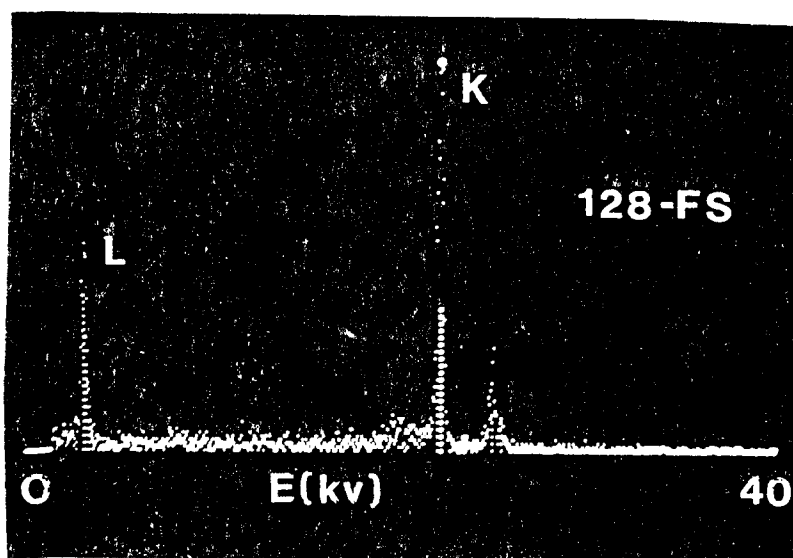

Figure 7 - Ag hole count from Ag disk specimen. A Pb plug
          has been inserted beneath the C_2 aperture. Full
          scale is 128 counts.

However the intensity ratio of the $Ag_{K\alpha}$ to $Ag_{L\alpha}$ peaks is very different
than that obtained from the normal X-ray spectrum from the Ag disk (Figure 6).
Goldstein and Williams[32] attribute such a hole spectrum primarily to
effect (e) (continuum X-rays from the C_2 aperture producing a strong $Ag_{K\alpha}$
peak). A small amount of stray electrons from the primary beam scattered
by the sides of the hole in the C_2 aperture, effect (c), probably produce
the reduced L_α peak and the relatively small continuum background.

The X-ray continuum produced from the C_2 aperture as column electrons
are absorbed appears to be the most serious problem, effect (e), (Figure 5)
with respect to spurious X-ray generation from the specimen. The generated
X-ray flux cannot be decreased below the C_2 aperature and it has a direct
line of sight to the entire specimen ($\sim$ 3 mm in diameter) and its surrounds.
Analyses of $\leqslant$ 100 nm areas are obviously compromised by this effect. Calcu-
lations of continuum intensity as a function of energy and its transmission
through Pt apertures of various thickness were produced by Goldstein and

Williams.[32]   These results are shown in Figure 8 for 25, 50, 100 and

200 μm thick apertures. For relatively thin apertures (25, 50 μm) or

thin regions near the hole of thicker apertures, continuum X-rays with

energies below 25 kV are transmitted and bombard the sample in turn.

X-rays in this energy range are quite efficient in fluorescing the speci-

men where characteristic X-rays of < 15 kV energy are used for analysis.

For thicker apertures, only continuum X-rays with energies above 25 kV

are transmitted. Therefore thick apertures with a minimum of thin region

around the hole are most desirable for minimizing spurious X-rays produced
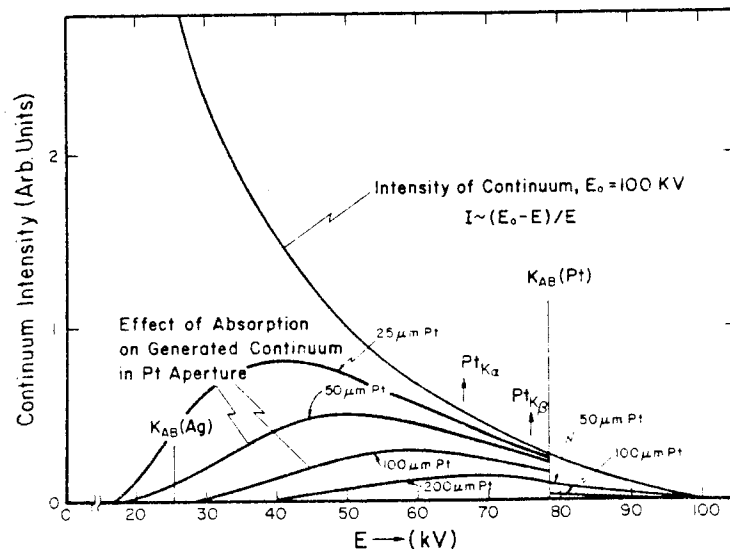
by continuum X-rays.

Figure 8 - Continuum X-ray production in and trans-
           mission from Pt C_2 apertures of various
           thicknesses.

The amount of spurious X-rays which are produced by the continuum

X-rays is a strong function of atomic number and specimen thickness.[32]

Less spurious X-rays are produced in thinner specimens.   At constant

thickness, low Z specimens show less of a spurious X-ray signal. In fact

for < 100 nm evaporated films of low atomic number (Al, Si, etc.), the

spurious X-ray signal, the "hole count," is very small. For ion thinned

or jet electropolished specimens where major portions of the specimens

are thick (> 1 μm), the absorption of continuum X-rays is very severe.

At a 1 μm thickness upwards of 3 - 15% of the incoming X-rays are absorbed.

In 10 μm thick regions of the foil over 25% of the 20 to 30 kV continuum

is absorbed in Cu, Ag and Au.[32]

In summary, for STEM microanalysis, there is a contribution of C_2 aperture continuum X-rays which fluoresce the specimen, supporting grid and surrounding holder. The specimen type (i.e., self supporting disk, or thin evaporated film) will have a marked effect on the generation of spurious peaks. If possible, thick C_2 apertures ($\sim 200\,\mu m$) as initially suggested by Russ[30] should be used. In addition, uniformly thin specimens (evaporated films on carbon substrates or thin window-polished flakes supported on Be grids) are the ideal specimens for analysis in the STEM. For specimens where chemical jetting or ion beam polishing must be used resulting in disk specimens, thick C_2 apertures are recommended. The process of subtracting the spurious X-ray spectrum as suggested by Kenik and Bentley[31] cannot be guaranteed to leave the correct spectrum, since moving the specimen or beam to obtain the hole count may itself result in a change in the distribution of spurious X-rays. When X-rays from an inhomogeneous region of unknown thickness are contributing a large fraction of a spectral peak which is to be used for quantitation, it is considered that the only way to ensure accurate data is to identify and remove the source of the hole count by one of the methods suggested above. When the counts in the spurious specimen peak(s) obtained down a hole in the specimen are less than the continuum background over the same energy range, it can be confidently stated that the STEM system is optimized for in-situ quantitative X-ray microanalysis.

Specimen Preparation

Thin foil specimens are conventionally produced by either electro-chemical polishing, or ion-beam bombardment. Both techniques have their drawbacks which may affect the microanalysis. The electropolishing bath is a very severe environment for very thin specimens. Heating occurs and may be substantial even in cooled and stirred solutions. Dissolution and redeposition of particular species have been observed in many alloys. For example Figure 9 shows the variation in relative intensity of $Al_{K\alpha}$ and $Cu_{K\alpha}$ X-rays, away from the edge of a conventionally electropolished thin foil of An al alloy. The $Cu_{K\alpha}$ intensity increases markedly towards the thin edge of the specimen.[34] This has been interpreted in terms of Cu deposition as a thin surface film $\sim 15\,nm$ thick during electropolishing, but attempts to remove such films by ion-beam thinning alloys have met
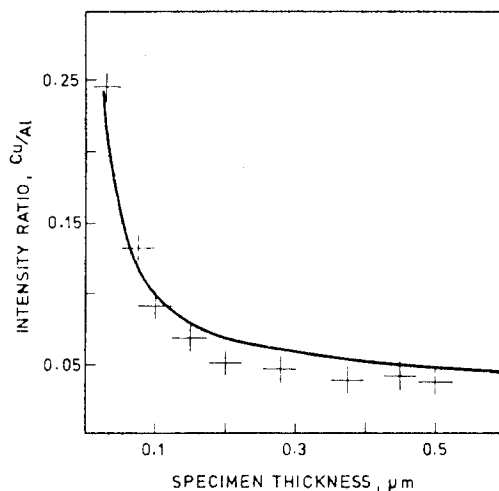
Figure 9 - Plot of copper K/aluminum K count intensity
ratio as a function of specimen thickness.
The crosses are the experimental points, the
line is calculated for an enriched surface layer
copper 15 nm thick.

with different degrees of success. In a companion study Doig and Flewitt[35]
concluded that enriched surface films in Al-Zn-Mg-Cu and Fe Ni alloys were
responsible for the $Cu_{K\alpha}/Al_{K\alpha}$ and $Fe_{K\alpha}/Ni_{K\alpha}$ intensity increases in the
thinnest regions of the alloy films. Ion beam thinning did not remove
the effect. On the other hand Morris, et al.[36] were able to eliminate
similar intensity increases by ion thinning with an instrument which
operated at low residual partial pressures. A similar enrichment effect
has been observed in Ni-Al alloys,[29] but was ascribed to the spurious
X-ray continuum background of the type discussed earlier. The problem is
still unresolved.

Oxide films produced during specimen preparation are not uncommon,
and may be enriched in a particular alloy component, thus giving spurious
results similar to that in Figure 9. Impurities may be introduced from
the chemicals used in the polishing solutions, for example Cl from perchloric
acid solution is particularly common. Finally, the resulting thin films
may be very nonuniform in thickness particularly in a two phase material.
This poses obvious problems in comparing results from different regions of
the same specimen as discussed in detail in the following section of this
paper. Similarly ion bombardment thinning almost invariably produces speci-
men heating and may give rise to substantial oxidation.[37] Invariably
foils produced in this manner are nonuniform in thickness even in single
phase regions.

It can only be concluded that specimen preparation should be performed with care, and close attention paid to the cleanliness of the preparation environment. At this point it is not even possible to eliminate specific film formation on the surface even during ion beam thinning. Until a more complete understanding of the surface enrichment effect, which occurs during specimen preparation, is available, each case of microanalysis must be treated on its own merits. The area of specimen preparation is clearly a very important topic for active research.

Spatial Resolution

The spatial resolution for chemical analysis in a thin foil is a function of atomic number, specimen thickness and the accelerating voltage. Goldstein, et al.[18] have estimated the effective beam broadening b by assuming that scattering takes place at the center of the thin film, that the dominant process causing beam spreading is elastic scattering by atomic nuclei and that the electron beam is a point source. This development yields an equation for broadening:

$$b = 625 \frac{Z}{E_o} \left(\frac{\rho}{A}\right)^{\frac{1}{2}} t^{3/2} \tag{9}$$

where b is in cm, Z is the atomic number, A is the atomic weight, E_o is in keV, ρ is in g/cm^3 and t is the film thickness in cm. The broadening varies inversely as E_o and increases with film thickness. As an example, for 500Å Au films b equals 173Å, for 3000Å Cu films b equals 1117Å, and for 5000Å Al films b equals 909Å at 100 kV operating potential. All of these film thicknesses are typical of electron microscope thin film specimens.

For a point source electron beam the spatial resolution-broadening can therefore be substantial. The broadening equation assumes that the size of the electron beam impinging on the sample is vanishingly small. The total X-ray spatial resolution is therefore equal to the sum of the broadening b and the size of the electron beam d impinging on the sample.

The broadening predicted by Eqn. (9) is plotted for Al, Cu and Au in Figure 10.[3] This Figure clearly shows the importance of the use of a high accelerating voltage and very thin specimens if a spatial resolution of a few hundred Angstroms is to be obtained. These results indicate that it is not possible to obtain a spatial resolution of a few tens of Angstroms

polyvinylpyrrolidone (PVP), hydroxyethyl starch (HES) and dextran have been established. The vitrified polymer solutions exhibit a characteristic microspherical substructure (15-40 nm in diameter) which is <u>not</u> induced by the quench cooling process but is an inherent feature of the solutions themselves.

We have found that 25% solutions of PVP (M. Wt. 44,000), HES (M. Wt. 450,000) and dextran (M. Wt. 68,500), when made up in isotonic salt solution, have little adverse physiological effect on a wide range of cells and tissues and are much less toxic than similar concentrations of glycerol and DMSO. The polymers appear not to penetrate cell membranes but nevertheless control intracellular freezing to such an extent that in freeze-fracture specimens no evidence of ice crystallization can be observed. Dextran is less useful in this respect for at the concentrations at which it is an effective cryoprotectant (25-40%) it has adverse physiological effects. The period of incubation in the cryoprotectant necessary before freezing is short (i.e. < 30 min) compared to the long infiltration for low molecular weight cryoprotectants. X-ray analytical studies show that these polymeric cryoprotectants do not cause ions and electrolytes to leak from cells and it is possible to measure concentration gradients across tissues which are embedded in these materials, although the possibility must remain that elemental redistribution can occur within a given cell. The reduction in size of ice crystals to nanometre dimensions in HES and PVP cryoprotected tissues makes this unlikely, but we need to carry out further analysis on cells in which one can unequivocally distinguish the major compartments. Quantitative X-ray analytical studies can only be effectively carried out on sectioned material. Both PVP and HES when used at concentrations at which they are good cryoprotectants are also useful embedding agents with excellent sectioning properties at low temperatures. Small pieces of tissue may be encapsulated in PVP and HES and sections cut from the frozen material at low temperature. Such sections may be used for low temperature scanning microscopy and X-ray microanalysis.

The use of polymeric cryoprotectants in morphological
and analytical studies of biological material

by

Felix Franks[*], Patrick Echlin[*] and Helen Le B. Skaer[**]

[*]Botany School and [**]Zoology Department,
University of Cambridge, U.K.

Cryogenic techniques appear to offer one of the most satisfactory solutions to the vexed question of biological and highly hydrated specimen preparation for both ultrastructural and analytical studies in electron beam instruments. By freezing small pieces of tissue the liquid phase of the cytoplasm is converted to a solid. If the cooling rate is fast enough, it should be possible to preserve structures and diffusible ions and electrolytes _in situ_ because the ice crystals become progressively smaller with an increased rate of cooling. In practice this phase change is, unfortunately, a crystallization process which may severely distort the morphology of the specimen. As ice crystals form at the expense of water in the system, the remaining liquid phase becomes progressively more concentrated causing ions to move away from their original positions in the cell and in extreme cases to be precipitated as salts. Low molecular weight cryoprotectants such as glycerol and dimethyl sulphoxide, although toxic to cells, are sufficiently effective in modifying ice crystal morphology to make them useful cryoprotectants for morphological studies. However they cause such gross changes in membrane permeability that they are of little use in analytical studies of unbound and freely diffusible ions.

It has been known for some time that concentrated aqueous solutions of some polymers will, upon quench cooling, yield vitreous states and recent experiments have shown that such vitrified solutions are able to act as effective ultrastructural cryoprotectants. The solid states formed by vitrified and frozen aqueous solutions of these hydrophilic polymers have been studied by differential scanning calorimetry, freeze fracture electron microscopy and electron probe X-ray microanalysis. Glass transitions, devitrification, recrystallization and melting behaviour of aqueous solutions of

Conditions For Avoidance of Ice Crystallization in Cells. Lionel I. Rebhun,
Department of Biology, University of Virginia, Charlottesville, Va. 22901.

Three cell types were investigated, marine eggs of clams and sea
urchins, rat liver and rat pancreas. In order to avoid accidental
evaporation of water during tissue handling, cells were sandwiched
between formvar films on small freezing platforms and plunged into
quenching fluid with a sling shot type of device. Tissue was then removed
with the freezing platform and substituted in ethanol, acetone or tetra-
hydrofuran at temperatures between -70 and -95°C in the presence or absence
of osmium. A final change in substituting fluid at low temperature removed
excess osmium if it had been used. Samples were allowed to come to room
temperature and were embedded in plastic, sectioned and stained by con-
ventional methods. Ice crystals were almost always seen in cells treated
by these methods, the only exceptions appearing in a small number of marine
eggs where ice crystal-free areas appeared immediately adjacent to ice
containing regions in the same cell. In addition, when formvar sandwiching
was not used ice-crystal free regions appeared in a small proportion of all
cells. If eggs were deliberately made hypertonic before freezing, the
proportion of ice-crystal-free regions increased greatly and after five
minutes in double strength sea water or higher, all cells had large ice-
crystal-free areas. Liver or pancreas deliberately partially air dried
for a minute or two showed surface regions ice crystal-free while that
handled in a moist chamber never showed ice-crystal free regions. Liver
put into 2x hypertonic sucrose in normal saline showed extensive ice
crystal-free regions. Impregnation of liver or pancreas with DMSO or
glycerol to a maximum of 25% in saline allowed large areas of ice crystal-
free regions to be obtained, the morphology of which is comparable to that
seen after chemical fixation. Our total experience suggests that chemical
fixation and freezing techniques yield similar morphology only when the
latter occur under conditions in which cells are partially dehydrated prior
to freezing either by accidental evaporation from the cell surface, which
can occur in seconds in ordinary low humidity laboratory air, or when water
is deliberately removed osmotically or by replacement with freeze-protective
agents. Since chemical fixation also involves a change in waterprotein
interactions which may stimulate a dehydration, it is perhaps this common
step which is important in consideration when comparing well fixed and well
frozen cells.

Another fine structure nearer the edge has been observed which is associated with the transition of the ejected photoelectron to one of the many empty states lying above the Fermi level. Since this is more or less a measure of the local band structure, this fine structure is sensitive to the chemical and crystallographic environment of the atom.

SCHEMATIC OF BEAM-SPECIMEN INTERACTIONS

incident electron beam

Auger electrons

X-rays

e⁻

electron transparent specimen

elastically scattered electrons
(Bragg diffraction)

thermal phonons (special case
of inelastic scattering)

inelastically scattered electrons
1. plasmons
2. single electron excitations
    a. inter-, intra-band
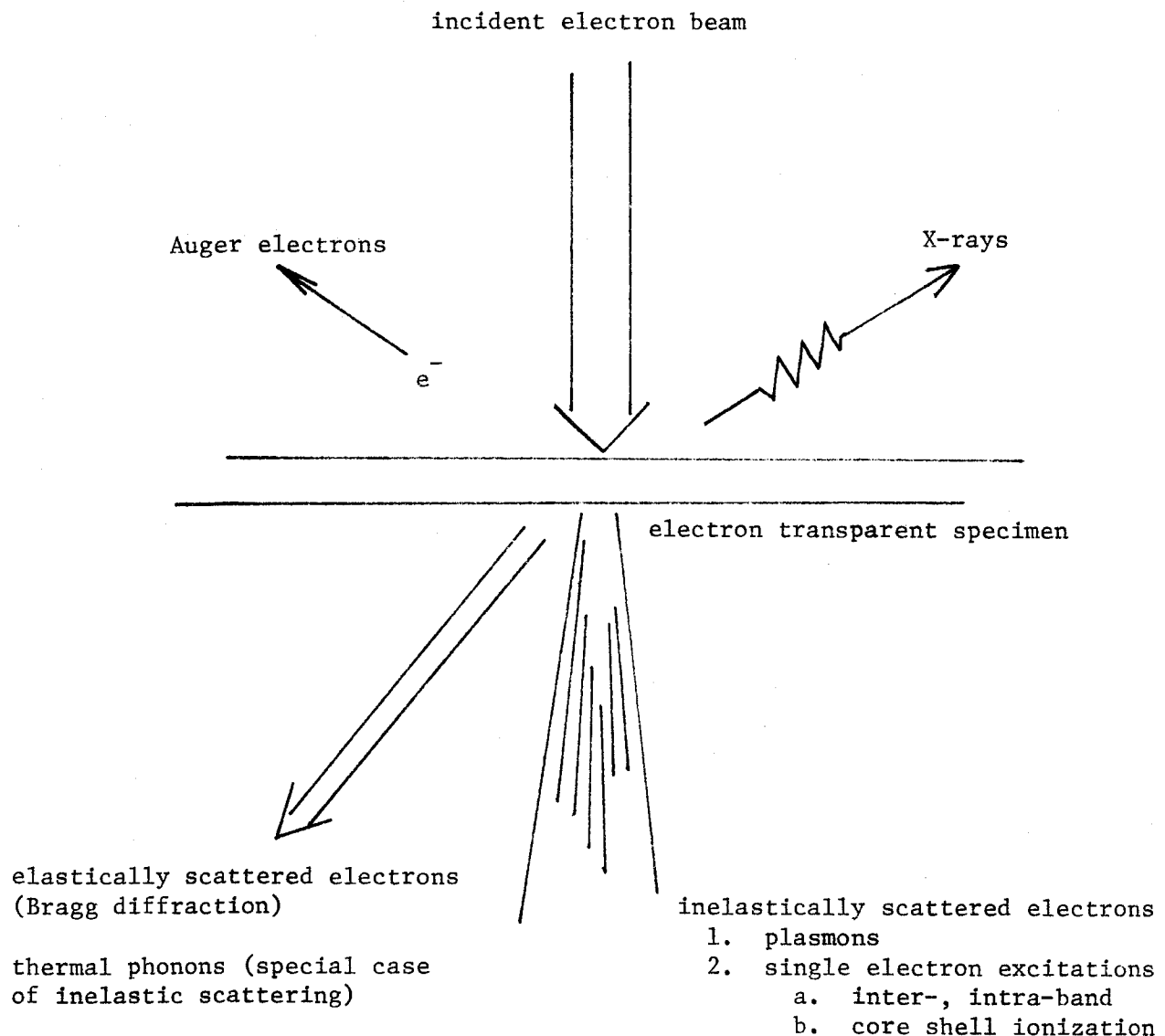   b. core shell ionization

Figure 1. Beam-Specimen Interactions

As is well known, characteristic X-rays are emitted when a vacancy created by the ejection of a core shell electron, say in K shell ionization, is filled by an electron from an outer shell, say the L shell. The difference in quantum energy between the two shells, which is equal to the difference in potential energy of the initial and final states of the transition electron is released as an X-ray photon. In the example given, K shell ionization, the emitted X-ray is called K-radiation. However, the energy released by the transition is not always emitted as X-radiation but may be used instead to eject an electron from an outer shell of the atom creating an Auger electron.

The transmitted fast electrons will sustain energy losses equivalent to the energy difference between the initial and final states of the ejected photoelectron, the magnitude of which can be hundreds or even thousands of eV. The electron energy loss spectra (EELS) of these transmitted electrons is particularly useful for detecting low atomic number elements ($Z < 13$) for which X-ray methods have poor sensitivity due in part to low fluorescence yield. (Auger electrons have a high excitation probability for low Z elements; however, experimental requirements of an ultra high vacuum limit Auger detection to very specialized equipment.) The characteristic core losses are observed as edges in the EELS at unique energies with the area under the edge proportional to the amount of the element present. In addition, there may be fine structure following the edge which is analogous to the fine structure which has been observed above the X-ray edges in X-ray absorption spectra (EXAFS). Such fine structure can extend over several hundred eV and is a measure of the short range order about the excited atom since it is thought to arise from scattering of the ejected photoelectron (say, from the K shell) by nearby surrounding atoms.

Plasmon scattering results from the Coulomb interaction between the incident fast electrons and the quasi-free electron gas in a solid (conduction electrons in a metal) causing the latter to oscillate about their equilibrium positions. These collective oscillations create a region of space charge which propagates as a longitudinal wave through the crystal with a characteristic energy, $E_p = h\omega_p$. This energy packet is called a plasmon and typically has an energy ranging from 10 to 30 eV. Accordingly, the incident electron beam loses this plasmon energy and also undergoes an angular deflection; however, this deflection is usually quite small so that most of the inelastically scattered electrons remain close to the forward direction and will pass through objective apertures of standard size.

Plasmon spectra have been used in chemical analysis; however, such investigations do not strictly involve chemical analysis but rather are studies of variations in the electron density of the free electrons.

SINGLE ELECTRON SCATTERING

The incident fast electron may interact with the atomic electrons in still another manner, that is, by the direct transfer of energy to a single electron. If this atomic electron is an outer shell, or valence electron, the energy transfer involves an intra- or inter-band transition of the atomic electron to a higher energy level. The energy transfer here is typically a few electron volts. These transitions are little used in the analysis of the energy loss spectrum. On the other hand, if the incident electron displaces an atomic core (K, L or M shell) electron, either characteristic X-rays or Auger electrons are excited. Both may be used for microanalysis of the elements in the specimen.

sensitive intensity. As the degree of atomic order increases, the subsidiary peaks become sharper until complete order is achieved as in the case for crystalline materials. Such peaks appear at characteristic angles described by the diffraction of coherently scattered electrons. Thus the fraction of electrons elastically scattered is contained in the intensity of the Bragg diffraction spots observed in diffraction patterns. Any other intensity must thus be due to inelastic scattering.

INELASTIC SCATTERING

Following the description of Egerton,[1] inelastic scattering which occurs in a thin film may be divided into three types: phonon, plasmon and single electron scattering. Of primary interest is the latter since it is from the single electron scattering process that most of the chemical information about the specimen is generated via x-rays, Auger electrons and absorption edge structure in the energy loss spectra of the transmitted electrons. A brief discussion of phonon and plasmon scattering will be given first.

Phonon scattering is a consequence of the thermal motion of the atoms causing them to be displaced from their exact lattice positions. As a result the structure sensitive intensity function previously discussed generates diffuse tails which are superposed on the sharp diffraction maxima which occur at Bragg angles. This diffuse scattering is considered equivalent to the creation and annihilation of phonons and corresponds to changes in energy of the incident electron beam on the order of kT (i.e., approx. 0.1 eV at room temperature). Consequently, the diffuse peaks associated with phonon scattering are analogous to the diffuse peaks arising from slight structural disorder as discussed under elastic scattering from an array of atoms, and are associated with Bragg diffraction peaks.

ELASTIC SCATTERING

The elastic scattering of an electron incident on an isolated atom is similar to the classical collision between a moving light billiard ball and a heavy one at rest. That is, the light billiard will be deflected through some angle with essentially no change in energy while the heavy billiard ball remains at rest. Elastic scattering of fast moving electrons by atoms is usually described as either Rutherford scattering or scattering by the electron cloud Coulomb potential. Rutherford scattering takes place when the electron passes close to the nucleus while electron cloud scattering occurs when the incident electron passes through the outer part of the atom where the field of the nucleus is more or less screened by the orbital electrons. Following standard mathematical arguments describing electron scattering, one obtains an expression for the amplitude of the atomic scattering by an atom of atomic number Z.

$$f(\theta) = \text{const.} \ (\frac{\lambda}{\sin \theta})^2 \ (Z - f_x)$$

In this equation the first term in the bracket is due to Rutherford scattering and the second term due to scattering by the electron cloud. f_x is the atomic scattering factor for x-rays and λ the electron wavelength. The term with $(\sin \theta)^{-2}$ decreases very rapidly so one would expect most electron scattering to be at small angles, typically less than 10^{-2} radians.

Elastic scattering from a material consisting of a random array of atoms will be incoherent in phase since there is a non-uniform spacing between atoms. This gives rise to a distribution of scattered intensity consisting of a monotonically decreasing radial intensity on which is superposed diffuse subsidiary maxima and minima derived from the interatomic separations - a structure

INTRODUCTION

Analytical electron microscopy in the context of today's technology means utilizing an electron microscope, usually in transmission, to characterize very small volumes of materials. Frequently, some form of scanning electron microscope is used, either an attachment to a TEM giving a (S)TEM as provided by Philips, JEOL, Hitachi, etc., or a dedicated STEM as manufactured by VG and Siemens, etc. The (S)TEM instruments are becoming commonplace in both university and and industrial materials research laboratories in this country, while the newer dedicated STEM instruments are located in just a few university laboratories, e.g., MIT, Illinois, Arizona State.

Materials characterization in a TEM can range from the simple problem of taking micrographs of surface replicas to the complex analysis of many of the signals from electron beam – materials interactions. That is, when a high energy electron probe is incident on a thin specimen a large number of scattering processes may occur which are conventionally labeled either elastic – no energy loss but directional changes, or inelastic – some energy loss in the incident electron energy. The most common use of elastically scattered electrons is in the formation of diffraction patterns, while inelastically scattered electrons are most frequently analyzed either directly or indirectly to give information about the chemical nature of the material.

The plan of this paper is to give a brief phenomenological discussion of the dominant electron beam – materials interactions and present some results appropriate to small area diffraction and elemental analysis.

PRINCIPLES AND PRACTICES OF STEM MICROSCOPY

BY

R. H. Geiss
IBM Research Laboratory
Dept. K41/281
San Jose, California   95193

ABSTRACT:

A p henomenological review of the interactions between a high energy electron and an electron-transparent specimen are presented relative to the modern-day concept of analytical electron microscopy using scanning transmission electron microscopes. Instrumentation is discussed and data presented showing the achievement of better than 30 Å area resolution in electron diffraction and 125 Å point to point resolution in EDS elemental analyses.

18. J. I. Goldstein, J. L. Costley, G. W. Lorimer and S. J. B. Reed, SEM/1977, ed. O. Johari, IITRI, Chicago, Illinois, 1977, Paper #46.

19. J. C. Russ, Proc. 8th National Conference on Electron Probe Analysis, 1973, 30.

20. R. König, Electron Microscopy in Mineralogy, ed. H. R. Wenk, Springer-Verlag, Berlin, 1976, 526.

21. G. W. Lorimer, G. Cliff, and J. N. Clark, Developments in Electron Microscopy and Analysis, EMAG 75, J. A. Venables, ed., Academic Press Inc., London, 1976, 153-156.

22. D. C. Joy and D. M. Maher, Proc. 33rd Annual EMSA Meeting, 1975, 242-3.

23. P. M. Kelly, A. Jostsons, R. G. Blake and J. G. Napier, Phys. Stat. Sol. 31, 1975, 771-780.

24. P. Rao, Proc. 34th Annual EMSA Meeting, 1976, 546-7.

25. R. H. Geiss and T. C. Huang, X-ray Spectrometry, 4, 1975, 196.

26. R. B. Bolon and M. D. McConnell, SEM/1976, ed. O. Johari, IITRI, Chicago, Illinois, 1976, 164.

27. H. Shuman, A. V. Somlyo and A. P. Somlyo, Ultramicroscopy, 1, 1976, 317.

28. J. J. Hren, P. S. Ong, P. F. Johnson and E. J. Jenkins, Proc. 34th EMSA Meeting, ed. G. W. Bailey, Claitors Publishing Division, 1976, 418.

29. N. J. Zaluzec and H. L. Fraser, Proc. 34th EMSA Meeting, ed. G. W. Bailey, Claitor's Publishing Division, 1976, 420.

30. J. C. Russ, SEM/1977/I, ed. O. Johari, IITRI, Chicago, 1977, 335.

31. E. A. Kenik and J. Bentley, Proc. 8th ICXOM/12th Annual MAS Conference, 1977, 114.

32. J. I. Goldstein and D. B. Williams, "Spurious X-ray Produced in the STEM," SEM/1978, ed. O. Johari, 1978, in press.

33. M. N. Thompson, (Philips, Eindhoven, Netherlands), Private Communication.

34. M. N. Thompson, P. Doig, J. W. Edington and P. E. J. Flewitt, Phil. Mag, 35, 1977, 1537.

35. P. Doig and P. E. J. Flewitt, J. Microscopy, 110, 1977, 107.

36. P. L. Morris, N. C. Davies, J. A. Treverton, EMAG, 1977, in press.

37. D. J. Barber, J. Mat. Sci., 5, 1970, 1.

38. D. F. Kyser and R. H. Geiss, Proc. 12th Annual Conference MAS, 1977, 110.

39. K. E. Easterling, J. Materials Science, 12, 1977, 857.

40. L. S. Lin, J. I. Goldstein and D. B. Williams, Geochim. Cosmochim. Acta, 41, 1977, 1861.

41. D. C. Joy and D. M. Maher, SEM/1977, ed. O. Johari, IITRI, Chicago, Illinois, 1977, 325.

42. H. Shuman and A. P. Somlyo, Proc. Nat. Acad. Sci., 1976, 1193.

43. C. S. Pande, M. Suenaga, B. Vyas, H. S. Isaacs and D. F. Harling, Scripta Met. 11, 1977, 681.

44. P. Rao and E. Lifshin, Proc. 12th Annual Conference MAS, 1977. 118.

Summary

It is clear from this tutorial that STEM X-ray microanalysis is not only feasible but has already yielded important information about the materials being studied. However it is also clear that at the present time the technique is not straightforward. The effects of spurious X-ray generation and specimen preparation appear to be the most serious problems at this time. Much research still needs to be done to overcome these problems as well as to establish the X-ray resolution and the sensitivity and accuracy of the thin film quantitation scheme. The field of STEM micro-analysis is just beginning and one looks forward to the important discoveries that will be made as a result of its continued development.

Acknowledgments

References

1. G. W. Lorimer, Analytical Electron Microscopy, Proceeding of a Workshop, Cornell University, 1976.
2. G. W. Lorimer, Proc. 12th Annual Conference, MAS, 1977, 108.
3. D. R. Beaman, Modern Techniques for the Detection and Measurement of Environmental Pollutants, 10th Rochester International Conference on Environmental Toxicity, 1977 in press.
4. J. I. Goldstein and D. B. Williams, SEM/1977, ed. O. Johari, IITRI, Chicago, Illinois, 1977, 651.
5. R. Castaing, Thesis, University of Paris, ONERA Publ. #55, 1951.
6. Practical Scanning Electron Microscopy, eds. J. I. Goldstein and H. Yakowitz, Plenum, New York, 1975.
7. S. J. B. Reed, Electron Microprobe Analysis, Cambridge University Press, Cambridge, 1975.
8. P. Duncumb, J. de Microscopie, 7, 1968, 581.
9. J. Philibert and R. Tixier, Brit. J. Appl. Phys. 1, 1968, 685.
10. R. Tixier and J. Philibert, Proc. 5th Int. Cong. on X-ray Optics and Microanalysis, eds. G. Mollenstedt and K. H. Gaukler, Springer-Verlag Berlin, 1969, 180.
11. M. J. Nasir, Proc. 5th European Cong. on Electron Microscopy, Manchester, The Institute of Physics, Bristol, 1972, 142.
12. J. Philibert and R. Tixier, Physical Aspects of Electron Microscopy and Microbeam Analysis, ed. B. M. Siegel and D. R. Beaman, J. Wiley, N.Y., 1975, 333.
13. M. H. Jacobs and J. Baborovska, Proc. 5th European Cong. on Electron Microscopy, The Institute of Physics, Bristol, 1972, 136.
14. M. H. Jacobs, J. Microscopy, 99, 1973, 165.
15. G. Cliff and G. W. Lorimer, Proc. 5th European Congress on Electron Microscopy, Institute of Physics, Bristol, 1972, 140.
16. G. Cliff and G. W. Lorimer, J. Microscopy, 103, 1975, 203.
17. J. W. Sprys and M. A. Short, Proc. 11th Annual Conference MAS, 1976, 9.

degree of tilt of the sample (36°) necessary for X-ray analysis and the small size of the structures. This is the first study in which the concentration gradient at the α/γ interface in iron meteorites as well as the composition of the various phases in plessite were measured in detail.
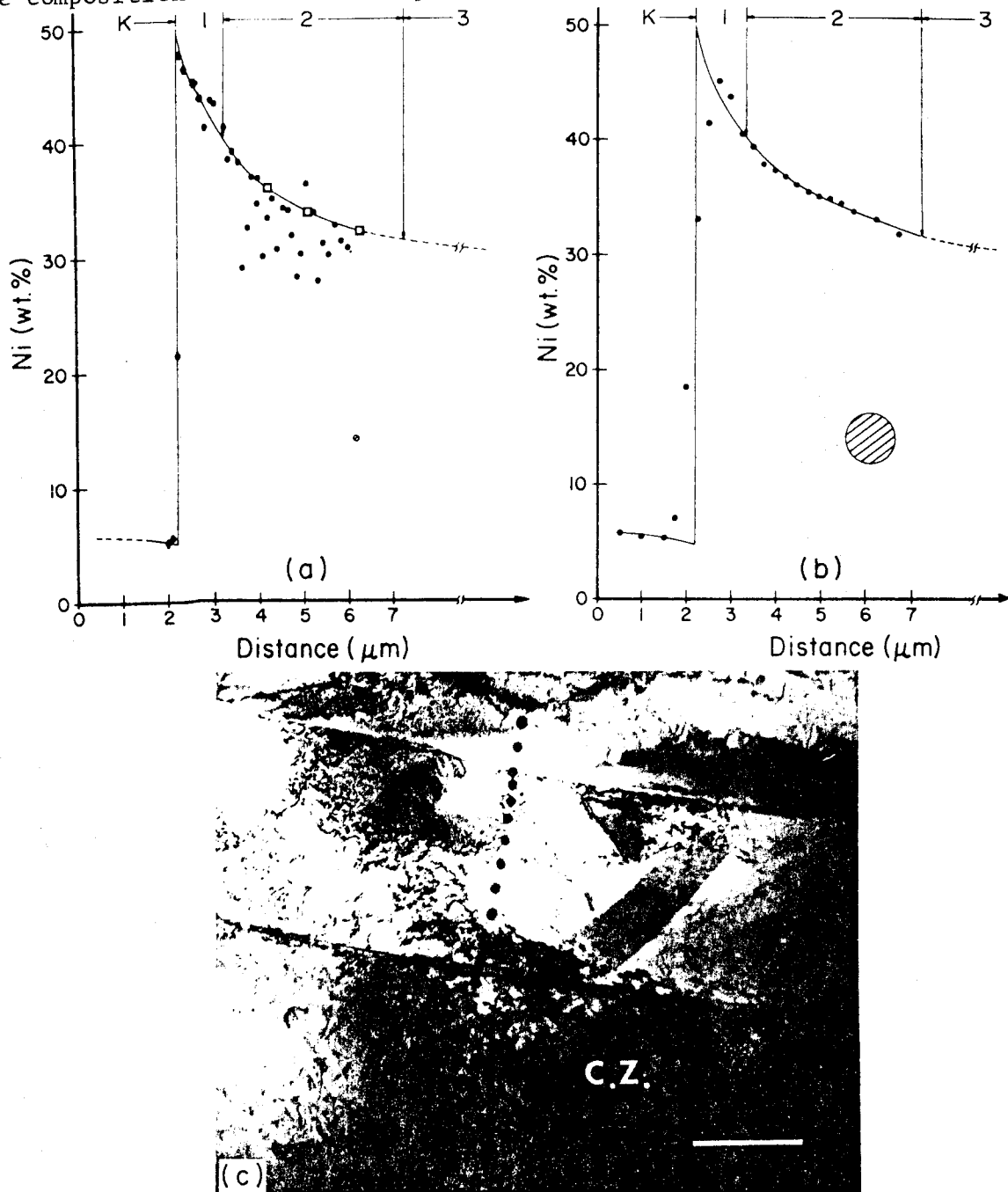

Figure 13 - a) Ni distribution in plessite (regions 1 and 2) as obtained by STEM X-ray analysis. The single circle below the plotted data indicates the X-ray spatial resolution obtained in this technique. b) Ni distribution in plessite (regions 1 and 2) as obtained by EPMA. The large circle below the plotted data indicates the X-ray spatial resolution obtained in this technique. c) TEM photomicrograph of the STEM X-ray analysis area. The black round contamination spots show the analysis points which correspond to the data points in a). Marker = 0.5 μm.

Lin, et al.[40] have investigated the various mechanisms for the formation of the fine structure (plessite) in iron meteorites using analytical electron microscopy techniques. The plessite is decomposed γ FeNi obtained on slow cooling of the iron meteorite. The study of plessite was complicated because approximately five different types or regions of microstructure are apparent and each region corresponds to different ranges of Ni content from 50 to 10 wt%. The plessite is also surrounded by the normal Widmanstätten pattern where plates of low Ni ($\sim 5 - 7\%$) bcc α FeNi have nucleated on the original {111} planes of the γ FeNi. The plessite structures are often submicron in size and contain platelets of γ FeNi, a honeycomb structure of γ and α FeNi and martensitic FeNi as well.

Lin, et al.[40] used a Philips EM 300 STEM operating at 100 kV to measure the Ni gradients at γ/α boundaries and within specific plessite structures. The thin foils were prepared by ion thinning. The electron beam was focused to a 20 - 30 nm diameter and the Cliff-Lorimer thin film method[16] was used to convert the X-ray intensities into wt%. Special precautions were taken to orient the thin film and α/γ interfaces in such a way to minimize spatial resolution. Figure 13 shows the Ni profiles across the kamacite/clear taenite I interface obtained by both STEM thin foil X-ray analysis (Figure 13a) and EPMA (Figure 13b) on a bulk specimen of the Carlton iron meteorite. In STEM X-ray analysis, data points were taken at steps of 50 - 100 nm. A TEM photomicrograph of the STEM X-ray analysis area is shown in Figure 13c. The improvement of spatial resolution in STEM (≤ 100 nm) as compared to EPMA (1 - 2 μm) is clearly shown. In addition, the Ni concentration at the interface obtained by STEM is always higher than by EPMA. The highest Ni content at the α/γ interface obtained by STEM X-ray analysis was 48 wt% (Figure 13a). The absolute accuracy of any one STEM analysis is approximately $\pm$ 5% relative. In the cloudy zone, (region 2) Ni concentrations were measured by both area scan and point modes. The square symbols in Figure 13a represent the data obtained by area scan mode (1 μm x 1 μm scan) and the solid circles represent the data obtained by point mode. The scattering of the point analysis data as obtained by STEM X-ray analysis is due to the presence of the fine α FeNi exsolution. The kamacite regions were too small to be resolved by the ~ 50 nm diameter X-ray source. The Ni distribution in each individual cell (γ phase) or surrounding wall (α phase) cannot be defined due to the high

critical value of ∼ 12 wt% in the vicinity of heat treated carbide-matrix interfaces. Diffusion calculations show that Cr depletion should only extend 1000-2000Å into the matrix from the chromium rich carbide ($M_{23}C_6$) matrix interface. The SEM-EPMA with its 1 μm spatial resolution is certainly inadequate for the task.

Pande, et al.[43] and Rao and Lifshin[44] used a JEOL 100C STEM and a JEOL 200 STEM respectively to measure such gradients at grain boundaries and at carbide-matrix interfaces in thin films of sensitized stainless (18 - 21% Cr, 8 - 12% Ni). Many of the precautions discussed in the earlier part of this tutorial were employed, particularly to minimize spurious X-rays. Special efforts were made to correctly orient the thin foil for maximum X-ray resolution. The Cliff-Lorimer thin film method[16] was employed for quantitative microanalysis. Values of k_{AB} were obtained directly using measurements with a defocused beam on known compositions of the matrix phase. Figure 12 shows the systematic determination of Cr, Fe and Ni concentrations by Rao and Lifshin[44] as a function of distance perpendicular to grain boundaries. The alloy was heat treated at $1121°C$ for 10 minutes and then water quenched. Subsequently it was heavily sensitized at $677°C$ for 24 hours and water quenched. Note the drop in grain boundary chromium concentration from about 21% in the austenite matrix to 5% at the grain boundary. These were the first studies[43,44] which were able to demonstrate that the postulated mechanism for sensitization was correct.
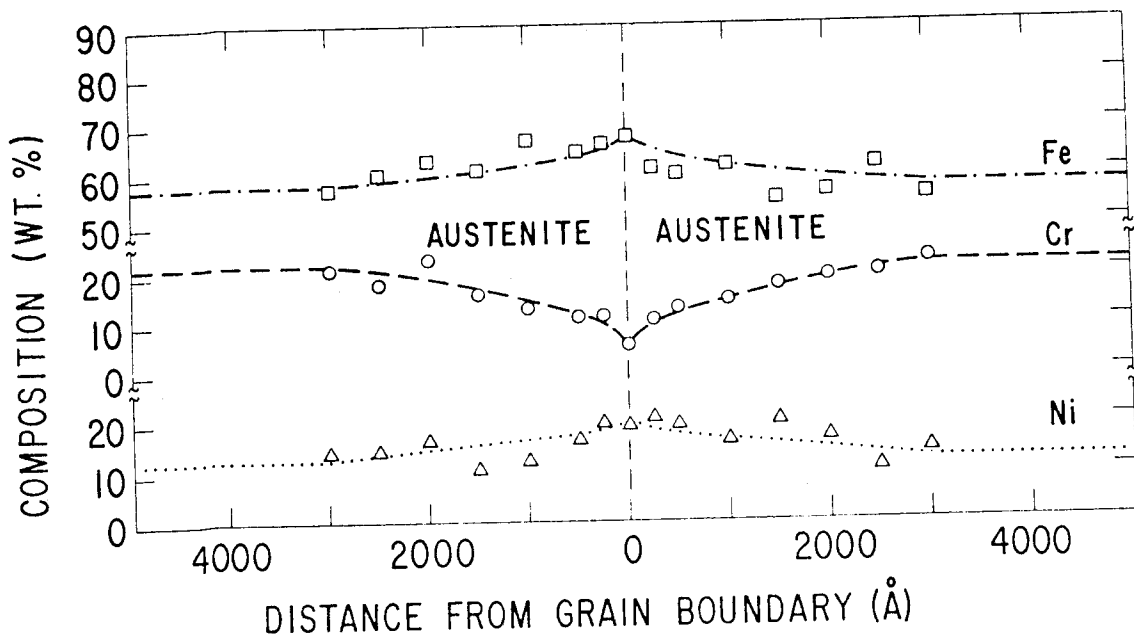

Figure 12 - Chromium, iron and nickel concentration profiles as a function of distance perpendicular to the grain boundary. Heavily sensitized condition-solution annealed, followed by 677°C heat treatment for 24 hours and water quenched.

$100A/cm^2 - 1000\text{Å}$). For the smaller probe diameter of 100Å the MMF ($15 < Z < 40$) is only ~ 3 wt% at 100 kV. In this case the MDM is $\sim 3 \times 10^{-19}$ g. If the precipitate is larger, $> 1000\text{Å}$, or if the compositional gradient occurs over regions of a micron or more, it is advantageous to use a larger spot size, $\sim 1000\text{Å}$, and higher current densities. In this case, the MMF ($15 < Z < 40$) is reduced to 0.2 wt% at 100 kV. The minimum detectable mass increases however to $\sim 1.5 \times 10^{18}$ g. As a comparison MMF values of ~ 0.01 wt% at 30 kV are typical for a SEM-EPMA using a wavelength dispersive detector.[6] The probe diameter is $\sim 1 \mu m$ and the minimum detectable mass is $\sim 10^{-15}$ g.

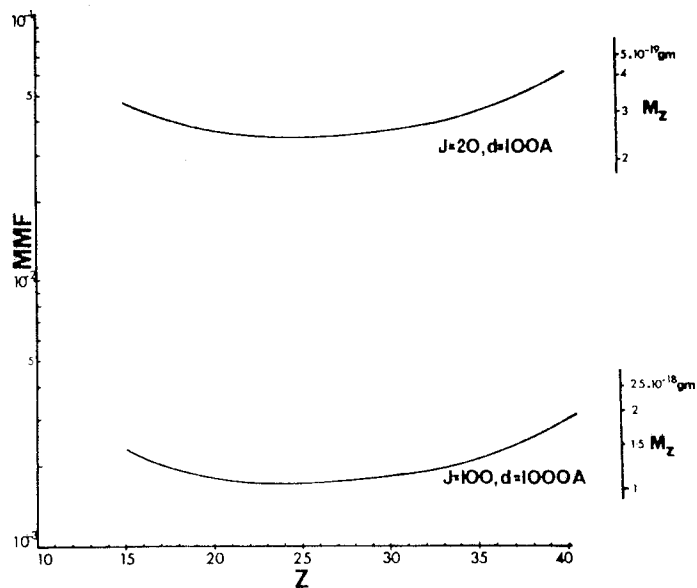
Figure 11 - Calculated minimum mass fraction (MMF) and minimum detectable mass (M_Z) versus element Z in a silicon matrix (see text for details).

Applications

The number of published STEM microanalysis papers through 1977 is still relatively small. Rather than attempting to summarize all the reported data in the literature, a few successful applications of the technique will be cited as examples of what can be accomplished with the present instruments, quantitative analysis schemes, and a lot of hard work. Pande, et al.[43] and Rao and Lifshin[44] have explored the mechanism of sensitization in stainless steels which is responsible for intergranular stress corrosion cracking in weld heat affected zones. The mechanism for sensitization postulated over 40 years ago was that chromium was depleted to below a

Sensitivity Limits

The sensitivity limits for STEM analysis are defined by the minimum detectable mass (MDM) and the minimum mass fraction (MMF). These limits are determined by several factors such as the spurious X-ray count rate, the efficiency and collection geometry of the EDS detector and the cross sections for the production of characteristic and continuum X-radiation. The spurious X-ray effects were discussed in a previous section. Clearly these effects must be minimized, that is decreased below the continuum count rate from an average sample if minimum sensitivity limits are to be achieved. Joy and Maher in a recent paper[41] have discussed the optimization of sensitivity limits and some of their conclusions are summarized here.

The MDM is a measure of the sensitivity in identifying an unknown element where they are free, or in a weakly scattering matrix. The background from the STEM system is the limiting factor in the analysis and the background from the substrate can be neglected. The MDM is the important parameter in analyzing individual particles on extraction replicas, sputtered thin films, stained biological sections, etc. Joy and Maher[41] have developed the appropriate equations for describing this type of sample and have shown that the MDM of an element $(10 < Z < 40)$ is of the order 5×10^{-20} gms for 100 sec counting time, an incident current density from a thermionic emitter of $20A/cm^2$ and accelerating voltages in the range 60 - 100 kV. This result is based on measured and calculated ionization cross sections and the use of Poisson statistics to assess the validity of a characteristic peak. Shuman, et al.[27] have also developed a method to optimize the MDM and have shown the MDM, in a 100 sec. collection time using a thermionic gun, to be $\sim 10^{19}$ g in agreement with previous analyses of the iron core of single ferritin molecules.[42]

The MMF is a measure of the sensitivity of detecting one element in the presence of another. The continuum radiation from the matrix is the limiting factor in the analysis. The MMF is the important parameter in analyzing precipitates or compositional gradients in a metal alloy, silicate, oxide or other material. Joy and Maher[41] have also developed theoretical expressions for the minimal mass fraction in STEM microanalysis. Figure 11 shows the calculated MMF and minimum detectable mass (M_Z) versus Z in a 1000Å thick crystal of silicon for 100 kV operation.[37] Two sets of current densities and probe diameters are considered $(20A/cm^2 - 100Å$, and

with conventional (electropolished and ion thinned) thin specimens, even if the analysis probe had, effectively, zero diameter.
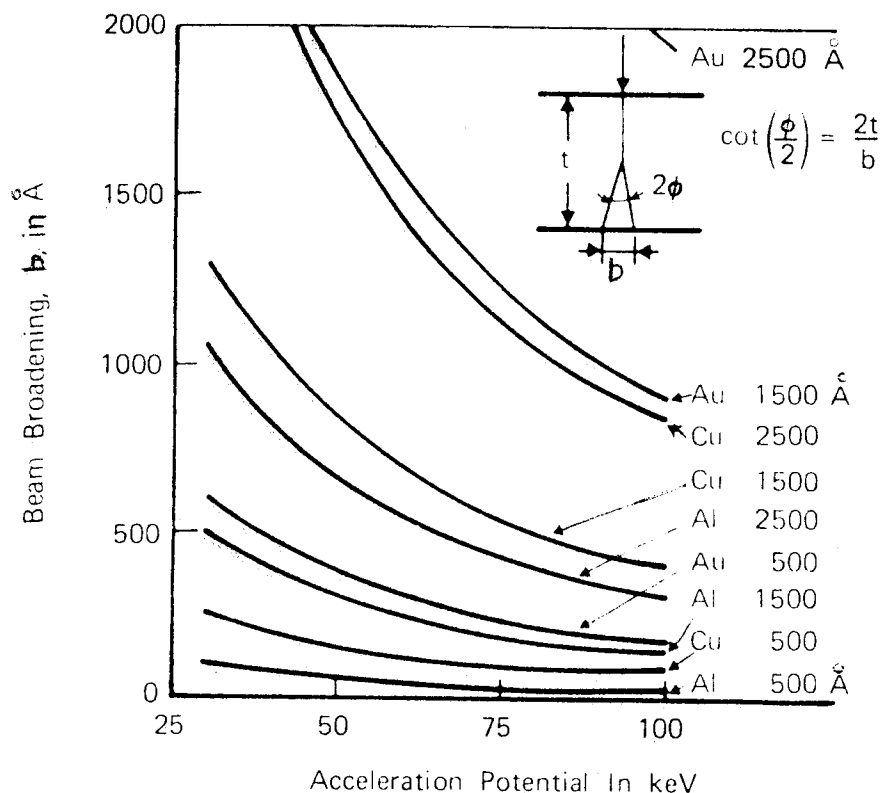

Figure 10 - Electron beam broadening, b, due to elastic scattering predicted by Eqn. (9). The broadening is plotted as a function of primary electron beam energy for various thicknesses (500, 1500, and 2500Å) of Al, Cu, and Au. The schematic inset illustrates the relationship between broadening and thickness suggested by Goldstein, et al. [18]

Monte Carlo calculations of beam broadening have been performed by Kyser and Geiss. [38] These calculations should be expected to provide the best results because they include such effects as the electron beam size, electron back scattering, multiple scattering, etc. In general, the relatively good agreement between the results of the simple scattering model and the Monte Carlo model tends to validate Eqn. (9). Few experimental measurements of X-ray resolution are available in the literature. [3] Although at present direct comparisons between measured and calculated resolutions have not been made both Easterling [39] and Lin, et al. [40] report X-ray spatial resolutions of ∼ 50 nm in TEM/STEM instruments. These measurements were made from point by point analyses across phase interfaces of Ag rich precipitates in an Al matrix and Ni poor precipitates in an Fe-Ni matrix respectively. Each of these show considerable broadening of the electron probe in the thin film.

The effectiveness of these non-penetrating cryoprotectants in suppressing the formation of intracellular ice to nanometre dimensions in single cells and tissue blocks has been used to advantage in elucidating the fine structural details of cells.

Both the PVP and HES used in our studies have molecular weights of a magnitude that render penetration of the cell by diffusion very unlikely. Under these circumstances, the content of the cells is unlikely to be seriously altered by treatment with these solutions. As a result, pre-fixation of the tissues is unnecessary and opens up the possibility of deep intracellular etching of cells, quench cooled in a physiologically active state. The polymers have also been used to provide mechanical support for cells and tissues fractured at low temperature and examined in the frozen-hydrated state in the scanning electron microscope. Because the polymer does not penetrate the cells and tissues it is possible to etch the fracture surfaces to reveal further morphological details.

The exact way in which these polymers protect cells during freezing is not entirely clear. It is unlikely that extracellular vitrification can promote similar vitrification of the cell contents, because it is difficult to envisage a mechanism of freeze prevention below the homogeneous nucleation temperature of the cytoplasm which must be in the neighbourhood of 230 K. An alternative explanation for the observed results is that the rigorous exclusion of heterogeneous nuclei in the extracellular spaces makes it possible for the cytoplasm to subcool to the homogeneous nucleation temperature, and that freezing at this temperature results in very small ice crystals.

The cryoprotective effect of PVP and HES is not limited to cells in direct contact with the polymer solution. Blocks of tissue up to 1 mm in diameter show evidence of good protection right into the centre of the tissue mass. This would imply that the polymers influence the degree to which the extracellular water in the intercellular spaces can be subcooled as well as in the cells themselves.

Radiation Damage In Biological Specimens At Low Temperatures.

Robert M. Glaeser, Division of Medical Physics, University of California, Berkeley and Donner Laboratory, Lawrence Berkeley Laboratory.

Organic materials are susceptible to severe structural damage when exposed to ionizing radiation in doses as high as 10^9 rad or more. Bond rupture and the loss of crystalline order are perhaps the most fundamental effects that are of concern to those who are interested in direct imaging at high resolution. Net mass loss, selective loss of certain elements, beam induced migration of materials, and bizarre dimensional or morphological changes are among the consequences of radiation damage that can be observed at lower resolution. Some of these latter problems appear to be even more severe in frozen hydrated specimens than in dried specimen materials. Very low temperature (about 10°K to 20°K) can essentially stop mass loss from occuring in anhydrous specimens, but mass migration on a scale of at least 100Å has still been observed to occur. Bubbles or voids with dimensions of a few hundred Ångstroms form in frozen hydrated specimens at -120°, but experiments at lower temperatures have not yet been reported. Most radiation damage experiments have been designed with high resolution microscopy in mind, so it is not yet clear what all the consequences and limitations will be in the area of microanalysis. A program of experimental investigation that is of direct importance to applications in microanalysis is clearly going to be needed in the near future.

FRACTURING OR CUTTING FROZEN SECTIONS
FOR ELECTRON PROBE MICROANALYSIS?

R. Gary Kirk and Gary H. Dobbs, III

Department of Physiology, Yale University, New Haven, CT. 06510
and
Department of Biology, Washington and Lee University, Lexington, VA. 24450

The controversy in cryo-ultramicroscopy studies as to whether or not a "cut" section is produced in the cryotome, or whether the knife is fracturing along structural planes in the biological sample, has been of special interest in our electron probe studies of single red blood cells. We have used human red blood cell membranes as structural planes to decide this basic issue because it is well documented that membrane fracture faces are formed by the fracturing of biological membranes within the structural plane of the lipid bilayer.

Surfaces of cut or fractured frozen red blood cells were replicated with platinum-carbon. Replicas were examined in an electron microscope for fracture faces. Our electron micrographs demonstrate that membrane fracture faces are only observed when sample and cryotome temperatures are less than -70°C. Fracture faces were never observed at temperatures above -70°C, which are routinely used in cryo-ultramicrotomy. We feel this to be strong evidence in support of the conclusion that sections are indeed being "cut" at the warmer (greater than -70°C) temperatures and "fractured" at the colder (less than -70°C) temperatures.

CRYOSECTIONING OF BIOLOGICAL SPECIMENS FOR X-RAY MICROANALYSIS.

Albert J. Saubermann, M.D. Department of Anaesthesia, Harvard Medical School, Boston, MA 02215.

Cryosectioning has been a major problem largely because of unpredictable consistency, and is perhaps one of the most problematic steps in cryospecimen preparation. Although cryosectioning is used for morphological reasons, histological reasons and for analytical reasons, this discussion will center around the use of cryosections for X-ray microanalysis of biological specimens. Cryosectioning is a poorly understood process and has been, historically, approached as a variant of conventional sectioning. However, at warmer temperatures sectioning is a shearing or cutting process while at colder temperatures cryosectioning becomes a fracturing process. Evidence for this can be found through direct measurement of the force of sectioning and by direct observation of surfaces of frozen hydrated sections. Sectioning can effect morphology and compartment identification, however there is not evidence for translocation or smearing effects upon elemental distribution in sections cut at warmer temperatures where fracturing is not occurring. The work of sectioning provides enough energy, were it all to go into the section to cause transient melting. Evidence against this is the appearance of a rough surface which occurs at lower temperatures (-80°C and below) while the absence of a rough surface at warmer temperatures suggest that there may be true cutting or melting. Sectioning can be optimized by using narrow angle knives, slow hand speeds, and clearance angles > 6°. The size of ice crystals within the tissue can effect sectioning, therefore good freezing is important for successful cryosectioning.

Low temperature scanning electron microscopy and X-ray
microanalysis of biological material

by

Patrick Echlin

Botany School, University of Cambridge, U.K.

The techniques of low temperature scanning electron microscopy
encompass both the examination and analysis of specimens on a cold stage
inside the microscope and the use of low temperatures during sample
preparation. The types of investigation which may be carried out using
low temperature methods may conveniently be divided into morphological
and analytical studies, although they are frequently interdependent.

The morphological studies include the examination of the external
features of soft labile specimens or the internal features of such
specimens which have been exposed using cryofracturing or cryosectioning
techniques. It is also possible to carry out dissection and
micromanipulation of frozen specimens inside the microscope. Although
new and interesting morphological information has been obtained using
low temperature techniques, the real advantage of these methods is to
be found in analytical studies. All the evidence suggests that the
analysis of diffusible ions and electrolytes can best be carried out
either on frozen-hydrated samples in which the cell fluids have been
immobilized and converted to a solid state, or on frozen-dried samples
in which the water component of the cell fluids is removed by
sublimation during tissue drying or freeze-substitution. The two
approaches are being used successfully in connection both with X-ray
microanalysis where the microscope is used as an analytical instrument
and cathodoluminescence where low specimen temperatures have been shown
to increase the chance of fluorescence by excited molecules.

Both types of work take advantage of the speed of cryofixation and
the substantial increase in the mechanical strength of water as it is
converted from a liquid to a solid state. There are other advantages
which may accrue from using low temperature methods. Cryofixation is
a physical process and as such can avoid the use of wet-chemical
preparative techniques which are now generally accepted as being
unsuitable for analytical studies involving unbound, diffusible elements.

Low temperatures immobilize the liquid state, arrest physiological processes and diminish the movement of dissolved substances in all but a few biological systems. Where specimens are examined at low temperatures inside the microscope the presence of large areas of cold surface result in a significant reduction in contamination, a higher vacuum pressure, and in the rate of thermal damage to the specimen. It had been expected that low temperatures would result in a substantial reduction in radiation damage to the specimen, but these earlier hopes have not been realized.

Low temperature techniques which avoid entirely any contact with chemicals or solutions should not, however, be considered as the panaceae for all morphological studies. In many instances, specimen preparation for the scanning electron microscope can be achieved more conveniently and effectively using ambient temperature methods alone or in combination with low temperature techniques. There are still problems with specimen preparation, manipulation and transfer at low temperatures, together with an incomplete knowledge of the freezing process in biological material, the redistribution of soluble constituents during freezing and the behaviour of frozen specimens during short- and long-term storage at low temperatures. Even if the specimen has been prepared adequately, there are very few cold stages which can maintain the specimen at 123 K or below, which is the temperature range needed to be able to carry out low temperature microscopy and microanalysis with little chance of the specimen melting.

There are four main types of specimen which may be prepared and examined using low temperature techniques. These are, thin sections (less than 100 nm), thick sections (0.1 μm to 2.0 μm), single cells or isolated organelles, and bulk samples. Each of the four types presents its own problem both from the point of view of specimen preparation and the information which it can provide. Some parts of the preparative procedure are common to all four types. By rapidly freezing small pieces of tissue it is possible to solidify the liquid phase of the cytoplasm and hopefully preserve structures and diffusible ions in situ. This phase change is, unfortunately, a crystallization process. Depending on the size, form and physiology of the specimen, and the speed at which the tissue is cooled to below the recrystallization point of ice, there are invariably ice crystals of varying size in the

sample. These ice crystals form at the expense of water in the system, and the solutes become progressively more concentrated. Under these circumstances the diffusible ions must move from their original positions in the cell, and if the ice crystals are particularly large, there may be serious distortion of the cell and tissue structure.

There is a popular misconception that water in biological samples can be converted to amorphous ice provided the sample is cooled at a sufficiently high rate. Unfortunately this cannot be achieved in practice as the amorphous state cannot be obtained by cooling <u>liquid</u> water because homogeneous nucleation starts at 233 K. (However, amorphous ice can be formed when water <u>vapour</u> condenses onto a very cold surface.) The situation is more complicated in biological materials because of the additional process of heterogeneous nucleation and the fact that samples vary in the amount of free water in their cells. The ideal solution to the problem would be to avoid crystallization entirely and attempt to convert the cell fluids to a solid aqueous state where no crystallization has occurred - the so-called vitreous or glass state. Only very small biological samples can be vitrified either as thin films up to 5 μm thick or droplets up to 10 μm in diameter. Under these circumstances the only acceptable alternative for most biological specimens is a microcrystalline state in which the water is converted to a large number of small ice crystals.

Although microanalysis could be carried out on thin films and small droplets of biological material, the main areas of current interest are centred on the analysis of small (c. 1-2 mm) pieces of tissue. As these specimens are a hundred times larger than the samples in which it is claimed that vitrification has occurred, serious ice crystal damage and re-location of dissolvable substances invariably occurs. Some of the problems associated with ice crystallization have been overcome either by infiltrating the specimens with penetrating cryoprotectants, or encapsulating the samples with non-penetrating cryoprotectants. Penetrating cryoprotectants such as glycerol and dimethyl sulphoxide although they are effective in preserving the morphological features of cells, cause such gross changes in membrane permeability that they are of little use in analytical studies of unbound and freely diffusible elements. Non-penetrating cryoprotectants such as polyvinylpyrrolidone (PVP) or hydroxyethyl starch (HES) do not suffer from these

disadvantages, and are effective in the preservation of ultrastructure as their penetrating counterparts. Studies have shown that these polymeric cryoprotectants do not appear to cause diffusible ions to leak from cells and tissues and that it is possible to measure concentration gradients across plant tissues which are embedded in these materials.

Quantitative X-ray analytical studies can only be effectively carried out on sectioned material. Although cryosectioning is now a fairly standardized procedure, there is considerable variation in the ease of sectioning different materials. Frozen animal material is more easily sectioned than plant material, and it is likely that the presence of cellulosic cell walls and large water-filled vacuoles are contributory factors to these difficulties. It has been shown that both PVP and HES when used at concentrations at which they are effective cryoprotectants are also effective embedding or encapsulating agents with excellent sectioning properties at low temperatures.

The material which is to be examined may be cut or fractured on some form of cryomicrotome. Thin sections are usually cut at temperatures between 130 K and 200 K on one or more of the various cryoultramicrotomes which are commercially available. The cutting temperature appears to be influenced more by the type of specimen than by any other factor, and it is clear that the actual process of cutting is far from understood. Thicker sections are prepared in a similar fashion although the cutting temperatures are somewhat warmer (240 K to 190 K). It is necessary to provide some sort of support for the sections and single cell and organelle isolates. Ideally this support should be electron transparent, conductive and make a minimal contribution to the signals generated in the section.

Depending on whether the analysis is to be carried out using energy dispersive or wavelength dispersive spectrometers, it may be necessary to apply a conductive coating to the specimen. This coating layer is usually 10-15 nm of carbon or aluminium deposited in a clean environment on the specimen maintained at least at 140 K. Sections which are analysed using diffracting spectrometers usually require a conductive coating because of the higher beam current used in this method. This is, however, not always the case and is the exception rather than the rule with specimens analysed using energy dispersive spectrometers.

Whether or not the specimens have to be coated, it is necessary to transfer them to the electron beam instrument which is to be used for the examination and analysis. This transfer must be done under conditions which ensure that the specimen remains frozen-hydrated and does not melt, sublime or become contaminated. Similarly, it is necessary to ensure that the specimen is kept sufficiently cold and clean during the actual process of analysis. Changes in the mass of the specimen, either by contamination or sublimation of ice, can seriously distort the experimental result and elemental mass ratios. The specimens must also be maintained at low temperatures inside the microscope during examination and analysis. The specimen temperature should not be allowed to exceed 130 K during analysis, and lower temperatures are preferable.

The environment surrounding the specimens must be carefully monitored during all phases of preparation, examination and analysis. Constant checks must be made on the temperature of the specimen, the total pressure and partial pressure of water in the system and on the level of residual gases surrounding the specimen. This is necessary, certainly in the initial phases of any investigation, to ensure that the specimen remains in the frozen-hydrated state.

Applicability of the Biochamber to Preparation

of Cold Biological Samples for X-ray Microanalysis

by James Pawley

Donner Lab, UC Berkeley

In the microanalysis of biological material it would seem safe to say that isolating the sample and introducing it into the appropriate instrumentation pose even greater practical and theoretical problems than the subsequent analysis of the resulting spectra. Although much effort has been expended on the latter, until recently only a few individuals have developed workable systems for the former. Recently several companies, ETEC, CAMECA, and AMR, have introduced cold sample handling equipment as attachments to their electron probe instruments. This paper will discuss our experience with the last of these: the AMR Biochamber.

This unit consists of a separately pumped high vacuum specimen preparation chamber which communicates with the specimen chamber of an AMR-100A SEM through a gate valve. Frozen samples may be inserted into this chamber through an airlock using a holder which prevents condensation of atomospheric water vapor onto the sample. This airlock is also used to attach carbon or metal evaporating devices to the system, and permits them to be removed to recharge their evaporants at any time. During evaporation, the sample and the source can be viewed through windows and the sample can be tilted (0-90°) and rotated while mounted on a shuttle attached to a cold copper block. The shuttle can be moved by an insulated push rod between stations for coating/insertions, fracturing and SEM examination. In the fracturing position atop the LN_2 reservoir, a cold knife, whose height can be adjusted in 5 μm increments.

moves horizontally across the sample surface. Its action can be viewed with a 10-100x stereo microscope.

The SEM cold stage is cooled by a Joule-Thomson refrigerator which permits high pressure (1500 psi) nitrogen gas to expand in a counter-current heat exchanger. The temperature of the shuttle can be measured and controlled (using ohmic heating) in the fracturing and examination positions. Sample temperatures need not rise above -170°C during the entire preparation of a freeze fracture sample and temperatures as low as -196°C can be attained in the SEM.

The features of this system which commend it to the X-ray micro-analysis are its ability to introduce sample without frost contamination and to coat cold samples with carbon as well as metals. Complementary fractures of thin films of frozen liquids have been observed and the ability to analyse both sides of such a fracture may be important in some studies.

At the present time there is no system for the handling and examination of transmission samples but we plan to develop these in the near future.

FROZEN-HYDRATED SECTIONS. P.D. Peters. Department of Anaesthesia,

Harvard Medical School, Boston, Mass. 02215.

The first step when tackling a new problem of elemental distribution

determination in biological tissue is to decide upon the best approach

for that particular problem. Assuming that the tissue is to be examined

by X-ray microanalysis, there is a choice between chemical or cryo-

fixation. It has been adequately established that chemical fixation

can distort the ionic distribution, so cryofixation must be used.

There is then the choice of whether to analyse frozen-dried, frozen-

substituted or frozen-hydrated tissue. Because of the difficulty of

determining whether ionic relocation has occurred with the first two

methods, frozen-hydrated analysis is the method of choice.

Small cubes of tissue ($\sim 1mm^3$) are frozen in either melting freon

or solid/liquid nitrogen slush. The tissue is transferred under liquid

nitrogen to the cryochamber of a Sorval MT2 microtome. There is then a

choice of cutting temperature, cutting speed, section thickness, knife

angle, knife material and clearance angle. These parameters will be

discussed.

For transfer to the cold stage in the electron microscope, the

sections are transferred on an eyelash onto a carbon-coated nylon

film stretched over a C or Be specimen stub. The sections are

encouraged to adhere to the film by the application of light pressure.

The stub is then transferred to the cold stage of a vacuum-transfer

system, and subsequently transferred to the cold stage of the electron

microscope.

It is then possible to see just what has been happening during

the "sectioning" process, and decide what information can be obtained

from this piece of frozen tissue. A secondary electron image will

show the surface contours of the section and so it can be inferred how the cutting has occurred, and this is correlated with information on the forces during cutting. A scanning transmission electron image shows the cellular detail within the tissue, and enables areas to be selected for analysis. The tissue can be further analysed when it is dry, to obtain an idea of additional morphological detail, and also to ascertain that the tissue had previously been fully hydrated. The electron images can also be correlated with stained tissue viewed in a light microscope.

A study on mouse liver will be described and the choice of optimum values of the various parameters will be discussed.

A NEW PROCEDURE FOR PREPARING BULK FROZEN-HYDRATED BIOLOGICAL
SPECIMENS FOR X-RAY MICROANALYSIS

P.A. Burgio*, W.C. Low** and M. Lawrence*

*Kresge Hearing Research Institute, University of Michigan Medical School,
 Ann Arbor, Michigan 48109.
**Bioelectric Sciences Laboratory, University of Michigan, Ann Arbor,
 Michigan 48109.

INTRODUCTION

A new procedure has been developed to prepare bulk frozen-hydrated specimens for quantitative x-ray microanalysis. This approach is unique because several important features are incorporated into one method: 1). The specimen is maintained at temperatures colder than -160°C from the time the tissue is in the animal until it is viewed in the scanning electron microscope. 2). A flat and smooth surface can be rapidly and reliably exposed in any plane of the specimen. 3). The take off angle can be determined and adjusted for maximum collection efficiency. 4). Also, intracellular details can be revealed in any part of the specimen.

METHODS

Animals were anesthetized and prepared for surgery. The tissue of interest was surgically exposed and quenched in freon -22 chilled by liquid nitrogen (LN). From this point on, the specimen is maintained in a LN bath until it is transported to the cold stage. A small circular saw was used to remove the tissue from the animal and to prepare it for the specimen holder.[1]

The specimen was precisely shaped to conform to the shape of the receptacle in the specimen holder by a thin cutting wheel. The wheel was driven by a variable speed Dremel 280 moto-tool. The precisely shaped surfaces of the specimen were fine polished to assure good thermal conduction between the specimen and the holder. Thermal conduction was further enhanced by a thin layer of aluminum foil between the tissue and the holder. The tissue was then secured in the receptacle of the holder and the viewing surface prepared.

Under a dissecting microscope the area of interest on the specimen was exposed by high speed cutting with the Dremel 280 moto-tool. It is essential this be done well below the surface of LN and the cutting surface of the Dremel be cooled to LN temperature. The cutting tool is guided by a jig to assure that the surface of interest is flat and smooth and is on the same plane as the surface of the specimen holder. At this point a polaroid picture or a sketch of the prepared surface can be made, to assist in the identification of cell groups and even individual cells during the initial stages of observation when minimal surface morphology is evident. This information is an aid in locating specific cell types or specific cells of interest when minimal amount of morphology is evident during the initial stages of sublimation.

The specimen is transferred from a LN bath to the cold stage of the SEM in a specimen holder[1] which was designed to prevent the generation of artifacts. When the specimen reaches the cold stage, the specimen temperature is about -160°C. The flat surface of interest is normal to the electron beam when the holder is placed on the cold stage, so the goniometer can be used to adjust the take off angle for maximum collection efficiency.

1. A description of the design and unique features of the specimen holder is in preparation.

THIRTEENTH ANNUAL CONFERENCE

OF THE

MICROBEAM ANALYSIS SOCIETY

PROCEEDINGS

MECHANISM OF OXYGEN ENHANCEMENT OF SPUTTERED ION YIELDS

Peter Williams

Materials Research Laboratory
University of Illinois
Urbana, Illinois 61801

Introduction

There exists to date no detectable consensus concerning the mechanism of secondary ion emission. Unanswered questions include whether ion emission is controlled by atomic effects ("bond-breaking"[1]), bulk effects (band structure[2]) or surface effects (work function[3]), and whether ion yields are determined by collision events within the surface[1] or by electron transitions external to the surface.[2] The most striking phenomenon in secondary ion studies -- oxygen enhancement of positive ion yields -- can be rationalized using almost any of the existing models.[1-3]

We have recently demonstrated that oxygen enhancement of negative ion yields[4] is a general phenomenon.[5] If we insist that a general model of sputtered ion emission should explain oxygen enhancement of both positive and negative ion yields from the same bombarded surface, then the bond-breaking model (efficient formation of M^+ by sputtering from an ionic M^+O^- lattice) fails, and the simple work function and band structure models are inadequate. Our observations are extended here to substantiate a model in which ion yields are determined by electron transitions between the surface and the departing sputtered atom, and in which the probability of electron transitions to or from the atom depends on the height of the local surface potential barrier at the sputtering site. This barrier height is determined by the strength and orientation of the surface dipole at the sputtering site.

Experimental

The effects of oxygen gas on ion yields from an Ar^+ ion-bombarded semiconductor, silicon, and a metal, copper, are shown in Figures 1 and 2. Positive ion yields are dramatically enhanced by oxygen; negative ion yields exhibit a more modest increase. When the oxygen is pumped out, the two ion yields return to the clean surface values, but with marked differences in initial behavior and overall decay rate, as illustrated in Figures 3 and 4. Both Cu^+ and Si^+ yields fall rapidly, at a rate consistent with the pumping speed of the sample chamber for oxygen. However, the Cu^- and Si^- yields show an initial sharp increase, when the oxygen inlet valve is closed, and thereafter fall only slowly. Other elements show similar behavior.

The rapid decay of positive ion yields is consistent with the rate of removal by sputtering of an adsorbed oxygen layer. The negative ion increase is correlated with the positive ion decrease, and therefore also with adsorbed layer removal. These results indicate that adsorbed oxygen must inhibit negative ion emission, as would be predicted by the existing ion

emission models.[1-3] The slow decay of the negative ion signal is consistent with the rate of removal of a recoil implanted oxygen component.[2] Enhancement of negative ion yields thus appears to be caused by recoiled, i.e., subsurface, oxygen.

Ion Emission Models

The effects reported here are completely at variance with the predictions of the bond-breaking model,[1] and with the simple work function model.[3] They may be rationalized by either a surface polarization model, which considers the effects of surface heterogeneity on an atomic scale, or by extending band structure concepts to incorporate the effects of oxygen on electron excitation within the sputtered surface.

Resonant and Auger electron transitions between a surface and a departing sputtered atom are thought to be extremely rapid.[6] The probability of such transitions is an inverse exponential function of the distance of the atom from the surface, i.e., the interaction is short-range. We postulate: (i) the charge state of the sputtered atom is overwhelmingly determined by electron transitions occurring as the atom departs (ii) the surface region with which the atom interacts is electronically excited, due to the inelastic surface collisions accompanying the sputtering event.

Surface Polarization Model (Figure 5)

We must rationalize the fact that oxygen enhances both positive and negative ion emission from the same macroscopic ion-bombarded surface. A logical conclusion is that the surface is microscopically heterogeneous. The availability of electrons in the surface region at an appropriate energy to neutralize a departing positive ion or to attach to a departing neutral will depend strongly on the energy difference between the acceptor states in the sputtered species and the electron distribution in the surface. A change in the surface potential barrier can change this energy difference. Oxygen adsorption on the surface can increase the potential barrier. Conversely, oxygen incorporation beneath the layer of surface atoms can result in a lowered potential barrier due to the orientation of the surface dipole formed by the oxygen and the more electropositive surface atom. On an oxygenated, ion-bombarded surface, both adsorption and incorporation (recoil implantation) occur. The sputtered atoms interact strongly only with those few atoms immediately surrounding the sites which they vacate. We postulate that the sputtered surface contains many sites, consisting of one to several atoms, at which either oxygen is incorporated beneath the surface (producing an electron-emissive, or negative ion-forming site) or oxygen is adsorbed on the surface (leading to an electron-retentive, or positive ion-forming site). Such sites are postulated to dominate the emission of negative and positive ions, respectively, giving rise to the observed oxygen enhancement effects.

Band Structure Model

As illustrated in Figure 6 for the case of silicon, oxygen enhancement of positive and negative ion yields can also be rationalized using oxide

band-structure concepts. Oxygen may enhance positive ion yields by lowering the energy of valence band electrons to such a level that they become unavailable for neutralization of departing positive ions.[2] We may postulate that negative ion formation proceeds by attachment, to departing sputtered atoms, of electrons collisionally excited into the conduction band. Because thermalization is extremely rapid, such electrons in pure Si, or metals, rapidly become unavailable for attachment. In the oxide the conduction band edge is raised and thermalized electrons may retain the appropriate energy for resonant attachment. Thus _if_ oxygen adsorption/ recoil implantation produces oxide-like band structure, negative ion enhancement may be rationalized. Similar arguments can be adduced for metals and other semiconductors.

Test of Model

To distinguish between the surface polarization and band structure models, the influence of oxygen on ion yields from gold was studied in detail. On ion yields from pure gold under Ar^+ bombardment oxygen has only a minor effect, as shown in Figure 7. The lack of polar Au-O bonds is consistent with this observation. Incorporation of aluminum into the gold lattice should (a) provide active adsorption sites, (b) produce highly polar Al-O dipoles with oxygen. As illustrated in Figure 8 these sites should then act to strongly enhance the yields of _gold_ ions -- both $\underline{Au^-}$ and $\underline{Au^+}$. That this prediction is verified, for an Au-5 at% Al alloy, is shown in Figure 9.

Because the solubility of Al in Au at room temperature is only 0.3 at.%,[7] a 5 at.% alloy will contain Al-rich precipitates. It is arguable that, upon adsorption of oxygen, Al_2O_3 -type band structure could result in such precipitates. A further experiment was therefore performed, using samples of gold into which aluminum had been introduced by ion implantation. In many systems it is known that ion implantation to levels in excess of the solubility limit does not result in precipitation.[8] However, to avoid any question of precipitation, a sample of gold was examined in which the _peak_ Al concentration was about 0.3 at.% i.e. below the solubility limit. Figure 10 shows the results obtained with this sample when a depth profile through the Al implant region was performed using Ar^+ bombardment and high ambient oxygen pressure. Al segregation to the surface is responsible for the initial high yield of Au^- ions. After the surface layer has been sputtered, the increase (20%) in Al concentration to the peak of the implant profile _is_ seen to cause a small(5%), but statistically significant increase in the Au^- ion yield. For this dilute sample (containing _atomically dispersed_ aluminum) bulk Al_2O_3 band structure concepts cannot apply. Thus the ability of single, highly polar, atomic sites to influence sputtered ion yields is confirmed.

Conclusion

Secondary ion emission is a complex process. If bulk oxide band structure concepts are to be applied to the case of oxygen adsorption, it is essential to consider what is the band structure at an ion-bombarded, oxygenated sputtering site _during the sputtering event_. It may well be that the simple bulk band structure concepts outlined here are inapplicable, but that the

overall effect of oxygen should still be to lower ground state electron energies and to retard thermalization of excited electrons.

With this work we have demonstrated that models in which ion formation is controlled by the probability of electron transfer between the surface and the sputtered species can qualitatively explain oxygen enhancement of both positive and negative ion yields. Electron transfer, in turn, is strongly influenced by the polar nature and orientation of the sputtering site and it has been shown in accordance with the surface polarization model, that isolated, highly polar sites of atomic dimensions are capable of significantly influencing sputtered ion yields.

Acknowledgements

References

1) G. Slodzian and J-F. Hennequin, Compte Rendu (Paris), 263, 1246, (1966).

2) R. Kelly and C.B. Kerkdijk, Surface Science 46, 537 (1974).

3) V. Krohn, J. Appl. Phys. 33, 3523 (1962).
   C.A. Andersen, Int. J. Mass Spec. & Ion Phys. 3, 413 (1970).

4) J.M. Morabito, R.K. Lewis and J.C.C. Tsai, Appl. Phys. Lett. 23, 260 (1973).

5) P. Williams and C.A. Evans, Jr., To be published.

6) H.D. Hagstrum, Phys. Rev. 122, 83, (1961).

7) M. Hansen, "Constitution of Binary Alloys", 2nd Ed. McGraw-Hill 1958.

8) J.M. Poate, J.A. Borders, A.G. Cullis and J.K. Hirvonen,
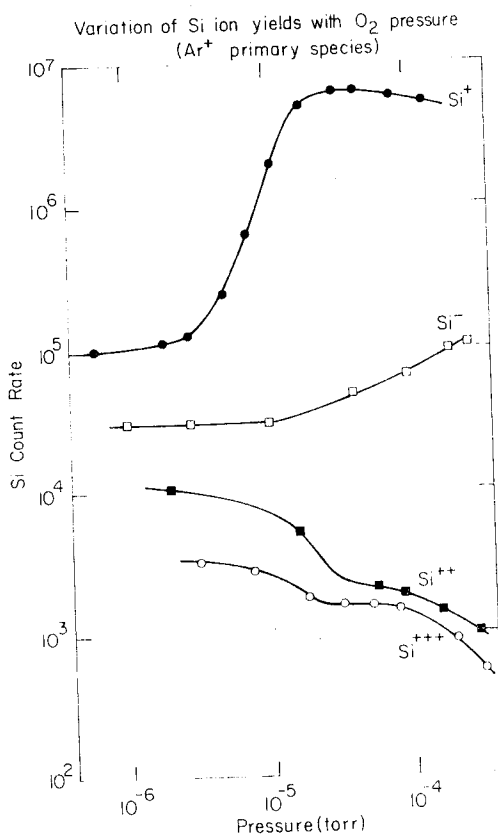   Appl. Phys. Lett. 30, 365, (1977).
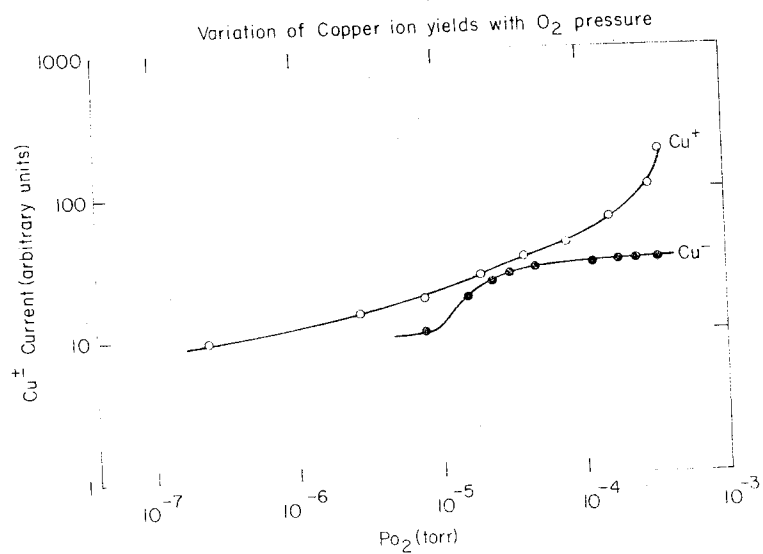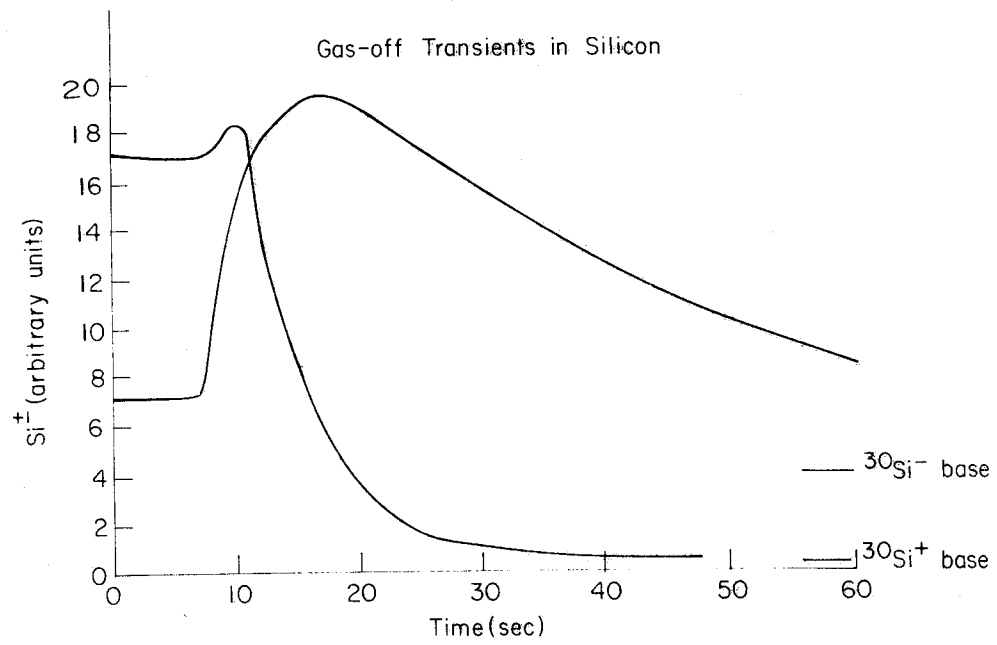
Variation of Si ion yields with O_2 pressure
(Ar+ primary species)

Figure 1

Variation of Copper ion yields with O_2 pressure

Figure 2

Figure 3

Figure 4

Positive Ion Site   Negative Ion Site

Surface Polarization Model
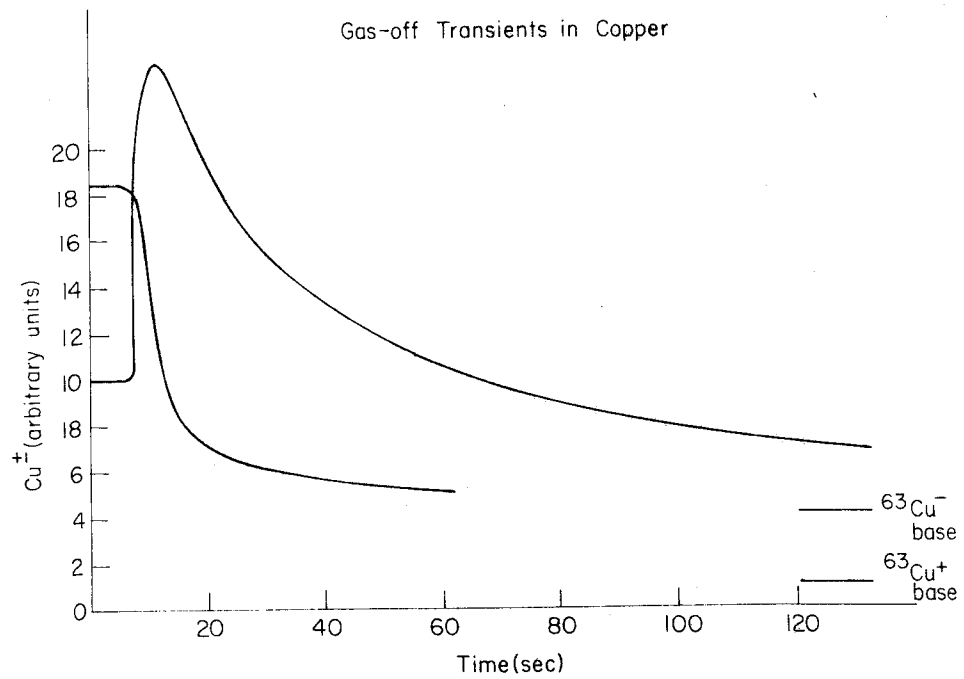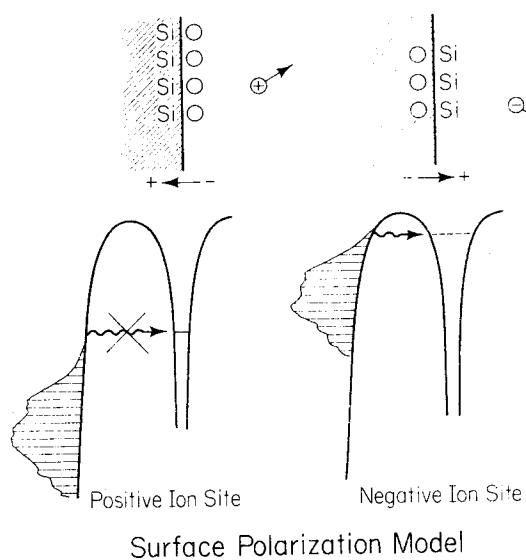
Figure 5

Oxygen Enhancement of ± Ion Yields
Band Structure Model

Silicon   Si Atom/Ion

Silicon Dioxide   Si Atom/Ion
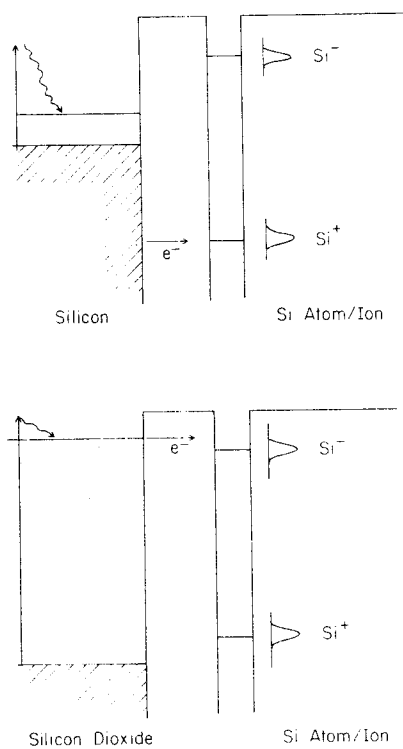
Figure 6

OXYGEN ENHANCEMENT – PURE Au
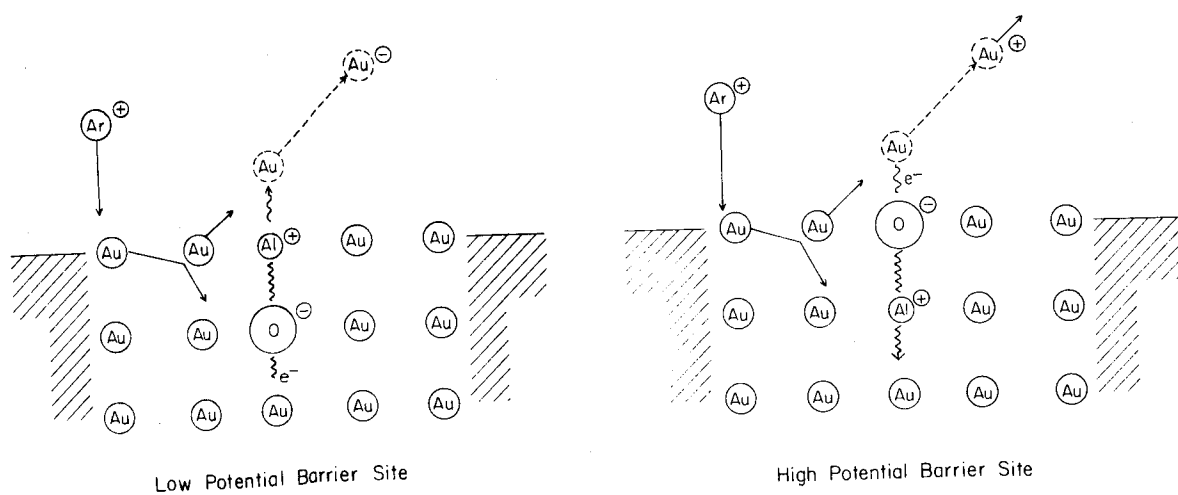

Figure 7

Low Potential Barrier Site

High Potential Barrier Site
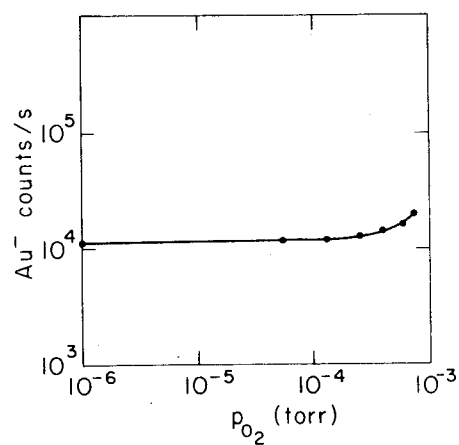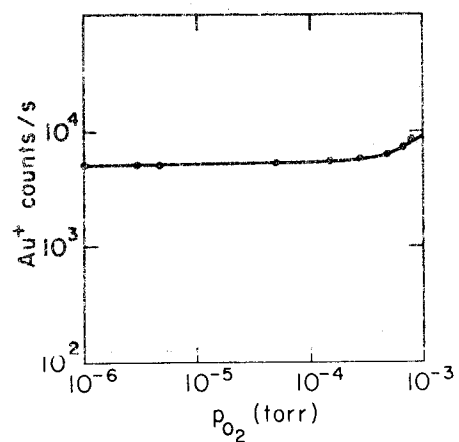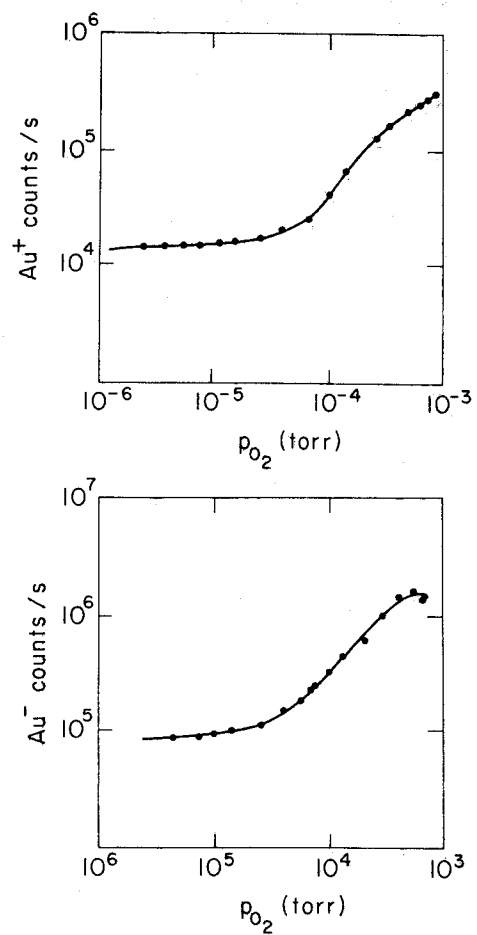
Figure 8

OXYGEN ENHANCEMENT – Au (5% Al)
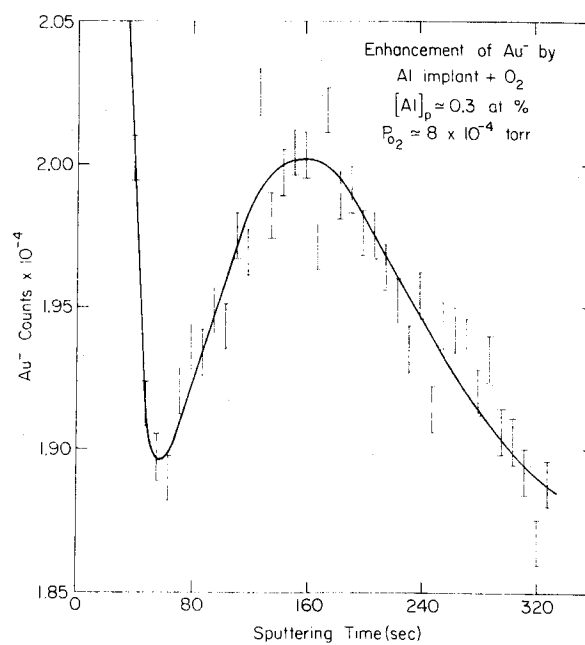

Figure 9

Figure 10

A ONE FITTING PARAMETER METHOD FOR QUANTITATIVE SIMS

A.E. Morgan and H.W. Werner

Philips Research Laboratories

Eindhoven, The Netherlands

Quantitative SIMS analyses to an accuracy of a few % will most probably always require the use of standards of a similar matrix. Our aim has been to obtain a semiquantitative analysis directly from the measured ion currents without recourse to the tedious preparation of suitable standards. To this end, we have been examining the usefulness of an LTE-type approach utilising only one fitting parameter, "the ionisation temperature" T_i. This parameter may be derived directly from the sample if one or more concentrations are known (internal standards). Of more practical interest, however, is the ability to analyse a specimen with no known concentrations which therefore entails prior knowledge of T_i. We have thus been investigating the properties of this parameter using metal, oxide and halide standards.

Positive secondary ion currents I resulting from 6 keV Ar^+ or O_2^+, or 15 keV O^- bombardment of the standards have been measured using the Cameca IMS 300 instrument (single-focussing with ion mirror). Oxygen gas was introduced when necessary to saturate the secondary ion emission. A 20 eV energy window was used, and optimisation of the instrumental settings for each mass number of interest was found necessary to obtain satisfactory and reproducible results.

For each standard, a plot of $\log(I_M + M_i^{\frac{1}{2}} Z_{MO} / c_M Z_{M^+})$ vs. E_M was made where M_i is the mass number of the measured isotope, c_M is the atomic concentration of the element M, Z represents an electronic partition function (which is temperature-dependent), and E_M is the first ionisation potential. The origin of the empirical $M_i^{\frac{1}{2}}$ term, whose inclusion was found always to reduce the scatter of experimental points around the straight line, is presently under investigation. T_i was derived from the least-squares slope ($= (kT_i)^{-1}$). Computer iteration was made until the temperature used for Z coincided to within 1 % with that calculated from the slope.

Ordinate values deviating by less than a factor of two from the least-squares fit were considered satisfactory for

analytical purposes. This criterion could not always be met if insufficient oxygen was present to saturate all M^+ currents, Fig. 1. The T_i value of a given sample increased with oxygen
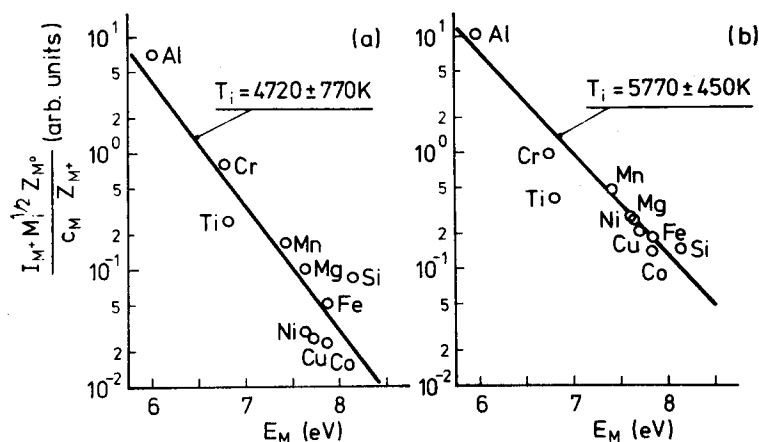

Fig. 1. Plots of $(I_{M^+}M_i^{\frac{1}{2}}Z_{MO}/c_M Z_{M^+})$ vs. E_M for 6 keV Ar^+ bombardment of a NiO standard (NBS 671) utilising 0-20 eV sec. ions; a) from measurements in vacuum, b) from measurements in an O_2 atmosphere.

admission until saturated secondary ion emission was achieved and then remained essentially constant. The factor by which the ordinate value for a given element deviated from the least-squares line turned out for most elements to be fairly constant from one standard to another. Knowledge of these factors permits empirical corrections to be applied to measured ion currents in order to improve analytical accuracy. However, far too high secondary ion yields were sometimes found for those elements beyond $E_M \approx 12$ eV. For instance, a large deviation was measured for oxygen unless $T_i \gtrsim 8500$ K. The reason for this behaviour is uncertain.

Relatively low atomic ion yields were found for those elements (e.g. see Ti in Fig. 1b)) with appreciable MX^+ (and sometimes also MX_2^+) currents, where X represents an oxygen or a halogen atom. In these instances, the ordinate deviation was directly related to the amount of molecular ion formation, Fig. 2; several values for one standard were obtained by
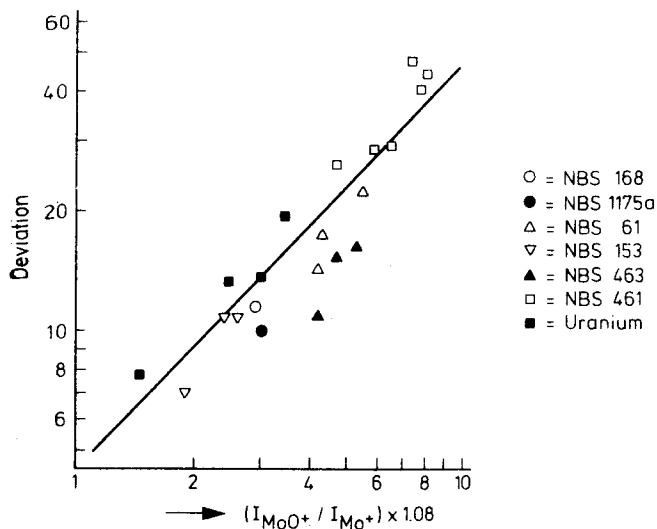
Fig. 2. The factor by which the ordinate value for Mo in
various standards is too low as a function of the
measured monoxide to atomic ion current ratio
(corrected by $M_i^{\frac{1}{2}}$); 0-20 eV sec. ions.

varying the oxygen ambient pressure. The discrepancy arises
from the preferential emission of molecular ions in place of
the low energy atomic ions. Such correction curves may be
employed for analytical purposes. An alternative method is to
restrict measurements to those secondary ions with initial
energies in the 40-60 eV range, where relatively few molecular
ions are present; such a procedure led to satisfactory semilog.
plots being obtained but with usually a higher T_i value.
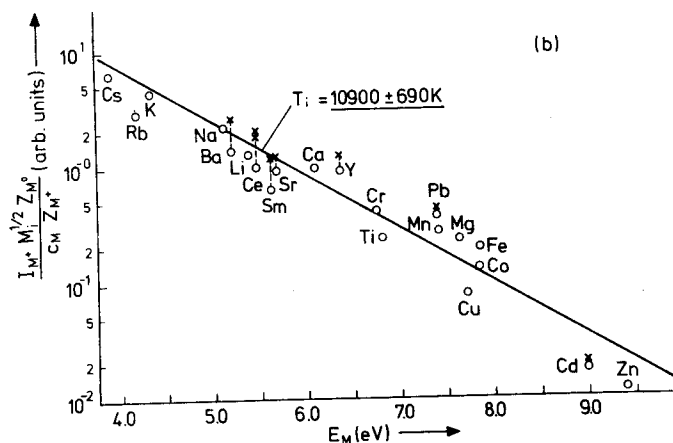Fig. 3 illustrates this for the case of PbF_2. The amount of
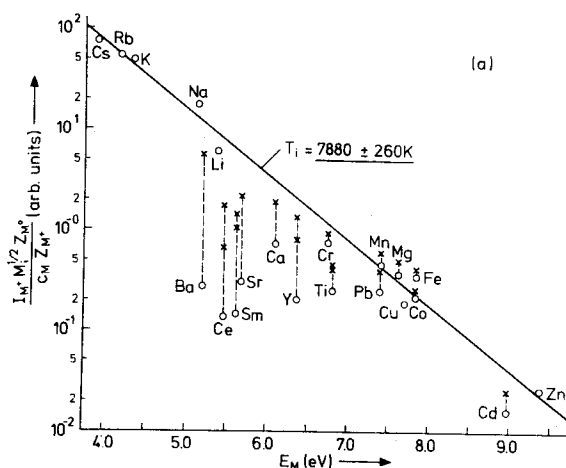
Fig. 3. Plots of $(I_{M^+} M_i^{\frac{1}{2}} Z_{MO}/c_M Z_{M^+})$ vs. E_M for 6 keV Ar$^+$ bombardment of PbF$_2$ samples in vacuum; a) 0-20 eV sec. ions monitored, b) 40-60 eV sec. ions monitored.

molecular ion formation can be gauged from the extent of the dotted lines; a cross results from adding the monofluoride ion current (corrected by $M_i^{\frac{1}{2}}$) to the corresponding atomic ion current whilst a second cross indicates that the MF$_2^+$ current has been added as well.

Fig. 4 demonstrates that molecular ion emission is determined essentially by stability considerations. The temperature obtained from such plots was about equal to T_i for halide matrices, but was close to $2T_i$ for oxide samples. This might prove to be a convenient way of estimating T_i.

Under conditions of saturated positive ion emission, T_i can vary markedly with different matrices; no dependence upon primary ion mass, current density and energy was found. Samples of a given matrix but with different minor components have very similar T_i values. This important result means that a definite value can be assigned to each matrix, and that standardless analyses are possible once this quantity has been measured or estimated. The T_i value for an oxide is not necessarily the same as that measured for the corresponding element plus oxygen. Also, the magnitude is influenced by the matrix cationic element. It would appear that T_i is independent of composition for a matrix composed of elements
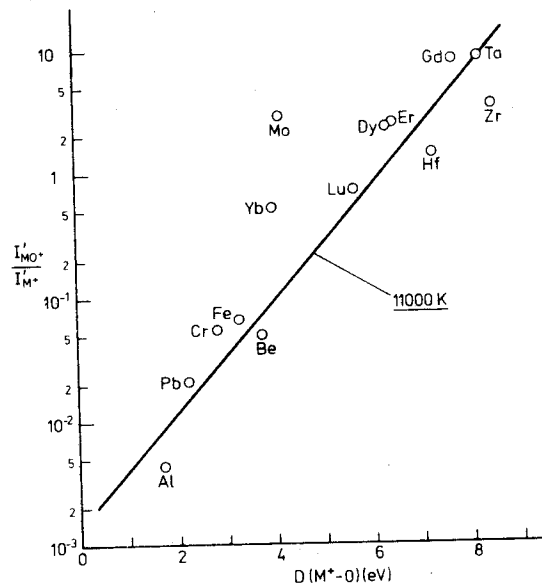
Fig. 4. Plot of (I'_{MO+}/I'_{M+}) against the bond dissociation energy $D(MO^+)$ for 6 keV Ar^+ bombardment of PbO and Bi_2O_3 samples in vacuum; I' signifies that the ion current (0-20 eV sec. ions) has been multiplied by $M_i^{\frac{1}{2}}$.

or of oxides of similar T_i values, and that T_i for an alloy can be estimated from the T_i values of its main constituents. Investigations are in progress using glass standards to study the situation with mixed oxide matrices.

ENERGY DISTRIBUTION OF POSITIVE IONS OF GROUP III AND GROUP V
ELEMENTS SPUTTERED FROM SEMICONDUCTORS

D. B. Wittry

Department of Materials Science and Electrical Engineering
University of Southern California
Los Angeles, California   90007

and

T. A. Whatley

Applied Research Laboratories, Inc.
P. O. Box 129
Sunland, California   91040

In semiconductor technology, elements from group III and group V
have a special significance--these elements are common dopants in
elemental semiconductors from group IV and are also the basis for
binary, ternary and quaternary compound semiconductors. Hence, it is
important to establish the relative sensitivity for detection of
group III and group V elements in semiconductors by secondary ion
mass spectrometry (SIMS).

Important factors in the relative sensitivities of SIMS for various
elements are a) the energy distribution of the sputtered ions and
b) the energy band-pass of the secondary ion spectrometer. In order to
evaluate the importance of these factors, we have studied the energy
distribution of positive ions from group III and group V from various
compound and elemental semiconductors. A typical result, shown in Figure 1
indicates that the group V elements generally have a much wider energy
distribution than the group III elements when the specimen is a III-V
compound or a III-V mixed crystal. In general, it is found that the
width of the energy distribution of the group V element is largest for
light elements and for elements that have a high ionization potential.

It is possible to understand these results in the light of non-equilibrium thermodynamic models if we recognize that the slow ions are more readily neutralized during escape than the fast ions. For the elements with a high ionization potential only the very energetic ions will be able to escape without neutralization.

An important consequence of the differing energy distribution is that the relative intensities measured will be influenced by the energy band pass of the spectrometer. While this complicates the quantitative interpretation, it can sometimes be used advantageously to improve detection of elemental peaks in the presence of interfering oxide peaks, since oxide peaks generally have a narrow energy distribution (e.g. PO in Figure 1).

Additional investigations of the energy distribution of group V elements present as impurities in a group IV semiconductors show a remarkable difference from the energy distribution obtained from III-V compound semiconductors. For example, Figure 2 shows the energy distribution of As from an As implanted Si specimen. We propose that the difference in the energy distribution of As in this case and in the case of III-V compounds is due to a difference in oxygen saturation which results from a difference in sputtering rate. The III-V compounds such as GaAs sputter at a rate much faster than Si and therefore there is a lower degree of oxygen saturation for these compounds than for silicon. However, another important factor determining the composition of the surface layer is the relative sputtering rates of the various constituents of the specimen. For GaAs bombarded by 10 kV oxygen ions it is expected that the surface will be enriched in Ga due to the volatility of As and arsenic oxides. Further work is in progress to clarify this situation.
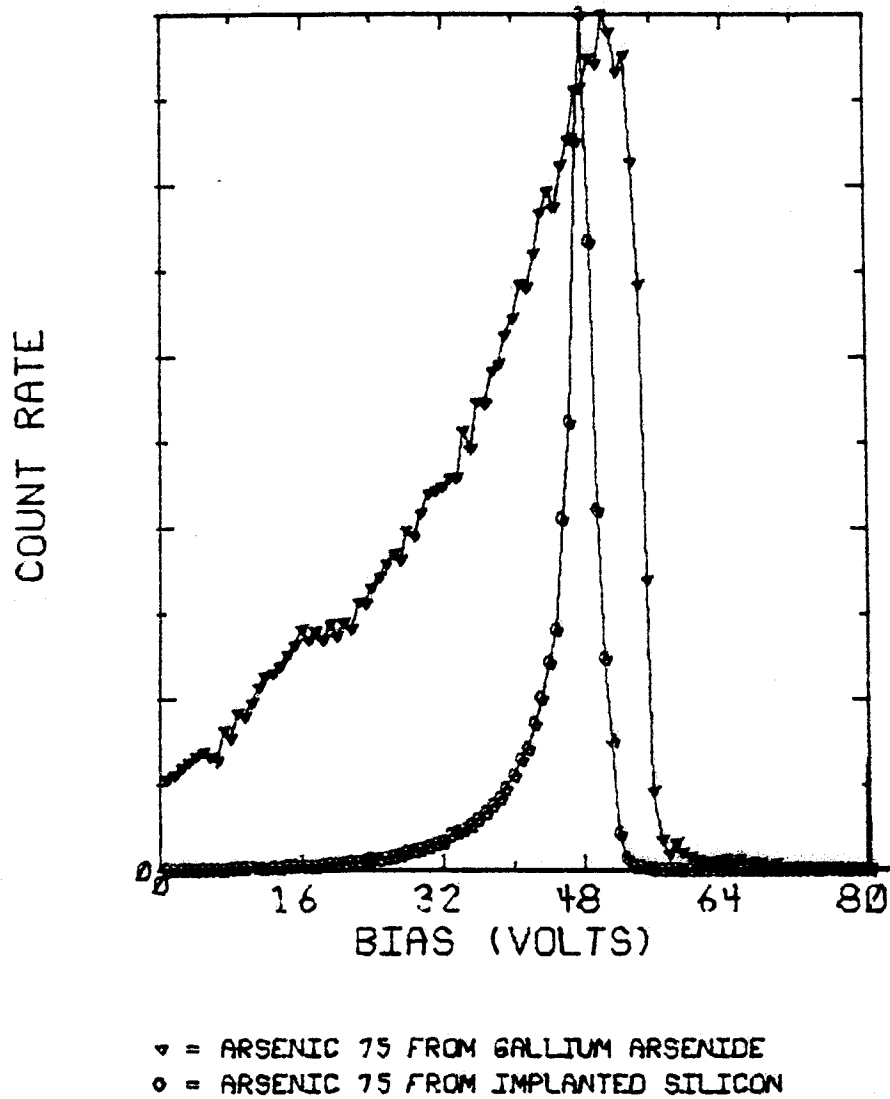
GALLIUM ARSENIDE PHOSPHIDE
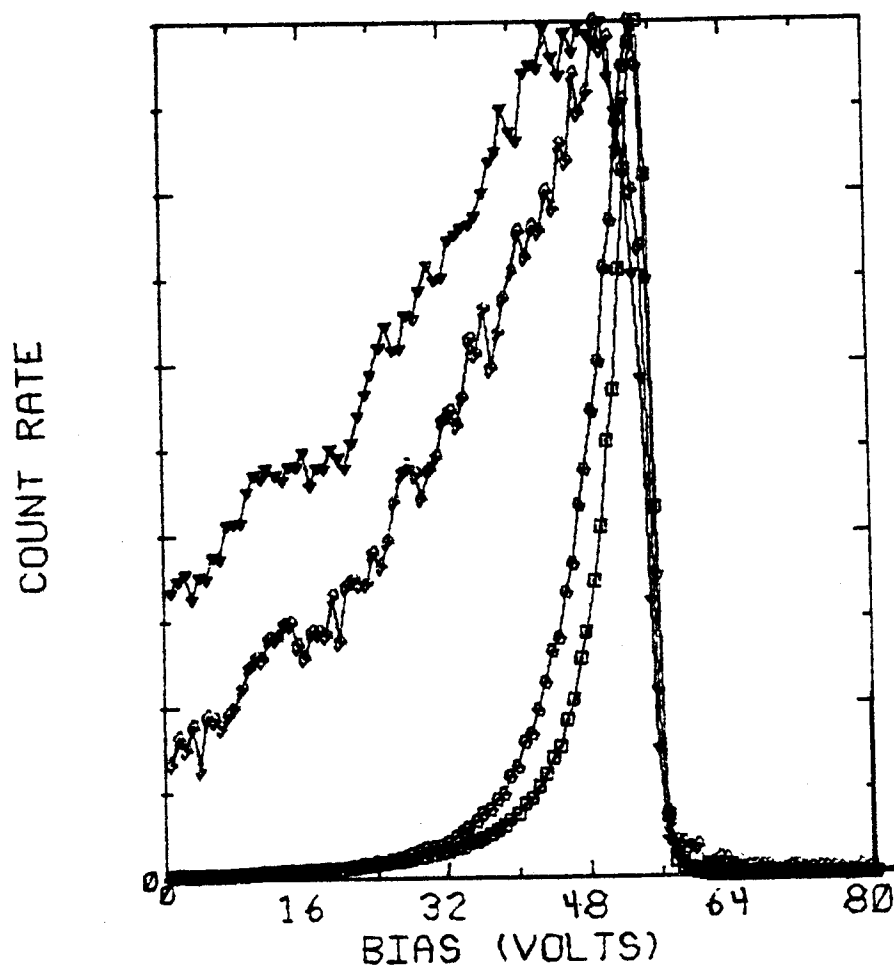
- ▼ = 31 PHOSPHOROUS
- ◇ = 47 PO
- ◻ = 69 GALLIUM
- ◇ = 75 ARSENIC

ARL 1/23/77

Fig. 1 Energy distribution of positive ions from $GaAs_{1-x}P_x$ normalized for the peak count rate. Ion energy increases from right to left, with zero energy at approximately 56 volts.

ARSENIC FROM GAAS   VS   AS/SI

COUNT RATE

BIAS (VOLTS)

▽ = ARSENIC 75 FROM GALLIUM ARSENIDE
◇ = ARSENIC 75 FROM IMPLANTED SILICON

ARL 1/23/77

Fig. 2 Energy distribution of As$^+$ ions from GaAs and from As-implanted
silicon. The offset of the curves is real and indicates that either
the Si specimen is charging positively or the GaAs specimen is charging
negatively.

SIMS Analysis: The Determination of Detection Limits -
Sample Volume Relationship Using Microdot Standards

R.D. Dobrott and G.B. Larrabee

Texas Instruments

Materials Characterization Laboratory

13588 N. Central Expw., M.S. 147

Dallas, Texas 75222

The problems in quantitative microbeam secondary ion mass
spectroscopy analysis are numerous. Wittry[1] has presented many of the
problems associated with sputter rates, ionization efficiency and
detection efficiency. Most of these problems can be avoided by using
standards which are chemically and physically identical to the material to
be analyzed. For single crystal solid state materials, standards
preparation by ion implantation can closely approach the ideal match
between standard and specimen to be analyzed. For silicon device
analysis, silicon has been implanted with several common dopants or
contaminate elements in microdots or small islands of various sizes to
simulate both the macro and micro area conditions that would be
encountered in the analysis of actual silicon devices . These standards,
similar to most devices, have physical volume constraints where the actual
surface area is limited and the analyte concentration in depth is
constantly changing. Therefore, these standards are of considerable value
in the development of analytical procedures and the determination of
detection limits or sensitivities. This paper will illustrate an
application of the analysis of a series of ion implanted microdots to
determine the detection limits on an ARL Ion Microprobe Mass Analyzer
(IMMA) operated under a fixed set of parameters. The effects of area
analyzed and background on these detection limits will be discussed.

Both depth resolution and sensitivity are important in depth profiling for any analytical system. To gain sensitivity while maintaining depth resolution the area analyzed must be increased. However, in many systems, such as solid state circuits, the area as well as the depth is limited. As a result, the detection limit or sensitivity becomes a strong function of the sample geometry. A relationship between the detection limit and area analyzed with a fixed depth profiling resolution can be derived from the analysis of increasing area microdots. For this relationship it is convenient to define an efficiency factor, E,

$$E = \frac{dose}{(\Sigma C_i) (\Delta d)} \tag{1}$$

where the dose is the number of analyte atoms per cm^2 implanted in the silicon; C_i is the analyte ion count obtained for the i-th depth interval; and Δd is the constant interval of depth sputtered for each C_i. If C_i is expressed in counts and Δd in cm, then E will have the units atoms-cm^3-count[1]. Some assumptions must be made to actually relate this efficiency factor to detection limit. First, Δd must be small enough (i.e. 2-3-nm) that the concentration over the incremental depth is constant; second, C_i can only be a function of the concentration; and, third, C_i must be linearly proportional to the concentration. The first assumption is justified by the smoothness inherent in ion implanted profiles. The second assumption is reasonable since all analysis parameters including sample surroundings are kept constant during the profiling. The validity of the third assumption is supported by the observed linearity between analyte-matrix count ratios and analyte concentrations reported by many investigators[2,3,4]. Under these conditions C_i is linearly proportional to the area, A, analyzed. Therefore, for microdot samples, E is inversely proportional to the microdot area provided the entire implanted volume is consumed.

A straight line relationship of the type shown in equation (2) can

$$E = a \left(\frac{1}{A} \right) + b \qquad\qquad (2)$$

A = area

a = slope

b = intercept

quite accurately be established by the analysis of increasing size microdots. The area implanted is well known and ΣC_i is completely dominated by the high concentration region of the depth profile. The phosphorus profile shown in Figure 1 demonstrates that the background and noise have little effect on ΣC_i. With E and its relationship to A an analysis detection limit can be calculated from the background count of the analysis with only the area, A, containing the analyte species. Also, the relationship shows that as a/A approaches b, little improvement in detection limit will be achieved by increasing the analyzed area.

Data taken from a series of four phosphorus implanted silicon microdot standards fit the straight line relationship between the efficiency factor and area shown in Eq. (3),

$$E = 4.246 \times 10^{19}/A + 6.225 \times 10^{15} \qquad\qquad (3)$$

with a multiple correlation coefficient of 0.89. In this expression E has the units of atoms/cc-count and A in $(\mu m)^2$. The relationship is shown graphically in Figure 2. The data consisted of the total phosphorus ion count (ΣC_i) obtained while profiling 5 sizes of microdots on each sample. The crater area sputtered was a nominal 125x100μm and kept constant throughout the entire analysis. The largest microdot was 100x75μm so each implanted volume was entirely consumed during analysis, eliminating crater wall problems. No electronic aperture (electronic signal rejection) was used in these data. A nominal 19.4* kV-$^{32}O^+$ beam was used to sputter the sample. The secondary ions were analyzed using a 1500 V acceleration, a

1.2 mm entrance and a 0.6 mm exit apertures on the energy analyzer, and a 254 mm momentum analyzer exit slit which gave a mass resolution, $m/\Delta m$, of 420. All these parameters were kept constant throughout the 20 profiles. The only parameter which varied slightly from day to day was the primary beam density which could account for much of the spread seen in Figure 2. The count rate obtained at the inner tail of each profile was assumed to be the background for that particular profile. The total phosphorus count was corrected using this background determination.

The detection limits for these analyses can be calculated with equation (3) and the experimental backgrounds. Table 1 tabulates the calculated detection limits obtained from various microdot sizes for 80 KV, 1.2×10^{15} atom/cm^2 phosphorus implanted silicon samples. Two statistical methods for the number of counts needed above background for phosphorus to be detected are included. One method uses a Poisson statistical formula developed by Currie[5] where the detection limit is given by equation (4).

$$L_D = 2.71 + 4.65 \sqrt{\mu_B} \tag{4}$$

where μ_B is the experimental background. The other used only $\sqrt{\mu_B}$.

As would be expected the detection limit improves as the implanted area increases but not very dramatically between the two largest areas. In this particular example the loss in detection limit improvement with increasing area occurs at about 3000 $(\mu m)^2$. The loss in this particular case is a result of the high background which is normally assumed to be the SiH^+ molecular ion interference. Consequently, unless some scheme is employed to reduce this background it would be fruitless to analyze areas larger than 3000 $(\mu m)^2$. Examination of equation (3) reveals that even if the background could be reduced to essentially zero, an area of about 10,000 $(\mu m)^2$ would closely approach the best detection limit possible.

The power of three-dimensional microdot standards for the quantitative calculation of IMMA has been presented in a previous paper [2] The ability to use these microdots to develop analysis parameters and to predict their effect on the results are demonstrated in this paper through the experimental determination of the efficiency factor-area analyzed relationship. Another application for these microdot standards is the development of specialized quantitative techniques which address unusual situations. Many other applications await only the imagination of the researcher and/or the analysis need.

TABLE 1

Detection Limit as a Function of Area Determined From a

80 KV - 1.2×10^{16} Atom cm^2 Phosphorus Implanted Silicon Microdot Series

Area $(um)^2$	μ_B counts	L_D counts	$C(L_D)$ atoms/cm^3	$C(\mu_B)$ atoms/cm^3
171	216	71	1.8×10^{19}	3.7×10^{18}
665	314	85	5.9×10^{18}	1.2×10^{18}
2621	518	108	2.4×10^{18}	5.1×10^{17}
4792	497	106	1.6×10^{18}	3.4×10^{17}
7540	645	120	1.4×10^{18}	3.0×10^{17}

ACKNOWLEDGEMENT

REFERENCES

1. Wittry, D.B., Proceedings of the Eighth International Conf. on X-Ray Optics and Microanalysis, p.129A, Boston, Mass., August 18 (1977).

2. Dobrott, R.D., Larrabee, G.B., and Keenan, J.A., 3rd Annual Meeting of the Federation of Analytical Chemistry and Spectroscopy Societies, Philadelphia, Pa, Nov. 15 (1976).

3. Colley, J., Proceedings of the Eighth National Conference on Electron Probe Analysis, p.4, New Orleans, La, Aug. 13 (1973).

4. Morabito, J.M., Anal. Chem., 46, 189 (1974)
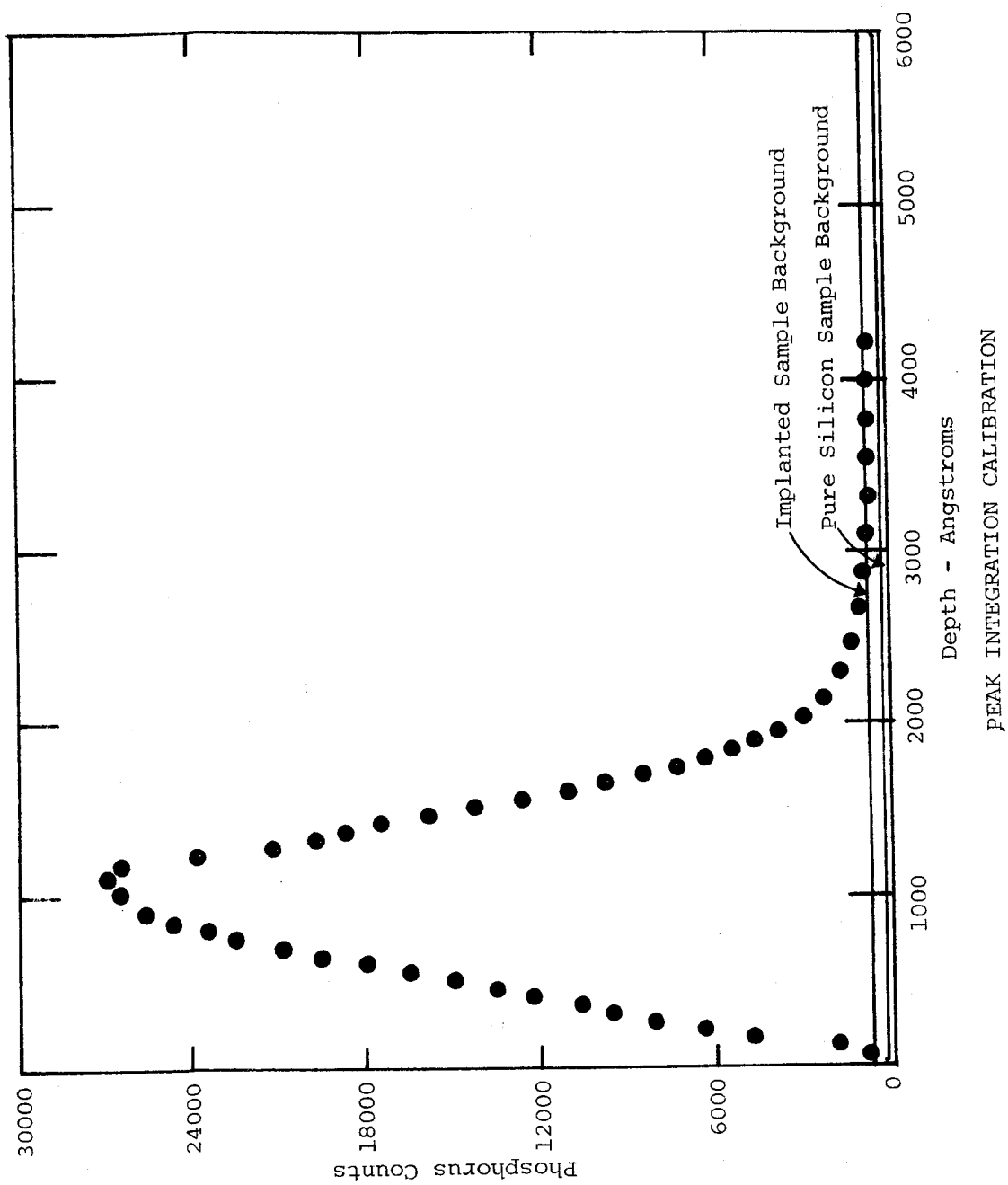
5. Currie, L.A., Anal. Chem., 40, 586 (1968)

Figure 1: Linear Plot of Phosphorus Counts versus Depth for an IMMA
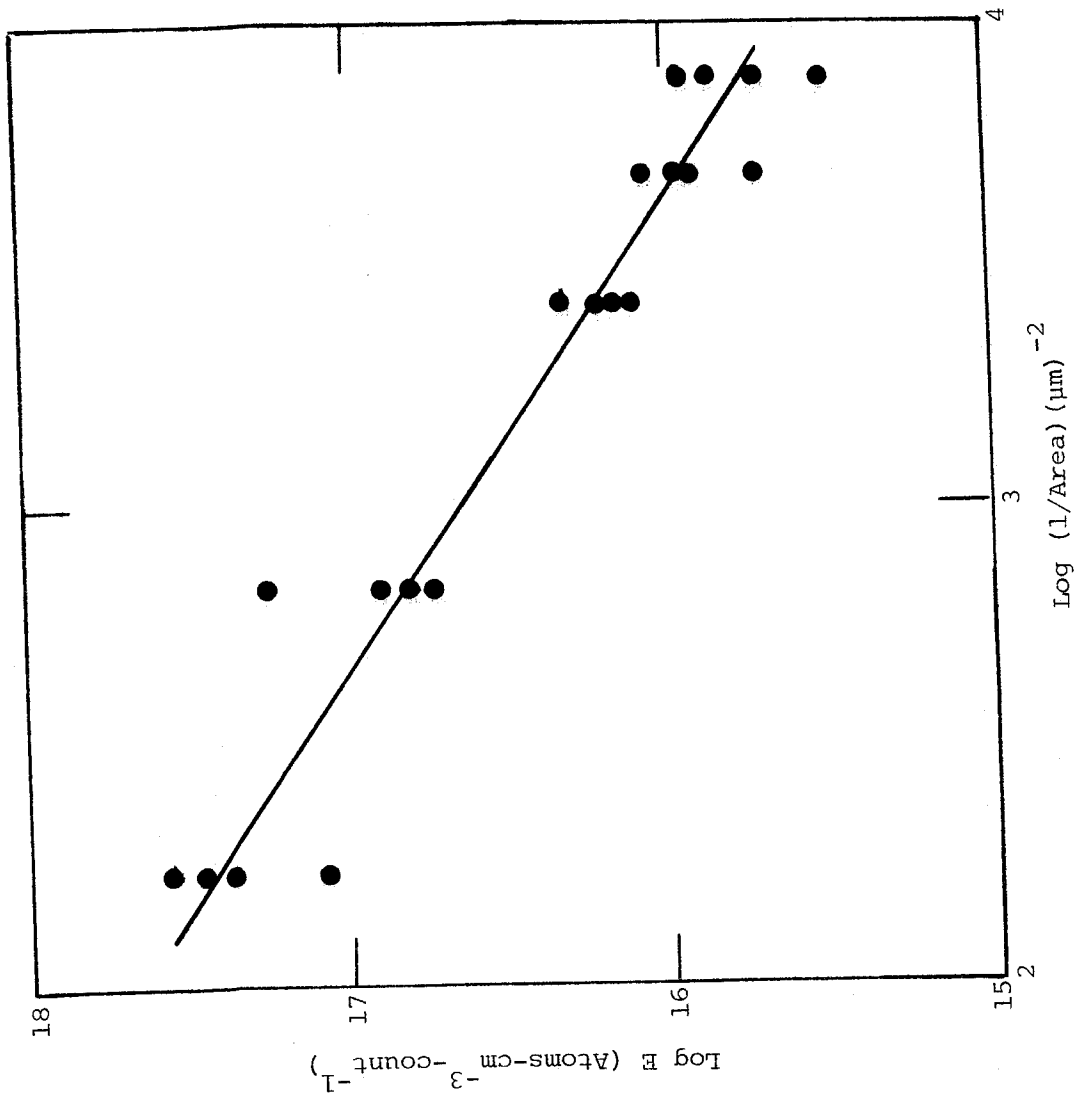In-Depth Analysis of a Phosphorus-Implanted Sample

Figure 2. The relationship between the efficiency factor, E, and area, A.

ADVANCES IN QUANTITATIVE STUDIES

USING Cs$^+$ SECONDARY ION MASS SPECTROMETRY

V. R. Deline,* P. Williams, and C. A. Evans, Jr.*

Materials Research Laboratory
and
*School of Chemical Sciences
University of Illinois at Urbana-Champaign
Urbana, IL 61801

The growing interest in solid state materials has fostered the development of many surface and thin film analytical techniques. Most of these techniques are capable of providing valuable information on major and minor elemental composition and structure, however they lack the sensitivities to acquire trace elemental information. Secondary ion mass spectrometry has aided in bridging this limitation, and is the only micro-analytical technique to analyze most elements with part per million detection limits. However, matrix effects have produced ion yield variations which influence detection limits and makes it difficult to quantitatively analyze heterogeneous materials such as multiphase alloys and multilayer thin film systems.

It has been known for several years that oxygen has the ability to greatly enhance positive ion yields for elements on the left side of the periodic table.[1,2] The value of this strong oxygen enhancement effect lies not only in increasing ion yields and sensitivities, but also in "overwhelming" or at least reducing other matrix effects. This has erased some of the problems associated with yield effects between matrices and has provided substantial benefits for the analysis of electropositive elements. Therefore, oxygen primary beams and oxygen backfilling has been used extensively in the SIMS technique. On the other hand, it has long been known that the presence of cesium on the sputtering surface leads to the enhancement of negative secondary ion yields,[3,4] but cesium has not been analytically employed because of the lack of a reliable Cs$^+$ ion source.

Recently, a Cs^+ primary ion source has been developed and put into service in our laboratory.[5,6] Evaluation of this source is being carried out using electronic materials. These materials represent an ideal system for the investigation and application of negative secondary ion mass spectrometry, because many of the elements of interest are from the right side of the periodic table where suitable electron affinities enhance electron attachment.

Generally, studies best suited for analysis have been those involving no matrix variations. A relatively straightforward example of this is the characterization of the physical phenomena associated with ion implantation.[7,8] Depth profiles of selenium implanted gallium arsenide samples have been measured as a function of substrate temperature during ion implantation, Figs. 1 and 2. It has been found that from liquid nitrogen temperature to room temperature (25°C), the implant profiles are virtually identical, but as the substrate temperature is increased from room temperature to 150°C, Se diffusion increases rapidly resulting in significantly deeper selenium distributions. At temperatures between 150°C and 500°C only small changes in profile distributions were detected. The behavior of post-implanted thermal diffusion has also been investigated. Figure 3 illustrates the magnitude of post-implant diffusion and a value for the diffusion constant has been determined. This study has provided valuable information on some unanticipated characteristics of Se implanted GaAs.

Ion implantation not only provides interesting samples for analysis, it can also furnish elemental standards for quantitating unknown compositional distributions. Demonstration of this unique capability is shown in Fig. 4, which gives the in-depth distribution for 3 different doses of O_2^+ implanted Si. A graph of peak $^{16}O^-$ ion intensity versus fluence of implanted O_2^+ (5×10^{14}, 1.5×10^{15}, and 5×10^{15} atoms/cm^2) demonstrates a linear relationship which intersected the origin. Furthermore if one assumes a Gaussian distribution, the peak concentration of the chemical profile can be calculated according to the formula:

$$\text{Peak Concentration} = \frac{\phi}{\sqrt{2\pi} \cdot \sigma_p}$$

where σ_p is the calculated standard deviation of the projected range obtained by range theory and published in tables,[9] and ϕ is the fluence of implanted ions in ions/cm^2. Quantitation is accomplished by assigning the peak concentration calculated from the above equation to the secondary ion intensity at the peak of the in-depth distribution, and assuming a linear ion intensity versus concentration relationship.

Multilayered samples pose a significant problem because of the secondary ion yield variations produced by the dissimilar matrices. Ion implantation has been applied to quantitate the redistribution of dopants during silicon oxidation. An example of this sample type is shown in Fig. 5 where the bulk arsenic is rejected during the oxide growth and concentrated at the SiO_2/Si interface. This is the so-called "snow-plow" effect. Ion implantation of arsenic into the grown oxide and the underlying doped silicon after oxidation will be used to correct for variation in the secondary ion yields from these two regions. This will permit the quantitative determination of the redistribution coefficient of arsenic in this multilayered system. Dopants of boron, phosphorus, and antimony will also be studied applying this same procedure.

This paper will demonstrate that Cs^+/SIMS can be used to provide a quantitative characterization of chemical and physical processes associated with electronic materials.

References

1. G. Slodzian and J. -F. Hennequin, C. R. Hebd. Seances Acad. Sci., Ser. B, 263, 1246 (1966).

2. C. A. Andersen, Int. J. Mass Spectrom. Ion Phys., 2, 61 (1969).

3. V. Krohn, J. Appl. Phys., 33, 3523 (1963).

4. C. A. Andersen, Int. J. Mass Spectrom. Ion Phys., 3, 413 (1970).

5. P. Williams, R. K. Lewis, C. A. Evans, Jr., and P. R. Hanley, Anal. Chem., 49, 1399 (1977).

6. P. Williams and C. A. Evans, Jr., Applied Physics Letters, 30, 559 (1977).

7. A. Lidow, J. F. Gibbons, V. R. Deline, and C. A. Evans, Jr., Applied Physics Letters, 32, 15 (1978).

8. A. Lidow, J. F. Gibbons, V. R. Deline and C. A. Evans, Jr., Applied Physics Letters, (In Press).

9. J. F. Gibbons, W. S. Johnson and S. W. Mylroie. "Projected Range Statistics," (2nd Edition), Halstead Press, 1975.

FIGURE 1. SIMS profiles of Se implanted into GaAs at 120 keV to a dose of $1 \times 10^{15} cm^{-2}$. Substrate temperatures during implantation were $-196°C$ (open squares), $25°C$ (open triangles), $100°C$ (closed circles), and $150°C$ (open circles).
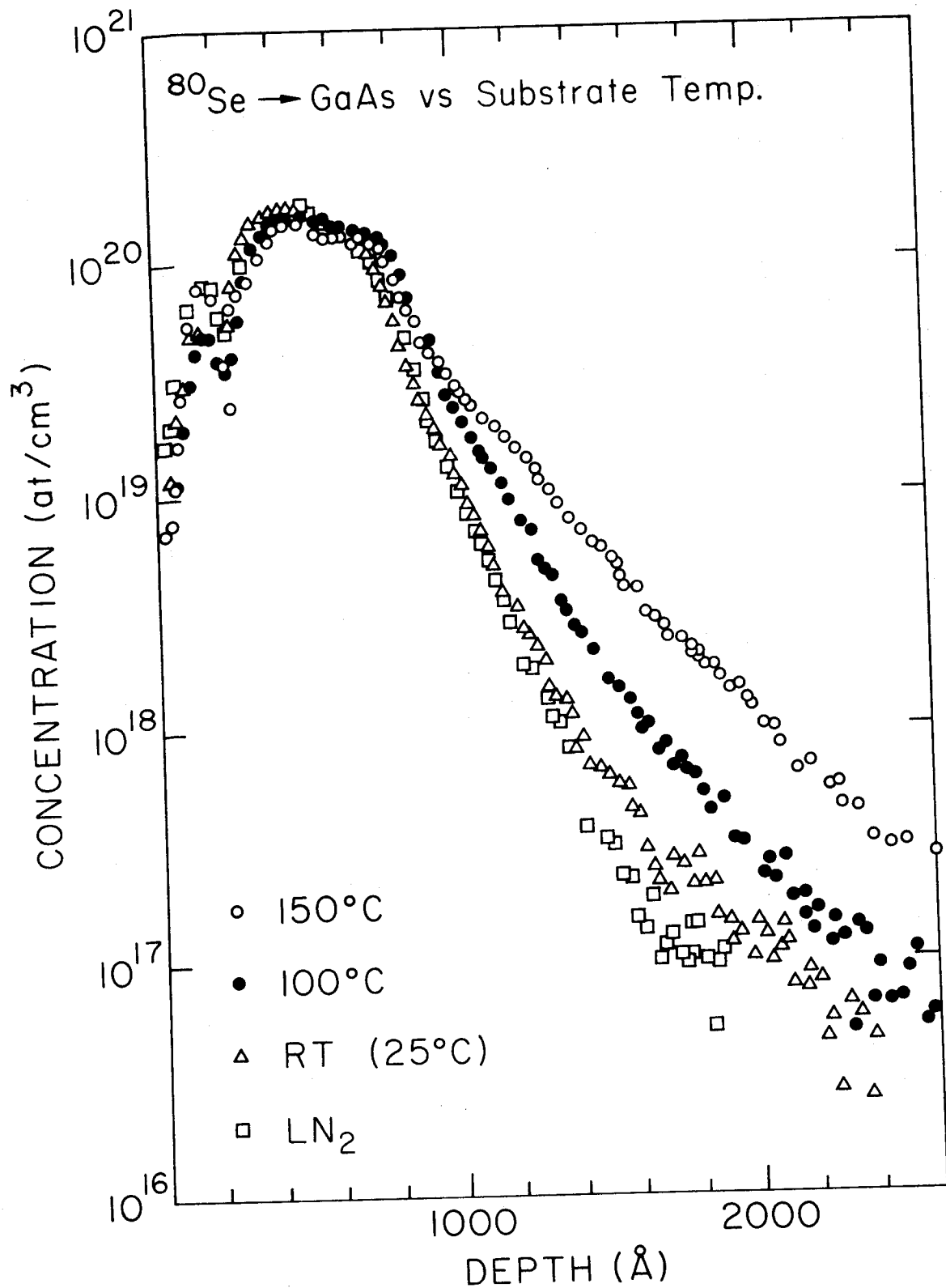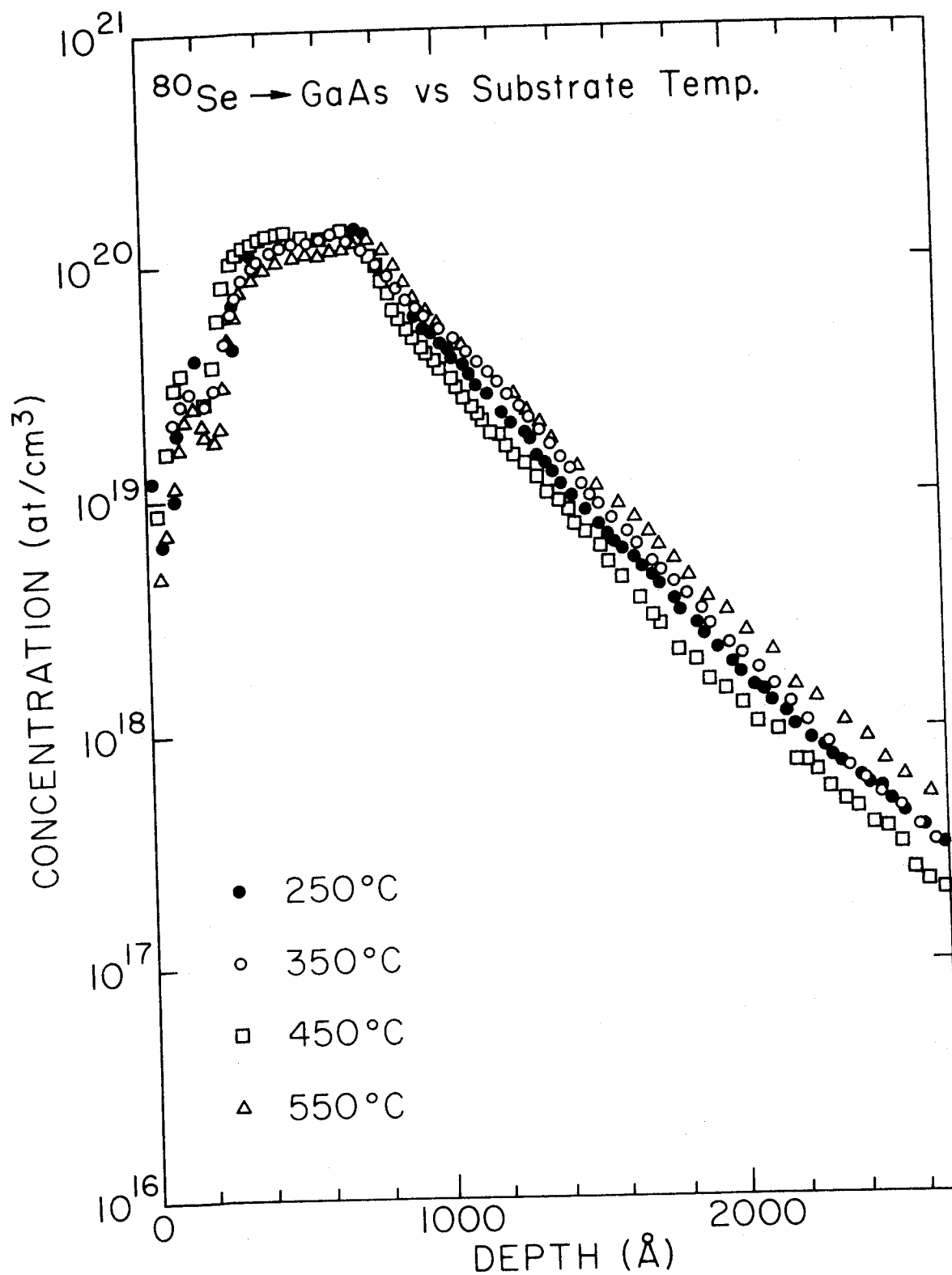
FIGURE 2. SIMS profiles of Se implanted into GaAs at 120 keV to a dose of $1 \times 10^{15} cm^{-2}$. Substrate temperatures during implantation were 250°C (closed circles), 350°C (open circles), 450°C (open squares), and 550°C (open triangles).
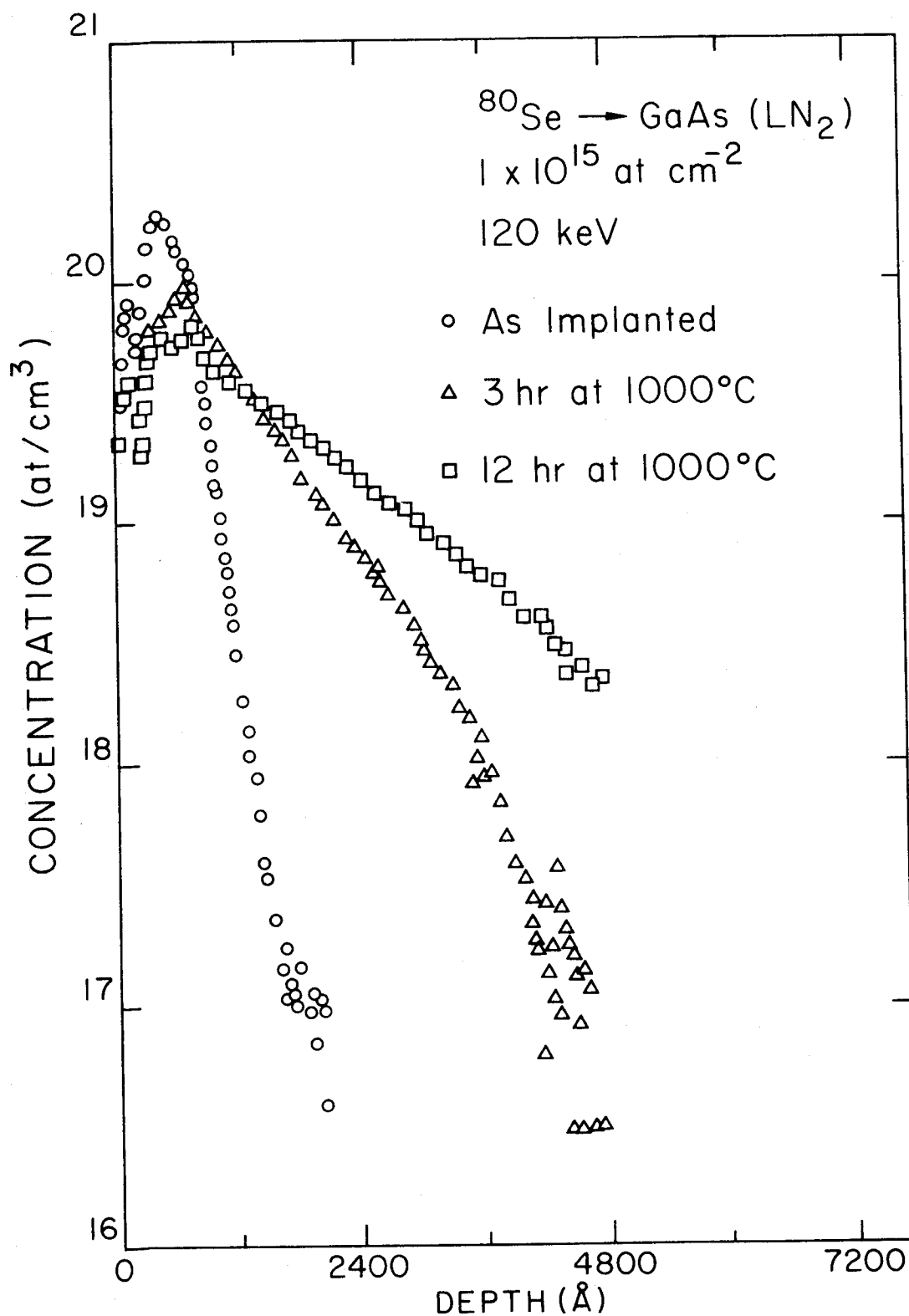
FIGURE 3. SIMS profiles for 120 keV Se implantation into GaAs to a
dose of $1 \times 10^{15} \text{cm}^{-2}$. Shown are an as-implanted (circles), a 1000°C for
3 hours anneal (triangles), and a 1000°C for 12 hours anneal (squares).

FIGURE 4. SIMS profiles for as-implanted O_2^+ in silicon at 100 keV to doses of $5\times10^{14}cm^{-2}$ (squares), $1.5\times10^{15}cm^{-2}$ (triangles), and $5\times10^{15}cm^{-2}$ (circles), and a graph of peak ion intensity versus implant dose.

FIGURE 5. SIMS profile demonstrating the redistribution of As in arsenic doped silicon after the growth of an oxide layer.

On the Accuracy of Quantitative Analysis in Secondary Ion Mass Spectrometry — Round Robin Results

Dale E. Newbury
Microanalysis Section
National Bureau of Standards
Washington, D.C. 20234

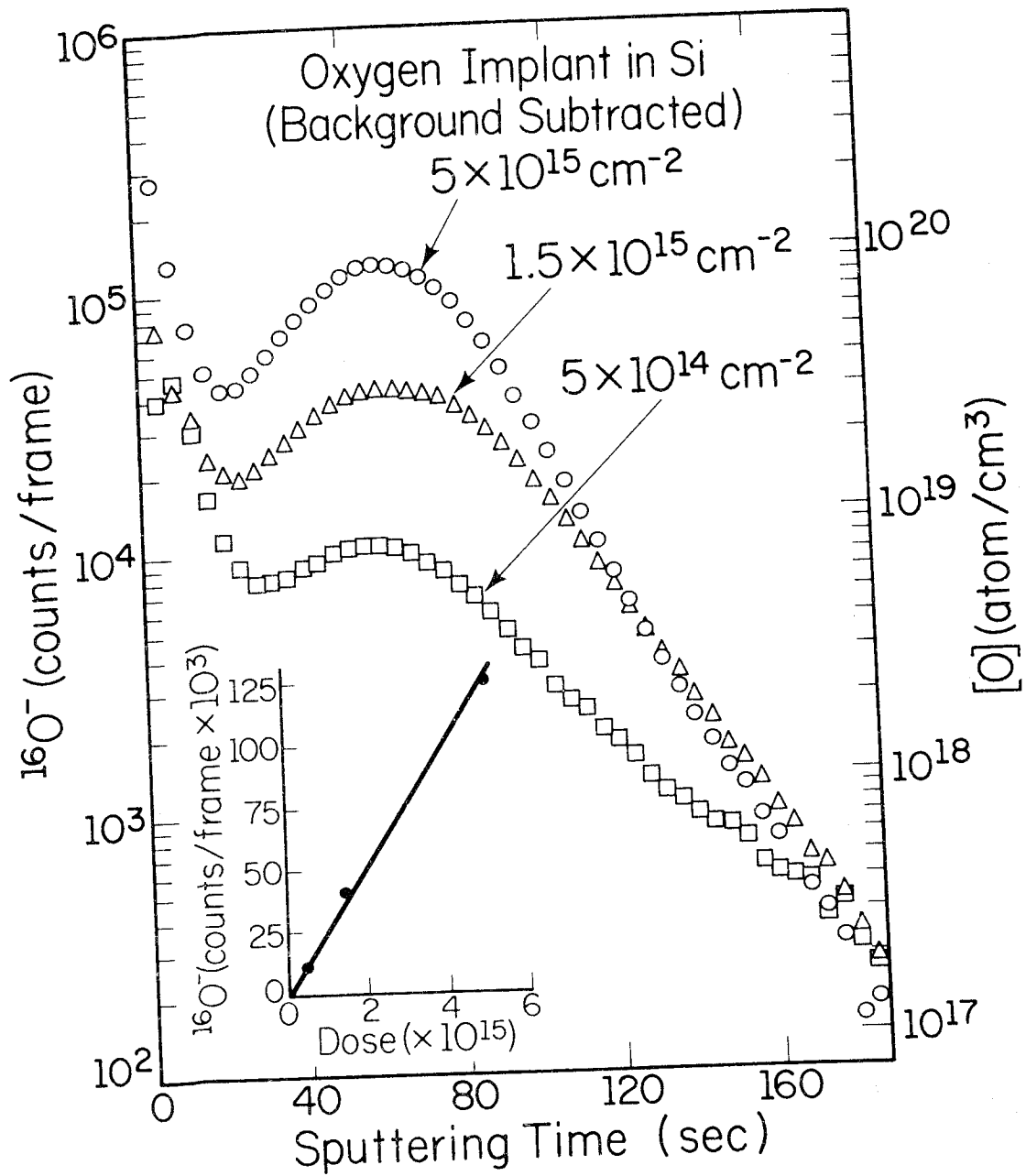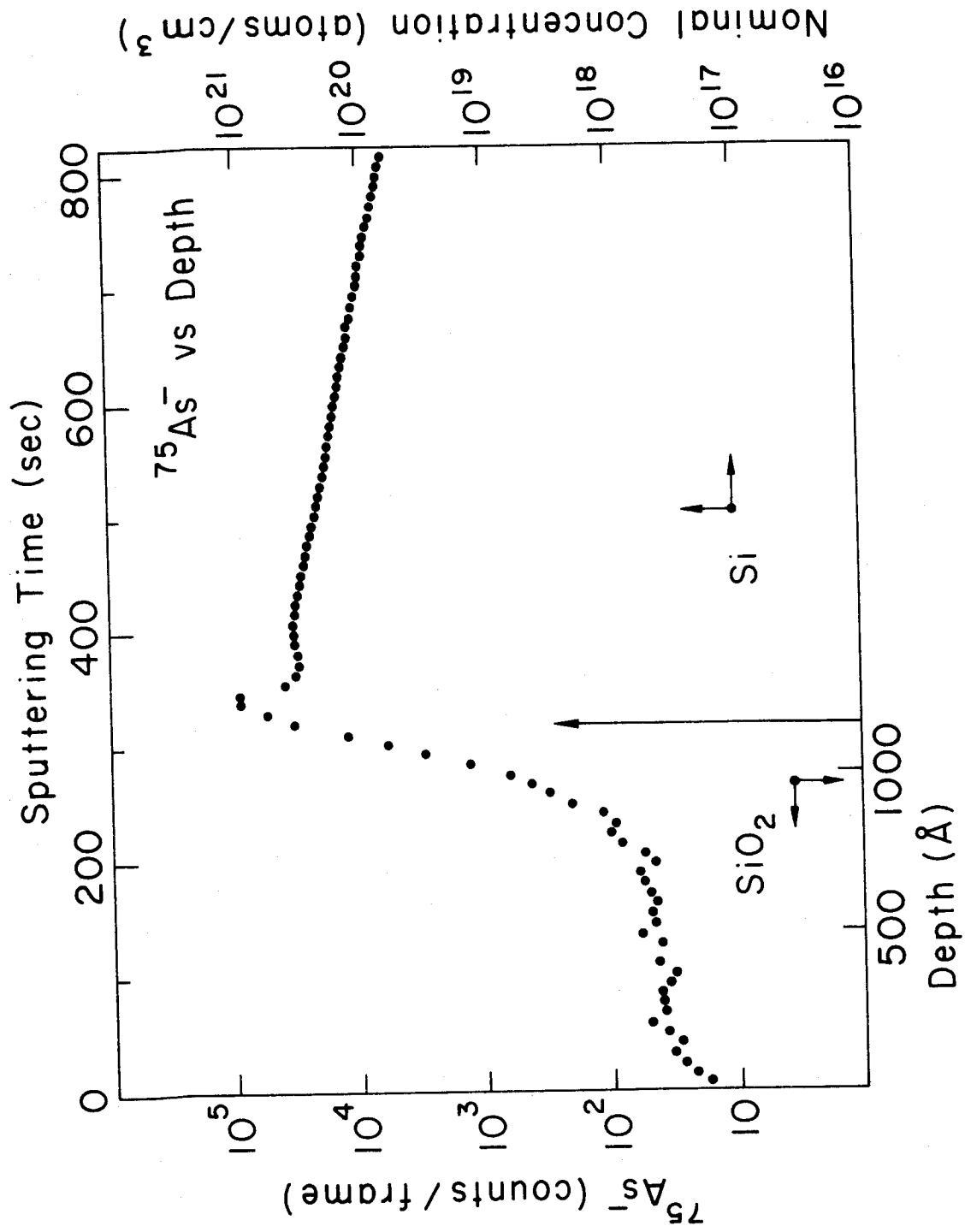In previous papers, the accuracy of quantitative analysis of glasses by secondary ion mass spectrometry (SIMS) has been tested for analysis with a physical model of secondary ion emission[1] and for analysis with relative elemental sensitivity factors[2]. The sensitivity factor approach has been shown to produce significantly more accurate analyses as compared with the physical model. The level of performance observed with sensitivity factors is such that about 55 percent of the analyses fall within 20 percent relative of the known composition, 83 percent within a factor of 2, and 99 percent within a factor of 5.

Such a level of accuracy of analysis by SIMS is quite encouraging, considering the strong matrix effects which are observed. However, a test of the accuracy of analysis under rigorous conditions which are representative of the analysis of unknowns is needed to determine realistic confidence limits. To this purpose, a program of analysis of blind samples has been carried out in cooperation with four independent SIMS laboratories employing similar ion microprobes. The laboratories were previously supplied with a suite of glasses prepared by the National Bureau of Standards with a wide variety of elements. The suite included the glasses offered as Research Materials 30 and 31[3]. Using either the synthetic composition or the analytic composition where available from independent measurements, relative elemental sensitivity factors were determined by each laboratory for its particular instrument configuration and operating conditions.

The sensitivity factor is generally described by an equation of the form:

$$S_{X/M} = (i_X/C_X f_X)/(i_M/C_M f_M) \qquad (1)$$

where i is the measured secondary ion intensity, C is the atomic concentration, f is the isotopic abundance of line measured, and X and M denote any two elements. Ideally, X should be a solute element and M a solvent or matrix element. For quantitiative analysis, the relative ion intensities measured from an unknown can be related to concentration ratios by the general formula (taking I_X as the total secondary ion signal over all isotopes for an element, $I_X = i_X/f_X$):

$$C_X/C_M = (1/S_{X/M})(I_X/I_M) \qquad (2)$$

The absolute concentrations are then derived with the equation:

$$C_M + \Sigma (C_M/S_{X/M})(I_X/I_M) = 1 \qquad (3)$$

Each of the participating laboratories was asked to analyze four glasses with no prior information as to their content. A wide range of concentration, from 0.1 to 22 atomic percent, was covered in the study. Twenty-three different elements in groups of seven to ten were present in the glasses, providing complicated samples for a demanding test of both qualitiative and quantitative analysis procedures. The choice of appropriate standards for sensitivity factors was left to each analyst.

Examples of the level of analytical accuracy achieved by the participating laboratories are given in Tables 1-4. Examination of these tables reveals an impressive level of accuracy of both the qualitative and quantitative analyses. The results are summarized in the error factor histogram shown in Figure 1.

The error factor, F, as used in this plot is arbitrarily defined as

$$F = C(\text{true})/C(\text{measured}) \qquad (4)$$

The distribution of errors indicates that 57 percent of the analyses fall within 20 percent relative, and 91 percent within a factor of two. This compares very favorably with the earlier study on known samples[2], with the present results actually improving on the former. This improvement can be ascribed to the use in the present case of standards for sensitivity factors which are as similar as possible to the unknown. In the former study, averaged senstivity factors for the whole suite of glasses were employed for analysis.

Examination of the results in Table 1-4 reveals that, for any particular glass, large errors of a factor exceeding two are occasionally observed. Moreover, there are a few instances of major elements being overlooked in the qualitative analysis. Due to the complex nature of SIMS spectra, containing signals for dimer and trimer molecules, compound ions, and multiply-charged ions as well as the isotopes of the elements, such errors are difficult to eliminate entirely. Elimination may be possible with computer automation systems where the rapid data flow encountered by the SIMS analyst can be more readily controlled.

Acknowledgements

References

(1) D. E. Newbury, R. L. Myklebust, and K. F. J. Heinrich, "Local Thermal Equilibrium Analysis of Secondary Ion Mass Spectra from Multi-Element Glasses" in Proc. 11th Ann. Conf. Microbeam Analysis Society (Miami, 1976) 42A.

(2) D. E. Newbury, "Quantitative Analysis of Glasses by Secondary Ion Mass Spectrometry," in Proc. 12th Ann. Conf., Microbeam Analysis Society (Boston, 1977) 140A.

(3) Research Materials 30 and 31, "Glasses and Glass Fibers for Microchemical Analysis," available from the Office of Standard Reference Materials, Room B311, Chemistry Building, National Bureau of Standards, Washington, D.C., 20234.

Table 1.   Round Robin Analysis of Glass K-873

Element	nom.comp. atom %	Lab A	rel. error	Lab B	rel. error	Lab C	rel. error	Lab D*	rel. error
Al	0.39	0.45	+15%	0.35	+10%	0.31	-21%	0.53	+36%
Si	16.16	21.95	+36%	14.0	-13%	11.31	-30%	11.34	-30%
Mn	0.23	0.15	-35%	0.21	-9%	0.15	-35%	0.24	+4%
Ge	9.28	8.42	-9%	8.91	-4%	12.38	+33%	6.53	-30%
Ba	6.33	6.83	+8%	9.20	+45%	8.90	+40%	8.35	+32%
Ce	0.12	n.d.	--	0.16	+33%	0.16	+33%	0.16	+33%
Ta	0.09	n.d.	--	0.084	-7%	0.20	+122%	0.21	+133%
Pb	4.35	4.75	+9%	5.25	+21%	4.36	+0.2%	9.64	+121%
energy		21.5keV		16.5keV		16.5keV		16.5keV	

n.d. - not detected.

*   also reported Na (0.05%); K (0.009%); Ca (0.009%); Fe (0.01%); Bi (0.12%).

** also reported B (0.07%); Fe (0.07%).

Table 2. Glass K-919

Element	nom.comp. atom %	Lab A	rel. error	Lab B	rel. error	Lab C	rel. error	Lab D	rel. error
Si	22.6	22.4	-0.8%	19.86	-12%	21.77	-3.6%	22.6	**—
Cr	0.415	nd	nd	0.67	+61%	0.40	-3.6%	0.425	+2.4%
Mn	1.09	1.33	+22%	1.11	+1.8%	1.08	-0.9%	1.04	-4.6%
Fe	1.18	1.40	+18.6%	1.26	+6.7%	1.15	-2.5%	1.49	+26.2%
Co	1.14	1.24	+8.7%	1.34	+17.5%	1.36	+19.3%	0.92	-19.2%
Ni	1.27	1.55	+22%	3.93	+209%	1.42	+11.8%	1.54	+21.3%
Cu	1.19	1.03	-13.4%	1.25	+5%	1.09	-8.4%	0.92	-22.6%
Ba	7.82	3.6	-54%	7.63	-2.4%	9.28	+18.7%	8.34	+6.6%
Ce	0.55	nd	nd	1.32	+140%	0.58	+5.4%	0.60	+9.1%

n.d. - not detected.

* reported in weight percent of the element; converted to atomic percent.

** values reported relative to silicon.

6-F

Table 3. Glass K-961

Element	nom.comp. atom %	Lab A	rel. error	Lab B	rel. error	Lab C	rel. error	Lab D	rel. error
Na	2.73	2.81	+2.9%	3.36	+23%	3.41	+24.9%	9.45	+246%
Mg	2.63	3.11	+18.3%	2.60	-1.1%	2.82	+7.2%	3.47	+31.9%
Al	4.57	3.99	-12.7%	4.74	+3.7%	4.45	-2.6%	4.42	-3.3%
Si	22.55	24.6	+9.1%	22.9	+1.6%	22.42	-0.5%	22.55	**
P	0.149	nd	--	nd	--	nd	--	nd	--
K	1.35	2.20	+63%	1.38	+2.2%	1.26	-6.7%	3.11	+130%
Ca	1.89	2.42	+28%	2.00	+5.8%	1.30	-31%	1.93	+2.1%
Ti	0.530	0.90	+70%	0.60	+13.2%	0.450	-15%	0.419	-21%
Mn	0.122	0.118	-3.3%	0.14	+14.8%	0.087	-29%	nd	--
Fe	1.33	0.58	-56%	0.84	-37%	1.00	-25%	1.24	-6.7%

n.d. - not detected.

* reported in weight percent of the element; converted to atom percent.

** values reported relative to silicon.

Table 4. Glass D-312

Element	nom.comp. atom %	Lab A	rel. error	Lab B	rel. error	Lab C	rel. error	Lab D	rel. error
Ca	11.9	20.2	+70%	11.84	-0.5%	10.98	-7.7%	10.6	-11%
Al	14.3	19.7	+38%	15.77	+10%	13.34	-6.7%	15.2	+6.3%
Be	9.25	nd	--	7.96	-14%	9.12	-1.4%	6.71	-27%
Zr	1.26	1.84	+46%	1.17	-7%	1.26	0%	0.99	-21%
Si	5.16	7.96	+54%	4.98	-3.5%	6.48	+25.6%	5.16**	--
Sn	0.507	nd	--	0.53	+4.5%	0.66	+30%	0.51	+0.5%
Ta	0.345	1.08	+213%	0.26	-25%	0.34	+1.4%	0.09	-73%

nd — not detected.

*   analyses reported in weight percent element; converted to atomic percent.

** analyses reported relative ot silicon.

Figure 1. Error factor distribution observed in blind sample round-robin analysis.

Blind Sample Round Robin

$0.83 \leq F \leq 1.2$ 57%
$0.50 \leq F \leq 2$ 91%

$(1/F) > 2.4$
1 case

$F > 2.4$
3 cases

1/F F
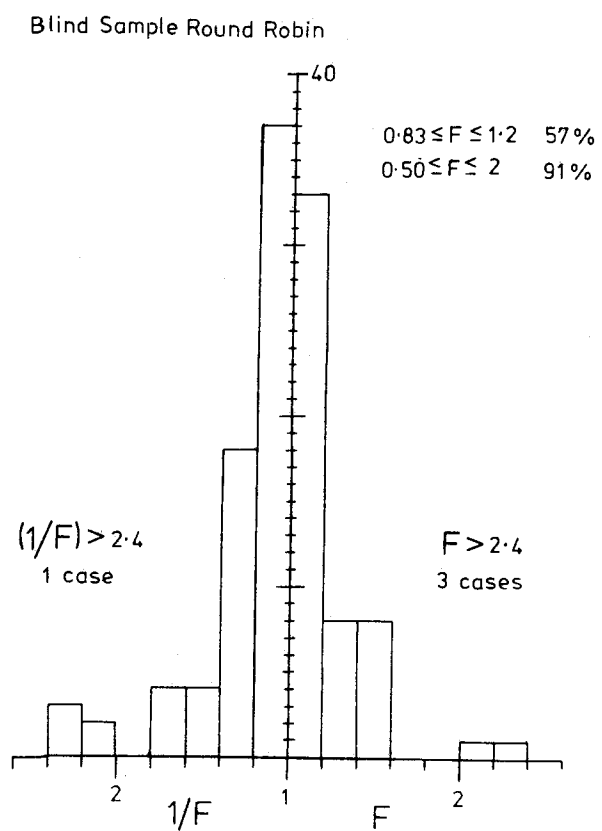
SELECTION OF PRIMARY ION SOURCE FOR SIMS

Howard A. Storms
Vallecitos Nuclear Center
General Electric Company
Pleasanton, CA 94566

A variety of primary ion sources (1-19) is being used today in secondary ion mass spectrometry (SIMS). The types of sources and their utilization appear to be increasing with the developing maturity of SIMS. Whereas, the duoplasmatron remains the workhorse of ion sources (1-4) and the ions it produces (e.g., O_2^+, O^-, Ar^+, N_2^+) are used in over 90 percent of the SIMS studies, more attention is recently being directed toward other kinds of ion sources (5-20). In particular, bombardment with Cs^+ ions (5-10) has been receiving increasing interest because enhanced secondary ion emission results for a number of elements for which there is considerable analytical interest and for which less than desired sensitivity had previously been achieved. These elements include carbon, hydrogen, the noble metals, and the Group V, VI, and VII elements (9). Several laboratories (11-14) have been investigating iodine as a possible substitute for oxygen in the analysis of electropositive elements. Other studies (18,19) are being conducted using conventional ion sources, usually Ar^+, and then directing a stream of the desired vapor or gas onto the sample surface. Oxygen has been used extensively in this manner (19). Recently, Slodzian's group has reported very promising results using cesium vapor (18). There appears to be considerable untapped potential for the utilization of specialty ion sources and chemical enhancement techniques to attack surface analytical problems.

Pioneering SIMS studies generally employed conventional inert gas primary ion sources, including the duoplasmatron, for various reasons. These ion sources were reliable, had long lifetimes, and conveniently produced stable high intensity beams of ions. Inert gases were considered desirable primary ions because they had minimum effect on the surface chemistry. Reactive elements were initially avoided except as curiosity. However, the demonstrations that oxygen bombardment results in generally enhanced and chemical matrix stabilized secondary ion yields while ion yields for the electronegative elements are further improved by cesium bombardment have given rise to increasing interest in the application of selected primary ions for analytical applications. The secondary ion yields shown in Figure 1 and 2 for O^- and Cs^+ bombardment demonstrate the advantages of selectivity in primary ion sources. These two primary ions complement one another as

evidenced by the trends shown in Figure 2 being nearly the inverse of those in Figure 1. Most of the elements can be determined with high sensitivity using either O^- or Cs^+ bombardment. Relatively higher detection sensitivities are obtained for the electropositive elements with O^- and for the electronegative elements with Cs^+.

The ion species and types of ion sources shown in Table 1 illustrate the variety available for SIMS. There will undoubtedly be substantial increases in ion source selection in the future.

Discussion will be given on chemical enhancement and primary ion sources. As an example, emphasis will be given to experience with an experimental cesium ion source.
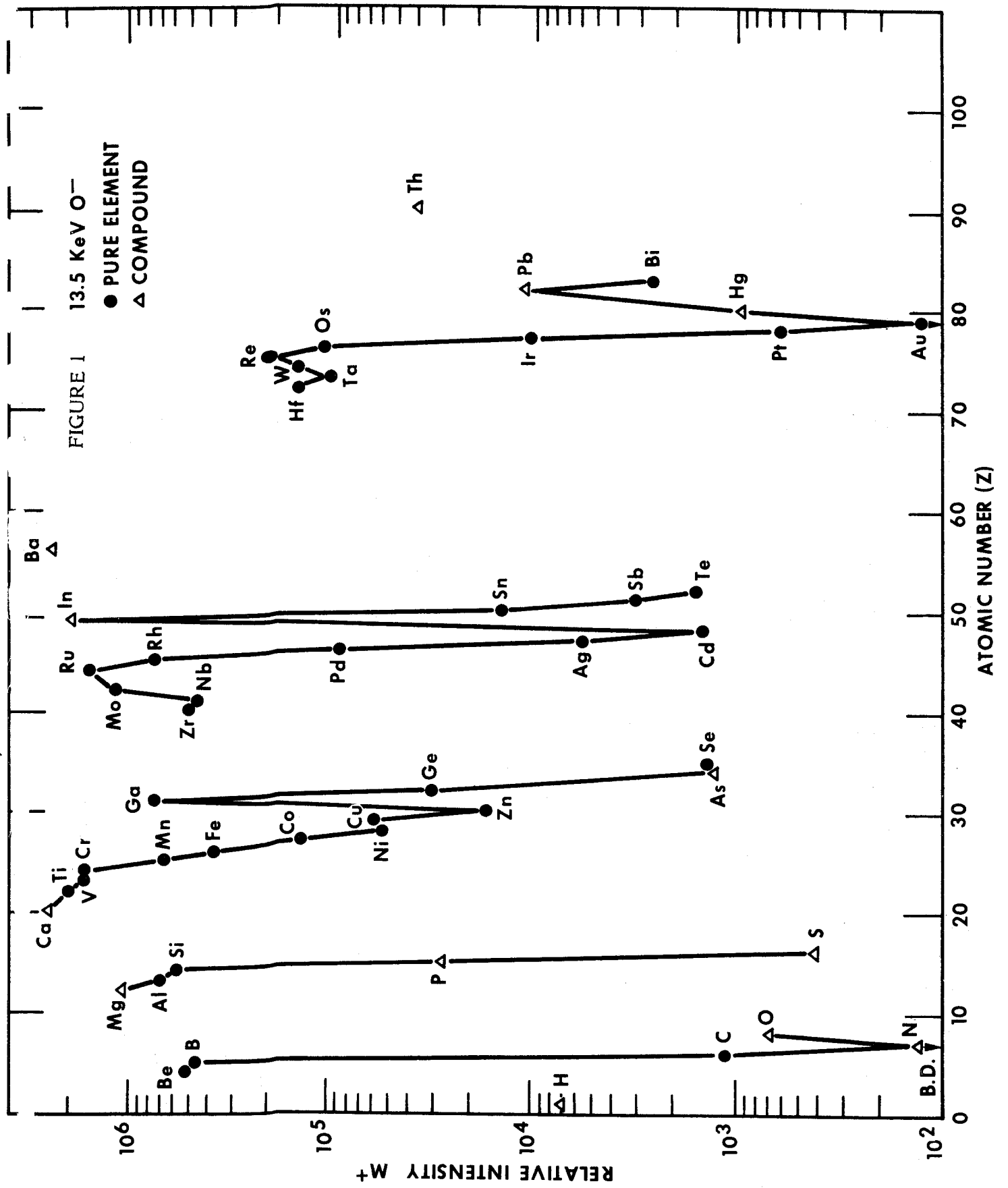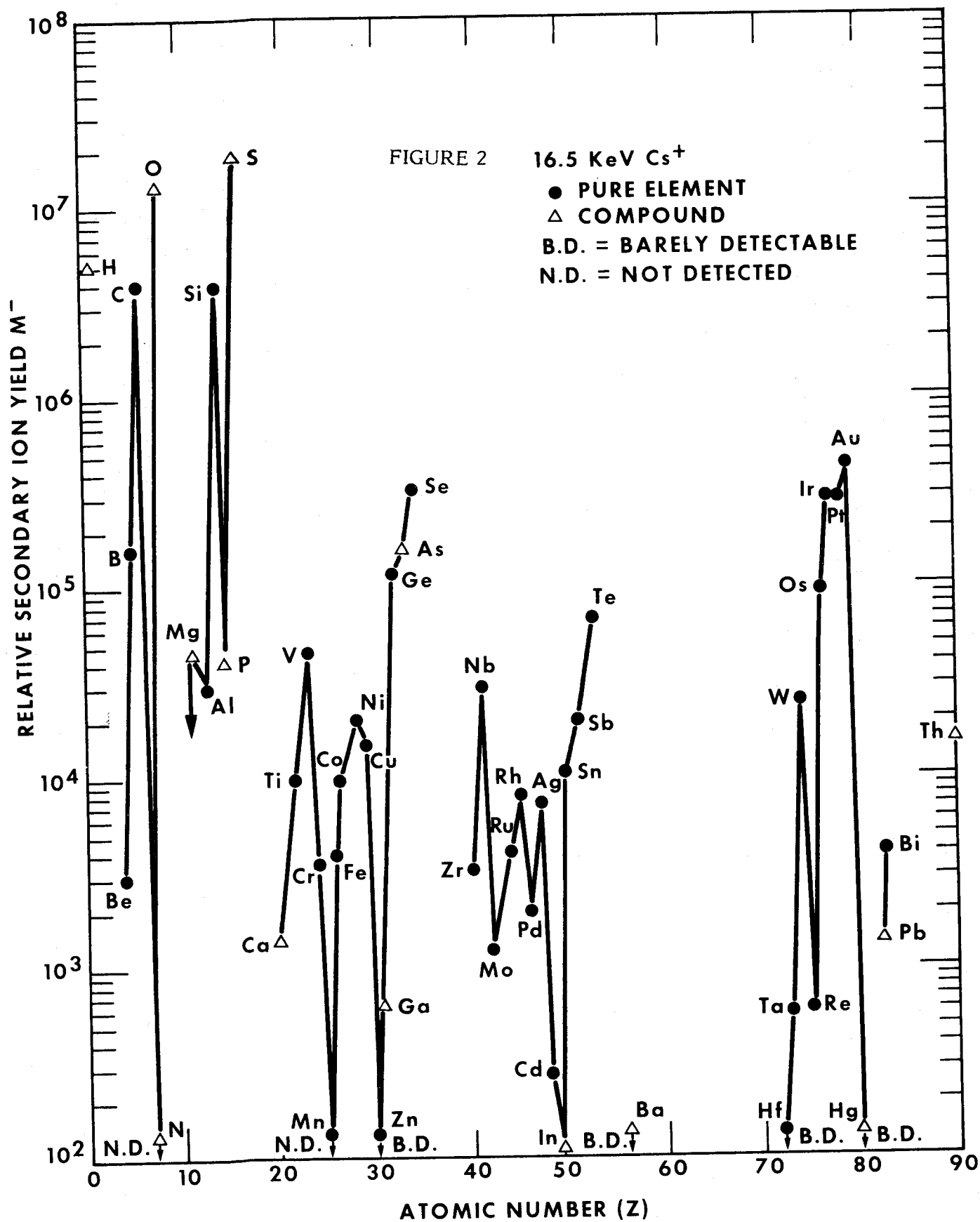
REFERENCES

(1) C. Lejeune, Nuclear Instr. and Meth. 90, 417 (1974).

(2) Ibid., 429.

(3) H. J. Roden, Proc. Second Symposium Ion Sources and Formation of Ion Beams, Berkeley, 1974, Paper VII-7.

(4) J. A. Samson and H. Liebl., Rev. Sci. Instr. 33, 1340 (1962).

(5) V. E. Krohn, J. Appl. Phys. 33, 3523 (1962).

(6) V. I. Veksler, Soviet Phys.-JETP 11, 235 (1960).

(7) C. A. Andersen, Int. J. Mass Spectrom. Ion Phys. 3, 413 (1970).

(8) P. Vallerand and M. Baril, Int. J. Mass Spectrom. Ion Phys. 24, 241 (1977).

(9) H. A. Storms, K. F. Brown, and J. D. Stein, Anal. Chem. 49, 2023 (1977).

(10) P. Williams, R. K. Lewis, C. A. Evans, Jr., and P. R. Hanley, Anal. Chem. 49, 1399 (1977).

(11) M. Bayard, unpublished, 1973.

(12) H. Liebl and W. W. Harrison, Int. J. Mass Spectrom. Ion Phys. 22, 444 (1976).

(13) D. E. Zuccaro and C. R. Dulgeroff, Proc. Second Symposium Ion Sources and Formation of Ion Beams, Berkeley, 1974, Paper VIII-8.

(14) N. Kashihira, E. Vietzke, G. Zellermann, Rev. Sci. Instrum. 48, 171 (1977).

(15) V. E. Krohn, J. Appl. Phys. _45_, 1144 (1974).

(16) C. A. Evans and C. D. Hendricks, Rev. Sci. Instrum. _43_, 1527 (1972).

(17) J. F. Mahoney, A. Y. Yahiku, H. L. Daley, D. Moore, and J. Perel, J. Appl. Phys. _40_, 5101 (1969).

(18) M. Bernheim and G. Slodzian, J. de Physique-Lettres _38_, L-325 (1977).

(19) M. Bernheim and G. Slodzian, Int. J. Mass Spectrom. Ion Phys. _20_, 295 (1976).

(20) R. Middleton and C. T. Adams, Nuclear Instr. and Meth. _118_, 329 (1974).

TABLE 1. Primary Ion Sources for SIMS

Species	Ion Source Type	Comments	References
O^-, O_2^+	duoplasmatron	in general use	1-4
Ar^+	duoplasmatron	in general use	1-4
N_2^+	duoplasmatron	in frequent use	1-4
Cs^+	thermal ionization	low emittance	5-8
Cs^+	contact ionization	Cs metal reservoir and porous W ionizer	9, 10
I^-	duoplasmatron	I_2 in Ar carries gas	11, 12
I^-	contact ionization	iodine reservoir, LaB_6 ionizer	13
X^-	contact ionization	source for negative halogen ions, LaB_6 ionizer	14
Ga^+	electrohydrodynamic	also produces other ions (e.g., Cs^+)	15, 16, 17
Cesium	vapor deposition	no ion source, used with duoplasmatron	18
Oxygen	partial pressure	no ion source, used with duoplasmatron	19
$Li^-, B^-, C^-, O^-, F^-, Si^-, S^-$	sputter ion source	ions generated by bombardment with alkali metal ions, not now available for SIMS	20

FIGURE 1

13.5 KeV O⁻

● PURE ELEMENT
△ COMPOUND

FIGURE 2   16.5 KeV Cs$^+$
● PURE ELEMENT
△ COMPOUND
B.D. = BARELY DETECTABLE
N.D. = NOT DETECTED

A SYSTEM FOR COMBINED SIMS-AES-XPS ANALYSIS OF SOLIDS

M. A. Frisch, W. Reuter and K. Wittmaack*

IBM Thomas J. Watson Research Center
Yorktown Heights, New York 10598

It is well known that three-dimensional characterization of the chemical composition of a solid can be achieved by means of Secondary Ion Mass Spectrometry (SIMS). All elements (isotopes) including hydrogen are detectable. Sophisticated SIMS instrumentation allows surface analysis, depth profiling and a display of the lateral distribution of isotopes at the instantaneous sputter-eroded surface (ion imaging). The sensitivity in trace analysis by means of SIMS exceeds the sensitivity of other surface analytical techniques by several orders of magnitude. The main disadvantages of SIMS are (i) the lack of a quantitative theory of secondary ion production and (ii) the strong variation of the ionization probability in the presence of either electropositive or electronegative elements, e.g. oxygen. Presently, (semi-) quantitative analysis can only be achieved by artificial control of the matrix effects, e.g. by sample saturation with oxygen (bombardment with oxygen primary ions and/or bombardment at elevated oxygen pressure).

In view of the difficulties encountered in quantitative SIMS analysis, we have designed a system for combined SIMS-AES-XPS analysis of solids. One of the objectives is to characterize the composition and chemical state of the sample by means of Auger Electron Spectroscopy (AES) and X-ray excited Photoelectron Spectroscopy (XPS), and to use SIMS for trace analysis. The system has been designed so that these SIMS-AES investigations can be performed in situ. For XPS inspection, the sample must be transferred to the respective spectrometer. All studies can be done under UHV conditions (base pressure in the 10^{-10} Torr range) without intermediate sample exposure to air.

The primary ion source can be operated with both non-reactive and reactive gases at acceleration potentials up to 15 kV. The ion gun chamber is differentially pumped so that the total pressure in the target chamber during analysis is mainly determined by the beam current passing through the pressure step (for Ar^+: $\Delta p/\Delta i \simeq 2 \times 10^{-9}$ Torr/μA). As a special feature, the set-up comprises a movable einzel lens and raster scanning unit. The position of this unit with respect to the sample can be varied during the experiment so that both microanalysis (spot size $\lesssim 10\mu$) and large area bombardment (10 mm x 10 mm) are achievable. Bombard-

*On leave from Gesellschaft für Strahlen-and Umweltforschung mbH, Neuherberg/Munich, West Germany.

ment of large sample areas is required because of the large field of view of the XPS spectrometer. To achieve high purity ion beams a mass filter (Wien filter) has been added to the primary beam line. Using a very simple design, a mass resolution $m/\Delta m \simeq 12$ could be achieved. This is sufficient for SIMS operation where separation of O_2^+ from Ar^+ is the main concern. Studies of the purity of argon beams extracted from the metal sealed, hot filament ion source revealed impurity levels of less than 10^{-4}. At 10 kV a mass separated beam current of more than $1\mu A$ has been obtained at the target (with a 1 mm diameter entrance aperture of the einzel lens).

The single path cylindrical mirrow analyzer (CMA) used for AES-studies is mounted $70°$ with respect to the primary ion beam. For combined SIMS-AES studies the primary ion beam enters the target at an angle of $45°$ while the electron beam hits the target at an angle of $65°$ with respect to the sample surface. In this configuration SIMS and AES studies can be performed without movement of the target. The sample holder, the quadrupole mass filter, and the CMA are mounted on bellows to permit accurate alignment with respect to each other. For combined SIMS-AES-XPS studies a Hewlett Packard 5950 B x-ray photoemission spectrometer is connected to the SIMS-AES chamber via an isolation value. The samples are mounted on a rod similar in design to the one used in the standard XPS spectrometer. The sample is moved from the loading position into the SIMS-AES chamber and finally into the XPS position via a metal bellow,

The automation of the SIMS-AES system is achieved using an IBM system 7 computer. Two important instrument parameters are under the control of the computer via high precision digital analog converters: 1) the mass filtered by the quadrupole mass spectrometer; this allows the performance of a variety of complex scanning routines and 2) the potentials applied to the energy filter; this permits the operator to take advantage of the variation in the energy distribution of either atomic or molecular secondary ions. In addition, several programs are available for data analysis: *i*) the calculation of the count averages and their statistics, *ii*) plotting of mass spectra for a specified time window, corresponding to a given depth in the profile and *iii*) the display of one or more ion species as a function of time, corresponding to the depth profile of the sample.

Wide dynamic range in ion signal detection is obtained by the use of high speed pulse counting techniques, with the gating of the scaler controlled by a programmable timer. An important feature of the timer is the ability to inhibit the scaler during unwanted portions of the raster. By this technique crater wall effects in depth profiling measurements are eliminated.

THE SECONDARY ION OPTICS OF A QUADRUPOLE ION MICROPROBE*

J. C. Potosky and D. B. Wittry

Department of Materials Science
University of Southern California
Los Angeles, California   90007

At present the determination of the chemical composition of a microvolume of solids by ion microprobe analysis is semi-quantitative. The technique is largely limited by the present understanding of secondary ion emission processes. An ion microprobe using a quadrupole mass filter has been developed[1] to study this phenomena with the aim of making the technique of Secondary Ion Mass Spectrometry (SIMS) more quantitative.

A vital component of this instrument is the secondary ion optical system. These electrodes extract the sputtered ions from near the sample surface and focus them into the quadrupole mass filter for subsequent mass separation. A schematic of the system is shown in Figure 1. Additionally there must be a significant amount of energy filtering before the ions enter the quadrupole. This is accomplished by the chromatic aberration of the extractor geometry.

The ion optical elements are diagramed in Figure 2. A unique point in the design is the high angle of incidence of the primary beam relative to a normal to the specimen's surface (75°). This angle was chosen for three reasons. First, the sputtering yield for most materials is greatly enhanced by oblique incidence of the primary ion beam. Second, the important function of depth profiling should be done with greater depth resolution. Lastly the configuration allows a large solid angle

of sputtered ions to be collected.

Considerable computer analysis was used in the design to determine the spatial response and energy bandpass of the system. This information is very important in correcting ion microprobe raw data for instrumental characteristics. Corrections of this nature are necessary for increasing the confidence in quantitative SIMS analysis.

References

1. J. C. Potosky and D. B. Wittry, "A Quadrupole Instrument for Investigations of Electron and Ion Beam Interactions with Solids," Proceedings 10th Annual Conference on Microbeam Analysis 1975, pp. 76 A-C.

PRIMARY
BEAM
TO ±20kV

SIGNAL

PM
TUBE

SCINTILLATOR

ELECTRON
BOMBARDMENT
IONIZER

QUADRUPOLE
MASS
FILTER

EXTRACTOR
LENS

0-15 kV

SPECIMEN

CONVERTER

±0-3kV

IONIZER
POWER
SUPPLY

±0-100V

±0-15kV

Fig. 1

Objective Lens

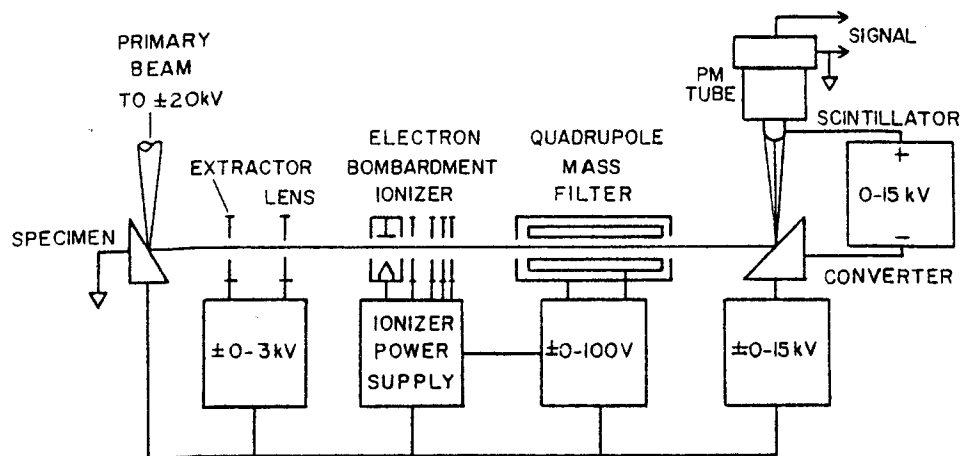Ionizer

Lenses

Quadrupole

Stage

Extractor

Backplane

Icm
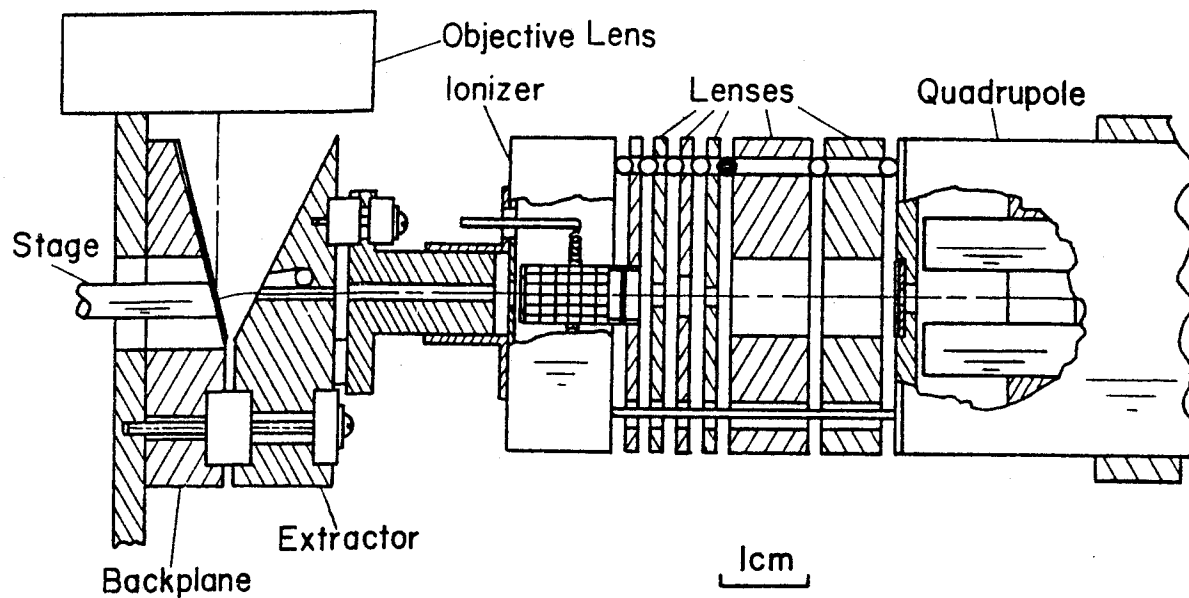
Fig. 2

INSTRUMENTAL DISCRIMINATION EFFECTS IN SIMS

M. A. Rudat and G. H. Morrison

Department of Chemistry
Cornell University
Ithaca, N. Y. 14853

Introduction

Two main approaches have been used in the attempt to obtain quantitative analyses using SIMS: empirical methods and what we call the semi-theoretical approach. The former requires standards, but a technique has recently been developed whereby the standards provide a special type of reference curve which must only be determined once (1). This Matrix Ion Species Ratio method has proven to be very successful, obtaining accuracies of 10% or better. The semi-theoretical approach utilizes a theoretical model of the ionization process in concert with the experimental data to determine the ionization efficiencies of the ions detected, and thereby calculates the composition of the sample being sputtered from the signal intensities. The most widely used of these models is the local thermodynamic equilibrium (LTE) model first proposed for use in SIMS by Anderson and Hinthorne (2), and put into practice with their CARISMA computer program, as well as with the many simplified and modified versions of that program used by other laboratories. In principle, the use of a good theoretical model in these calculations could allow standardless quantitative analysis since the sum of the concentrations of all of the elements present must be 100%. The main unspoken requirement in the use of such an approach is that the signal levels from the SIMS instrument must have a one-to-one correspondence with the secondary ion populations in the vicinity of the sample surface. It is here that instrumental discrimination effects can play an important role.

The instrument used in our laboratory, the CAMECA IMS-300, has been evaluated for discrimination effects induced by the detector system, the collection optics, and the energy bandpass of the spectrometer. The detector effects were evaluated for a large number of atomic, dimer, and monoxide positive ions representing 50 elements. The energy spectra for positive ions from more than 40 elements were determined, and the discrimination effects of the collection optics and energy bandpass were extracted from them. The results will be applied to the evaluation of several theoretical models for use in quantitative analysis with SIMS.

Experimental Results

Detector Effects: In the detector discrimination study, a Faraday cup was
used as a reference for the true ion current entering the detector section of
the IMS-300. The output current of the Faraday cup was amplified and con-
verted to a voltage, which was then used as the reference. An aperture en-
sured that the Faraday cup and the instrument's Cu/Be ion-to-electron conver-
ter were exposed to the same portion of the ion signal from the sample. The
electrons emitted by the Cu/Be electrode due to the impact of the 46.5 KeV
ions, were accelerated and magnetically directed toward a plastic scintillator,
the light output from which was monitored by a pair of coincidence-mode pulse
counting photomultipliers. The pulse count rate was determined using a com-
puter interfaced to the instrument. The result of the comparison was a ratio
given in counts per second/volt, with the values on the order of 10^5 cps/v.

Figures 1, 2, and 3 show the results of this study for the M^+, MO^+, and
M_2^+ types of ions, plotted versus the mass of the element M. There is clearly
a strong periodicity in the detector yields for the various ions, which seems
to be related to the electronic structure of the neutral atoms: for ions
beyond Sc the maxima in the detector yield curve for the M^+ ions occur for
elements in the IIA to IVB columns, and the minima occur for the IIIA elements.
This type of oscillation in yield has been reported for ions striking electron
multipliers at much lower energy, and it has been suggested that the behavior
is due to variations in the electronic stopping power (s_e) for the various
ions (3). The locations of the maxima and minima on the mass scale are com-
parable to the rather limited results previously reported (4,5,6,7).

The results for the MO^+ and M_2^+ ions have also been shown to vary periodi-
cally, and in fact are directly related to the yields of their constituent ele-
ments M^+. The smooth curves on Figures 2 and 3 are actually the curve from the
M^+ graph least-squares fit to the MO^+ and M_2^+ data which have been plotted vs.
the mass of M. The correlation is surprising, but is helpful in estimating
the detector yield factors for ions not detectable by the Faraday cup in this
study. The MO^+ ion result might be explained by the fact that a multiple-atom
ion tends to break up on impact and contribute an electron yield from each
piece (4,8) so that the additional atom (oxygen) tends to contribute a constant
amount, increasing the yields to be an average of about 35% higher than that
for the corresponding atomic ion. However, this does not explain why the dimer
ions also tend to have a yield about 30% higher than the M^+ ions, and correlate
with the M^+ yields about as well as the MO^+ yields do.

There is obviously a significant effect on the SIMS spectra, since to obtain a true measure of the secondary ion current entering the detector one must use the expression:

$$\text{true relative ion current} = \frac{\text{apparent current}}{\text{detector yield factor}} \cdot$$

For the M^+ ions, the detector yield factors vary by more than a factor of two, and by nearly that amount for the MO^+ and M_2^+ ions. The atomic ions are most used in the semi-theoretical analysis schemes, occasionally having their signal level supplemented by the MO^+ signal. Obviously, since the apparent signal is not related to the true signal in the same way for all ions, the effects will be significant, especially when using internal standards. For example, if zinc and gallium were used as internal standards for a semi-theoretical type of quantitation program, the concentrations of calcium and titanium would be overestimated by a factor of 1.8-1.9, even if the ionization model being used were correct. Adding the MO^+ signal to the M^+ signal simply complicates matters.

Ion Energy Effects: The variation in the energy spectra of positive ions between ions of different types is illustrated in Figure 4 for the case of vanadium. In general, as the number of atoms forming the ion increases, the energy spectrum becomes narrower and peaked at somewhat lower energies. Because of this dramatic variation, the effect of instrumental energy discrimination must also be taken into account.

The energy discrimination effect of the IMS-300 is severe; the approximate effect of the ion extraction lens is illustrated in Figure 5. In addition, the instrument employs an electrostatic mirror as a high energy cutoff, which is normally operated in our laboratory so as to obtain a bandpass of 0-15 eV initial energy. The combined effect is illustrated in Figure 6 for vanadium. The smaller curve represents the uncorrected energy spectrum (having been attenuated due to the extraction lens) and the shaded portion indicates the portion of the original signal actually being sent to the detector. The ratio of the shaded portion to the total integrated corrected ("true") energy spectrum (the upper curve) gives a direct measure of the collection and transmission efficiency of the instrument for the ion being measured, and will be referred to as the bandpass efficiency.

The energy spectra for essentially all detectable ions not having mass interferences for many pure elements and many elements dispersed in a silver matrix were determined under high vacuum conditions (5×10^{-8} torr), with O_2^+ bombardment at 5.5 KeV. The bandpass efficiencies were then determined from the

spectra. The variation in the bandpass efficiency is larger between ion types than within a class, there being more than a factor of three range in efficiencies between the large polyatomic ions (typically 23%) compared to the atomic ions (typically 7%); ions composed of two atoms tend to have an inter-mediate value (about 15%). The bandpass efficiencies for ions of a given type tend to fall within a narrow range (e.g., 7 ± 3% for the atomic ions) although some ions have unusually narrow or broad energy spectra which tend to make their bandpass efficiencies very much higher or lower than other ions of the same type. A systematic investigation of these effects is being completed at this writing, and the results will be presented.

Conclusion

Wide variations in the bandpass efficiency of any SIMS instrument can dramatically affect the appearance of the mass spectra, as can variations in the detector yield for various ions. These significant contributions to the instrument discrimination have been evaluated for the CAMECA IMS-300, and have been found to be of a surprisingly large magnitude. Since they represent the largest sources of discrimination for this instrument, the combined effects will be taken into account and used for the evaluation of the efficacy of the various semi-theoretical quantitation methods that have been proposed over the last several years. It is expected that this will reveal which of these models, if any, will be able to be used for quantitative analysis of any samples, and which best describes the ionization process in SIMS.

REFERENCES

1. J.D. Ganjei, D.P. Leta, and G. H. Morrison, Anal. Chem., in press.
2. C.A. Andersen and J.R. Hinthorne, Anal. Chem., 45 (1973) 1421.
3. U. Fehn, Int. J. Mass Spectrom. Ion Phys., 21 (1976) 1.
4. C. La Lau, Adv. Anal. Chem. Instrum. 8 (1970) 93.
5. R.C. Lao, R. Sander, and R.F. Pottie, Int. J. Mass Spectrom. Ion Phys., 10 (1972/73) 309.
6. U. Fehn, Int. J. Mass Spectrom. Ion Phys., 15(1974) 391.
7. G. Staudenmaier, W.O. Hofer, and H. Liebl, Int. J. Mass Spectrom. Ion Phys., 11 (1976) 103.
8. M. Van Gorkom and R.E. Glick, Int. J. Mass Spectrom. Ion Phys., 4 (1970) 203.
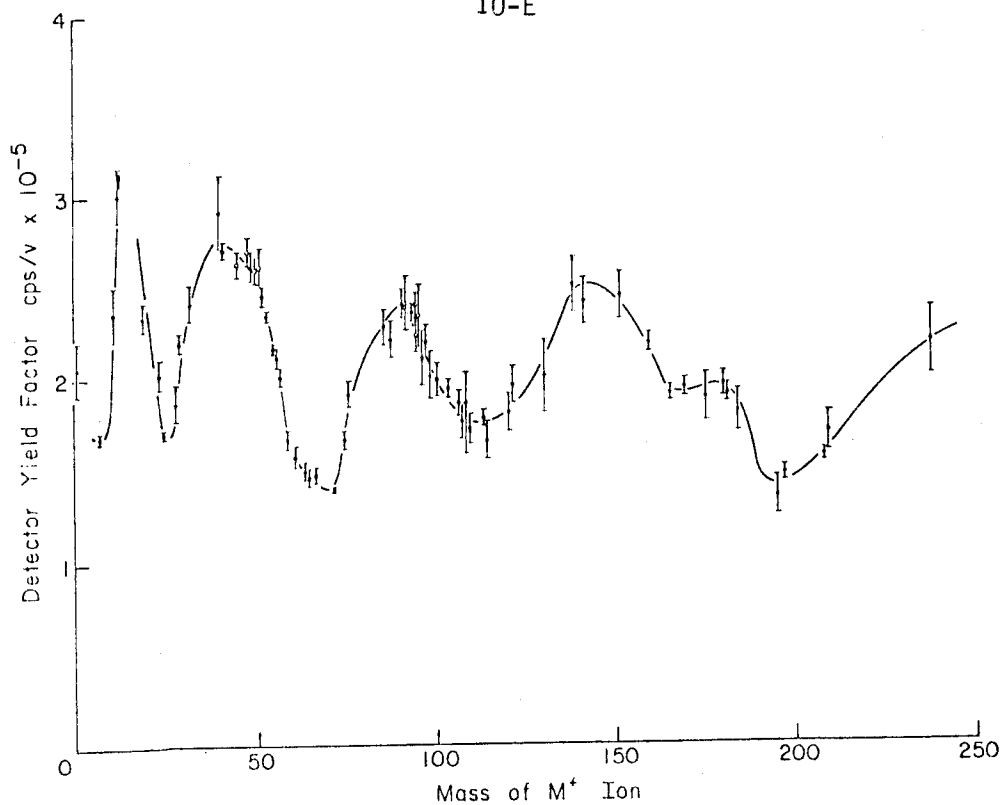
Fig. 1. Detector yield factors (instrument output compared to Faraday cup output) for atomic ions, including a number of isotopes (open circles).
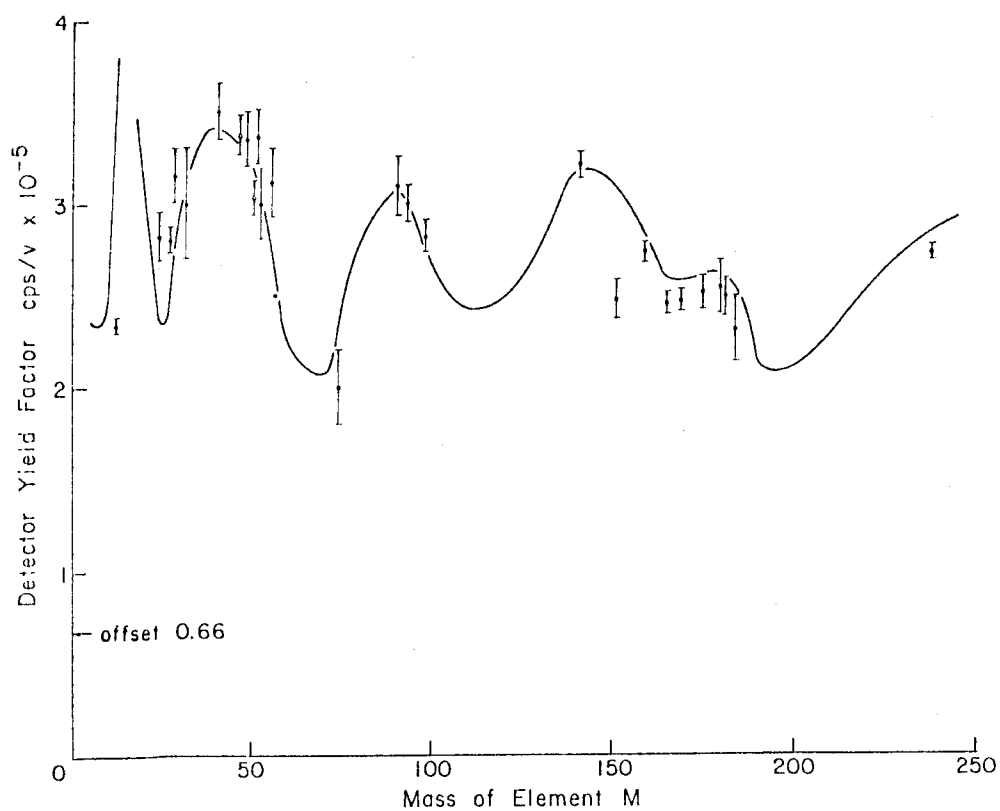

Fig. 2. Detector yield factors for monoxide ions (MO$^+$) vs. mass of element M. Curve is from Fig. 1, offset by 0.66 units.
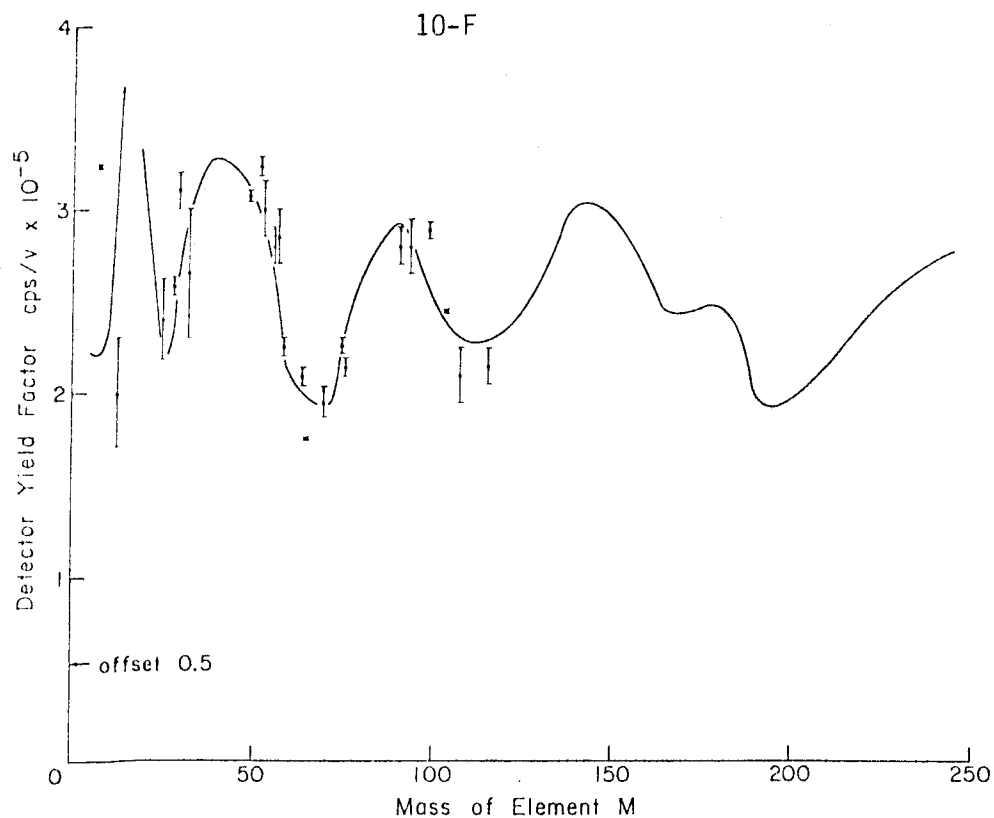
Fig. 3. Detector yield factors for dimer ions (M_2^+) <u>vs</u>. mass of element M.
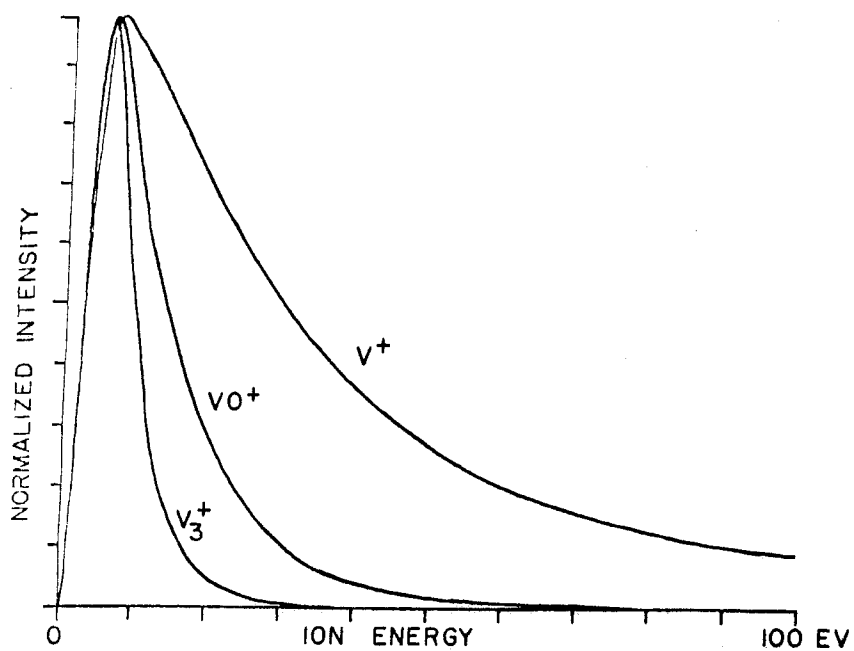Curve is from Fig. 1, offset by 0.5 units.

Fig. 4. Normalized energy spectra for typical atomic, monoxide, and
polyatomic ions.

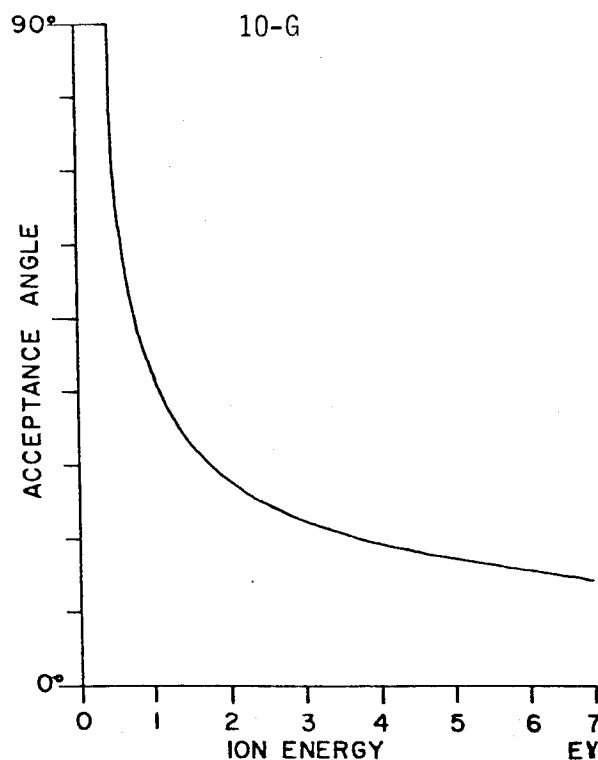Fig. 5. Extraction lens characteristics for a 400 μm contrast aperture. Angle of acceptance as measured from the surface normal defines the solid angle of acceptance for ions of a given energy and angle of emission from the sample.
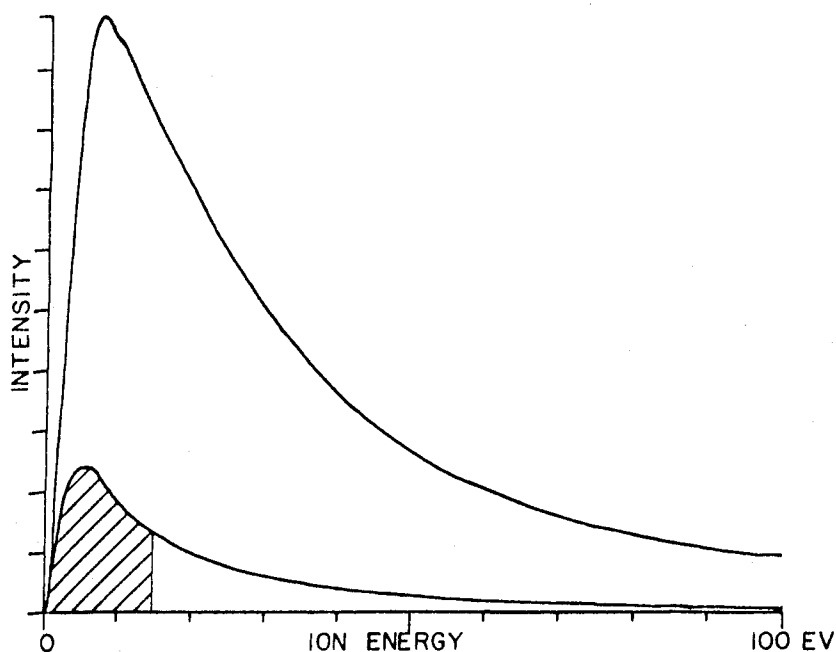

Fig. 6. Corrected (upper) and uncorrected (lower) energy spectra. Shaded area shows the portion of the signal reaching the detector due to the 0-15 eV bandpass of the instrument as used.

OPTIMIZATION OF RECORDING SECONDARY ION MASS SPECTRA*

D. B. Wittry

Departments of Materials Science and Electrical Engineering
University of Southern California
Los Angeles, California   90007

Secondary ion mass spectroscopy using a magnetic spectrometer places severe demands on analog recording systems. The problems are due to the following: a) the large dynamic range of signals, b) the large change in peak width over the mass range, involving very narrow peaks at small mass numbers, and c) limited recorder slewing rates.

The problems due to the wide dynamic range of the signal can be overcome to a large degree by using logarithmic recording of the counting rate, or by using periodic pulse counting followed by digital-to-analog conversion with logarithmic recording. The first of these approaches is not very satisfactory because of limitations due to ratemeter circuitry for signals of a large dynamic range and because of the limited range of typical logarithmic converters operating on analog signals. The second approach is more satisfactory and is the basis for computerized recording systems using digital data storage and subsequent display in a logarithmic mode. An alternative and less expensive solution is to utilize commercially available photon counting systems with digital to analog conversion and logarithmic output. One such system manufactured by Princeton Applied Research Corporation provides 8 decades of dynamic response and a wide range of integration times. Hence the large dynamic range of the signals obtained in SIMS spectra is not a serious limitation to accurate recording of secondary ion mass spectra.

The problems due to the change in peak width over the mass range have not been satisfactorily addressed in existing instruments. In many cases,

the magnetic field is scanned linearly with time t. For this case the mass

number is proportional to t^2. This yields a slower mass scan rate at

low mass number than at high mass number as desired because of the

narrower peaks at low mass number. However, this type of scan is not

optimal because the time spent in scanning each mass peak is not a constant.

As a result, if one selects a scan speed for detection of low mass peaks

to a given accuracy, the speed is too low for high mass peaks. Alternatively,

if one selects a scan speed based on a given accuracy for detection of high

mass peaks, the scan speed is too fast at low numbers. In the former case

we spend more time than necessary to perform a mass scan, while in the

latter case we can encounter errors at low mass numbers due to inadequate

counting statistics or due to limited slewing speed of the recorder.

It can be shown that for a spectrometer having $\Delta M/M$ = constant, the dwell

time over each peak will be a constant if the mass number increases expo-

nentially with time, i.e. $M = M_o e^{t/\tau}$. Since M is proportional to B^2,

the magnetic field should also increase exponentially with time. This

is easily implemented by a linear ramp followed by a functional module

that provides an output proportional to the antilog of the input, as

shown in Figure 1. The expected theoretical improvement in scanning time

for an exponential scan is indicated in Figure 2. In this figure a

scan time over a peak at mass number 6 is taken to be 0.5 seconds for

all cases. The exponential scan would require a scan time of ~8 minutes

to go from mass no. 6 to 150. A mass scan proportional to t^2 (conventional

method) would require $\approx$ 20 minutes. Also shown in this figure is the

scan time required for a mass scan that is linear in time (time required

$\doteq$ 60 minutes). It should be noted that although the mass scan may be

nonlinear with time, the x deflection of the recorder will be proportional

to the mass if a signal from the magnetic field detector is squared as

shown in Figure 1.

An additional advantage of the exponential mass scan is that the dwell time over each mass peak can be independent of the starting mass number. Thus, if only species of higher mass number are of interest, the time required for a mass scan can be further reduced without affecting the dwell time on each mass peak.

Comparison of experimental results for an exponential mass scan ($M \propto M_o e^{t/\tau}$) and a conventional mass scan ($M \propto t^2$) will be given.
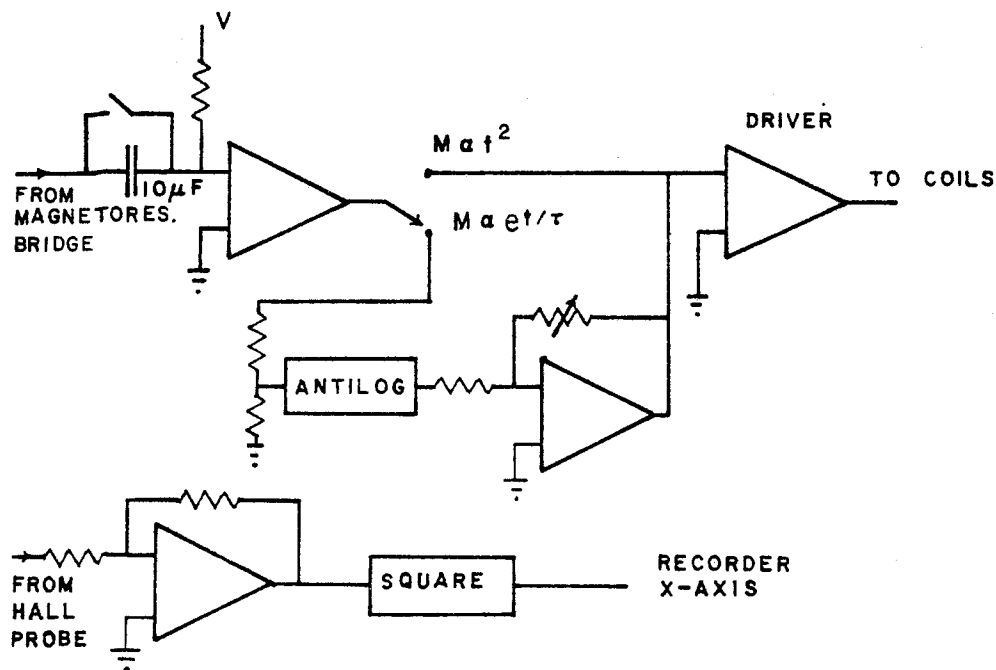

FROM MAGNETORES. BRIDGE

$M \alpha t^2$

$M \alpha e^{t/\tau}$

DRIVER

TO COILS

ANTILOG

FROM HALL PROBE

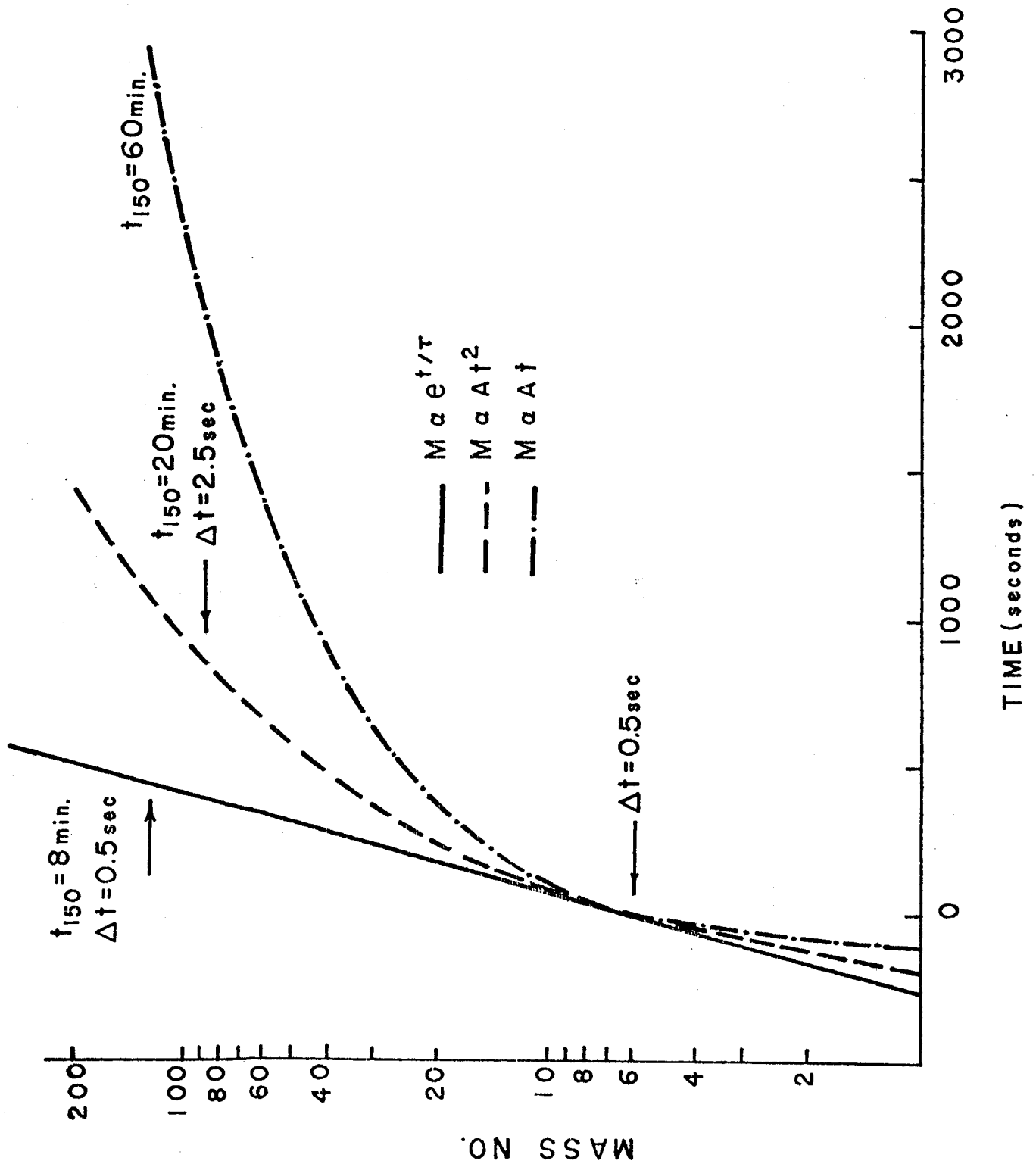SQUARE

RECORDER X-AXIS

FIG. 1

FIG. 2.

MULTIFEATURE MASS ANALYSIS UTILIZING
DIGITAL IMAGE PROCESSING OF SECONDARY ION MASS SPECTROMETRIC IMAGES

J. D. Fassett and G. H. Morrison

Department of Chemistry
Cornell University
Ithaca, N. Y. 14853

The ion microscope is a unique analytical tool combining ion sputtering, mass spectrometric filtering, and ion optics to give a spatially resolved mass analysis of the surface of a solid (1). An ion micrograph produced photographically has up to 250 μm diameter field of view with a 1 μm point-to-point resolution. Thus, an ion micrograph potentially contains over 50,000 information bits, where each information bit is related to the number of secondary ions of a particular mass sputtered from a particular point on a sample. A series of ion micrographs, surveying a range of masses of interest, increases the dimensionality of an analysis, providing both spatial and extended elemental information for the sample.

A system has been developed in this laboratory that combines scanning microphotodensitometry and digital image processing to analyze the large number of information bits in an image (2). Whereas previously ion images have been studied for only the obvious qualitative information available, that is, relative correlations between elements and phases and features, quantitative spatial and elemental correlations are possible with computer processing of micrographs. The original ion micrograph film negative is digitized into a point density matrix of size 256 square with 256 levels of density resolution by the microphotodensitometer. Thus, both spatial resolution and intensity resolution is maintained in the digitization process. From previous work procedures have been developed that determine the characteristic curve of the film relating density to ion intensity. Therefore, a digitized and quantized ion micrograph can be equated to a summation of 50,000 microprobe analyses.

Computerization of images is a well established method of qualitatively and quantitatively handling image information in many fields of science, although neglected in chemical analysis. Feature analysis which is one aspect of digital image processing, entails the identification and quantification of features where features can be defined by one or a number of parameters such

as intensity, shape, or size. This study is an example of one important application of feature analysis to ion microscopy illustrating the ability to extract and correlate compositional information from a series of micrographs of a multifeatured specimen.

A polycrystalline iron specimen was analyzed and a series of ion images spanning atomic and molecular positive secondary ion species of iron and oxygen was taken. The features in this sample are the different crystal grains. These different crystal grains exhibit relative intensity contrasts due to differential primary ion beam-crystal orientation interactions, a well noted phenomenon of SIMS (3). The micrograph negatives were digitized and a feature map isolating the individual grains in the image area constructed by a combination of derivative and threshold techniques on one of the micrographs. This feature map was then aligned relative to each individual image in the series and the compositional information collated. Table I illustrates the results; Figure I presents two images from the series and the feature map. This work is part of a study on the effect of crystal grain structure and differing instrumental modes of operation in quantitative analysis.

Literature Cited

1. G. H. Morrison and G. Slodzian, Anal. Chem., 47, 932A (1975).
2. J. D. Fassett, J. R. Roth, and G. H. Morrison, Anal. Chem., 49, 2322 (1977).
3. M. Bernheim, Radiation Effects, 18, 231 (1973).

TABLE I. FEATURE MASS ANALYSIS

FEATURE Mass	Exposure(sec)	I	II	III	IV	V	VI
		---- I N T E N S I T I E S ----					
^{16}O	300	.68	.52	.82	.39	.67	.85
^{56}Fe	20	94.	78.	120.	96.	78.	130.
^{72}FeO	200	1.8	1.8	2.1	1.7	1.7	2.6
$^{112}Fe_2$	50	30.	34.	21.	14.	21.	47.
$^{128}Fe_2O$	50	17.	16.	15.	9.0	12.	26.

Characteristic Curve

$$Dc = -0.896 + 1.033 \log (t \cdot I/100)$$
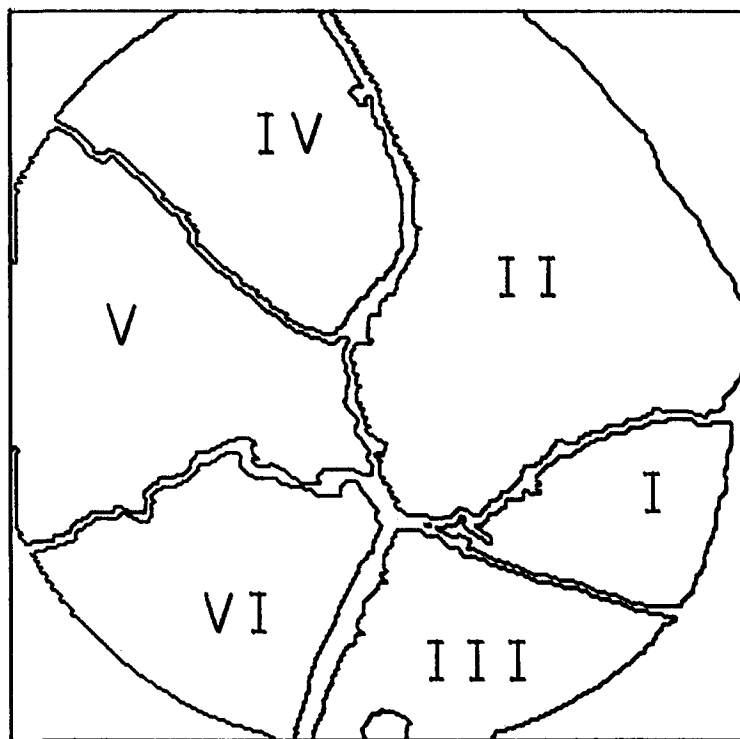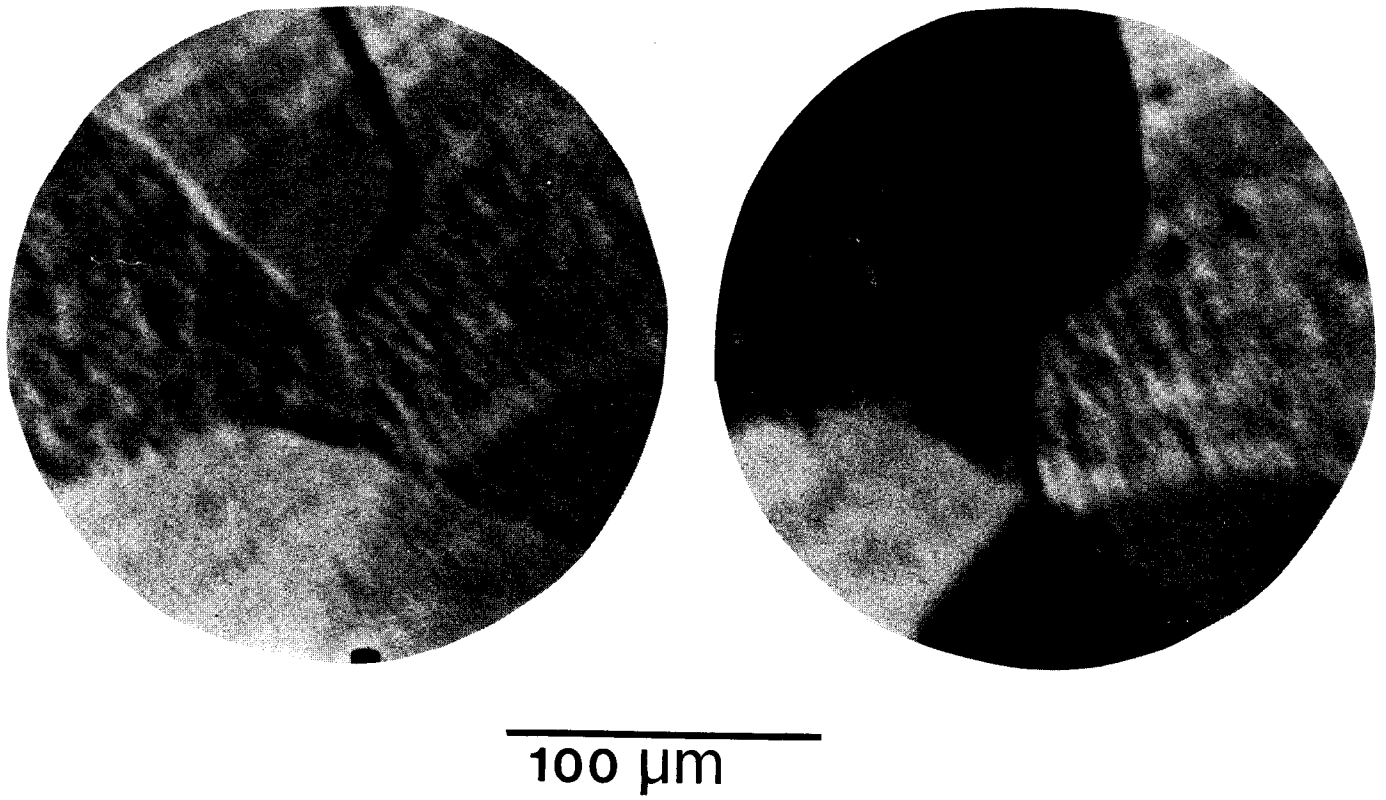
$$I(Fe_{avg.}) = 1.00$$

100 µm

Figure 1: Fe and Fe$_2$ micrographs representative of ion image mass series, and the feature map used to quantify features.

USE OF SPECIMEN CURRENT INTEGRATION IN SIMS*

F. Guo and D. B. Wittry
Departments of Materials Science and Electrical Engineering
University of Southern California
Los Angeles, California   90007

In secondary ion mass spectroscopy, depth profiles are usually obtained by assuming that the depth is directly proportional to the sputtering time; subsequently the relationship between depth and sputtering time is determined by measuring the pit profiles by interference microscopy or by stylus techniques. This works well if the beam is swepth in a faster fashion, if electronic aperturing is used and if the incident ion current does not fluctuate during the depth profile. Under these conditions it is also possible to determine sputtering rates from the primary ion current, the scanned area and the time the beam is actually on (it is usually desirable to blank the beam during retrace).

Because of errors that can occur when the primary ion current varies, it is desirable to also monitor specimen current during a depth profile and most SIMS instruments are provided with this capability. However, up to now, little use has been made of specimen current as a signal that could aid in improving quantitative measurements. Two possible applications are immediately apparent, namely 1) the value of the integrated specimen current over a short period could determine the secondary ions counted and 2) the value of the integrated specimen current from the beginning of a depth profile could be used in place of time as variable related to depth. A simple system for beam current integration that we have constructed for use with a prototype IMMA instrument is shown in Figure 1.

Results obtained with specimen current must be interpreted with caution because sputtering rates are not always uniquely related to specimen current. Because of secondary processes, it is essential to determine the relationship between specimen current and primary ion current as measured on a Faraday cage for each specimen of interest. It is also important to insure that sputtering yields do not vary with depth for a given specimen (the same problem is also present when time is used as a coordinate instead of integrated specimen current). For this reason, it is expected that integrated specimen current will be useful in providing more reproduceable results mainly on specimens for which the concentration of major constituents is nearly independent of depth. Because of surface charging and associated secondary electron or ion processes, it is also expected that integrated specimen current may be less useful in studies of insulators than in studies of metals or semiconductors.

Experimental results concerning the utility of integrated specimen current for studies of III-V semiconductors will be given.
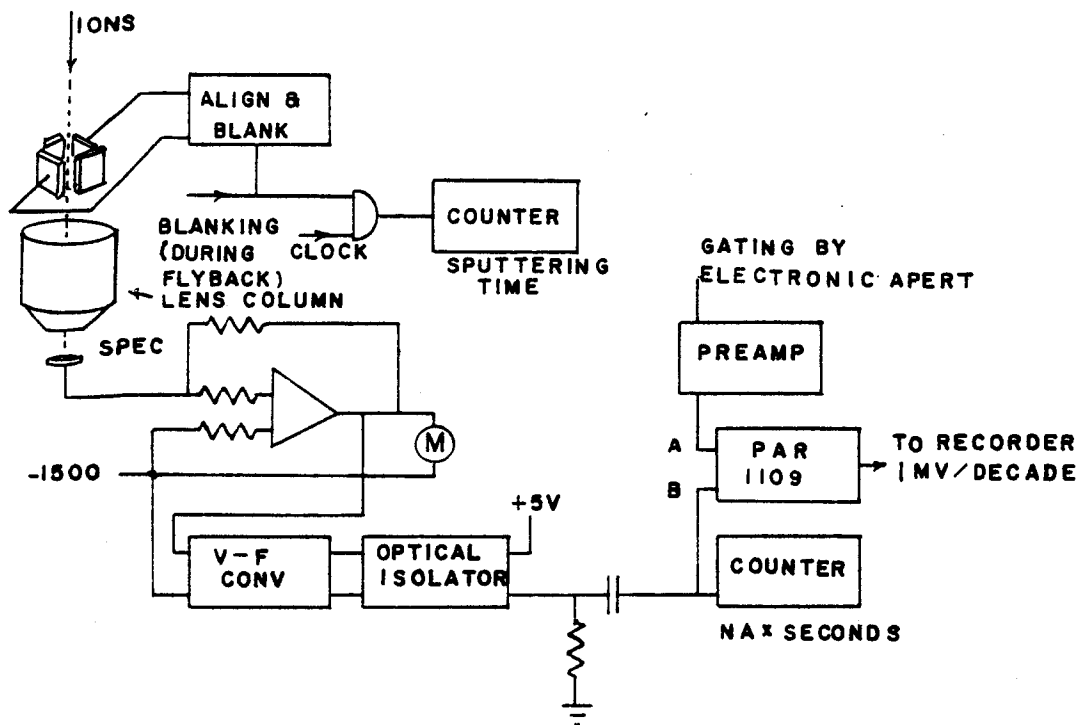
FIG. 1

APPLICATION USING SECOND GENERATION HIGH
RESOLUTION ION MICROANALYZER

BY

C. Conty
CAMECA
Courbevoie, France

The completely new instrument concept of the IMS 3F Ion Microanalyzer allows us to analyze large areas (400 sq. microns) as well as small ones (a few sq. microns) with a high sensitivity.

With such a high sensitivity, lower detection limits of impurities can be achieved in both in-depth profiles of dopants in semi-conductors and isotopic ratios in geological samples.

Some applications data will show:

1) The sensitivity, precision and reproductibility of analysis on geological samples for the isotopic ratio measurement on one of several elements.

2) The detection limit of dopants in semi-conductors, notably in-depth analysis of, as Sb and B implanted or diffused in Si wafers. These examples will show the transfer optics efficiency for analysis of small surfaces.

3) Ion images will show the distribution of several elements and stress the improved lateral resolution.

4) High resolution mass spectrum will show the separation of doublest or triplets, notably those of Cu and Ti at masses 63 and 65.

ELECTRON ENERGY-LOSS SPECTROSCOPY (EELS) AND ITS

APPLICATION TO BIOLOGY

David Joy and Dennis Maher
Bell Laboratories
Murray Hill, NJ   07974

INTRODUCTION

Recent developments in the electron microscope have made it possible to combine high-resolution imaging with chemical information. The most familiar technique for such microanalysis is that which uses the fluorescent X-rays produced by the interaction of the incident beam with atoms in the specimen. When an energy dispersive x-ray spectrometer is combined with a 100 kV (scanning) transmission electron microscope, all elements from about sodium upwards in the periodic table can be studied simultaneously with a minimum detectable mass of the order of 10^{-19} gm[1] and a spatial resolution of the order of a few hundred angstroms. The utility of this technique is demonstrated by the large volume of papers dealing with its application. However there are many problems for which x-ray analysis is of very limited value because the elements of interest are those of low atomic number such as carbon, nitrogen or oxygen.

This fall off in sensitivity is because of the characteristics of the detector. The number of x-ray photons N actually counted into the multi-channel analyser can be written as

$$N_z = J \cdot \sigma_z \cdot W_z \cdot M_z \cdot Q \quad \text{counts/sec.} \quad \text{--- (1)}$$

where J is current density, σ_z the ionization cross-section, W_z is the fluorescent yield, M_z is the mass of the element z present and Q is a term representing the efficiency of the detector. For light elements ($Z \leq 12$) the fluorescent yield W_z is falling as about z^4, but the cross-section σ_z is rising rapidly and the product $\sigma_z W_z$ is about constant. However the window in front of the detector and the gold "dead-layer" on the detector have an absorption characteristic which rises extremely rapidly for photons having energies lower than 2 kV or so. For photons of only a few hundred eV the detection efficiency is effectively zero. There is also the problem that, at this energy, the resolution of the spectro-meter is a very large fraction of the separation between peaks, and interent electronic noise is of the same order of magnitude as the signal. Consequently even with greatly improved detectors, light element analysis with X-rays using an energy-dispersive spectrometer could never be very satisfactory.

Electron energy-loss spectroscopy (EELS) circumvents all of these problems. The incident electron which excites the atom loses an amount of energy equal to the that required to complete the ionization. This energy loss is as characteristic of the atom excited as the x-ray produced and therefore can equally well be used for microanalysis. During the ionization event the incident electron is deflected, but only by a relatively small angle typically a few milli-radians. All the electrons which passed through the sample and interacted with it are therefore contained in a narrow cone. Thus, in principle, almost every electron can be collected and passed into an

electron spectrometer which measures its energy loss. By analogy with the x-ray case (Equation 1), Q is therefore very high and essentially independent of the energy loss (which in any case is only 1% or less of the incident energy of the beam). In addition there is no fluorescent yield factor to include since it is the ionization of the atom that is measured, not its subsequent decay. Consequently the efficiency of EELS for the detection of light elements will actually increase as Z decreases because of the increase in σ_z.

THE ELECTRON SPECTROMETER

The characteristic energy losses that contain the required micro-analytical information are measured, relative to the incident beam energy, by an electron spectrometer. This disperses the transmitted electrons as a function of their energy by passing them through magnetic or electric fields. Figure 1 shows a typical arrangement for a magnetic electron spectrometer fitted to an electron microscope, in this case a JEOL JEM 100 B. Electrons transmitted through the sample are brought to a focus at about the level of the fluorescent view-ing screen of the microscope. This focus is the object point for the spectrometer which is simply an electromagnet which bends the electrons through a 90° arc. Those electrons which have lost energy relative to the incident energy of 100 keV are bent more strongly and are thus deflected in the vertical plane as shown. On the system shown here, this deflection is about 4 μm

per eV of energy lost. The energy spectrum can then be obtained by scanning this dispersion over a narrow slit behind which is a scentillator and photo-multiplier detector arrangement. A slit width of 80 µm gives an effective resolution of 20 eV, which is comparable to the resolution of a crystal (wavelength-despersive) x-ray spectrometer. The spectrum collected in this way is then stored in a multichannel analyser [2] for observation and analysis.

Spectra can be obtained in either TEM or STEM modes of operation. In TEM the size of the area analysed is set by the intermediate ("selected area") aperture, or by focussing the illumination. Typically regions ~0.5 µm or more in diameter are achieved. In STEM the area is determined by the area scanned or, with a stationary probe, by the probe size. Since, unlike the x-ray case, these is no extra scattering the resolution of the analysis will be set only by the area illuminated and regions down to one or two hundred angstroms are possible. The angular range of scattered electrons accepted by the spectrometer is controlled by the objective or intermediate apertures, and with an appropiate choice [3] the signal/noise ratio of the spectrum can be optimized. Additionally in STEM, images in any selected energy-loss windows can be obtained. The application of these two modes of operation will now be considered.

SPECTRAL ANALYSIS

Figure 2 shows the spectrum obtained from a thin carbon film. The most prominent feature is the peak at zero energy loss due to the electrons transmitted without losing any energy. As is clear from the logarithmic scale all the other features in the spectrum are of much lower intensity.

In this case, at 283 eV loss, the carbon K-edge is visible. It has the form of a sharp discontinuity on top of the monotonically falling background. The energy at which the discontinuity occurs identifies the element concerned, listings of values can be found in standard x-ray tables or on charts [4]. K-edges have a triangular appearance, L edges a more rounded "sleeping whale" shape.

In principle the process of analysis is similar to that for x-ray systems. The spectrum from the selected area is recorded, the time usually being of the order of 100 seconds for a 0 - 1 KeV loss range, and then examined from the display of the multichannel analyzer. The spectrum is swept out in the direction of increasing energy loss and because the signal level falls steadily, occassional gain adjustments are necessary to maintain a suitable amplitude. Figure 3 shows a portion of the spectrum recorded from thin crystals of cytrochrome oxidase, indicating the variety of elements that can be detected. It is clear that, even for relatively heavy elements such as iron, the sensitively of this technique is high since the iron edge present represents the signal from only 2 atoms of iron per 120,000 units of molecular weight. In this case the spectrum was recorded using a 300 $\overset{\circ}{\text{A}}$ diameter spot and a beam current of about 10^{-10} amp. The thickness of the specimen is of critical importance in determining the quality of the spectrum. If the specimen is too thick, probably in excess of 1000 $\overset{\circ}{\text{A}}$ at 100 kV, then multiple scattering effects will swamp small edges and distort larger ones. Specimen charge-up will also adversely affect the quality of the spectrum, but conventional techniques to avoid this such as the

deposition of carbon must not be used or else the spectrum will contain a dominant carbon edge and little else! A final problem is that of mass loss during analysis. Preliminary studies show that the rate of loss of some elements such as oxygen, lithium and nitrogen under the beam is very high. This can only be minimized by reducing the beam dose, keeping the beam moving to fresh areas of the sample, and only scanning that part of the spectrum which contains the edge of interest.

THE ENERGY SELECTED IMAGE

In the STEM mode of operation energy filtered images can be formed by adjusting the spectrometer so that the desired energy loss falls over the slit. One use of this is simply to collect only the zero-loss image and filter out all the inelastic signals which tend to reduce the image contrast. Alternatively any chosen edge can be set over the slit. In this case when the corresponding element is present the signal level at the slit will be higher than the background level without the element present. An image taken at this loss will thus map the presence of the chosen element. Figure 4 shows an example of this technique in operation. Blood platelets, incubated with a sulfur analog of seratonin, were imaged in the sulfur L_{23} loss. The image clearly shows the localization of the sulfur to the dense bodies and their corresponding fibers. This technique can be applied to any element, but it is most advantageously used for elements which are specifically used as tracers and are not otherwise present, for example fluorine[5].

The sensitivity of the method is high and the quality of the images compares very favorably to x-ray elemental maps.

Resolutions of the order of several hundred angstroms are readily obtained. However care must be used in interpreting the images as a direct visualization of the amount of the element present since other effects, such as changes in thickness, can also cause contrast. Images taken below and above the edge can be used to alleviate this problem, or alternatively the map can be compared with a dark-field "mass thickness" image.

REFERENCES

1. D. C. Joy and D. M. Maher, Proc. 10th Ann. SEM Symposium (ed. O. Johari), IITRI Chicago, p. 325 (1977).

2. D. C. Joy and D. M. Maher, "Electron Microscopy and Analysis 1977". Institute of Physics, London p. 357.

3. D. C. Joy and D. M. Maher, Ultramicroscopy (in press), 1978.

4. D. C. Joy and D. M. Maher, Proc. 35th Annual EMSA Meeting Boston (ed. G. W. Bailey), p. 244, (1977).

5. J. L. Costa, D. C. Joy, D. M. Maher, K. L. Kirk and S. W. Hui, Proc. 35th Ann. EMSA Meeting, Boston (ed. G. W. Bailey), p. 238, (1977) Also Science, (in press), 1978.
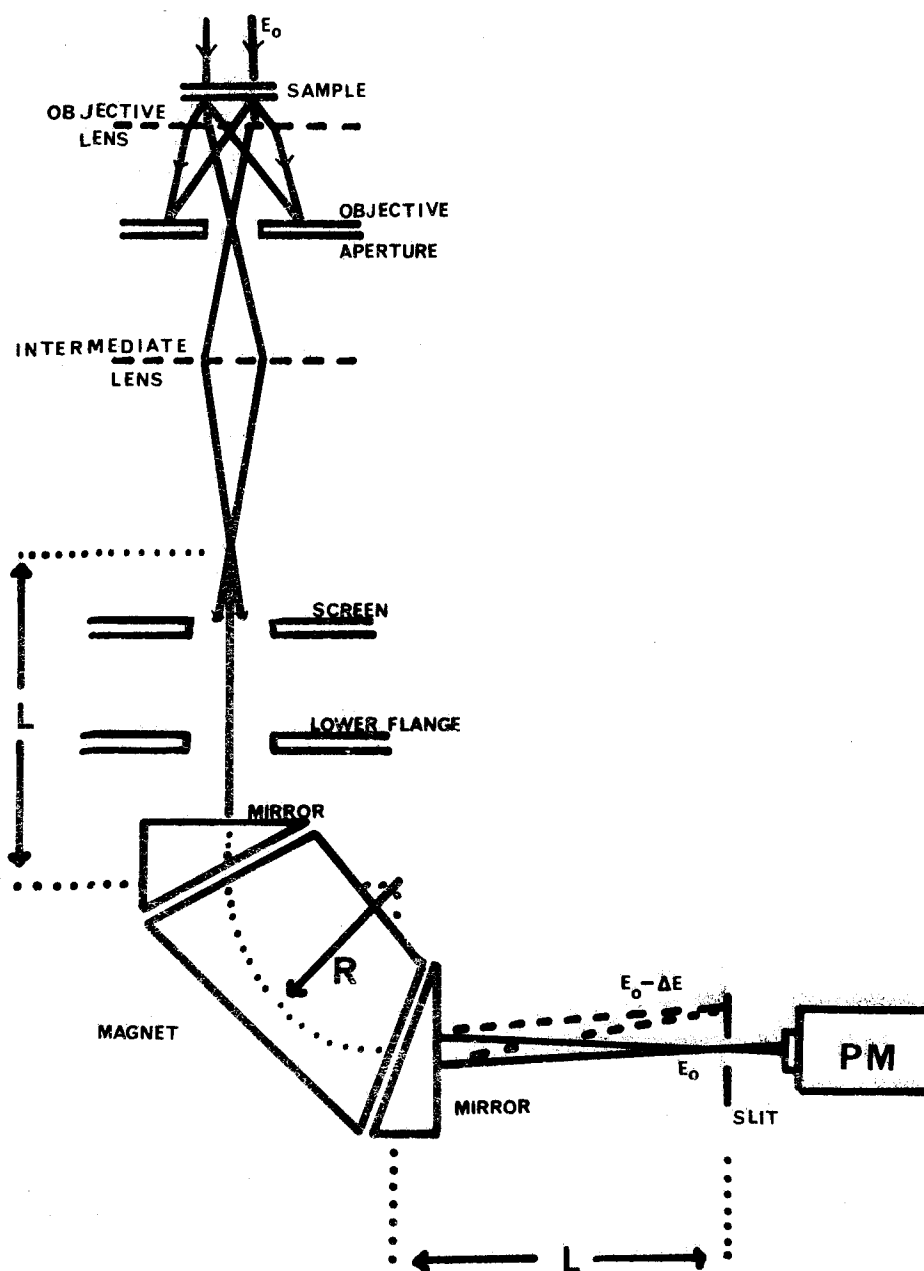
Fig. 1

Schematic diagram of electron optics for an energy-loss spectro-
meter. In a practical version of this system fitted to a JEOL
JEM 100B the radius R of the arc into which electrons are deflected
is 16 cms and the focal length L is 33 cms. The dispersion in the
plane of the slit is 4 μm per eV of energy loss at 100 kV.
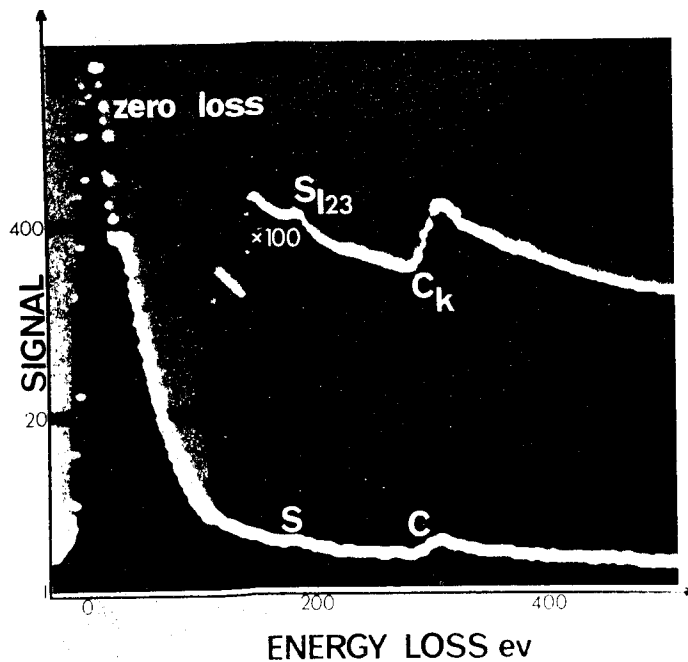
Fig. 2

EEL spectrum from a thin carbon film contaminated with sulphur, showing the relative intensities of the zero loss and characteristic loss regions.
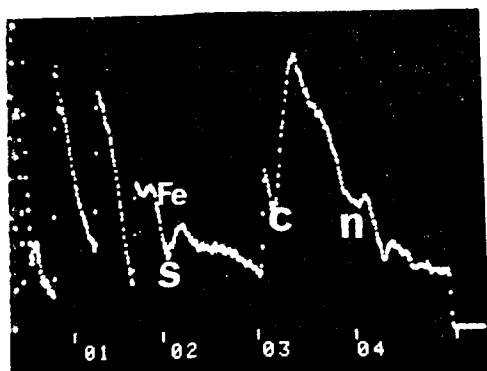
Fig. 3

EEL spectrum from a crystal of cytochrome oxidase. The breaks in the spectrum at about 100 eV intervals are where the gain of the recording system has been changed. Spectrum was obtained in STEM at 100 kV.
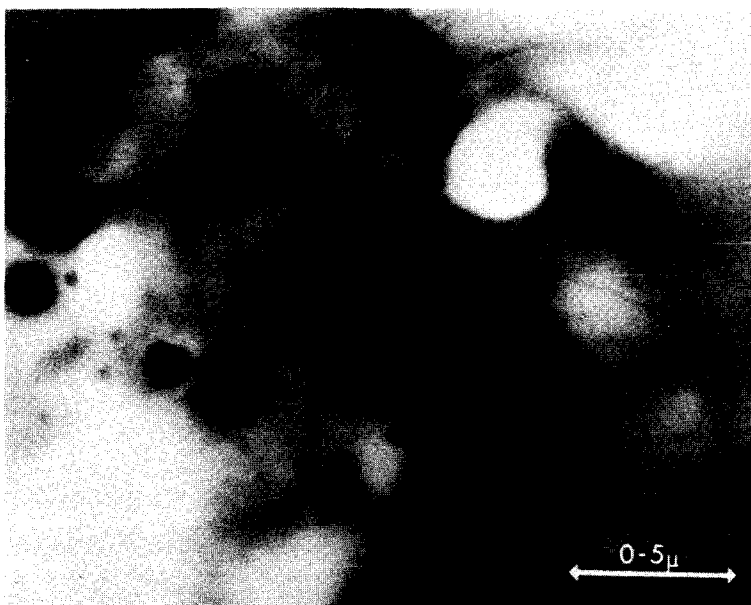
Zero Loss
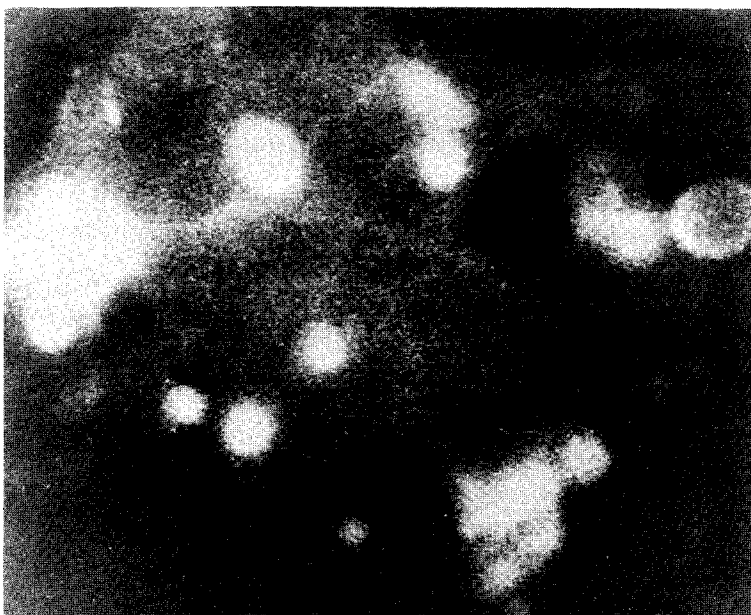
S$_{L23}$ Loss

Fig. 4

Zero loss, and S$_{L23}$ loss images of blood platelets which have been incubated with a sulphur analog of serotonin. The sulphur image shows that the serotonin has localized in the dense bodies (the dark areas in the zero loss image).

The LAMMA instrument: A new Laser Microprobe Mass Analyzer for biomedical purposes.

R. Kaufmann[1], F. Hillenkamp[2], R. Nitsche[1], M. Schürmann[1], H. Vogt[3], R. Wechsung[3].

1) Physiologisches Institut der Universität Düsseldorf, Lehrstuhl für Klinische Physiologie
2) Institut für Biophysik der Universität Frankfurt, Physik für Mediziner
3) Firma Leybold-Heraeus, Köln, Zentralstab Forschung und Entwicklung

The rapidly improving performance of microprobe instruments such as electron probe and ion probe microanalyses has attracted the interest of many biomedical research workers. However, despite a lot of successful applications, the techniques available so far did not in every respect fulfill the particular needs of biology and medicine. It became clear that an instrument we are looking for must include the following features:
1) Spatial resolution (imaging as well as analytical) must be better then 1 μm.
2) Analytical information should basically cover all elements of the periodic table. Additional information about organic constituents would be desirable.
3) Analysis should provide for quantitative or at least semiquantitative information.
4) Sensitivity should be high enough to detect trace elements even in the sub-ppm range.
5) To study kinetics of the compounds under investigation isotopes should be distinguished.
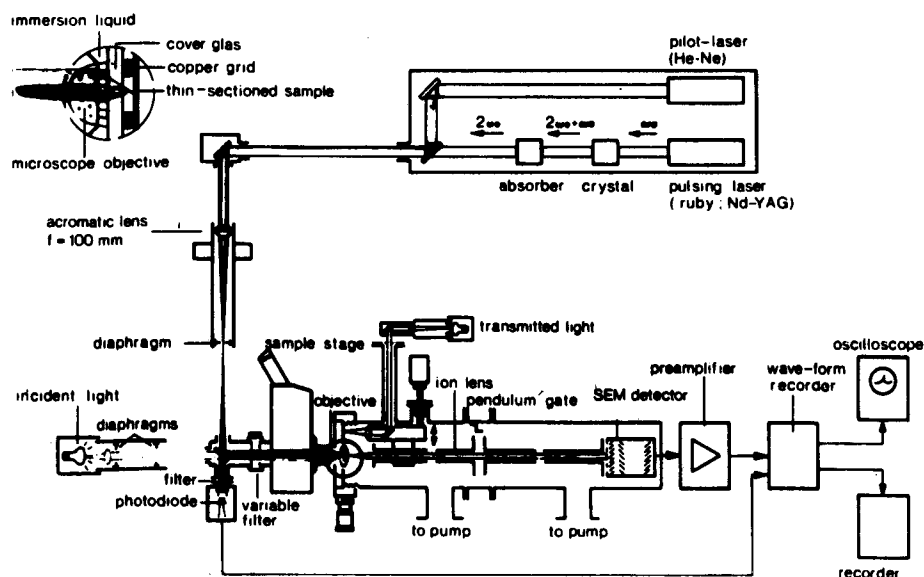
Fig. 1: A schematic diagram of the Laser Microprobe Mass Analyser (LAMMA). See text for further explanation.

To reach this goal an instrument has been designed which we call
LASER MICROPROBE MASS ANALYSER = LAMMA, the basic configuration of
which is schematically shown in Fig.1.

An optical microscope is used to image the specimen but, at the
same time, to focus the light of a Q-switch pulse laser onto a se-
lected spot of interest. The lasers used so far were either a fre-
quency doubled ruby (λ = 347 nm) or a frequency quadrupled Yag-Nd
laser (λ = 265 nm).

The specimen to be analyzed is preferably a thin section (2-3000 Å)
of embedded tissue material supported by a usual electronmicroscop-
ic grid. It is located in an evacuated specimen chamber right un-
derneath a thin cover slide (quartz) which serves as optical window
for the microscope and as vacuum seal at the same time.

The laser shot (pulse duration 25 μs, power density at the focus
$10^{10}-10^{11}$W/cm^2) creates a perforation the diameter of which can be
brought down to a diffraction limited spot size of about 0.5 μm.

The probed material (about 10^{-13}g) is evaporated and converted into
a plasma which is allowed to expand freely into the entrance of a
TOF mass spectrometer. The plasma contains neutral fragments, but al-
so atomic and molecular ions representing the constituents present

Fig. 2: Time of flight mass spectra obtained from a 0.1 μm thick
foil of epoxy resin, doped with Li 6x10^{-6}, Na 20x10^{-6},
Rb 80x10^{-6}, Cs 120x10^{-6} (weight fraction). Sampled volume:
10^{-13}cm^3. The electronically added laser signal serves as
zero time mark of the time-of-flight scale and as laser
output control.

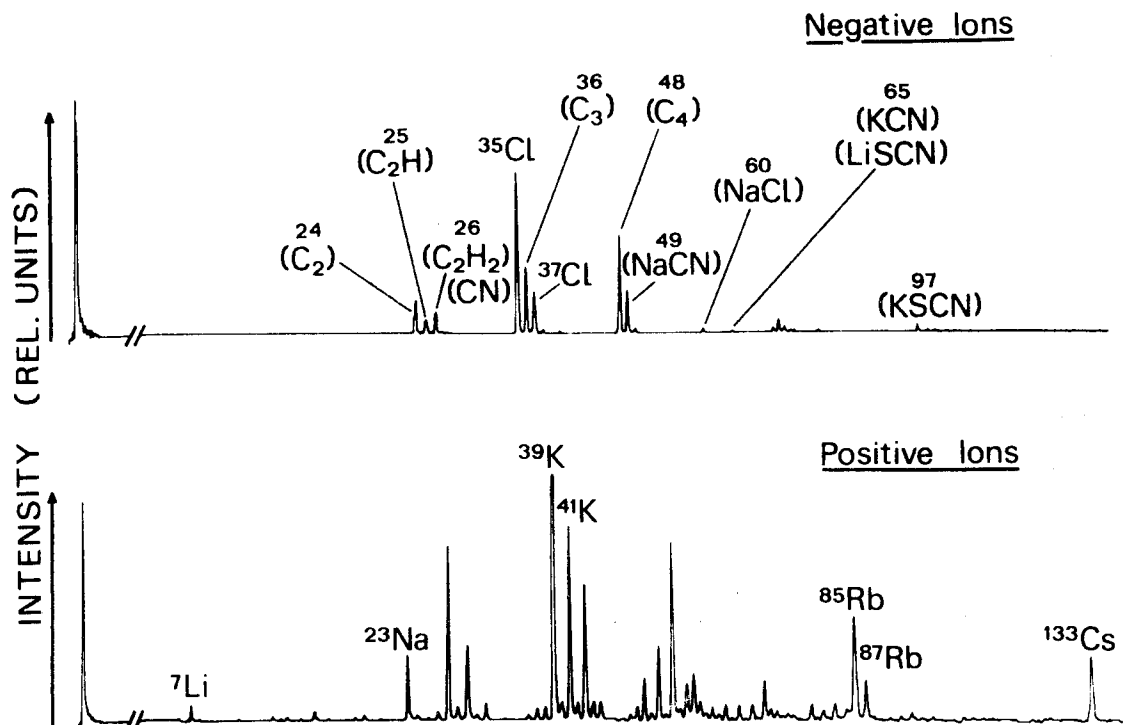in the probed material. It has been shown that the ion yield for the various elements differs (depending on the ionization energy level) but that most of the physiological cations (Na, K, Ca) or of the toxic metals (Hg, Cd, Pb) gave rather high ion yields and, therefore, optimal detection limits. Other elements, such as F or Cl, which have not been obtained as positive ions due to their high ionization potential were found to show up as negative ions at a rather good ion yield (see Fig.2).

The spectrometer consists of an ion lens which collimates and accelerates the ions to their drift energy of 2-3000 V, a field free drift tube of either 1,2 or 2,4 m length in which the various ion species are separated according to their (m/e dependent) flight time and an open SEV serving as an ion detector at the end of the spectrometer. Due to the rather high aperture and the collimating properties of the ion lens, the spectrometer transmission is high and can reach 50-80% of the ions produced in the microplasma.

The ion signals emerging at the output of the SEV, that means the whole mass spectrum, are further amplified and are stored in a fast digital transient recorder for visualization and further evalutation. To test sensitivity and selectivity standard specimen were prepared from epoxy resin (Spurr's low viscosity medium) containing dotations of trace metals at known concentrations. The relative and absolute detection limits established so far are shown in Table I. For most of the physiological cations this sensitivity is much higher than needed. For the detection of toxic trace metals the limits appear acceptable in most cases.

Table I: detection limits of the LAMMA instrument

	absolute (g)	relative (ppm)
Li	5×10^{-20}	0,5
Na	2×10^{-20}	0,2
K	1×10^{-20}	0,1
Ca	2×10^{-19}	1
Cu	4×10^{-18}	20
Rb	5×10^{-20}	0,5
Cs	3×10^{-20}	0,3
Ag	4×10^{-18}	20
Pb	1×10^{-17}	20

In Fig.2 original mass spectra of one of our standard specimen are shown. Dotation used in this case was Li (6 ppm), Na (20 ppm), K (35 ppm), Rb (80 ppm), Cs (120 ppm). The relevant ion signals in the mass spectrum are labelled. The large number of additional mass peaks present in these spectra are molecular fragments of the organic matrix (in this case of the epoxy resin used). This observation raises two points: First, the large number of molecular ion species creates a background problem when searching for trace elements at low concentration levels. In this situation the ion signals of say, Zn or Cu, may be hidden in larger peaks of organic fragments with nominally the same m/e numbers.

The second aspect of the molecular mass spectra appearing in our instrument is much more favourable. That is the possibility of identifying organic constituents of the specimen by mass spectrometric fingerprinting. Fortunately, enough laser induced organic mass spectra are much simplier than spectra emerging from conventional thermal ion sources. Therefore, it is not too unrealistic that conditions will be found where particular organic constituents can be identified even when present in a specimen of highly heterogeneous composition.

Fig.3 demonstrates the selectivity of our instrument, that means the lowest difference in mass number which can be discriminated. The mass spectrum shown contains the 3 isotopes of Pb separated one from another by 1 mass number. From this a selectivity (or mass resolution) of $m/\Delta m \simeq 400$ can be derived.
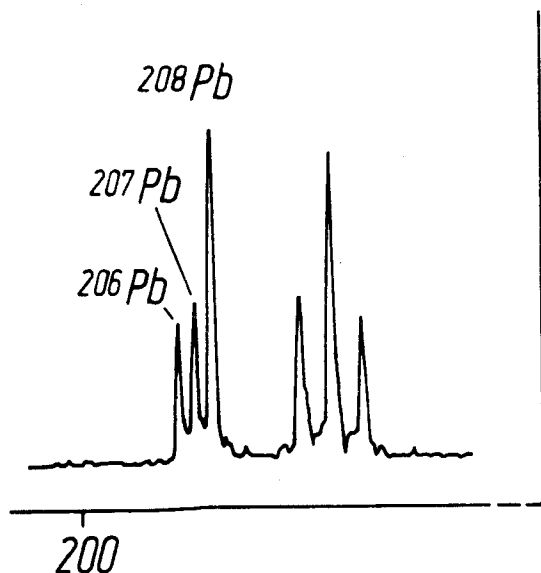
Fig. 3:

The request for quantitative analysis can be fulfilled although some reservations have to be made Accuracy of every analytical device depends on reproducability of the processes involved. In our case the interaction of the laser light with the specimen is a highly nonlinear process and, hence, rather sensitive to statistical fluctuations of the laser parameters and to variations of the specimen (thickness, spatial orientation). Therefore, we are still concentrating much effort to improve the stability and reproducability of the laser used and to optimize the specimen preparation technique. The reproducability reached so far in the LAMMA-instrument is in the range of 20-40% SD which, certainly, is comparable or even better than accuracy in other microanalytical systems.

For absolute calibration one must either refer to a standard specimen or to an inner standard for which, in the simpliest approach, the integrated mass spectrum could be taken.

Finally, a biomedical application of this instrument is demonstratet. In Fig.4 several mass spectra are shown which were obtained from different fibres of a freeze dried frog skeletal muscle. Muscle fibres control their contractile activity by a rather complicated system of Ca-movements occuring between various subcellular compartments such as the sarcoplasmic reticulum, the myofibrils and the mitochondria resp. However, most of our knowledge so far is inferential since direct measurements of the subcellular Ca-distribution in muscle fibres were not possible. In the LAMMA instrument we have obtained for the first time not only direct evidence for the highly compartimentized distribution of the cellular Ca but also for the dependence of intracellular

Ca-accumulation on the Na/K ratio (Fig. 4).
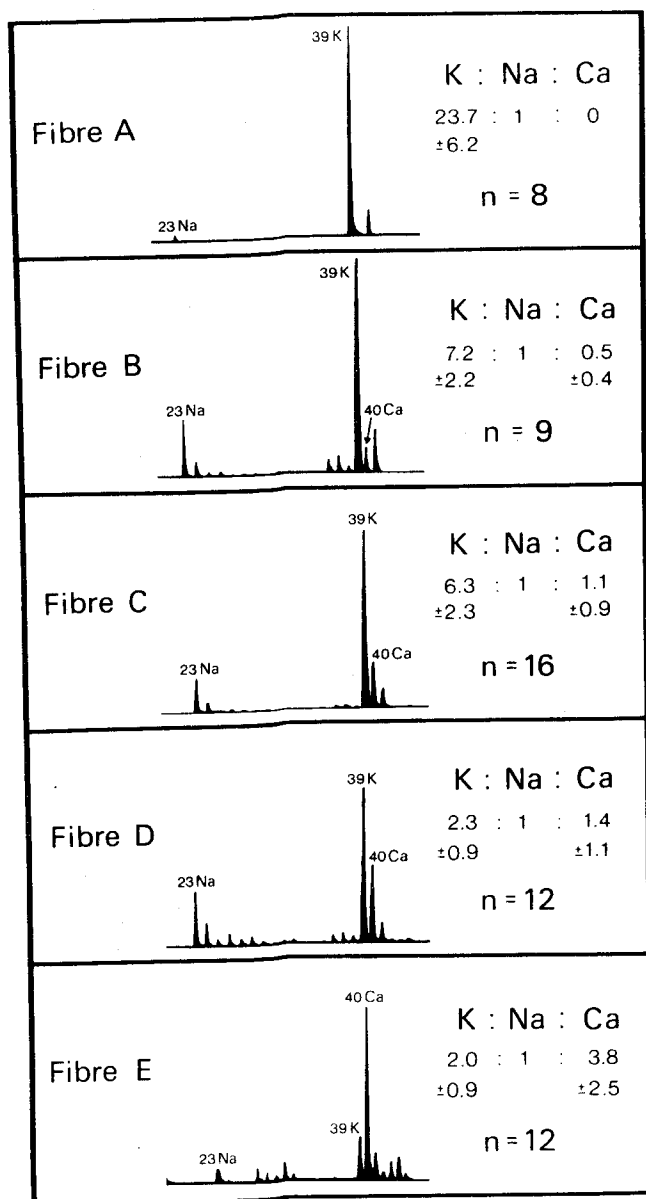
Fig. 4:
Mass spectra and K:Na:Ca ratios from different fibres of an isolated frog sartorius muscle. The fibres were carefully dissected, soaked in a 7% albumin Ringer solution and tested for vitality by applying electrical stimuli. Visible signs of fibre damage present only in fibre E.

References:
HILLENKAMP, F., R. KAUFMANN, R. NITSCHE und E. UNSÖLD:
Laser Microprobe Mass Analysis of Organic Materials
Nature, 256, 119-120 (1975)

HILLENKAMP, R., UNSÖLD, R., KAUFMANN, R. and NITSCHE, F.:
A High-Sensitivity Laser Microprobe Mass Analyzer.
Appl. Phys. 8, 341-348 (1975)

KAUFMANN, R., HILLENKAMP, F., NITSCHE, R., SCHÜRMANN, M., UNSÖLD, E.:
Biomedical Application of Laser Microprobe Analyses.
J. de Microscopie 22, 389-398 (1976)

ZAF-CORRECTION PROCEDURES IN ELECTRONPROBE X-RAY MICROANALYSIS
OF BIOLOGICAL BULK SPECIMENS

A.Boekestein[1], G.M.Roomans[2], A.L.H.Stols[1], and A.M.Stadhouders[1]

[1]Laboratory for Submicroscopic Morphology, Faculty of Medicine, and

[2]Department of Chemical Cytology, Faculty of Science,

R.C.University of Nijmegen, Nijmegen, The Netherlands.

INTRODUCTION

In electronprobe X-ray microanalysis special mathematical procedures are
applied to correct characteristic X-ray peak intensities in an X-ray spectrum
for those effects which result from the particular chemical composition of
the specimen.When analyzing bulk specimens there are four of such effects:

   a.deceleration of beam electrons (stopping power) ⎫
   b.backscattering of beam electrons   ⎬ (Z)
   c.absorption of X-rays   (A)
   d.secondary fluorescence   (F)

The effects a and b are often considered together as the atomic number
effect (Z).Corrections for these four effects are called ZAF-corrections.
In this study various alternatives in ZAF-correction (as developed primarily
in the material sciences) have been compared for their applicability to
biological X-ray microanalysis.Furthermore there are several important
differences between biolohical and metallurgical specimens when considered
for electronprobe X-ray microanalysis (Boekestein, et al.,1977).These
differences are mentioned in table 1.

variable	specimen		comment
	metallurgical	biological	
contribution of non-detectable elements	small	large	elements like C,N,O in energydispersive analysis
knowledge of:			
local geometry	good	poor	complex surface topography
eff.accel.voltage	good	poor	depending on specimen charging
specific mass	good	poor	partially depending on the preparation method

Table 1.Some important differences between metallurgical and biological
specimens when considered for electronprobe X-ray microanalysis.

Therefore we traced the influence on the calculated concentrations of
(1) the accelerating voltage, (2) the specimen-spectrometer geometry,
(3) the specific mass of the specimen, and (4) the composition of the
organic matrix because very soft X-rays cannot be detected in energydispersive
X-ray microanalysis when the spectrometer is equipped with a beryllium
window.

MATERIALS AND METHODS

Spectra were obtained with an energydispersive X-ray spectrometer (EDAX)
with an energy resolution of 170 eV at 5.894 keV and a beryllium window
thickness of about 7.5 μm.This spectrometer was attached to a scanning
electron microscope (Philips SEM 500).The angle between the spectrometer
axis and the horizontal plane was 7°.
In the ZAF-correction procedures the total correction factor was calculated
according to the following authors (table 2):

$Z \begin{cases} \text{stopping power} \\ \text{backscattering} \end{cases}$	Bethe (1930); Philibert and Tixier (1968) formulae for the backscatter factors were fitted to the data of Duncumb and Reed (1968) and Reed (1971) (Boekestein, unpublished)
A absorption	Philibert and Weinryb (1963) with the Lenard coefficient according to Heinrich (1968)
F secondary fluorescence	Reed and Long (1963)

Table 2.Components of the applied ZAF-correction.

For the calculation of the stopping power correction there are a number
of alternatives.Firstly there are several ways to acquire the mean ionisation
potential (Bloch, 1933; Duncumb and Da Casa, 1967).Secondly there is the
possibility to neglect the ionisation cross section (Bethe, 1930).
With a ZAF-correction program, written in Fortran IV, we processed typical
biological spectra (real or fictitious) on a DEC PDP 11/45 computor after
the background was subtracted.Spectra were obtained from e.g. the mould
Neurospora crassa-after freezedrying-with a gelatine/glycerol/KH_2PO_4
mixture as a standard (Roomans and Boekestein, 1978).
A deviation in % of one of the above mentioned variables which causes
a variation of 2% in the calculated concentrations is taken as a criterion
for the admissable deviation and is called the 'tolerance' of that variable.

RESULTS AND DISCUSSION

We compared a number of alternatives to calculate the stopping power
correction.It turned out that the differences in the outcome of these
alternatives did not exceed 2%.We also compared the calculated concentrations
when the stopping power and the backscattering corrections were supposed
to be either dependent or independent on the atomic number of the
element for which the corrections were performed.In the last case only
one atomic number correction value was used for all the elements present
in the specimen.It appeared that the differences in the calculated concentrations
obtained with these two alternatives did not exceed 2%. We concluded that
the various ways in which the stopping power corrections could be computed
yielded relative differences in the calculated concentrations which were
well below the overall accuracy of the analytical method (Shuman, et al.,1976).
Further we calculated the tolerance of some of the variables for a
difference of 2% in the calculated concentrations (table 3).

variable	tolerance
accelerating voltage	6
tilt angle	10
specific mass	Ca: 6
	Na: 3

Table 3.Tolerances of some variables involved in electronprobe
X-ray microanalysis.

From table 3 it follows that for a 2% difference in the concentrations
and for an accelerating voltage of 20 kV a charging of the biological
specimen of 1.2 kV is permitted.
The tolerance of the specific mass for light elements (e.g. Na) was smaller
than for heavier elements (e.g. Ca).This is primarily due to the fact that
the absorption correction is larger for low-Z elements.
Another characteristic of the specimen is the composition of its organic
matrix.We concluded that this matrix could be represented by only one
element and that the deviation in the concentrations which occurred by this
substitution did not exceed 2%.The atomic number of the element used for this
substitution should be the nearest integer mass-weighted mean atomic number
of the organic matrix.

We found that in soft biological specimens nitrogen was in most cases the substituting element which resulted in minimal differences when compared to the unchanged situation (fig 1).
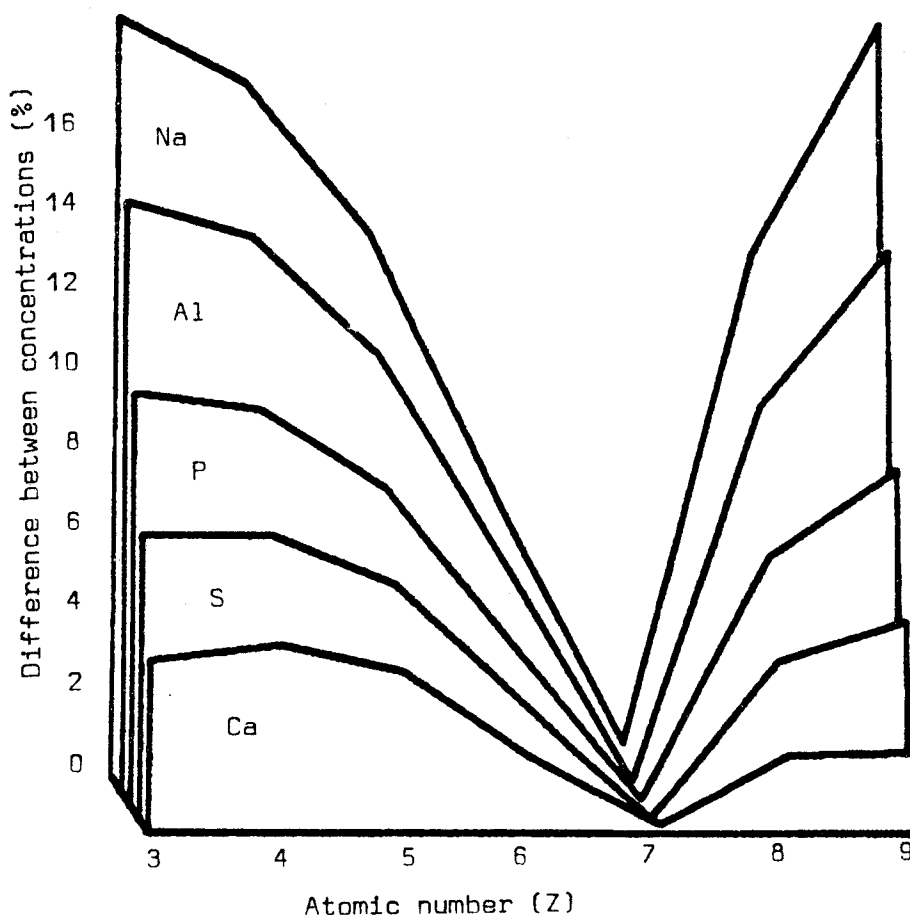
Fig 1.The relative difference in the concentrations (vertical scale) versus the substituting atomic number (horizontal scale) for some light elements.

Finally we examined the influence of the magnitude of some of the variables on the sensitivity of the correction procedure for a slight change in that variable.There existed an optimum for the accelerating voltage where the sensitivity of the total correction factor for such a slight change was minimal.This optimum was strongly dependent on the atomic number of the element for which the correction was calculated (table 4).

element	optimal accelerating voltage (kV)
Na	13
Al	22
P	35
K	51
Ca	58

Table 4.Optimal accelerating voltages for minimal sensitivity
       of the total correction factor for a slight change in
       the accelerating voltage.

It appeared that these optimal accelerating voltages are higher than
those for metallurgical specimens (Büchner and Stienen, 1976).This is
probably due to the lower absorption in biological bulk specimens.

We checked our conclusions with spectra obtained from biological
specimens, e.g. the mould Neurospora crassa, a gelatine/glycerol/KH_2PO_4
standard and dentine.We found that tolerances were within the experimental
accuracy.

LITERATURE

Bethe, H. (1930) Ann.Phys.Leipz. 5,325

Bloch, F. (1933) Zeit.Phys. 81,363

Boekestein, A., Stols, A.L.H., Roomans, G.M., and Stadhouders, A.M. (1978)
   (in press)

Büchner, A.R., and Stienen, J.P.M. (1976) Mikrochim.Acta Wien 2,635

Duncumb, P., and Da Casa, C. (1967) Paper presented at Conference on Electron
   Probe Microanalysis, London

Duncumb, P., and Reed, S.J.B. (1968) In: Quantitative Electron Probe
   Microanalysis (K.F.J.Heinrich, ed.) Natl.Bur.Stands. Spec.Publ. 298
   (Washington, U.S. Dept.Commerce), p.133

Heinrich, K.F.J. (1968) Quantitative Electron Probe Microanalysis,
   Natl.Bur.Stands. Spec.Pub. 298 (Washington, U.S.Dept.Commerce)

Philibert, J., and Weinryb, E. (1963) In: X-ray optics and X-ray microanalysis
   (H.H.Pattee, et al., ed.) New York, p.451

Philibert, J., and Tixier, R. (1968) J.Phys. D 1,685

Reed, S.J.B., and Long, J.V.P. (1963) In: X-ray optics and X-ray microanalysis

Reed, S.J.B. (1971) J.Phys. D 4,1910

Roomans, G.M., and Boekestein, A. (1978) (submitted for publication)

Shuman, H., Somlyo, A.V., and Somlyo, A.P. (1976) Ultramicroscopy 1,317

ENVIRONMENTAL CHAMBERS FOR MICROANALYSIS

Donald F. Parsons

Electron Optics, Division of Laboratories and Research

New York State Department of Health, Albany, NY 12201

1. Design Principles of Environmental Chambers for Electron Beam Devices

Early attempts to encapsulate a specimen in a water vapor, or other gaseous environment, inside an evacuated electron microscope column proved impractical due to frequent breakage and contamination of the thin film windows required (see review by Parsons et al. 1974). Today, it is realized that small apertures (50 to 200 μm hole size) can replace the thin film windows in a differentially pumped arrangement that allows rapid exchange and examination of wet specimens in a pressure and temperature controlled gaseous environment (Parsons, 1974).

This extension of the capabilities of electron microscope and electron probe devices overcomes some basic obstacles in electron imaging and microprobe analysis technique. The advantages are:

(a) Vacuum drying or other types of drying cause distortion of fine structure and loss of electron diffraction spectra in many types of biological specimens

(b) Contamination and specimen charging are reduced in environmental chambers

(c) Whole wet cells can be viewed and analyzed with the minimum disturbance of intracellular fluid composition.

For each type of electron beam instrument the design should aim at placing the environmental chamber (E.C.) so that the wet specimen is placed in the usual specimen plane of the objective lens. This is easy in some instruments with large gap, side entry pole pieces (e.g., high voltage electron microscopes) or with long focal length (conventional scanning electron microscopes). It is more difficult in most conventional CTEM's where the objective gap is small and the side entry ports are limited in size and number. In the past, to overcome this difficulty, we have selected instruments with large top entry access and built the E.C. into the upper half of the objective pole piece. This need not affect electron diffraction operation but leads to decreased resolution due to increased spherical aberration. In the future, the best solution to the problem for high resolution CTEMS lies in the redesign of the pole-piece as a pin-hole lens of moderate gap so that the gap of the pole piece itself becomes the E.C. and the pole-piece bores are the limiting apertures (such pin-hole pole piece have also attractive electron optical characteristics).

The basic design of the differentially pumped EC for CTEM's (with or without a scanning attachment) or for high voltage electron microscopes is shown in Fig. 1. The chamber and its four co-axial apertures (inner pair, 50 to 100 μm and outer pair, 200-250 μm hole size) is centered close

to the optic axis by its close fit to the movable upper pole piece. (Slight displacement of the pole piece gives exact centering on the beam). The E.C. is thermally insulated from the microscope and can be heated or cooled by a Peltier device in the range of -35°C to 40°C. The grid end of the specimen rod is in contact with the E.C. and in temperature equilibrium with it, but the grid end is thermally insulated from the rest of the specimen rod and the microscope. The specimen grid temperature is monitored by a thermocouple.

Inside the E.C. and close to the specimen grid there is a water reservoir (0.2 to 0.5 ml capacity) sufficient for several hours operation. The water vapor pressure (plus any added gases) is monitored by a manometer or pressure transducer. Gases are pre-mixed by an anesthiology type array of manometers. In situations where precise gas concentrations are required a flow-through arrangement is used.

The inner compartment of the E.C. forms a "thermodynamic black box" with saturated water vapor pressure in the dynamic equilibrium when the E.C. is adjusted to any temperature in the range -35° to +40°C. In order to ensure that no leaks exist in a new system the water vapor pressure at a given E.C. temperature is compared to that given in tables. A more sensitive test of the equipment is to record the electron diffraction pattern of the wet crystalline protein catalase (Matricardi et al., 1972). This protein, and most others, are irreversibly disorganized and do not give detailed electron diffraction patterns, if the equilibrium water vapor pressure falls below 95% of the equilibrium value. In this case, the water vapor equilibrium is being tested directly in the electron beam and on the axis of the apertures under conditions identical to those of actual operation.

The outer compartment, limited by a pair of 200-250 μm hole size apertures, acts as a vacuum buffer for the leak of escaping gas. This is pumped away by connection of this compartment to a small rotary pump. The remaining gas leak from the outer apertures is readily taken care of by the normal microscope pumping system.

The electron beam passes through the upper apertures, the wet specimen and the lower apertures. The resolution loss due to chromatic aberration is related to the height of the compartments, their gas pressures, type of gas (helium, exygen, etc) and the thickness of the wet specimen (see Parsons, et al., 1974). At 200 kV we have produced a 20 Å Fresnel fringe in water vapor at room temperature and expect to improve on this with our HVEM chamber.

It is also now realized that the wet specimen preparation must be carried out quantitatively in a water vapor saturated glove box. Insertion of uncontrolled wet specimens with blobs of water will result in large resolution loss, blockage of the beam or boiling of the water! We use an interference microscope placed in the humidity box to control water thickness. The ideal specimen is a wet object sitting on a dry surface but it is possible to control the thickness of a water layer on a hydrophyllic surface.

2. Adapting Environmental Chambers to Microbeam Analysis

We have shown by using an E.C. fitted to a 1 MeV high voltage microscope

with its increased penentration, that whole mounts of wet cells grown on gold grids can be viewed in a thin layer of medium without any stain or fixation (Parsons et al., 1972; 1974). Fig. 2 shows mitochondria in the cytoplasm of a spread 3T3 cell and Fig. 3 shows whole red blood cells in a thin layer of phosphate buffered medium. Contrast can be enhanced in thin portions of the cytoplasm by using dark field (Fig. 4).

However, increased penetration with decreased loss of resolution can also be obtained with cheaper STEM machines. The costly Field Emission gun type would be desirable but tungsten or lanthanum hexaboride guns should suffice for low resolution work. The ultimate in penetration and analytical usefulness would be an HVEM in the scanning mode. However, it is difficult to mechanically or electronically stabilize the beam position after passing down the long acceleration tube.

We are developing an E.C. for the ETEC STEM (Fig. 5 and 6). This is currently in use for STEM imaging of wet chromatin and chromosomes. Removal of the scintillator and addition of a magnetic analyzer will allow us to carry out electron energy loss elemental analysis on wet specimens. Initial energy loss analysis work on the Albany 1.2 MV HVEM will use point by point placement of the beam (1000 Å diameter). Later we hope to develop a method of stabilizing and scanning the 1.2 MV beam.

Ideally, we would like to have the superior sensitivity of electron energy loss analysis coupled with simultaneous x-ray detection. However, a large collection angle for x-rays is not easily compatible with E.C. design and reliance most be placed on the development of minature, room temperature, solid state detectors. The extent to which further development of E.C.'s for elemental analysis is justified must await the all important initial cytoplasmic composition determinations on whole wet cells. Hopefully they will be closer to the known physiological data then current results with frozen, freeze dried or critical point dried cells.

References

Matricardi, V. R., Moretz, R. C., and Parsons, D. F. (1972) Science, 177, 268

Parsons, D. F. (1974) Science 186, 407

Parsons, D. F., Matricardi, V. R., Moretz, R. C., and Turner, J. N. (1974) Adv. Biol. Med. Phys. 15, 161.

Parsons, D. F., Matricardi, V. R., Subjeck, J., Uydess, I and Wray, G. (1972) Biochim. et Biophysica Acta, 290, 110.

Parsons, D. F., Uydess, I., and Matricardi, V. R. (1974) J. Microscopy (U.K.) 100, 153

Acknowledgements
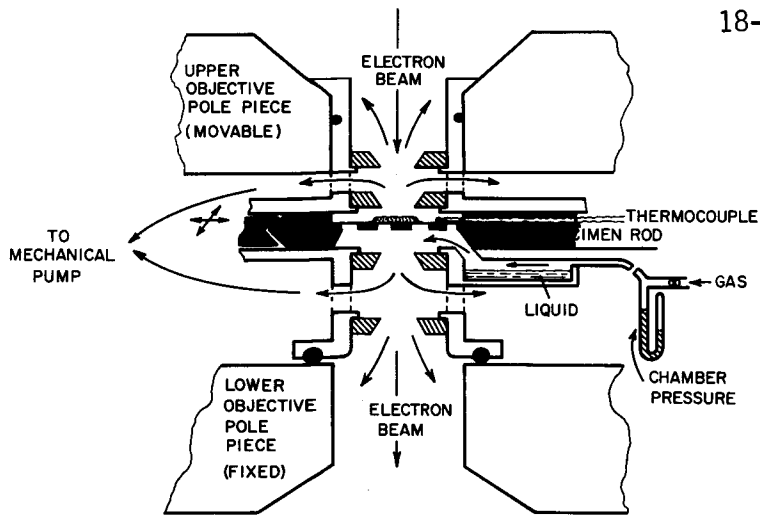
Fig. 1. Schematic drawing of a differentially pumped, aperture limited, environmental chamber placed in the gap of the electron microscope objective lens. See text for details.

10 μm

Fig. 2. Wet, unfixed and unstained 3T3 cell grown on a carbon coated gold grid., Elongated mitochondria are visible (800 KV).

Fig. 3. Wet Mouse red blood cells in phosphate buffered saline. The cells have the characteristic RBC shape Mag. X3260. (800 KV).

STEM HYDRATION CHAMBER
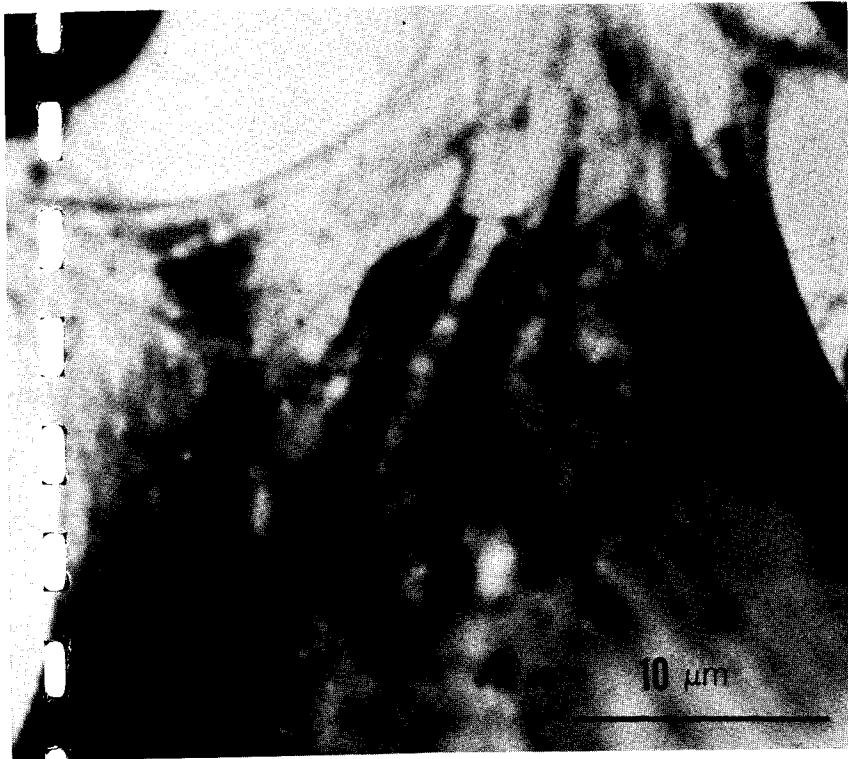
Fig. 4. Spread unstained 3T3 cell. Dark-field image at 800 KV showing enhanced ontrast for fine processes of cytoplasm.
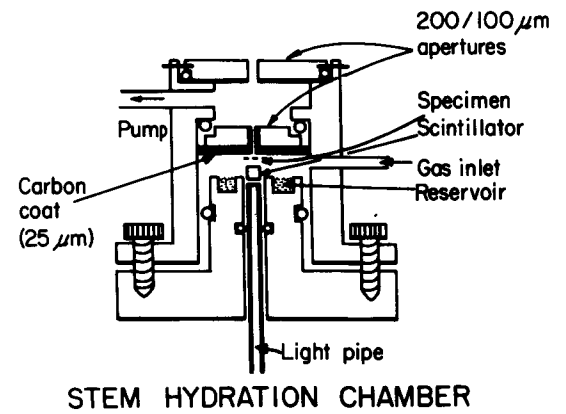
Fig. 5. STEM (ETEC) environmental chamber (Diagramatic) for imaging. The light pipe connects to a photomultiplier tube. The carbon coat reduces backscatter image formation.
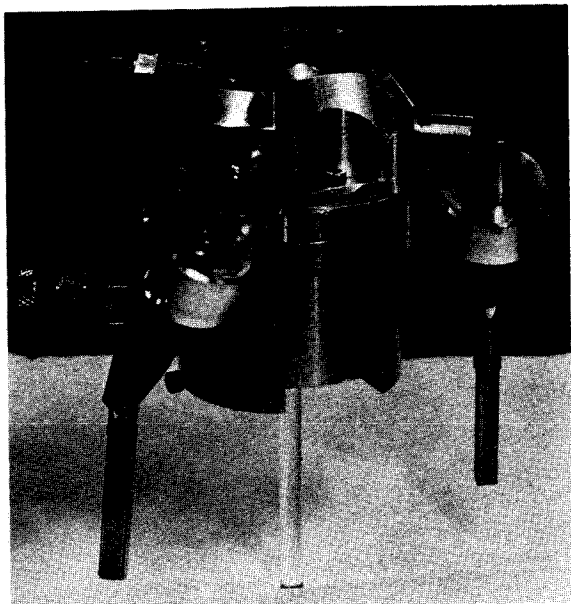
Fig. 6. Photograph of the STEM E.C. of Fig. 5 showing the specimen grid drives, pump-out lines and scintillator.

SOME EFFECTS OF ELECTRON IRRADIATION OF BIOLOGICAL SPECIMENS*

by

John W. Edie, Dows Institute for Dental Research, University of Iowa,
    Iowa City, Iowa 52242

and

Paul L. Glick, V.A. Hospital and College of Dentistry, University of
    Iowa, Iowa City, Iowa 52242

It has been speculated since the inception of electron probe micro-analysis (EPMA) that biological applications for the technique are virtually boundless. For tissues, a major portion of the effort expended to date has been to develop methods of sample preparation which maintain the chemical integrity of the specimen. There is an apparent trend toward examination of frozen hydrated tissues as representing the least ambiguous preparatory procedure for assuring against ionic redistribution. Of course, the preparation methodologies are of fundamental importance, but, regardless of the existence of an "ideally representative specimen", there are several physical phenomenon involving electron beam-specimen interactions which can severely handicap attempts to obtain quantitative results.

An excellent means of observing limitations on absolute quantitation exists in the EPMA of mineralized tissues. The high count rates that exist for Ca and P allow one to easily observe dynamic counting conditions which are fundamentally dependent upon the light element portion of the specimen.[1,2] Variations also exist, usually in an opposite manner, in continuum count rates[3]. The error in absolute quantitative predictions has been observed to exceed 50% unless these dynamic effects are accounted for and an appropriate interpretation of the results is made. Similar types of effects are believed to exist in all biological specimens in which a substantial organic matrix and/or light element composition exist. The effects occur for electron doses $\geq 10^{-8}$ C/um^2--which would be within one second duration for focused beam analyses and operating conditions commonly employed in tissue examinations. The dynamic counting conditions in soft tissues are masked by this short duration, as well as the statistical fluctuations of much reduced count rates, and what appear to be stable count rates are the end product of prolonged electron doses.

An examination of a multitude of different specimens has lead to the following apparent generalizations regarding specimens which exhibit dynamic counting conditions:

(1) Transient specimen current variations are induced from the onset of of the electron beam.

(2) Electron irradiation results in a physical alteration of the analysis surface.

(3) The specimen possesses a significant proportion of light element content--such as exhibited in organic specimens.

(4) Some specimens with chemically active light element content (e.g., F and Na) exhibit count rate dynamics of an irregular nature.

These observations all support the concept that electron irradiation results in energy transfer to the specimen. The light elements are removed from the matrix and the resulting matrix of higher average atomic number has substantially different x-ray absorption characteristics than the original matrix.

A quadrupole mass analyzer* was adapted to an ARL EMX-SM microprobe so that these effects could be examined in greater detail. The detector was positioned 6 cm from the specimen and was line-of-sight to the x-ray excitation volume (see Figure 1). The residual gas mass spectrum is shown in Figure 2-a for mass numbers 1 through 50. The light element portion of this spectrum ($1 \lesssim M \lesssim 16$) is displayed in Figure 2-b. Few ambiguities exist in the identification of these peaks and particular attention is drawn to $M = 2$ ($_1H_2^1$, or less likely $_1H^2$). Figure 3-a shows the $M = 2$ peak displayed in one second intervals with no beam incident upon the specimen. The envelop of these peaks therefore represents a semi-quantitative portrayal of H_2 content in the vacuum as a function of time and displays the statistical variation to be anticipated in sampling this peak. Figure 3-b is an equivalent spectrum for H_2, but with an electron beam made incident on a nonvolatile specimen (a fluoro-apatite crystal) while the mass sampling was taken. A slight decrease in H_2 composition is noted and is a result of specimen charging by the electron beam. If a specimen exhibiting dynamic count rates (mid-dentine region of a plastic embedded rat tooth incisor) is similarly irradiated, the mass spectrum shown in Figure 3-c results. From the onset of the beam, the H_2 composition increases rapidly, then gradually diminishes as electron dosage increases. Hydrogen is evidently sputtered from the surface as a result of electron bombardment.

Other light element sputtering may be examined in a similar manner. By far the most volatile component is Hydrogen, with the volatility of other elements decreasing with atomic number. The magnitude of the sputtering is dependent upon the accelerating voltage employed, the current density incident on the specimen and the conducting state of the specimen.

A simplified model for the sputtering may be advanced assuming elastic collisions occur between electrons of energy E_0 and stationary atoms of mass number M within the specimen matrix. The energy gained by the atom is assumed to at least equal the dissociation energy to permit the atom to escape from the specimen. The mass number of the largest atom which can escape the matrix under these assumptions is predicted by

$$M \lesssim 2\, E_0(\text{kev})/E_b(\text{ev})$$

*Quadruvac Q200, Leybold-Heraeus GMBH & Co.

where M is the mass number of the ejected atom, E_o is the energy of the incident electrons in kev and E_b is the binding energy necessary to dissociate the atom from the matrix in electron volts. This model neglects accumulated thermal effects, inelastic interactions and relativistic effects and is only a first order approximation to mass loss from the specimen.

The model agrees with experimental observation in the following ways:

(1) For a given accelerating voltage, the likelihood of an atom being ejected from the specimen as a result of electron bombardment is dependent upon its mass and on the magnitude of the energy by which it is bound to the solid.

(2) For a given dissociation energy, only light elements are ejected at lower accelerating voltages. As mass number increases, it would be necessary to use increasingly higher accelerating voltages to sputter these atoms from the specimen.

(3) The rate atoms of mass M would be ejected from the matrix would be proportional to the number of atoms present in the matrix. As a result, the sputtering phenomenon would follow an approximately exponential process.

It is believed that these effects are limiting factors in any attempt to quantify the chemical composition within biological specimens. Light elements, especially Hydrogen, play an extremely important role in the x-ray absorption characteristics of the matrix. The effects must be controlled, or the results interpreted in view of these processes, if reliable quantitative information is to be obtained in the EPMA of biological tissues.

In view of the above observations, it is relavent to conjecture what dynamic effects will occur in the EPMA of frozen hydrated specimens. The binding energy for ice molecules at $0\ ^oC$ is $\sim$12 kcal/mole, or $\sim$.5 ev/molecule. Ice cooled to LN_2 temperatures would further require $\sim$1.5 kcal/mole, or $\sim$.06 ev/molecule, to raise the temperature to $0\ ^oC$. In view of the above theory, even super-cooled ice should be very volatile under the electron beam and beam energies of one kev would be sufficient to sputter these specimens. This may well be an important factor for the biologist to consider in the preparation of tissues for EPMA.

References

1. Edie, J. and P. Glick. Dynamic effects on quantitation in the electron probe analysis of mineralized tissues, Proc. 11th Annual Conference, Microbeam Analysis Society, Miami (1976), 65A-65F.

2. Edie, J. Electron probe analysis of fluorine uptake in mineralized tissues, Proc. 12th Annual Conference, Microbeam Analysis Society, Boston (1977), 173A-173F.

3. Hall, T. A. and B. L. Gupta. Beam-induced loss of organic mass under electron-microprobe conditions, J. Microscopy, Vol. 100, Pt. 2, 1974.
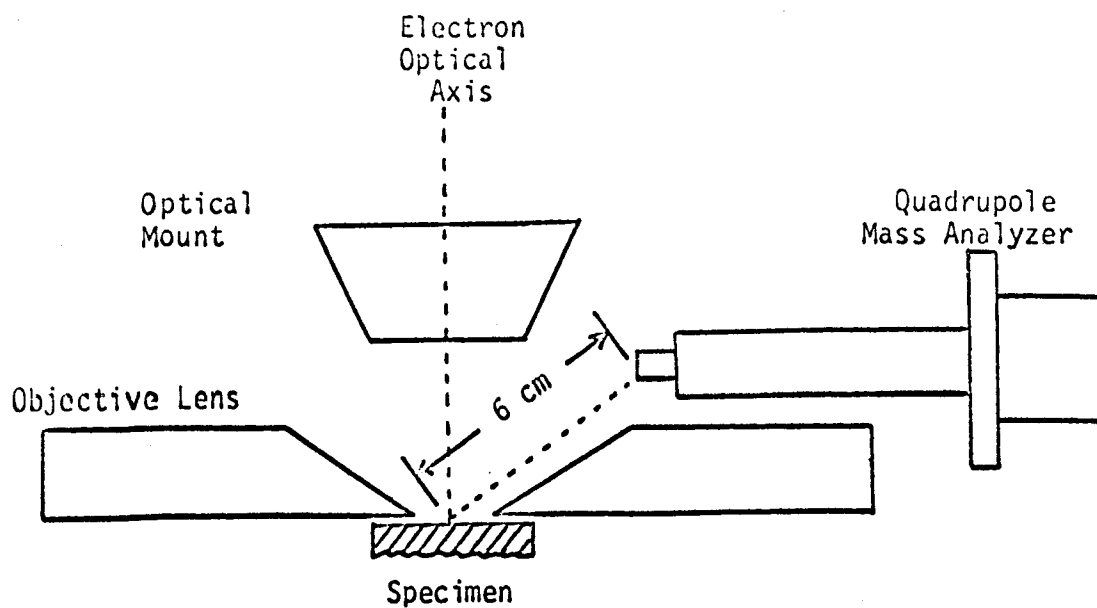
Figure 1. Geometrical arrangement for the adaptation of a quadrupole
mass analyzer to an ARL EMX-SM microprobe.

Mass Number
(a)

Mass Number
(b)
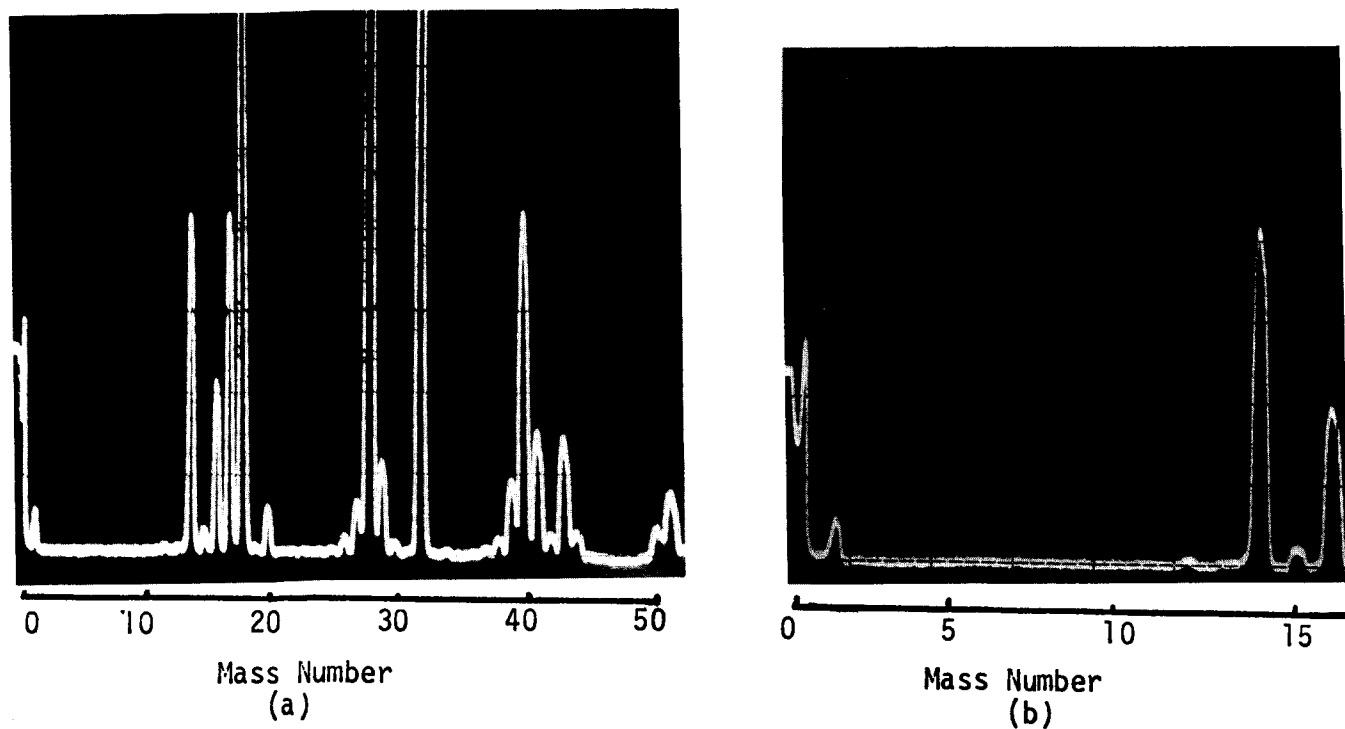
Figure 2. (a) Mass spectrum, $1 \leq M \leq 50$, of the residual gas within the
microprobe at 10^{-5} torr. (b) Light element portion, $1 \leq M \leq 16$,
of the residual gas mass spectrum.
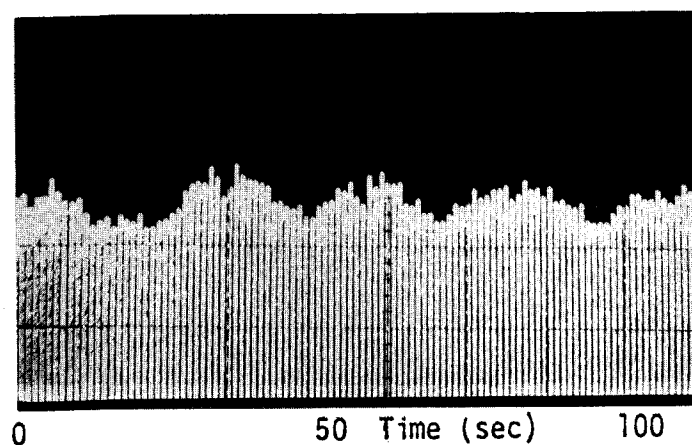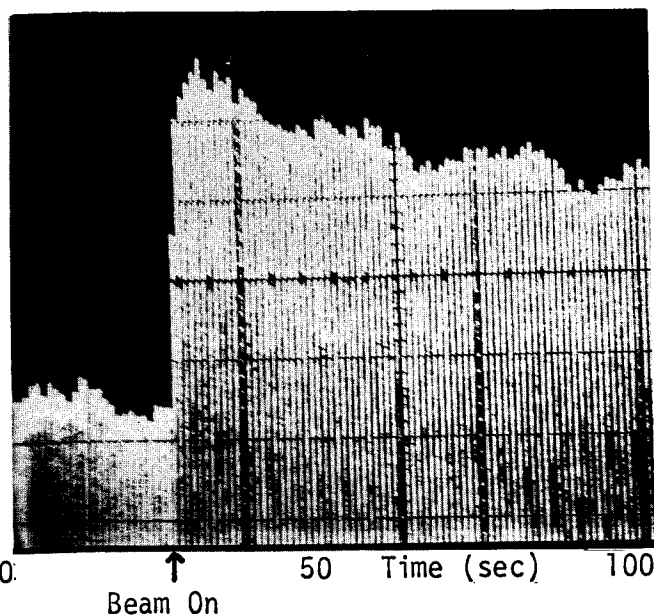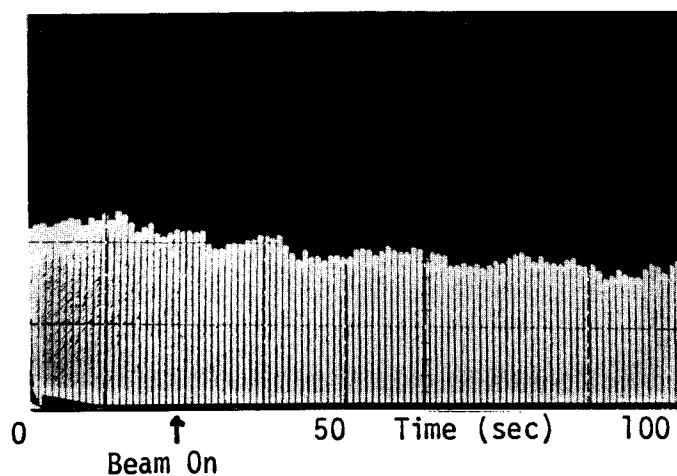
Figure 3. The H_2 mass peak (M = 2) is displayed in one second intervals. The envelope of these peaks represents H_2 variation as a function of time. (a) H_2 peak heights with no electron irradiation of a specimen. (b) H_2 peak heights when an electron beam is made incident upon a nonvolatile specimen (a fluoro-apatite crystal) during the mass sampling. (c) As in (b), but when irradiating a volatile specimen (mid-dentine region of a plastic embedded rat incisor).

MICROPROBE ANALYSIS IN MINERALIZING TISSUES

E.R. Krefting, H.J. Höhling, R.H. Barckhaus
   Institut für Medizinische Physik der Universität
   D-4400 Münster

Hard tissue formation is a complex process consisting of
different steps. Although much research on individual stages
of this process has be done, no general calcification theory
has emerged. Hard tissue formation thus belongs to one of the
basic unsolved problems in biology. Electron probe micro-
analysis can contribute to the solution of some of the unsolved
questions.

Vesicle mineralization

In the last years it has become apparent that the onset of
hard tissue formation is connected with the mineralization of
collagen-free extracellular matrix vesicles.

We have found, that the mineralization starts in the lower
proliferation zone of the epiphyseal plate in round (or elliptic)
microcompartments (dense clusters), in which needle like
apatitic formations appear mostly radially arranged (1). Most
probably they are the (mineralized) matrix vesicles. These
"dense clusters" are preserved into the fully mineralized long
septa. To answer the question whether these "dense clusters"
contain more mineral substance per volum than the surrounding,
secondarily mineralized compartments (light regions) we have
measured the Ca- and P-counts in both regions. For the analysis
we have used the scanning device of the Philips EM 301 with an
energy dispersive detector. The area of each measurement was
250 x 250 nm^2. It was found that the Ca- and P-counts were 70%
to 90% higher in the "dense clusters" compared with the "light
regions". As absorption corrections could be neglected the
difference in mineral content should be the same. So it could
be concluded that in a first stage a large amount of mineral
substance is deposited in clusters (probably the vesicles) and
in a second stage the surrounding matrix (including the collagen)
is mineralized to a lesser extent.

Mineralization without vesicles

After a sheath of mineral substance has been deposited in dentine and bone, matrix vesicles are no more necessary for a further mineralization. Also those stages of the mineralization of turkey tibia tendon which we have analyzed seem to be not connected with matrix vesicles.

The turkey tibia tendon mineralizes in a physiological way at an age of about 11 weeks. They offer an excellent model for the (topological) analysis of hard tissue formation. Using a static electron beam in the EM with a diameter of about 5o nm we have found that the countrate of Ca and P in single minera- lized collagen fibrils is only half of that found in the mineralized surrounding groundsubstance, which is free of collagen and originally rich in proteoglycans (2). From this and other systems being analyzed one can conclude that the noncollagenous matrix can deposit more mineral substance than the collagen.

In order to analyze the Ca/P relation, proceeding from the unmineralized into the mineralized regions, quantitative measurements, using wavelength dispersive spectrometers, were carried out across the border of mineralization (using a microprobe with an analyzed area of about 25 x 25 μm^2). The Ca- and P-contents increased from o.2% $^w\!/\!w$ for each element in the unmineralized region to about 2o% (Ca) and 8% (P) in the mineralized region. So the Ca/P-ratio increased from about 1 in the unmineralized to more than 2 in the mineralized region (apatite value: 2.16). Such an increase in the Ca/P-ratio from values below the apatite value up to the apatite value has been registered by us in the predentine/dentine border and in mineralizing aortas with isthmus stenosis too. Further it was found in measurements across the aorta wall that the shape of the distribution curve for Ca and Mg are similar.

Special problems concerned with the microanalysis of mineralizing tissue

In the following only some of the special problems can be discussed. The problem to keep all elements without loss or

displacement in situ is the same in the electron probe microanalysis of mineralizing tissue as it is in the analysis of soft tissue.

Fully mineralized tissue can be analyzed, with morphological correlation to the crystallites, on ultrathin sections. Except for enamel it is not too difficult to cut ultrathin sections on a microtome with a diamond knife. Hard tissue can also be analyzed on polished surfaces of bulk material or on polished slices. As this preparation is the same being used in mineralogy and metallography, microanalysis of biological material started with these preparations.

It is more difficult to cut tissue in which soft tissue (in the prestage of mineralization) appears together with mineralized one. Nevertheless the analysis of such material is fundamental for the research of hard tissue formation.

Soft and hard tissue differ not only in their chemical composition but also in their density and hardness. Cutting mineralizing dentine in the cryostat we have observed, that the peripheral dentine can be pushed into the predentine.

Another problem may arise concerning the great difference in density and absorption of x-rays and the scattering of electrons. Using ultrathin sections there is no x-ray absorption in the section itself (not even in the mineralized region), but quite a lot of radiation may originate in the surrounding of the specimen, not in the specimen itself.

To analyze larger areas (e.g. the element distribution in the arterial wall) one has to use cryostat sections, cut with 5 μm thickness. Such sections can be analyzed in a conventional microprobe with a wavelength dispersive detectorsystem (beam diameter ca. 1 μm). In such specimens the absorption in the mineralized region is large (while the soft tissue is still "thin" in regard to the method of Hall (3). For quantitative work we use this method of Hall, which needs the ratio of P (characteristic counts) to W (count-rate of a suitable region of the white x-ray spectrum). This ratio P/W can vary with film thickness (up to a factor of three)(4). But we have clarified,

that P/W is not dependend on film thickness, when the energy
region of W is taken very close to that of P (a method which
Cobet has used for bulk specimens).

Often one is interested in the analysis of the elemental
distribution of some mm in one direction. As it will not be
possible to cut ultrathin frozen sections of such a width
the cutting and analysis of normal cryostat sections will be
necessary also in the future, especially, when proceeding from
the soft tissue into the mineralized one. For those projects
in which small, normally adjacent, microcompartments are to
be analyzed the elemental analysis of cryoultrathin sections
in the EM will be necessary.

References:

(1) Barckhaus R.H., Höhling H.J. - Cell Tiss. Res. in press

(2) Höhling H.J., Barckhaus R.H., Krefting E.R., Schreiber J.
      - Cell Tiss. Res. 175, 345-35o (1976)

(3) Hall T.A. - In: Physical Techniques in Biological Research,
      1A, 2nd Ed., Academic Press, New York, 157-275 (1971)

(4) Krefting E.R. - Beitr. elektronenmikroskop. Direktabb.
      Oberfl. 9 in press

ELECTRON PROBE ANALYSIS OF SMOOTH AND STRIATED MUSCLE

Andrew P. Somlyo*, Avril V. Somlyo*,
Henry Shuman*, Bonnie F. Sloane* and Antonio Scarpa**

* Pennsylvania Muscle Institute, Presbyterian-University of Pennsylvania
Medical Center, 51 North 39th Street, Philadelphia, Pa. 19104

**Department of Biochemistry-Biophysics, Richards Building/4, University
of Pennsylvania, Philadelphia, Pa. 19104

The use of electron probe analysis for determining the subcellular composition of skeletal, cardiac and smooth muscle has provided some direct answers to questions related to excitation-contraction coupling. We shall summarize here results obtained in our laboratory, details of which have been presented elsewhere (1-7).

METHODS

Specimen Preparation:

The preservation of diffusible elements prior to electron probe analysis is an essential requirement for obtaining physiologically valid information. Because of the high cooling rates required for obtaining vitreous (or near vitreous) freezing, material that is sufficiently well frozen for electron microscopy is generally limited to a tissue depth of approximately 10-20μm (1). Therefore, cubing of tissues prior to freezing is not desirable, because it leads to the influx of extracellular ions (e.g., Na, Ca) and the efflux of intracellular constituents through cut surfaces. Muscle, however, is a rather suitable tissue to be prepared for electron probe analysis, since small bundles and even single fibers can be obtained without injury.

Cryoprotectants have not been used in our experiments. The addition to the extracellular solutions of 4% bovine serum albumin (BSA), while

not a true cryoprotectant, yields frozen specimens showing reduced ice crystal formation in the extracellular space (1, 2, 6).

Optimal freezing has been obtained with supercooled Freon 22 (1) at approximately $-164 \pm 2^{\circ}$C by shooting the tissue into the constantly stirred coolant, thus exposing it continuously to consecutive layers of cold Freon 22. Observations on cryo sections of muscle (1, 2, 3, 5, 6, 7) as well as the measurement of cooling rates (8) indicate that supercooled Freon 22 employed in this manner yields better freezing rates than liquid N_2 slush.

Approximately 100-200nm thick sections are cut at -130°C, placed on thin carbon foil that has been glow-discharged to improve adhesion and flattening, and then dried at 10^{-6} Torr at -80°C (1). The details of the preparatory techniques summarized above have been published (1). Only un-fixed preparations obtained without cryoprotectants are suitable for electron probe analysis. However, frozen thin sections can also be used for structural studies and have the advantage that the osmication and dehydration steps are eliminated. These morphological, but not electron probe, studies are most suitably done on preparations fixed with glutaraldehyde prior to freezing and negatively stained after sectioning (Fig. 1; see also 9).

Electron Probe Analysis:

The instrumentation and the computer program used for quantitation, based on Hall's method of characteristic peak/continuum for concentration measurements (10) and the minimal detectable limits have been published in detail elsewhere (11, 12, 13). Recent experiments have been done on a Phil-ips EM 400 high vacuum microscope with a single crystal LaB_6 gun (Kim-

ball Physics), a 30mm^2 Kevex detector and 5100 multichannel analyzer interfaced with a NS 880 system. Specimens are cooled to approximately -165°C to reduce contamination and mass loss (12).

RESULTS

Striated Muscle:

Elemental concentrations (mmoles/kg/dry wt. $\pm$ S.E.M.) determined by electron probe analysis of frozen dried cryosections of frog striated muscle of the type shown in Fig. 2 were: K 404 $\pm$ 4.3, Mg 39 $\pm$ 2.1, P 302 $\pm$ 4.3 and Cl 24 $\pm$ 1.1. In the instances where reliable measurements of these elements have been obtained by independent methods (K, Mg and P), those values are in good agreement with the results of electron probe analysis (1). The Cl concentration measured with the electron probe is in excess of that predicted by a passive Gibbs-Donnan distribution. Some recent studies with Cl sensitive electrodes report similar values indicating that this excess Cl is not bound (14), although others report Cl activities indicative of a passive Cl distribution under conditions of normal pH (15).

The terminal cisternae (TC) of the sarcoplasmic reticulum (SR) contains high concentrations of calcium (66 $\pm$ 4.6 in frog and 77 $\pm$ 0.9mmoles/kg dry wt. $\pm$ S.E. in toadfish striated muscle). A major question of excitation-contraction coupling was resolved unambiguously by electron probe analysis (for review see 1), i.e., the SR does not contain extracellular concentrations of NaCl.

Hypertonic solutions cause vacuolation of frog striated muscle, and the vacuoles contain high concentrations of the predominantly extracellular

solutes Na and Cl (1). In cryosections of muscles vacuolated with hyper-tonic solutions, compartmentalization of NaCl in the vacuoles could be dem-onstrated with sharp boundaries at a spatial resolution of 50-100nm (1). Structural studies on freeze-substituted material show that the vacuoles are part of the transverse tubule system (16). In muscles treated with hypertonic solutions there were also electron dense granules in the longi-tudinal SR. These granules consisted mainly of Ca, Mg and P in a ratio of approximately $(Ca + Mg)/P = 1.1 \pm 0.35$ S.D.

Fatigued (stimulated to exhaustion) frog striated muscle develops vacuoles that are part of the transverse tubule system and contain high con-centrations of NaCl (5). The Ca content of TC in fatigued muscles was normal, or possibly increased, indicating that calcium depletion of the se-questration sites is not the cause of fatigue. Similarly, uncoupling of mito-chondria due to calcium accumulation could also be ruled out as a cause of fatigue, in view of the normal Ca content (2.2 ± 1.7mmoles/kg mitochon-drial dry wt.) of the mitochondria in fatigued striated muscle.

In cardiac muscle, the subject of earlier preliminary studies, mi-tochondrial Ca granules were found when the (mouse) hearts became ischem-ic and/or had undergone fibrillation during dissection (7). No similar gran-ules were found in normal cardiac muscle after improvement in dissection. This finding further emphasizes the importance of the preparatory tech-niques necessary to obtain undamaged tissues for electron probe analysis.

Smooth Muscle:

Cytoplasmic analysis of rabbit portal-anterior mesenteric vein smooth muscle showed a Cl content significantly in excess of that expected on the basis of Gibbs-Donnan distribution which ranged, in different experimental series, from 190 ± 2.6 to 335 ± 3.4 mmoles/kg dry wt. $\pm$ S.E.M. This finding is in agreement with Cl-flux measurements (17, 18, 19) and, in addition, provides direct evidence that the high Cl content of smooth muscle is not due to compartmentalization in organelles, but represents Cl generally distributed throughout the cytoplasm.

In elements of the SR of smooth muscle that had been depolarized with high K solutions to increase Ca influx, localized concentrations of Ca were present, confirming the role of the SR (20, 21) as a calcium seuestration site in smooth muscle.

Mitochondrial calcium content in portal-anterior mesenteric vein smooth muscle was low (1.8 ± 1.7 mmoles/kg dry wt. $\pm$ S.E.M.), even in preparations that had been depolarized for 30 minutes with high K solutions. This finding, in conjunction with the apparent K_m of isolated vascular smooth muscle mitochondria for Ca (22, 23), suggests that mitochondria do not play a significant role in the physiological regulation of cytoplasmic Ca in this smooth muscle. Only in cells that were judged to be damaged, as indicated by high cytoplasmic Na and low K, were there significant concentrations of mitochondrial calcium in the form of granules.

Isolated Mitochondria:

Mitochondria isolated from bovine vascular smooth muscle (main

pulmonary artery) contained high concentrations of Ca, in contrast to the low Ca content of in situ and isolated rabbit vascular smooth muscle mitochondria. The mean concentration of Ca, as determined by atomic absorption spectroscopy, in normal bovine vascular smooth muscle mitochondria was 82nmol/mg mitochondrial protein. The mean concentration of Ca was significantly higher (169nmol/mg mitochondrial protein) in mitochondria isolated from fatty (atherosclerotic) vessels. Electron probe analysis of individual mitochondria which were isolated from atherosclerotic tissue and which contained electron dense granules showed that the Ca content of these mitochondria was 280mmoles/kg dry wt. Occasional mitochondria (up to 10%) isolated from rabbit vascular smooth muscle also contained granules. The latter could be differentiated into two types: a) relatively large, electron dense granules with a circular profile called "dense granules" and b) smaller, less electron dense granules having a more irregular outline, called "fluffy" granules. Electron probe analysis of individual mitochondria containing the two types of granules showed that the Ca to Mg ratio was much higher (8.6 ± 1.1) in the "hard" than in the "fluffy" (1.9 ± 0.2) granules.

CONCLUSION

Electron probe analysis has resolved major questions concerning subcellular composition, such as the ionic content of the sarcoplasmic reticulum, the role of mitochondria in controlling cytoplasmic Ca levels and the distribution of Cl in smooth muscle. The results of quantitative electron probe analysis of thin dried cryosections of muscle are also in good

agreement with the available, independent measurements of bulk concentrations. We limited our discussion to results obtained in our laboratory on adult tissues. Cell cultures are also suitable for rapid freezing, the localization of tagged drugs and composition measurements of intracellular ionic compartments (24, 25). No attempt was made to review publications using precipitating agents in fixed muscles or the use of frozen hydrated material (26, 27, 28, 29). In our experience the use of trapping agents, such as pyroantimonate or silver nitrate, does not reliably preserve the distribution of ions and results in a total loss of non-precipitable ions of physiological interest. Therefore, while simpler preparatory techniques may be suitable in partially preserving relatively insoluble deposits of compartmentalized elements (30), the major advantage of electron probe analysis is its potential in establishing subcellular distribution of diffusible, as well as non-diffusible, ions in muscle, and this is critically dependent on the rapid freezing of uninjured muscle fibers.

The most important biological results obtained to date show that the sarcoplasmic reticulum of striated muscle does not have an ionic composition similar to that of the extracellular space, that mitochondrial calcium granules appear under pathological conditions and in cells injured during dissection, and that the non-Donnan distribution of Cl in smooth muscle is not due to compartmentalization of Cl in organelles.

REFERENCES

1) Somlyo, A. V., Shuman, H. and Somlyo, A. P. J. Cell Biol. 74:828-857, 1977.

2) Somlyo, A. V., Shuman, H. and Somlyo, A. P.   Nature 268:556-558, 1977.

3) Somlyo, A. P., Somlyo, A. V., Shuman, H., Sloane, B. and Scarpa, A. In: Ann. N. Y. Acad. Sci., In press.

4) Somlyo, A. P., Somlyo, A. V., Shuman, H. and Garfield, R. E. In: Ionic Actions on Vascular Smooth Muscle with Special Regard to Brain Vessels, E. Betz ed., Springer-Verlag, pp. 17-20, 1976.

5) Gonzalez-Serratos, H., Somlyo, A. V., McClellan, G., Shuman, H., Borrero, L. M. and Somlyo, A. P.   Proc. Nat. Acad. Sci., In press.

6) Somlyo, A. V., Shuman, H. and Somlyo, A. P.   Proc. 34th Ann. EMSA Mtgs. 334, 1976.

7) Somlyo, A. V., Silcox, J. and Somlyo, A. P.   Proc. 33rd Ann. EMSA Mtgs. 532, 1975.

8) Costello, M. J. and Corless, J. M.   J. Micros. 112:Part 1, 1978, In press.

9) Sjöström, M., Thornell, L. E. and Cedergren, E.   J. Micros. 99:Part 2, 193-204, 1973.

10) Hall, T. A.   In: Physical Techniques in Biological Research, Vol. IA, G. Oster ed., Academic Press, Inc., New York, 1971.

11) Shuman, H. and Somlyo, A. P.   Proc. Nat. Acad. Sci. 73:1193-1195, 1976.

12) Shuman, H., Somlyo, A. V. and Somlyo, A. P.   Ultramicroscopy 1:317-339, 1976.

13) Shuman, H., Somlyo, A. V. and Somlyo, A. P.   Scan. Elect. Micros. IIT Res. Inst. 1:663-672, 1977.

14) Armstrong, W. McD., Wojtkowski, W. and Bixenman, W. R.   Biochim. Biophys. Acta. 465:165-170, 1977.

15) Bolton, T. B. and Vaughan-Jones, R. D.   J. Physiol. 270:801-833, 1977.

16) Franzini-Armstrong, C., Heuser, J. E., Reese, T. S., Somlyo, A. P. and Somlyo, A. V., Manuscript in preparation.

17) Casteels, R.   J. Physiol. (Lond.) 214:225-243, 1971.

18) Kao, C. Y. and Nishiyama, A. Am. J. Physiol. 207:793-799, 1964.

19) Jones, A. W., Somlyo, A. P. and Somlyo, A. V. J. Physiol. (Lond.) 232:247-273, 1973.

20) Somlyo, A. V. and Somlyo, A. P. Science 174:955-958, 1971.

21) Somlyo, A. P., Somlyo, A. V., Devine, C. E., Peters, P. D. and Hall, T. A. J. Cell Biol. 61:723-742, 1974.

22) Somlyo, A. P., Vallieres, J., Garfield, R. E., Shuman, H., Scarpa, A., and Somlyo, A. V. In: Biochemistry of Smooth Muscle, N. L. Stephens ed., University Park Press, Maryland, pp. 563-583, 1977.

23) Vallieres, J., Scarpa, A. and Somlyo, A. P. Arch. Biochem. Biophys. 170:659-669, 1975.

24) Garfield, R. E. and Somlyo, A. P. Exp. Cell Res. 109:163-179, 1977.

25) Garfield, R. E. and Somlyo, A. P. In: Factors Influencing Vascular Smooth Muscle Reactivity, S. Shibata and O. Carrier eds., Igaku Shoin Ltd., Japan, In press.

26) Gupta, B. L., Hall, T. A., Maddrell, S. H. P. and Moreton, R. B., Nature (Lond.) 264:284-287, 1976.

27) Gupta, B. L., Hall, T. A. and Moreton, R. B. In: Transport of Ions and Water in Animals, B. L. Gupta, R. B. Moreton, J. L. Oschman and B. J. Wall eds., Academic Press, London, pp. 83-143, 1977.

28) Saubermann, A. J. and Echlin, P. J. Micros. 105:155-191, 1975.

29) Lechene, C. P. Am. J. Physiol. 232:F391-F396, 1977.

30) Burton, K. P., Hagler, H. K., Templeton, G. H., Willerson, J. T. and Buja, L. M. J. Clin. Invest. 60:1289-1302, 1977.

FIGURE LEGENDS

Fig. 1 a) Longitudinal and b) transverse section of a glutaraldehyde fixed frog muscle. Frozen sections were cut from the fixed tissue, picked up on frozen drops of sucrose, melted and negatively stained with ammonium molybdate. Sections prepared in this way are not suitable for electron probe analysis, but are useful for morphological studies as they circumvent the use of osmium and organic solvents. Note the A and I bands and M line as well as the Z line. Magnification a) x60, 000 and b) x312, 000.

Fig. 2 Frozen-dried section of unfixed normal frog toe muscle showing A band, I band, Z and M lines. Note knife marks and fine compression lines at right angles to the knife marks. Unstained. Bar, 1 μm. Magnification x22, 500. From (1)

Fig. 3 Longitudinal section of toadfish swimbladder muscle processed by freeze-substitution to illustrate the depth of ice crystal-free tissue. The outer aspect of the muscle that is free of ice crystals formed the leading edge of the specimen when it was shot into supercooled Freon. Note the increments of ice crystal size towards the interior of the muscle. The A band is 1.5μm long. Magnification x10, 000. For frozen sections the outer 5-10μm of similarly frozen tissues are utilized.

Figure 1a
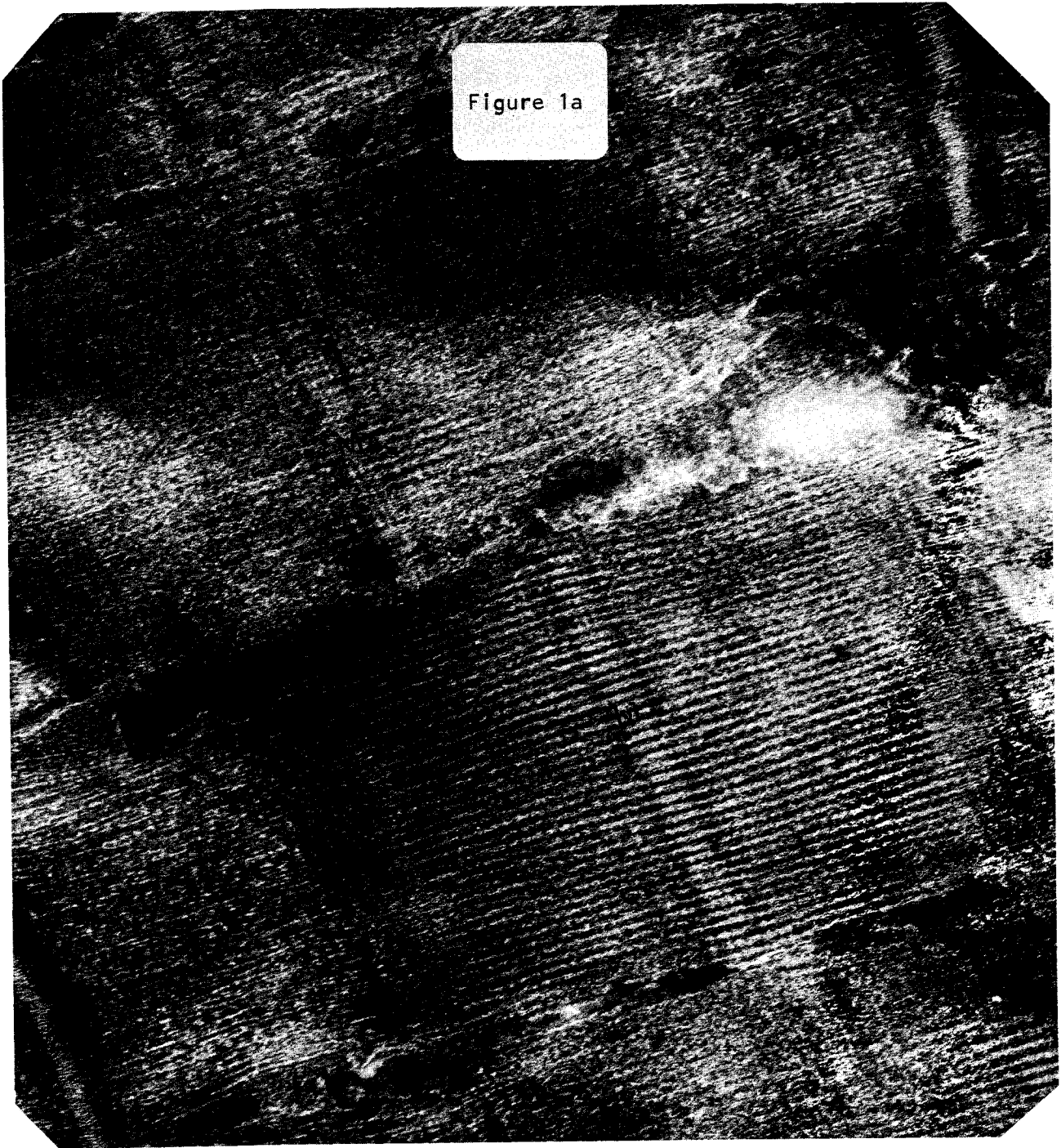
Figure 1b

Figure 2

Figure 3
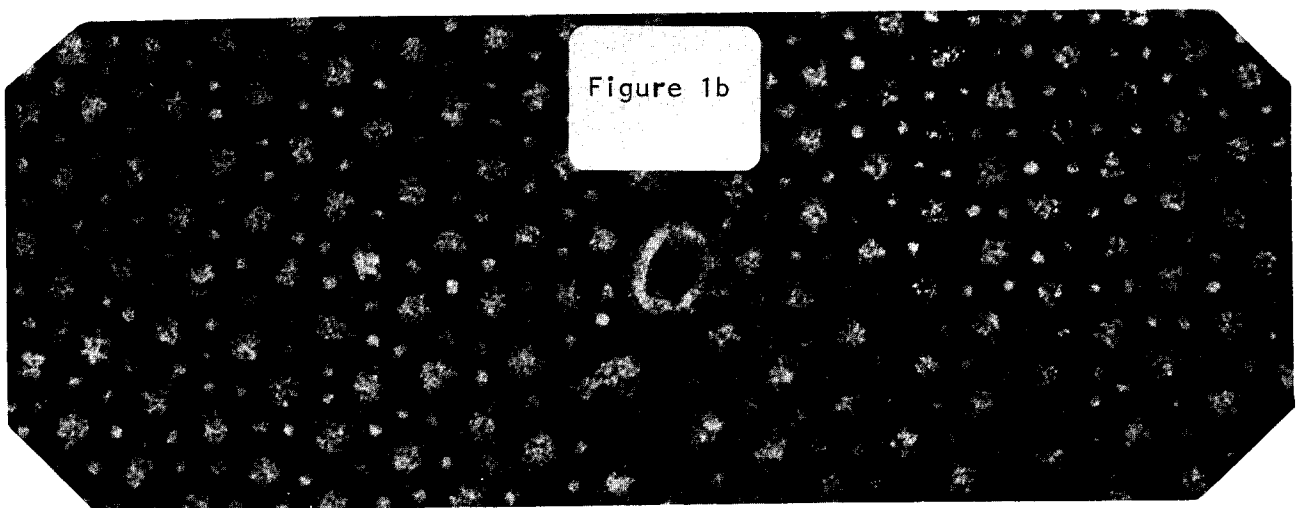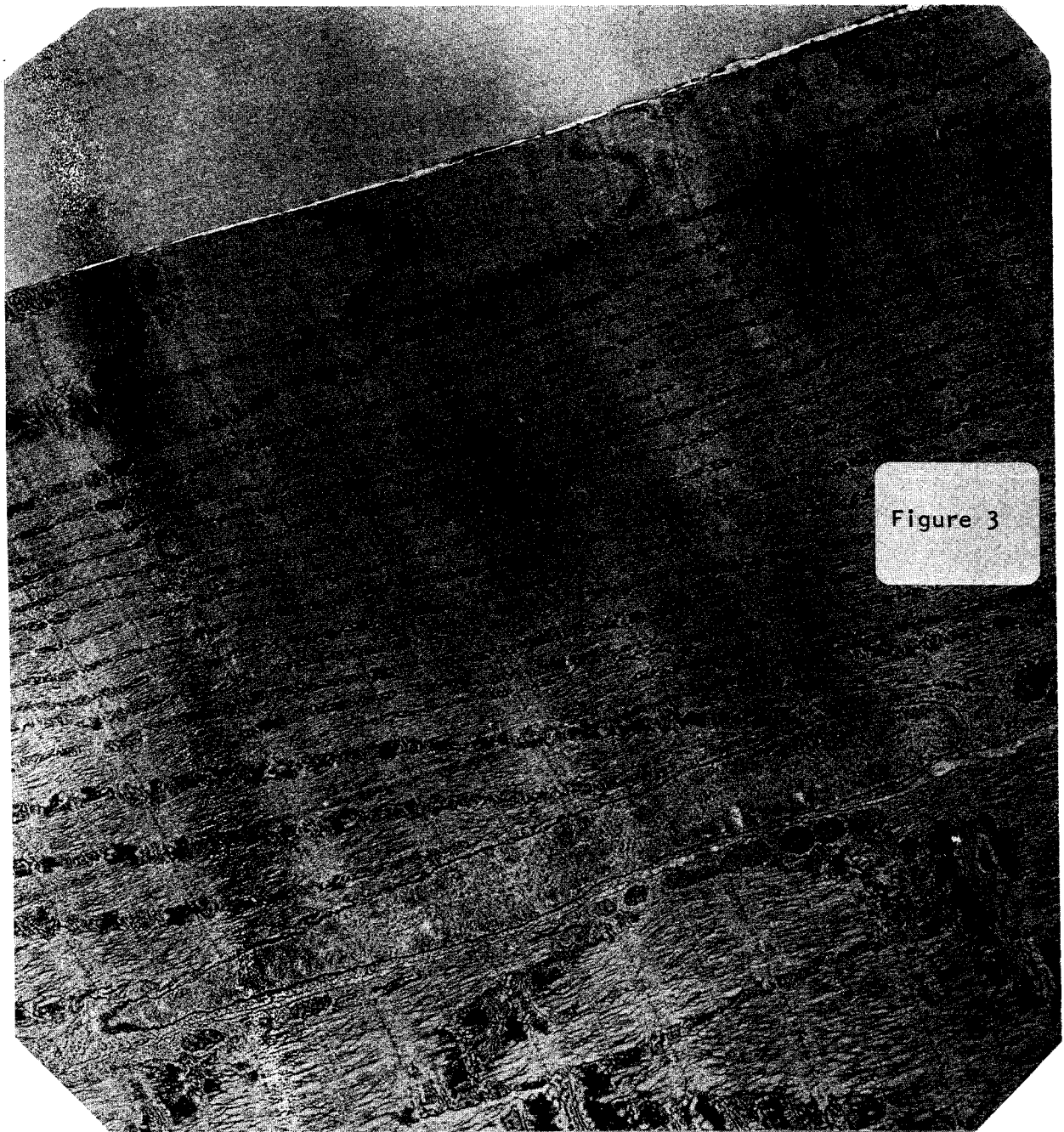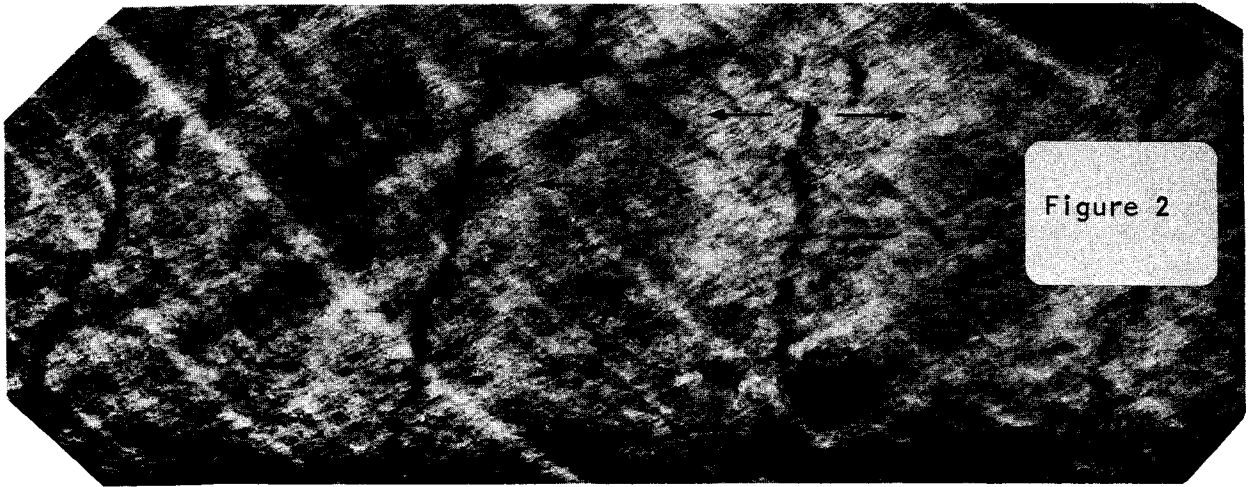
IMPROVEMENT OF PEAK/BACKGROUND RATIOS FOR ANALYSIS OF FROZEN-HYDRATED
TISSUE SECTIONS. P.D. Peters, A.J. Saubermann and W.D. Riley.
Department of Anaesthesia, Harvard Medical School, Boston, Mass. 02215.

In microanalysis of frozen-hydrated biological specimens the
concentration of the light elements of interest is often low, giving
poor peak/background (P/b) ratios on a Si(Li) detector, and consequently
poor statistics. Since the peak count cannot be increased other than
by increasing the probe current or counting time, the P/b ratio has been
improved by reducing the background.

Two major elements which it was necessary to remove from the spectra
were Al and Cu, both of which gave inconvenient overlaps with peaks of
interest, as well as a high level of continuum radiation. The frozen-
hydrated sections had been routinely mounted on an aluminized nylon
film, stretched over a 3 mm hole in an Al cylinder. This specimen
stub was then mounted on a Cu holder for transfer onto the cold stage
in the AMR 900 electron microscope.

The specimen stub has been redesigned so that the Si(Li) detector
"sees" less metal, and specimen stubs of the modified shape made out of
C and Be are now used. To remove the Al characteristic peak entirely,
the evaporated Al coating has been replaced by C; to remove the Cu
peak entirely, the stub holder is being replaced with Be.

A range of combinations of stage height, specimen tilt and Si(Li)
position has been tested to find the optimum, and collimators on the
nose of the Si(Li) detector have been used to prevent extraneous
radiation from the sub-stage reaching the detector. Spectra will
be shown to illustrate the improved background shape and how it is
now possible to acquire more significant data.

ELECTRON MICROPROBE LOCALIZATION OF ALUMINUM DEPOSITS IN RAT LUNG
AFTER INHALATION EXPOSURE TO ALUMINUM CHLORHYDRATE

W. J. Hamilton
Applied Research Laboratories
9545 Wentworth Street
Sunland, California 91040

N. Woodside
Experimental Pathology Laboratories, Inc.
P. O. Box 474
Herndon, Virginia 22070

Aluminum chlorhydrate is used extensively as an active incredient
in aerosol antiperspirants. The present work was conducted as
part of a larger investigation to determine the possible patho-
logical effects of inhalation of aluminum chlorhydrate on lung
tissue. After inhalation exposure, rat lung cells obtained by
direct tissue sectioning or by lung lavage are found to contain
particulate materials and membrane bound, electron dense bodies.
Wavelength dispersive x-ray analysis has been used in conjunction
with scanning transmission electron microscopy to localize
aluminum within the electron dense bodies in ultrathin sections
of rat cells from lung lavage of rats after inhalation exposure
to aluminum chlorhydrate.

METHODS & MATERIALS

Male and female rats were intermittently exposed in inhalation
chambers to aluminum chlorhydrate at levels from 0.25 mg/m^3 to
2.5 mg/m^3.

The micrograph in Figure 1 was obtained by direct tissue section
from a female rat given a one year intermittent exposure of
2.5 mg/m^3 for 6 hours/day for 5 days/week. The micrographs in
Figures 4 and 5 were obtained from a lung lavage from a male rat
given a similar six month intermittent exposure of 2.5 mg/m^3.

Lung lavage was performed by washing intratracheally with normal saline. The washings were centrifuged and the pellets treated as fresh tissue.

Tissue and pellets were fixed in 3% gluteraldehyde in s-collidine buffer for 30 minutes, quartered and post-fixed for one hour in the same fixative followed by 90 minutes in 1% osmium tetroxide after a thorough wash. Routine dehydration, infiltration and embedding was performed with Epon 812. A dispersion of aluminum chlorhydrate was also embedded to act as a reference standard. Gold sections (700-800 Angstroms thick) were produced with glass knives on an LKB 3 ultramicrotome to optimize x-ray signal while retaining electron transmission.

Transmission electron microscopy was performed on an Hitachi HU-12A at 75kV. Scanning·transmission electron microscopy (STEM) was obtained at 25-50kV and 5-150 picoamp beam current on an Applied Research Laboratories' SEMQ. X-ray area mapping was performed on the ARL SEMQ using the aluminum K_α line on a light element x-ray scanning spectrometer fitted with a thallium acid phthalate crystal and a flow proportional detector. The Al K_α peak wavelength position was located using the alumunum chlorhydrate standard (Figures 2 and 3) in order to avoid possible wavelength shifts. The x-ray images were obtained at 15-20kV and 10-15 nanoamps beam current (specimen current measured on the copper grid).

X-ray intensity data were obtained for cell components, bare epoxy and electron dense bodies. The points (labeled A-E in Figure 5) were selected by placing the beam position indicator cross of the SEMQ video display over the point in the scanning image and switching to the point mode. At least three 10 second integrations were averaged for each position. The beam conditions used were not altered from those used for x-ray mapping.

RESULTS

The appearance of rat lung tissue after exposure to aluminum chlorhydrate is shown in the transmission electron micrograph of Figure 1. A number of the abnormal, irregular-shaped electron dense bodies are visible in the cell and cell debris. The shape and sizes of these dense bodies are typical of those found

associated with cells in lung sections and lavages. The number
of these bodies are exposure and dose related.

In order to ascertain that the dense bodies were a primary
result of the inhalation of aluminum chlorhydrate and not a
secondary response of the cell, the localization of aluminum
within the bodies by x-ray mapping was performed. Initial
attempts at use of energy-dispersive x-ray mapping using a solid
state detector were only marginally successful; the high x-ray
background level made spatial localization difficult.

Scanning transmission electron images and wavelength dispersive
x-ray images were obtained on the sections of aluminum chlor-
hydrate reference standard (Figures 2 and 3) and on rat lung lavage
(Figures 4 and 5). In each case, the STEM images were first
located and photographed at high accelerating voltages and very
low beam currents and the beam conditions changed to optimize
x-ray imaging to lower accelerating voltages and much higher
beam currents. The resulting STEM image of the lung lavage
(Figure 4) clearly shows the cell components and electron dense
bodies. The x-ray image (Figure 5) unequivocally locates the
aluminum x-ray source principally within the electron dense
bodies.

The x-ray intensities determined with a static beam corroborate
the x-ray data for the location of the aluminum.

Location	Point	Al K_α X-ray counts/ 10 seconds
Irregular, electron dense body	A	321 (±16) (±1σ)
Crescent-shaped dense body	B	275 (±2)
In Epon, external to cell	C	13 (±5)
Cell cytoplasm	D	15 (±4)
Cell nucleus	E	16 (±1)

Within the electron dense bodies the aluminum x-ray intensities
were high; in the normal cell components and external to the cell,
the counts were just detectable.

DISCUSSION AND CONCLUSIONS

Rat lungs exposed to aluminum chlorhydrate by intermittent inhalation contain exposure and dose related, electron dense inclusion bodies. The use of wavelength dispersive x-ray imaging in conjunction with scanning transmission electron microscopy has permitted the localization of aluminum within the electron dense bodies. This localization substantiates the hypothesis that the dense bodies are a direct result of the aluminum chlorhydrate inhalation and are not due to some other experimental parameter.

The use of a wavelength dispersive spectrometer enhanced the detection and imaging of the aluminum x-ray signals relative to the energy dispersive detector. This is most likely due to: (1) the much higher inherent peak to background ratio of the wavelength dispersive spectrometer; (2) the lowered sensitivity of the energy dispersive detector to the longer wavelength x-rays from the lighter elements and (3) the increased aluminum x-ray background resulting from the use of aluminum in the construction of instrument stages and columns and the wide angle of acceptance of the energy dispersive detector allowing x-rays to be collected from those areas.

It is important to note that the ability to image transmitted electrons at high accelerating voltage and very low currents to locate areas of interest, followed by rapidly switching to low accelerating voltage and high currents for optimal x-ray work was critical in the success of the localization of aluminum in ultrathin sections.

ACKNOWLEDGEMENTS
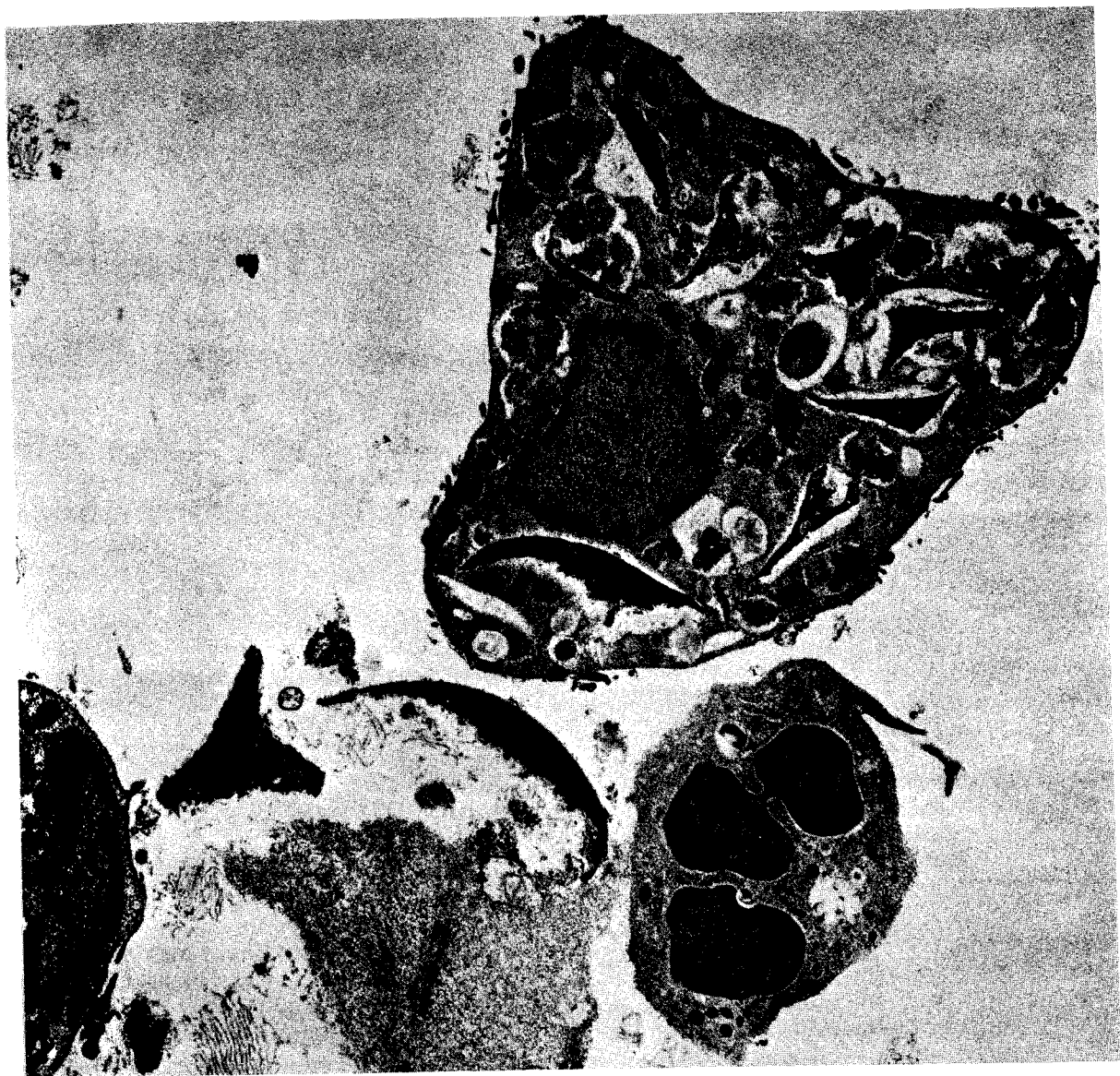
Figure 1: Rat Lung Exposed by Inhalation to Aluminum Chlorhydrate

Conventional Transmission Electron Micrograph

9000X   1μm |———|

Figures 2 & 3: Aluminum Chlorhydrate Embedded in EPON 812

Figure 2: Scanning Transmission Electron Micrograph
           12.5kX   30kV   150 picoamp

Figure 3: Aluminum Kα X-ray Image
           12.5kX   20kV   15 nanoamp
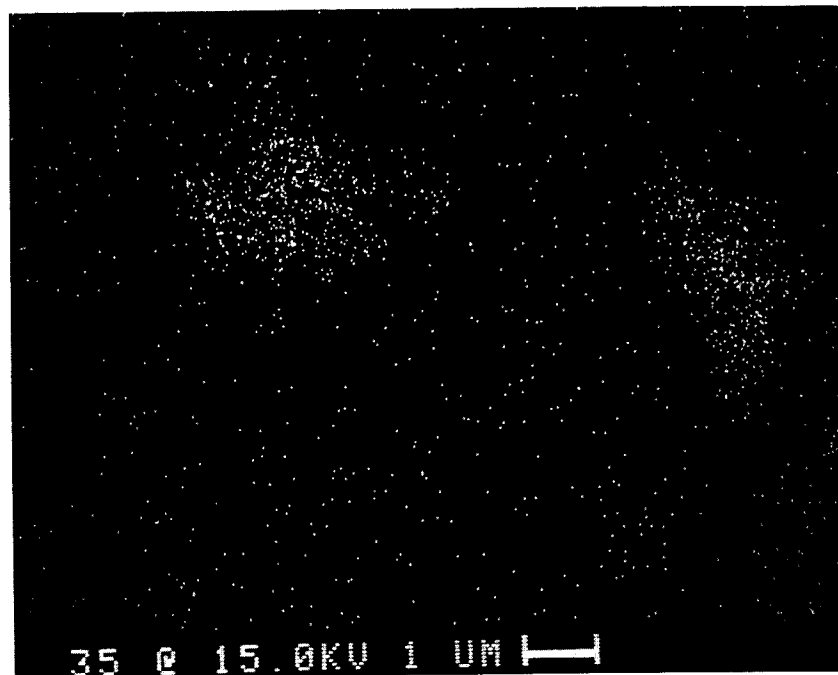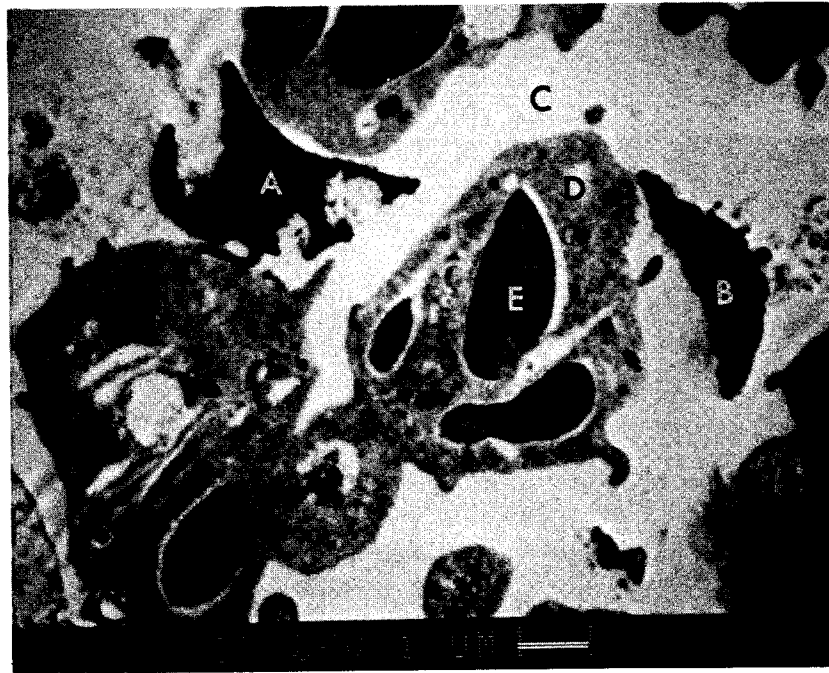
Figures 4 & 5: Rat Lung Exposed by Inhalation
                to Aluminum Chlorhydrate

Figure 4: Scanning Transmission Electron Micrograph
           10kX   35kV   50 picoamp

Figure 5: Aluminum Kα X-ray Image
           10kX   15kV   12 nanoamp

ELECTRON PROBE ANALYSIS IN KIDNEY PHYSIOLOGY

R. R. Warner and C. P. Lechene

Harvard Medical School
Boston, Massachusetts

The role of the kidney is to maintain homeostasis of body fluid and electrolytes. To perform this function the plasma is filtered into kidney tubules (nephrons); the ultrafiltrate flows along the nephron where the epithelial cells modify the electrolyte and fluid content of the filtered plasma by reabsorption and secretion. Of interest is knowing (a) what the kidney cells are doing at various places along the nephron under different physiological conditions and (b) how the cells are performing these functions. The first question can be answered by measurement of changes in the tubular fluid due to epithelial cell functions; however, all nephrons have segments that penetrate deep into the kidney, and in these regions the tubular fluid is inacessible to conventional sampling techniques (micropuncture). The latter question is not well understood in any tissue and is a major unsolved problem in physiology. A major step towards understanding cellular transport processes would be the analysis of the electrolyte content and distribution within a single cell. Whereas this is potentially possible with an electron microprobe, the lack of a specimen preparative technique that would preserve the in situ distribution of diffusible ions and water in the cells and their microenvironment has limited its application.

Previous attempts at measuring cellular electrolyte content and distribution in the kidney have utilized available techniques of freeze drying (1) or freeze drying followed by plastic embedding (2). Whereas some element retention was obviously obtained, problems of element loss and translocation could not be avoided. Infiltration of freeze-dried tissue by plastic has been shown to extract and redistribute elements (3). Problems of freeze drying are particularly crucial in kidney tissue which has extensive extracellular compartments devoid of any supportive protein

structure that could "trap" or "hold" ions in place as water is removed. After freeze drying these extracellular spaces are totally empty of solutes (4,5); in addition, some of this translocation could be a result of "mini-explosions" caused by the drying process, which could distribute fragments of the extracellular matrix over extensive areas (4). The fact that the extracellular compartments are empty precludes their analysis in regions deep within the kidney, regions of great interest due to their inaccessibility by conventional techniques of renal physiology.

Whereas techniques for direct analysis of kidney cells and compartments continue to be investigated, a general and routine technique has been developed for analysis of the electrolyte content of the small volumes of tubular fluid collected by conventional methods. With this liquid droplet technique (6,7), much smaller volumes can be analyzed than previously possible; and in these small volumes one can analyze for as many elements above boron as one wishes, nondestructively, and with an absolute specificity, provided the concentration exceeds approximately 0.1mM. With this technique, inter-element correlative studies are not only feasible but now routine; the analysis for elements that were previously measured only with difficulty are now measured quite simply; and experiments are now possible that previously were limited or made impossible by sample sizes that were too small.

The advantages of the liquid droplet technique have insured a wide application, and the technique has been established in a number of laboratories in transport physiology (8, 9, 10, 11). In our laboratory, the technique has been used to study how the kidney handles a number of electrolytes. Sulfate reabsorption along the nephron has been studied in rats undergoing mild saline diuresis (12) as well as in sulfate-loaded rats (13). Parameters affecting phosphate reabsorption along the nephron have been studied (14, 15, 16), and the movement of phosphate into the proximal tubule from the plasma has been investigated (17). Inter-element effects of parathyroid hormone (18) and drugs (19, 20) were studied,

and mechanisms of fluid and electrolyte movement in the proximal tubule have been delineated (21, 22). On-going projects involve the study of calcium transport in isolated nephron segments from deep within the kidney, the effect of the drug furosemide on kidney function, the transport of K in distal regions of the nephron, and the reabsorption of Ca and Mg in the most distal regions of the nephron deep within the kidney. Our laboratory has extended the use of the liquid droplet technique by developing new procedures for ultrafiltration of microliter volumes (unpublished), for the analysis of organic compounds (22, 23), and for distinguishing between chemically bound and free elements (12, 13).

The success of the liquid droplet technique has provided valuable new information on what kidney cells are doing in the modification of tubular fluid in some nephron regions. However, these studies remain limited by conventional techniques for obtaining fluid samples from accessible regions of the kidney. Techniques for obtaining fluid samples from inaccessible regions in frozen kidneys by collecting chips or melts of the extracellular ice have not given encouraging results (24), nor could these techniques directly answer questions of how kidney cells are performing their functions. Attention remains centered on developing new techniques for the analysis of kidney tissue in the frozen-hydrated state, in which the element content and distribution within cells, between cells and in the tubular and peritubular fluid can be determined throughout the nephron at any level of the kidney. The feasibility of analyzing frozen-hydrated bulk kidney tissue has been demonstrated in our laboratory with regard to diffusible element localization (25), potential for quantitation (4), and acceptable morphological identification (unpublished). Sample preparation with this technique is relatively easy now that the required hardware is developed (26). This frozen-hydrated technique has been applied to the analysis of the cortico-papillary gradient in antidiuretic and water diuretic rats (27); the observation of sharp discontinuities in this gradient differs from previous observations of a uniform, steadily

increasing gradient observed with other techniques and with microprobe
analysis of frozen-dried sections (28). Although the ultimate resolu-
tion using this technique is "limited" to a few cubic microns, meaning
investigations are limited to the cellular rather than organelle level,
this "limit" is not a barrier but a horizon. Knowledge of transport
phenomena at this level of resolution is practically non-existent. A
great number of truly fundamental problems could be answered, and in-
deed must be answered at this level if higher resolution studies are
to be effective. Whereas the development of routine procedures for
analysis of ultrathin frozen-hydrated tissue remains the ultimate goal,
providing resolution at the cell organelle level, results from these
studies can only be interpreted within the framework of events occur-
ring at the cellular level.

Although problems of charging, frost accumulation, surface drying
and accurate quantitation remain to be definitely solved for the analysis
of frozen-hydrated bulk tissue, these problems should present no major
barrier to be overcome. Similarly, the problem of finding an appropriate
ultrafiltered volume marker required to assess fluid absorption should
present no barrier. The use of metrizamide or sodium iothalamate com-
pares well with the conventionally used inulin, and has the advantage
that iodine can be detected with the microprobe (Table 1). An analysis
of the interaction between tubular fluid composition and cellular elec-
trolyte distribution at any region of the frozen-hydrated in vivo kidney,
as well as a comparison of this cellular distribution with measured fluxes
in the in vitro isolated tubule, are likely to significantly advance the
basic understanding not only of what kidney cells are doing along the
nephron, but how they are doing it.

TABLE 1

Comparison of glomerular filtration rate (GFR) measured in the sample by ^{3}H inulin liquid scintillation counting and by microprobe analysis of metrizamide or iothalamate iodine.

INULIN GFR	IODINE GFR
.92 ±.13	.96 ±.14
n = 8	n = 8

REFERENCES

1. Rosenstiel, A.P.V., H.J. Höhling, J. Schnermann and W. Kriz. Electron probe microanalysis of electrolytes in kidney slices. Proc. 5th Nat'l Conf. Electron Probe Analysis, New York City, New York (1970) 33A-33B.

2. Ingram, F.D., M.J. Ingram and C.A.M. Hogben. An analysis of the freeze-dried, plastic embedded electron probe specimen preparation. In: Microprobe analysis as Applied to Cells and Tissues; Hall, Echlin and Kaufmann, eds. Academic Press, New York (1974) 119-146.

3. Morgan, A.J., T.W. Davies and D.A. Erasmus. Changes in the concentration and distribution of elements during electron microscope preparative procedures. Micron 6 (1975) 11-23.

4. Lechene, C., T. Strunk and R. Warner. Perspectives in electron probe microanalysis of biolgical samples kept frozen. Proc. 10th Annual Conf., Microbeam Analysis Society, Las Vegas, Nevada (1975) 49A-49E.

5. Dörge, A., R. Rick, K. Gehring, J. Mason and K. Thurau. Preparation and applicability of freeze-dried sections in the microprobe analysis of biological soft tissue. J. Microsc. Biol. Cell 22 (1975) 205-214.

REFERENCES, Cont'd.

6. Lechene, C. The use of the electron microprobe to analyze very minute amounts of liquid samples. Proc. 5th Nat'l Conf. Electron Probe Analysis, New York City, New York (1970) 32A-32C.

7. Lechene, C. Electron probe microanalysis of picoliter samples. In: Microprobe Analysis as Applied to Cells and Tissues; Hall, Echlin and Kaufmann, eds. Academic Press, New York, (1974) 351-367.

8. Le Grimellec, C., N. Rionel and F. Morel. Simultaneous Mg, Ca, P, K, Na, and Cl analysis in rat tubular fluid. Pflügers Arch. 340 (1973) 181-210.

9. Agus, Z.S., L.B. Gardner, L.H. Beck and M. Goldberg. Effects of para- thyroid hormone on renal tubular reabsorption of calcium, sodium and phosphate. Am. J. Physiol. 224 (1973) 1143-1148.

10. Rick, R., M. Horster, A. Dörge and K. Thurau. Determination of electro- lytes in small biological fluid samples using energy dispersive X-ray microanalysis. Pflügers Arch. 369 (1977) 95-98.

11. Quinton, P.M. Energy dispersive X-ray analysis of picoliter samples of physiological fluid. Proc. 10th Ann. Conf. Microbeam Analysis Society, Las Vegas, Nevada (1975) 50A-50B.

12. Lechene, C., E. Smith, and K. Blouch. Site of sulfate reabsorption along the rat nephron. Kid. Int. 6 (1974) 64A.

13. Lechene, C.P., E. Abraham and R.R. Warner. Effect of sulfate loading on ionic distribution along the rat nephron. Clin. Res. 23 (1975) 432A.

14. Knox, F.G. and C. Lechene. Distal site of action of parathyroid hormone on phosphate reabsorption. Am. J. Physiol. 229 (1975) 1556-1560.

15. Knox, F.G., J.A. Haas and C. Lechene. Effect of parathyroid hormone on phosphate reabsorption in the presence of carbonic anhydrase inhi- bition. Kid. Int. 10 (1976) 216-220.

16. Colindres, R.E., E. Pastoriza-Munoz, W.E. Lassiter and C. Lechene. Effect of extracellular volume expansion on phosphate reabsorption along the nephron in acutely thyroparathyroidectomized rats. Kid. Int. 10 (1976) 488.

17. Gregor, R.F., F.C., Lang, F.G., Knox and C. P. Lechene. Absence of sig- nificant secretory flux of phosphate in the proximal convoluted tubule. Am. J. Physiol. 232 (1977) F235-238.

REFERENCES, Cont'd.

18. Abraham, E., R.R. Warner and C. Lechene. Electron probe analysis of the
    effect of parathyroid hormone on inorganic ions in the rat kidney.
    Proc. 10th Ann. Conf. Microbeam Analysis Society, Las Vegas, Nevada
    (1975) 47A-47F.

19. Lechene, C.P., T. Strunk and K. Blouch. Effect of furosemide after sul-
    fate loading on chlorine transport in the rat kidney. Kid. Int. 8
    (1975) 483.

20. Roman, R.J., J.S. Davis and C. P. Lechene. Dose related effect of clon-
    idine on water and electrolyte excretion. Proc. 7th Int. Cong.
    Nephrology, Montreal, Canada (1978).

21. Warner, R.R. and C. Lechene. Standing droplet limiting transepithelial
    ion concentration differences across rat proximal tubule: A myth?
    Kid. Int. 10 (1976) 601.

22. Warner, R.R. and C. Lechene. Analysis of standing droplets in rat proxi-
    mal tubules; 1: Na, Cl and raffinose limiting concentrations, con-
    vection coupling and active transport. Submitted for publication.

23. Bonventre, J.V. and C. Lechene. A method for electron probe microan-
    alysis of organic components in picoliter samples. Proc. 9th
    Ann. Conf. Microbeam Analysis Soc., Ottawa, Canada (1974) 8A-8D.

24. Strunk, T., R. Warner and C. Lechene. Methods for electron probe
    analysis of tubular fluid and cells deep within the kidney. Fed.
    Proc. 34 (1975) 393.

25. Lechene, C., R.R. Warner and T.H. Strunk. Electron probe analysis of
    ultra small volumes in physiology. Proc. 12th Ann. Conf. Micro-
    beam Analysis Society, Boston, Massachusetts (1977) 161A-161E.

26. Conty, C. Mouvement-object refroidi pour applications biologiques et
    physiques. J. Micros. Spectrosc. Electron. 1: 475-484.

27. Lechene, C.P. and J.V. Bonventre. Electron probe study of the urinary
    concentrating mechanism; elemental cortico-papillary gradient in
    frozen-hydrated rat kidney. Proc. 11th Ann. Conf., Microbeam
    Analysis Soc., Miami, Florida (1976) 61A-61G.

28. Koepsell, H., W.A.P. Nicholson, W. Kriz and H.J. Höhling. Measurements
    of exponential gradients of sodium and chlorine in the rat kidney
    medulla using the electron microprobe. Pflügers Archiv. 350 (1974)
    167-184.

ELECTRON PROBE MICROANALYSIS AND THE CELLULAR BASIS OF
INTESTINAL CALCIUM ABSORPTION

James R. Coleman

It was early recognized that the absorption of calcium by the intestine and the retention of calcium by the kidney were essential to the prevention and cure of the debilitating disease of rickets. The intestine and kidney, along with bone, formed the three elements of the complex mechanism which controls calcium metabolism, and maintains the concentration of calcium in blood between narrow and rigid limits. In addition to the effect of calcium on rickets, it has become increasingly evident in recent years that calcium plays an extremely important role in intracellular metabolism. That increased calcium concentration in muscle cells resulted in contraction has been clearly documented, and current investigations center on the mechanisms that cyclically release and sequester calcium within the muscle cell (1-5). Other investigations have shown in several different types of cells that calcium serves as a signal to increase or decrease the operation of serveral metabolic processes (6). A series of investigations, most notably in nerve and muscle, have shown that resting cells maintain a constant and relatively low, e.g. 10^{-7} M, concentration of calcium in the cytoplasmic space. Since it appears that calcium constantly "leaks" into cells, this low concentration of calcium is reached by the operation of a plasma membrane "pump" that operates to move calcium out of the cell. In addition, there is reason to believe that mitochondria may participate in the overall maintenance of low calcium concentrations by acting as a "buffer" for calcium; that is, when relatively large influxes of calcium (such as occur in response to hormones) raise the cytoplasmic calcium concentration, beyond the level that can be handled by

the plasma membrane, the mitochondria transport calcium into their matrix space, and consequently lower the concentration of calcium free in the cytoplasm.

Whether the same mechanisms operate in all cells is not known; but it is of special interest to know whether they operate in the special class of cells that are involved in calcium absorption by the intestine. In essence, the interest in these cells concerns the question of whether another mechanism peculiar to calcium transporting cells operates to maintain the constant low cytoplasmic calcium concentration necessary for other cells.

Microprobe methods offer distinct advantages for investigating such questions: microprobe analysis is sensitive to the very small amounts of calcium contained in a calcium transporting cell; microprobe analysis is capable of sufficient spatial resolution that the location of calcium within a cell may be determined. Since individual cells may be analyzed, it is not necessary to deal with the uncertainties associated with measuring the average properties of a population of cells, some of which may be inactive or engaged in other processes. Consequently, in our studies of calcium absorption we turned to microprobe analysis to obtain some greater insight into the cellular mechanisms involved.

We began our studies using two tissues: although our main interest was in calcium absorption by the small intestine, it was more convenient and economical to use another simpler, calcium absorbing tissue, the chick chorioallantoic membranes; and the small intestine of both rat and chick. Our first aim was to determine whether all cells in the absorptive layer absorbed calcium; and if so, did they do so at the same rate. To begin our studies we used oxalate to precipitate cellular calcium and thus prevent the loss or translocation during the preparative processes, including fixation, dehydration, embedding in epoxy, and sectioning, that precede microprobe examination. Our first results showed that only a few cells absorbed calcium at any one time; and further, the calcium being absorbed was sequestered within the absorbing cell (7,8). This latter finding

was surprising at first, but simple calculations indicated the necessity of some
such compartmentalization. For example, if the calcium in a chorioallantoic mem-
brane were uniformly distributed throughout the total water space of the tissue,
calcium concentrations would reach 150 mM, and in intestine, 5 mM; values far
higher than have been reported for even extracellular fluid which is usually
about 3 mM (9.10). This was confirmed by studies of manganese absorption, a
process apparently carried out by the same mechanisms responsible for calcium
absorption. Because manganese is paramagnetic, electron paramagnetic resonance
spectrometry can be employed to gain information about the _milieu_ encountered
by the manganese during transport. Such studies showed that most of the manga-
nese in the tissue was in a "spin exchange" form which indicated close packing
of the manganese ions, as would occur if they were sequestered within the tissue
(9).

The use of oxalate is not without drawbacks for the study of calcium absorp-
tion: calcium absorption is affected by sodium, and the sodium content of cells
is not preserved by oxalate; the role of potassium and phosphate are also of in-
terest, and these are not preserved by oxalate; cell membranes are permeable to
oxalate, and impermeable to calcium, thus oxalate can diffuse to cellular calcium
but not vice-versa; however, calcium oxalate crystals could grow by accretion, re-
sulting in some small scale translocation. Therefore, to circumvent the drawbacks
of oxalate, we turned to snap-freezing and freeze-drying tissue which was sub-
sequently embedded in epoxy and sectioned. These preparations offered reasonably
good morphology, and the distribution of calcium, phosphorus, sodium and potassium
when determined by electron probe X-ray microanalysis, appeared to be preserved.
In general, analyses of tissue prepared in this manner, confirmed the results
obtained with oxalate (11). However, it was felt that preparations might be im-
proved if the tissue were snap frozen, sectioned while frozen, and the sections

freeze dried. At least, this procedure would minimize the opportunity for translocation and loss through such effects as dissolving in the epoxy embedding material. At present, morphological preservation is inferior to freeze-drying, but results to date confirm those of freeze-drying.

The major disadvantage of any procedure involving freezing is that freezing may destroy membranes and produce translocations by ice crystal formation (12,13), thus making identification of the cell organelles which sequester calcium difficult. Consequently, we have turned to cell isolation techniques to identify the cell organelles which sequester calcium in transport. Others have found that Golgi membrane preparations from intestine show an ATP-dependent calcium sequestering capability (14). We have identified a cell membrane fraction that also sequesters calcium and has ATPase activity. We are investigating the composition and calcium kinetics of this cell fraction.

ACKNOWLEDGMENTS

REFERENCES

1. Haynes, D. and V.C.K. Chiu (1977); In: Calcium Binding Proteins and
        Calcium Function. (R.H. Wasserman, R.A. Corradino, E. Carafoli,
        R.H. Kretsinger, D.H. McLennan and F.L. Siegel, eds). North Holland,
        New York, page 135.

2. Katz, A.M., D.I. Repke, G. Fudyma and M. Shikegawa (1977); ibid, p. 137.

3. Green, N.M., G. Allen, G.M. Hebdon and D.A. Thorley-Lawson (1977); ibid,
        p. 155.

4. Shamoo, A.E. and J.J. Abramson (1977); ibid, p. 164.

5. Somlyo, A.P., A.V. Somlyo and H. Shuman (1977); Proc. 8th International
        Conference on X-Ray Optics and Microanalysis and 12th Annual Conference
        of Microbeam Analysis Society - Boston, MA, p. 164.

6. Rasmussen, N. and P. Bordier (1974); The Physiological and Cellular Basis
        of Metabolic Bone Disease. Williams-Wilkins, Baltimore, MD, p. 363.

7. Coleman, J.R. and A.R. Terepka (1972a); Electron probe analysis of the
        calcium distribution in cells of the embryonic chick chorioallantoic
        membrane. I. A critical evaluation of techniques. J. Histochem.
        Cytochem. $\underline{20}$:401.

8. Coleman, J.R. and A.R. Terepka (1972b); Electron probe analysis of the calcium
        distribution in the cells of the embryonic chick chorioallantoic mem-
        brane. II. Demonstration of intracellular location during active trans-
        cellular transport. J. Histochem. Cytochem. $\underline{20}$:414.

9. Terepka, A.R., J.R. Coleman, H.F. Armbrecht and T.E. Gunter (1976);
        Transcellular transport of calcium. In: Calcium in Biological Systems;
        XXX Symposium of the Society of Experimental Biology, Cambridge Univer-
        sity Press, Cambridge, pp. 117-140.

10. Wasserman, R.H. and F.A. Kallfelz (1970); Transport of calcium across biologi-
        cal membranes. In: Biological Calcification: Cellular and Molecular
        Aspects, (ed. H. Schraer), Appleton-Century-Crofts, New York, p. 301.

11. Coleman, J.R. (1976); Electron probe studies of calcium transport. Proc. XI
        Conference Microbeam Analytical Society, Miami Beach, FL, p. 58A.

12. Echlin, P. and A.J. Saubermann (1977); Scanning Electron Microscopy Vol. I,
        p. 621.

13. Gupta, B.L., T.A. Hall and R.B. Moreton (1977); In: Transport of Ions and
        Water in Animals (B.L. Gupta, R.B. Moreton, and J.L. Ochsman, eds),
        Academic Press, London, p. 83.

14. Freedman, R.A., M.W. Weiser and K.J. Isselbacher (1977); Proc. Natl. Acad.
        Sci. $\underline{74}$:3612.

APPLICATION OF ELECTRON PROBE MICROANALYSIS
IN REPRODUCTIVE BIOLOGY

by

C. Lechene

Harvard Medical School, MA

(Abstract not received in time for printing)

ORGANIC SIMS

By

A. Benninghoven

University of Munster

Germany

(Abstract not received in time for printing)

A REVIEW OF SECONDARY ION MASS SPECTROMETRY IN
BIOLOGICAL RESEARCH

Margaret S. Burns-Bellhorn, Albert Einstein College
of Medicine, Bronx, N.Y.

Use of sophisticated instruments for elemental
and surface analysis is just beginning for answering
questions of interest to biologists.
Simultaneous localization and measurement of
elements is of paramount importance in a variety of
common biological problems. Technical specifications
of SIMS indicate that it could be ideal for solving
these problems. Each individual problem has different
and specific requirements for solution, depending upon
such factors as: the quantitative elemental content;
the change in elemental content as a result of physio-
logical change; the spatial resolution required for a
meaningful solution; the amenability of the biological
system to elemental manipulation; the specimen prepara-
tion necessary.
These factors, and their interrelationships
will be evaluated by consideration of a few illustrative
biological problems and their potential solution by
SIMS. The utilization of four modes of data analyses
will be emphasized: ion imaging; ion counting; mass
spectra analysis; and depth profiling. Practical appli-
cations will be shown. Problems unique to both hard
and soft biological material as well as organic compounds
will be discussed. Future applications of SIMS analysis
of biologically important problems are numerous and will
benefit from improved instrumental design and data
analysis capabilities.

ELBERS [1], P.F., GRAS [2],D.J. ,von Rosenstiel [2], A.P. and BROWN [3], J.D.

1) Section of Electron Microscopy, Dept. of Molecular Cell Biology,
   University of Utrecht, The Netherlands.
2) Metaalinstituut TNO, Apeldoorn, The Netherlands.
3) University of Western Ontario, London, Canada.

ION MICROPROBE ANALYSIS OF Li IN SNAIL EGGS IN EARLY CLEAVAGE STAGES.

INTRODUCTION

Li ions cause disturbances of development in animal eggs,but the site and mode
of action are unknown. For Lymnaea eggs chemical analysis is excluded because
of the limited sample volume and the lack of suitable radioisotopes.

Normally these eggs develop into gastrulae after 3 days.
Li ions, when applied at the second division in a concentration of 50 mM, cause
a disturbance of development called exogastrulation. At other cleavage stages
the eggs are insensitive to the treatment. The side and mode of action of the
Li ions were unknown so far nor was it ever shown that Li actually enter the
cells.

ANALYTICAL PROCEDURE

Washed cells were air dried on a gold coated stainless steel substrate.
Thin smears of hen eggyolk, with appropriate salt additions served as standards
for quantification purposes.
Depth profile analysis for Li, Na, Mg, Ca, Sr, P, Fe, Cr and C were performed
for both samples and standards with a 10 Na, 10 kV, O_{32}^{+} primary beam, under
computer control including an "on line" sample voltage adjustment for these
poorly conducting uncoated specimens; a 70x70 μm area with a 25% electronic
aperture was used for each analysis.

An oxygen primary beam was chosen rather than nitrogen because it yielded
smoother crater bottoms. After an equilibration period of several seconds a
steady-state secondary ion yield was obtained, indicating the absence of
gross elemental inhomogenities (salt crystals) in either eggs or standards.

As the carbon content per analyzed volume is similar in dried eggs and standards, the measured intensities (see fig.1) are expressed as count rates relative to carbon for calculation of chemical concentration in the fresh state.

Li countrates were also determined relative to Na, K and Ca using a second set of improved standard specimens,with nearly identical sputter etch characteristics with respect to the egg cells and similar concentration of Na, K and Ca.

RESULTS

The first column of fig. 1 shows that Li ions are reliably detected down to the 0.1 mM level or about 1 p.p.m. in a dry biological matrix. The other relative count rates correspond to 30 mM Na, 28 mM K, 54 mM Mg and 35 mM Ca known from chemical analysis of hen egg yolk.
In the second column this is supported by the known addition of 50 mM of each of these elements.
The third column gives the relative count rates in Lymnaea eggs. No Li could be detected in untreated eggs. L. eggs contain 80% water compared with 50% in the hen egg yolk. Thus, to obtain chemical concentrations the relative count rates have to be divided by a factor of 2.5.
Columns 4, 5 and 6 show that Li ions enter the egg cells to the mM level ir-respective of average concentration or number of cleavage stages.
The Li ions are not washed out as is shown in the analysis of 4 cell eggs (column 6) that were treated in the insensitive 2 cell stage with 50 mM LiCl. These 4 cell eggs contained the same amount of Li as those that were treated at the very sensitive 4 cell state (column 5). It is concluded that the dis-turbance of development is not caused by Li ions that may be present in the cytoplasm of the eggs but by the outside Li concentration at the sensitive stage. This means that the site of morphogenetic action of Li ions has to be sought at the level of the cell membrane.

Count rates relative to carbon for Li, Na, K, Ca, Mg, Sr and P

Figure 1

	Li	Na	K	Ca
	Mg	Sr	P	

Axis labels: 10^2, 10^1, 10^0, 10^{-1}, 10^{-2}

50 mM, 10 mM, 1 mM, 0.1 mM
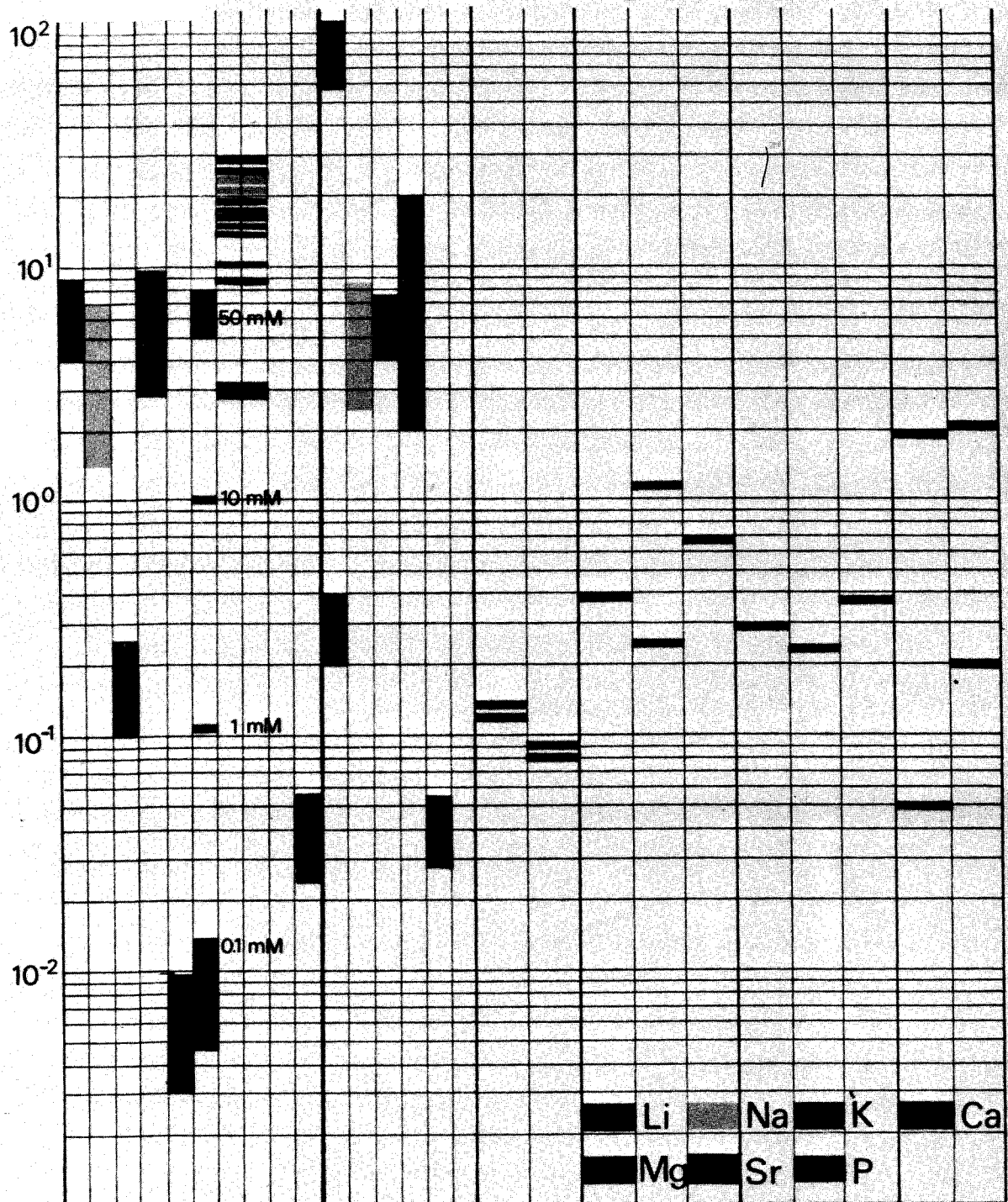
├ Hen egg yolk ┤ ├──── Lymnaea eggs ────┤

| with added 0.1; 1; 10 and 50 mM LiCl | further added 50mM NaCl, KCl, CaCl$_2$, MgCl$_2$, SrCl$_2$ | 2 and 4 cell stages experimental and control | 2 cell + 5 ; 10 mM LiCl | 4 cell + 5 , 10 ; 50, mM LiCl | 4 cell from 2 cell + 50 mM LiCl | 4 cell + 10mM LiCl + 50 mM \| 30 mM CaCl$_2$ \| SrCl$_2$ |

ION MICROPROBE ANALYSIS OF ^{30}Si
DIFFUSION IN α-SiC

J. D. Hong and R. F. Davis
Department of Materials Engineering
and Division of Engineering Research
North Carolina State University
Raleigh, North Carolina 27607

and

D. E. Newbury
Analytical Chemistry Division
National Bureau of Standards
Washington, D. C. 20234

For many Si-containing materials, accurate knowledge of the coefficients and the activation energies of Si self-diffusion is critical to the elucidation of the physical mechanisms involved in such processes as creep, sintering, phase transformations, crystal growth and the numerous historical and on-going geologic processes. However, until recently, considerable experimental difficulties have confronted the investigators in their attempts to measure the diffusion profile of this element, as noted in the following review.

Silicon exists in three natural isotopes of various abundance: ^{28}Si (92.21%), ^{29}Si (4.70%) and ^{30}Si (3.09%), as well as, several artifically produced radio-isotopes. For obvious reasons, the most frequent Si self-diffusion studies have been conducted on single crystals of the elemental semiconductor; however, there is poor agreement among the different sets of results. Peart (1) and Fairfield and Masters (2) employed the neutron activated ^{31}Si isotope as the tracer; however, its short half-life (9.36 x 10^{3}s) drastically limited the diffusion times and, therefore, the temperatures that could be investigated. In order to investigate this problem, Ghostagore (3) diffused the stable ^{30}Si isotope into the pure Si and subsequently activated this species to ^{31}Si via the ^{30}Si (n·γ)^{31}Si reaction. Unfortunately the introduction of Na as a minor impurity during the preparation of the crystal/tracer couple was impossible to prevent, and simultaneous activation of this impurity to the 1.37 MeV ^{24}Na during the irradiation of each section produced an energy peak whose position overlapped that of the ^{31}Si. To further compound the problem, the intensity and half-life (5.4 x 10^{4}s) of the ^{24}Na exceed that of the ^{31}Si.

Schaeffer (4) used a mass-spectrometric method to determine the enriched ^{30}Si self-diffusion profiles produced in silicate glasses. However, this author's serial analysis required that the Si atoms in the removed sections of the solid be reacted to form a gaseous compound . This is impractical for the α-SiC of the present authors' research, as this stable compound will only react with extremely

oxidizing and corrosive gases such as F_2 (5), Cl_2 (6-8) or a few gaseous compounds containing these elements (e.g., BF_3 (4)) which are difficult to use and control.

In the only research similar to that reported herein, Ghostagore (9) attempted to determine the Si profile in α-SiC by diffusing pure ^{28}Si into the crystal and activating the residual ^{30}Si in the profile to ^{31}Si. The results (only data for two temperatures were reported) showed a considerable variation in the diffusion coefficient from different sections because of a) the low maximum possible value (3.09 isotopic percent) of the ^{31}Si in the profile and b) the interference from the ^{24}Na as described above. No Si diffusion coefficients as a function of temperature were reported.

In the present research, secondary ion mass spectrometry incorporated with an Ion Microprobe Mass Analyzer (10) was employed to elucidate the ^{30}Si diffusion profile in α-SiC. There are several advantages inherent in using this technique for Si relative to those procedures described above. These include a) good isotope ratio reproducibility and sensitivity, b) easy sample preparation and c) accurate step scanning with a small diameter beam along the profile. The last factor permits the sample size to be quite small: it was possible in this research to use sections of the same crystal for many of the profiles.

Experimental Procedure

The α-SiC single crystals employed in this research* were of two types: high purity, essentially electronically intrinsic and N-doped (10^{24} atoms/m^3), n-type. All other impurities were in very low concentrations. The crystals were shaped with a thin diamond saw to a size of $\simeq$ 2mm x 3mm x 1 mm thick and lapped to a flatness of one light band of He and a parallelism between the top and bottom surfaces of 1×10^{-6}m. These surfaces were the (0001) plane in the hexagonal (6H polytype) crystals; thus, the Si diffusion occurred along the <0001> direction.

The tracer materials consisted of a thick ^{30}Si deposit on the highly polished single crystals which was, in turn, covered by a thick layer of ^{30}SiC applied via a slurry technique. The ^{30}Si layer, as well as additional amounts of this material placed in the closed crucible, sufficiently slowed the evaporation of the isotope during the diffusion anneals. This allowed reaction of the ^{30}Si with the SiC crystal such that the former could be easily treated mathematically as an "infinite" source. The diffusion source was not derived from any existing vapor phase as only the side of the crystal exposed to the molten ^{30}Si revealed the presence and profile of the isotope.

The crystal/tracer combination was placed in a small covered inner SiC-coated graphite crucible which was positioned in a second, larger graphite outer crucible for the sake of equalizing the heat distribution. An electronically controlled ($\pm$7K at 2300K) graphite resistance tube furnace was employed for the

*Grown by Drs. J. Blank and R. Potter, General Electric Lamp Division, Nela Park, Ohio.

annealing. The furnace was evacuated to 0.13 Pa, purged three times with pure (99.999) argon, sealed in this gas at a static pressure of 9×10^4 Pa and heated to the diffusion temperatures (2273-2573K) from 2073K within ten minutes.

After diffusion annealing, the samples were cut in half perpendicular to the tracer surface. The two resulting sections were polished to a 1×10^{-6}m finish, mounted flat on a glass plate with a very thin layer of Duco cement, enveloped by the small holes drilled in a 1.5×10^{-2}m diameter $\times 0.5 \times 10^{-2}$m brass holder, fixated with epoxy casting resin and coated at two sample/brass interfaces with silver epoxy by heating to 373K for 2 hours to ensure the conduction between samples and brass holder. The last process was necessary to prevent charge buildup in the ion microprobe.

Ion microprobe analysis* of the ^{30}Si as a function of diffusion distance was conducted by scanning a 5×10^{-6}m diameter positively charged oxygen ion beam (18.5 kev) over the sample. A scan width of 50×10^{-6}m was employed. The profile penetration distance was established by the center of the ion beam and the profile shape determined by moving the beam from the tracer into the crystal at 1×10^{-6}m steps. Initial calibration of the instrument was made by scanning a standard semiconductor grade silicon sample in the same manner as the SiC samples, coupled with continuous adjustment until the $^{28}Si/^{30}Si$ ratio was approximately 30:1 (i.e., the ratio in the natural material). The ion beam current was adjusted such that the absolute ^{30}Si count was not below 2000 in a period of 20 seconds (sample current of $1 \sim 3 \times 10^{-9}$ A). The center region of the sample was chosen as the scan area to eliminate any possibility of a contribution to the ^{30}Si counts from surface diffusion. All values of the diffusion parameters reported below were determined from a least-squares analysis of the diffusion data obtained using the equation for an infinite source, i.e.

$$C(x,t) - C_0' = (C(0,t) - C_o')\text{erfc} \frac{1x1}{2(Dt)^{1/2}} \qquad (1)$$

and the standard Arrhenins equation

$$D = D_o \exp (-Q/kT) \qquad (2)$$

Complete details of the experimental and mathematical procedures may be found in reference (11) and will be reported in a subsequent paper.

Results
───────

Figure 1 shows a ^{30}Si concentration vs distance profile typical of both the high purity and the N-doped α-SiC crystals. This figure was produced by plotting the ^{30}Si enrichment, calculated from the total counts of ^{30}Si and ^{28}Si using the equation

$$^{30}Si(\%) = \frac{^{30}Si/^{28}Si}{1 + {}^{30}Si/^{28}Si} \times 100 = \frac{^{30}Si}{^{30}Si + {}^{28}Si} \times 100 \qquad (3)$$

─────────

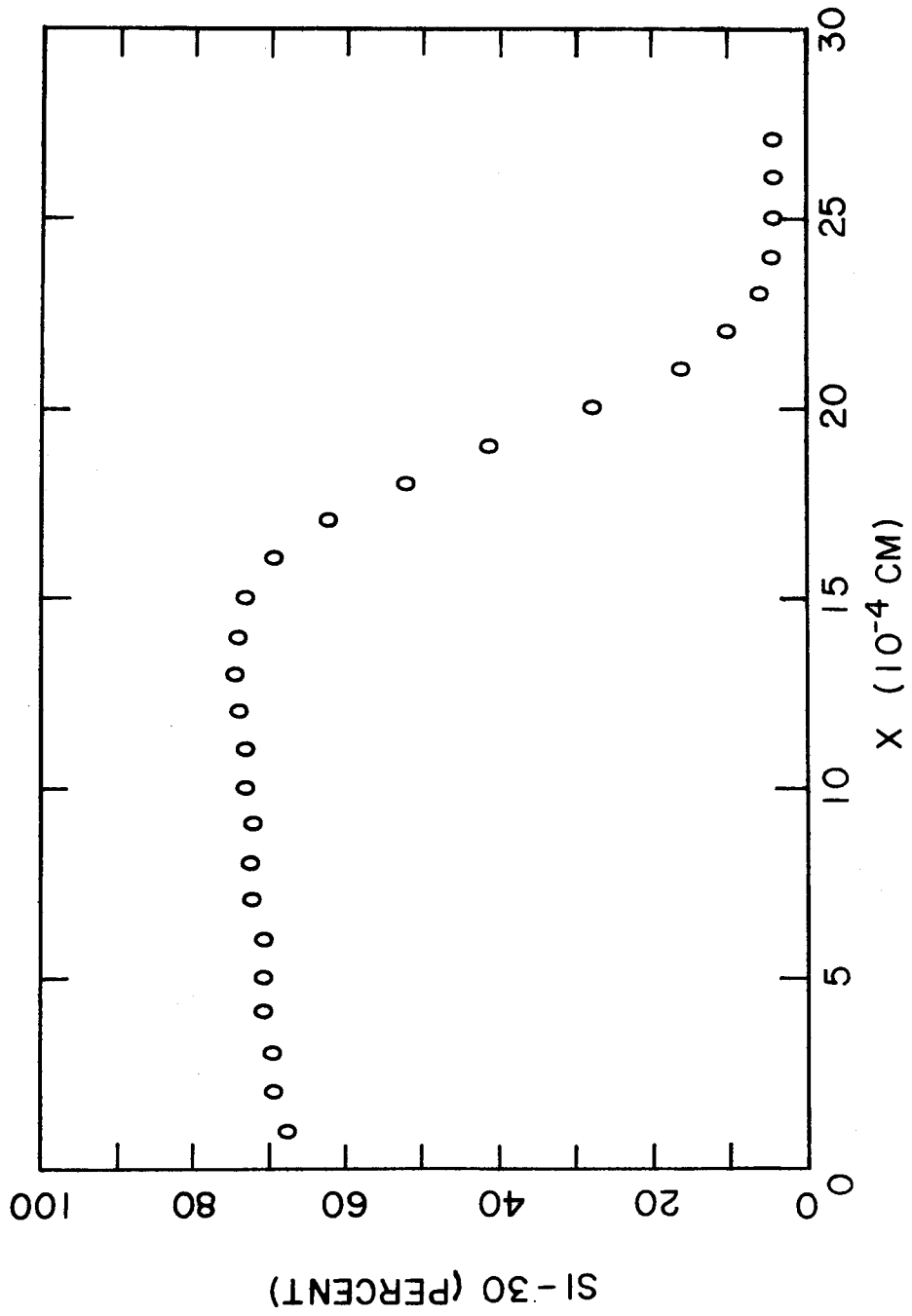*Ion microprobe Mass Analyzer (IMMA), Applied Research Laboratory, Glendale, California.

Figure 1.   Typical Concentration Profile of ^{30}Si in α-SiC Single Crystal Along <0001> Direction.

where ^{30}Si and ^{28}Si are the intensities measured by the ion microprobe at each point along the profile. In this case, the presence of the 3.09% natural abundance of ^{30}Si is advantageous, as the microprobe can analyze the $^{30}Si/^{28}Si$ ratio without concern for the correctness of the absolute value of either individual species. It should be noted that the isotope intensity of ^{29}Si falls within the limits of experimental accuracy ($\approx 5\%$) and is thus neglected.

Plots of the concentration gradient calculated from the difference in ^{30}Si enrichment per unit length (1×10^{-6}m), versus the penetration distance for each sample were also produced in order to determine the tracer-crystal interface position (x = 0) in the profile (i.e., the point at which the concentration gradient is a maximum). Plots of the logarithm of the concentration gradient versus the square of the penetration distance at each point resulted in a straight line having a slope equal to $1/(4Dt)$ which indicated that the use of an infinite source solution is indeed correct.

Silicon-30 self-diffusion coefficients calculated from the concentration gradient curves are plotted in figure (2) as a function of 1/T. The resulting curves can be expressed as follows:

(1) for high purity, essentially intrinsic α-SiC single crystals along the <0001> direction

$$D_{Si}(cm^2/sec) = (5.01\pm1.71)\times10^2 \exp\{\frac{-(7.22\pm0.07)}{kT}\} \qquad (4)$$

(2) for diffusion in the N-doped, n-type α-SiC single crystals along the <0001> direction

$$D_{Si}(cm^2/sec) = (1.54\pm0.78)\times10^5 \exp\{\frac{-(8.18\pm0.10)}{kT}\} \qquad (5)$$

Discussion

From Figure 2 and equations 4 and 5, one may note that Si diffuses faster in the N-doped, n-type crystals than in the high purity, essentially intrinsic materials. The principal reason for this phenomenon is the interaction between charged defects such as vacancies and impurities. In semiconductors, the number of electrons and holes and the degree of ionization of acceptors and donors depend on the position of the Fermi level. However, the Fermi level itself depends, in turn, on the concentration of donors and acceptors. The concentration of donors therefore influences the degree of ionization of acceptors and vice-versa.

In semiconductors at any temperature, there exists a definite number of charged and neutral vacancies. The latter represent the thermal equilibrium number which is constant at a given temperature. Although no direct measurement of the character of the charged Si vacancies in SiC has been conducted, the results of photo-luminescence (12) and self (3) and impurity (13) diffusion measurements in this material strongly indicate that these vacancies are acceptors and therefore negatively charged. Thus, on the Si sublattice in any SiC crystal the total
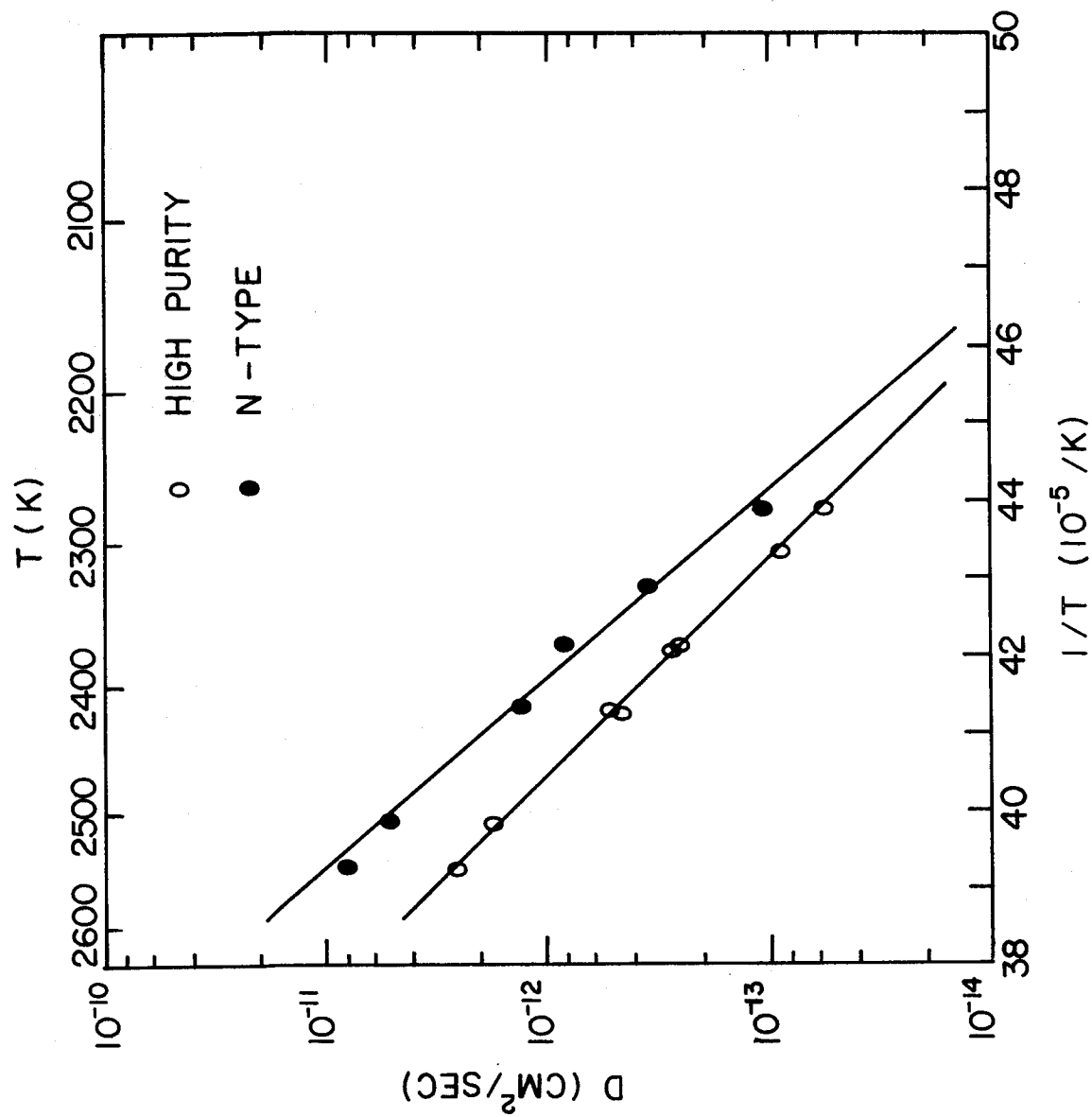
Figure 2. Self-Diffusion Coefficients of Si in α-SiC Single Crystals
Along <0001> Direction as a Function of 1/T.

concentration of vacancies is given by $[V] = [V^{\circ}] + [V^{-}]$. The concentration of charged vacancies can be related to $[V]$ by the Fermi-Dirac function

$$[V^{-}] = \frac{[V]}{1+1/2\exp\left(\dfrac{E_A-E_F}{kT}\right)} \qquad (6)$$

where E_A and E_F are the vacancy acceptor level and Fermi energy, respectively. If two semiconductors are considered, one doped and the other intrinsic, a ratio of equations analogous to (6) can be established and the energy differences related to electron concentrations. From this mathematical manipulation is derived the relationship (see any book on semiconductor theory, e.g., Tuck (14)).

$$\frac{D_d}{D_i} = \frac{[V]_d}{[V]_i} = \frac{n_d}{n_i} \qquad (7)$$

where D_d, $[V]_d$, n_d, D_i $[V]_i$ and n_i are the diffusion coefficients, vacancy concentrations and electron concentrations for the doped and intrinsic crystals, respectively. A substitutional mechanism of diffusion is assumed in the derivation and use of equation (7). This equation predicts that if vacancies act as acceptors in a crystal, any substitutional-type diffusion process on this lattice should show a larger coefficient in the donor-doped, n-type than in the pure or acceptor-doped, p-type material. Therefore, since 1) Si has been shown to diffuse by a vacancy mechanism (11), 2) N is a donor impurity and 3) the character of the charged Si vacancies is of the acceptor type, the presence of the N impurity and the excess electrons contributed by this element will act to increase the charged and, therefore, the total vacancy contribution. This, in turn, will increase the rate of Si self-diffusion over that of the pure material. A complete discussion of the physical and chemical aspects of the ^{30}Si transport process will be reported in a later paper.

Summary

The utilization of the ion microprobe mass analyzer allows the determination of the self-diffusion parameters of ^{30}Si and αSiC and, doubtless, in other Si-containing substances, if the initial experimental details are carefully controlled. The accuracy of this profile measurement technique is superior to mechanical removal methods which are coupled with neutron activation or mass-spectrometric analyses for this element. Furthermore, this method can readily determine the differences in ^{30}Si diffusion rates between the high purity SiC and crystals which are doped with only 10^{24} atoms/m^3 (=36 ppm) of an impurity such as N.

Bibliography

1. R. F. Peart, Phys. Stat. Sol. 15, K119 (1966).
2. J. M. Fairfield and B. J. Masters, J. App. Phys. 38, 3148 (1967).
3. R. N. Ghoshtagore, Phy. Rev. Let. 16, 890 (1960).

4. H. A. Schaeffer, Phys. Stat. Sol.(a) 22, 281 (1974).
5. P. T. B. Shaffer, J. App. Phys. 39, 5332 (1968).
6. V. J. Jennings, Mat. Res. Bull. 4, S199 (1969).
7. R. C. Purdy, J. Am. Cer. Soc. 17, 42 (1934).
8. L. F. Lowe, H. D. Thompson and J. A. Cali, Silicon Carbide, A High Temperature Semiconductor, J. R. O'Connor and J. Smiltens, eds., pp. 221-226, Pergamon Press, New York (196).
9. R. N. Ghostagore and R. L. Coble, Phys. Rev. 143, 623 (1966).
10. H. Liebl in Secondary Ion Mass Spectrometry, NBS Special Pub. No. 427, K. F. J. Heinrich and D. E. Newbury, eds., pp. 1-31 (1975).
11. J. D. Hong, Ph.D. thesis, North Carolina State University, Raleigh, North Carolina, May 1978.
12. W. J. Choyke and L. Patrick, Phy. Rev. B. 2, 4959 (1970).
13. Yu. A. Vodakov and E. N. Mokhov, in Silicon Carbide, 1973, R. C. Marshall, J. W. Faust, Jr. and C. E. Ryan eds. pp. 508-519, Univ. South Carolina Press, Columbia, South Carolina (1974).
14. B. Tuck, Introduction to Diffusion in Semiconductors, IEE Monograph #16, Peter Peregrinus LTD, 1974.

ELEMENTAL IMAGING FACILITIES OF THE ION
MICROPROBE APPLIED TO NODULAR CAST IRON

J.H. Schilling, P.A. Büger and H. Fidos

National Physical Research Laboratory,
Pretoria, South Africa

Introduction

Despite the widespread use of cast iron extensive research
is still being done into its morphology [1] since the properties
depend strongly on the structure of the material. One particular
structure, containing graphite nodules, is obtained by
spheroidising and inoculating the melt with additives. Many
attempts have been made to explain the formation [2] of such
nodules but no definite model has yet been accepted. This is
mainly due to the lack of experimental data concerning the dis-
tribution of elements and especially the movement of the elements
during the formation of the nodules. Since trace elements are
expected to influence this process, analytical data of this kind
would be of great interest.

The ion microprobe mass analyser [3] is capable of measuring
distributions of all elements at concentration levels down to the
ppm range with a spatial resolution of a few μm. It appears there-
fore that the use of this instrument could furnish data on trace
element distribution in nodular cast iron.

Experimental

Common grade cast iron was spheroidised by adding 0.8 wt %
Ni-Mg alloy to the melt at 1450°C. Subsequently, 1.4 wt % Fe-Si
was added to initiate heterogeneous nucleation of graphite. The
composition of these materials is given in Table 1 as obtained by
spark source mass spectrometry. Two samples were prepared at
different cooling rates: The first sample was cooled at a rate of
185 K/min (slow cooled) and a second one at 370 K/min (fast cooled).
At the faster cooling rate the time for solidification was insuffi-
cient for the proper formation of the graphite nodules. Thus, an
early stage of the nodule formation is obtained in the final product.
The graphite nodules obtained cover a range of sizes from 15 to 50 μm
in the fast cooled sample and 15 to 80 μm diameter for the slow cooled
sample. The conditions for nodule formation could now be investigated.

Polished cross-sections* were prepared from the samples. As

---

* It must be kept in mind that such cross-sections do not necessarily
  cut through the centre of the nodules. Thus, "small" nodules may
  be the top or bottom of a larger one.

can be seen in Fig. 1 the nodules are each surrounded by a halo, i.e. a region of different appearance between the nodule and the surrounding bulk material.

Elemental distributions were measured with an ARL-type ion microprobe mass analyser [3]. The samples were bombarded with a beam of $^{14}N_2^+$ ions which was focused to approximately 5 μm at a current of a few nA thus compromising between resolution and sensitivity. The resulting sputter rate is in the order of 20 atomic layers per second. The beam was rastered stepwise under computer control across a grid of points on the sample. Counts of sputtered ions were accumulated for .25 s from each point in the sample area under investigation. Only the distribution of those elements which sputter as positive ions were measured**. The count rates obtained for each measured point were punched onto paper tape during the experiments for subsequent analysis, which was carried out on a CDC 174 computer equipped with a VERSATEC plotter.

Discussion and Results

The experiments yield sputtered ion intensities, which do not relate directly to element concentrations, because the sputtered ion yield does not only depend on the element being sputtered but is also strongly affected by matrix effects. Also topography, charge build-up on the surface, residual gas in the sample chamber, and transmission of the analysing system influence the actual count rates of sputtered ions differently for the elements. Therefore, the measured count rates have to be converted to concentrations before they can be used in the interpretation of element distribution. Since such a conversion is usually subject to large inaccuracies even in homogeneous samples [5], a first order approximation had to be used [6], in this examination of an inhomogeneous sample to obtain quantitative data. Correction factors, as given in Table 2 were obtained from a control specimen by comparing the sputtered ion intensities with the concentrations as determined by a spectrochemical analysis using a glow discharge. These factors

---

** This was due to the problem of realignment of the coordinate origin on the sample after a change in beam polarity. (A shift of approx. 150 μm is experienced after such a change.)

were used for the nodular cast iron and maintained constant across the area under investigation.

This procedure has been shown to give more reliable results of element distributions [6] than the direct interpretation of the sputtered ion intensities. Since in this investigation two samples of the same average composition and similar structure are compared, errors in the individual correction factors are not expected to have an adverse influence on results. The quantified element distributions are displayed in Fig. 2. For this purpose the range from the lowest to the highest concentration for each element is divided linearly or logarithmically into 10 classes (zero to nine) and displayed in different grey scales. The concentrations related to the different classes are given in Table 2. Obviously, the low intensity details of the distributions are enhanced in the logarithmic scale.

To demonstrate the matrix effects that occur, Fig. 3 shows the distribution of the sum of weighted count rates as used for the quantifying procedure.

A 3-dimensional form of display is shown in Fig. 4. This gives a good indication of the steep changes in element concentrations at the perimeter of the graphite nodules. A few distributions are given in numerical form which allows comparison of concentrations at different points or for different elements.

Because the differences between the samples are so small, a further method of data analysis was used. An attempts was made to plot the correlation of elements in the sample. Since not all the possible graphs of combinations of two elements can be shown, Fig. 4 displays a few important examples. This form of data analysis correlates element combinations not only in single points but across the whole sample area under investigation. Thus, it is possible to relate the occurrence of an element and its spatial position relative to the graphite nodule and by using all the measured data and not by a few accidentally chosen points in the sample area. Furthermore, it will be possible to obtain information about how stronly the changes in concentration of two elements depend on each other.

Table 2 also gives average concentrations which are obtained from all points in the measured area. Since the cross-section used for the measurement must not be representative of the bulk material,

these values can not be used to establish the correction factors, but they allow further comparison between the samples.

For the following interpretation of the data presented, it must be borned in mind that only a first order approximation for the quantifying procedure was used. In such an inhomogeneous matrix the correction factors applied in the bulk (iron) may not be identical to those in the nodule (graphite), thus limiting the accuracy of the quantitative analysis.

These sums of weighted intensities (Fig. 3) cover a range of three orders of magnitude thus influencing the results of the element distribution and the actual concentrations significantly.

Iron and carbon are clearly separated, though in the logarithmic scale it can be seen that both elements occur in low concentrations also in the region of the complementary element.

Boron gives the most striking feature in the region of the halo. Its concentration is higher in the nodule than outside.

Oxygen, aluminium, silicon, phosphorus, potassium, titanium, vanadium, chromium and manganese as well as antimony and tantalum in the case of the fast cooled cast iron, are mainly present outside the graphite nodules.

Sodium behaves differently in each sample: In the fast cooled sample it is mainly present outside the nodule, the contrary occurring in the slow-cooled sample.

Calcium and titanium as well as the spheroidising elements, magnesium and nickel, exhibit precipitates of high concentration. Except for titanium these appear in the centre of the nodules as can be expected in nodulisers. In the fast cooled sample nickel also occurs in high concentration in the halo whereas it is, like magnesium, much more evenly distributed in the other sample.

Since nitrogen was used as the bombarding species no comment could be made on the nitrogen distribution. Values of up to 18 at.% have been measured as could be expected with nitrogen bombardment.

The correlation pattern (Fig. 5a) shows a very distinct separation between iron and carbon with a much larger scatter at low carbon concentrations, that is outside the nodules. This scatter is less for the slow cooled sample thus indicating a more complete precipitation. The highest iron concentration occurs in the halo region. The high boron concentration is to be found further outside the nodule

than the iron halo (Fig. 5b). The sodium correlation pattern (Fig. 5c) is much more distinct in the slow cooled sample with a strange behaviour at high iron concentrations: in this region low to high sodium concentrations occur.

In general, it can be noticed that all elements form much narrower bands in the correlation graphs of the slow cooled sample than in those of the fast cooled one. Exceptions to this are manganese and nickel.

The average concentrations show agreement between the samples for most elements. Exceptions are oxygen, sodium, potassium and calcium with higher concentrations in the slow cooled sample, whilst silicon and phosphorus yield lower concentrations in this sample.

Conclusion

Ion microprobe measurements of element distributions followed by extensive data analysis have yielded new data concerning the composition of the halo surrounding graphite nodules and differences in samples of different cooling rates. The data on these two samples could provide a basis for an interpretation of the development of graphite nodules. Work on this model will be continued.

Acknowledgements

References

1. R. H. McSwain, C. E. Bates and W. D. Scott, AFS Cast Met. Res., 10, 181, 1974.

2. R. H. McSwain and C. E. Bates, The Metallurgy of Cast Iron, Georgi Publ. Comp., St Saphorin, Switzerland, 1975.

3. C. A. Andersen and I. R. Hinthorne, Science, 175, 853, 1972.

4. F. G. Rüdenauer and W. Steiger, Proc. 7th Intern. Vac. Congr. & 3rd Intern. Conf. Solid Surf., Vienna, 1977.

5. D. E. Newbury, R. L. Myklebust and K. F. J. Heinrich, Proc. Microbeam Anal. Soc., 42E, 1976.

6. J. H. Schilling and P. A. Büger, Int. J. Mass. Spec. Ion Phys., in press, 1977.
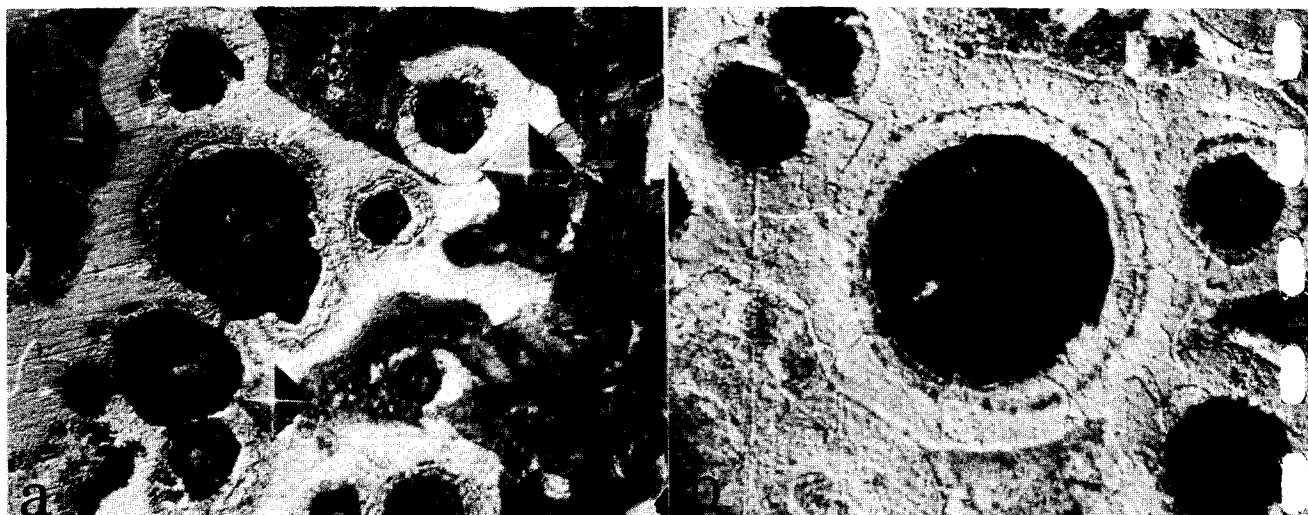
Figure 1: Microphotographs (200 x 150 µm)
(a) fast cooled nodular cast iron
(b) slow cooled nodular cast iron.

Figure 2a: Quantified images of the element distributions of fast cooled nodular cast iron (40 μm x 140 μm). The concentrations related to the different grey scales are given in Table 2.
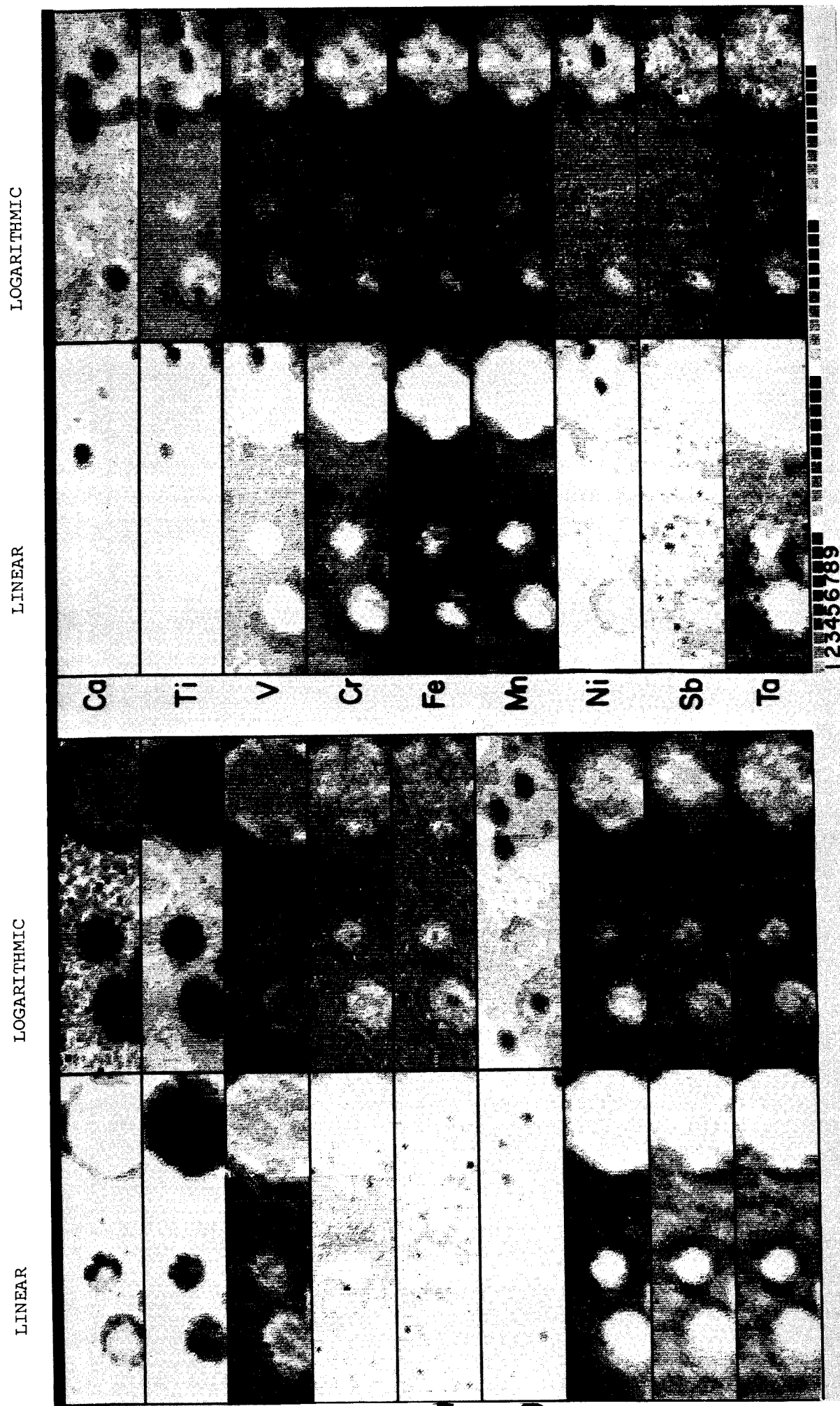
Figure 2b: Quantified images of the element distribution of slow cooled nodular cast iron (120 μm x 120 μm). The concentrations related to the different gray scales are given in Table 2.

Figure 3: Distribution of the sum of weighted concentrates.

LOGARITHMIC

Figure 4: As Figure 2a but in a 3-dimensional display

at. ppm boron

at. % iron

Figure 5b: correlation Fe-B
fast cooled cast iron
(logarithmic scales,
* means more than
9 occurrences)

at. % carbon

Figure 5a: correlation Fe-C
slow cooled cast iron
(logarithmic scales,
* means more than
9 occurrences)

at. % iron

```
2                      160                        13000
 +----+------------------+--------------------------+
2.9 +                    111                       .at. ppm sodium

                       1  11
                       1 12121
                         2  1
                         123231
                        11 21
                       1 212223
                       11132333 1
                       2 11 1452        11
                       2 2 2413
                       231 13422
                        211 222          1
                    1 111 312111         1
                   1 1  111 2121           2
                        41 2 212
                        31 211            1
                      1 12 111            2
                      11 1122  1
                      2 131 1 1 1         1
                      14   21  2
                   1      1 2 321         1
                    1 112 1   11
                      2 1 11              11
                      1 -2 2               2
                   1 1  1121              1
                   11 1  14
                   13    1   11
                          2  1
                   1   21311 1           1
                   1   111121  1
                    111121 1 1
                   1   12112
                        21  2
                       13131   2
                   1   1 33 1   1
                   1     1222 11          1
                   1
                   1  1 111     1         11
                        211               1
                   1 1    1               1
                   1 111211
                    1  21  2 1
                    11    1       1
                   11111   2  1  1
                   13 1   311  211 1
                   2 1  11     12 21  2
                   11321  12   21          1
                   111 111122111  21    1  1
                    2 1111    111 1        1
                    1   31 2       1
                   1   221 2 1 111    2 1
                   1 111112111 212331 2
                       122  11112  21 113
                   1 2112 121  1 213432211 1
                     12213 3 53    13 1121 1 11
                   2121443 7411   2641 3411 2  1
                   1122535*534142113124
                   11 34 37441659573733 411 11121 21 112 11
                   12 24566*********+.++**39*945755615 34134415   111
                   232125 v*+.;.***.***+.+.***.9**886556447622513522 4 113
                   121 11 5459*+c*+*69+*965+++***75*57555541   2        1
85. +1             1111 24311       1    131     1  1
```
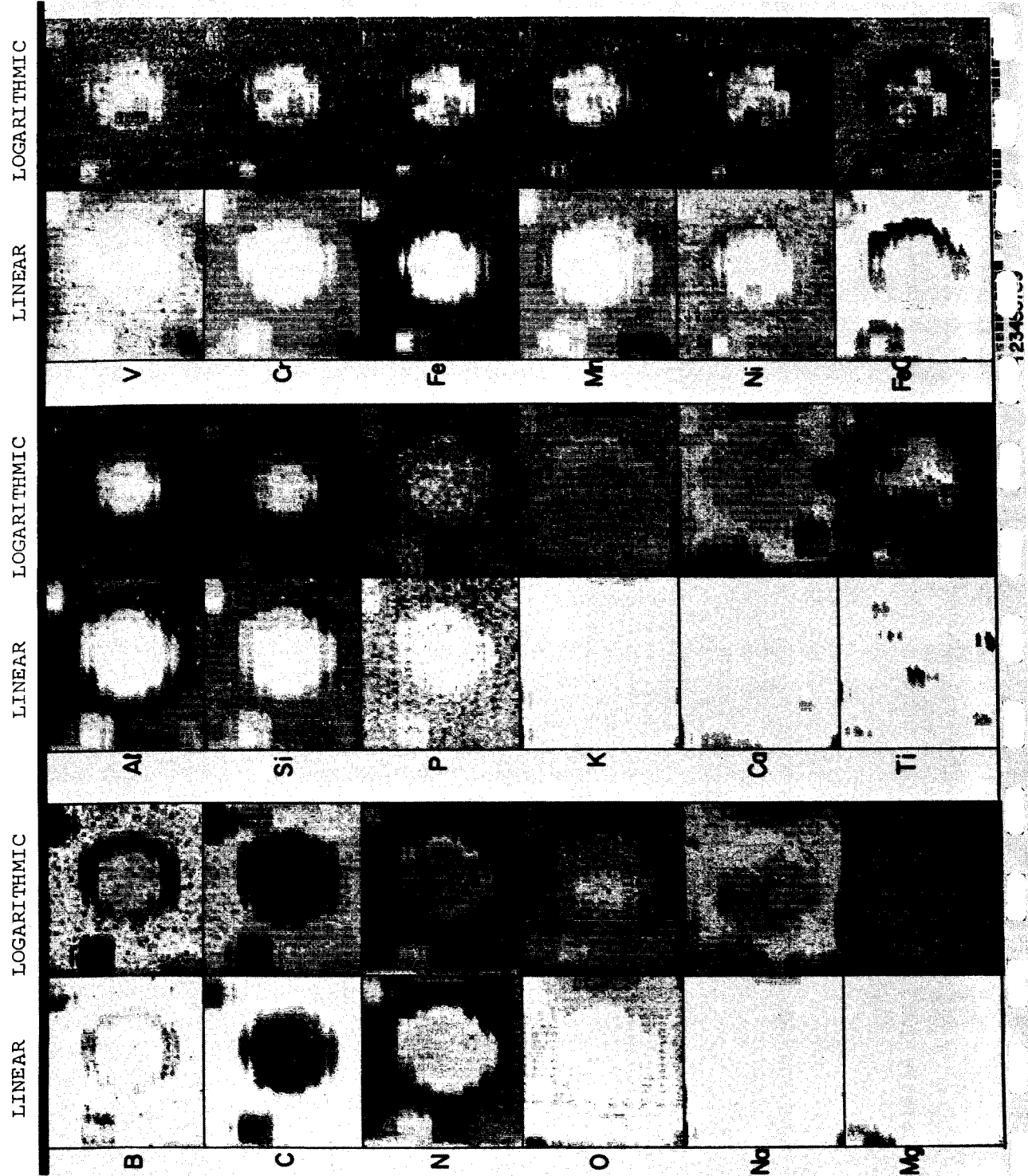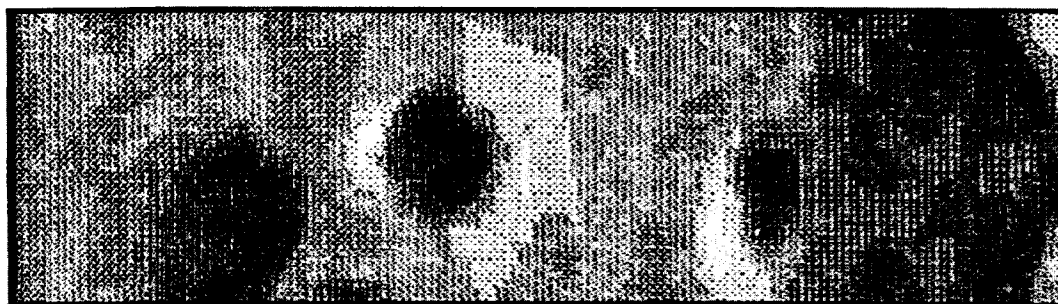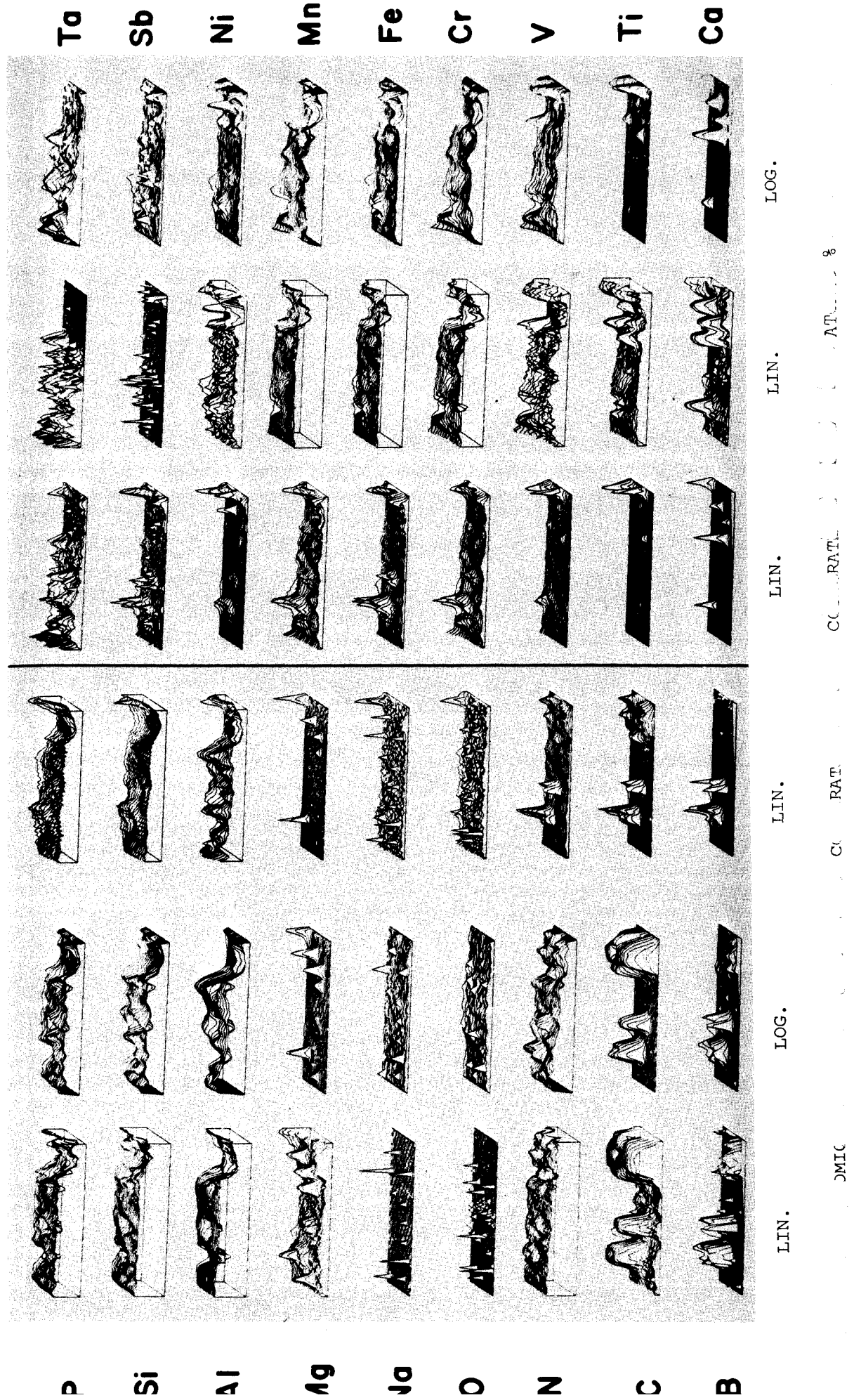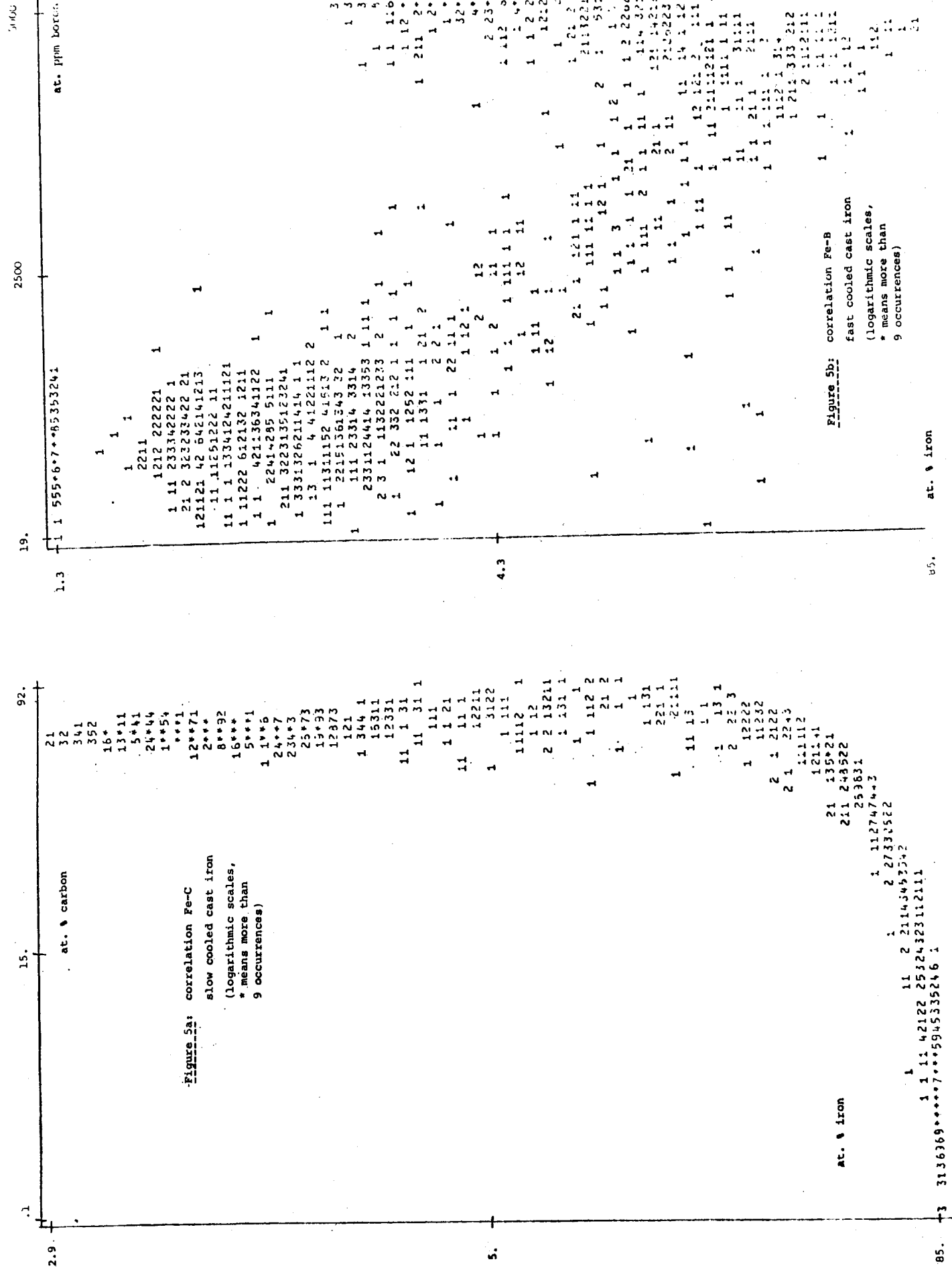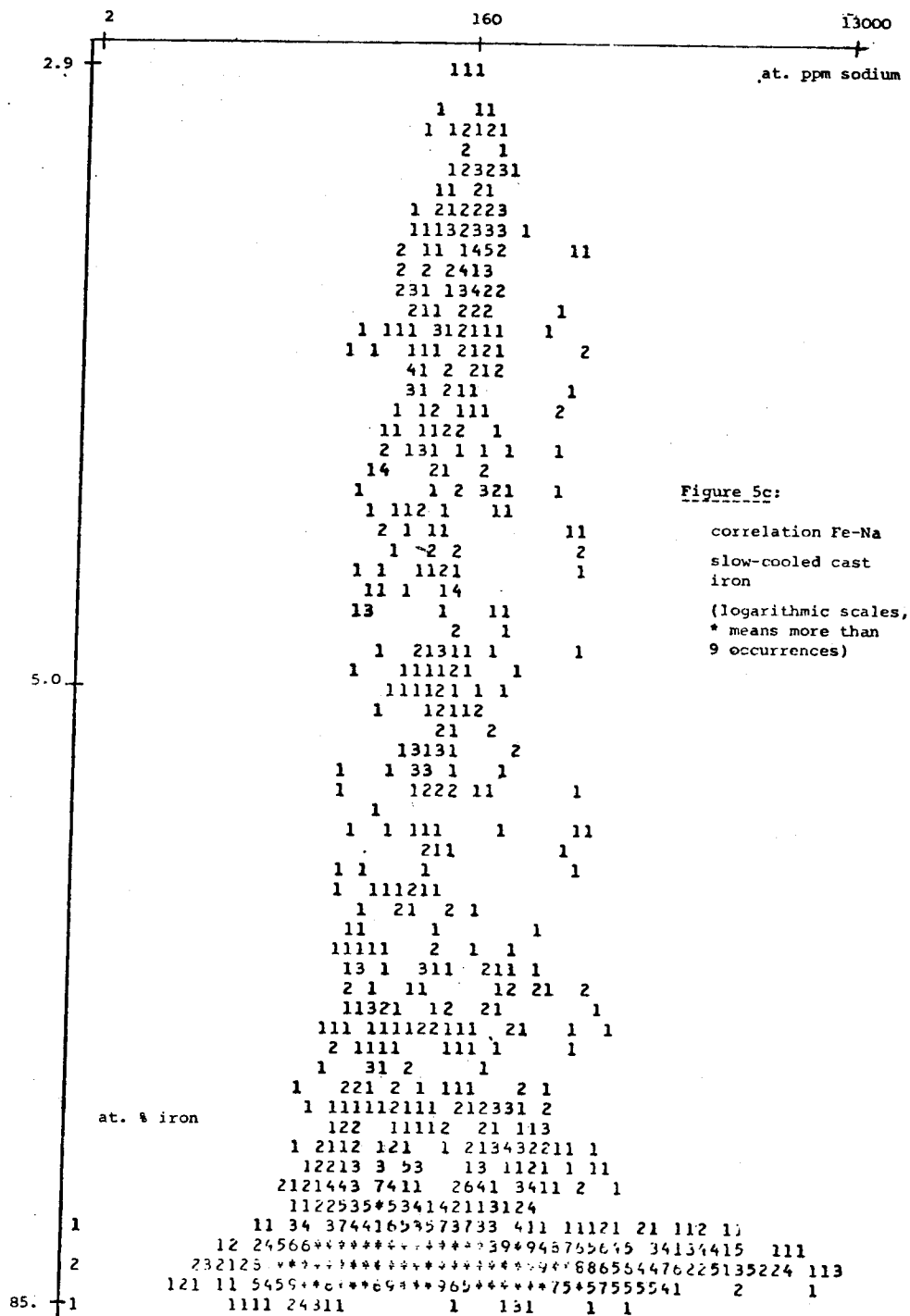
Figure 5c:

correlation Fe-Na

slow-cooled cast
iron

(logarithmic scales,
* means more than
9 occurrences)

at. % iron

TABLE 1. COMPOSITION OF MATERIALS USED AS OBTAINED BY
SPARK SOURCE MASS SPECTROMETRY

Element	Concentration (at. %)		
	Ni-Mg (.8 wt % added)	Fe-Si (1.4 wt % added)	Nodular cast iron
B	.008	.003	.013
C	-	-	3.5
N	.015	.015	.015
O	.1	.1	.08
Na	.003	.005	.01
Mg	16.	.1	0.5
Al	-	1.3	-
Si	-	75.	3.4
P	.005	.005	.08
K	.0005	.001	.002
Ca	.001	1.	.3
Ti	.002	.02	.04
V	.0002	.005	.03
Cr	.02	.02	.09
Mn	-	-	.9
Fe	-	22. (balance)	90. (balance)
Ni	83. (balance)	.02	.8
Sb	.005	.0001	.003
Ta	.002	.002	.002

TABLE 2: LINEAR CLASSES OF CONCENTRATIONS (ppm or at %)

Element / class	B	C	N	O	Na	Mg	Al	Si	P	K	Ca	Ti	V	Cr	Fe	Mn	Ni	Sb	Ta
Correction factor	20.	52.	190.	390.	1.7	3.3	3.2	6.1	9.6	1.6	1.6	2.8	1.8	2.4	64	2.7			
Slow cooled																			
	19.	.10%	2.7%	24.	2.	3.	55.	26.	2.	0.	5.	9.	1.	5.	.29%	70.	10.		
0	517.	9.3%	5.4%	2.4%	.13%	1.4%	.40%	.11%	40.	440.	.24%	.46%	70.	580.	8.8%	.75%	560.		
1	.10%	19.%	8.2%	4.7%	.27%	2.8%	.80%	.23%	78.	880.	.48%	.93%	140.	.12%	17.%	1.5%	.11%		
2	.15%	28.%	11.%	7.1%	.40%	4.2%	1.2%	.34%	120.	.13%	.72%	1.4%	210.	.17%	26.%	2.2%	.17%		
3	.20%	37.%	14.%	9.4%	.54%	5.7%	1.6%	.45%	150.	.18%	.96%	1.8%	280.	.23%	34.%	3.0%	.22%		
4	.25%	46.%	16.%	12.%	.67%	7.1%	2.0%	.56%	190.	.22%	1.2%	2.3%	350.	.29%	43.%	3.7%	.28%		
5	.30%	55.%	19.%	14.%	.81%	8.5%	2.4%	.67%	230.	.26%	1.4%	2.8%	420.	.35%	51.%	4.5%	.33%		
6	.35%	65.%	22.%	16.%	.94%	9.9%	2.8%	.78%	260.	.31%	1.7%	3.2%	500.	.40%	60.%	5.2%	.39%		
7	.40%	74.%	25.%	19.%	1.1%	11.%	3.1%	.89%	305.	.35%	1.9%	3.7%	570.	.46%	68.%	6.0%	.44%		
8	.45%	83.%	27.%	21.%	1.2%	13.%	3.5%	1.0%	340.	.39%	2.2%	4.2%	640.	.52%	76.%	6.7%	.50%		
9	.50%	92.%	30.%	23.%	1.3%	14.%	3.9%	1.1%	380.	.44%	2.5%	4.6%	710.	.58%	85.%	7.5%	.55%		
Average concentration	380.	22.%	17.%	2.3%	200.	.30%	1.8%	.42%	810.	82.	.47%	.17%	160.	.16%	53.%	2.2%	.15%		
Fast cooled																			
	2.	.10%	3.1%	440.	1.	320.	88.	1.2%	190.	0.	14.	40.	2.	30.	1.3%	420.	44.	2.	16.
0	600.	9.0%	6.1%	.44%	10.	2.6%	.41%	2.2%	.19%	16.	1.0%	2.6%	150.	530.	9.6%	.60%	.18%	140.	38.
1	.13%	18.%	9.1%	.83%	19.	5.2%	.81%	4.3%	.37%	33.	2.0%	5.3%	300.	.10%	18.%	1.2%	.35%	280.	75.
2	.19%	27.%	12.%	1.2%	28.	7.8%	1.2%	6.3%	.55%	50.	3.0%	8.0%	450.	.15%	26.%	1.7%	.52%	420.	110.
3	.25%	36.%	15.%	1.6%	36.	10.%	1.6%	8.4%	.72%	60.	4.0%	11.%	600.	.20%	35.%	2.3%	.70%	560.	150.
4	.32%	45.%	18.%	2.0%	45.	13.%	2.0%	10.%	.90%	83.	5.1%	13.%	750.	.25%	43.%	2.8%	.87%	700.	190.
5	.38%	53.%	21.%	2.4%	54.	16.%	2.4%	13.%	1.1%	100.	6.1%	16.%	900.	.31%	51.%	3.4%	1.0%	830.	220.
6	.44%	62.%	24.%	2.8%	63.	18.%	2.8%	15.%	1.3%	120.	7.1%	19.%	.10%	.36%	60.%	4.0%	1.2%	970.	260.
7	.51%	71.%	27.%	3.2%	72.	21.%	3.2%	17.%	1.4%	130.	8.1%	21.%	.12%	.41%	68.%	4.5%	1.4%	.11%	300.
8	.57%	80.%	30.%	3.6%	80.	23.%	3.6%	19.%	1.6%	150.	9.1%	24.%	.13%	.46%	76.%	5.1%	1.6%	.12%	340.
9	.63%	89.%	33.%	4.0%	89.	26.%	4.0%	21.%	1.8%	170.	10.%	26.%	.15%	.51%	85.%	5.6%	1.7%	.14%	570.
Average concentration	380.	25.%	18.%	.69%	14.	.31%	1.7%	5.9%	.51%	50.	.11%	.40%	180.	.15%	45.%	2.2%	.14%	100.	120.

Note: "31-N" appears in the blank Sb/Ta region of the Slow cooled block.

THE EFFECT OF PREFERENTIAL SPUTTERING ON ION MICROPROBE DEPTH PROFILES IN MINERALS

E. Zinner, McDonnell Center for the Space Sciences, Washington University, St. Louis, Mo. 63130

Introduction: One of the attractive features of SIMS is the capability to measure concentration depth profiles with high spatial resolution. McHugh (1,2) has reviewed SIMS depth profiling and has discussed the various effects that influence and distort the true concentration profiles. One of the major factors is the so-called "chemical" effect of the implanted primary ion. For example, the use of a negative oxygen beam results in an enhanced yield of positive ions from metallic surfaces (3,4). The sputter ionization varies greatly for different matrices containing oxygen or no oxygen affecting the secondary ion signal correspondingly (5). In depth profiling of homogeneous insulating matrices like glasses or minerals with O^- ions the chemical effect does not seem to play any role. There the most important factor for the distortion of true concentration profiles seems to be the preferential sputtering of different elements from the matrix. Experiments performed in metallic oxides (6,7) as well as in a variety of alloys and other compounds (8) showed changes in the composition of sputtered surfaces attributed to preferential sputtering effects. Such effects were also noticed by Housley (9) for silicate glass under Ar bombardment. Solar wind sputtering has been invoked as the cause of elemental and chemical fractionation effects on the surface of lunar material (10-12). In the course of ion microprobe studies of implanted ions in terrestrial and lunar minerals (13-15) we investigated also the question of preferential sputtering effects under the primary ion beam.

Experimental Procedure and Results: Depth profiles were measured with an ARL ion microprobe mass analyzer in polished sections of Lake County labradorite samples in a way described previously (14,15). Samples were uncoated but a metal grid with holes of $\sim$ 100 x 100 μ in size was placed on top of the sample surface to insure the collection of secondary ions. A $^{16}O^-$ or NO_2^- primary beam of typically 0.3 - 1.0 nA was rastered over areas of $\sim$ 60 x 90 μ. Profiles were obtained at low mass resolution ($\sim$300) for masses where we could be sure that molecular ions would not interfere substantially with atomic ions. This was the case for the major element isotopes ^{23}Na, ^{27}Al, ^{28}Si and ^{40}Ca but also for ^{7}Li and ^{24}Mg. Figure 1 shows depth profiles for these elements measured with an NO_2^- beam at 9 kV. The depth scale in the graphs has been obtained by monitoring the profile of ^{52}Cr ions implanted at 62 kV and using the LSS (16) theory to calculate their projected range.

Discussion: All the depth profiles show the same qualitative behavior: an initial increase or decrease of varying length after which the secondary ion signal reaches a constant level. Although it is difficult to eliminate any contamination of Na on our samples, surface contamination can be ruled out for the major elements Na and Si as the source for the initial enhancements seen. Both elements exist in much higher concentrations in the matrix than can be expected for any surface contaminants. A possible explanation for the initial transients of the depth profiles is ion migration resulting from surface charging (17). However, this is unlikely, even for the alkali metals Li and Na. Firstly, Hughes et al (17) observed this effect for Na implanted into a foreign matrix as compared to Na which is part of the crystal structure as in our case. Secondly, the relative behavior of Mg, Al and Ca vs. Si could not be explained this way. The most likely interpretation of the depth profiles is to consider them to be the result of the different sputtering rates of different elements. At the beginning ion yields will be proprotional to sputtering rates and bulk concentrations of the different elements. Preferential sputtering will lead to elemental enhancement or depletion in a thin surface layer until a steady state is reached in which the ion yields must be proportional to the bulk concentrations only (8). This steady state is characterized by the constant signal in the profiles of Figure 1. If S_i are the sputtering rates for different elements and c_i their bulk concentrations in the mineral, the average steady state concentrations n_i of the surface layer from which secondary ions are sputtered off must be

$$n_i = \frac{c_i}{S_i} \bigg/ \sum_{\substack{all \\ elements}} \frac{c_i}{S_i}$$

The ratio of the ion signal at the beginning of the profile to that of the steady state is then

$$R_i = \frac{c_i}{n_i} = S_i \sum_{\substack{all \\ elements}} \frac{c_i}{S_i}$$

and for two elements

$$\frac{R_i}{R_j} = \frac{S_i}{S_j}$$

A simple model that requires that atoms lost by sputtering are replaced by atoms with the average composition of the mineral in the thin sputtering layer will yield the time or depth evolution of the secondary ion signal. The detailed form of individual profiles depends on the sputtering rates and concentrations of the elements in the matrix considered. The characteristic depth at which the steady state is reached is a function of the depth from which atoms are sputtered and the depth at which

atomic mixing takes place under the ion beam (8). We observe this depth to be roughly proportional to the range of incident ions for a beam of O^- at 15 kV and NO_2^- at 9 kV. From the R-values above we can derive the relative sputtering rates of different elements. While we do not consider our measurements to be accurate enough to obtain quantitative values for the sputtering rates, it can be seen from Figure 1 that $S_{Li} > S_{Na} > S_{Si} > S_{Mg} > S_{Al} > S_{Ca}$. In agreement with Housley and Grant (9) we find that the sputtering rates are not just a function of the atomic masses of the elements as expected from simple kinetic or diffusion models (20, 21) based on momentum transfer in the collision cascade. Our results thus favor sputtering models which include some thermodynamic considerations (7, 11, 18) or take into account thermal sputtering.

Conclusion: Preferential sputtering effects under the primary ion beam have to be taken into account for the interpretation of SIMS depth profiles in multielement matrices. The transient part at the beginning of depth profiles can in principle be used to determine relative sputtering rates which do not follow a simple mass dependence. Extension of this work to different matrices and to the measurement of isotopic sputter fractionation might have important implications for the interpretation of the presence or absence of such effects on the lunar surface (10-12, 22).

References:

(1)   J. A. McHugh, Methods of Surface Analysis, p. 223, Elsevier, 1975.
(2)   J. A. McHugh, Secondary Ion Mass Spectrometry, p. 179, NBS Special
        Publication 427, 1975.
(3)   C. A. Anderson, Int. J. Mass Spectrom. Ion Phys., 2, 61, 1969.
(4)   C. A. Anderson, Int. J. Mass Spectrom. Ion Phys., 3, 413, 1970.
(5)   R. D. Fralick, et al., Abstract no. 387, 3rd Annual Meeting FACSS,
        Philadelphia, 1976.
(6)   R. Kelly and N. Q. Lam, Rad. Effects 19, 39, 1973.
(7)   H. M. Naguib and R. Kelly, Rad. Effects 25, 1, 1975.
(8)   Z. L. Liau, et al., Appl. Phys. Letters 30, 626, 1977.
(9)   R. M. Housley and W. R. Grant, Proc. Lunar Sci. Conf. 8th, 3885, 1977.
(10)   T. Gold, et al., Proc. Lunar Sci. Conf. 6th, 3285, 1975.
(11)   C. T. Pillinger, et al., EPSL, 33, 289, 1976.
(12)   P. K. Haff, et al., Proc. Lunar Sci. Conf. 8th, 3807, 1977.
(13)   E. Zinner and R. M. Walker, Proc. Lunar Sci. Conf. 6th, 3601, 1975.
(14)   E. Zinner, et al., Proc. Lunar Sci. Conf. 7th, 953, 1976.
(15)   E. Zinner, et al., Proc. Lunar Sci. Conf. 8th, 3859, 1977.

(16) J. Lindhard, et al., Mat. Fys. Medd. Dan. Videnskab. Selskab 33, (14), 1, 1963.

(17) H. L. Hughes, et al., IEEE Trans. Nucl. Sci., NS-19, 256, 1972.
(18) K. S. Kim and N. Winograd, Surface Sci. 43, 625, 1974.
(19) R. Kelly, Rad. Effects 32, 91, 1977.
(20) P. Sigmund, Phys. Rev. 184, 383, 1969.
(21) D. T. Goldman and A. Simon, Phys. Rev. 111, 383, 1958.
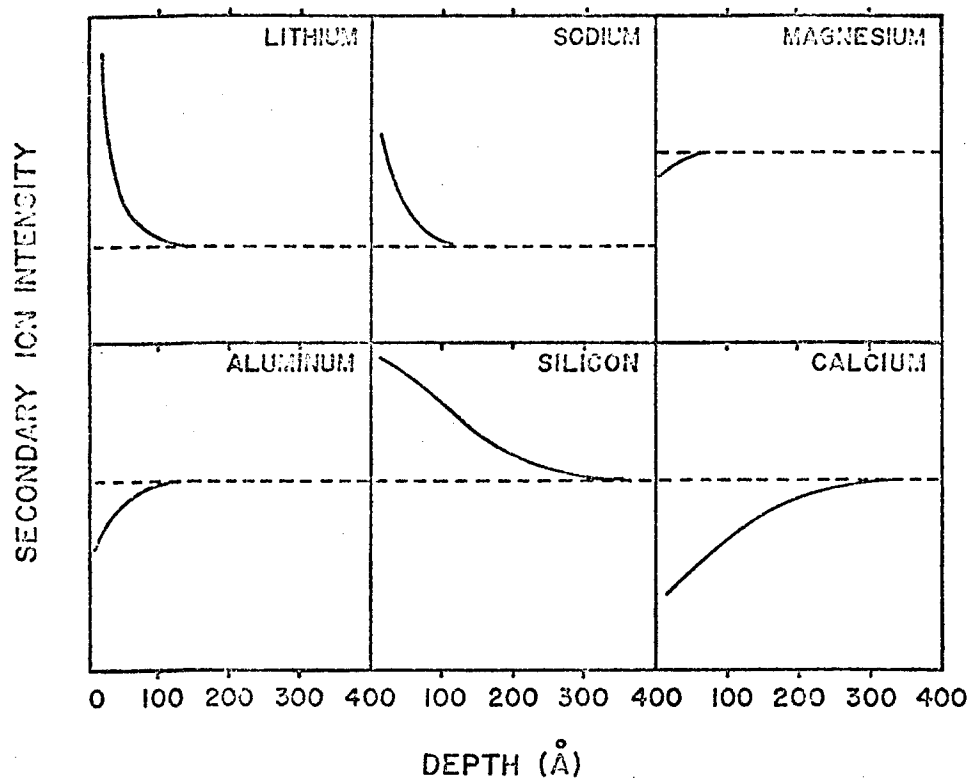(22) W. A. Russell, et al., Proc. Lunar Sci. Conf. 8th, 3791, 1977.

Figure 1. Depth profiles measured with ARL IMMA in a polished section of Lake County labradorite. The primary NO_2^- beam of 9 kV and 0.3 nA was rastered over 72 x 48 µm. An electronic aperture selected the signal only from the central 40% of the area. The ordinate scales are normalized in a way that the steady state signal (dashed lines) is the same for all the elements except for lithium and sodium where, for reasons of space, this steady state value was chosen as one half of that of the other elements.

Historical Comments on Electron Beam Induced

Current Methods in the Scanning Electron Microscope

T.E. Everhart

Department of Electrical Engineering and Computer Sciences
University of California, Berkeley, California 94720

While working as a research student in the Cambridge University Engineering Laboratories under the supervision of Mr. C.W. Oatley (now Professor C.W. Oatley, FRS) on a scanning electron microscope developed by D. McMullan and K.C.A. Smith, it was my good fortune to observe voltage contrast on various semiconductor p-n junctions. Our best sample was a germanium alloyed p-n junction obtained from Dr. J.R. Tillman and Mr. Dennis Baker of the Post Office Engineering Research Station. After examining this sample in the SEM on May 1, 1957, I wrote the following words in my laboratory notebook: "While taking micrographs for Dennis Baker today, I noticed that the beam could make a large difference in the back current taken by the p-n junction.... This effect could be due to hole-electron pairs being created by the beam. Knowing the beam current, the energy needed for hole-electron pair creation, and the beam energy, we should be able to derive the maximum suspected increase in junction current."

To the best of my knowledge, that entry recorded the first observation of electron-beam-induced current (EBIC) that was measured in a scanning electron microscope, although as a later search of the literature showed, others had certainly observed electron-bombardment conductivity earlier.[1-3] The effect was duly noted in my doctoral thesis,[4] where figure 9.6(b) showed the increase in reverse bias current due to the SEM electron beam (see Fig. 1 below).

A few years later, during 1962-63, it was my pleasure to collaborate at the Westinghouse Research Laboratories with Dr. O.C. Wells, with whom I shared our laboratory room at Cambridge from 1955 to 1957. At Westinghouse, we were interested in observing passivated silicon integrated circuits in the SEM using the voltage-contrast mode. Many persons who heard this idea forecast failure because 1) voltage contrast wasn't very well understood and 2) the insulating SiO_2 layer on the silicon was sure to charge-up and change the surface potential anyway! Stubborness and a hunch based on many hours of observing aluminum samples (with their inherent thin oxide layers) had convinced us that we had a chance of success, and when we placed our first IC in the SEM, applied reverse bias, and looked at the image--behold, voltage contrast.[5] The doubters had neglected to consider the electron-beam-induced conductivity that electrically connected the surface of the insulating SiO_2 to the silicon.

During this period of collaboration, Oliver Wells suggested that the

electron-beam induced current across a selected junction could be displayed on the micrograph directly, giving an EBIC micrograph which showed information about junctions underneath the surface. This was successful, and we also found micrographs generated by adding EBIC signals to the secondary electron signal gave considerable additional information over either signal displayed alone.[5,6]

About this same time, interesting work at Bell Labs by Lander, Czaja, and collaborators was showing crystal imperfections using EBIC collected by p-n junctions.[7-10] The imperfections caused more rapid recombination of the hole-electron pairs created by the primary beam, and hence showed up as dark regions. This work is being followed up even today, as the papers following this one in this conference will demonstrate.

In conclusion, the EBIC signal has been used in the SEM to provide information below the surface of certain samples, especially those in which an electric field can be induced for the separation of hole-electron pairs generated by the primary electron beam. This signal, which complements the secondary electron signal, should prove even more useful in the future, as we move forward semiconductor devices with dimensions so small that mechanical probing proves virtually impossible.

It is an honor to be invited to provide this lead-off paper, and a pleasure to thank publicly Prof. C.W. Oatley, Dr. K.C.A. Smith, Dr. O.C. Wells, and many others who have helped me understand the electron optics and signal generation in scanning electron microscopes. I wish also to thank Dr. Wells for reading this paper for me.

References

1. K.G. McKay, Phys. Rev. 74, 1606-1621 (1948); Phys. Rev. 77, 816-825 (1950).

2. L. Pensak, Phys. Rev. 75, 472-   (1949).

3. F. Ansbucher and W. Ehrenberg, Proc. Phys. Soc. A64, 362-379 (1951).

4. T.E. Everhart, "Contrast Formation in the Scanning Electron Microscope," Ph.D. dissertation, Cambridge University, 1958.

5. T.E. Everhart, O.C. Wells, and R.K. Matta, J. Electrochem. Soc. 111, 929-936 (1964).

6. T.E. Everhart, O.C. Wells, and R.K. Matta, Proc. IEEE 52, 1642-1647 (1964).

7. J.J. Lander, H. Schreiber, T.M. Buck, and J.R. Mathews, Appl. Phys. Lett. 3, 206-207 (1963).

8. W. Czaja and G.H. Wheatley, J. Appl. Phys. 35, 2782-2783 (1964).

9. W. Czaja and J.R. Patel, J. Appl. Phys. 36, 1476-1482 (1965).

10. W. Czaja, J. Appl. Phys. 37, 918-919 and 4236-4248 (1966).
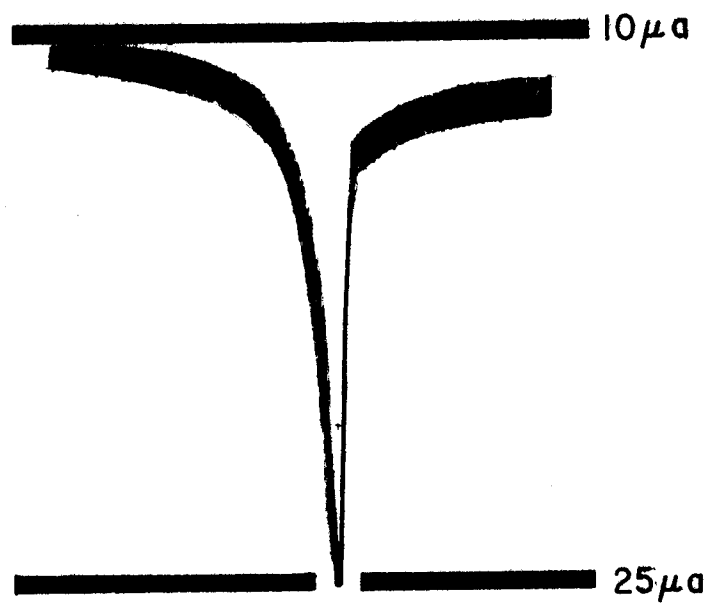
Fig. 1. Variation of reverse-bias current through a p-n junction vs. primary electron-beam position measured normal to the plane of the p-n junction. Abcissa is distance transverse to the p-n junction, ordinate is reverse-bias current (increasing downward). (From Fig. 9.6, reference 4)

Charge Collection Microscopy

H. J. Leamy

Bell Laboratories, Murray Hill, New Jersey 07974

Charge collection occurs whenever the motion of electrons and holes in semiconductors is perturbed by an electric field. During collection, the nonrandom component of carrier motion induces a compensating current in an external circuit. When used as the video signal in an SEM, this current reflects the efficiency with which carriers created by the SEM electron beam are collected within the semiconductor sample. Charge collection is therefore the mechanism by which images are produced in the familiar electron beam induced current (EBIC) mode of scanning electron microscopy.

The charge collection process is very sensitive to inhomogeneities in carrier mobility, lifetime, and diffusion length. This sensitivity may be used to advantage to study defects in semiconductor materials. The advent of large scale integration of many devices on one semiconductor crystal makes such study not only scientifically interesting but technologically imperative. Defect examination may be most easily accomplished if the collection field is supplied by a thin Schottky barrier, through which the SEM beam injects charge carriers. Because sample preparation consists only of metallization, the influence of the defects upon charge collection is unaltered and the influence of various processing steps, heat treatments, etc. may be determined. This paper contains a review of our experience with the surface barrier method (1-5) of charge collection microscopy.

Charge collection micrographs with resolution better than 0.5 μm may be produced by operating the SEM at low accelerating voltage, E. Resolution generally scales with the electron range, R, which increases as $E^{1.75}$. Defects are generally revealed as carrier recombination centers. Combination of charge collection microscopy and x-ray topography or etching studies thus allows the determination of electrically inactive defects and changes in electrical activity induced by processing. The energy levels of localized defects, dislocations, stacking faults, precipitates, etc. may be determined by temperature dependent charge collection microscopy. The depth location of defects beneath the sample surface may also be determined to within 1.0μm by varying R. Finally, correlation of the crystallographic nature of the defect with its electrical activity is possible when charge collection microscopy is combined with transmission electron microscopy.

In addition to localized defects, inhomogeneous distributions of small, individually unresolvable defects such as

point defects and dopant atoms may also be imaged. These generally alter the geometry of the collection field and thus cause a change in the background or base level of charge collection. Quantitative determination of diffusion length and lifetime is possible in such instances.

References

[1] A. J. R. de Kock, S. D. Ferris, L. C. Kimerling, and H. J. Leamy, "Investigation of Defects and Striations in As-Grown Si Crystals by SEM Using Schottky Diodes" Appl. Phys. Lett. 27, 313-315 (1975)

[2] H. J. Leamy, L. C. Kimerling, and S. D. Ferris, "Silicon Single Crystal Characterization by SEM" Scanning Electron Microscopy/1976 (Part IV), (O. Johari ed.) IIT Res. Inst., Chicago, 1976 pp. 529-537

[3] L. C. Kimerling, P. Petroff, and H. J. Leamy, "Injection-Stimulated Dislocation Motion in Semiconductors", Appl. Phys. Lett., 28, 297-300 (1976)

[4] L. C. Kimerling, H. J. Leamy and J. R. Patel, "The Electrical Properties of Stacking Faults and Precipitates in Heat-Treated, Dislocation-Free Czochralski Silicon", Appl. Phys. Lett., 30, 217-219 (1977)

[5] A. J. R. de Kock, S. D. Ferris, L. C. Kimerling, and H. J. Leamy, "SEM Observation of Dopant Striae in Silicon", J. Appl. Phys., 48, 301-307 (1977)

STUDY OF DOPANT STRIATIONS FOR HIGHLY DOPED SILICON IN SOLAR CELL STRUCTURE BY SCANNING ELECTRON MICROSOCOPY

J. Y. Chi and H. C. Gatos
Department of Materials Science and Engineering
Massachusetts Institute of Technology
Cambridge, Massachusetts 02139

Contrast due to variation of impurity concentration (striation) in highly doped silicon (above 10^{18}cm^{-3}) was observed with SEM in the EBIC mode. For impurity concentration below 10^{17}cm^{-3} dopant striations have been observed in the EBIC mode by preparing a Schottky barrier.[1] In contrast to the Schottky barrier technique, the present contrast was found to be due to the diffusion length variation in the base material. A quantitative analysis has been carried out.

Solar cell structure, i.e., a large-area shallow p-n junction, was prepared using the standard spun-on boron oxide source and photomasking techniques on Czochralski grown Sb-doped silicon slices. The depth of the junction (0.19 μm) was measured nondestructively by an EBIC technique developed by the present authors.[2]

Due to the shallow junction and high doping level, the thickness of the diffused region and the depletion region was less than 0.25 μm. The high energy electrons (above 30 keV) lose almost all of their energy in the neutral base region. The generated electron-hole pairs diffuse in the neutral base region and the minority carriers are accelerated by the high electric field in the depletion region to produce the EBIC. Thus the measured EBIC is almost completely due to the electron-hole pairs created in the neutral base region.

Using the depth-dose function,[3] dE/dZ, and modulating the excitation strength, the EBIC normalized with respect to the incident electron beam can be calculated by the following equation

$$I_i/I_b = \frac{1}{\varepsilon} \int_0^R \frac{dE}{dZ} e^{-Z/L} dZ$$

where I_i is EBIC, I_b is the incident current, ε is the average ionization energy for electron-hole pair in silicon (3.67 eV[4]) R is the range of the energetic electron, L is the diffusion length, Z is the depth. The diffusion length can be calculated from the measured EBIC by a graphical method. Fig. 1 shows representative results. The normalized EBIC trace along the EBIC micrograph (Fig. 1a) is shown in Fig. 1b, and the calculated diffusion length variations are shown in Fig. 1c. Using an empirical relationship between the diffusion length and the doping concentration[5,6] the concentration variation was also obtained; the result is shown in Fig. 1d. The shape and the value of the profile is common for Czochralski grown Si.[7] Using the concentration dependent mobility,[8], D, the minority carrier lifetime $\tau = L^2/D$ can also be determined (see Fig. 1e).

References.

1. L.C. Kimberling, H.J. Leamy, J.L Benton, S.D. Ferris, P.E. Freeland and J.J. Rubin, "Semiconductor Silicon 1977", p. 468-480, The Electrochemical Society, Inc., Princeton, 1977.

2. J.Y. Chi and H.C. Gatos, IEEE Trans. on Electron Devices, <u>ED-24</u>, 1366 (1977).

3. T.E. Everhart and P.H. Hoff, J. Appl. Phys. <u>42</u>, 5837 (1971).

4. R.H. Pehl, F.S. Goulding, D.A. Landis and M. Lenzlinger, Nucl. Instrum. Methods <u>59</u>, 45 (1968).

5. D. Kendall, Conf. Physics and Application of Lithium Diffused Silicon, NASA-Goddard Space Flight Center (Dec. 1969).

6. P.A. Iles and S.I. Soclof, Proceedings of 11th Photovoltaic Specialists' Conference, p. 19 (1975).

7. A. Murgai, H.C. Gatos and A.F. Witt, J. Electrochem. Soc. <u>123</u>, 224 (1976).

8. J.C. Irvin, Bell System Tech. J. <u>41</u>, 387 (1962).

(a)
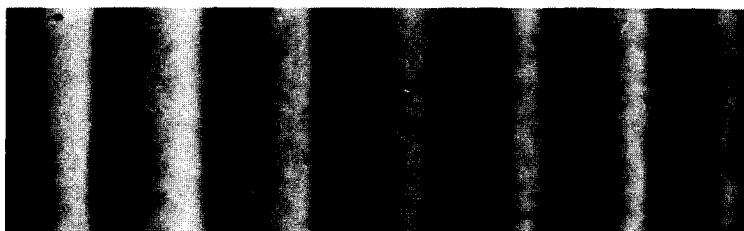
(b)
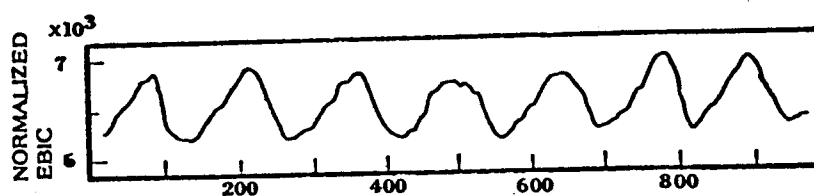
(c)
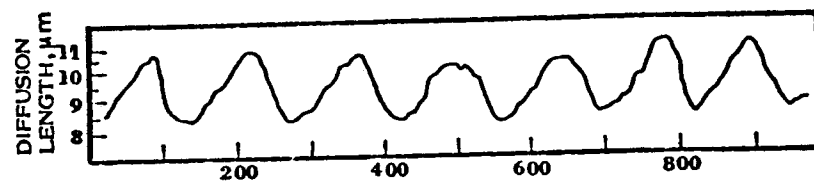
(d)
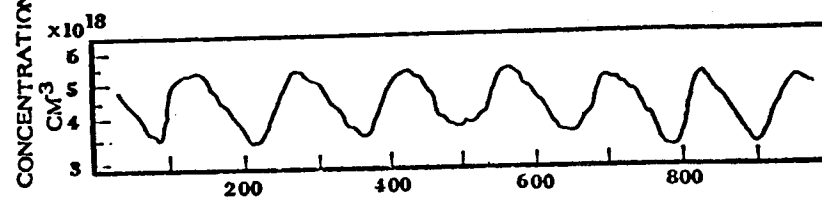
(e)
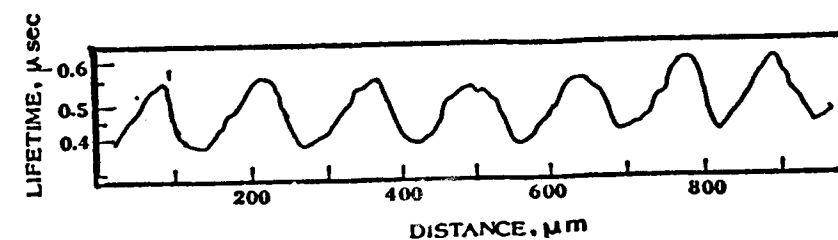
Figure 1. An EBIC micrograph (a) showing variations in diffusion
length in a Czochralski Si crystal. The graphs show
variations of the normalized EBIC, diffusion length,
dopant concentration and lifetime as a function of
distance.

Electron Beam Induced Currents in Metal Oxide Silicon Devices

P. Roitman

National Bureau of Standards
Electronic Technology Division
Washington, DC 20234

The scanning electron microscope is by now widely used for the study of semiconductor crystals and devices. The electron beam induced current (EBIC) or charge collection mode has particular utility in this application since its use can reveal subsurface structures and since it is sensitive to the electrical properties of the material, which are usually the ones of interest. This technique has been used extensively to investigate p-n junctions[1,2]. Schottky barriers have also been used[3,4] and are the preferred device structure for the investigation of crystalline defects as perturbation of the sample during preparation is minimized. Metal-oxide-silicon (MOS) structures are the third basic electronic device component of integrated circuits. The detailed interactions of the electron beam with this structure and the signals produced are slightly different than those of the other two diode structures. The measuring circuit, consisting of a low noise current amplifier and a voltage source, is identical to that used for diode measurements.

Three mechanisms for generating induced currents in MOS structures are illustrated schematically in figure 1. The device is illustrated as having a negative bias on the gate (metal). In process (a) an electron is ionized from the valence band by the incident electron, producing an electron in the conduction band of the oxide and a hole in the valence band. These drift in the field in the oxide to the silicon and the metal respectively. While they are drifting a current is measured in the external circuit which is proportional to the number of pairs generated. Since holes in silicon dioxide move several orders of magnitude more slowly than electrons, the observed current is essentially entirely due to the electrons. Also, the electrons may recombine with the holes before reaching the edge of the oxide. This last process is field-dependent and explains the contrast in figure 2, which shows what appears to be a scratch at the silicon surface. Where the oxide thickness changes the field changes, resulting in a change in the measured current. (The signal was differentiated to enhance contrast).

In process (b) in figure 1 electrons are excited from the metal over the barrier into the oxide, where they drift to the silicon. Electrons may similarly be injected from the silicon under positive bias conditions. In practice the contribution of these currents is usually several orders of magnitude below the contribution of the currents due to processes (a) and (c).

While most of the applied bias appears across the oxide, a significant field penetrates the surface region of the semiconductor, causing a depletion layer to form. A large number of electrons and holes may be generated in this region by the incident high energy electrons (process (c) in figure 1). This plasma will screen the field, causing the band to flatten and the space charge capacitance to change. These effects generate a displacement current. As the incident electron beam penetrates the sample it spreads laterally due to scattering, into a circular shape with a gaussian intensity profile. Consider this circular beam

scanning across a test point. As the front part of the beam crosses the test point the bands start to flatten and a displacement current flows in a direction determined by the applied bias and the conductivity type of the silicon. As the beam passes over the test point, the bands bend back causing a displacement current to flow in the opposite direction. These two contributions will cancel unless the beam is scanned across a point at which the electrons and holes re-combine more quickly than in the rest of the crystal. At such a "recombination center" the contributions from the front and back of the beam will not cancel and contrast will be observed. Such features are shown in figure 3. The small fuzzy dots are oxidation-induced stacking faults in the silicon. A particular feature of this contrast mechanism is that the magnitude of the contrast depends on the speed the beam is scanned across the sample. This point is illustrated in figure 4, which shows two line scans across the same stacking fault at beam scan velocities of (a) 0.43 cm/s and (b) 0.12 cm/s.

The above examples indicate some of the ways the SEM, operated in the EBIC mode, can be used as a very sensitive probe of MOS devices.

References

1. Hoff, P., and Everhart, T. E., Carrier Profiles and Collection Efficiency in Gaussian *p-n* Junctions, *IEEE Trans. Electron Devices* ED-17, 458-465 (1970).

2. Ravi, K. V., and Varker, C. J., Oxidation Induced Stacking Faults in Silicon, *J. Appl. Phys.* 45, 263-287 (1974).

3. Leamy, H. J., Kimmerling, L. C., and Ferris, S. D., Silicon Single Crystal Characterization by SEM, *Scanning Electron Microscopy/1976/IV*, p. 529-537 (IIT Research Institute, Chicago, IL, 1976).

4. de Koch, A. J. R., Ferris, S. D., Kimmerling, L. C., and Leamy, H. J., SEM Observation of Dopant Striae in Silicon, *J. Appl. Phys.* 48, 301-307 (1977).

5. Bottoms, W. R., Guterman, D., and Roitman, P., Contrast Mechanisms in Electron Beam Images of Interface Structures, *J. Vac. Sci. Technol.* 12, 134-139 (1975).

6. Bottoms, W. R., and Roitman, P., SEM Studies of Metal-Oxide-Silicon Capacitors, *Scanning Electron Microscopy/1977/I*, p. 731-738 (IIT Research Institute, Chicago, IL, 1977).
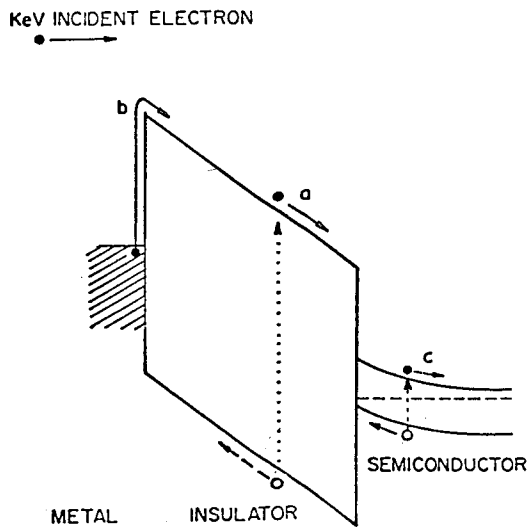
Figure 1. Induced current mechanisms in metal-oxide-silicon structures. (a) Electrons and holes generated in the oxide. (b) Electrons excited from the metal into the oxide. (c) Electrons and holes generated in the silicon. The device is shown with the metal biased negatively.
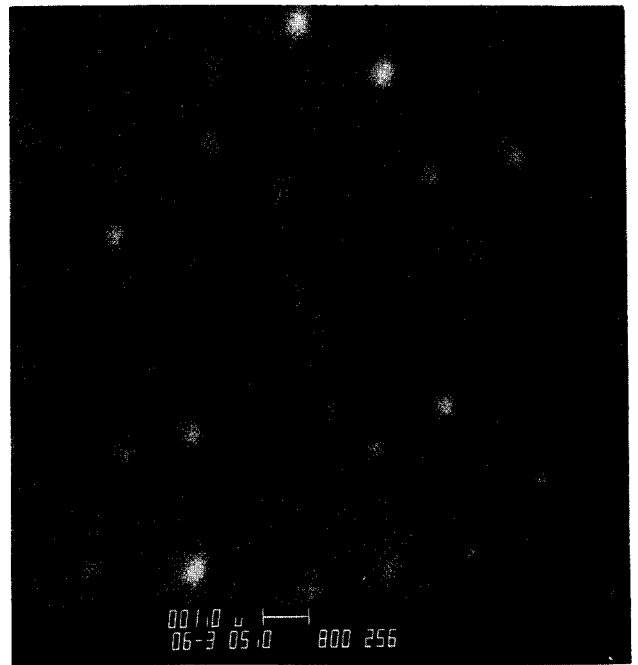

Figure 3. Induced current micrograph of stacking faults in silicon. 4-keV beam, 0.05-μm aluminum on 0.1-μm silicon dioxide on p-type silicon.
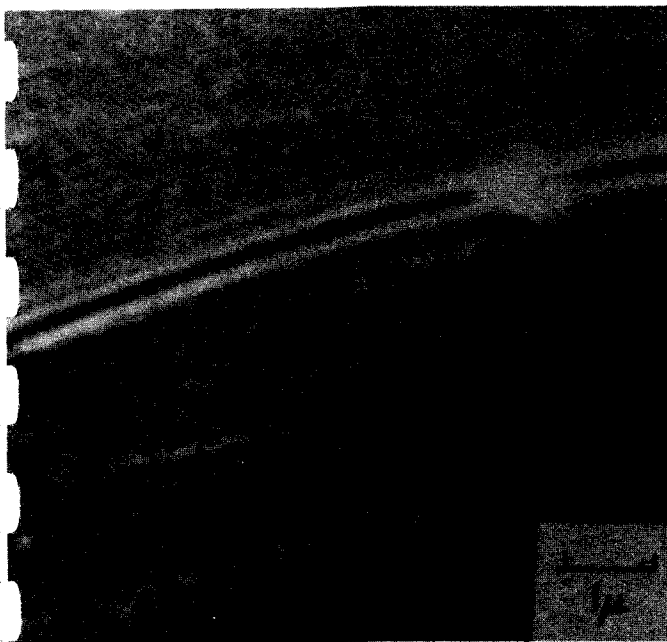

Figure 2. Induced current micrograph of a scratch at the silicon/oxide interface. 30-keV beam, 0.01-μm gold on 0.3-μm silicon dioxide on n-type silicon.
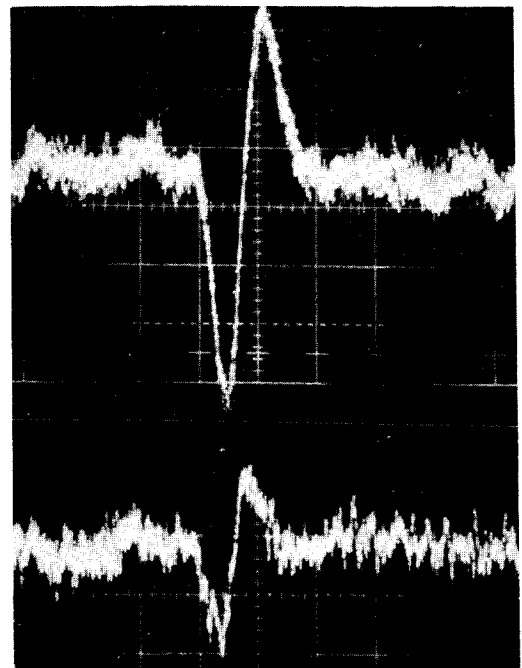
Figure 4. Line scan across a stacking fault. Vertical scale: 5×10^{-10} A/div. Horizontal scale: (a) 1.3 ms/div.
(b) 4.8 ms/div.
Scan speed: (a) 0.43 cm/s.
(b) 0.12 cm/s.

Electron Beam Induced Current Examination of Defects in Solar Cells

C. V. Hari Rao

Mobil Tyco Solar Energy Corporation, 16 Hickory Drive,

Waltham, Massachusetts 02154

The interest in alternate energy sources has led to the development of a variety of low cost techniques for photovoltaic power generation. Some of the techniques for growth of silicon are the edge-defined film-fed growth (EFG) technique, the deposition of thin polycrystalline film on low cost substrates, the Web-dendritie growth of ribbons, the casting of silicon in graphite molds followed by slicing the castings to yield large area polycrystalline sheets etc. In addition to silicon, the use of other materials such as Cds and GaAs for solar cells is also being explored. Consequences of many of the low cost solar cell technologies are the crystal imperfections and the tendency for the incorporation of lifetime-reducing impurities into the crystals. Several techniques have been used to characterize both the crystallographic and electrical properties of the low-cost substrates and solar cells. The Scanning Electron Microscope used in the Electron beam induced current (EBIC) mode is a powerful tool for characterizing both the starting material and the finished solar cell and for examining the electrical effects of crystal defects and defect-impurity complexes.

Solar cells for photovoltaic applications are large area devices (several tens of square centimeters in area) with shallow junctions (< 1 μm). The three important electrical parameters that characterize the solar cell are (i) the short-circuit current, I_{sc}, (ii) the open-circuit voltage, V_{oc}, and (iii) the curve fill factor, CFF. Defects and defect-impurity interactions have different effects on these parameters.

(i) Short-circuit current (I_{sc}):

The short-circuit current of a solar cell is a function of the minority carrier lifetime in the bulk of the material. Since the diffusion length, L, of minority carriers is related to the lifetime, τ, through the relationship $L=\sqrt{D\tau}$ (where D is the diffusion coefficient) either the lifetime or diffusion length can be used to characterize the base material properties. The presence of recombination centers at defect sites could lead to local lifetime degradation of minority carriers. An example of such recombination is shown in Fig. 1 which is an EBIC image of a solar cell fabricated on silicon ribbon. The

incorporation of impurities at crystallographic defects is essential for reduction in the diffusion length. An example is shown in Fig. 2, which is an EBIC image of a portion of a ribbon solar cell. In Fig. 2(a) is an EBIC image of the cell. Fig. 2(b) is a secondary electron image of the cell, while Fig. 2(c) is a high magnification image of the electrically active boundary, both (b) and (c) were obtained after a preferential silicon etch. Notice that the electrically active boundaries in Fig. 2(a) form a very small fraction of the total density of defects present in the material, and that not all the boundaries act as recombination sites.

Data on density of electrically active defects and local diffusion lengths will be presented in the paper.

(ii) Open-Circuit Voltage (V_{oc}):

Lifetime in the depletion region of the device is reflected in the open-circuit voltage. The presence of certain crystallographic defects in the junction area lead to a reduction in the V_{oc} by causing non-uniform junction profiles and hence, the junction field. An example of the effect of crystal defects is shown in Fig. 3, which is an EBIC scan of a solar cell fabricated on polycrystalline silicon sheet obtained from Wacker-Chemitronic Inc. Notice the enhanced recombination at the grain boundaries. The V_{oc} value of these cells are typically lower than those observed in solar cells fabricated in other defective silicon materials. Data will be presented to compare the effects of particular type of defects on V_{oc} in solar cells.

(iii) Curve Fill Factor:

The curve fill factor is a strong function of the I-V characteristics of the solar cell, and is dependent on the leakage current of the device. Examples of the kinds of EBIC response obtained from cells with different fill factors will be shown and the results discussed.

A solar cell is a device that is forward biased during operation. Therefore, EBIC data obtained while the device is in active mode of operation are of interest. Fig. 4 shows the influence of illumination on the degree of recombination at electrically active boundaries. Notice the decrease in recombination contrast at the defects. Data on diffusion lengths of solar cells fabricated on defective material also show an enhancement as a function of incident light intensity (1). The enhancement in diffusion lengths and the "illuminated" EBIC data can both be explained on the basis of filling of 'trap centers' in these materials.

References.

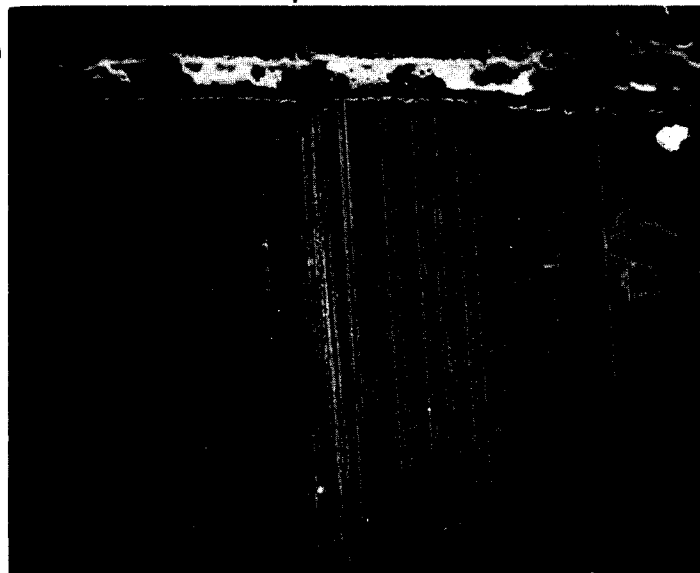1. C. T. Ho, R. O. Bell, and F. V. Wald, App. Phys. Lett., 31, 463, (1977).

Fig. 1. EBIC micrograph of a solar cell fabricated on EFG ribbon silicon. Notice recombination along boundaries. The positions A refer to current collecting metal grids.
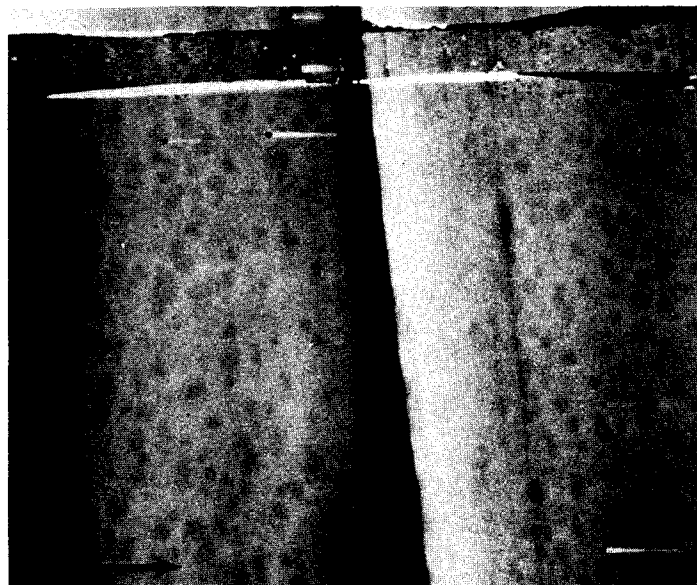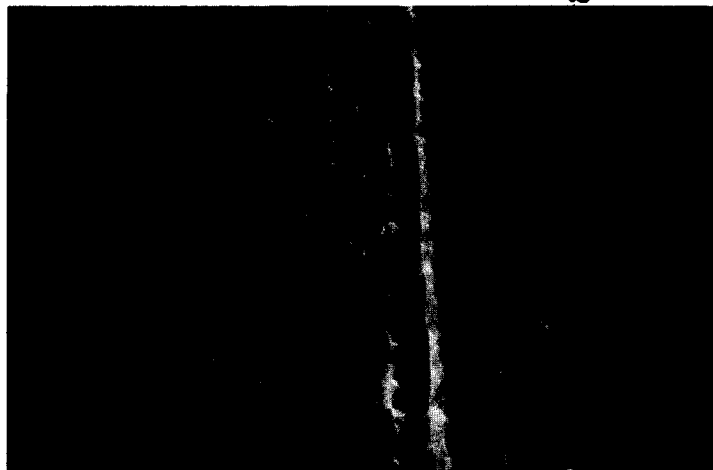
Fig. 2. (a) EBIC image of linear boundaries in a ribbon silicon solar cell, (b) secondary electron image of the region shown in (a), (c) high magnification secondary electron image of the electrically active defect shown in (a). Both (b) and (c) were obtained after a preferential silicon etch.
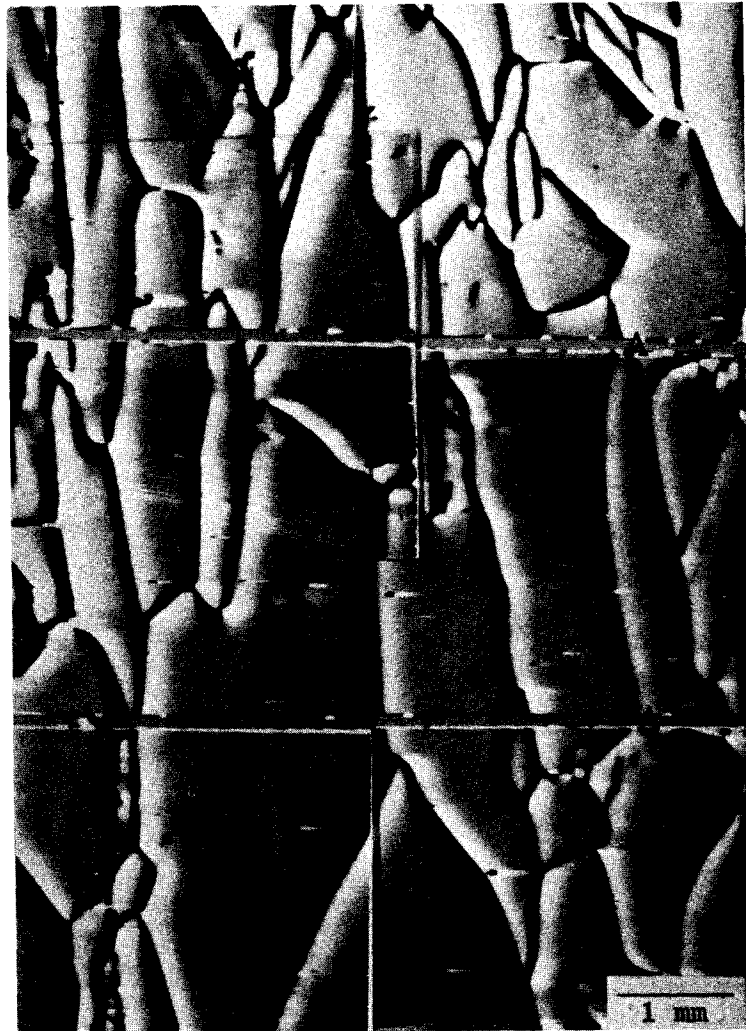
Fig. 3. EBIC micrograph of a solar cell fabricated on polycrystalline silicon
sheets manufactured by Wacker-Chemitronic, Inc. Notice enhance re-
combination at grain boundaries. The current collecting metal grids
are denoted by the letters 'A'.
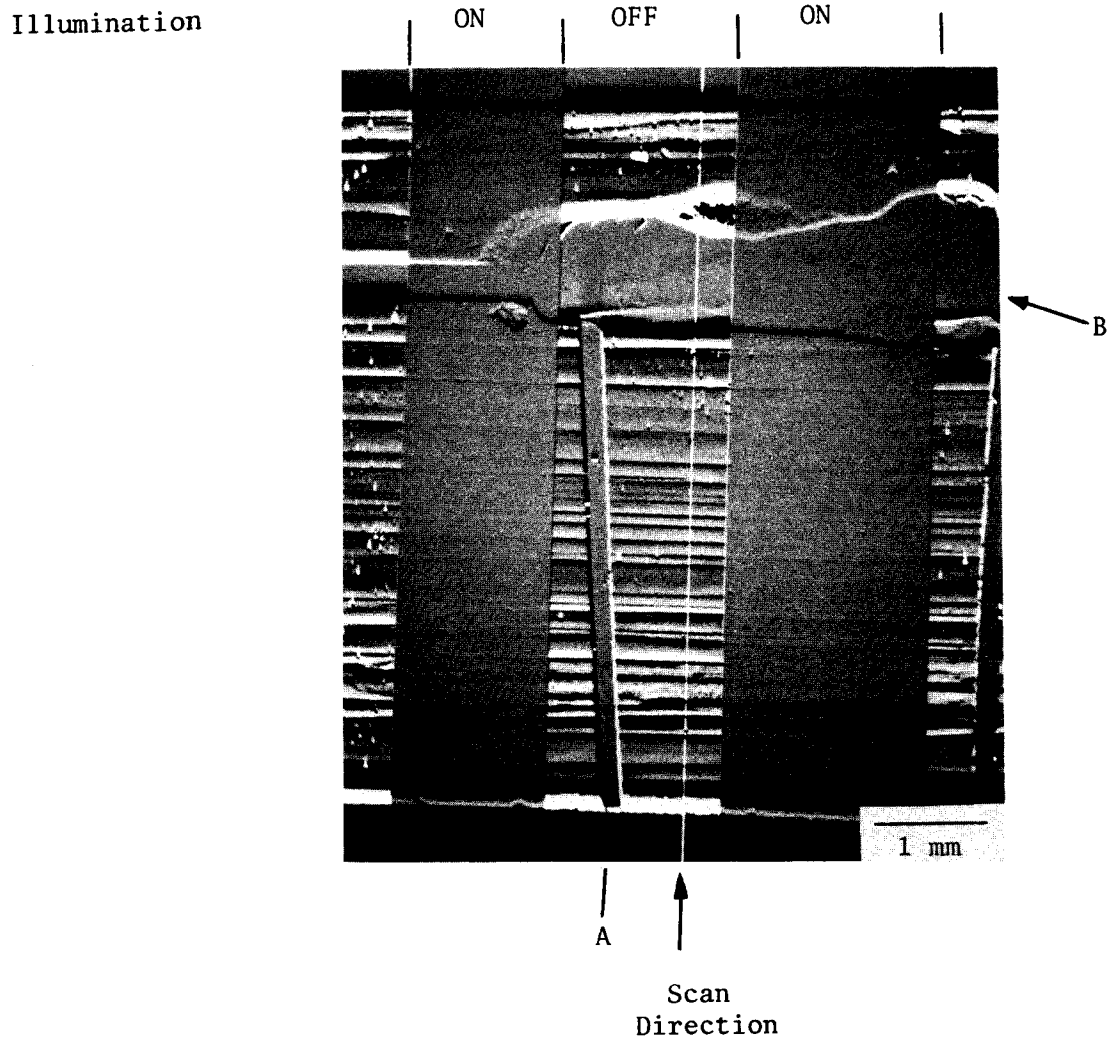
Fig. 4. Effect of illumination (intensity = 5 mW/cm^2) on local recombination in an EFG silicon ribbon solar cell. Illumination was incident on cell at positions marked 'ON'. A and B are current collection metal grids.

A CONTAMINATION EFFECT WHEN EXAMINING EITHER SILICON SOLAR CELLS OR GALLIUM ARSENIDE LASER DIODES BY THE EBIC METHOD.

Oliver C. Wells

IBM Thomas J. Watson Research Center
P.O. Box 218, Yorktown Heights, NY 10598

Some unexpected contamination effects have been found in electron beam induced current (EBIC) images of either silicon solar cells or gallium arsenide laser diodes.

Fig. 1 shows an EBIC image which was obtained with an accelerating potential E_o of 10 kV from a 55CL solar cell[1] which was being evaluated for use as a backscattered electron detector[2]. The three dark circular regions represent a reduction in collected current of between 5% and 10% within those regions. The observations that have been made with this particular sample include the following:

(1) These dark regions are formed when the specimen is left in position for a period of time with the accelerating potential applied to the electron gun. The diameter of the dark region is the same as the diameter of the aperture in the final lens. If the specimen is moved at suitable intervals, then a sequence of dark areas can be formed on the specimen.

(2) These dark regions can only be observed with this particular sample if the operating potential is 30 kV or less.

(3) On the other hand, they only _form_ if the operating potential is higher than this. Thus, in Fig. 1, starting with the smallest circular dark region in the top left corner of the micrograph, the deposition conditions were as follows:

A. 10 mins. at 60 kV operating potential with 100 μm final aperature in position.

B. 10 mins. at 60 kV with 200 μm final aperture in position.

C. 90 mins. at 40 kV with 200 μm final aperture in position.

In all cases, the beam was scanned over the entire area of the micrograph (with a current of about 10^{-10}amp) when these depositions were carried out. The vacuum level was 10^{-6} torr. At lower accelerating potentials the dark regions are formed much more slowly. According to this single set of observations, it would appear that the time taken to form a dark region of the intensity shown in Fig. 1 varies inversely as the fifth (or higher) power of the accelerating voltage.

An EBIC image obtained from a gallium arsenide laser diode is shown in Fig. 2. The diameter of the aperture in the final lens was 400 μm. In this case, the dark regions were both formed and observed with an accelerating potential of 30 kV. This micrograph was taken with an angle of incidence of 45°. The elliptical dark areas had appeared to be circular when they were deposited with a more nearly glancing angle of incidence. With reference to this sample, McMullin[3] wrote "A reduction in the induced current has sometimes been observed in circular areas in the line-of-sight from the lanthanum hexaboride electron gun".

At the time when Fig. 2 was obtained it was supposed that the dark region was caused by lanthanum hexaboride evaporating from the electron gun[4]. When Fig. 1 was obtained, it was while measurements were being made of the current gain of the diode as a function of the incident electron energy, and the voltage-dependence of the deposition rate was discovered.

In order to explain these effects it is probably necessary to assume that negative ions are generated at the cathode surface and are then accelerated by the field in the electron gun before moving down the column and onto the specimen. One way in which these ions could be excited would be because of bombardment of the cathode surface by positive ions caused by interactions between the electron beam and the residual gases in the column, but this explanation is, of course, still tentative at this time.

After these experiments had been completed, we discovered that very similar dark regions had been found in the cathodoluminescent image of cadmium sulfide by Bröcker and Reimer[5]. They had also found that the sizes of the dark regions were determined by the size of the final aperture in the SEM column. They proposed an explanation in terms of negative oxygen ions. They had operated with a tungsten hairpin electron gun, whereas our experiment had been done with a rod-type lanthanum hexaboride gun. Our results provide evidence in favor of their comment: "The phenomenon will also be of interest for the inspection of integrated circuits".

I would like to thank L. W. Landermann for technical help.

References

(1) Manufactured by Optical Coating Lab., Inc., City of Industry, CA 91746. According to the manufacturers, these diodes consist of a 2 μm thick boron diffusion into an n-type silicon substrate.

(2) O. C. Wells, "Effect of collector position on type-2 magnetic contrast in the SEM", Scanning Electron Microscopy, Ed. O. Johari, Los Angeles, 1978.

(3) P. G. McMullin, "Quality evaluation of GaAs-AlGaAs heterostructure wafers using the electron beam induced current technique", Scanning Electron Microscopy/1976, Ed. O. Johari, **1**, 543-550 (1976).

(4) A. N. Broers, "Electron gun using long-life lanthanum hexaboride cathode", J. Appl. Phys., **38**, 1991, 1992 and 3040 (1967).

(5) W. Bröker and L. Reimer, "Specimen damage by negative oxygen ions from SEM cathode detected by cathodoluminescence", Scan, **1**, to be published in the opening issue.
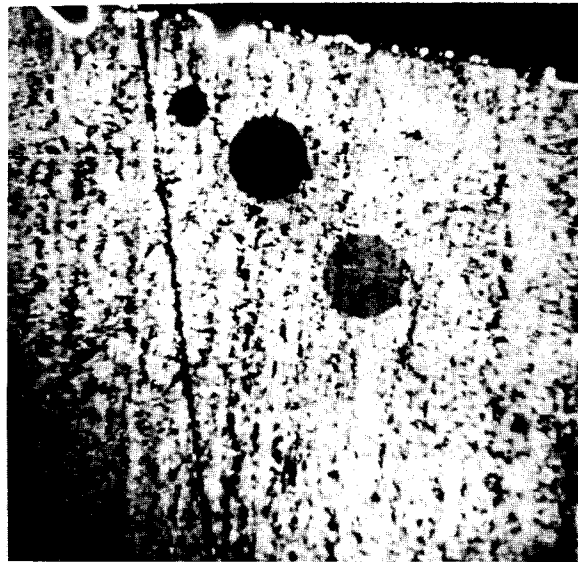
Fig. 1   Electron-beam induced current (EBIC) image of 55CL silicon solar cell obtained at normal incidence with E_o = 10 kV. The three dark circular regions are believed to be caused by ion bombardment of the specimen while it is being examined in the SEM.
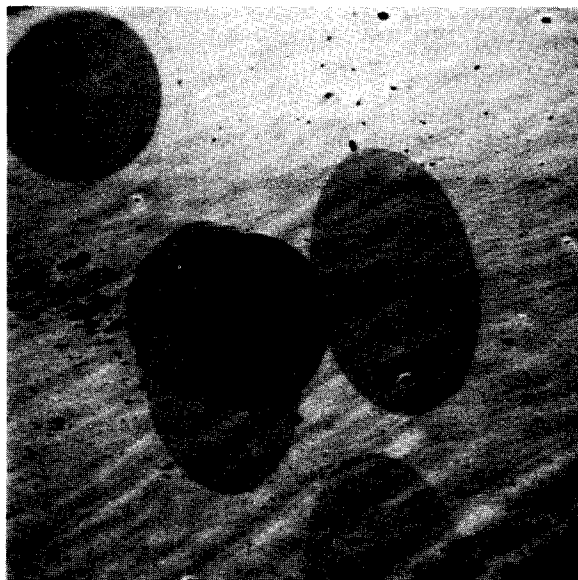

Fig. 2   EBIC image of gallium arsenide laser diode. Angle of incidence = 45°; E_o = 30 kV. The elliptical dark regions had appeared to be circular when they were deposited with a more nearly glancing angle of incidence.

A New Correction Procedure for Quantitative Electron Probe Microanalysis

G. Love and V.D. Scott

School of Materials Science,
University of Bath, U.K.

Introduction

In order to convert microanalysis measurements into weight concentrations, correction factors are applied to take into account atomic number, X-ray absorption and fluorescence effects. Most commonly, the atomic number correction of Duncumb and Reed (1), the absorption correction of Philibert (2) with Heinrich's constants for σ and h (3), and Reed's characteristic fluorescence correction (4) are used, the majority of computer programmes for quantitative work being based upon these. For much work this correction procedure is reasonably satisfactory, due mainly to the fact that input parameters used in both the atomic number and the absorption corrections have been optimised to give the best overall fit to microanalyse results. Despite empirical adjustments, however, the method fails to work satisfactorily for heavily absorbing systems, especially when analysing for light elements and, furthermore, is difficult to extend to non-normally incident probe geometries.

Our new correction procedure removes, in principle, these limitations and should, on completion, provide a universal correction procedure. In the present paper it is shown that it works well at normal incidence for a wide range of systems including light elements. These results are then compared with those obtained using the established correction method.

The Correction Method

Our new atomic number correction (5) is treated conventionally by considering separately the stopping power factor, S, and the backscatter factor, R,

i.e.
$$\frac{Isp}{Ist} = Ci \; \frac{Rsp}{Rst} \cdot \frac{Sst}{Ssp}$$

where the ratio Isp/Ist refers to the intensity of X-rays emitted by the ith element of a multi-element specimen to that in a pure element standard and Ci is the weight fraction of the ith element. Analytical expressions for S and R have been derived which take into account atomic weight A, and atomic number Z, of the target, incident electron energy, Eo, and overvoltage, Uo, (Uo = Eo/Ec, where Ec is the critical ionisation potential of the X-ray line being measured). R is established using Monte Carlo calculations (6).

$$\frac{1}{S} = \left[1 + 16.05 \left(\frac{J}{Ec}\right)^{\frac{1}{2}} \left[\frac{Uo^{\frac{1}{2}} - 1}{Uo - 1}\right]^{1.07} \right] \Bigg/ \sum \frac{CiZi}{Ai}$$

$$R = 1 - \eta \left[I(Uo) + \eta \; G(Uo) \right]^{1.67}$$

where I(Uo) and G(Uo) are functions of overvoltage , Uo, and are given by

$$I(Uo) = 0.33148 \ln Uo + 0.05596 (\ln Uo)^2 - 0.06339 (\ln Uo)^3 + 0.00947(\ln Uo)^4$$

and

$$G(Uo) = \frac{1}{Uo} \left[2.87898 \ln Uo - 1.51307 (\ln Uo)^2 + 0.81312 (\ln Uo)^3 - 0.08241 (\ln Uo)^4 \right]$$

J is the mean ionisation potential of the X-ray line being measured and we take $J/Z = 0.0135 keV$ (6). For a multi-element specimen, J is averaged as follows

$$\ln(J) = \sqrt{\frac{c_i z_i}{A_i}} \, \ln(J_i) \Big/ \sqrt{\frac{c_i z_i}{A_i}}$$

The parameter, η, is the backscatter coefficient. It is a function of Z and Eo and may be expressed (7) as

$$\eta = f_1(Z) \left[1 + f_2(Z) \ln\left(\frac{Eo}{20}\right) \right]$$

where $f_1(Z) = (-52.3791 + 150.48371Z - 1.67373Z^2 + 0.00716Z^3) \times 10^{-4}$

and $f_2(Z) = (1112.8 + 30.289Z - 0.15498Z^2) \times 10^{-4}$

The absorption correction we develop is based upon the treatment outlined by Bishop (8). The fractional transmission of the target for X-rays, $f(\chi)$, is expressed by

$$f(\chi) = \frac{1 - \exp(-2\chi\overline{\rho z})}{2\chi\overline{\rho z}}$$

where $\chi = \mu/\rho \, \mathrm{cosec} \, \theta$, θ is the X-ray take-off angle and μ/ρ is the relevant mass absorption coefficient. The mean mass depth of X-ray generation, $\overline{\rho z}$, is given by

$$\overline{\rho z} = \rho s_m \frac{(0.49269 - 1.09870\eta + 0.78557\eta^2) \ln Uo}{(0.70256 - 1.09865\eta + 1.00460\eta^2) + \ln Uo}$$

where ρs_m, the average path length of an electron in the target, is given by

$$\rho s_m = \frac{(0.773 \times 10^{-5} J^{\frac{1}{2}} Eo^{3/2} + 0.735 \times 10^{-6} Eo^2}{\sum \frac{c_i z_i}{A_i}}$$

We have used the characterisation fluorescence correction of Reed (4), but have not included a correction for continuum fluorescence since this is sufficiently small to have little effect upon our results.

Application of the Proposed Correction

The results of applying our new correction procedure to 430 published microanalysis data (9, 10) are summarised in Table 1.

Table 1

Model	RMS error %	% of results within 2½% of true conc.	% of results within 7½% of true conc.
New correction procedure	5.3	54	87
Established method	6.8	49	84

Comparison with results obtained by applying the established procedure, see also Table 1, shows that our method is an improvement.

Table 2 shows the results obtained by applying our method to some light element data, oxygen analysis of oxides (11, 12).

Table 2

Model	RMS error %	% of results within 2½% of true conc.	% of results within 7½% of true conc.
New correction procedure	5.6	38	82
Method incorporating full Philibert absorption correction	6.0	46	84

Since the simplified Philibert absorption model used in the established correction procedure is inappropriate for light element analysis (9), for comparison it has been replaced by the full Philibert expression with Duncumb and Melford's constants (13), see Table 2. Out model is at least as good as the alternative method but the full Philibert treatment is, of course, not particularly accurate when applied to heavy element systems (9).

In conclusion, our model must be regarded as a genuine advance towards a universal correction procedure for quantitative electron-probe microanalysis since it does not rely upon a best fit analysis approach which adjusts empirically input parameters. Next it will be developed for use on inclined specimens.

References

1. P. Duncumb and S.J.B. Reed, NBS Spec. Tech. Publ. 298 ed. K.F.J. Heinrich, U.S. Dept. of Commerce, Washington, 133. 1968.
2. J. Philibert, X-ray Optics and Microanalysis. eds. H.H. Pattee, V.E. Cosslett and A. Engstrom, Academic Press, New York, 379, 1963.
3. K.F.J. Heinrich, Trans. of Second Nat. Conf. on Electron Probe Microanalysis, Boston, U.S.A., Paper No. 7, 1967.
4. S.J.B. Reed, Brit. J. Appl. Phys., 16, 913, 1965.
5. G. Love, M.G.C. Cox and V.D. Scott, J.Phys.D : Appl. Phys., 11, 7, 1978.
6. G. Love, M.G.C. Cox and V.D. Scott, J.Phys.D : Appl. Phys., 10, 7, 1977.
7. G. Love and V.D. Scott, to be published.
8. H.E. Bishop, J.Phys.D : Appl. Phys., 7, 2009, 1974.
9. G. Love, M.G.C. Cox and V.D. Scott, J.Phys.D : Appl. Phys., 8, 1686, 1975.
10. G. Love, M.G.C. Cox and V.D. Scott, J.Phys.D : Appl. Phys., 9, 7, 1976.
11. G. Love, M.G.C. Cox and V.D. Scott, J.Phys.D : Appl. Phys., 7, 2131, 1974.
12. G. Love, M.G.C. Cox and V.D. Scott, J.Phys.D : Appl. Phys., 7, 2142, 1974.
13. P. Duncumb and D.A. Melford, X-ray Optics and Microanalysis. eds. R. Castaing, P. Deschamps and J. Philibert, Hermann, Paris, 240, 1966.

A TRANSPORT EQUATION THEORY OF ELECTRON
BACKSCATTERING AND X-RAY PRODUCTION

D. J. Fathers[*] and P. Rez[†]

[*]Department of Metallurgy and Science of Materials,
University of Oxford, Oxford OXI 3PH, ENGLAND

[†]Department of Materials Science and Engineering
University of California, Berkeley, California 94720

To calculate the rate of x-ray production or backscattering a knowledge of the distribution of electrons in depth and velocity is needed. The behavior of the electron distribution function (the probability of finding an electron at a given point with a given velocity) is governed by the Boltzmann transport equation

$$\frac{\partial f}{\partial t} + \underline{v} \text{ grad } f = \iiint v'\sigma'(\underline{v}',\underline{v})f(\underline{v}', \underline{r}' t) - v\sigma'(\underline{v},\underline{v}') f(\underline{v},\underline{r},t)d\underline{v}' \quad (1)$$

where $\sigma(\underline{v}',\underline{v})$ is the probability per unit distance of an electron with initial velocity $\underline{v}'$ being scattered to a final velocity $\underline{v}$. Rather than solve this integro-differential equation directly the usual approach has been to simulate the behavior of many electron trajectories by Monte-Carlo methods (see for example Shimizu, et al. [1]). The transport equation can be simplified by assuming solutions are stationary with respect to time and that the electron beam has infinite extent in the x,y plane (parallel to the specimen surface). Integrating over the azimuthal angle removes it from the equation as the cross section is a function of the difference in azimuthal angles of the incident and scattered states. Dependence on it can easily be calculated by fourier transformation with respect to this variable. It is also convenient to rewrite the equation in terms of fluxes which can easily be related to observed currents

$$I(\theta,E,z) = v \, f(\theta,E,z) \qquad\qquad 2.$$

$$\cos\theta \, \frac{dI}{dz}(\theta,E,z) = \int_0^\pi \int_0^{E_0} [\sigma(\theta,E;\theta'E') \, I(\theta',E',z) \left(\frac{E}{E'}\right)^{\frac{1}{2}}$$

$$3.$$

$$-\sigma(\theta,E';\theta,E) \, I(\theta,E,z)] \sin\theta' \, d\theta' \, dE'$$

In many treatments further approximations are made at this stage. Bethe et al. [2] derive the corresponding Fokker-Plank equation and this has been solved by Brown, et al. [3] numerically using a grid in angle, depth, and integrated path length. It is also usual to expand in Legendre polynomials [4], [5], [6], but applying the boundary conditions is not easy and sometimes only spatial moments in an infinite foil with a source at the center were calculated [4], [5]. Integrated path length was nearly always used instead of energy to describe the electron state and this means that energy distributions were calculated assuming a continuous loss law. This has also been a problem with earlier Monte Carlo calculations [7].

Equation 3 is put into a matrix form by segmenting the angle and energy variables

$$\frac{dI_m^i}{dz} = \sum_j A_m^{ij} \, I_m^j + \sum_{nj} c_{mn}^{ij} \, I_n^j \qquad\qquad 4.$$

where

$$I_m^i = I(\theta_i, E_m, z) \qquad\qquad 5(a)$$

$$A_m^{ij} = \sigma(\theta_i, E_m; \theta_j, E_n) \sin\theta_j \sec\theta_i \, \Delta\theta\Delta E \qquad i \neq j$$

$$A_m^{ii} = (\sigma(\theta_i, E_m; \theta_i, E_m) - \sum_{nj} \sigma(\theta_j, E_n; \theta_i, E_m)) \sin\theta_i \sec\theta_i \, \Delta\theta\Delta E \qquad 5(b)$$

$$c_{mn}^{ij} = \sigma(\theta_i, E_m; \theta_j, E_n) \sin\theta_j \sec\theta_i \qquad\qquad 5(c)$$

Dashen [8] uses a similar approach but derives a nonlinear equation for the matrix relating forward and backward traveling fluxes. As electrons only lose energy and it is also a good approximation to assume that they are only scattered

from one energy level to the next equation 4 can be rewritten as a coupled supermatrix differential equation. The diagonal matrixes represent the elastic scattering and the "absorption" due to inelastic scattering and those on the next lower off diagonal represent the coupling between the energy states due to inelastic scattering

$$\frac{d}{dz} \begin{vmatrix} I_0 \\ I_1 \\ I_2 \end{vmatrix} = \begin{vmatrix} A_0 & 0 & 0 & . & . \\ C_{10} & A_1 & 0 & . & . \\ 0 & C_{21} & A_2 & . & . \\ . & . & . & & \end{vmatrix} \begin{vmatrix} I_0 \\ I_1 \\ I_2 \end{vmatrix} \qquad 6.$$

A further simplification is to assume only one energy loss equal to the incident energy and this means that absorption from the incident state is the only effect of the inelastic scattering. The resulting matrix differential equation has a simple solution

$$I(t) = \exp At \, I(0) \qquad 7.$$

which can be evaluated by diagonalizing the matrix. As there is a symmetry between forward and backward scattering before applying the boundary conditions the eigenvalues and eigenvectors can be partitioned

$$\begin{vmatrix} I_F(t) \\ I_B(t) \end{vmatrix} = \begin{vmatrix} V1 & V2 \\ V2 & V1 \end{vmatrix} \begin{vmatrix} \exp \lambda t & 0 \\ 0 & \exp -\lambda t \end{vmatrix} \begin{vmatrix} V1 & V2 \\ V2 & V1 \end{vmatrix}^{-1} \begin{vmatrix} I_F(0) \\ I_B(0) \end{vmatrix} \qquad 8.$$

This can be solved for $I_B(0)$, $I_F(t)$ subject to the boundary conditions $I_F(0) = \delta_{i,i_0}$, $I_B(t) = 0$ and gives

$$I_F(t) = (V2 - V1V2^{-1}V1) \exp -\lambda t \, V2^{-1}(I + V1 \exp -\lambda t \, V2^{-1} \, V1 \exp -\lambda t \, V2^{-1}) \qquad 9(a).$$

$$I_B(t) = (V1V2^{-1} - V2 \exp -\lambda t \, V2^{-1} \, V1 \exp -\lambda t \, V2^{-1})(I + V1 \exp -\lambda t \, V2^{-1} \, V1 \exp -\lambda t \, V2^{-1})$$
$$9(b).$$

As can be seen if t tends to infinity the backscattered flux becomes

$$I_B(0) = V1V2^{-1} \, I_F(0) \qquad 10.$$

and this is the solution matrix of Dashen's nonlinear equation. The forward and backward traveling fluxes at depth z are:

$$I_F(z) = V2 \exp{-\lambda z} \, V2^{-1} \, I_F(0), \quad I_B(z) = V1 \exp{-\lambda z} \, V2^{-1} \, I_F(0) \qquad 11.$$

The solution for the supermatrix differential equation (6) where many energy levels are considered proceeds in a similar way. The supermatrix is diagonalized in two stages. The first step is to bring it to a block diagonal form analogous to an eigenvalue matrix with the matrices A^m along the diagonal. This can be done by solving matrix commutator equations involving these matrices by diagonalization. The supermatrix eigenvalues and eigenvectors are found by expressing the diagonal matrices A^m in terms of their eigenvalues and eigenvectors and a numerical procedure was devised where the solution for each energy is found using the eigenvector elements of the previous energy. The time taken to diagonalize the supermatrix by this method is proportional to the number of energy levels. The partitioning can then be done and the solution is similar to that given previously except that the matrices now have indices corresponding to energy. The backscattering at energy i is given by

$$I_B^i(0) = \sum_j V1_{ij} \, V2_{j0}^{-1} \, I_F^0(0) \qquad 12.$$

From the energy distribution of electrons at different depths various other quantities such as the rate of x-ray production, the secondary electron and Auger yield can be calculated. If x-rays with absorption coefficient μ are produced at the rate Φ_i by electrons at energy level i and the detector makes an angle θ_D with the specimen normal the observed rate of x-ray production would be

$$\frac{\sum \Phi_i (V1_{ij} + V2_{ij}) \, V2_{j0}^{-1} \, I_F^0(0)}{\left(\lambda_j + \dfrac{\mu}{\cos\theta_D} \right)} \qquad 13.$$

As the depth integration is analytic there is no extra effort in calculating x-ray yield as opposed to backscattering.

In calculations using this theory it was found that 10 angle elements in 90° were necessary for convergence at 10~15 energy intervals were needed for energy distributions of backscattered electrons. For the elastic scattering

a screened Rutherford cross section was used and for the inelastic scattering a cross section was derived from the Bethe loss low using the formula

$$\sigma(\theta_i, E_n; \theta_i, E_m) = \frac{1}{E_n - E_m} \frac{dE}{ds} \left(\frac{E_n + E_m}{2} \right) \qquad 14.$$

was used.

It was found that the results were not very sensitive to small changes in screening parameter or ionization potential. However the theory is quite general and other cross sections could be used. For calculations of distribution of backscattering with atomic number and angle the single energy step theory where only absorption is considered was found to be quite adequate. Probably the most important parameter affecting backscattering is the ratio of elastic to inelastic scattering. This is illustrated in Fig. 1 which shows a plot of backscattering as a function of atomic number. The density was assumed to be $.234Z$ gm cm^{-3} and the mean ionization potential $11.5Z$ eV. The agreement between calculated points and experimental points is good, the discrepancy being mainly due to the simple expressions assumed for density in the calculations. To investigate whether single large angle events are more important than many small angle events the cross section was cut off so that electrons were only scattered by 20° or less. Large angle events appear to be more important in light elements as the inelastic scattering is stronger and so there is less chance that electrons which have been scattered many times will leave the specimen. Fig. 2 shows the variation of backscattering with angle of incidence for 50 kV electrons. At grazing incidence the backscattering is more or less independent of atomic number. This agrees with the experiments of Kanter [7] and Monte Carlo calculations. In Fig. 3 polar plots of backscattering for 30 keV electrons at normal incidence are presented. For thin specimens the flattened distribution dominated by single scattering is apparent, for bulk specimens the distribution follows a cosine law.

The energy dissipation of 30 keV electrons for copper as a function of depth can also be calculated using this approach and this is shown in Fig. 4 with the results of Spencer's [5] calculations scaled to 30 keV. The main discrepancy is that the single energy step calculation decreases too slowly at large depths and is too low at small depths. This is to be expected as there is too much absorption of electrons near the incident energy and not enough absorption of the lower energy electrons at greater depths in the

specimen. If more energy levels are considered this can be corrected and about 5 energy levels are needed for convergence the remaining discrepancy probably being because Spencer did not use the correct boundary conditions. Similar effects due to the treatment of absorption can be seen in calculations of forward and backscattered fluxes from specimens of different thicknesses or of fluxes at various depths in a semi-infinite specimen.

In Figs. 5, 6, and 7, the energy distribution of backscattered electrons for copper, aluminum,and gold is plotted and compared with the experimental results of Darlington [10]. The agreement is good and the calculations show a broadening of the peak of the distribution with a shift in the maximum to lower energies for lower atomic number. This is a result of the ratio of inelastic to elastic scattering, the greater inelastic scattering for light elements giving rise to more energy dispersion.

One advantage of these methods over Monte Carlo calculations is the reduced computer time. For a CDC 7600 angular distributions assuming the single energy low approximation can be calculated in 0.2 sec, energy and angular distributions or x-ray production in 3 sec. and detailed energy spectra at 20 different depths in about 30 sec. This method is readily applicable to layer problems and perturbations can be easily handled. It is also possible in principle to invert the equations to calculate quantities of interest (e.g. thickness of an overlayer) from backscattering observations.

ACKNOWLEDGMENT

REFERENCES

1.   R. Shimizu, T. Ikuta and K. Murata, J. Appl. Phys. 43, 4233 (1972).
2.   H.A. Bethe, M.E. Rose and L.P. Smith, Proc. Amer. Phil. Soc. 78, 573 (1938).
3.   D.B. Brown, D.B. Wittry and D.F. Kyser, J. Appl. Phys. 40, 1627 (1969).
4.   H.W. Lewis, Phys. Rev. 78, 526 (1950).
5.   L.V. Spencer, Phys. Rev. 98, 1597 (1955).
6.   J.H. Jacob, Phys. Rev. 8A, 226 (1973).
7.   H.E. Bishop, Proc. Phys. Soc. 85, 855 (1965).
8.   R.F. Dashen, Phys. Rev. 134, 1025 (1964).
9.   H. Kanter, Brit. J. Appl. Phys. 15, 555 (1964).
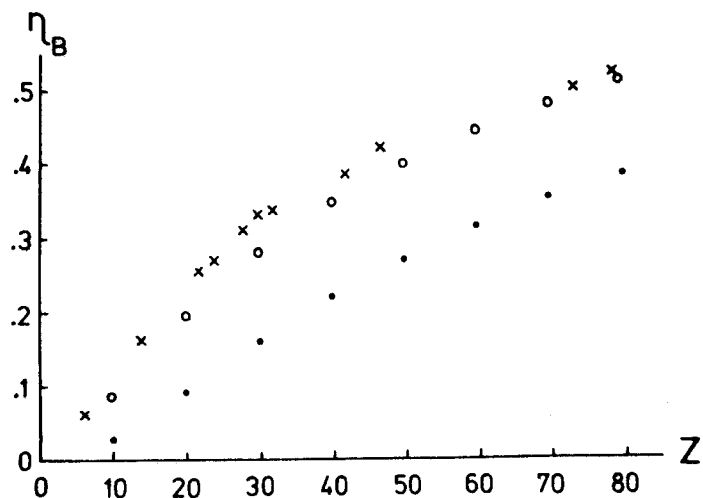10. H. Darlington, J. Phys. D 8, 85 (1975).

Fig. 1 Backscattered fraction η_B as a function of atomic number Z. The open circles 'o' are calculated points, the crosses 'x' are experimental points and the dots '.' are calculated points for scattering of 20° or less.
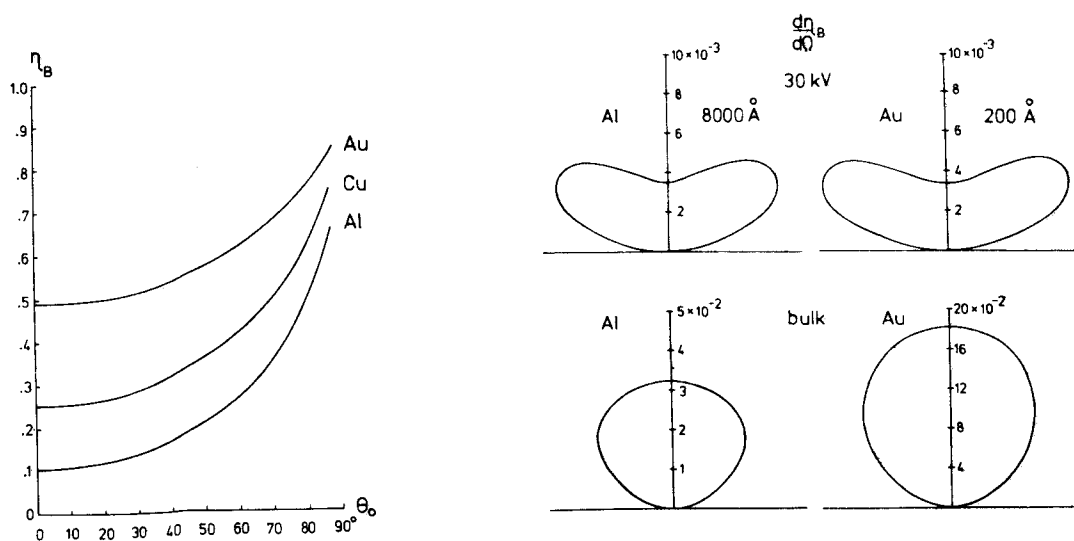

Fig. 2 Backscattered fraction η_B as a function of angle of incidence Θ_0.

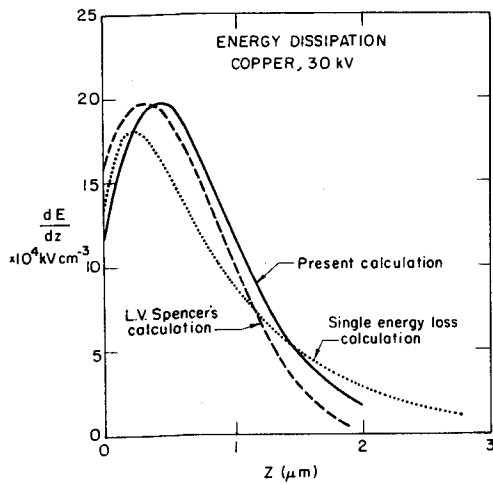Fig. 3 Angular distributions of backscattered electrons.

XBL 781-6971

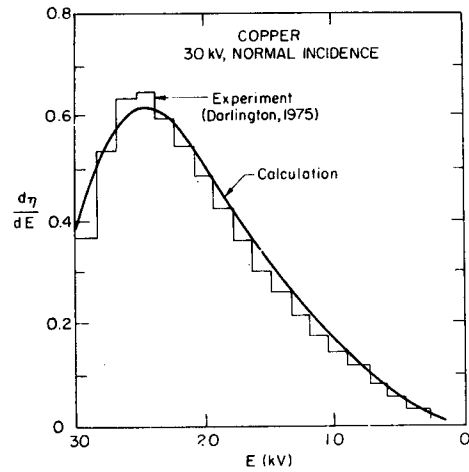Fig. 4 Energy dissipation dE/dz as a function of depth, z, in a bulk specimen.

Fig. 5 Energy distribution of backscattered electrons for copper.
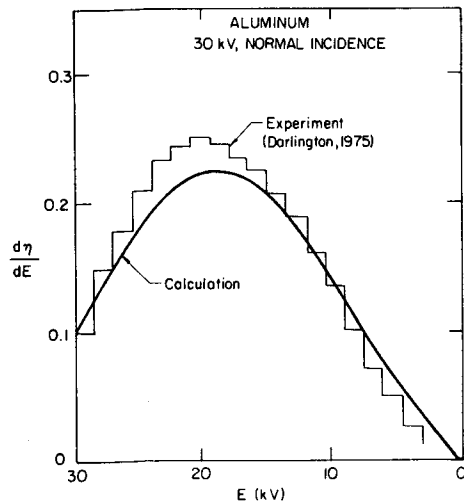
Fig. 6 Energy distribution of backscattered electrons for aluminium.
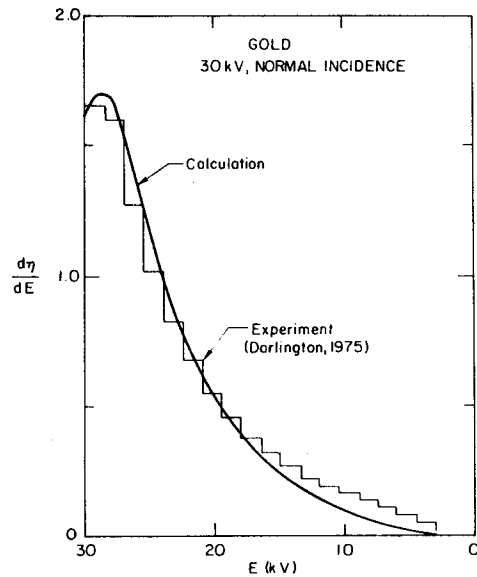
Fig. 7 Energy distribution of backscattered electrons for gold.

XBL 781-6996

Limit Spatial distribution of electrons
in a homogeneous and isotropic target

Claude LANDRON - Physics department

Faculté des Sciences et Techniques -SFAX-

TUNISIA

A point source, placed on the surface of a semi-infinite, homogeneous and isotropic target sends electrons towards Ox, perpendicular to the plane surface of the target (1). In consequence of the collisions between the constituents of the target and the electrons of the incident beam, the latter lose energy and sometimes leave the target by back scattering.

In quantitative electron probe microanalysis it is particularly interesting to state an analytic formulation of the spatial distribution of the electrons with residual energy, and to compare the results with those obtained by means of the simulation technique such as the MONTE-CARLO method (2) .

Let's call $g(x, r, \theta, s)$ the number of electrons situated inside an elementary ring defined by the axial and radial parameters (x, r, dx, dr). This $g(x, r, \theta, s)$ function verifies BOLTZMANN'S transport equation (3) :

$$\frac{\partial g}{\partial s} + \frac{\partial g}{\partial x} \cos \theta + \frac{\partial g}{\partial r} \sin \theta = N\sigma_E g - N \int g (\cos \theta') \sigma (\eta) d\omega$$

In this expression $\sigma = \sigma_E f(\theta)$ is the differential cross section scattering.

The evolution of the electron distribution in the target is the solution to this equation which is subject to :

1° The boundary conditions of a semi-infinite specimen.

2° The initial conditions for $E = E_o$.

$$g(x, r, \theta, s) = \delta(x) \delta(r) \delta(\theta) \delta(s)$$

Owing to the isotropicness of the electronic paths at the end
of the trajectories, a FOURIER transformation of the transport equation
permits a decomposition of the latter into two limit equations. The first
of which exlusively depends on the radial variable and the second on
the axial variable.

The electronic distributions at the end of the trajectories are
then as follows :

$$g(x, r, s) = f(x, s) \times h(r, s)$$

These limit distributions being calculated with a method developed
by LOEVE (4) in the theory of probabilities, which consists in determinir
the conditions necessary and sufficient enough for a great number of
variables - linked or not linked - to converge.

Determining the characteristic functions of the distributions of
electrons in the target leads to the following statement related to the
axial and radial distributions in an infinite target :

$$f(x, s) = \frac{(s-x)^{\nu-1} \exp(-\frac{s-x}{b})}{b^{\nu} \Gamma(\nu)}$$

$$h(r, s) = \frac{\exp(-\frac{r^2}{2 <r^2>})}{\sqrt{2 \pi <r^2>}}$$

The b and ν parameters are connected at the first moments of the
$f(x, s)$ distribution by the relations :

$$b = \frac{<x^2> - <x>^2}{s - <x>}$$

$$\nu = \frac{(s - <x>)^2}{<x^2> - <x>^2}$$

The $<x>, <x^2>, <x>^2$ moments are obtained by an integration
of the transport equation on the whole space by multiplying the cor-
responding variable by the appropriate power.

Now remains the problem of the distribution of the electrons in a semi-infinite target. This is treated by considering the conditions as to the limits imposed by the surface of the target which plays the role of a transmission barrier in such a way that the electrons that cross it once leave it definitively. Owing to the linearity of the transport equation with regard to x and s, the limit distribution of the electrons in a semi-infinite target is this (fig. 1).

$$g_{si}(x,r) = \frac{\left[(s-x)^{\nu-1} \exp\left(-\frac{s-x}{b}\right) - (s+x)^{\nu-1} \exp\left(-\frac{s+x}{b}\right) \right] \exp - \frac{r^2}{2<r^2>}}{b^{\nu} \Gamma(\nu) \sqrt{2} \pi <r^2>}$$

The surface of equal probability of presence of the electrons diffused by a semi-infinite target for a given loss of energy have the following equation (fig.2) :

$$x^2 = 2 <r^2> \text{Log} \left[\frac{k f_{si}(x)}{\sqrt{2 \pi <r^2>}} \right]$$

These distributions of the electrons in the semi-infinite targets permit to visualize the scattering of a beam of electrons in a homogeneous and isotropic target ; the numerical results associated with these distributions show good agreement with the characteristic parmeters of the distributions determined with the aid of the MONTE-CARLO method (5).

This model permits to tackle in the most general way the problem of the multiple scattering of particles - whether they be charged or not - whose interactions with the constituents of the targets are subject to well defined assumptions.

REFERENCE :

1) C. LANDRON, M. ANDREANT, P. AZOU : Eighth
   International Conference on X Ray optics and
   Microanalysis, Boston, 1977.

2) MAURICE F. Journal de Microscopie, 1972, 15, 3

3) LEWIS H.W. ; Phys. Rev. 1950, 78, 526.

4) LOEVE M. Jour. Math. Pure et Appl., 1945, 24, 32.

5) BISHOP H.E., Brit. J. Appl. Phys.? 1968, 1, 673.
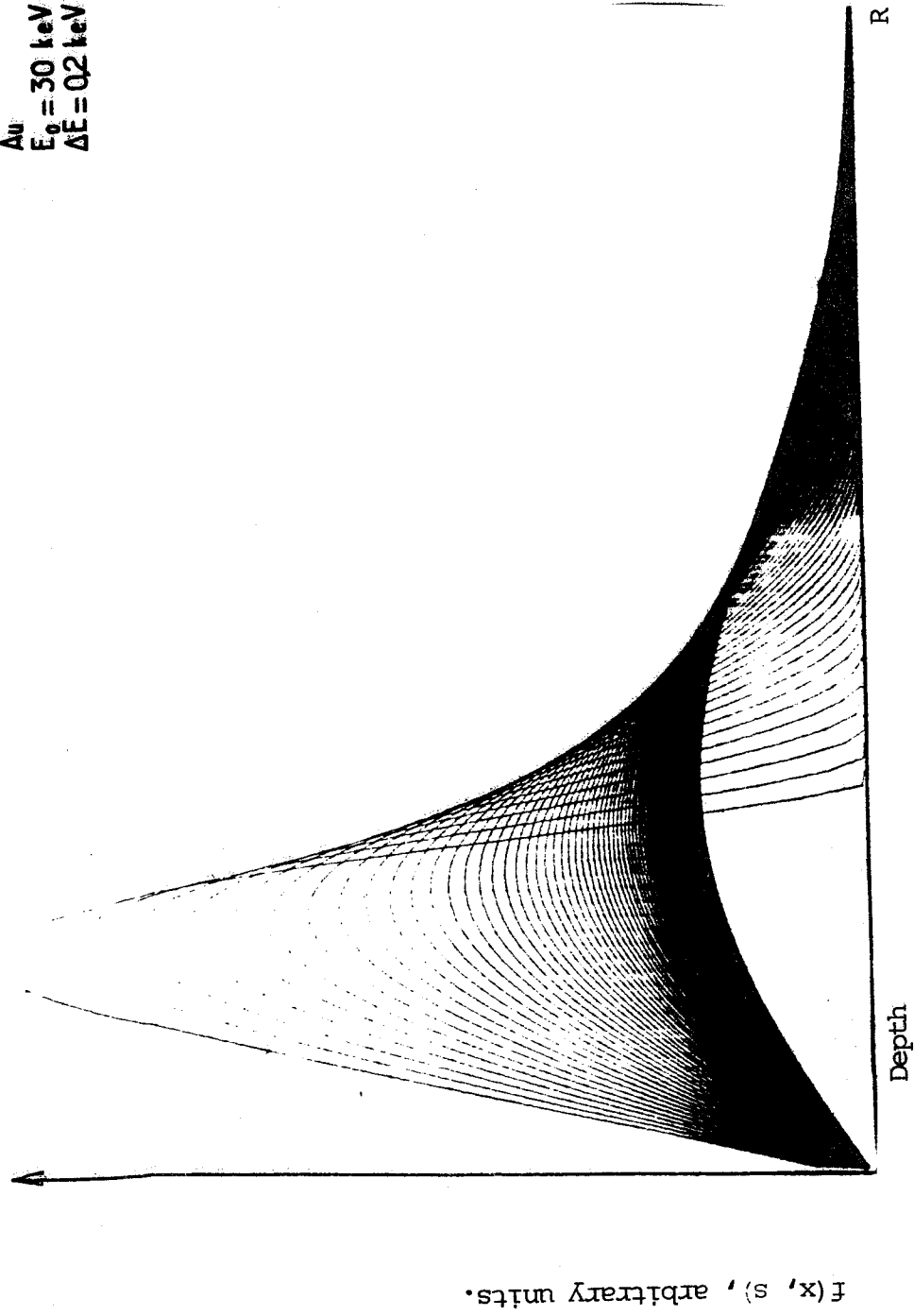
Fig.1 Distribution with residual energy of electrons in a semi-infinite gold target

Au
E₀ = 30 keV
ΔE = 0.2 keV

gold surface incident beam
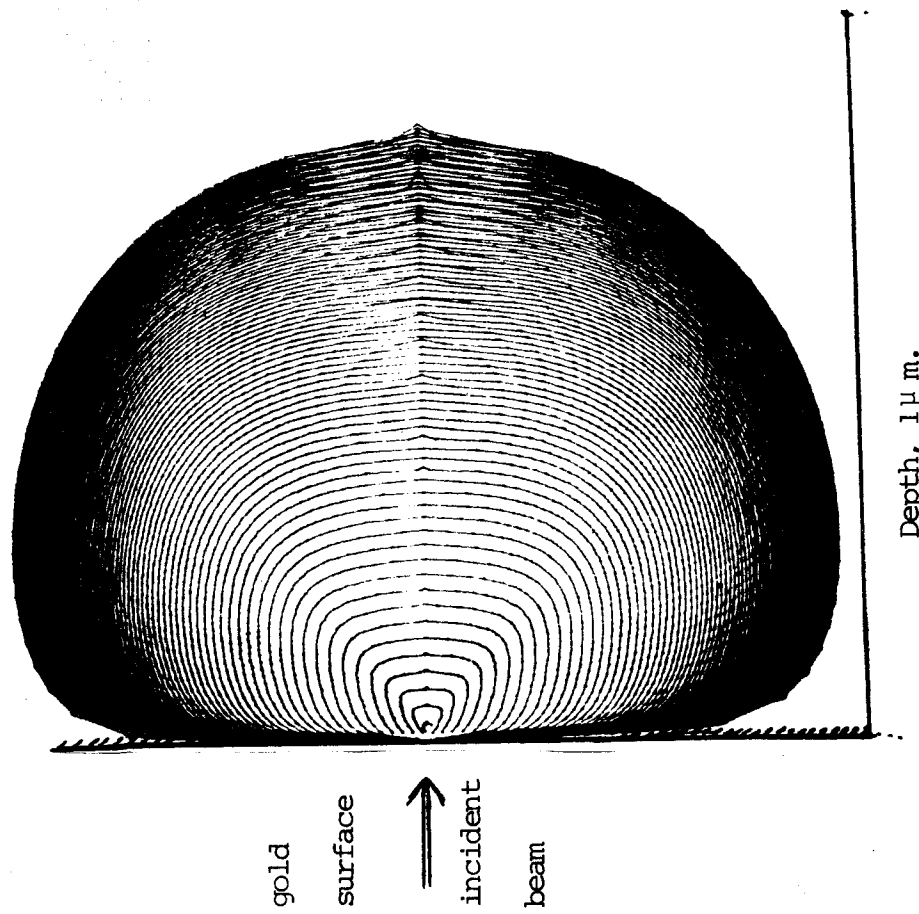
Depth, 1 μm.

Fig.2   Surfaces of equal probability of présence of electrons in a semi-infinite gold target.

EFFECT OF ELECTRON INCIDENCE ANGLE ON QUANTITATIVE CORRECTIONS IN ELECTRON PROBE MICROANALYSIS

W. Robinson and J.D. Brown

Faculty of Engineering Science and
The Centre for Interdisciplinary Studies in Chemical Physics
The University of Western Ontario
London, Canada   N6A 5B9

Many different geometries of electron beam incidence angle Φ and x-ray take-off angle ψ exist in commercially available Electron Probe Microanalysers. The increased use of Scanning Electron Microscopes with energy dispersive X-ray spectrometers has further expanded the geometries routinely used during quantitative analysis. At the same time, most studies of correction equations for quantitative analysis have been performed on instruments in which the electron beam strikes the specimen perpendicular to the specimen surface, leaving unanswered the question of how the corrections vary as the electron incidence angle varies.

The two important angles in establishing the magnitude of the corrections are shown in Figure 1. Changes in Φ affect not only the production of X-rays as a function of distance from the specimen surface, but the magnitude of electron backscattering as well. ψ must be accurately known to allow proper calculation of the absorption correction. Of the two factors, the effect of Φ is least well known.

Reed[1] found that the backscattering coefficient changes significantly in changing Φ from 90° to 45°. To correct f(x) values for $\Phi \neq 90°$, Bishop[2] suggested the simple factor $(1 - 1/2 \cos^2 \Phi)$ which has since been shown to be inaccurate.[3,4]

Monte Carlo techniques have been used to study the effect of Φ on backscattered electrons[5] and the interaction volume. Duncumb[6] has reported the variation of calculated $\phi(\rho z)$ curves as a function of Φ shown in Figure 2 in which the maximum in the curves shifts to smaller depths with decreasing Φ as expected.

Measurement of depth distribution of X-ray production, $\phi(\rho z)$ curves, as a function of electron incidence angle, can establish the effect of Φ on both the absorption and atomic number effects.[7,8] Measurements on specimens previously used by Brown and Parobek[8] have been performed on an AEI SEM II electron microprobe using a special sample stage to allow specimen tilt. The electron energies used varied from 20 to 30 KeV. These energies have been verified, using an electrostatic voltmeter to check the potential on the electron gun.

$\phi(\rho z)$ curves measured from the same sandwich specimen composed of a zinc tracer in a silver matrix are shown in Figure 3. The angles are

$\Phi = 90°$ and $\Phi = 60°$. The $\phi(0)$ values are taken as the ratios of intensity from the tracer layer to that from the pure element with the same value of Φ. The effective thickness of the tracer layer increases as Φ decreases but this change does not entirely account for the increase in $\phi(0)$ values. The shift of the interaction volume to smaller depths also contributes. The peak of the $\phi(\rho z)$ curves shifts to smaller depths with decreasing angle. This change is greater than would be predicted by the correction factor suggested above. The effect of Φ on $\phi(\rho z)$ curves and hence the absorption correction will be examined in detail.

References

1. Reed, S.J.B., J. Phys. D. (Appl. Phys.) 4, 1910 (1971).

2. Bishop, H.E., Proc. Phys. Soc., 83, 435 (1964).

3. Brown, J.D., "Electron Probe Microanalysis", Suppl. to Advances in Electronics & Electron Phys. p. 45 (1969), Academic Press.

4. Bishop, H.E., J. Phys. D. (Appl. Phys.) 1, 673 (1968).

5. Shimizu, R., Ikuta, T. and Murata, K., J. Appl. Phys. 43, 4233 (1972).

6. Duncumb, P., Electron Microscopy and Analysis, W.C. Nixon, ed., Conf. Series 10, 132 (Inst. Phys., London 1971).

7. Castaing, R. and Henoc, J., Proceedings of the Symposium on X-ray Optics and Microanalysis, Orsay, 120, 1965 (Hermann, Paris, 1966).

8. J.D. Brown and L. Parobek, Proceedings of the Sixth International Conference on X-ray Optics and Microanalysis, University of Tokyo Press, 163 (1972).
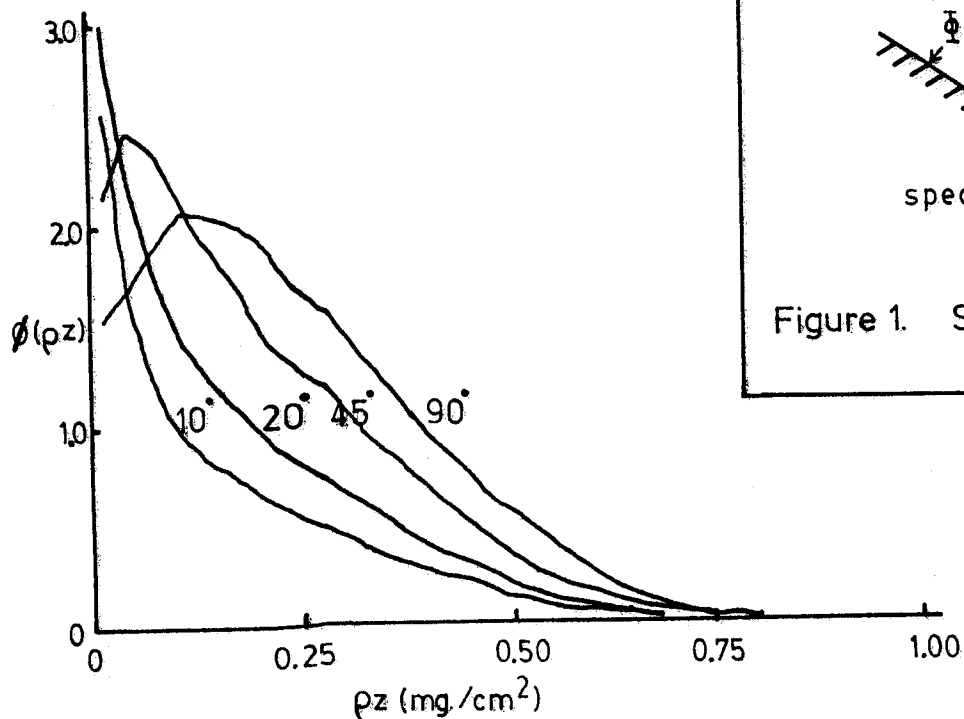
Figure 2. Distribution of X-ray production with depth, ∅(ρz) for copper at 20kV and various angles Φ. From Duncumb[6].

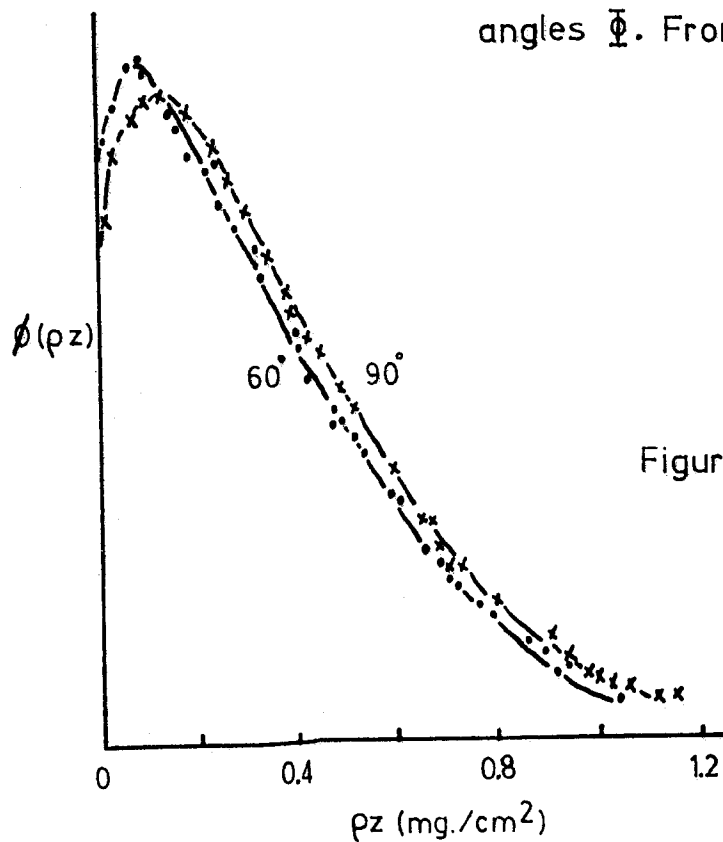Figure 1. Specimen geometry.

Figure 3. Measured ∅(ρz) curves for zinc tracer in silver matrix at 25kV and two angles of Φ.
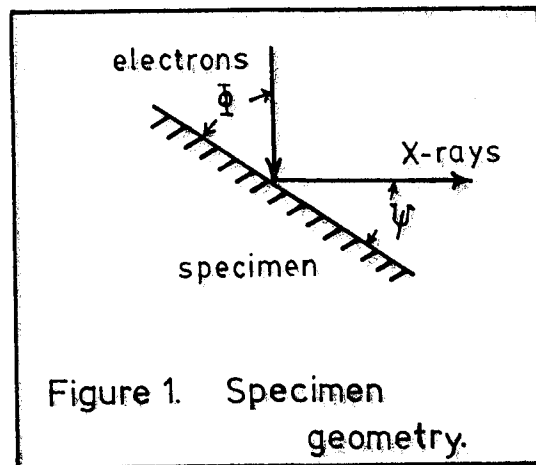
INFORMATION, PROBABILITY, AND MICROPROBE ANALYSIS

Norman M. Walter, Materials Engineering, The Boeing Vertol Company

As is well known, chemical analysis by gravimetric methods is based on the separation of individual atoms from a sample volume, with subsequent weighing to determine the mass fraction present. It would be difficult to perform this type of chemical analysis in outerspace. On the other hand, excitation of the individual atoms by use of electrons, or other suitable radiation, permits one to determine the mass of a specific element present in a specimen volume by measuring the Intensity of the characteristic radiation emitted.

The basic relationships for performing a microprobe analysis were set forth by R. Castaing in 1951(1), and need not be detailed here. Subsequent theoretical work has been concerned with methods of data correction to bring experimental results of Intensity measurement into concordance with the known mass fraction of standards, and thus be able to measure unknown quantities with reliability. The techniques have centered on the determination of three correction factors: 1. Atomic Number; 2. Absorption; and 3. Fluorescence. Again it is not necessary to detail the varied methods which have been specified and are currently being practiced. Great strides have been made during the past twenty-seven years, and yet the approach to accuracy has been slow. The quest continues for the "General Solution" which will give the closest value to the "intuitive" relationship

$$Ca = Ia/I(A) = k = (Pa\text{-}Ba)/(P(A) - B(A)) \qquad (I)$$

This preliminary report is given to review the development of a slightly different approach to the problem of radiation measurement, which has been formulated over the past twenty years. Although significant results have been obtained in areas of x-ray diffraction, this is the first exposition of a complete outline of its application to microprobe analysis. It must be emphasized that these results are of a preliminary nature, and much work is planned to investigate the possible validity of the proposed relationships.

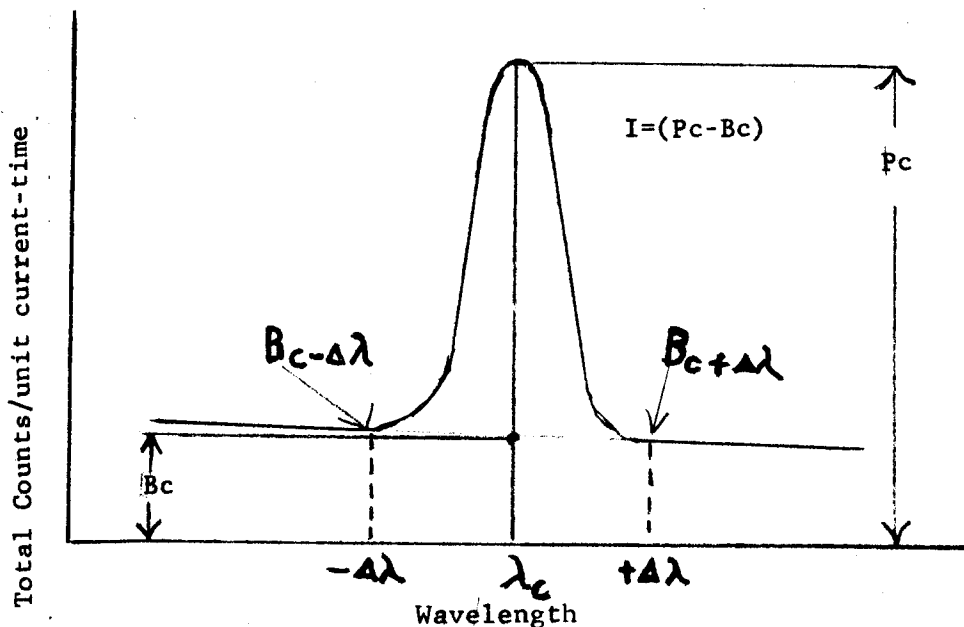Referring to Figure 1. we find the basic definition of Intensity.

Figure 1.

where Pc is the total number of counts recorded at the characteristic wavelength, λ_c,

and Bc is the total number of counts from the white radiation generated by the specimen, characteristic radiation from other elements, and system noise at the same wavelength. System noise consists principally of radiation entering the energy window, i.e. cosmic, and random pulses in the equipment that are accepted by the detector circuitry. The value of Bc cannot be measured directly. A possible measure of it can be obtained by measuring the background at $\lambda_c - \Delta\lambda$ and $\lambda_c + \Delta\lambda$, and extrapolating to a value at λ_c. In addition, it is not possible to determine whether a photon detected at λ_c was generated by an atomic inter-action with the radiation or by an interaction with the individual electrons of the specimen. Therefore, to be able to assign a possible value to Ic, a minimum of three pieces of information are needed. These are $B_{\lambda_c - \Delta\lambda}$, Pc, and $B_{\lambda_c + \Delta\lambda}$. Since one is not able to distinguish between a photon at λ_c generated by an atom and one generated by the background, we can only say with a certain probability, P, that the photon was indeed a characteristic one. It can be definitely stated that a pulse did occur if it is detected. The problem is to find a function which will be related to the mass of an atom species in the specimen. The chosen function must vary from 0 for 0% concentration, to 1 for 100% concentration. The following function was selected as having reasonable potential to describe our relationship.

$$P = \int_{-\infty}^{+\infty} \frac{1}{2^x} dx = 1$$

In addition it must be positive. On integration the probability becomes:

$$P = 1 - \frac{1}{2^{+\infty}} = 1 \qquad\qquad II$$

The measure of the value of e^x is taken to be Pc/Bc, the Peak-to-Background ratio. Then

$$P_c = 1 - \frac{B_c}{P_c} = \frac{P_c - B_c}{P_c}$$

This gives us the probability that a given detected photon was a characteristic one.

The conditions of the experiment are chosen such that the accelerating voltage is constant, and a constant specimen current is collected for a fixed time in-terval. For example: 0.1 microamp. at 15 KV for 100 sec. Preliminary data were collected for copper and zinc in five brass standards and "pure" copper and zinc. A plot of the weight fraction vs. P/B is shown in Figure 2. It is seen that the data are fairly linear with a maximum P/B for each element.
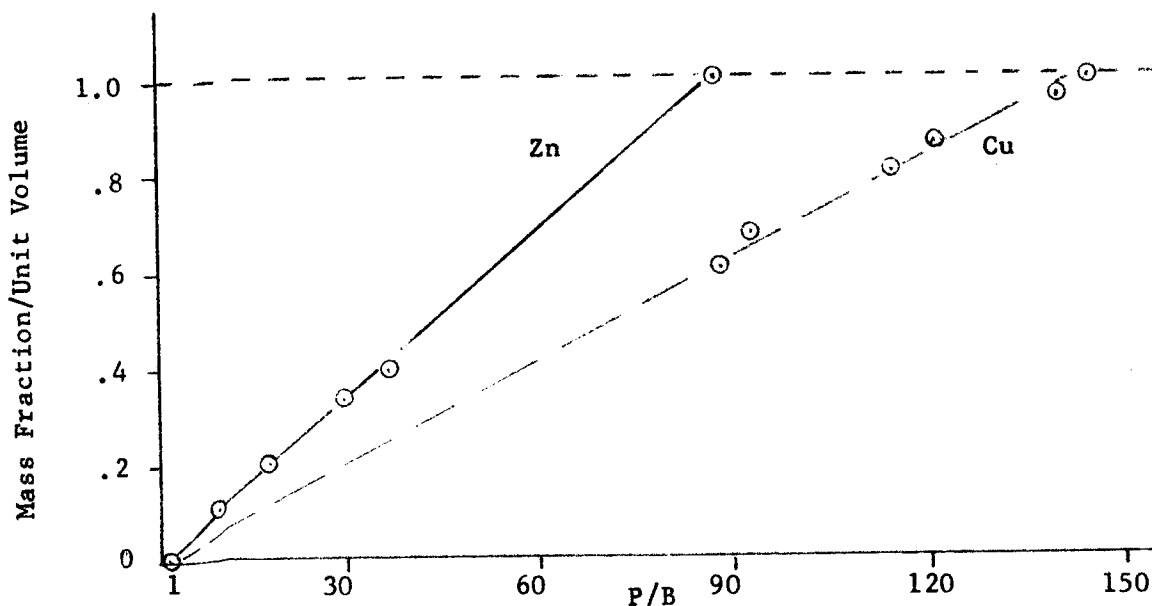

Figure 2.

The results of this experiment were used to derive a relationship between the probability, P, and the mass fraction/unit volume. This was achieved by modifying our original definition of P in Eq. II to

$$P_P = \int_0^{x_{max}} \frac{1}{e^x} dx = 1 \qquad \text{III}$$

The final relationship between the probability and the concentration was found to be the following:

$$y_i \text{ (mass fraction)} = \frac{\left(\frac{P}{B}\right)_{x_i} - 1}{\left(\frac{P}{B}\right)_{p_i} - 1} = \frac{\frac{(P_{x_i} - B_{x_i})}{B_{x_i}}}{\frac{(P_{p_i} - B_{p_i})}{B_{p_i}}} \quad \begin{array}{l}(Alloy)\\[20pt](Pure)\end{array}$$

$$y_i = \frac{P_{x_i} - B_{x_i}}{P_{p_i} - B_{p_i}} \times \frac{B_{p_i}}{B_{x_i}} \qquad \text{IV}$$

The function is hyperbolic and relates the probability of detecting a characteristic photon to its mass fraction/unit volume. An interesting sidelight is that the ratio P-B/B as a function of take-off angle is constant, within the accuracy of their experiments, as shown by Abelman and Jones(2). This should also hold for any characteristic line above a background, i.e. P-B/B is a constant as a function of $\emptyset$.

A more complete expression relating the mass fraction to to the "k" factor is the following:

$$y_i = \sum_{j=1}^{i} \alpha_{ij} N_i = \frac{P_{x_i} - B_{x_i}}{P_{p_i} - B_{p_i}} \times \frac{B_{p_i}}{B_{x_i}} \qquad \text{V}$$

where α_{ij} are the interaction coefficients, N_i is the mass fraction of the ith atom species, and $\sum N_i = 1$. If there are no interactions between each of the atoms, then all of the α_{ij} should be equal to zero when $i \neq j$.

To assess the effect of atomic number on the derived expression IV, measurements were made on "pure " copper and "pure" gold giving some insight to the possible magnitude of the background factor. The results are the following:

BG of	Cu(Kα)	Au(Mα)	on
	2524	154	Cu
	8247	718	Au

Future work will now be concerned with the development of better Peak-to-Background ratios with the present instrument, and the collection of data from known specimens. Additional data and suggestions will be presented to support the direction which the present investigation has taken.

1. Castaing, R., Doctoral Thesis, University of Paris, 1951

2. Abelman, R.A., and Jones, R.E., Pitts. Conf. on Anal. Chem. and Spec., February 1966

Quantitative Microanalysis
with Si Detector and CAMAC Automated Microprobe

J.C. Rucklidge

Department of Geology, University of Toronto

A basic Etec Autoprobe fitted with a Kevex Si detector has been interfaced to a PDP11/10 computer with 28k memory through an interface consisting of CAMAC modules. The three stepping motors for stage control are driven from Borer modules, which have been modified slightly to allow manual joystick control as well as computer controlled operation. Control of lens current is from a Kinetic Systems 8 channel 12 bit D/A converter and measurement of beam current and probe is through a K.S. 16 channel stepping 11 bit A/D converter. The signal from the Si detector is processed via a Canberra linear amplifier and LeCroy QVT multichannel analyser. This latter, which is NIM module, has a CAMAC interface which lets it be started, stopped, read out, written into and cleared by the computer. The display of the memory is provided through a laboratory oscilloscope. Beam blanking control is provided through one line of a CAMAC output register, and detector count rates are monitored by one channel of a KS 6 channel 24 bit CAMAC scaler. A CAMAC live time clock completes the instruments required to operate the system. Fig. 1 is a schematic of this layout. The Branch Highway, shown in this diagram, is the CAMAC data transfer route which connects to Branch controller, and ultimately to the PDP11 Unibus.

Two RK05 disk drives are included in the computer system, which is run under the RT-11 operating system. Programming is done mainly in Fortran

with minor use of Assembler and advantage is taken of the overlaying
options provided by RT-11 for running programmes which require memory in
excess of that available in the computer.

Operation

The mode of operation of the instrument is dominantly on suites of similar
minerals for which good quantitative analyses are required, but which
rarely present any problems in the identification of the elements present.
Consequently little attention is given to the display and interpretation
of spectra, and the normal mode of operation is to select a point for
analysis, collect a spectrum, and store it for subsequent reduction.
Remote control and sensing of the beam current and count rates allow for
collecting spectra at a constant count rate rather than the more conven-
tional constant probe current. We have found that maintaining the count-
rate constant gives superior analyses, probably because operating
conditions for the detector, which is the most sensitive part of the
system, remain constant. Use is made of a Faraday cage to provide cali-
bration measurements from which the probe currents can be calculated for
all spectra. Element standards may also be used but stored default
standard values are usually adequate. It is however necessary to establish
the calibration of the detector with each run, so that channel numbers
and X-ray energies are accurately related.

Data Reduction

Data reduction is performed off line by a modified version of EDATA (Smith
1975). The modifications are to adapt it to run on the minicomputer and to

allow for the rather specialised method of collecting and storing spectral and beam current data. The reduction is relatively slow, taking 3-4 minutes per spectra, but out of this come high quality analyses with positive data on 21 elements each time. The elements are Na→Zn, Zr, Ba, which are selected for their geochemical affinities. Programmes are also available for subsequent interpretation of data through plotting, tabulation etc.

Conclusions

The flexibility offered by CAMAC interfacing and a superior Fortran based operating system, gives rise to a wide range of hardware and software possibilities in running laboratory instruments. The system described above is only one third of the total configuration; the other two thirds consisting of a Siemens SRS XRF spectrometer, and another energy dispersive detector on an ARL-EMX microprobe. All three of these instruments may be operated simultaneously, and even under these conditions, the computer is underused in time, though memory limitations prevent much expansion with the present CPU. When time and money permit, the CPU can be updated to larger and faster model, while the rest of the system, both hardware and software, will be unaffected by the change. It is precisely this built in non-obsolescence which has paid and will continue to pay dividends.

Reference

Smith, D.G.W. 1975. An approach to fully quantitative energy dispersive electron microprobe analysis. Proc. M.A.S. Conf. Las Vegas. Paper #21.
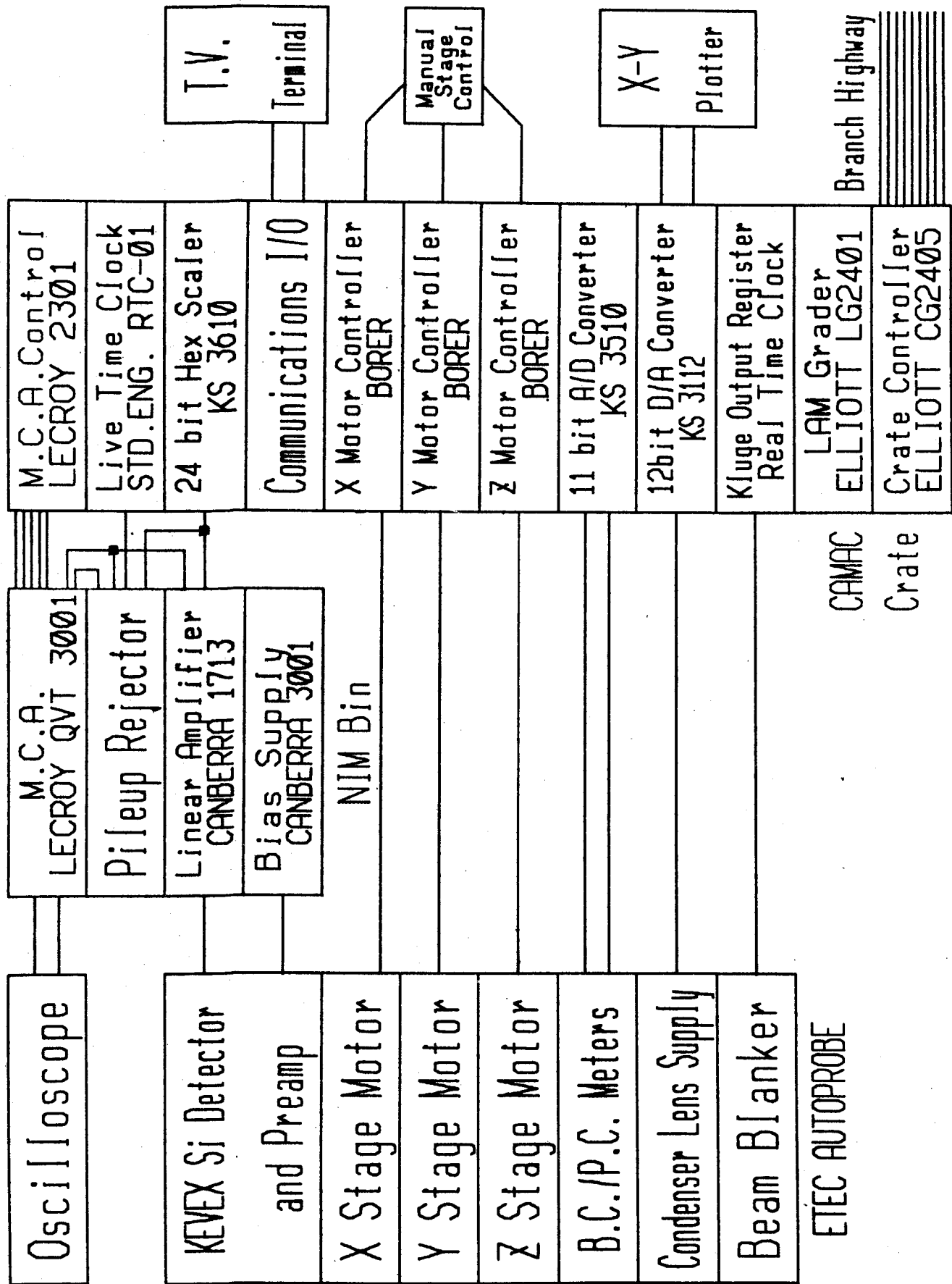
Fig. 1. Schematic layout of the essential components and interconnections for automatic control and F.D.A. data collection of an ETEC Autoprobe, using the CAMAC interface standard.

AN ENERGY DISPERSIVE TECHNIQUE FOR THE QUANTITATIVE ANALYSIS OF CLAY MINERALS BY THE ELECTRON MICROPROBE

D.G.W. Smith and P.A. Cavell, Dept. of Geology, University of Alberta
Edmonton, Alberta, Canada T6G 2E3

Although the electron microprobe has become the principal tool for investigating mineral compositions, one large group, the clay minerals, has remained almost untouched by the technique. Clays are usually extremely fine-grained with many particles appreciably less than 1 μm in their largest diameter. This property alone makes it difficult to prepare mounts which are suitable for quantitative microprobe analysis. In rare cases, where particles are relatively large, a mount can be made by impregnation with an epoxy resin followed by careful grinding and polishing. In most cases, however, particles are too fine-grained and too soft for such preparation and a means had to be found of preparing an aggregate of grains for analysis. Attempts to analyse films of oriented clay particles such as those used in X-ray diffraction studies, proved totally unsuccessful because they could not be made sufficiently conductive by coating with carbon or even gold. A new type of mount was therefore developed in which colloidal graphite is mixed with the clay. This additive renders the films conductive and permits analysis by normal microprobe methods.

The <1 μm clay fraction is obtained by standard settling techniques [1] after disaggregation of the sample in distilled water using a common blender and, where necessary, an ultrasonic vibrator of the probe type [2]. The <1 μm fraction was chosen to minimise the amount of impurities which are present in most clays in the form of relatively coarse grains of other minerals. Flocculation can be prevented either by adding a chemical dispersant [3] [(NaPO3)6] or by repeated washing and centrifuging to remove electrolytes. A known weight of the <1 μm fraction in suspension is then combined with a predetermined amount of colloidal graphite also in suspension. Tests showed that the amount required to give adequate conductivity is usually in the range 10 - 12 wt.% (graphite). The mixture is then deposited by suction onto a porous ceramic disc [4,5]. These are cut from unglazed tile and ground to a thickness of 3 mm. Deposition is effected by means of a specially designed suction apparatus illustrated in figures 1 and 2. Although this device fits over a standard suction flask and is operated using a line vacuum, it was carefully machined and balanced so that it can also be used in a centrifuge. Before being removed from the suction device, the film is washed with 5 ml of distilled water to remove any dispersant and other soluble ions present in the residual liquid still trapped by the clay. The film is then dried for a few minutes before being inverted on a fluorotelomer-coated glass slide, where it is left to air dry completely. The weight of the ceramic disc (∿2.5 gm) is sufficient to keep the film from cracking and peeling as it dries, and the fluorotelomer prevents it from sticking to the glass, while still giving a smooth upper surface. When dry, conductivity of the film is checked using an ohmeter on the MΩ range. For the operating voltage and probe current used, a resistance of 50 MΩ from edge to edge of the disc is entirely adequate to prevent charging. The sample is now ready for microprobe analysis. It can also be used for X-ray diffraction studies, should these prove necessary or desirable, the graphite acting as a convenient internal standard for accurate measurement of peak positions.

Figure 1: Photograph of the suction device mounted on a standard vacuum flask, accompanied by clean and coated discs, the microprobe mount, and the graphite and fluorotelomer used.
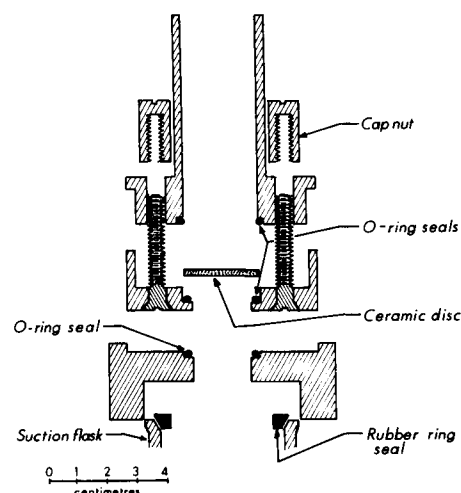
Figure 2: Exploded cross-section of the suction device, showing the ceramic disc and the well into which it fits. The O-ring in the upper section just seals the upper edge of the disc when the screws are tightened.

In defocussed beam analysis, more than one type and composition of particle is excited by the electron beam. In such cases normal correction procedures for matrix effects are inapplicable and special procedures must be adopted that involve separate corrections for matrix effects in the various phases present.[6] Although such procedures are essential for accurate results when individual particles make up a relatively large part of the analysed volume, they become progressively less important as particle size is reduced and randomness on an atomic scale, as occurs in a glass, is approached. In the analytical method reported here a volume of about $2 \times 125 \times 125$ μm^3 is analysed by rastering a focussed beam over the sample surface. This volume contains more than 300,000 particles of clay, with colloidal graphite filling the interstices. At any instant in time, the analysed volume will contain about 50 clay particles with interstial graphite. Figure 3 shows SEM photographs which indicate that the distribution of clay and graphite in the film is rather homogeneous and that it forms a compact mass. These characteristics render the special procedures adopted for defocussed beam analysis unnecessary and allow matrix corrections to be applied sufficiently accurately by assuming homogeneity. Furthermore, the energy dispersive technique used does not suffer from the spectrometer defocussing effects encountered in wavelength dispersive analysis when the beam is rastered over such an area.
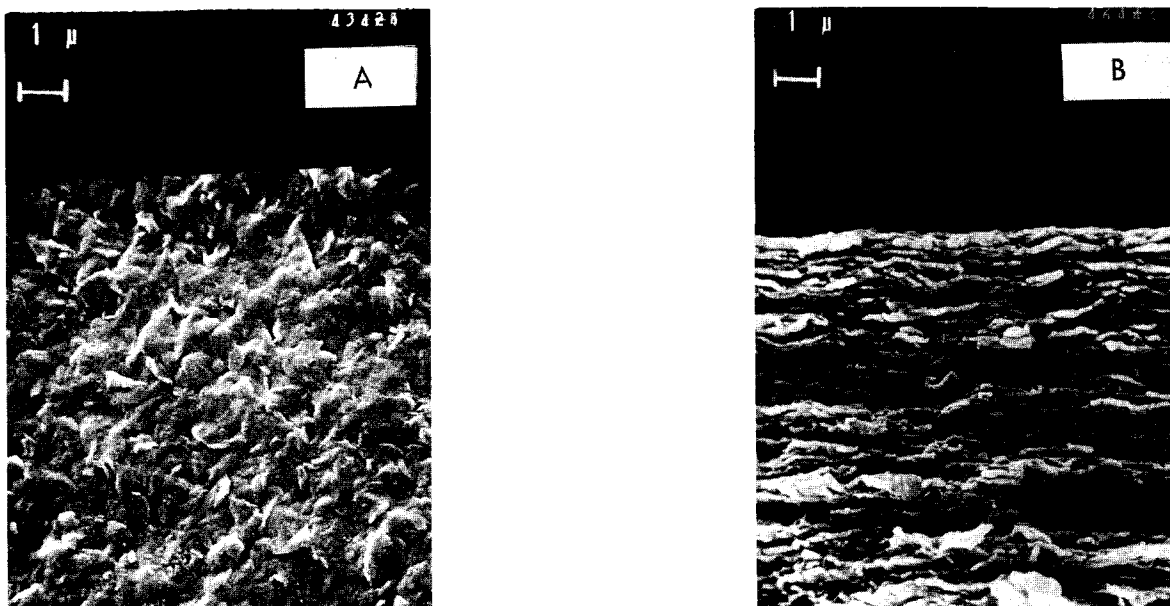
Figure 3: SEM photographs of A) top surface of a smectite film and B) edge view of the upper part of a smectite film. Note that in neither case is there any obvious seggregation of clay and graphite.

Twenty-two elements (Na to Zn incl. plus Zr and Ba) are determined simultaneously by energy dispersive techniques described by Smith[7]. An operating voltage of 15 kV is used with probe currents of about 20 nA. Data is processed through the FORTRAN IV program EDATA[8] which, in addition to integrating peak intensities and making full matrix corrections (atomic number, absorption, characteristic and continuum fluorescence), accurately calculates background throughout the spectral range of interest, strips escape peaks, makes deadtime corrections, deals rigorously with complex overlap possibilities, determines system resolution, corrects for miscalibration in the energy of spectra acquired and takes into account any fluctuations in probe current during analysis.

Special subroutines are used to deal with elements known to be present but which lie outside the analytical range of the technique. These elements are principally H, C and O, but may sometimes include Li. The amount of colloidal graphite added is entered, the oxygen equivalents of metals determined by the analysis computed and the difference between the total of all of these elements and 100% is assigned to water. All of these calculations are reiterated during each loop of the correction procedure. Entry of carbon values which were deliberately in error by as much as 50% was found to have a very small effect on the final results. This is so because replacement of carbon by water in the calculations has minimal effect on the size of ZAF corrections. The colloidal graphite suspension used ("Aquadag") contained small amounts of impurities. These were determined on a film of the graphite, entered into the program and subtracted from the results after correction.

In the treatment of clays to obtain particular size fractions, a chemical dispersant such as $(NaPO_3)_6$ is commonly added. When this was done during preparation of clays by the techniques outlined here, it became clear that a significant amount of phosphorus remains on the clays and it was found that this cannot be removed even by persistent washing. The problem is, however, avoided by using an ultrasonic vibrator followed by repeated washing and centrifuging to remove electrolytes that cause flocculation.

The water and hydroxyl content of clay minerals is variable, depending not only on the species and its composition, but also on the preparation techniques and to some extent the temperature and humidity in which it is stored. It was found that water contents calculated for clays by the method outlined above varied with the details of the analytical technique used. Thus, if the beam was rastered over a larger area, thereby decreasing the electron flux/unit volume/sec, the indicated water content tended to increase (Table 1). Furthermore, different clay mineral species behaved in somewhat different fashions. Thus, smectites which can contain 1, 2 or 3 layers of water molecules in their structure depending on the conditions under which they are prepared and stored, rapidly lose water even when the area over which the beam is rastered is very large. However, under the analytical conditions selected, they appear to stabilize with an amount of water equivalent to one structural layer.

Table 1

VARIATION OF INDICATED WATER CONTENT WITH RASTERING AREA
FOR KAOLINITE, MACON, GEORGIA

	Computed wt. % oxides				Elements recalculated water-free, to 100%				
	$500{\times}500\mu m^2$	$125{\times}125\mu m^2$	$31{\times}31\ \mu m^2$	$15{\times}15\mu m^2$	$500{\times}500\ \mu m^2$	$125{\times}125\mu m^2$	$31{\times}31\ \mu m^2$	$15{\times}15\mu m^2$	
SiO_2	45.79	47.14	49.77	49.13	25.46	25.50	25.40	25.53	Si
Al_2O_3	34.76	35.70	37.87	37.34	21.88	21.87	21.88	21.97	Al
Fe_2O_3	0.41	0.37	0.45	0.36	0.34	0.30	0.34	0.28	Fe^{3+}
MgO	0.49	0.55	0.54	0.58	0.35	0.38	0.36	0.39	Mg
CaO	0.49	0.49	0.52	0.48	0.42	0.40	0.41	0.38	Ca
Na_2O	0.05	0.05	0.05	0.05	0.04	0.04	0.04	0.04	Na
K_2O	trace	trace	trace	trace	trace	trace	trace	trace	K
TiO_2	2.08	2.11	2.40	2.03	1.49	1.46	1.57	1.35	Ti
P_2O_5	0.24	0.25	0.22	0.28	50.02	50.04	50.00	50.05	O
H_2O	15.69	13.34	8.18	9.75					
Total	100.00	100.00	100.00	100.00					

In view of the behavior of water during analysis and the possible addition of phosphorus when a chemical dispersant is used, for comparative purposes all results are calculated on a carbon, water and phosphorus-free basis. Such data can be easily converted back to the conventional form for the purpose of comparison with data in the literature, by the addition of H_2O and (OH) based on the ideal structural formula.

To test precision, twenty discs of Fithian illite[9] were prepared and each was analysed in two different locations on the film. Statistical treatment of the results did not indicate any significant differences between inter- and intra-sample variances for any element present.

Table 2 summarises the data. Also shown for comparison, recalculated on the same carbon, water and phosphorus-free basis, is the average of 7 chemical analyses[10]. These previously published values show a large scatter, presumably because of factors such as the different samples and size fractions used, the different analytical techniques and analysts employed, the presence of impurities, differences in preparation techniques and, not least, the variability of the water content.

Table 2

FITHIAN ILLITE ANALYSES

	Average Wet Chemical Analysis	Microprobe Analysis		
		Mean Wt.%	Standard Deviation	Standard Error
Si	26.59	25.96	0.06	0.010
Al	13.95	14.17	0.05	0.009
Fe^{3+}	3.51	} 4.60	0.06	0.009
Fe^{2+}	0.93			
Mg	1.32	1.46	0.03	0.0004
Ca	0.76	0.86	0.05	0.008
Na	0.30	0.07	0.04	0.006
K	5.10	5.65	0.04	0.006
Ti	0.45	0.46	0.03	0.004
O	47.09	46.76	0.03	0.004

The techniques described in this paper have now been successfully applied to a whole range of clay minerals including members of the illite, smectite, kandite and palygorskite groups. The techniques are rapid, non-destructive and, assuming the availability of an electron microprobe, relatively inexpensive. A typical analysis for the 22 elements, including data processing time, takes about 10 min. Sample preparation time is similar to that for X-ray diffraction studies and, in fact, the same mount can be used for both purposes. The method should have a wide range of applications in clay mineralogy and in the earth sciences in general, as well as in other fields such as soil science, forensic science and ceramics. The general method for the microprobe analysis of powdered samples may have an even broader sphere of application.

REFERENCES:

1. Folk, R.L. (1959): Petrology of sedimentary rocks. 154 pp. Hemphill's, Austin, Texas.
2. Genrich, D.A. and Bremner, J.M. (1972): A re-evaluation of the ultrasonic-vibration method of dispersing soils. Soil Sci. Soc. Amer. Proc., 36, 944-947.
3. Grimshaw, R.W. (1971): The chemistry and physics of clays. 1024 pp. Benn, London.
4. Kinter, E.B. and Diamond, S. (1956): A new method for preparation and treatment of oriented aggregate specimens of soil clays for X-ray diffraction analysis. Soil Sci. 81, 111-120.
5. Gibbs, R.J. (1965): Error due to segregation in quantitative clay mineral X-ray diffraction mounting techniques. Amer. Mineral. 50, 741-751.
6. Bower, J.F., Wood, J.A., Richardson, S.M., McSween, H.Y.Jr. and Ryder, G. (1977): Rock compositions by defocussed beam analysis. Proc. 8th Internl. Conf. X-ray Optics & Microanal. and 12th Ann. Conf. Microbeam Anal. Soc., Boston (1977), p. 182A-182C, Microbeam Anal. Society.
7. Smith, D.G.W. (1976): Quantitative energy dispersive analysis. In: Short Course in Microbeam Techniques Handbook, 64-106. Mineralogical Association of Canada.

8. Gold, C.M. and Smith, D.G.W. (1976): EDATA - A FORTRAN IV program for calculation of chemical compositions from spectra obtained by energy dispersive microbeam analysis. Dept. of Geology, Univ. of Alberta, Edmonton, Alberta, Canada.

9. Kerr, P.F. et al. (1951): Analytical data on reference clay minerals. In: Amer. Petrol. Inst. Research Project #49, Prelim. Rpt. #7, 161 pp.

10. Weaver, C.E. and Pollard, L.D. (1973): The chemistry of clay minerals. Developments in Sedimentology, 15, 213 pp., Elsevier.

A Fast, Self-Contained, No-Standards Quantitative Program for EDS

John C. Russ
EDAX Laboratories
P.O. Box 135
Prairie View, IL 60069

To properly occupy a useful position between qualitative analysis and optimized quantitative analysis using conventional standards, a "no-standards" program should be fast, require minimum operator input, and be self-contained (ie. require no mass storage of either library spectra or data such as energies). This paper describes such a program, which was written originally in simple BASIC; a FORTRAN-compiled version is even faster in operation, and the typical times quoted here are reduced by 2 to 4 times in most cases.

The steps in the program are described below. Required information from the user (accelerating voltage V, angles S = surface tilt, A = azimuth to detector, E = elevation to detector, detector parameters such as resolution and Be window and dead layer thickness) are normally entered only once, unless they change. The list of elements (symbol or atomic number and K, L or M shell) is also re-used until changed, and may also be taken directly from a list of elements identified during qualitative analysis.

The spectrum is first corrected for escape and sum peaks [1]. Then a first approximation of continuum background is fit by a curve of the form:

$$B = a_1 (V-E)/E + a_2 (V-E)^2/E$$

where the constants a_1 and a_2 are determined by least squares fits to 4 background points, either from a list of user selected points, or automatically chosen as points in the spectrum meeting the criteria that 1) they do not exceed either neighboring point by two standard deviations (possible peaks), and 2) they are not lower than both neighbors by two standard deviations (possible valleys between peaks). This fit is performed segmentally along the spectrum. It is similar to the semi-theoretical form of background equations [2] except that the absorption correction is missing. Hence the ratio of actual height to that calculated by this fit can be stored and subsequently divided by an F (χ) correction without further fitting.

Intensities are determined by simultaneous fitting of non-Gaussian peaks [3] generated for all of the energies of elemental lines. These in turn are calculated (energies and relative heights) from polynomial functions of atomic number; five K, ten L, and five M lines are used. The total area of peaks for the selected shell of each element are summed and listed as counts per second. The use of total shell intensities gives a significant improvement over earlier "no-standards" calculations [4] which incorporated factors for the relative intensity in a given line. Displays of the fitted background and peaks, or of the remainder after peak stripping can be selected to visually confirm the results.

The intensities are converted to relative K-ratios by dividing by the calculated pure intensity, obtained with the equation

$$P = Q\omega R \ T \ F/A$$

in which

$Q = U \log U + U - 1$ $; U = V/E_{abs}$

$\omega = Z^4/(a + Z^4)$ $; a_K = 10^6, a_L = 10^8, a_M = 7.5 \ 10^8$

R = effective current calculated as in FRAME [5]

T = spectrometer efficiency calculated for actual detector and window thickness

F = absorption correction calculated after Heinrich [6]

A = atomic weight (the only table of numbers used in the program)

Other needed parameters, such as absorption edge energies, mass absorption coefficients, etc. are calculated from polynomial fits.

The K-ratios are normalized and processed in a ZAF program based on NBS FRAME [5]. The sum of K-ratios is re-normalized after each iteration to bring the calculated concentrations to 100%. It is also possible to select oxide normalization, by inputting the presumed oxygen/cation stoichiometric ratio.

Program output includes atomic and weight percent, Z, A and F factors, and the mass absorption coefficient table if requested. The user can choose to have the initial background approximation improved by the introduction of matrix absorption after each iteration, and the intensities re-determined. This typically doubles the total calculating time, and in tests so far has not generally made a significant difference in final results.

Several examples illustrate the application of the program to complex samples:

Example 1 Analysis of steel (NBS 348) with mixtures of K and L shell elements, and major and minor lines, some of which (V, Mn) are completely overlapped.

Figure 1 measured spectrum
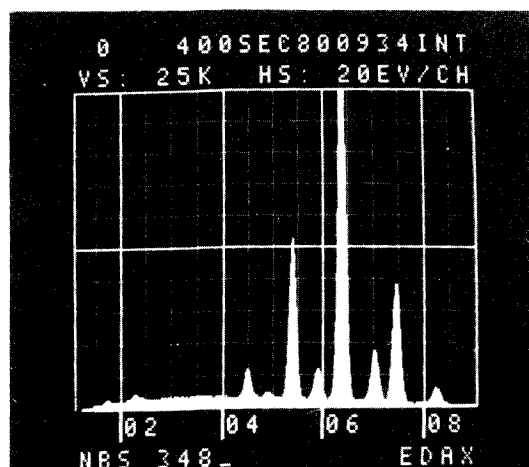
the necessary input parameters from the user are:

```
NEXT? 1 PARAMETERS:
   KV= 25  RES'N @ MN= 152  DET.THICK.(MM)= 3.2
   WINDOW THICK. (UM): BE= 10  SI= .15
   ANGLES:  S= 20  E= 16  A= 40
   OXIDE OR ELEMENT NORMALIZATION? E
```

The element and shell designations are shown in the list below. The program will handle twelve elements (plus oxygen). The total time required to obtain final answers was 5:20 (1:25 to collect intensities and 3:55 for ZAF calculation).

ELEM(Z)		SHELL	INTEN.
FE	26	K	728.82
CR	24	K	279.65
NI	28	K	236.53
TI	22	K	46.47
MO	42	L	10.93
SI	14	K	3.81
AL	13	K	0.59
CU	29	K	2.75
MN	25	K	21.90
V	23	K	3.93

ELEM(Z)	K	Z	A	F
26	.5193	.996635	.936947	1.03638
24	.16234	.992936	.96063	1.13866
28	.21165	1.01578	.837972	1
22	.02273	.993611	.923255	1.09655
42	.01093	.922723	.727921	1.00517
14	.00142	1.10479	.261495	1.0017
13	.00025	1.07349	.162208	1.0011
29	.00296	.969428	.870595	1
25	.01428	.976564	.9762	1.02837
23	.00213	.973885	.950812	1.10029

```
ELEM(Z)        %
  26          53.66
  24          14.947
  28          24.865
  22          2.259
  42          1.619
  14          .489
  13          .145
  29          .351
  25          1.457
  23          .209
MASS ABS COEFF TABLE (1=YES, 0=NO)? 1
EMITTER:  26        24        28        22        42        14
ABSORBER
  26      71.7     113.3     379.4     186.3    1182.2    2509.7
  24     473.6      88.3     310.4     145.2     921.4    1955.9
  28      90       142.2      58.9     234      1484.3    3151
  22     380.5     601.7     249       110.3     699.7    1485.4
  42     295.7     466.8     193.8     767.2     733.4    1502.1
  14     116.4     185.2      75.7     307.2    2007.7     328
  13      94.5     150.6      61.5     250.1    1640.4    3529.8
  29     100.1     158.2      65.6     260.3    1651.4    3505.8
  25      63.5     100.3     343.9     165      1046.8    2222.1
  23     425.6      77.2     278.7     127       805.8    1710.6
EMITTER:  13        29        25        23
ABSORBER
  26    3855.5     310.8      89.7     144.5
  24    3004.8     254.1      69.9     112.6
  28    4840.8      48.2     112.6     181.4
  22    2282       203.7     476.2      85.5
  42    2260.9     158.7     369.8     595.2
  14     503.8      61.8     146.1     237.2
  13     385.4      50.1     118.8     193
  29    5385.8      53.7     125.3     201.8
  25    3413.8     281.7      79.4     127.9
  23    2627.9     228.1     532.6      98.5
```

Figure 2 printout for example 1

The NBS certified values for bulk composition are:

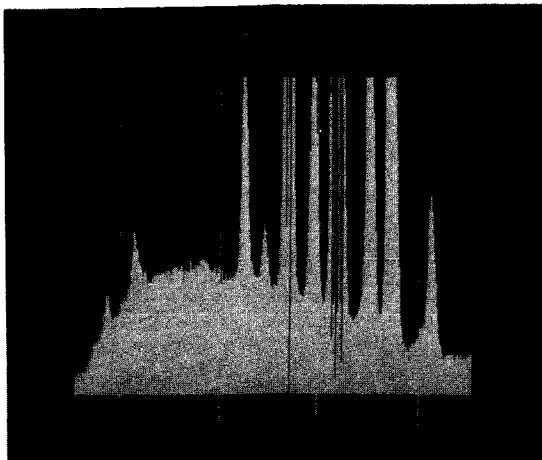| Fe | 53.30 | Si | 0.54 |
Cr	14.54	Al	0.23
Ni	25.80	Cu	0.22
Ti	2.24	Mn	1.48
Mo	1.30	V	0.25

Figure 3 display of expanded spectrum showing background and minor element peaks
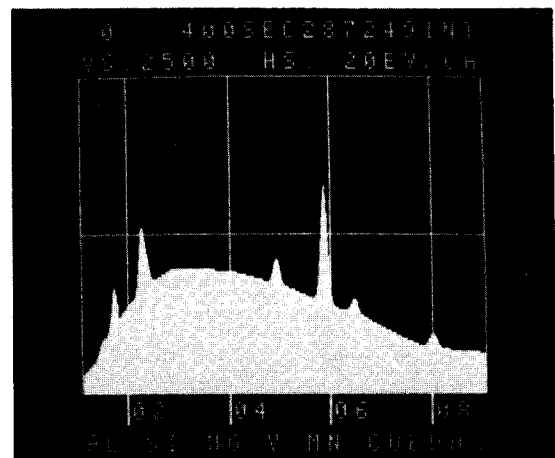

Figure 4 display of generated spectrum with background and minor element peaks (Al, Si, Mo, V, Mn)

Example 2 Analysis of ilmenite mineral[7] showing the use of the oxide normalization routine. Again, several elements are present in small amounts and/or overlapped.

The necessary input parameters are:

```
NEXT? 1 PARAMETERS:
   KV= 12  RES'N @ MN= 152  DET.THICK.(MM)= 3.2
   WINDOW THICK. (UM): BE= 9  SI= .15
   ANGLES:  S= 20  E= 20  A= 40
   OXIDE OR ELEMENT NORMALIZATION? O
```

The calculated intensities, concentrations, and ZAF factors are listed below. The total time required for the BASIC version of the program was 1:05 to collect the intensities 3:20 and to calculate the final results.

ELEM(Z)		SHELL	INTEN.	OXIDE RATIO
MG	12	K	384.73	1.0
AL	13	K	14.09	1.5
SI	14	K	7.75	2.0
ZR	40	L	8.49	2.0
TI	22	K	1518.82	2.0
CR	24	K	73.96	1.5
MN	25	K	5.84	1.0
FE	26	K	506.25	1.0

ELEM(Z)	K	Z	A	F
12	.03312	1.06196	.513322	1.0003
13	.00111	1.02965	.623943	1.0006
14	.00058	1.05462	.739336	1.00119
40	.00145	.828913	.953767	1.00286
22	.2882	.92309	.997857	1.01948
24	.021	.916357	.973094	1.03132
25	.00215	.897478	.981708	1
26	.24011	.911584	.986389	1

ELEM(Z)	%	OXIDE %
12	6.074	10.071
13	.173	.327
14	.074	.159
40	.183	.247
22	30.69	51.192
24	2.284	3.338
25	.244	.315
26	26.703	34.352
8	33.576	33.576

```
MASS ABS COEFF TABLE (1=YES, 0=NO)? 1
```

EMITTER:	12	13	14	40	22	24
ABSORBER						
12	453.1	4354.6	2810.2	1800.2	198.1	119.2
13	613.5	385.4	3529.8	2263.2	250.1	150.6
14	802.1	503.8	328	2768.2	307.2	185.2
40	3019.8	1939.4	1288.5	850.1	671.3	408
22	3632.9	2282	1485.4	959.9	110.3	601.7
24	4783.6	3004.8	1955.9	1264	145.2	88.3
25	5434.6	3413.8	2222.1	1436	165	100.3
26	6137.8	3855.5	2509.7	1621.8	186.3	113.3
8	2140.6	1324.2	849.8	541.3	57.9	34.6

EMITTER:	25	26
ABSORBER		
12	93.9	74.7
13	118.8	94.5
14	146.1	116.4
40	323.1	258.2
22	476.2	380.5
24	69.9	473.6
25	79.4	63.5
26	89.7	71.7
8	27.2	21.6

```
*READY
```

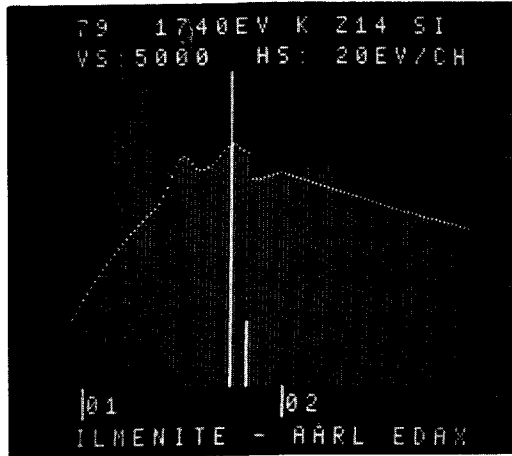Figure 5 printout for example 2

Figure 6   Comparison of original spectrum with generated Al and Si peaks plus background.
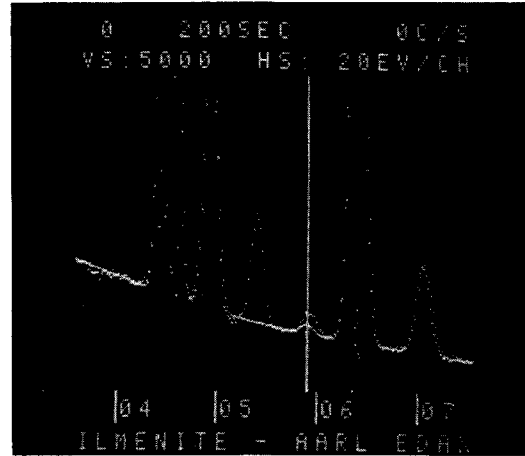

Figure 7   Comparison of original spectrum to generated spectrum with all peaks except Cr. Note minor Mn peak (marker).

Example 3 Analysis of 58% Sn - 42% Sb alloy[8]. This sample is a severe test of stripping performance, because of the thoroughly overlapped L lines.
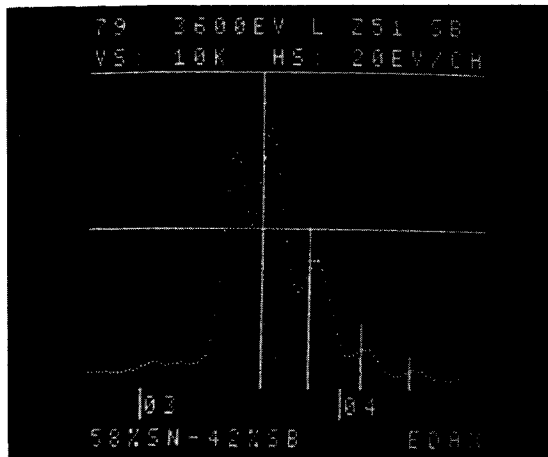

Figure 8   Separation of Sb from Sn: original spectrum (dots) and fitted Sn L-series peaks.

The analysis conditions are identical to example # 1. The printout is reproduced below.   Total   time   required   was   to   collect   intensities,   and   to   calculate concentrations.

ELEM(Z)		SHELL	INTEN.		
SB	51	L	686.62		
SN	50	L	998.22		
ELEM(Z)		K	Z	A	F
51		.41411	.996135	1.01164	1
50		.58539	1.00273	.991045	1
ELEM(Z)		%			
51		41.093			
50		58.907			

MASS ABS COEFF TABLE (1=YES, 0=NO)? 1
EMITTER: 51   50
ABSORBER
  51   412.3   464.4
  50   387.5   436.5

Figure 9 printout for Example 3

References

1. P.J. Statham, "Escape Peaks and Internal Fluorescence for a Si (Li) Detector and General Geometry", J. of Physics E: Sci. Instrs. 1976, Volume 9.

2. C.E. Fiori, R.L. Myklebust, and K.F.J. Heinrich, "Prediction of Continuum Intensity in Energy Dispersive X-Ray Microanalysis", Analytical Chemistry Volume 48, No. 1, Jan. 1976, p. 172-176.

3. J.C. Russ, "Resolving Spectrum Interferences Using Non-Gaussian Peaks", EDAX EDITor, Volume 7, No. 3, 1977, p. 12-16.

4. J.C. Russ, "Quantitative Microanalysis with Minimum Pure Element Standards", MAS 1974, p. 22a-c.

5. H. Yakowitz, R.L. Myklebust, K.F.J. Heinrich, "FRAME: An On Line Correction Procedure for Quantitative Electron Probe Microanalysis", U.S. Natl. Bur. Stds. Technical Note 796, U.S. Government Printing Office Washington, D.C., 1973.

6. K.F.J. Heinrich, Analytical Chemistry, Vol 44, 1972, p. 350.

7. Specimen and analysis courtesy Dr. C.E. Feather, Anglo American Research Laboratories, Republic of South Africa.

8. Specimen and analysis courtesy Mr. E. Groenewoud, ELCOMA, Eindhoven, Netherlands.

COMPUTER TECHNIQUES FOR ANALYSIS OF "ENERGY-DISPERSIVE X-RAY SPECTRA

Peter J. Statham

LINK SYSTEMS , Halifax Road,High Wycombe,Bucks HP12 3SE , England.

SPECTRAL CHARACTERISTICS

In energy-dispersive spectrometry we are dealing with a digitised x-ray-energy spectrum and are primarily interested in determining peak areas. Peaks are nominally Gaussian in shape, but may be distorted due to malfunctions in the recording electronics or due to fundamental physical processes within the x-ray detector itself. Although this distortion is usually constant for a particular system and a particular x-ray energy, the characteristics can vary appreciably from system to system. When spectra are generated by electron-excitation, the peaks are superimposed on a background where the ratio of peak height to background height is of the order of 100 when the peak corresponds to 100% of a chemical element. The background is fairly smooth, but exhibits high curvature in the low-energy region below 2 keV and also has steps due to x-ray absorption which are each smoothed out by a Gaussian instrumental response function appropriate to the energy of the step. Spectra are digitised into channels where there are typically about 10 to 15 channels spanning the full width at half maximum (f.w.h.m.) of a peak and if the number of counts in channel i is y_i, then the statistical standard deviation for this channel can be approximated by $y_i^{\frac{1}{2}}$ for most practical purposes. The statistical variation is uncorrelated from channel-to-channel and with typical channel-counts of 200 for the background the statistical "noise" in the spectrum is very noticeable. These features are summarised by fig. 1.

In addition to these fundamental components, there are artefacts introduced by the spectrometer. Silicon $K\alpha$ "escape peaks" appear at an energy of 1.74 keV below each major peak in the spectrum and are invariably less than 2% of the major peak in height. They are the result of escape of Si $K\alpha$ x-rays from the detector and can be removed quite easily as shown below.

When two large peaks at energies E_1 and E_2 are present in the spectrum, a small "pile-up" or "sum" peak may appear at energy $E_1 + E_2$. These sum peaks can be eliminated by operating the spectrometer at a low counting rate at the expense of a longer accumulation time, but there may also be a "pile-up continuum" which extends downward in energy from $E_1 + E_2$ and constitutes a small but notice-able contribution to the observed background. These pile-up phenomena are highly dependant on the design of the spectrometer electronics and will not be considered in this paper, although methods of correction are discussed else-where (1).

ESCAPE PEAK REMOVAL

The mechanism of Si $K\alpha$ escape is well understood and the escape probability k (E) can be predicted from theory as a function of the energy of the incident x-ray, E. Since the escape fraction is very small it suffices to perform a channel-by-channel subtraction routine starting from the high-energy end of the spectrum. Thus, if channel I corresponds to E keV and IS corresponds to 1.74 keV, then the channel counts, N (I), are modified according to

$$N (I-IS) = N (I-IS) - k (E) . N (I) \qquad (1)$$

If a suitable polynomial approximation is available (2,3), then k (E) can be computed very rapidly as I is successively decremented.

BACKGROUND SUBTRACTION

Several methods of background subtraction are compared in (4) which can be conveniently divided into two groups: those where the background is removed explicitly from the spectrum prior to measurement of peak areas and those where the background is implicitly taken into account during the peak deconvolution process. One basic technique which falls somewhere in between is peak detection so this will be discussed first.

Peak Detection

The simplest method of peak detection involves searching for a maximum in the spectrum which is revealed by a change in the first derivative from positive to negative. Since statistical noise introduces many spurious maxima into the spectrum, some method of averaging the fluctuations over several channels must be used, and Savitzky and Golay's polynomial smoothing coefficients have often been used for this purpose (5). The more channels that are used, the more smooth the result so smaller peaks can be differentiated from statistical fluctuations. However, two peaks that are close together may not be resolved if too many points are averaged so a compromise is involved, although better resolution may be obtained by observing the changes in higher derivatives of the spectrum. The trade-offs involved in derivative search procedures are fully discussed by Barnes (6). Another popular technique makes use of a "zero-area correlator" which is convoluted with the spectrum to expose the peaks. One of the simplest forms is the "top-hat" where the convolution is described by

$$N(I) = \frac{1}{2M + 1} \sum_{S = -M}^{S = +M} N(I + S) - \frac{1}{2N} \left(\sum_{S = M+1}^{S = M+N} N(I-S) + N(I+S) \right)$$

$$-(2)$$

Where M and N are chosen to optimise resolving power and statistical precision; a suitable choice makes 2M+1 and 2N both close to the f.w.h.m. of a peak (7). Many ad-hoc variations on the above methods have been suggested but they invariably involve a test procedure applied to some linear combination of channel counts and the statistical accuracy should therefore be predictable so that spurious peaks can be effectively rejected. In a comparison of several techniques from this standpoint, Hnatowicz (8) has shown that the zero-area correlator approach appears to be the best for detecting small peaks on a high background.

In the above procedures it is assumed that the background is a smooth function of energy so that the operation of taking a derivative, or convoluting with a "top-hat" function, will effectively remove the background from consideration.

Explicit Background Removal

The simplest method of background subtraction involves interpolating the background with a straight line between two points on either side of the peak. Besides the obvious problems that occur when several peaks overlap, there is

the disadvantage that the statistical accuracy is limited by the choice of only 2 channels to determine the background; this limitation becomes severe when the peak is very small. When large peaks are present, the absorption step in the background associated with each major peak introduces curvature into the background in addition to the curvature which is present at low energies in all spectra and linear interpolation is totally unsuitable. To accommodate curved backgrounds, higher-order polynomials can be fitted to the few peak-free points that are available on either side of a region containing peaks. The danger here is that if too few points are used, or the statistical scatter on the data is large, the fitted function will be subject to large errors, especially when interpolated or extrapolated over regions greater than those used for fitting. A better solution is to find a function which accurately represents the background shape, then scale this to available peak-free points.

The shape of the bremsstrahlung continuum has been studied by several investigators and this has given rise to a number of background correction procedures where an estimate of specimen compositions is used to calculate the background shape (reviewed in (9) and (10)). In principle, this should completely correct for absorption steps and curvature but in practice the formulae usually have to be "fudged" to match the observed spectrum in regions which are free from peaks. A further problem with this technique is that the spectrometer efficiency has to be estimated which is particularly difficult at low energies where the efficiency falls off very rapidly. This problem can be avoided by using a background spectrum obtained form a standard of know composition (e.g. diamond) and then modifying the shape by multiplying each channel count by the calculated ratio of unknown to standard background. This ratio method not only eliminates the need to determine spectrometer efficiency, but also tends to compensate for uncertainties in the theory. In order to fully exploit the available statistical accuracy, as many background points as possible should be used to scale the calculated background. However, if one attempts to use a single scaling factor for the whole curve, systematic errors may exceed the statistical variation in some parts of the spectrum and it may be advantageous to calculate local scaling factors by using background points on either side of selected regions of interest.

Implicit Background Correction

Procedures where the background is removed prior to peak deconvolution are conceptually easy to appreciate which probably explains their popularity, but methods of peak deconvolution which are themselves designed to be insensitive to background are considerably more versatile and only demand an accurate knowledge of peak shape. In practice, the background may contain a number of spurious components such as bremsstrahlung radiation generated within the detector entrance window, a pile-up continuum from unresolved pulse pairs, counts from degraded events which appear as a long low-energy tail on each major peak and counts from energetic backscattered electrons which penetrate the detector window. These additions make characterisation of the background shape a difficult task, whereas characterisation of peak profiles is easily achieved by studying spectra where the peak-to-background ratio is high.

If we assume that the background is a slowly-varying function of energy when compared with the peaks then, instead of removing the background, we can remove the peaks until we are left with a smooth, peak-free residual. One method of doing this in a controlled fashion is "iterative stripping" (4).

This involves estimating each peak area in turn and subtracting a peak of the correct shape but with an area which is guaranteed to be less than the true peak area. After several iterations, this process will reduce all peaks to the background level and the peak area will be given by the sum of the areas stripped in each iteration. A suitable method of estimating peak area above local background is to use the "top-hat" function described by equation 2 and in fact the "iterative stripping" principle can be thought of as a method of reducing the spectrum until a peak detection procedure fails to find any peaks. Since all the mathematical procedures involved are linear, the solution obtained by iterative stripping can be defined uniquely and in fact the resulting equations are very similar to those for a least-squares fit of profiles to the spectrum. A logical extension of this method is thus to do a least-squares fit of profiles to the spectrum but only after pre-processing both the standard peak profiles and the spectrum of the unknown with a "top-hat" digital filter. Convolution with the "top-hat" will suppress smooth background components in both standard and unknown spectra, but since the convolution described by equation 2 is an inherently linear operation, the filtered spectrum will still be a linear sum of the filtered standard profiles. Thus, deconvolution and background subtraction can be accomplished simultaneously by this combination of digital filtering and least-squares techniques. Details of the method and analysis of performance are given in (11) and (12).

PEAK DECONVOLUTION

When peaks overlap, individual peak areas can be determined provided peak shapes are accurately known. For example, if the integrals over fixed energy ranges about each peak are recorded, and the fractional overlap of a given peak into the integration ranges of others is known, then a set of simultaneous equations can be derived and solved to obtain the integrals that would have been obtained in the absence of overlaps. The least-squares fitting technique is only a formal mathematical extension of the "overlap factor" idea, although it does demand knowledge of the complete peak profile for each component. However, once the profiles are determined the overlap with other peaks is automatically taken into account, so least-squares fitting is somewhat more versatile and, in fact, gives slightly better statistical accuracy because more data points are used in the calculation. Details of both methods are given in (4).

In practice, the principle errors in peak deconvolution tend to be due to inaccurate background subtraction and errors in the estimated peak shape rather than statistical uncertainty. Errors in the estimated peak shape can arise if the resolution of the spectrum alters or the gain on zero of the spectrometer tends to drift. In practice, this can be due to a variety of causes and the expected degree of shift and broadening can be used to predict the likely errors introduced in peak deconvolution (4).

One attractive solution to the problem of shift and resolution changes is to allow the parameters of the component peaks to vary and thus optimise the "fit" to an unknown spectrum. This is the idea behind "non-linear least-squares" or "adaptive profile fitting" techniques which employ a variety of search procedures to find that combination of parameter values which gives the best fit to the data (see for example (6), (13) or (14). Convergence can be a problem with such methods and the results are usually sensitive to both the initial guesses for the peak parameters and the choice of data points to be matched. Even when the true answer is known, it is possible to demonstrate that other combinations of peak parameters can give as good or even a better fit to the

noisy data (15) or in other words, a good fit to the data doesn't guarantee that the resulting parameter values will be correct.

In one computer simulation, two peaks of f.w.h.m. 15 channels, heights 5000 and 10000 counts respectively were positioned 4 channels apart, thus corresponding to a separation of 40 eV at 150 eV f.w.h.m. resolution. The data were fitted with two Gaussian peaks, both with f.w.h.m. = 15 channels, by the usual linear least-squares procedure and the calculated peak heights and X^2 values were observed for various combinations of peak positions. For a region of fit from channel i_1 to i_2,

$$X^2 = \frac{1}{(i_2 - i_1 + 1 - n)} \sum_{i_1}^{i_2} \frac{(y_i - \hat{s}_i)^2}{y_i} \tag{3}$$

where n ($=2$) is the number of "free" parameters, y_i is the count in channel i and $\hat{s}_i$ is the fitted curve so X^2 corresponds to the "chi-square" measure that is normally used to establish "goodness of fit". Fig. 2 gives a pictorial representation of X^2 as a function of the two centroid parameters, x_1 and x_2. The true values are $x_1 = 100$, $x_2 = 104$ for the centroids and $p_1 = 5000$, $p_2 = 10000$ for the peak heights and the corresponding X^2 value is 1.173. The fitted result, $p_1 = 5031$, $p_2 = 9996$ for $x_1 = 100$, $x_2 = 104$ gave $X^2 = 1.138$, so we see that in this particular example, the statistical error in the linear least-squares approach where the peak shapes are exact is 0.6% for p_1 and 0.04% for p_2. In this example, where there are only two variables, it is quite easy to understand the concepts of the non-linear search procedure. An initial guess of $x_1 = 99.4$, $x_2 = 103.4$ would place us at point A on the X^2 surface (fig. 2) and the particular search procedure employed would direct stepwise changes in x_1 and x_2, as shown by the dotted line, towards a minimum on this surface. (In practice, there are often more than two undefined parameters so the X^2 surface appears in (n + 1) - dimensional space which is difficult to visualise when n is greater than 2 but the essential behaviour can still be described with reference to the X^2 "landscape".) Thus the search would proceed down the valley from A and would continue past the point $x_1 = 100$, $x_2 = 104$ and in fact would finish up at a minimum point with $X^2 = 0.925$ at $x_1 = 101.2$, $x_2 = 105.0$. At this minimum, which corresponds to the best fit in the "chi-square" sense, $p_1 = 9119$ and $p_2 = 5903$ so the errors are + 82% and - 41% respectively. An additional constraint could be applied if the exact distance apart of the peaks were known and thus could be fixed at 4 channels. This would remove all but a diagonal line from consideration in fig. 2 and in fact, the point $x_1 = 100$, $x_2 = 104$ is a local minimum and as mentioned above, the results are quite reasonable at this point. However, if by some misfortune, the starting parameters were $x_1 = 100.8$, $x_2 = 104.8$, the search would converge toward an even lower minimum of $X^2 = 0.963$ at $x_1 = 101.4$, $x_2 = 105.4$ and at this point, $p_1 = 10130$, $p_2 = 4889$ so the errors in the results, + 103% and - 51% respectively, would again be totally unacceptable. In fact, to guarantee success with this particular example, the peak widths and separation have to be known and the initial guess for peak position must be accurate to within ± 0.4 channels (± 4 eV @ 10 eV/ch). Complete details are given in (15).

The above example illustrates a problem with non-linear profile fitting procedures that is induced by statistical noise. When the noise is very low, the "valley walls" in fig. 2 are very steep and the correct solution and "best fit" parameters tend to coincide. However, when the noise is significant, the landscape becomes more rippled and searches can reach minima which do not correspond to realistic solution vectors. Moreover, standard statistical procedures

are really only applicable when the constraints are well defined and the influence of "soft" constraints which allow parameters to alter by some degree is not easy to determine in general. Because non-linear methods are usually very complex, they are also very difficult to analyse theoretically so one cannot be certain that convergence is assured or how statistical noise affects the region of the X^2 landscape which is accessible to the search. With the statistical noise that is usually present in E.D.S. spectra, the constraints limiting parameter variations have to be very tight to prevent the search reaching spurious solution vectors.

The solution in linear profile-fitting methods is determined uniquely, statistical errors can be predicted and the consequence of peak profile inaccuracies can be established. Thus linear methods are "well-controlled" whereas non-linear methods are apt to be unstable in the presence of noise. When the statistical noise is very low, the non-linear approach can be advantageous provided that the parameterisation of peak profiles is exact, but in general non-linear methods should be treated with caution.

USE OF THE FOURIER TRANSFORM

The very nature of the spectrum, peaks buried in a "noise" of continuum background and statistical fluctuations, suggests that signal-processing techniques could be applied to the data. Unfortunately, the results are not as satisfying as one might hope for, primarily because useful information, such as knowledge of allowable peak positions (x-ray line energies), is not exploited as it is in most of the methods described so far.

Background Subtraction

Gaussian peaks are rapidly-varying functions compared to the underlying continuum so it should be possible to remove the background by filtering out the low-frequency components from the spectrum. However, the peaks have both D.C. and low-frequency components in common with the background, so this procedure leaves the peaks with large negative undershoots on either side. Frequency filtering via the Fourier transform is equivalent to convolution with the appropriate function and the results of this technique are essentially the same as those produced by the "top-hat" convolution (equation 2).

Resolution Enhancement

Peaks are fundamentally Gaussian in shape and can thus be thought of as δ - functions smeared out by a Gaussian instrumental response function. The smearing process is equivalent to attenuating high-frequency components so the resolution of a spectrum can be improved by performing a digital Fourier transform, multiplying by a suitable filter to restore the high frequency components then inverse transforming to obtain the result. Statistical noise, which has a "white" frequency distribution, imposes a limitation on this method because enhancing the high-frequency components will clearly exaggerate the noise in the spectrum, but if the high frequencies are not restored, the spectrum will be distorted so a compromise is involved. Various methods of selecting a suitable filter have been proposed (reviewed in (16)) as well as the equivalent linear iterative procedures for convolution (e.g. (17)) but the filter which gives the minimum total squared error can be calculated and used to demonstrate the fundamental limitations imposed by statistical noise (16). Thus, a peak with

a total area of 10^8 counts on a background of zero could be narrowed to about 65% of its original width with only 1% r.m.s distortion relative to the original peak height (16). However, in E.D.S spectra, the background is rarely zero, and peak areas are typically in the region of 10^5 counts for a large peak, so attempts to reduce the f.w.h.m. by more than 10% will give distortion in excess of 1% r.m.s. (16).

Although the use of Fourier transform techniques for resolution enhancement is rather limited with the levels of noise present in E.D.S. spectra, the optimal least-squares filter can be derived for noise removal (16) and spectrum smoothing by this method is considerably more effective than by the popular Savitzky and Golay smoothing procedure.

The limitations with respect to noise and distortion apply to linear procedures, but more spectacular results can be obtained with non-linear restoration techniques that can incorporate constraints such as the condition that the final result must be positive to represent a theoretically feasible x-ray spectrum (e.g. (18), (19)). However, the solution of large systems of non-linear equations can be very demanding on computer resources and, as with the non-linear profile-fitting technique, methods have not yet been developed to analyse the non-linear mathematics so that convergence can be guaranteed and reliable error estimates obtained.

REFERENCES

1. P.J. STATHAM, X-Ray Spectrom. 6, 94 - 103, 1977.

2. S.J.B. REED and N.G. WARE, X-Ray Spectrom. 2, 69 - 74, 1973.

3. P.J. STATHAM, J. Phys. E: Sci. Instrum. 9, 1023, 1976.

4. P.J. STATHAM, X-Ray Spectrom. 5, 16 - 28, 1976.

5. A. SAVITZKY and M.J.E. GOLAY, Anal. Chem. 36, 1627, 1964.

6. V. BARNES, IEEE Trans. Nucl. Sci. NS-15, 437, 1968.

7. A. ROBERTSON, W.V. PRESTWICH and T.J. KENNETT, Nucl. Instrum. and Meth. 100, 317 - 324, 1972.

8. V. HNATOWICZ, Nucl. Instrum. and Meth. 133, 137 - 141, 1976.

9. P.J. STATHAM, Proc. 11th Ann Conf. M.A.S., Miami Beach, Florida, U.S.A. 1976, 10A - 10I.

10. P.J. STATHAM, X-Ray Spectrom. 5, 154 - 168, 1976.

11. F.H. SCHAMBER, Proc. Symposium on "X-Ray Fluorescence Analysis of Environmental Samples", Chapel Hill, N.C., 1976, T. Dzubay, Ed., Ann Arbor Science Publications, Ann Arbor, Mich. 1977, pp 241 - 257.

12. P.J. STATHAM, Anal. Chem. 49, (14), 2149 - 2154, 1977.

13. R.G. HELMER, R.L. HEATH, M. PUTNAM and D.H. GIBSON, Nucl. Instrum. and Meth. 57, 46 - 57, 1967.

14. G.C. ALLEN, "Computer Analysis of Spectra by Deconvolution", Central Electricity Generating Board report, RD/B/N3068, Research Dept., Berkeley Nuclear Laboratories, England, 1974.

15. P.J. STATHAM, submitted to X-Ray Spectrometry, October 1977.

16. P.J. STATHAM, Proc. 12th Ann. Conf. M.A.S., Boston, Mass., U.S.A., 1977, 103A - 103E and Proc. 8th Int. Conf. X-Ray Optics and Microanalysis, 1977 (to be published).

17. J.E. STEWART, Applied Spectroscopy, 29, (2), 171 - 174, 1975.

18. P.A. JANSSON, R.H. HUNT and E.K. PLYER, J. Opt. Soc. Am. 60 (5), 596-599, 1970

19. B. ROY FRIEDEN, J. Opt. Soc. Am. 62 (4), 511 - 518, 1972.

FIGURE 1. Constituents of a typical
digitised x-ray energy
spectrum produced by electron
bombardment and measured with a
Si(Li) detector. Note the change in
scale for each component.

PEAKS (x1)

SPECTRUM ⟹

ENERGY ⟶

BACKGROUND
(x16)

NOISE (x8)
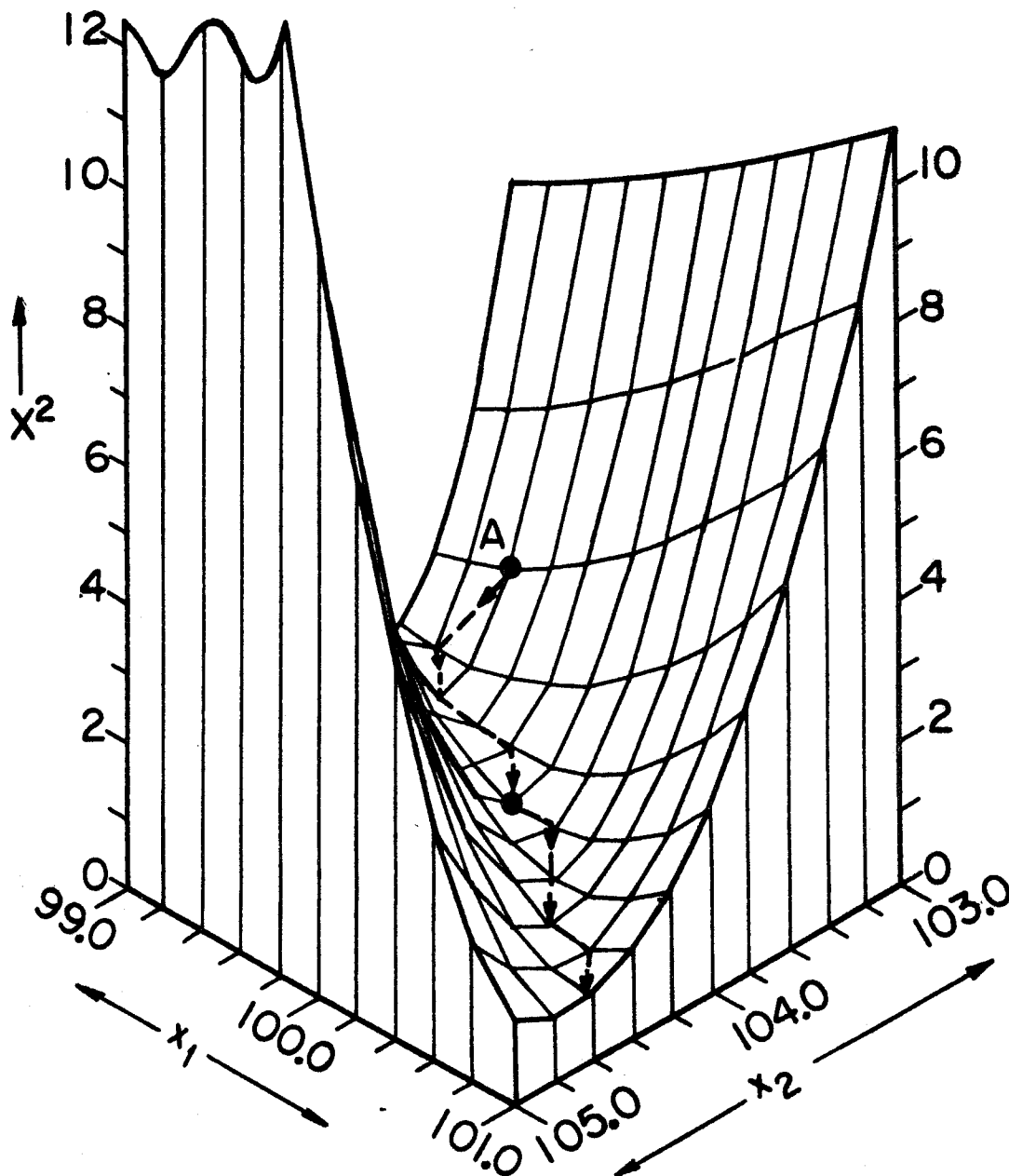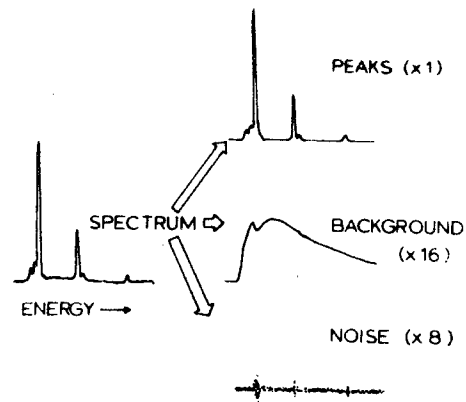
FIGURE 2. Pictorial representation of the X^2 surface for the simulated
profile fitting problem described in the text. The minimum
X^2 for different combinations of centroids, x_1 and x_2 is plotted.

Spectral Analysis Techniques in Auger-Electron Spectroscopy

C. J. Powell

National Bureau of Standards, Washington, D.C. 20234

Auger-electron spectroscopy (AES) is now being used extensively for surface analysis.[1] At this time, most analyses are qualitative rather than quantitative but there is growing interest in converting the observed intensities of AES spectral features to elemental concentrations.[2] The development of AES as an analytical tool will probably follow the pattern of development of the electron-probe microanalyzer (EPMA) although the much greater surface sensitivity of AES puts more stringent demands on the knowledge of sample homogeneity. The accuracy of surface analysis by AES will then generally be inferior to that of EPMA.

This paper will be divided into three main parts. First, the basic processes in Auger-electron spectroscopy will be described together with the factors that need to be considered in intensity measurements (background, inelastic scattering, chemical effects, topography). Second, the techniques now being used for spectral analysis will be described. Finally, reference will be made to a recent round robin conducted under the auspices of the ASTM Committee E-42 on surface analysis that provides a measure of the current state-of-the-art in AES.

References

1. C. J. Powell, Applications of Surface Science (in press).

2. C. J. Powell, in Quantitative Surface Analysis of Materials, edited by N. S. McIntyre (American Society for Testing and Materials, Philadelphia, 1978), ASTM STP 643 (in press).

THE ELECTRON ENERGY-LOSS SPECTRUM AND
REQUIREMENTS FOR ITS PROCESSING

by

David Joy, Dennis Maher and Peggy Mochel
Bell Laboratories
Murray Hill, New Jersey   07974

INTRODUCTION

Electron energy-loss spectroscopy (EELS) is a
powerful technique for the chemical microanalysis of thin
specimens. The energy distribution of electrons which
have passed through the sample has features ("edges") at
discrete energy losses and these are characteristic of
the elements contained in the specimen. Just as is the case
of X-ray analysis, there is a need to identify these features
and for quantitation to obtain an accurate measure of their
magnitude. Because EEL spectra are still relatively unfamiliar,
this paper will concentrate on the general characteristics of
the spectrum and describe the types of operations which need
to be performed upon it. Another paper in these same proceed-
ings will describe one particular data collection and reduction
scheme which is based on a commercial multi-channel analyzer
interfaced to a small computer.

THE SPECTRUM

The EEL spectrum is a plot of signal intensity
against the energy loss of the electrons relative to the

incident beam energy (which is typically 100 KeV). Figure 1 shows a spectrum recorded from a thin carbon film for the energy-loss range 0 to 500eV. The spectrum can be divided into two regions namely below and above 100 eV. In the range below 100 eV, the peak from the electrons which passed through the sample without being scattered inelastically (i.e., "zero-loss signal") dominates the spectrum. There are also plasmon scattering peaks from the interaction of the incident beam with the electron gas in the sample. While these events are characteristic[1], they are not widely used for microanalysis because of ambiguities in interpretation. Above 100 eV, the characteristic edges which are due to the ionization of K, L, M, etc. shells of the atoms are found and these edges are used for chemical analysis.

It can be seen from the logarithmic scale of the display that edges are very small in magnitude compared to the zero-loss peak. The first problem is thus the wide dynamic range which in extreme cases, such as for example a high energy-loss K edge (e.g., silicon at 1840 ev), may be 10^4 to 1. Since edge signals are usually small compared to the mean signal level at any loss, it is necessary to increase the recording gain at intervals in order to make them readily visible. However, this can present further problems where computer manipulation is required. If the system is adjusted so that the zero-loss peak is recorded at

the highest acceptable count rate, then the maximum count
in any channel is typically 100K. A subsequent gain change,
of say X100, will make it possible to record several thousand
counts in an edge. However, the **corrected** maximum count in
the zero-loss peak (corrected = original x gain change) will
now exceed the capacity of a 16-bit word. It may therefore
be necessary to break the spectrum into pieces for processing
even though this causes difficulties with operations such as
a Fourier transform which requires access to the entire
spectrum at a constant scale factor. Although these problems
are not insupperable, they are an inconvenience.

Figure 2 shows in more detail a K-edge (from carbon)
and the associated background on which it rides. The edge,
unlike an X-ray peak, is in principle of indefinite extent
only extrapolating into the underlying background for a
loss equal to the incident energy. The background at any
point in the spectrum is thus comprised of the sum of the
tails from all previous edges together with other types of
scattering events (for example non-characteristic single
electron excitations). This has two consequences. First,
the background must always be extrapolated under the edge of
interest. This is inherently less accurate than the inter-
polation procedures which can be employed for X-ray analysis.
Second, **the model** of the background which must be used will
clearly change each time another edge is passed.

To a good approximation the background can be modelled by the expression AE^{-r}, where A and r are empirically determined parameters and E is the energy loss. An analytical function of this type can be fitted to $\sim$ 100 eV of background proceeding an edge and extrapolated for several hundred electron volts past the edge with a considerable degree of success, as judged by the test that the edge should become asymtotic to, but not cross, the background. For the next edge, the parameters A and r must be redetermined because the principal contribution to the background will be the tail of the previous edge. A least squares fitting technique has been found adequate although more flexible procedures such as simplex optimization[2] might be better when the spectrum is noisy.

After the background has been stripped, an edge also can be described by a function of the type BE^{-s}, where again B and s are fitted parameters. However, precautions must be taken in fitting this expression. Low energy-loss events, such as plasmon peaks, are reflected in each edge because of multiple scattering. When multiple scattering is minimal, the shape of an edge is unchanged at energy losses $\sim$ 30 eV or more down from the edge, but when multiple scattering becomes appreciable (Figure 3), the edge is completely distorted and cannot be represented analytically. An analytical fit to the shape of an edge is required for microanalysis because it is necessary to find the total integral under the edge.

For practical reasons (e.g., the accuracy of the background extrapolation), the energy window over which the actual integration is carried out must be limited. If an accurate representation of the edge can be obtained analytically, then the true integral to infinity can be calculated from a measure of the integral in a finite window.

Theoretically[3] both the edge shape and the background would be expected to show an exponent of the order of 4, but experience obtained on a wide variety of spectra indicate that the number can range from as low as 2 to as high as 5. Consequently, correction routines which rely on an estimated value of the exponent for their validity will be in considerable error. For this reason, sufficient computing power must be available to rapidly fit these data.

FUTURE CONSIDERATIONS

Since quantition of edge data has been attempted only recently, considerable work remains to be done. As is clear from the discussion above, only empirical approaches to data reduction have been found to be useful. This is because very little accurate theoretical knowledge is available to enable either the background or the edge to be modelled realistically. There also may be "systems" contributions to the spectrum in the form of stray electron scattering, electronic non-linearities etc., which are presently insufficiently understood to make it possible to take them into account.
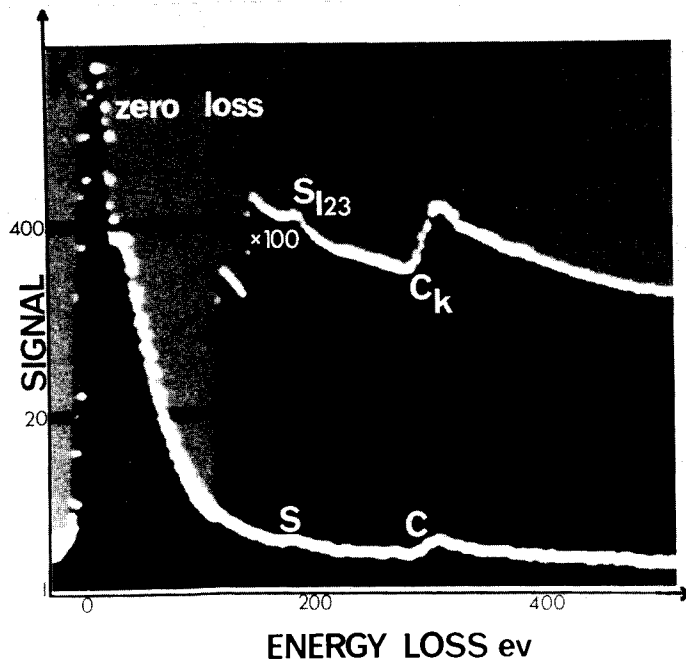
Fig. 1

EEL spectrum from a thin carbon film contaminated with sulphur. Note the large change in signal level between the zero-loss peak and the characteristic edges.
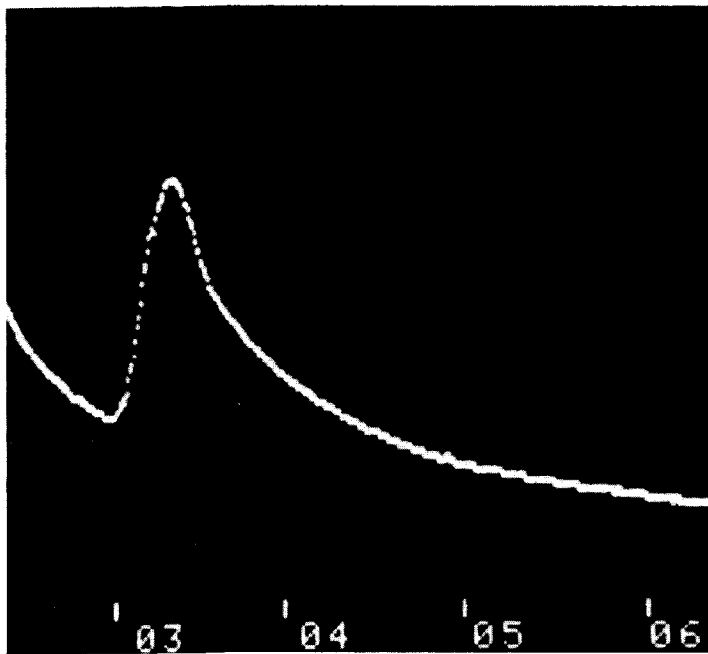
Fig. 2

Carbon K-edge from a thin film recorded at 100 kV. Units on the horizontal scale represent 100 eV increments of energy loss.
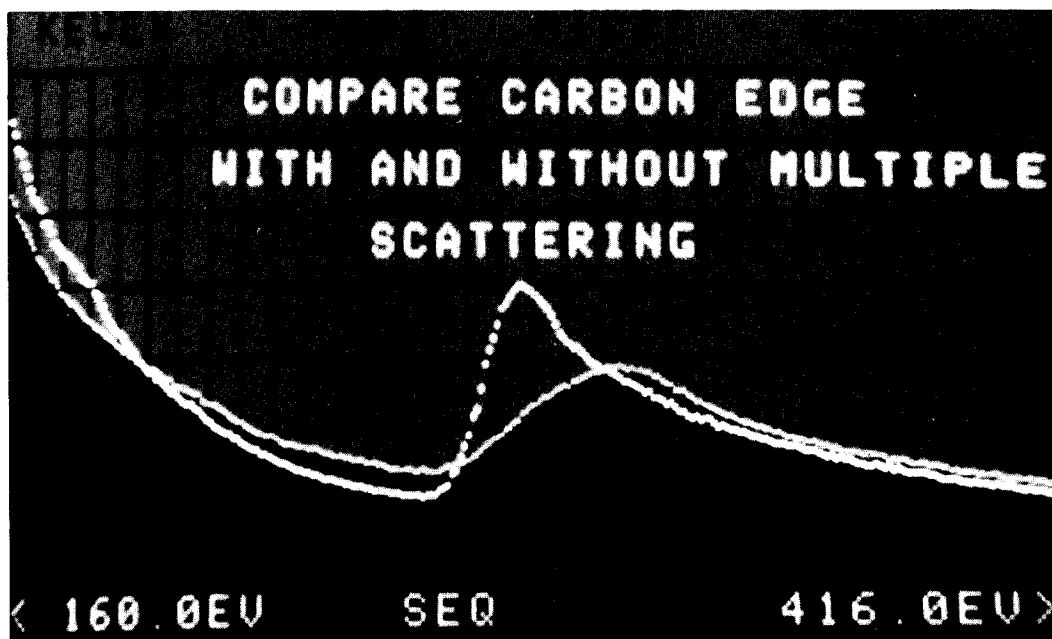
Fig. 3

Comparison of carbon K-edges from thin and thick regions
showing the distortion in edge shape which results from
multiple scattering.

AN OVERVIEW OF CURVE FITTING TECHNIQUES

F. H. Schamber

Tracor Northern, Inc.

Middleton, WI 53562

Introduction

Curve fitting procedures find application in nearly every branch of science and engineering which is concerned with quantifying collections of parametric data. Although many of the underlying principles of such procedures have been known for centuries, the routine application of these methods to large data sets was not practical prior to the modern high-speed computer. As a result of the current proliferation of sophisticated yet inexpensive minicomputers, curve fitting procedures have moved into the laboratory and may now be considered a practical tool for on-line data reduction.

Although the basic principles of curve fitting are actually quite simple and straightforward, there exists nonetheless a certain "mystique" which tends to intimidate many practical analysts. Several reasons can be advanced for this state of affairs:

(1) The sheer magnitude of the computational process (easily involving tens-of-thousands of mathematical operations) and the logistics of programming the problem on a computer have tended to obscure the fundamental simplicity of the procedures involved.

(2) Much of the available literature on the subject is written by "experts" and oriented towards theoretical concerns; there are relatively few readable texts which address the sort of practical problems which are of concern to the laboratory analyst.

(3) So many variants on the basic procedures have been employed and reported that the casual observer may fail to discern the common principles.

(4) Curve fitting techniques have all too frequently been applied improperly or inappropriately and the resulting "horror stories" have encouraged some to regard the methods as basically unreliable.

(5) There exists a suspicion that any subject which receives so much attention from statisticians must be entirely too complicated for rational mortals.

Although it is clearly impossible to deal with all such concerns within the constraints of a brief paper, it is nonetheless reasonable to examine some of the basic issues at an elementary level. It is the purpose of this paper to address the following questions:

(1) What are the basic premises of curve fitting?

(2) What are the principal methods used to compute a solution in a curve fitting problem?

(3) What are some of the basic pitfalls of curve fitting and how can these be avoided?

(4) What are some of the trade-offs between the various computational methods?

Overview

A common application of curve fitting in the laboratory is to "unfolding" problems. In such problems, the analyst is concerned with determining the amplitudes of the signals of interest (e. g. , peaks) in a multicomponent spectrum. Analysis may be complicated by interference between the signals of interest, the presence of an underlying "background" signal, and random statistical fluctuations in the data.

Addressing such a problem, let us assume that the measured spectrum is represented by an array of N data values $\bar{Y}(x_j)$ which are the amplitudes measured at the points x_j (j=1, N). It is then desired to synthesize a solution of the form

$$Y(x_j) = F_1(x_j) + F_2(x_j) + \ldots + F_M(x_j)$$

which is the "best fit" to the set of measured points $\bar{Y}(x_j)$ for the entire collection of N data points. The functions F_1, F_2, ... F_M represent the signals or structures (including background) which must be included to provide an accurate representation of the measured spectrum.

The most common criterion for a "best fit" solution is that of "least-squares" in which it is assumed that the "best" solution is that which minimizes the sum-of-the-squares of the differences between the measured data points and the fitted representation. That is, the quantity

$$\sum_{j=1}^{N} (\bar{Y}(x_j) - Y(x_j))^2$$

is a minimum for the best choices of the fitting functions F_1, F_2, ... F_M. Intuitively, the least-squares criterion is attractive since it tends to emphasize large differences between the measured and fitted points and is relatively insensitive to small deviations. At a more rigorous level it can be shown that the solution which minimizes the expression

$$\chi^2 = \sum_{j=1}^{N} (\bar{Y}(x_j) - Y(x_j))^2 w_j$$

(where the w_j are appropriately chosen statistical weights) is the "most probable" solution. This is commonly referred to as "error-weighted least-squares" or "chi-squared" minimization.

The first, and often the most difficult step in a curve-fitting problem is the formulation of a set of appropriate fitting functions. Each of the fitting functions must be

expressed as a function of the position x_j and one or more "free parameters" to be optimized. The simplest fitting problems are those in which the fitting functions can be expressed as linear functions of the fitting parameters; for example a polynomial function

$$a_1 + a_2 x_j + a_3 x_j^2 + \ldots + a_m x_j^{m-1}$$

or a linear superposition of predetermined functions (shapes)

$$a_1 f_1(x_j) + a_2 f_2(x_j) + \ldots + a_m f_m(x_j)$$

Often, the most appropriate fitting functions can only be expressed as non-linear functions of the fitting parameters, as in the problem of fitting to a Gaussian line shape of unknown amplitude, position, and width

$$a_1 e^{-(x_j - a_2)^2 / a_3}$$

The second step in a curve-fitting problem is to select a method for optimizing the fit (e. g., minimizing chi-squared). There are three general classes of methods which are employed:

(1) Pattern Search Techniques

The simplest of all such methods conceptually is to simply divide the range of reasonable parameter values into a grid of appropriate mesh size and evaluate the fit obtained at each point on the grid; the point at which the best fit is obtained is then taken as the solution. Such a "brute-force" method is extremely reliable but can consume inordinate amounts of computer time due to the large number of points which have to be tested. More efficient techniques in this class start from a set of initial parameter estimates and by evaluating the improvement or lack of improvement achieved for small variations of the parameters, select a new set of improved estimates. By repeating this process the program can be made to "walk" towards the optimum solution. The "simplex" method is a particularly elegant algorithm of this class.

(2) Gradient Search

This class of methods may be employed when the optimum solution is one which minimizes a function (such as chi-squared). The premise is that the value of the object function will smoothly decrease as one approaches the minimum of the function. Thus by evaluating the m-dimensional slope (gradient) of the object function at a starting point, one may infer the direction in which the parameters must be modified in order to move closer towards the minimum. Thus, the program proceeds from a trial point along the direction of "steepest descent" to a new trial point and the process is repeated until the minimum is located.

(3) "Matrix Inversion" Methods

This method in its purest form (linear parameters and no constraints) is the most mathematically elegant and potentially the fastest technique for optimizing a least-squares fit. One knows that at its minimum a function must have zero slope. Thus, by requiring that the first partial derivatives of chi-squared with respect to each of the m parameters be zero

$$\frac{\partial \chi^2}{\partial a_i} = 0 \qquad\qquad (i=1, m)$$

one obtains a set of m coupled equations in m unknowns (a_i). If the fitting functions are linear in the parameters then this set of "normal" equations is also linear and the problem reduces to that of solving the set of equations for the values of the parameters. This solution is commonly done by matrix-algebra methods involving the inversion of an m x m matrix; hence the designation as a "matrix inversion" method. However, any reasonable technique for solving the set of equations can be used equally well and there are a number of variants on this procedure which do not involve matrix inversion.

The first two classes of optimization techniques may be applied directly to non-linear as well as to linear parameterizations. The "matrix inversion" method is generally applicable only to linear problems due to the necessity of computing solutions to the coupled equations. However, this restriction can be circumvented by "linearizing" the problem. One occasionally applicable trick is to transform the non-linear data set to a representation in which the fitting function is linear (e. g., by fitting to the logarithm of an exponential data curve). A more generally applicable approach is to perform a first-order Taylor expansion of the non-linear function (Newton's method) so as to obtain a linear approximation. For example, the linear expansion of an exponential function would be stated as

$$e^{-a x_j} = e^{-a_o x_j} + b e^{-a_o x_j}$$

where a_o is an initial estimate and $b=(a_o-a)$. Substituting this linear approximation for the non-linear expression one treats b as the free parameter and optimizes chi-squared with respect to it. A new estimate of a is then computed as (a_o-b) and the process is repeated until the fit converges to the minimum. This method converges quite rapidly and reliably when the initial estimate (a_o) is reasonably close to the minimum but may behave erratically if the initial estimate is poor.

An important, but frequently overlooked final step in a fitting problem is the analysis of error. A major reason for the popularity of the matrix-inversion type of optimization is that the uncertainties of the fitted parameters can be readily computed from the inverse matrix. Estimation of uncertainties via the other two classes of methods is less direct. It is also imperative that the practitioner employ some sort of "reasonableness" check (e. g., inspection of

residuals or chi-squared) in order to verify that a reasonable fit has actually been obtained.

References

The following references contain readable and not overly-technical accounts of the theory and practice of curve fitting. The book by Bevington is highly recommended since it concentrates on practical problems and contains a number of sample Fortran programs.

(1) P. R. Bevington, Data Reduction and Error Analysis for the Physical Sciences, McGraw-Hill (1969).

(2) R. W. Hamming, Introduction to Applied Numerical Analysis, McGraw-Hill (1971).

(3) S. N. Deming and S. L. Morgan, "Simplex Optimization of Variables in Analytical Chemistry", Anal. Chem., 45 (3):379A (1973).

SYSTEMATIC ERRORS IN DIGITAL FILTER ANALYSES
OF EDS SPECTRA

by

R. A. Miller & M. A. Giles

Princeton Gamma-Tech, Inc.
P. O. Box 641
Princeton, N. J. 08540

Two prominent methods of background subtraction, currently being applied in quantitative energy dispersive x-ray analysis, are the 'theoretical' or 'modelled' background techniques and the digital filter methods. Digital filtering in this context usually means computing a spectrum proportional to the smoothed second derivative of the raw spectrum. The smoothing or filter width is selected to reduce the effect of fluctuations on the peaks of interest. Theoretical background subtraction consists of obtaining a model of the continuum using a variety of phenomenological and theoretical tools. In both cases, this is preliminary to a peak overlap correction and corrections for matrix effects.[1,2,3]

It may not be a question of which of these techniques is superior, but rather, that the techniques are complementary

SYSTEMATIC ERRORS IN DIGITAL
FILTER ANALYSES OF EDS SPECTRA

and of varied usefulness depending on the application. The
theoretical background subtraction has the advantage that
there is apparently no limit to its accuracy, i.e., it is
subject only to the amount of effort expended in determin-
ing the physical processes which produce the continuum, the
care in sample preparation, the experience of the operator,
etc. However, the physical processes which result in con-
tinuum production are complicated and not completely under-
stood. Various phenomenological techniques have been used
and the accuracy has been gradually increasing. Digital
filtering, on the other hand, cannot account for all the
subtleties in the background but has the advantage that it
is typically much faster. Shamber et. al.[3] and Statham[4,5]
have pointed out that by using experimentally obtained
standards, many of the inherent inaccuracies in the digital
filter method are eliminated or minimized.

Systematic errors remaining in digitally filtered
analyses performed on samples of known concentration will
be discussed. If these errors are truly systematic, com-
pensation may be possible.

REFERENCES

1. H. Yakowitz, R. L. Myklebust, and K. F. J. Heinrich,
    NBS Technical Note 796, 1973.

2. C. Maggiore and M. Foster, Proc. 10th Annual Conference
    of the Microbeam Analysis Society (1975), p. 24.

3. F. H. Shamber, N. F. Wodke, and J. J. McCarthy, Proc.
    8th International Conference of X-Ray Optics and Micro-
    analysis and 12th Annual Conference of the Microbeam
    Analysis Society (1977), p. 98A.

4. P. J. Statham, Proc. 11th Annual Conference of the
    Microbeam Analysis Society (1976), p. 10A.

5. P. J. Statham, Proc. 8th International Conference on
    X-Ray Optics and Microanalysis and 12th Annual Con-
    ference of the Microbeam Analysis Society (1977), p. 95A.

Observations on the Sequential Simplex Method and its Application to Peak Fitting in Energy-Dispersive X-ray Spectrometry

by

C. E. Fiori and R. L. Myklebust

Institute for Materials Research
National Bureau of Standards
Washington, DC 20234

Extended Abstract

Increasing use is being made of the lithium-drifted silicon (Si(Li)) detector in both X-ray fluorescence analysis and electron probe microanalysis. The increasing popularity of the Si(Li) detector is due to a number of factors including high quantum efficiency over a wide range of energy, simplicity and lack of moving parts, low cost and minimal maintenance. However, due to the limited resolution of the Si(Li) detector relative to the natural width of an X-ray line, considerable opportunity exists for interferences. For example, the natural width of an X-ray line is of the order of one electron volt, in the energy range of interest, measured at half the maximum of the peak intensity (the measured quantity is designated "full width, half maximum" (FWHM)). At the energy of Mn $K\alpha$ radiation (5.9 KeV), the FWHM is approximately 1.5 eV. The measured peak width from the Si(Li) spectrometer is degraded to a typical value of 150 eV for Mn $K\alpha$. Consequently, a natural peak of 1.5 eV width having 1000 counts amplitude would be degraded to a peak having a width of 150 eV and an amplitude of 10 counts.

This paper will describe an application of a mathematical procedure, the sequential simplex [1,2,3], which is used in our laboratory to deconvoive spectral overlaps in the X-ray energy range 1-20 KeV [4]. The procedure has been designed to work in a small computer. A sequential simplex procedure is a technique which can be used for selection of the parameters in a mathematical expression which describes a spectral peak. In this procedure, each of the n independent variables in the function to be fitted is assigned an axis in an n-dimensional coordinate system. A simplex, in this coordinate system, is defined to be a geometric figure consisting of n+1 vectors (in this discussion we will use the purely mathematical definition of a vector i.e. an ordered n-tuple $(X_1, X_2 ... Xn)$). In one dimension a simplex is a line segment; in two dimensions a triangle; and in three or more dimensions a polyhedron, the vertices of which are the above-mentioned n+1 vectors. The simplex is moved

toward the set of independent variables which optimize the fit according to a set of specific rules. The function used to determine the quality of the fit for any set of independent variables is called the "response function". The response function is evaluated at the n+1 vertices of a simplex and the value exhibiting the largest error (worst fit) is then replaced by another value obtained by reflecting the discarded vertex across the hyperplane of the remaining vertices. The methods for expanding and contracting the size of the simplex suggested by Nelder and Mead [2] have been adopted.

The energy-dispersive X-ray peaks in our method are assumed to be described by Gaussian profiles, figure 1. This assumption is based on 1) the known distribution of noise generated in the preamplifier of the Si(Li) detector and 2) the discrete nature of the counting process of charge carriers created by capturing photons of a single energy in the active volume of the Si(Li) detector. The assumption of a Gaussian distribution ignores the distortion on the low energy side of the observed peak caused by incomplete charge collection in the detector [5,6]. This effect can be seen in figure 2 for chlorine Kα and potassium Kα peaks. The deviation from a Gaussian distribution (shown as a solid line) is a function of energy. For example, the magnitude of the effect is significantly different for chlorine and potassium, which are seperated by only two atomic numbers. This effect tends to diminish as the energy of the X-ray line increases. In general, incomplete charge collection is a second order effect and can be neglected. For those situations, however, in which incomplete charge cannot be neglected (i.e. small peaks on the low energy side of large peaks), it is possible to determine an expression of the form

$$ y_j = aA_i (E_i - E_j)e^{-b(E_i - E_j)} \quad E_j \leq E_i \tag{1}$$

for a particular detector in a given experimental situation [7]. This equation can be functionally added to the Gaussian profile used to fit each peak in a spectrum. The terms in equation 1 are as follows: E_i is the centroid of the particular Gaussian profile to be modified and A_i the amplitude, y_i is the contribution due to the incomplete charge collection at energy E_j, and "a" and "b" are coefficients which will, in general, be different for peaks of different energy.

The simplex fitting procedure involves the calculation of the function which is then compared with the experimental data points. The purpose of the response function is to

provide a measure of the goodness of fit to the data points. The response function used is a normalized chi-square:

$$R = \sum_{j=1}^{M} \frac{-1}{z_j} \cdot \frac{(z_j - y_j)^2}{M-f} \qquad (2$$

where M is the number of data points, y_j is the measured intensity at each data point, y_j is the evaluation of the function to be fitted at the energy of the data point j, and f is the number of degrees of freedom (the number of independent variables). The weighting factor, $1/z_j$, equalizes the effect of all data points used in the fit.

The independent variables (coefficients) "amplitude", "energy", and "standard deviation" must be determined for each of the N peaks to be fitted. Consequently, the total number of coefficients (n) is

$$n = 3N \qquad (3$$

Here, values for n+1 sets of n coefficients are chosen to create the initial simplex and a R value is determined for each set. The procedure then minimizes the value of R to obtain the best set of coefficients.

If several overlapping peaks must be simultaneously fit, the method requires many coefficients and one may easily find false minima which generate incorrect estimates of the coefficients. We have introduced some simplifications which improve the final results by reducing the number of coefficients. Since the energies of X-ray lines are well known, it is unnecessary to include all of the peak energies (E_i) as coefficients. Only the energy of the principal peak (E_p) is used (to correct for small shifts in energy due to miscalibration of the multichannel analyzer). The energies of all other peaks are determined from energy E_p, thereby reducing the number of coefficients (the stability and linearity of present-day amplifiers permits this assumption). In addition, the standard deviation (σ_p) of only the principal peak must be included since the widths of the other peaks (σ_i) are given (for a lithium-drifted silicon detector [8]) by

$$\sigma_i = \frac{\sqrt{2500(E_i - E_p) + (2355 \, \sigma_p)^2}}{2355} \text{ (keV)} \qquad (4$$

The number of coefficients is, therefore, reduced from 3N to N+2. When more than several peaks are being fit this reduction in the number of coefficients significantly lowers the computation time. Furthermore, since the energies and widths of small peaks are determined as functions of the principal peak, the risk of obtaining a false minimum is considerably reduced.

Starting and stopping criteria for the simplex procedure will be discussed as will a technique to presmooth the data and use alternate data channels for the fit. We are presently applying this simplex method for determining some of the parameters needed in our quantitative electron probe microanalysis program FRAME C [7].

References

1) W. Spendley, G. R. Hext, and F. R. Himsworth, Technometrics, $\underline{4}$, 441 (1962).

2) J. A. Nelder and R. Mead, Computer J., $\underline{7}$, 308 (1965).

3) S. N. Deming and S. L. Morgen, Anal. Chem., $\underline{45}$, 278A (1973).

4) C. E. Fiori and R. L. Myklebust, to be published, J. Am. Nuc. Soc.

5) E. Elad, C. N. Inskeep, R. A. Sareen, and P. Nestor, IEEE Trans. Nucl. Sci. $\underline{20}$ (1), 534, (1973).

6) H. U. Freund, J. S. Hansen, E. Karttunen, and R. W. Fink, Proc. Intern. Conf. on Radioactivity and Nuc. Spect., 623, (1969).

7) R. L. Myklebust, C. E. Fiori, and K. F. J. Heinrich, 8th Intern. Conf. on X-rays, Optics, and Microanalysis, Boston, MA, paper 96 (1977).

8) C. E. Fiori and D. E. Newbury, SEM/78, Om Johari, ed., Tutorial paper 4, (1978).

$\sigma_A = \text{FWHM}/2.355$

$y = A_A \exp\left\{-\frac{1}{2}\left(\frac{E-E_A}{\sigma_A}\right)^2\right\}$
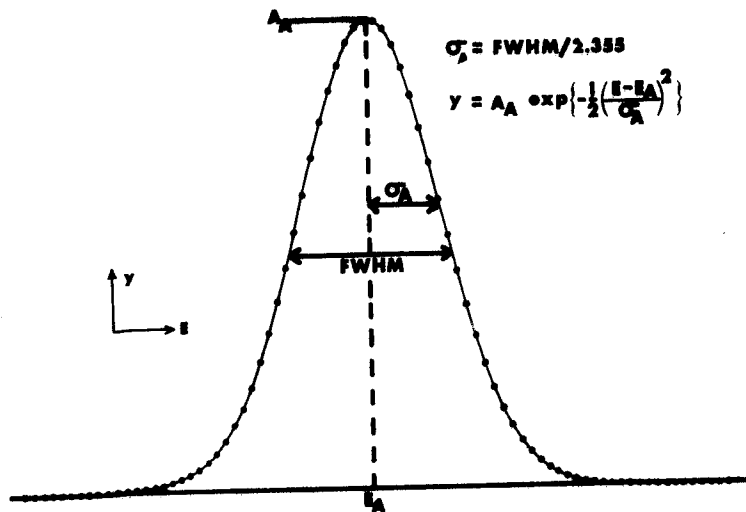
1. Theoretical Gaussian distribution which describes an X-ray peak observed on a lithium-drifted silicon detector. σ is the standard deviation of the distribution, A_A is the peak amplitude, and y is the amplitude at any energy.
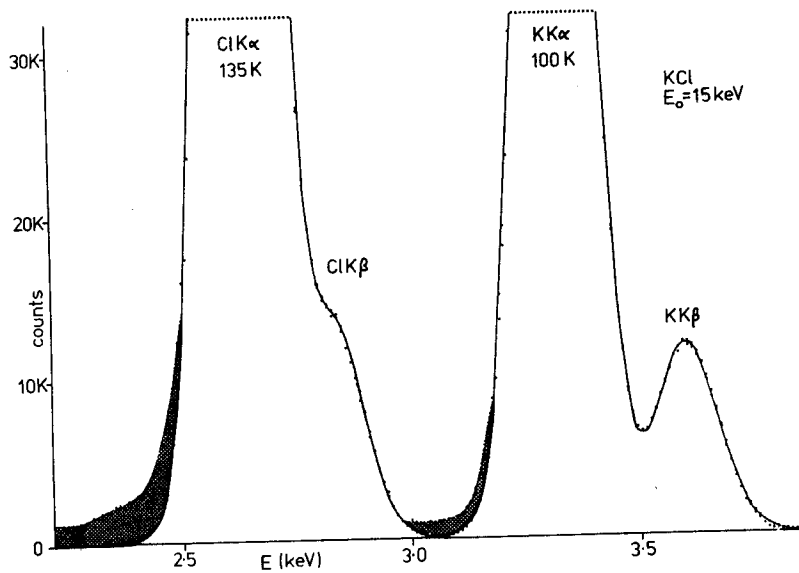
2. Si(Li) detector spectrum of kCl showing deviation between Gaussian fit (solid line) and real data.

A DATA COLLECTION AND REDUCTION SYSTEM FOR ELECTRON ENERGY-LOSS SPECTROSCOPY

by

Dennis Maher, Peggy Mochel and David Joy
Bell Laboratories
Murray Hill, N. J.   07974

Introduction

This paper describes a system for collecting, storing and processing electron energy-loss spectra. The hardware is built around the Kevex 7000 multi-channel analyser supported by a PDP11/03 computer, or by a separate remote time-shared computer. The software so far developed allows for full quantitation of EEL spectra   and is designed to be used in conjunction with the pre-set programs and routines which are available directly from the keyboard of the 7000 unit. The general features of EEL spectra and the requirements for the processing of such spectra are described in a previous paper in these proceedings.

The Hardware

A schematic diagram of the system is shown in Figure (1). The output from the photomultiplier detector system of the spectrometer is passed to a "voltage to frequency converter" module which generates a pulse train with an instantaneous repetition rate proportional to the magnitude of the input signal. This pulse train is stored in the multi-channel analyser operated in a scaling (sequential access) mode in which all the counts

arriving within a pre-determined interval of time are stored in one channel of the memory before stepping on to the next channel. The dwell time per channel is controlled from the keyboard and can be set in 0.1 ms increments from 1 millisecond to 1 second. Direct electron counting using fast pulse amplifiers is also possible but the restrictions on the maximum count rate in this mode limit its usefulness to those cases in which there is no need to examine the spectrum in the region of the zero-loss peak.

A digital scan ramp to drive the spectrometer is generated in synchronism with the display scaling by a counter chain and D/A converter in the 7000. A maximum of 4096 channels is available in blocks of 1024 or 2048. However, a selected group of channels in any block can be scanned by control from the keyboard so allowing limited "window" scans over a selected energy range. Any number of sweeps can be preselected from the keyboard and the analysis is started, or terminated by a single push key command. Under software control this sequential EELS analysis can be carried out while simultaneously performing a conventional EDS analysis into another block of memory channels.

The display can be calibrated from the keyboard to correspond to any chosen energy increment per channel. On the microscope used here (JEOL JEM 100B), calibrated accelerating voltage shifts of 980 and 1880 volts are

available, and these are used to set up a nominal 1eV/channel
increment on the display. After adjustment at the calibration
points a linearity of better than 1% over the loss range
0-2 KeV is achieved. The reset accuracy of the
spectrometer and the analyser electronics when performing
multiple sweeps has been found to be better than 1 channel.
The maximum allowed count rate is about 400,000 cps and
the memory range (bi-polar display) is $\pm 2^{19}$ counts ($\pm$ 524 K counts).
The contents of the memories, together with identification
tags can be transferred at high speed to the PDP11/03 or put
onto paper tape for processing on a remote computer.

Data Processing

A limited number of processing routines can be
performed directly from the keyboard of the 7000. In
particular the smoothing routines have been found to be
valuable for reducing the visibility of random noise on
the spectrum. 5, 7 and 9 point running smooths are available,
but because the resolution of the spectrometer is typically
15-20ev (and hence about 20 channels) the smallest number
of smooth points must be used to minimize degradation in
resolution. A numerical differentiation routine [1] has also
proved useful to identify weak edges in the spectrum.

The number of atoms n per unit area producing the
observed intensity in the edge is given by (see Figure 2)

$$n = \frac{I_k \, (\alpha, \Delta E)}{I_0 \, (\alpha, \Delta E) \, \sigma_k \, (\alpha, \Delta E)} \quad \ldots\ldots(1)$$

where α is the acceptance angle of the spectrometer, ΔE is the energy interval over which data is integrated, I_k is the integral under the edge, I_0 the integral under the zero-loss peak, and σ_k is the ionisation cross section. For convenience this expression can be rewritten as:

$$n = \frac{I_k \, (\alpha, \Delta E)}{I_0 \, (\alpha, \Delta E) \, \sigma_k \, \eta_\alpha \, \eta_{\Delta E}} \quad \ldots\ldots(2)$$

where α_k is now the total ionisation cross section (i.e. the X-ray cross section) and η_α and $\eta_{\Delta E}$ are efficiency factors to account for the limited angular and energy range over which the data is collected. The assumption that the angular and energy dependent contributions can be separated in this way has been found to be a very good approximation.

Of the quantities in equation (2), I_k and I_0 are measured experimentally from the spectrum, σ_k is a physical constant which can be calculated [2] and η_α and $\eta_{\Delta E}$ can be estimated theoretically [2,3] or calculated empirically. The program described in the rest of this paper measures or calculates all of these quantities and produces a value for n for each edge examined. The program is written in Fortran and requires about 12K of storage in the 11/03.

The integral I_0 is measured directly from the contents of the memory by summing over the number of channels under the zero loss peak corresponding to the chosen energy window ΔE. Because of the wide dynamic range in the EEL spectrum, in general, there will be one or more changes in the gain of the recording system between the zero-loss peak and the edge of interest. The correction factor for this change is measured directly by setting the display cursor to the relevant channels and the integral is then multiplied by the appropriate factor.

The integral I_k is the area lying above the extrapolated background and below the measured spectrum for an energy window ΔE starting at the edge energy loss E_k. The first requirement is therefore to accurately model and extrapolate the background. It has been found that a relation of the form

$$S_{BK} (E) = A E^{-r} \qquad ------(3)$$

(where S_{BK} is the background signal at the energy loss E and A and r are constants) is a good fit to experimental spectra although the fitted value of the exponent r is often far from the predicted theoretical value of 4[3]. In the program used here between 40 and 100 channels prior to the edge are measured to fit the background. The intensity and energy values for each channel in this range are converted to

logarithms and a linear least squares fit procedure used
to find A and r. This fitted background is then computed
for the full range of interest and stripped from the original
spectrum as shown in figure (3). This procedure although simple
has been found to work well. Typical fitted values of r
range from 2.5 to 5.

I_k is then found from the stripped spectrum for the
chosen energy window ΔE. The accuracy of this integration
is entirely dependent on the success of the background
extrapolation, and that in turn is dependent on the range
over which the extrapolation must be made. Although the
edge profile should be asymptotic to the extrapolation, if
there is any significant error in the modelling the edge may
intersect the extrapolation. In such an event the integral
is then terminated at the channel for which the two meet.

The cross section α_k is calculated from the standard
Bethe formula [2] and all the data required for this is
stored with the spectrum. The remaining task is thus to find
η_α and $\eta_{\Delta E}$ the efficiency factors which are the ratio between
α_k and α_k $(\alpha, \Delta E)$. It can be shown theoretically [2,3] that
η_α should be given by

$$\eta_\alpha = \frac{\ln\left[1 + \left(\alpha/\theta_{E_k}\right)^2\right]}{\ln\left(2/\theta_{E_k}\right)} \quad \ldots \quad (4)$$

where $\theta_{E_k} = (E_k + \Delta E/2)/2E_0$ and E_0 is the accelerating
potential. This variation is well confirmed by experimental
results and **therefore it is** used directly in the program.

On the basis of an assumption about the variation of the generalized oscillator strength with energy it would be predicted that the stripped edge would have a shape of the form BE^{-s} (where B and s are constants) after the leading edge. The value of s for small values of α should be the same as that expected for r, that is 4 . However, if a linear least squares fit for the function BE^{-s} is made to the stripped edge, it is found that s is usually between 2 and 5. The actual value is rarely the same as that fitted to the background, and is in any case influenced by multiple scattering effects. Because of the effects of multiple scattering, the spectrum is only fitted for the region starting well away (30 ev or more) from E_k to avoid the part in which shape changes due to these effects are most pronounced.

If the oscillator strength is assumed to be essentially constant as a function of energy above the edge, then the value of $\eta_{\Delta E}$ will be just the ratio between the areas under a curve of the form BE^{-s} measured for ΔE and a very large energy window. This is obviously given as

$$\eta_{\Delta E} = \left\{ 1 - \left(\frac{E_k}{E_k + \Delta E} \right)^{s-1} \right\} \qquad \ldots \quad (5)$$

by straightforward integration. Hence after curve fitting an empirical efficiency factor can be derived from the data and used to correct it. The success of this approach can be tested directly by noting from equation (2) that

$I_k(\Delta E)/(I_o(\Delta E) \cdot \eta_{\Delta E})$ should be a constant, independent of the choice of ΔE. Figure (4) shows a plot of the raw data. $I_k(\Delta E)/I_o(\Delta E)$ and the same data after correction with the derived value of $\eta_{\Delta E}$. The stability of the result is seen to be excellent. The dotted line shows the result of assuming that s=4.[3] It is seen that, although a constant value is achieved, the value derived is not correct. Hence the empirical approach is to be preferred. The data used in this case was from **a thin carbon film and the spectra** are shown in Figure (3). The failure of the theoretical $\eta_{\Delta E}$ correction to give an accurate result has been observed previously[4] but it has been difficult to document accurately until the background could be stripped efficiently.

Conclusion

The combination of the 7000 system and the PDP 11/03 provides a powerful tool for the acquisition and reduction of EEL spectra. The quantitization program has been extensively tested and been found to be reliable and accurate. All the necessary operator interventions are accomplished visually from the display and are relatively non-critical. The **limitations of the procedures described here are that only a first order correction for multiple scattering effects is made.** Since these effects significantly reduce the accuracy of the result, the development of appropriate deconvolution techniques to eliminate them is of high priority.[5]

REFERENCES

1. Savitzky, A., and Golay, M., Analytical Chemistry, 1627, July, 1964.

2. Egerton, R. F., and Joy, D. C., Proc. 35th Ann. EMSA Meeting (ed. G. W. Bailey), Boston, p. 252, (1977).

3. Isaacson, M. and Johnson, D., Ultramicroscopy 1, 33, (1975).

4. Egerton, R. F., Proceedings SEM 1978, Los Angeles. In Press.

5. Spence, J. C. H., Proc. 35th Ann. EMSA Meeting (ed. G. W. Bailey), Boston, p. 234, (1977).
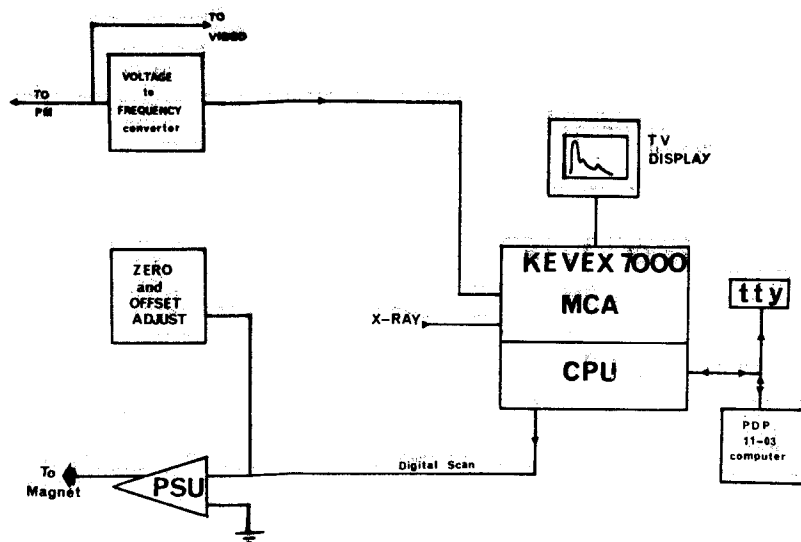
Fig. 1

Data collection system for EEL (and EDX) spectra based on a Kevex 7000 analyzer.
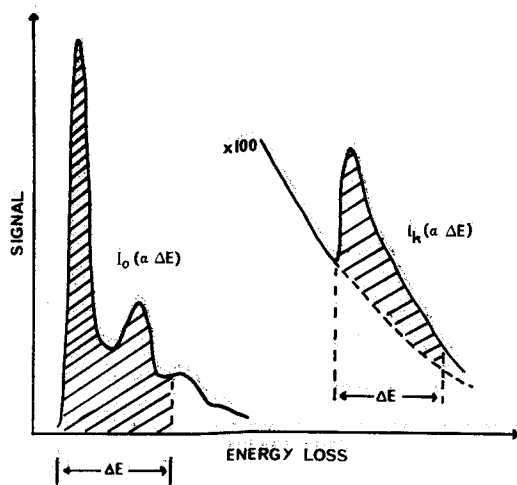
Fig. 2

Definition of variables required for the quantitation of EEL spectra. The acceptance angle α is set on the instrument, the energy window ΔE is chosen during data reduction.
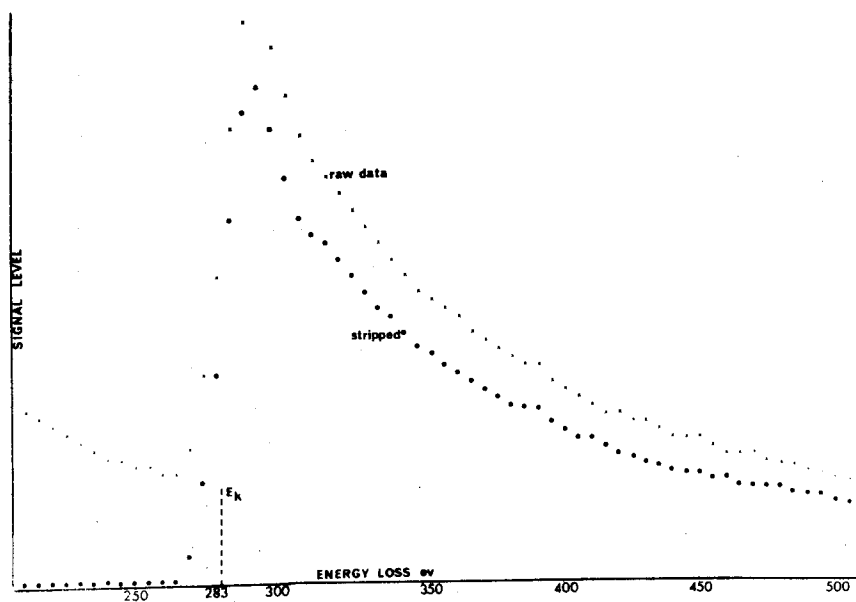
Fig. 3

Carbon K-edge as collect₁ 1 (raw data) and after a computer strip of the background. Each point represents a 5 eV loss increment.
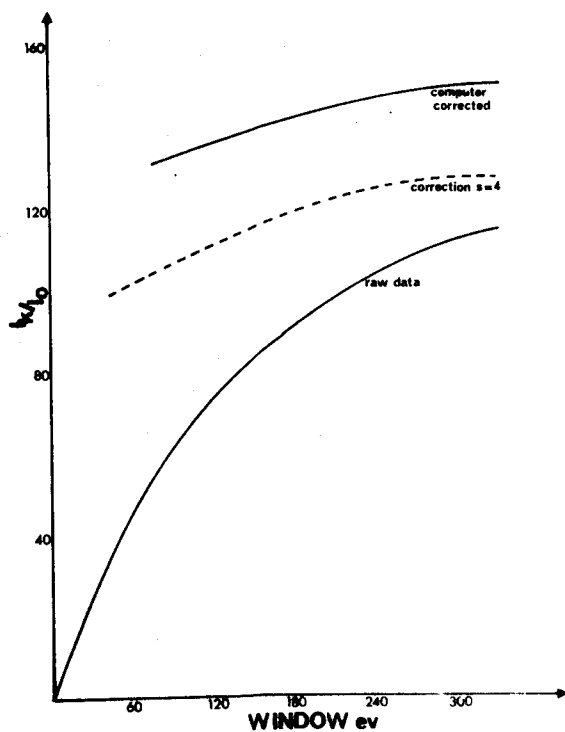
Fig. 4

Stability of quantitation result as a function of the window ΔE for two correction procedures. The data is from the carbon K-edge shown in Figure 3.

Interactive Displays and Simple Algorithms as an Aid to Qualitative Analysis of ED Spectra

J.C. Russ and V. Chopra
EDAX Laboratories
103 Schelter Road
Prairie View, IL 60069

Although the greatest emphasis in publications (and commercial brochures) is usually placed on quantitative aspects of processing Energy Dispersive spectra, experience suggests that most systems are actually used most of the time for qualitative, comparative, or at most semiquantitative analysis. In this mode of operation the user extracts the information he wants (element identification and perhaps "a lot", "a little", "more", or "less") from the visual display presented to him. We report here on the interactive use of the display information with simple, fast (and definitely not exact) algorithms to aid the user in obtaining this kind of information.

Most analyzers are equipped with some kind of markers used to indicate the positions of major lines and sometimes label the display with elemental symbols. We have expanded this peak identification algorithm by allowing it to be used in several ways, corresponding to four different questions the user may wish to answer. If the question is "Is there any lead present?", the user can select the ELEM button and enter either PB or 82 on the keyboard. The display then shows markers for up to twenty element lines (K_{α_1}, K_{α_2}, K_{β_1}, K_{β_2}, K_{β_3}, L_{α_1}, L_{α_2}, L_{β_1}, L_{β_2}, L_{β_3}, L_{β_4}, L_{γ_1}, L_{γ_2}, L_{γ_3}, L_ℓ, M_α, M_β, M_γ, M_{δ_1}, M_{2N_4}) plus six absorption edges (K, L_{1-3}, M_{4-5}). Figure 1 shows an example. The height of each marker reflects the actual relative height and varies with the element. To achieve a compact algorithm, all of the energies are calculated from a fifth order polynomial in atomic number, and the relative heights from a second order polynomial. If the user decides that the displayed KLM markers (each of which is labelled with the line designation) fit, and that the element is present, pressing the SAVE button will cause the markers to disappear but the elemental symbol to be saved below the main (α_1) peaks. The symbols move with the spectrum and the list of elements is available for further automatic routines to be described.

A second mode of operation, similar to many conventional KLM markers, is to scan through the periodic table. The user initiates this by pressing LIST. Then the markers start at C (Z = 6) and advance by one atomic number each time the user presses either SAVE or GO, up to Pu (Z = 94). If SAVE is pressed, the element label is written under the peak position.

A very different question is "What is that peak?". To answer it, the user can either use the cursor to mark the peak or enter its energy from the keyboard. Then the energy is compared to the table of energies for all twenty lines for elements from 6 to 94. The elements with lines within a test range (typically ± 40 eV, but settable by the user) are displayed, and by selecting any of them, all of the line markers and their symbols are displayed. The user can try any of the possible elements (as many as 8 or 10 in some cases) and SAVE the symbol for the one giving the best fit.

Peak identification also may be hampered by the presence of very small and large peaks in the same spectrum. Conventional logarithmic displays reduce the size of the large peaks, but do not use the full dynamic range of the display, so that small peaks are still hard to discern. Instead, we use an algorithm that displays an expanded log scale with the maximum corresponding to the highest peak, and covering 1, 2, 3 or 4 decades as specified by the user. Figure 2 shows the improvement this gives in viewability of small peaks.

Besides peak identification, the user often wishes to remove background and resolve (or strip) peak overlaps. A simple algorithm to approximately fit background in an interactive mode is to connect points selected by the user (and indicated either by the cursor or entering their energies) with a curve of the form (V - E)/E where V is the accelerating voltage and E the energy. This routine allows the user to either a) enter a series of points to be connected by this line (which is superimposed on the spectrum in the display as shown in Figure 3; b) re-use the last series of such points that he entered; or c) let the program select points by testing every 100 eV for points that neither exceed either neighbor by more than two standard deviations (a possible peak) nor lie two standard deviations below both neighbors (a possible valley between peaks). By examining the fitted background line, the user can quickly determine its reasonableness and change any doubtful points.

To resolve peak overlaps, the user can generate peaks above the fitted background for comparison to the spectrum. He can indicate the peak by a) entering its energy, b) indicating the energy with the cursor, or c) entering the element and line symbol. The height can either be entered by the user, or the program will fit it (by linear least squares) to the spectrum over a range of 1 FWHM. The comparison of the generated spectrum with the measured one allows the user to quickly spot gross errors in identification or missed minor peaks. Figure 4 shows an example. The area of each fitted peak is also given (in counts per second).

The peak fitting algorithm can be automatically applied for all of the elements previously identified using the peak markers. In this case the user obtains not only a list of the elements and their approximate total intensities, but can also examine the comparison of the fitted spectrum (background plus peaks) to the measured one. This tells him to what extent he may trust the element/intensity data, or whether he should fit some other elements himself. If the user has not already fit a background curve, as described above, the program will do so automatically. In addition to the use of the identified element list, the program will also proceed automatically through the K lines of elements from Na to Mo, giving a "hands-off" qualitative analysis of elements present. As Figure 5 shows, this can even detect rather small amounts of overlapped elements.

In addition to these algorithms, the user can also subtract from his measured spectrum either the fitted one (background and/or peaks) to see the residuals as shown in Figure 6, or a measured "blank" spectrum, which can be normalized by the ratio of intensities in any selected peak. Routines for smoothing, escape peak and/or sum peak removal, and spectrum labelling are also included.
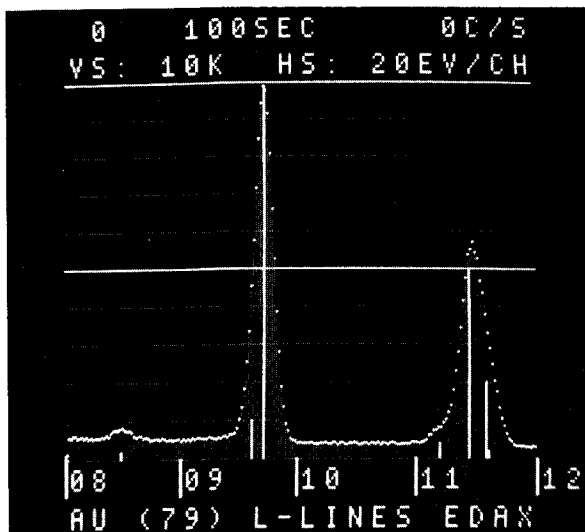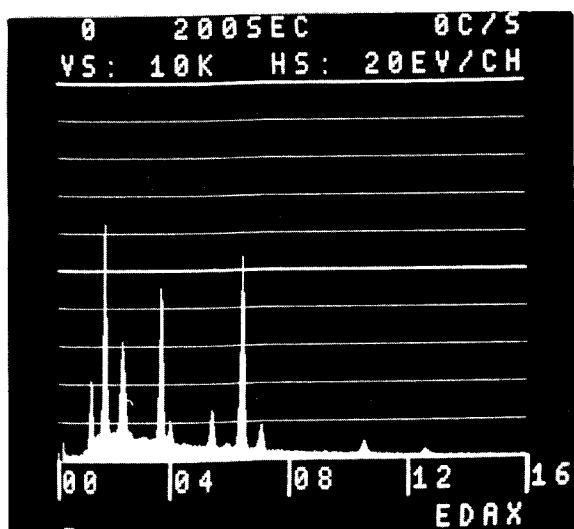
1a
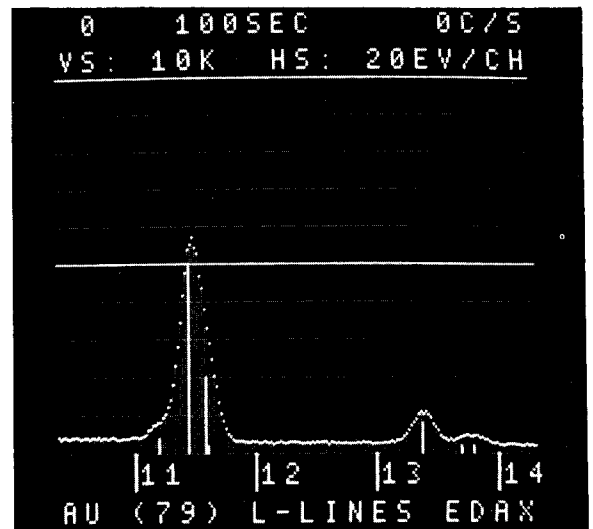
1b
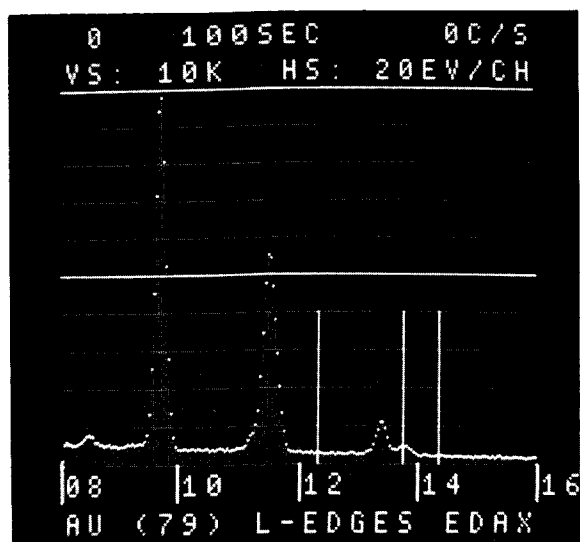
1c

Figure 1: L series markers for gold (Z = 79) superimposed on spectrum. Ten L lines are shown (a, b), with relative heights that vary with element; all three L edges are displayed (c).


2a

2b

Figure 2: Spectrum from a mineral sample: (a) as measured, linear calculation; (b) conventional log scale covering five decades, as may be produced by hardware in some MCA displays (note that very little of the total screen is used for the display, and both the large and small peaks are hard to see; (c) expanded log display covering two decades (now peaks are more easily visible).
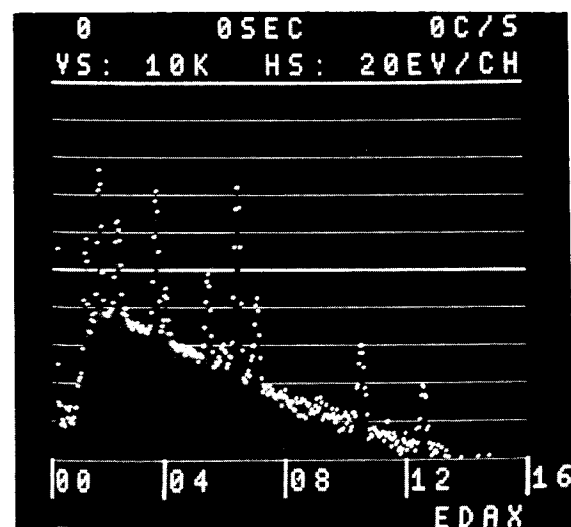
2c
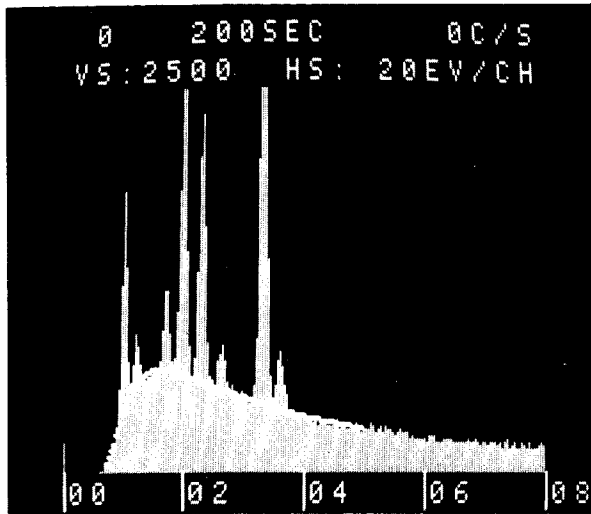
Figure 3: Approximate background curve fit to user selected points at 0.7, 1.5, 2.9 and 5 keV.
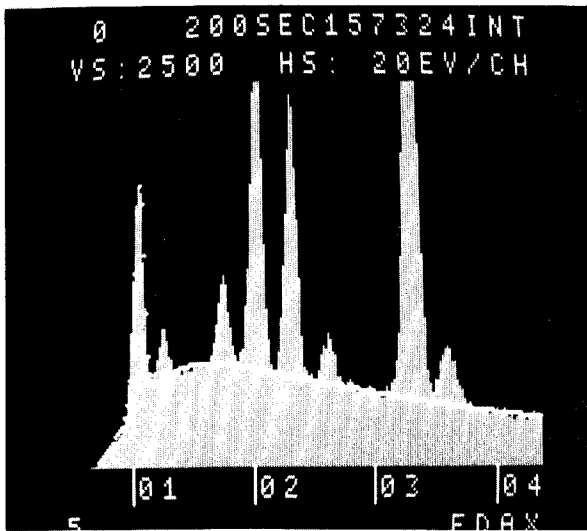
4a
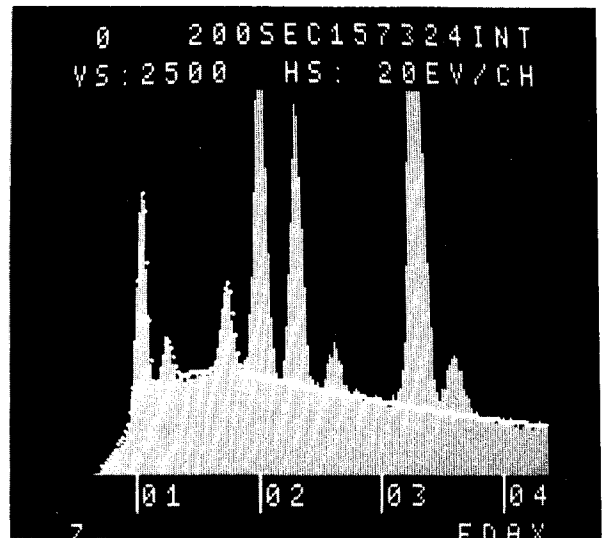
4b

Figure 4 Fitted background curve plus generated Na peak (a). User can then add Al and Si (b). Detail of potassium K_α is shown in (c).
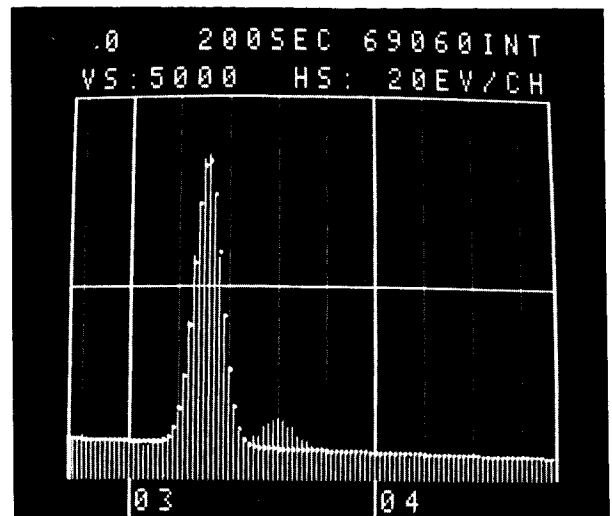
4c
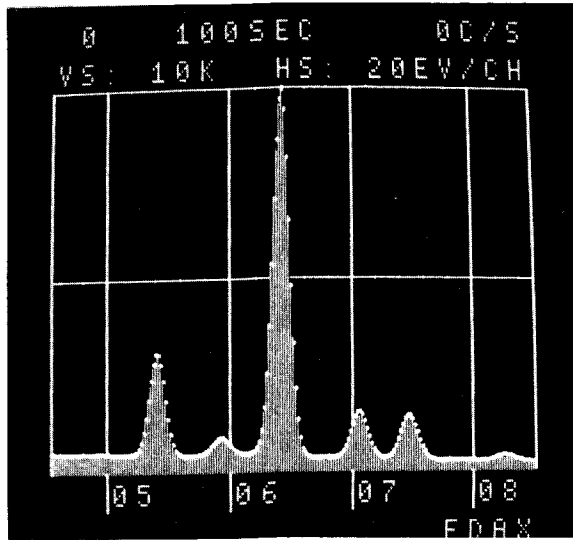
5a
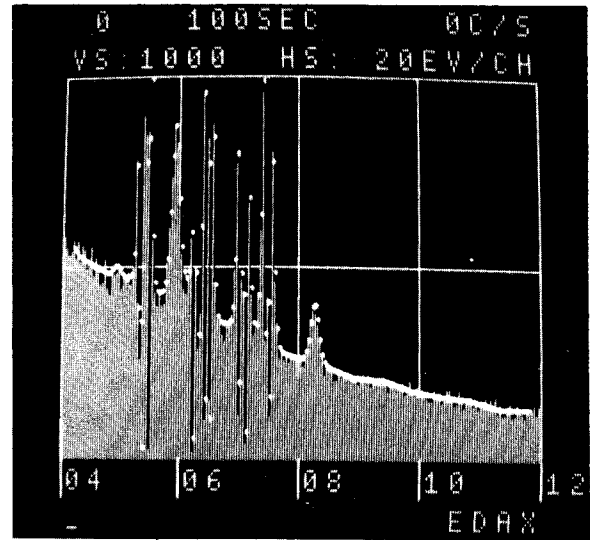
5b

```
-> 8 K!
   ELEM(Z)        NET CPS
     V -23           2.518
    CR-24          234.79
    MN-25           16.971
    FE-26          921.91
    NI-28          116.31
->
```

5c

Figure 5 Automatically fitted background curve and peaks (see printout) for a stainless steel. Note that trace V and overlapped Mn peaks are found, and that Co (which is not present) is not listed.
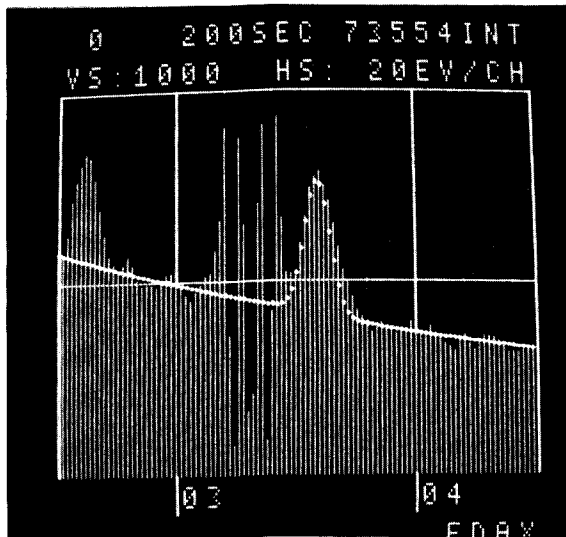
6a
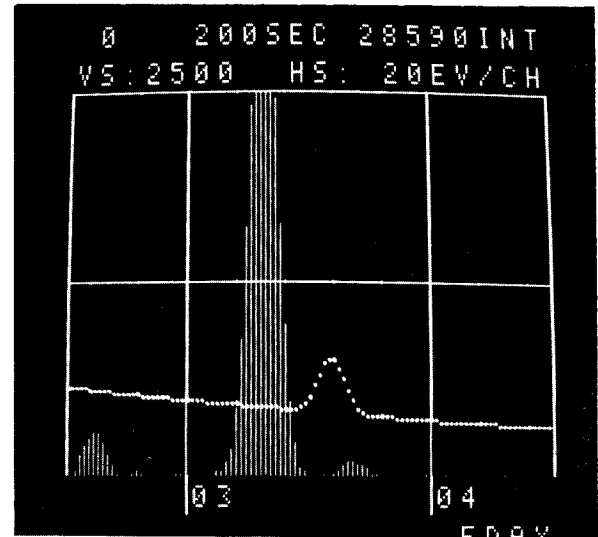
6b

Figure 6: Background curve plus generated potassium K_β line (a). Subtraction leaves small Ca K_α peak at 3.69 keV (b).

COMPUTER INDEXING OF X-RAY EMISSION SPECTRA

N. Spielberg
Department of Physics
Kent State University, Kent, Ohio, 44242

Most applications of computers to the analysis of x-ray spectra, whether generated in a microprobe or scanning electron microscope or in a fluorescence analysis instrument, deal with the conversion of x-ray spectral intensities to quantitative or relative amounts of various atomic species actually participating in the emission process. In these cases, the identifications of the pertinent spectral lines are known beforehand. Relatively few applications have been reported of the use of a computer to actually index or identify each and every x-ray line observed in the spectrum of a specimen. A given analytical specimen may be totally uncharacterized previously or contain components not previously expected. In principle, the x-ray spectrum emitted by the specimen can be used to completely characterize qualitatively or even semi-quantitatively its elemental composition for all atomic numbers greater than 5 or 6, depending upon the elemental range and sensitivity of the instrumentation employed. (Although variable specimen preparation procedures do have a drastic effect on the intensities of various observed spectral lines, this can only affect quantitative analyses.) This paper reports the results of an initial study of possible Fortran programs for accomplishing this task.

Simply put, the task requires the comparison of observed x-ray spectral lines with a reference table of wavelengths of the line emissions for all the elements. For the elements from atomic number 22 to 100, there are roughly 1600 spectral lines in the wavelength range from 0 to 3 Angstroms. The observed spectrum of an alloy steel sample, for example, may contain upwards of 30 or 40 lines. The "manual" identification of all these spectral features, based only on the wavelengths and intensities observed, and with no prior assumptions as to which elements are likely to be found in the specimen, may take as long as 30 to 60 minutes. The process requires that account be taken of the relative intensities of spectral lines in a given series, the instrumental resolution, the relative intensities of the various orders of diffraction, and the fact that certain orders may be missing or very weak. (Pulse height discrimination techniques may not always be available or completely effective.) For example, topaz cut parallel to the 101 planes is often used as an analyzer crystal. The principal reflection used is (303); but reflections from (606) and (909) are commonly obtained, and even other (h0h) reflections, starting with h = 1, may be observed. The cleavage planes of mica in third, fourth, or fifth order are used in one type of microprobe spectrometer, but all orders from first to eighth or tenth may be readily observed. Si (111) and (333) reflections are observed, while Si (222) is extinct.

A superficially simple computer indexing program would automate the table "look-up" process, assign all possible identifications of the observed spectral features by matching λ/n of the observed lines against tabulated values, where n is the order of diffraction, and then eliminate those identifications which fail to meet the following criteria: (1) The excitation potential used in the experimental measurements must be high enough to actually excite the assigned line. (2) If, for example, a $K\alpha_{1,2}$ line is identified, then the corresponding $K\beta_1$ line should also be present, at roughly 1/4 to 1/10 of the intensity of the $K\alpha_{1,2}$ line. Conversely the identification of a $K\beta_1$ line requires the presence of the $K\alpha_{1,2}$ line at 4 to 10 times greater intensity. Similar considerations apply to L-series lines. (3) A line observed in a given order of reflection should be observed in other orders, with due account taken of the relative reflectivities of the various orders. The application of these criteria is complicated by the possible presence of other unresolved lines superposed on a particular line, leading to multiple identifications and resulting ambiguity of intensity assignments, and by the possibility that the expected line intensity might be smaller than experimentally detectible.

Such a program was prepared for an IBM 1130 computer having a CPU memory of 16K 16-bit words, plus auxiliary disk storage. While this computer was chosen primarily because of its availability, its use also made it possible to draw conclusions as to the feasibility of this task for small computers in general, as contrasted to a large computer. For such a case, it is necessary to store the reference wavelength table in the disk memory, which has considerably longer access time than the CPU memory. Moreover, the simple approach described above is too cumbersome, and criterion (2) was applied before line identifications were assigned. In fact, the program as actually written was itself too large for the CPU, and was divided into some 11 segments to be called up from the disk as needed. In this process it was necessary to store intermediate results on the disk as well. The result was that more time was required for the "programmed" indexing than for "manual" indexing!

In order to get some idea of the relative effects of CPU speed and auxiliary memory access, the program was then transcribed, essentially without change, for a Burroughs B5500 computer. This larger computer has a CPU memory of 32K 48-bit words, plus auxiliary memory modules, disk storage, and tape storage. Although it has a much faster CPU cycle time than the IBM 1130, the access time to disk storage is about the same as for the IBM 1130. Although the various subprograms could now be stored in core memory, the storage of intermediate results, as well as the reference wavelength table, on disk was maintained. The results on two typical test spectra were total computer times of 18.62 minutes and 53.12 minutes, with input-output (I/O) times of 10.27 minutes and 29.43 minutes respectively. It is estimated that perhaps half the I/O time was involved in "table look-up", and half in the storage of intermediate results.

In order to obtain a faster indexing program, steps are required to reduce the amounts of time spent in "table look-up", in matching the observed spectral features against the reference table, and in testing various identifications for possible rejection at some later stage. Two obvious steps can be applied: (1) The excitation potential test should be applied to each line before any "look-up" or matching procedures are begun, particularly when indexing for higher orders of diffraction. (2) Moseley's Law can be used to calculate an estimated atomic number Z for each observed line, assuming that it is the $K\alpha_{1,2}$ line. The table "look-up" is then restricted to the wavelengths for that particular element, and for elements of atomic number Z-1 and Z+1. If a match is found, the observed spectrum is then searched for the corresponding $K\beta_1$ line. If the $K\beta_1$ line is indeed found, higher order reflections are searched for. Assuming these are found, subject to minimum detectibility considerations, then and only then are other K-series lines searched for. No separate search is made for other lines in the K-series than the $K\alpha_{1,2}$. A similar procedure can be followed with L-series lines. A supplemental higher order search is necessary to identify those lines for which the principal order reflections are beyond the range of the observed data.

It is estimated that the application of these procedures should substantially reduce the total length of the program and result in a total execution time reduced by a factor of several fold. This should facilitate the use of small computers for this purpose.

Progress in Quantitation of
Single-Particle Analysis with the Electron Probe

J.A. Small, K.F. Heinrich, C.E. Fiori,
D.E. Newbury, and R.L. Myklebust

Institute for Materials Research
National Bureau of Standards
Washington, DC 20234

Extended Abstract

During the past few years several groups of investigators have been studying the problem of quantitative electron probe analysis of particles. In addition to the quantitative methods discussed by Armstrong at last year's M.A.S. meeting[1], ratios of characteristic to continuous x-ray intensities are being used to correct for particle effects[2,3,4] and Monte Carlo simulations of electron trajectories are being used to predict x-ray emissions from particles[5].

The National Bureau of Standards is currently developing methods for the quantitative analysis of particles which are based on the energy distribution of the continuous x-rays generated as a result of the electron beam interaction within the sample. The methods being studied involve two major lines of research, both of which we feel are necessary in order to obtain a practical method for the analysis of real-world particles. The first line is to develop a general expression to describe the distribution of continuous x-radiation emitted from samples as a function of atomic number, accelerating voltage and particle parameters. The second line is the use of the ratio between characteristic and continuous radiation, which will hereafter be referred to as the line-to-background ratio (L-B ratio), to account for the difference between the volume of beam interaction within a particle and a bulk standard.

Only the results from the second line of research will be presented
here.

The use of L-B ratios to correct for particle effects was discussed
by us and by Statham and Pawley at the SEM meeting in April of this
year[3,4]. The method is a modification of the method used by Hall to
correct for the excited volume in thin films[6]. It assumes, as a first
approximation, that the depth distribution of generation for character-
istic x-rays is the same as that for continuous x-rays of the same energy.
For instance, a continuum x-ray emission generated in a particle at
6.4 keV would be influenced by particle effects to about the same extent
as a characteristic x-ray emission at 6.4 keV.

Experimental

The glass microspheres used in this study were made from NBS glass
K-309 which has a nominal composition listed in Table 1. A study of
cross-sectioned spheres has shown that the spheres have the same com-
position as bulk glass[3]. The microspheres were suspended in ethanol

Table 1

Composition of Glass K-309

Element	Weight Fraction[a]
O	0.388
Al	0.079
Si	0.187
Ca	0.107
Ba	0.105
Fe	0.134

[a] Composition has been confirmed by electron
probe microanalysis.

and mounted on a thin film which was supported by a beryllium
microscope grid. The samples were coated with approximately

10 nm of carbon before analysis. Experimental measurements were made on different size microspheres with a scanning electron microscope equipped with a lithium-drifted silicon x-ray detector. The accelerating voltage used for the measurements was 17.4 kV, the detector take-off angle was 30 degrees, and the beam current was 1×10^{-9} amps. Two raster methods were used for the analysis of the spheres. One set of spheres was analyzed by scanning the electron beam over an area slightly smaller than the cross-sectional area of the sphere (see fig. 1). The other set of spheres was analyzed by scanning the electron beam over an area larger than the cross-sectional area of the sphere.
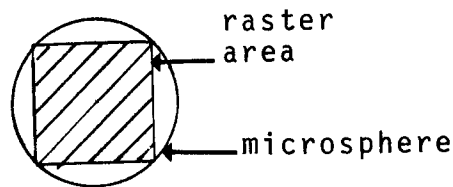
Figure 1: Diagram of the Small Area Scan.

Calculation of the Line-to-Background Ratios

The L-B ratios are calculated from equation (1) in which I_E equals the experimental intensity within a region of interest of photon energies for a characteristic line, I_{Bkg} equals the calculated background intensity, from the data reduction procedure, FRAME C[7], for the same region of interest and R is the ratio:

$$R = \frac{[I_E - I_{Bkg}]}{I_{Bkg}} \qquad (1)$$

The continuum from the carbon film is ignored and the particle spectrum is assumed to have a continuum which originates from only the analyzed particle. This is a reasonable assumption since the intensity from the carbon film is small in most cases as shown in figure 2 which is plots of the spectra from an 8 μm particle and the carbon film.
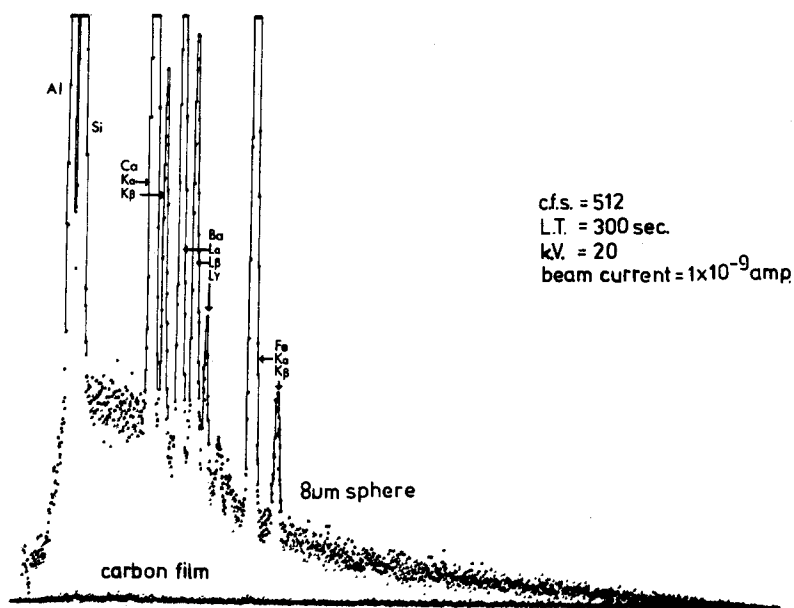

Figure 2: Spectra of an 8 μm Particle and the Carbon Mounting Film.

The continuum for a given particle is fit by a computer with equation(2).

$$I_E = [A \cdot (E_0 - E) + B \cdot (E_0 - E)^2] \cdot 1/E \ f(x) \cdot P_E \qquad (2)$$

I_E equals the intensity of the continuum at energy E, E_0 equals the

accelerating voltage, A and B are empirical coefficients, f (χ) is the

absorption term, and P$_E$ is the detector efficiency. Two experimental points

are used to determine the coefficients A and B. The equation is then

used to obtain the continuum fit through the two experimental points.

Equation 2 which is a modification of Kramer's equation was originally

derived for bulk specimens and is being used to calculate a first

approximation for the particle continuum. Work is currently underway

to derive a more exact expression for the continuum generated in

small particles. Figure 3 shows the spectrum from a particle

10 μm in diameter and the calculated background. The continuum

regions selected for the fit were taken between the Si K and

Ca Kα peaks and at an energy slightly greater than the Fe Kβ

peak. The fit is in good agreement with the experimental

continuum over the entire energy range,

Background Fit for
a 10um sphere

L.T. = 300 sec.
kV. = 17.4
beam current = 1x10^{-9} amp.
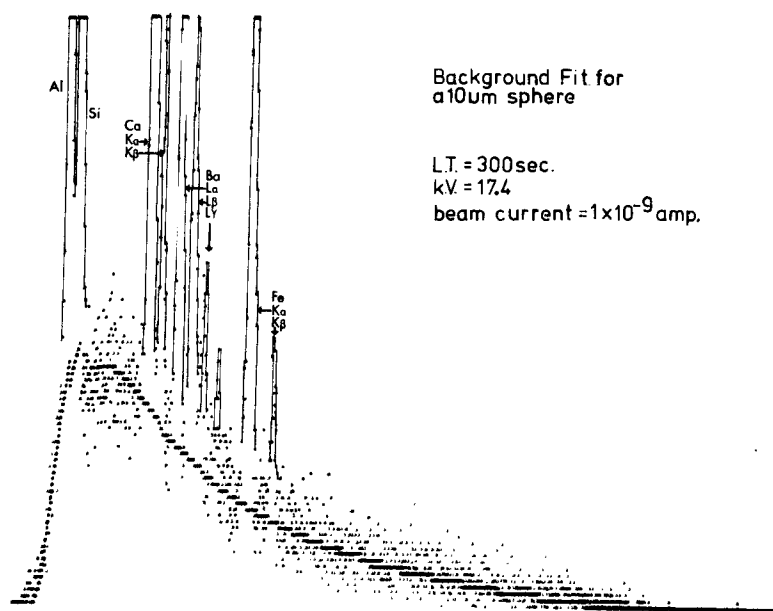
Figure 3: Spectrum from a 10 μm Particle and the
Calculated Continuum

Results

The results from the analysis of microspheres ranging in size from 1.5 to 29 µm in diameter are reported in tables 2 and 3. Table 2 contains the results from spheres analyzed with the small area scan and table 3 contains the results from spheres analyzed with the large area scan. The average L-B ratios from the spheres analyzed with a large area scan are closer to the bulk values than the L-B ratios obtained from spheres analyzed with a small area scan. The better agreement of the L-B ratios for spheres analyzed with the large area scan may be the result of averaging the particle geometry effects over the entire particle[8].

The average values of the L-B ratios for both raster methods are within 15 percent of those for the bulk glass except for the calcium value from table 2 which is within 21 percent of the bulk glass value. While the characteristic peak intensity ratios between the spheres and bulk glass show a strong dependence on particle diameter and scan area, the L-B ratios do not show any major variations with these factors. In addition the L-B ratios for the spheres are much closer to the bulk values than the ratios of the characteristic intensities.

Procedure for the Quantitative Analysis of Single Particles

Ideally, we would like to measure the spectrum from the particle and spectra of pure element or simple compound standards as the only data input for quantitative analysis,

Table 2

Line-Background and Characteristic Intensity
Ratios for K-309 microspheres*

Element	Al		Si		Ca		Ba		Fe	
Sphere Diameter in μm	a	b	a	b	a	b	a	b	a	b
1.5	1.2	0.76	0.89	0.77	0.89	0.74	0.95	0.72	0.93	0.73
1.8	1.2	0.44	0.94	0.35	0.79	0.36	0.66	0.32	0.93	0.44
1.8	0.95	0.40	0.96	0.43	0.74	0.41	0.66	0.39	0.80	0.47
3.4	0.92	0.70	0.94	0.73	0.90	0.81	0.76	0.71	0.90	0.80
6.2	0.87	0.77	0.91	0.84	0.93	0.95	0.81	0.86	0.91	0.90
8.0	1.0	0.64	0.98	0.67	0.93	0.75	0.96	0.80	0.92	0.77
Ave.	1.0	0.62	0.94	0.63	0.86	0.67	0.80	0.63	0.90	0.69

* Spheres were analyzed by scanning the beam over an area slightly
  less than the cross-sectional area of the sphere.

a Line-to-background ratios normalized to bulk values

b Characteristic intensity ratios

Table 3

Line-Background and Characteristic Intensity
Ratios for K-309 microspheres*

Element Sphere Diameter in μm	Al a	Al b	Si a	Si b	Ca a	Ca b	Ba a	Ba b	Fe a	Fe b
1.6	1.0	0.12	1.1	0.13	0.86	0.10	0.83	0.87	1.0	0.12
3.0	0.97	0.47	0.97	0.47	0.86	0.40	0.88	0.41	0.96	0.43
4.3	0.91	0.26	0.95	0.27	0.89	0.24	0.93	0.24	1.1	0.27
4.3	1.0	0.45	0.99	0.45	0.88	0.40	0.93	0.42	0.96	0.43
5.3	1.3	0.25	1.2	0.24	0.89	0.21	0.88	0.21	0.90	0.22
10.0	0.98	0.23	0.96	0.23	0.96	0.23	0.94	0.23	0.94	0.23
10.4	1.0	0.24	1.0	0.24	1.0	0.25	1.0	0.26	1.1	0.26
15.1	1.4	0.23	1.2	0.21	0.98	0.22	0.97	0.28	0.95	0.23
29.0	0.97	0.22	1.0	0.23	0.94	0.25	0.94	0.25	0.91	0.28
Ave.	1.1	0.27	1.0	0.27	1.0	0.26	0.92	0.26	0.98	0.27
Ave.**	1.0	---	1.0	---	0.89	---	0.90	---	0.98	---

* Spheres were analyzed by scanning the beam over an area larger
  than the cross-sectional area of the sphere.

** Average of spheres less than ten micrometers in diameter

a Line-to-background ratios normalized to bulk values

b Characteristic intensity ratios

The observation that the L∗B ratios are similar on particles and bulk material of the same composition (equation 3) suggests that the peak intensity of the particle can be scaled up to a value appropriate to bulk material (equation 4),

$$(P/B)_{particle} = (P/B)_{Bulk} \qquad (3)$$

$$P^*_{Particle} = P_{Bulk} = \frac{P_{Particle} \cdot B_{Bulk}}{B_{Particle}} \qquad (4)$$

The value of the scaled intensity, P^*, could then be used to form a k∗value which would be an appropriate input for FRAME as if no particle size effects existed. The difficulty in practice is that for a typical unknown particle we will not have a bulk material of the same composition to measure the values of B_{Bulk}. An appropriate value of B_{Bulk} can be determined from the continuum measured on any standard if we know the ratio of the average atomic number of the bulk unknown, $\overline{Z}_{Bulk}$, to the atomic number of the standard, (equation 5)

$$B_{Bulk} = \frac{\overline{Z}_{Bulk}}{\overline{Z}_{Standard}} , \quad B_{Standard} \qquad (5)$$

We can estimate an initial value of $\overline{Z}_{Bulk}$ with reasonable accuracy and use this in an iteration. The first estimate is used in equation 5 to obtain a value for B_{Bulk}. This value, B^1_{Bulk}, is then used in equation 4 to obtain the first estimate of the scaled particle intensity, P^{*1}. A set of k∗ratios are then calculated and used as the input to FRAME:

$$k^1 = P^{*1}_{Particle} / P_{Standard} \qquad (6)$$

The concentrations thus found are used to calculate a new value of $\bar{Z}_{Bulk}$ and the sequence is repeated. This procedure is a first approximation for quantitative analysis. It is expected to show the most serious discrepancies where absorption effects are most serious, such as in the case of an analytical line near an absorption edge.

Acknowledgements

We would like to acknowledge W.K. Haller, M.F. Dilmore and D.H. Blackburn of the inorganic materials division of NBS for the manufacture of the bulk glass and the glass microspheres.

Bibliography

(1) J. T. Armstrong and P. R. Buseck, Proceedings, 12th Annual Conference of the Microbeam Analysis Society, Boston, Mass., August 1977, No. 41.

(2) C. E. Fiori et al. Proceedings 7th I. M. R. Symposium 1974, NBS Special Publication 422, U. S. Government Printing Office, Washington, DC, 1976, 1283-1291.

(3) J.A. Small et al., Proceedings 11th Annual Scanning Electron Microscopy Symposium, Los Angeles, April, 1978 (in press).

(4) P. Statham and J. Pawley, Proceedings, 11th Annual Scanning Electron Microscopy Symposium, Los Angeles, April, 1978 (in press).

(5) R.L. Myklebust, D. E. Newbury, and H. Yakowitz, Use of Monte Carlo Calculations in Electron Probe Microanalysis and Scanning Electron Microscopy. NBS Special Publication 460. U. S. Government Printing Office, Washington, DC, 1976, 105-125.

(6) T. Hall, Quantitative Electron Probe Microanalysis, NBS Special Publication 298, 1968, p 269.

(7) R. L. Myklebust, C. E. Fiori, Proceedings 12th Annual Conference of the Microbeam Analysis Society, Boston, Mass., August 1977, No. 97.

(8) J. T. Armstrong and P. R. Buseck, Anal. Chem., 47, 2178-2192 (1975).

ESTIMATING MASS THICKNESS IN SEMI-THIN SECTIONS

M. A. Giles and N. C. Barbi
Princeton Gamma-Tech, Inc.
P. O. Box 641
Princeton, New Jersey 08540

In attempting to quantitate x-ray intensity data from small particles or thin sections, one must either invoke the thin film assumption or apply corrections consistent with the mass thickness of the sample. Thickness measurements and density calculations may be prohibitively difficult and inaccurate.

In one analytical scheme proposed for semi-thin sections, atomic number and absorption corrections are applied in proportion to the ratio, z/z_r, where z is the mass thickness of the analyzed region and z_r is the x-ray range.[1]

In order to estimate z/z_r internally from x-ray intensity measurements, it is assumed that the concentration of element i (C_i) is equal to the ratio of the intensity of element i in a sample of thickness t to that in a pure element section of the same thickness:

$$C_i = \frac{I_i^t}{I_i^{ot}} \qquad (1)$$

If C_i can be estimated (for example, from normalized k-ratios relative to the bulk pure element), I_i^{ot} can, in turn, be estimated from equation (1).

Combining the derivations of Philibert and Tixier[2] and Reed[3] for the ratio of the pure element thin section intensity to the bulk pure element intensity, equation (2) results:

$$\frac{I_i^{ot}}{I_i^o} = K \frac{(\ln(U)/U)(S)(z)}{R\,E_c^2} \qquad (2)$$

where I_i^{ot} = intensity from section of pure element i of thickness t

I_i^o = intensity from bulk pure element i

$U_i = E_o/E_c$

R = backscattering factor
S = stopping power factor
z = mass thickness of sample
E_c = critical excitation potential for a given x-ray line

The "constant", K, in equation (2) was evaluated at the following boundary condition:

$$\frac{I_i^{ot}}{I_i^o} = 1 \text{ when } z = z_r$$

K was found to be a function of E_o (accelerating voltage), E_c, Z (atomic number) and A (atomic weight), shown in equation (3) for K lines and equation (4) for L lines.

$$K = U^{0.3}(K' + K''(E_c^{0.1}/(Z/A))) \qquad (3)$$

where K' = -30137900 and K" = 37416750

$$K = K' + K''(E_c^{0.2}U^{0.39}/(Z/A)) \qquad (4)$$

where K' = 60920240 and K" = 10885660

A plot of K calculated using equation (3) versus K evaluated at the boundary condition is shown in Figure 1, where the 45° line represents perfect agreement between the two. The agreement obtained using equation (4) for L lines is similar.

The mass thickness calculation was tested by comparing the calculated thickness with visual estimates of particle thickness. The results were in good agreement but could not be critically evaluated since even visual estimates of thickness are difficult in the SEM except for the most regular particles.

REFERENCES

1. N. C. Barbi et al., "Estimating Concentrations in Small Particles Using X-ray Analysis in the Electron Microscope", submitted to SEM/78, April 1978.

2. J. Philibert and R. Tixier, "Some Problems with Quantitative Electron Probe Microanalysis", in Quantitative Electron Probe Microanalysis (K.F.J. Heinrich, ed.), NBS Spec. Publ. 268, U.S. Govt. Printing Office, Washington DC 20402, pp. 13-33.

3. S. J. B. Reed, Electron Microprobe Analysis, Cambridge University Press, Cambridge, England, 1975, p. 329.
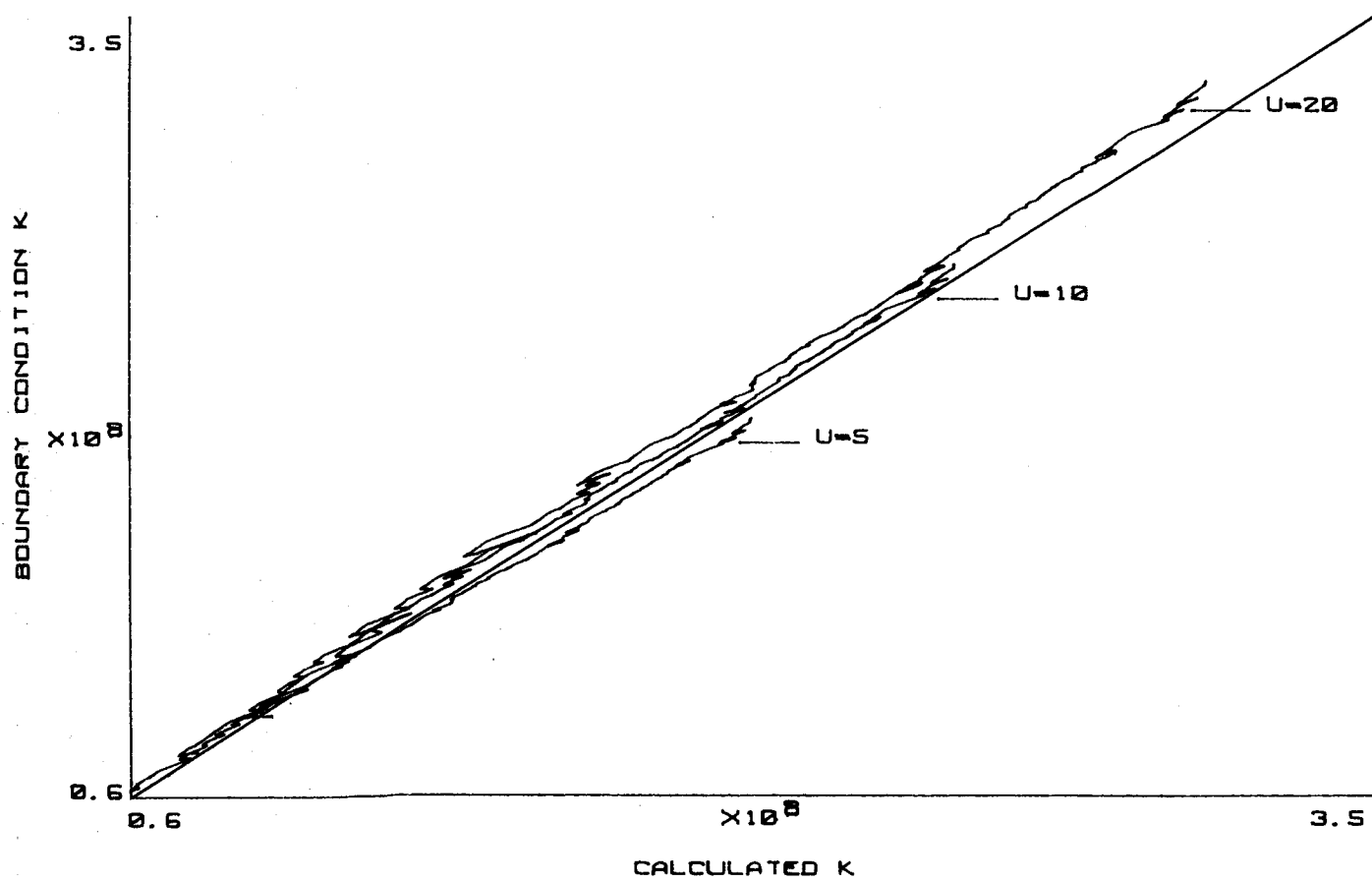
Figure 1

Variation in Intensity Ratios Used to Identify Asbestos Fibers

John C. Russ
EDAX Laboratories
P.O. Box 135
Prairie View, IL 60069

Identification of asbestos fibers and other small particulate matter observed in TEM and STEM is often based in whole or part on the ratios of elemental intensities[1,2]. The underlying principle in this method is the linear relationship between concentration ratio and intensity ratio, which has been proposed by many authors, some of whom measure the proportionality factors[3] and others calculate them from quasi-theoretical relationships[4].

To be able to routinely apply this method to confidently identify particles, it is necessary to evaluate the magnitude of variation that may be encountered, and the extent to which it may allow for confusion. We have analyzed a series of asbestos minerals and others which potentially could be mistaken for them. Table 1 lists the concentrations of the major elements which would normally be chosen for analysis, and Figure 1 shows the concentration ratios Mg/Si and Fe/Si, indicating that the materials are indeed all distinct.

Table 1
Bulk concentration (w/o) of major elements (by XRF)

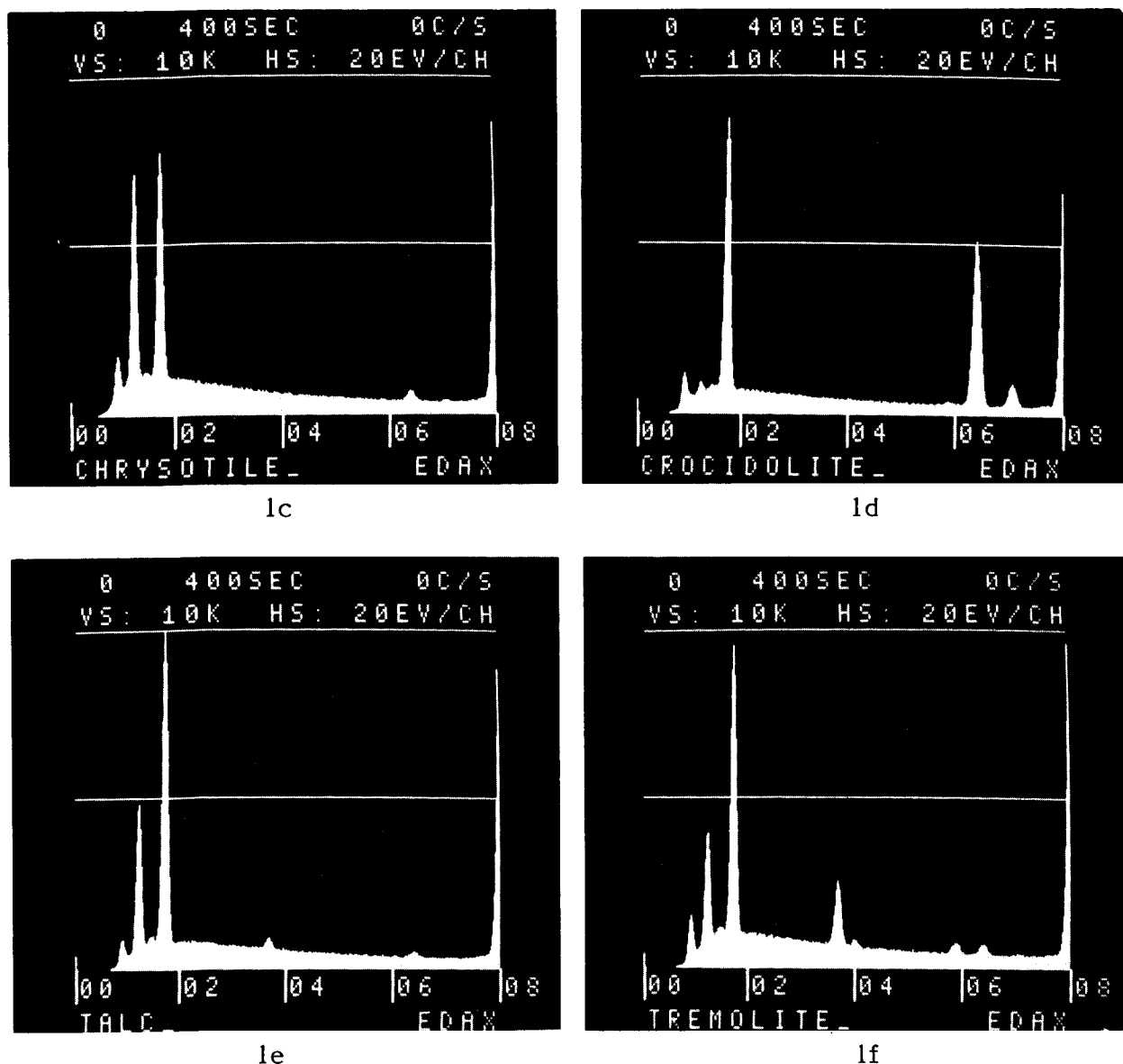| mineral	% Mg	% Si	% Fe
amosite	2.4 – 4.0	22.4 – 23.1	28.4 – 34.2
anthophyllite	12.7 – 17.2	21.5 – 27.1	4.3 – 8.4
chrysotile	24.0 – 25.9	18.3 – 19.6	1.4 – 2.4
crocidolite	0.6 – 1.60	22.7 – 23.8	27.9 – 29.5
talc	18.3 – 19.2	28.1 – 29.6	0.3 – 1.0
tremolite	14.4 – 14.8	26.5 – 29.6	1.0 – 3.3

1a

1b

1c

1d

1e

1f
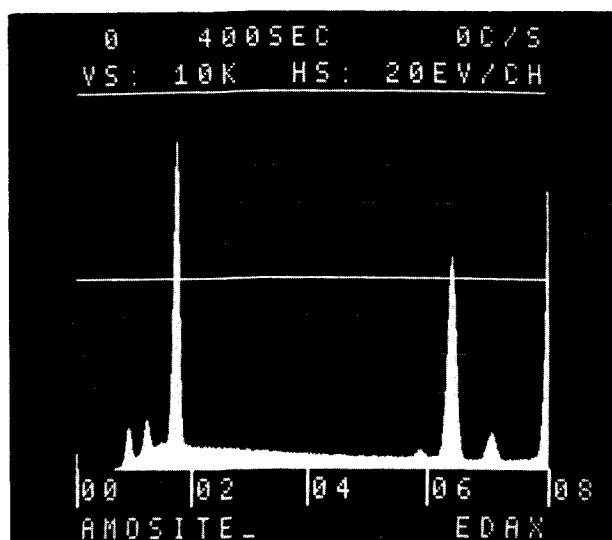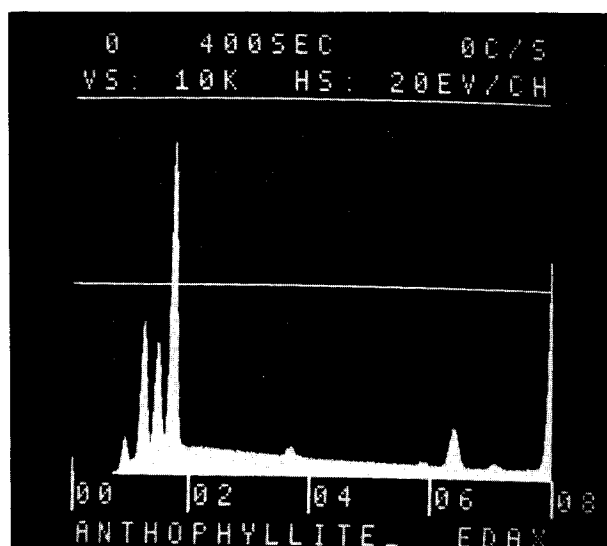
Figure 1 (a-f)   Representative spectra from various mineral particles.

Figure 2 shows representative electron-excited spectra of particles at 80kV in the STEM. From such spectra, measured for 400 seconds to obtain good counting statistics, we determined the factors k_{xSi} defined by the relationship:

$$\frac{Conc_x}{Conc_{Si}} = k_{xSi} \frac{Inten_x}{Inten_{Si}}$$

Since the k_{xSi} factor is not truly a constant, but depends to some extent on particle size, orientation and matrix composition, we measured a series of particles ranging from approximately 0.1 to 5 μm, and for the larger particles measured spectra both with the beam centered on the fiber or particle and with the beam scanning to cover the entire

area (or for some of the longer fibers, a representative section). The total peak area above a fitted background curve was integrated and the mean bulk composition used to calculate k_{xSi} factors, which ranged as shown in Table 2.

Table 2

Calculated k_{xSi} factors for different minerals and particle sizes

mineral	k_{MgSi}	k_{FeSi}
amosite	not determined	1.12 - 1.57
anthophyllite	1.30 - 1.58	1.09 - 1.61
chrysotile	1.29 - 1.42	not determined
crocidolite	not determined	1.22 - 1.59
talc	1.31 - 1.71	not determined
tremolite	1.31 - 1.65	not determined
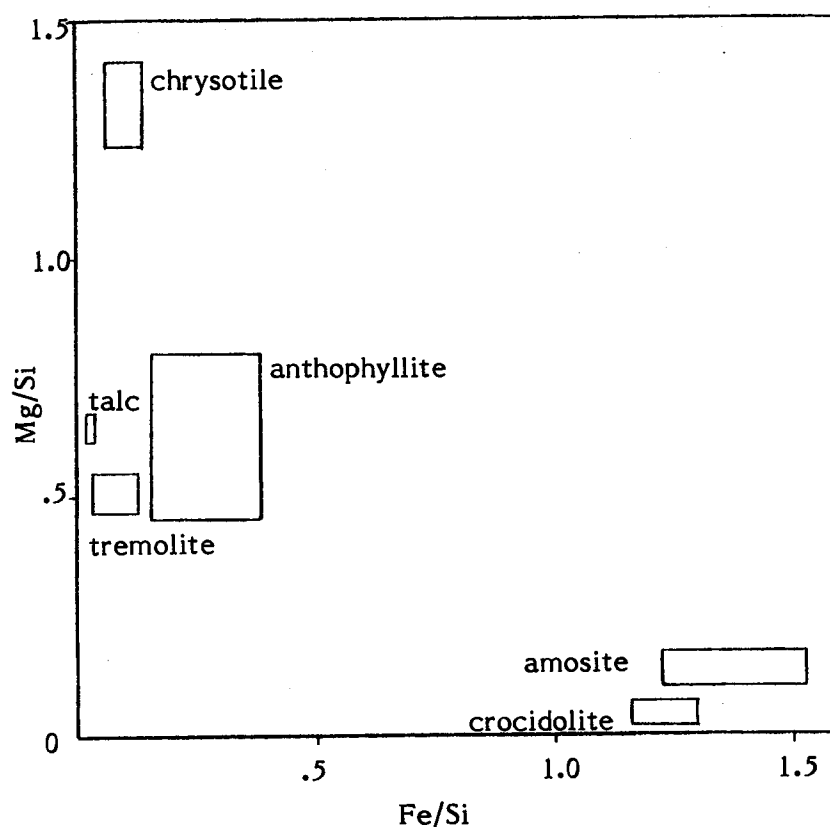
Figure 2 Plot of concentration ratios for minerals (see Table 1).

In general, the higher values of k_{MgSi} and lower values of k_{FeSi} represent the larger particles. The overall mean values for the factors were

$$k_{MgSi} = 1.41 \qquad\qquad k_{FeSi} = 1.48$$

These values include fundamental constants such as fluorescent yield, the influence of microscope parameters such as the accelerating voltage influence on ionization cross-section, and X-ray detector parameters such as beryllium window thickness, and so will vary from one experimenter and apparatus to another.

Since practical identification of mineral particles in the microscope normally involves many particles, it is necessary to restrict the analyzing time per particle. As an apparently practical compromise, we chose to count until the silicon peak reached 1000 full scale (at which point its integrated area was 5500-6000 counts). This required times varying from less than 20 seconds for the larger particles to more than 100 seconds for the smaller ones.

For a series of ten such measurements, all on a single particle of each type (each approximately 0.5 m in particle or fiber diameter), we then integrated the Mg, Si and Fe peaks and divided to obtain ratios. Table 3 shows the range of variation due to the statistics of counting, and Figure 3 shows a representative spectrum.

Table 3
Range of Intensity Ratios for Ten Measurements on same particle

mineral	Mg/Si	Fe/Si
amosite	0.023 - 0.181	0.917 - 1.008
anthophyllite	0.410 - 0.489	0.132 - 0.202
chrysotile	0.946 - 1.036	0.021 - 0.104
crocidolite	0.010 - 0.129	0.822 - 0.916
talc	0.402 - 0.511	0.006 - 0.051
tremolite	0.307 - 0.413	0.018 - 0.111
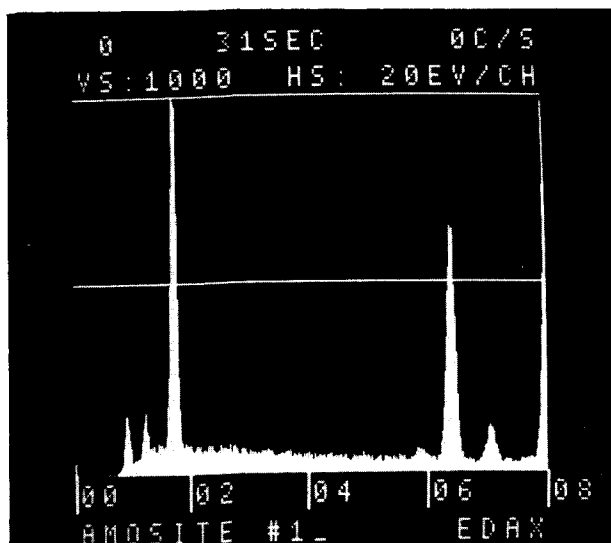
Figure 3 Repetitive short-time measurement on fiber of amosite, showing poor peak statistics.

Figure 4 shows these intensity ratio ranges graphically, and Figure 5 shows the same ranges enlarged by the error due to assuming the k_{xSi} factor is constant. It is clear that while many of the minerals can be readily distinguished, not all can. For amosite and crocidolite, some additional means of identification such as the presence of other elements, or electron diffraction must be added to the simple comparison of intensity ratios of the major elements. It is not practical to use a longer time to reduce the statistical spread, as the overlap would persist. Individual correction of the k_{xSi} factors for particle size, and conversion to concentration, is only useful for spectra having good counting statistics, and so is too time consuming for routine application to large numbers of analyses.
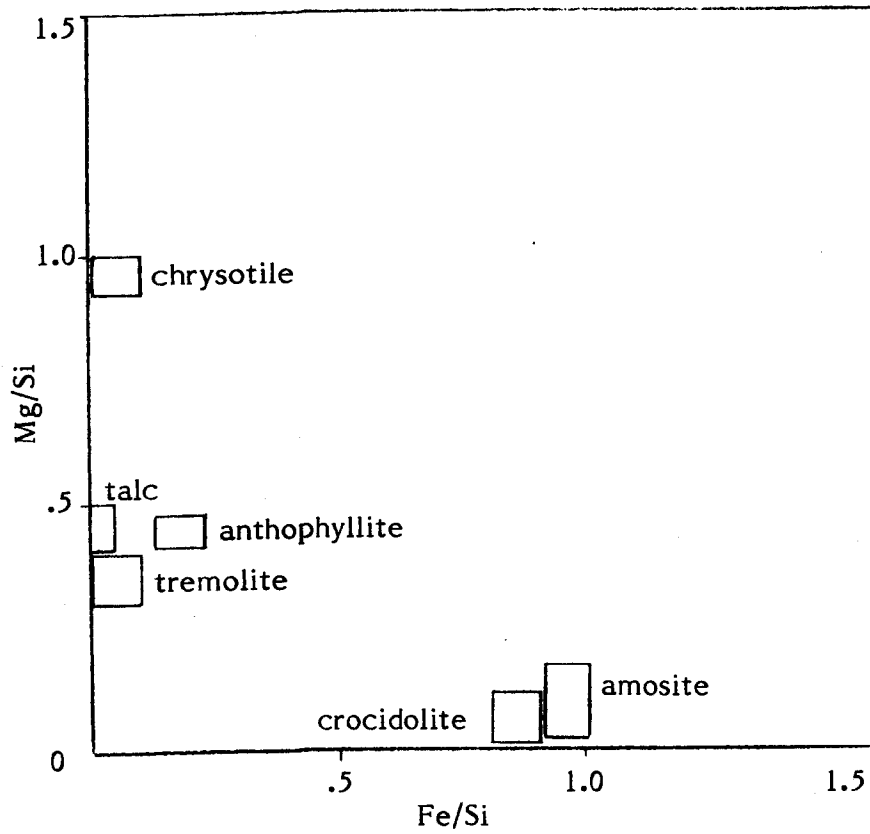
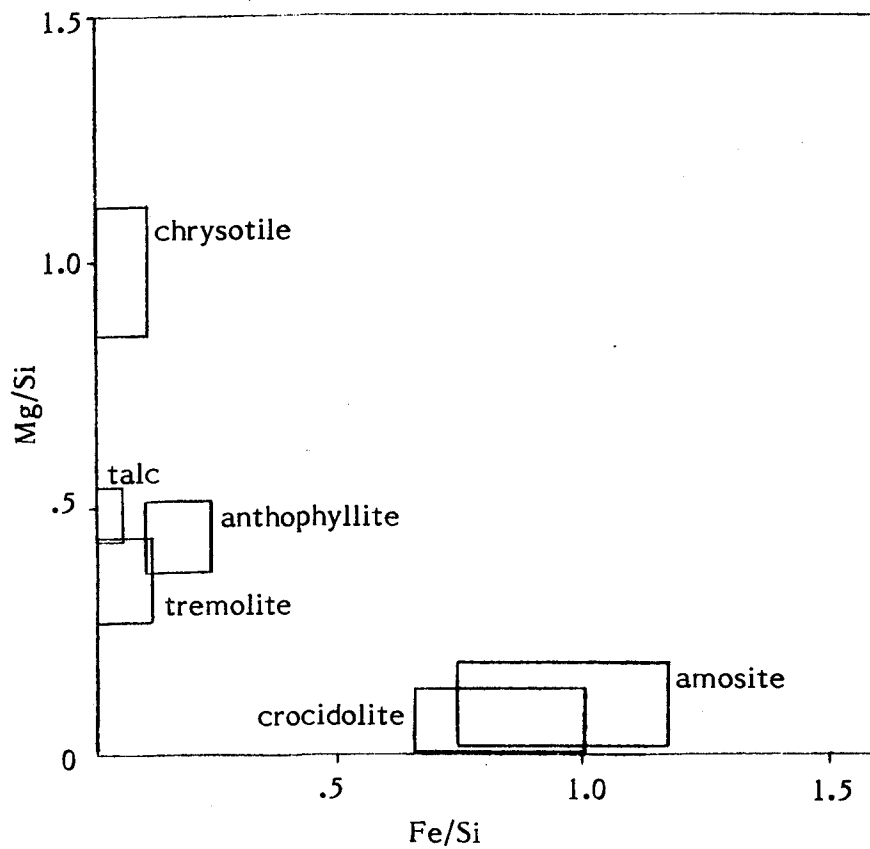Figure 4 Plot of intensity ratios for minerals (see Table 3).

Figure 5 Plot of total range of intensity ratios, including variation in k$_{xSi}$ due to particle size, geometry and matrix.

In general, the experimenter should be very careful in applying this fast and simple method. It is essential to first consider all probable overlaps of identification with other minerals which might be present.

References

1. D.R. Beaman and D.M. File, "Quantitative Determination of Asbestos Fiber Concentrations", Analytical Chemistry, Vol. 48, No. 1, January 1976, p. 101-110.

2. F.D. Pooley, "The Use of an Analytical Electron Microscope in the Analysis of Mineral Dusts", Phil. Trans. R. Soc. Lond. A. 286, p. 625-638, 1977.

3. G. Cliff and G.W. Lorimer, "Quantitative Analysis of Thin Foils Using EMMA 4 - The Ratio Technique", Proc. Fifth Europ, Congr. on Electron Microsc. Manchester, p. 140-141, London: Inst. of Physics.

4. J.C. Russ, "The Direct Element Ratio Model for Quantitative Analysis of Thin Sections", Microprobe Analysis as Applied to Cells and Tissues, T. Hall, P. Echlin and R. Kaufmann, 1974, p. 269-276.

CHEMICAL AND PHYSICAL CHARACTERIZATION OF COAL GASIFICATION
PARTICULATES, AND ITS RELEVANCE TO INHALATION TOXICOLOGY

D. L. Davidson and E. M. Gause

Southwest Research Center
P. O. Drawer 25810
San Antonio, Texas   78284

Introduction

The initial site of deposition of an inhaled particle depends primarily
upon its size; particles larger than 10 microns in diameter are trapped in
the nose, while particles between 10 and 3 microns are deposited in the upper
respiratory tract, and particles below 3 microns in diameter reach the deep
lung or alveolar region before being deposited. Particles smaller than 3
microns are generally referred to as being in the respirable size range.
(There are some exceptions to these generalizations as very long, narrow as-
bestos fibers have been found in the deep lung upon autopsy.)

Once respirable particles are deposited in the deep lung, clearance
mechanisms involve primarily phagocytosis by alveolar macrophages and solu-
bilization by lung fluids. After phagocytosis or ingestion by alveolar
macrophages, these cells attempt to break down the particles enzymatically;
however, enzymatic mechanisms are designed primarily for biological matter
and do not function effectively for disposal of combustion-derived parti-
culate matter. An exception to this statement is the class of mixed-function
oxidases which convert organic chemical compounds into water-soluble forms
which can be excreted from the body. Therefore, while polycyclic organic
compounds may be metabolized if they are adsorbed on particle surfaces, they
may be converted to more toxic forms which are carcinogenic or mutagenic be-
fore being released from the macrophage, and the particles, as well as metal-
lic or inorganic species will not be metabolized. If substances adsorbed on
the surfaces of the particles, or the particles themselves (such as silica)
are toxic to the macrophages, they will cause cell death resulting in release
of potent hydrolytic enzymes which can cause tissue damage and in release of
the particles themselves. The released particles may be taken up by another
macrophage to repeat the cycle. This effect may result in foci of dead and

dying macrophages — an observation which has been linked to tumor formation and to tissue necrosis;[1] it also results in local concentrations of the phagocytized particles or "hot" spots. There is evidence that particles which cannot be degraded by alveolar macrophages are eventually cleared from the lung by dissolution in lung fluids and transport into the circulation - a process which may take years or may never be successful.

Toxic chemical species can be concentrated on the surfaces of respirable particles by condensation and adsorption during the cooling of combustion products, resulting in much higher biologically available levels of such species than would be anticipated from bulk particle analysis.[2] In fact, high surface concentrations of species not even detectable by conventional bulk analysis or by single particle x-ray microprobe analysis can be attained. This surface form of presentation also maximizes biological uptake and biological impact of the toxic species, in that leaching of the toxic species by biological fluids is facilitated and contact of cells with surface-bound species is maximal. Surface deposition also results in a greater concentration of toxic trace element the smaller the particle diameter; and the smaller the particle diameter, the more likely it is to be inhaled and deposited within the deep lung.

The chemical nature and oxidation state, concentrations, etc., of species bound to the surfaces of respirable particles are determined by the inorganic components of fuels which may be present in extremely low concentrations and the conditions of the combustion process. The combustion process may result in condensation of minor fuel components upon surfaces of effluent particles leading to relatively high "environmentally effective concentrations." The capacity of particles resulting from a given process for producing serious adverse health effects is presently not understood, but is growing in importance as energy technology switches to alternate sources, both stationary and mobile.

Materials Examined

Particles described in this study were obtained from a European coal gasification plant. Details of the particle collection procedure are unknown. The particles were sieved to separate the most respirable particles from the bulk sample. Only the fraction below 20 microns in diameter was

directly examined; all information presented here was obtained from this material. The larger size fractions were ground in a ball mill with alumina grinding balls and re-sieved. The fraction of this ground material below 20 microns was also examined by surface analysis techniques, and the differences observed due to grinding are discussed.

For examination, a sample of particles was placed into reagent grade isopropyl alcohol. This slurry was then flooded onto sintered silver filter (Selas Co.) having a pore diameter of 0.45 μm.

Bulk Analysis

Because of the small size of the particles, electron penetration at the working voltages necessary for x-ray microprobe analysis causes fluorescence from most parts of the particle volume, as opposed to a true surface analysis by electron spectroscopy. The x-ray analysis was carried out at the University of Texas Health Science Center in San Antonio in cooperation with Dr. Nancy Smith using a JSM-35 Scanning Electron Microscope (SEM) equipped with a Tracor Northern model 880 energy dispersive x-ray spectrometer. Numerous particles were individually analyzed and photographed. The photographs of three typical particles are shown in Figure 1, and the x-ray spectroscopy of these particles is shown in Figure 2. The physical appearance of the silver filter may also be seen in the photographs; the chemical composition of the filter (after flooding with alcohol) is shown in Figure 3. From these illustrations and the data taken from a number of other particles, the particles we found to contain principally aluminum, calcium, iron, magnesium, silicon, sulfur, and perhaps small amounts of titanium or barium, chlorine and copper. The particles shown in Figure 1a and 1b have sufficient quantities of aluminum and silicon that they might be considered in the asbestos family. A quantitative analysis of the particle shown in Figure 1b indicated the constituents shown in Table I (excludes the silver filter components).

Table I

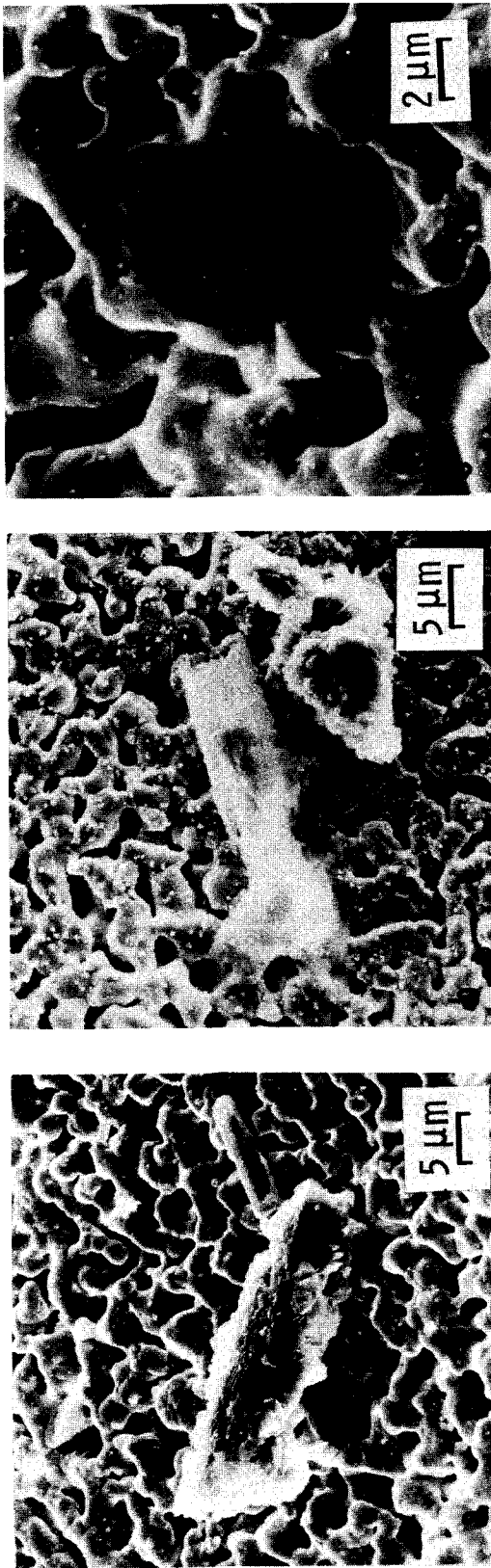| Element	Concentration (%)
Al	31.8
Si	30.6
Fe	3.5
Na	14.1
Cl	13.9

Figure 1. SEM Micrographs of Three of the Particles.
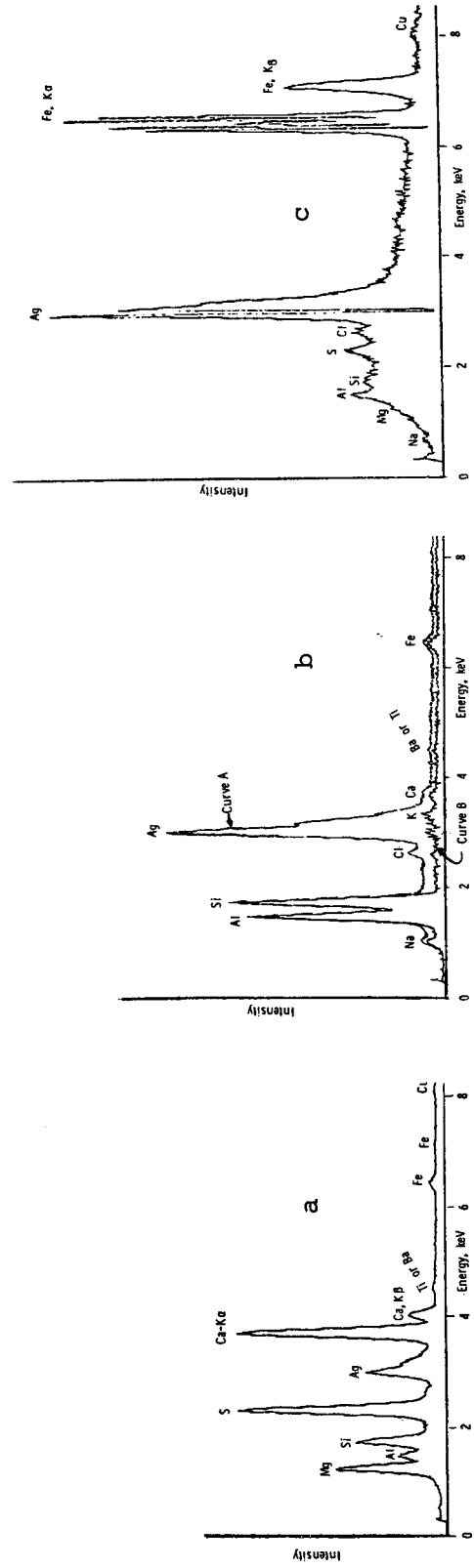

Figure 2. Energy Spectrums of the 3 Particles Shown in Figure 1 Showing their Bulk Elemental Chemistry.
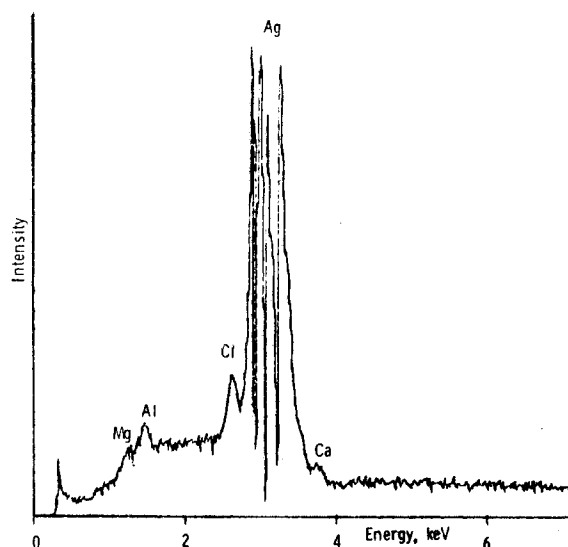
Figure 3. Energy Spectrum of the Silver Filter Carrier
for the Particles.

The techniques used in this analysis were the standard background sub-
traction and ZAF correction techniques furnished by the equipment manufac-
turer. The curve with silver filter spectrum subtracted is shown in Figure 2b
as curve B.

Surface Analysis

The same particulate material (but samples different than those examined
by energy dispersive x-ray analysis) was also subjected to surface analysis
by Auger Electron Spectroscopy (AES) and x-ray Photoelectron Spectroscopy
(XPS) also called ESCA. Because both of these techniques[3] depend on the
energy spectrum of relatively low energy electrons, only surface and near
surface material is included in the analysis, as opposed to the larger volume
of material from which x-rays originate in the microprobe analysis. Equip-
ment manufactured by Physical Electronics Industries was used for both the
AES and XPS analyses. The spectra shown in Figures 4 and 5 are representative
of several samples examined by both techniques. Detailed examination of the
XPS carbon and nitrogen peaks was made in order to determine the chemical
state of the compounds containing these elements.

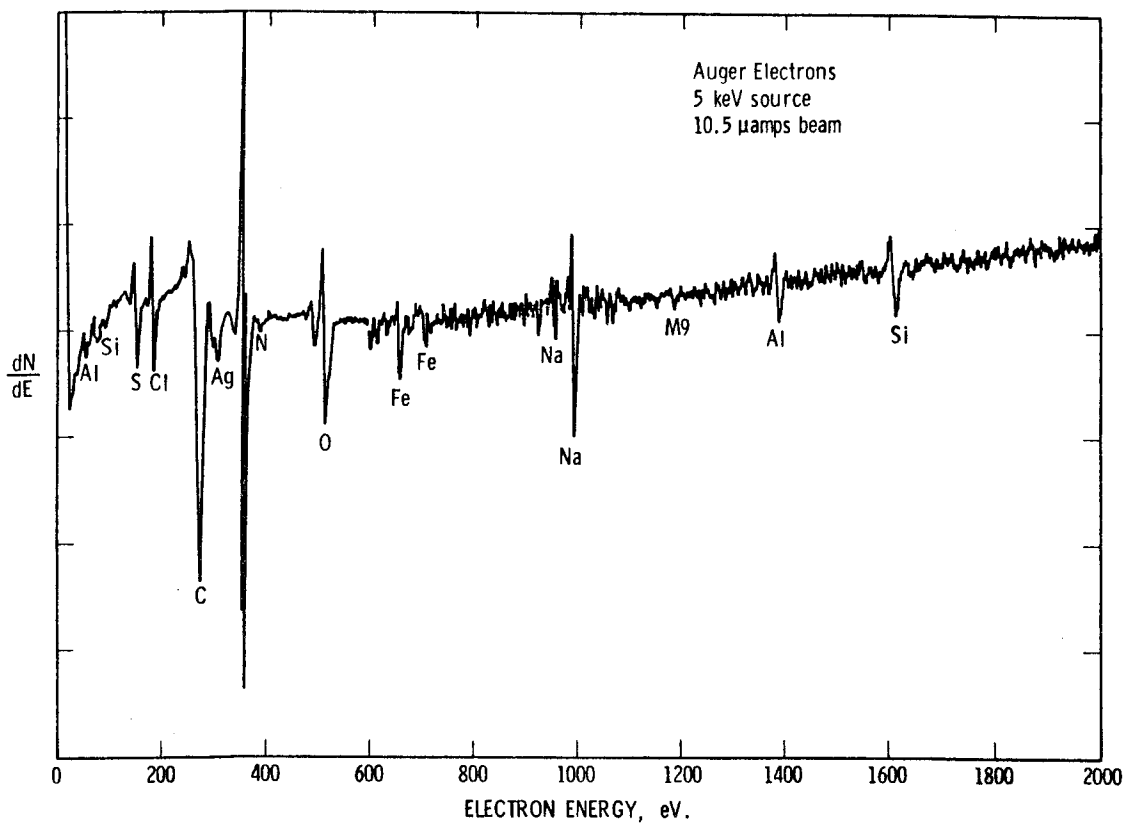The larger particles, separated out by sieving and subsequently reduced

Auger Electrons
5 keV source
10.5 μamps beam

$\frac{dN}{dE}$

Al Si S Cl Ag N Fe O Fe Na Na M9 Al Si

ELECTRON ENERGY, eV.

Figure 4. Auger Electron Spectrum of the Unground Particles,
Showing their Surface Chemistry.

X-ray Photoelectrons
Mg 400 watt source
4mm diameter irradiated

N(E)

3000
cycles per second

19   Ag 3p^3
20   Ag 3p^1
21   O Auger

1000
cycles per second

Line Number	Element Transition		
1	O 2s	10	C 1s
2	Ni 3p	11	Ca 2p^3
3	Al 2p	12	Ag 3d^5
4	Fe 3s	13	Ag 3d^3
5	Pb 4f^7	14	Pb 4d^5
6	Se 3p^3	15	Pb 4d^3
7	Cl 2p^1	16	Ni Auger
8	Mo 3d^5	17	O 1s
9	Na Auger	18	Fe Auger

BINDING ENERGY, eV
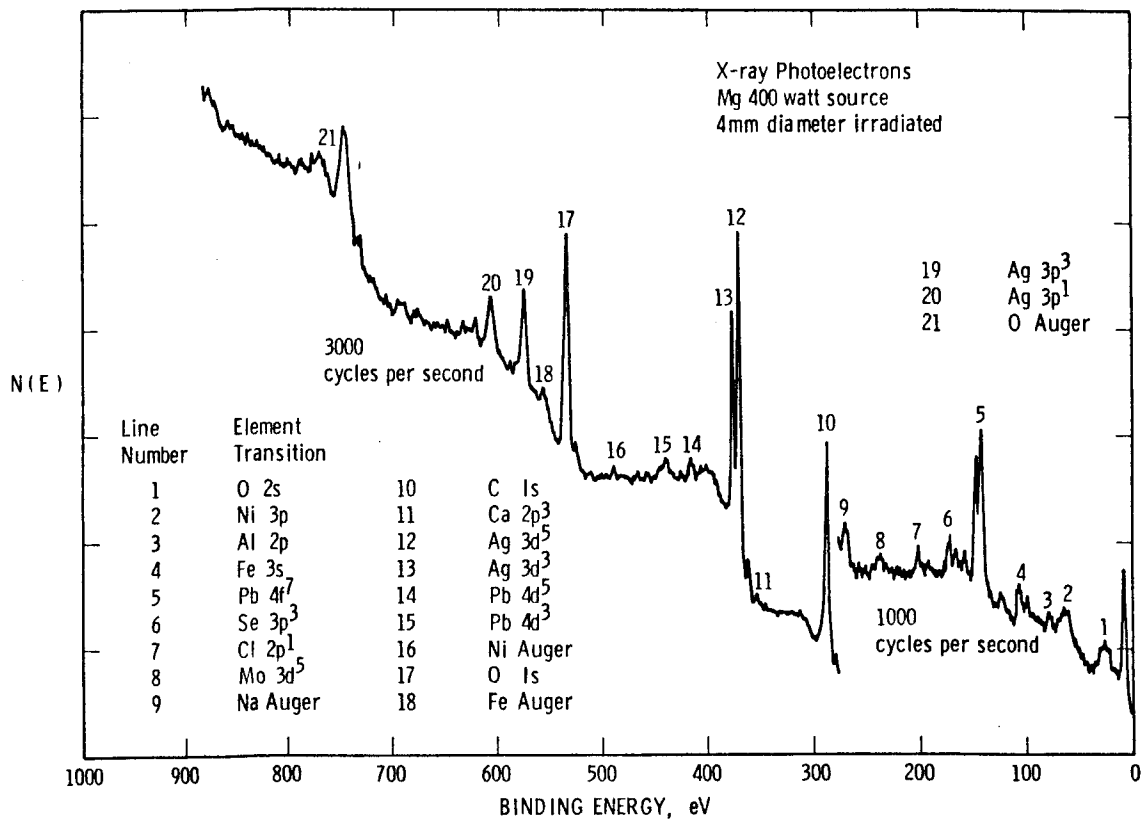
Figure 5. X-ray Photoelectron Spectrum of the Unground Particles.

in size by ball milling, were also examined by both AES and XPS. Examination of the XPS carbon peak from this material showed that it was very likely to have been bound as hydrocarbons and graphite, whereas from the unground material the carbon was all graphite. The ground material also evidenced a strong nitrogen peak which showed sufficient breadth and asymmetry to conclude that not only was nitrogen bound as in the gaseous state, but in more complex chemical states with hydrogen, oxygen, and perhaps the halogens and alkali metals. The unground material exhibited such a small nitrogen peak that no analysis of its probable bound states was possible. AES analysis of the ground material also showed a much less complex spectrum in which most of the minor elemental constituents were not detected, with the carbon peak becoming dominant. After argon sputtering for two minutes (an estimated 100% of material was removed) some of the elements found on the unground particles began to appear.

Discussion

Inhalation of particulates is a direct route of entry into the body. It has been reported that approximately 25% of inhaled particles in the respirable size range settle in lung tissue, a similar amount is exhaled, and the remaining 50% is diverted to the pharynx, where it is swallowed.[5] Combustion-derived particulates apparently possess a variety of chemical species condensed onto or adsorbed on their surfaces, including trace metals, organic compounds, and ionic species. Alveolar absorptive efficiency for most trace elements is 50-80%[2] and efficiency of absorption in the stomach is 5-15%[6]. Many trace elements are carcinogenic, mutagenic, cytotoxic, or can disturb vital biochemical equilibria causing a variety of toxicological manifestations. Organic compounds are either metabolized by phagocytic cells or solubilized by binding to proteins and transported to other sites; many representatives of this class of compounds are either cytotoxic (causing cell death), or carcinogenic and therefore capable of causing cancer of the lung or of other organs upon transport to distal sites in the body. The processes of carcinogenesis and mutagenesis are characterized by very long lag times (decades) between exposure and appearance of effect; these processes may also be initiated by extremely small amounts of material.

Both bulk and surface analyses indicated the presence of elements comprising the various minerals generically known as asbestos although the actual existence of these minerals has not been verified. Asbestos is, of course, capable of producing grave pulmonary disease, in that asbestos fibers too long to be taken in by phagocytosis cause collagen production and fibrogenesis or asbestosis. Asbestos can also cause lung cancer.[4] Surface analysis, however, indicated a number of other elements known to be biologically significant. Perhaps the most significant finding on the surface is that of lead. The biological effects of lead have been well-studied; it is known to interfere with heme biosynthesis, a biochemical pathway important to lung function since cytochrome a, cytochrome c, and cytochrome oxidase are essential components of the respiratory chain, and cytochrome P-450 or P-448, a mixed function oxidase responsible for metabolism of xenobiotics, all contain heme structures.

Grinding of the original particles resulted in surface exposure of hydrocarbons and nitrogen. Some of the nitrogen was observed to be chemically bound to other elements, an observation which could have biological significance in that many organic nitrogen-containing compounds such as aromatic amines are known to be carcinogens or mutagens. The reason hydrocarbons were found internal to the larger particles and not on the surface is not known. Perhaps the reason nitrogen was found internal to these particles has to do with the presence of hydrocarbons, in that the high temperature of the gasification process can promote compound formation between these two species.

Summary and Conclusions

Surface analytical techniques (Auger electron and x-ray photoelectron spectroscopies) have found biologically important chemical species not detected by bulk (x-ray microprobe) analysis.

From consideration of the chemical nature of surface-bound species, together with their concentration and biological accessibility, there is reason to believe that, for most types of respirable particles, the chemical species found on their surfaces may be more significant with respect to potential toxicological effect than the particles themselves.

References

(1) Mohr, U., Reznik-Schuller, H., Reznik, G., Grimmer, G., and Misfeld, J. (1976), Investigations on the Carcinogenic burden by air pollution in man. XIV. Effects of automobile exhaust condensate on the Syrian Golden Hamster lung. Zbl. Bakt. Hyg., I. Abt. Orig. B, Vol. 163, pp. 425-432.

(2) Natusch, D. F. S., Wallace, J. R., and Evans, C. A., Jr. (1974). "Toxic trace elements: Preferential concentration in respirable particles," Science, 183: pp. 202-204.

(3) Characterization of Metal and Polymer Surfaces, Vol. I and II, ed. by Lieng-Huang Lee, Academic Press, New York, 1977. p. 105 and p. 399.

(4) Harrington, J. S. and Allison, A. C. (1977) Tissue and cellular reactions to particles, fibers, and aerosols retained after inhalation. In: Handbook of Physiology, Sec. 9, Reactions to Environmental Agents, D. H. K. Lee, ed., pp. 263-283. Bethesda, Md., Americal Physiol. Soc.

(5) Schroeder, H. A., (1971), Environment, Vol. 13, p. 18.

(6) Patterson, C. C., (1965). Arch. Environ. Health, Vol. 11, p. 344.

QUANTITATIVE ANALYSIS OF SMALL PARTICLES USING WAVELENGTH AND ENERGY DISPERSIVE SYSTEMS IN AN ELECTRON BEAM INSTRUMENT

John Gavrilovic, PhD

Walter C. McCrone Associates, Inc.

Chicago, Illinois 60616

Microparticles in sizes down to 1 μm can be quantitatively analyzed in electron beam instruments using the standard ZAF correction procedure for solid (bulk) and infinitely large samples. The precision of such quantitative analyses is limited primarily by the particle size and subsequent loss of x-ray intensities which, in turn, increases experimental error. Such error cannot be effectively compensated by small particle corrections since it is mostly random and is caused by instrument instability and counting error. Ratios of x-ray intensities for particles below 1 μm and particularly below 0.3 μm are severely affected by particle size. The relative change measured in x-ray intensities on very small particles as compared to bulk samples is caused primarily by the decrease in x-ray absorption due to the shorter absorption path within the sample and is significantly higher than the experimental errors incurred during the analysis of such particles.

The total intensity of x-rays from small particles (below 6–10 μm) falls rapidly with particle size as can be seen in Figures 1 and 2. Particles larger than 6–12 μm have total x-ray intensities equal to that of the solid sample. The major cause of the significant drop in x-ray intensity for particles larger than 10 μm, observed by some researchers, is the result of local changes both in the incident angle of the electron beam and in x-ray

take off angle, both of which depend on particle shape. The optimum method for analysis of small particles therefore appears to be to collect x-rays from the small particle while it is being rastered by the electron beam. Such a raster normally also covers a certain portion of the substrate in order to incorporate the whole projected area of the small particle. To compensate for loss of x-ray intensity during rastering of the substrate one can use the following correction factor:

$$I_o = I_1 \times \frac{S_r}{S_p} \quad ,$$

where I_o is the corrected intensity from the element, I_1 the measured intensity, S_r the total rastered area, and S_p the projected area of the small particle. With this method the stability of the measurement is significantly increased and analysis of particles down to approximately 1 μm becomes routine. Even particles smaller than 1 μm down to 0.1 μm can be analyzed semiquantitatively with a relative accuracy of 20-40% without further correction except for the ratio of rastered to projected area.

Both wavelength and energy dispersive systems can be used for quantitative analysis of small particles without corrections provided suitable bulk standards of similar composition are available. Low concnetration elements (less than 1%) in small particles should be analyzed with wavelength dispersive systems because of the excessively high background inherent in the energy dispersive systems.

Figures 3, 4, 5 and 6 and Table 1 show experimental results obtained during analysis of microparticles of sizes 0.1 μm and larger mounted on a polished beryllium substrate. These microparticles were obtained by grinding two types of glasses produced by the National Bureau of Standards for electron microbeam analysis. As you can see from these diagrams the calculated composition for small particles, down to approximately 1 μm is the same as for the solid samples of glass without any corrections. Below approximately 1 μm the ratio of elements in the small

particles drastically changes due to the increase in the ratio of low energy to high energy x-rays because of reduction in self absorption in the sample. The wavelength dispersive system gave a lower background and higher sensitivity for trace elements, but the associated experimental errors were generally larger because of the more severe x-ray geometry requirements.

Table 1 illustrates the results of an EDS analysis of 30 small particles ranging in size from 0.1 to 11 μm, including the bulk (polished) standard glass K-230. These results were obtained on an ARL electron microprobe, EMX-SM type, at 10 nA specimen current on beryllium and 20 kV accelerating voltage with an electron beam of 0.1 μm. The probe is equipped with four wavelength dispersive spectrometers and a high resolution ORTEC energy dispersive detector along with a Sargent-Welch vertical turbomolecular pump which supplies 1×10^{-6} torr contamination free vacuum.

REFERENCES

1. J. T. Armstrong and P. R. Buseck, The Minimization of Size and Geometric Effects in the Quantitative Analysis of Microparticles with Electron Beam Instruments. Proceedings of the Tenth Annual Conference of Microbeam Analysis Society (1975).

2. J. T. Armstrong and P. R. Buseck, Quantitative Chemical Analysis of Individual Microparticles Using the Electron Microprobe. Analytical Chemistry, Vol. 47, No. 13, November (1975).

3. M. Bayard, Microprobe Analysis, C. A. Andersen. Ed., Wiley-Interscience, New York, NY, pp 323-348 (1973).

4. J. Gavrilovic, Common Errors in Subnanogram Particle X-ray Analysis, Microscope Vol. 22, pp 221-227 (1974).
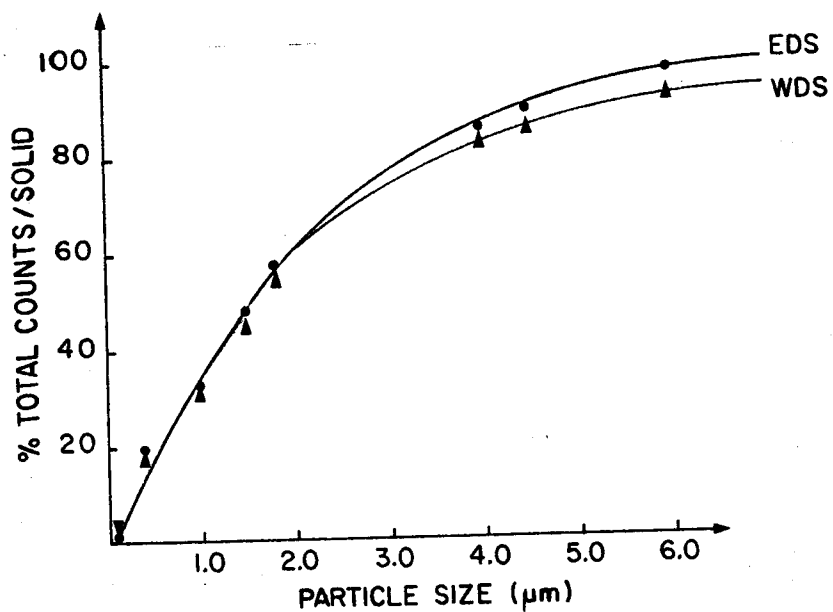
Size Distribution versus Total Intensity of Major Elements for K-489 Glass Particles

Figure 1
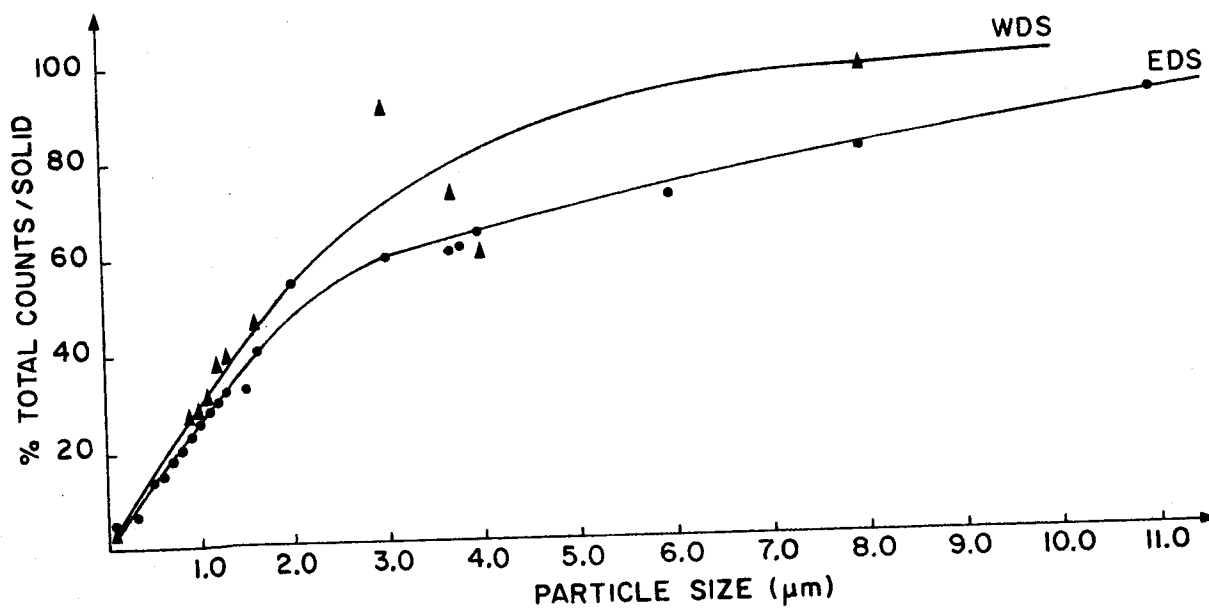
Size Distribution versus Total Intensity of Major Elements for K-230 Glass Particles

Figure 2
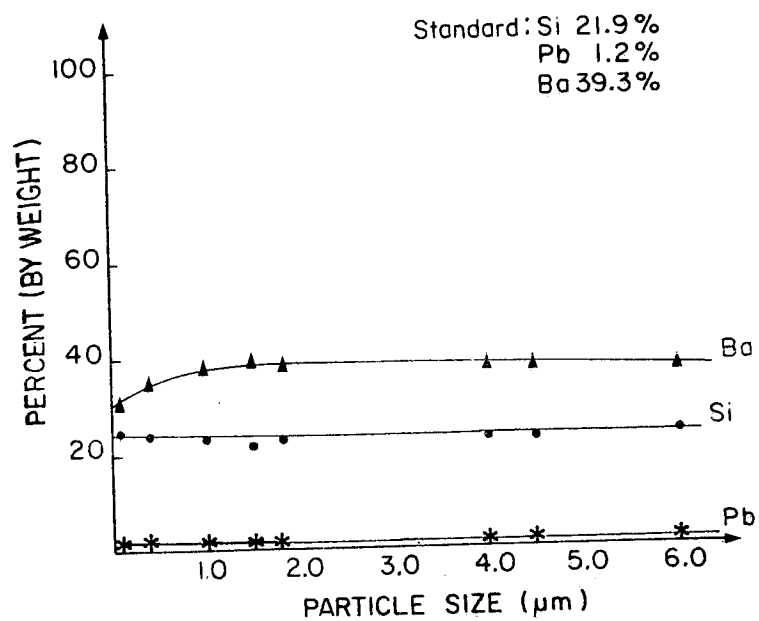
Figure 3. Percent by Weight of Major Elements versus Size as Determined by EDS for K-489 Glass Particles
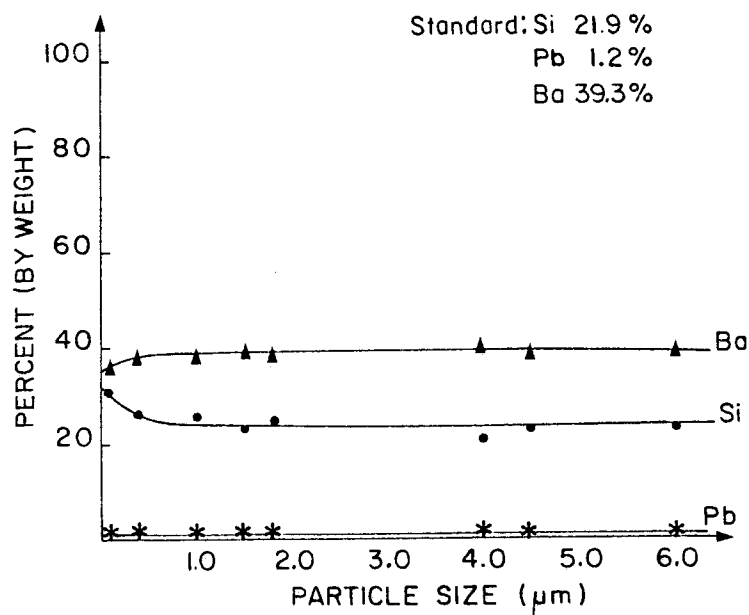

Figure 4. Percent by Weight of Major Elements versus Size as Determined by WDS for K-489 Glass Particles
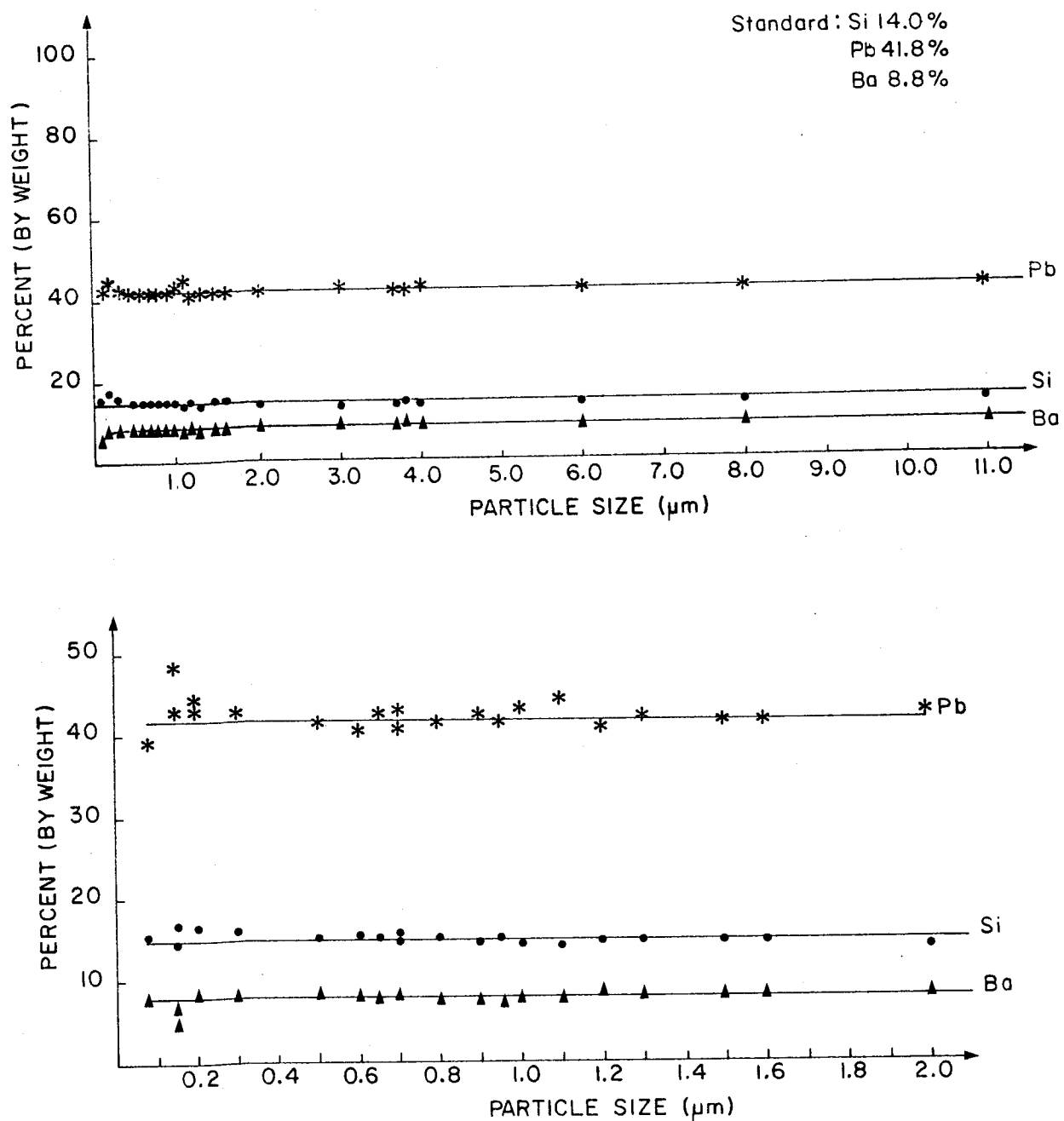
Figure 5. Percent by Weight of Major Elements versus Size as Determined by
EDS for K-230 Glass Particles
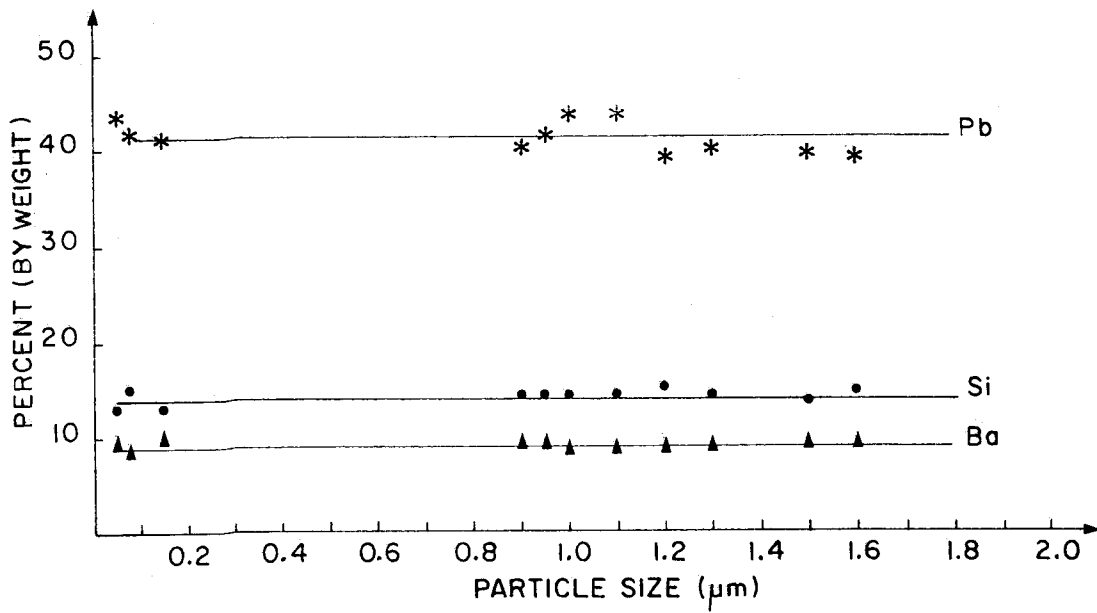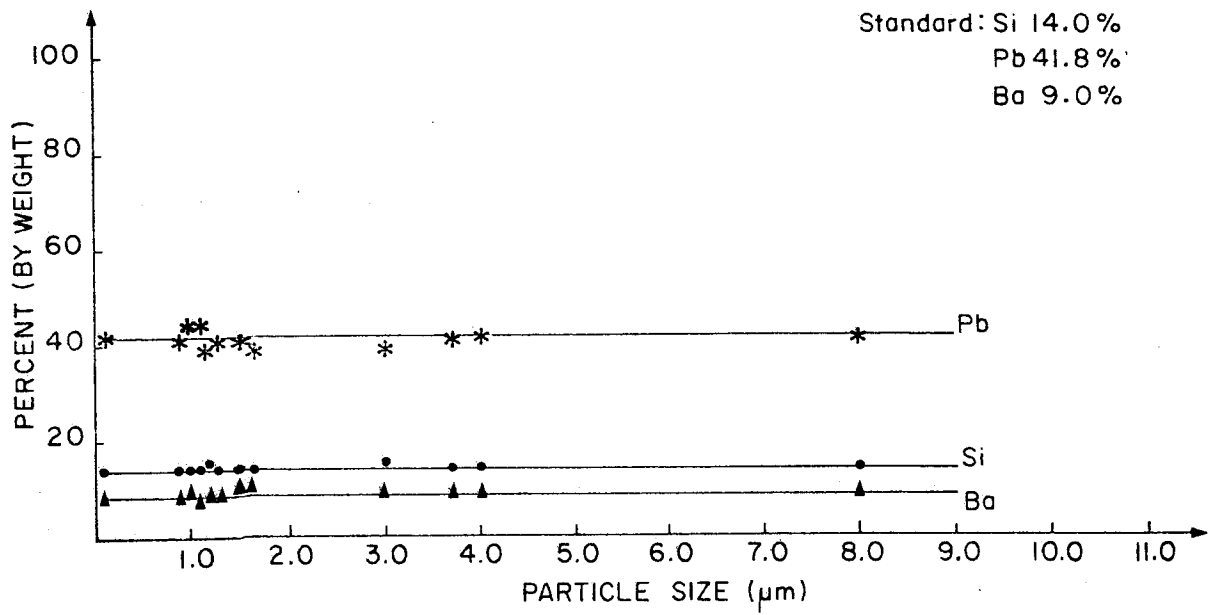(Bottom curves — expanded scale)

Figure 6. Percent by Weight of Major Elements versus Size as Determined by WDS for K-230 Glass Particles
(Bottom curves — expanded scale)

Table 1

Electron Microprobe Analysis
of Major Elements in K-230 Glass Particles

| Particle size (μm) | ---------- counts ---------- | | | | % by weight | | |
	Si	Pb	Ba	total	Si	Pb	Ba
0.08	2052	1790	1019	4990	15.8	39.2	7.4
0.15	2310	2191	1081	5718	14.8	42.9	6.9
0.15	2394	2254	976	5769	17.1	48.6	4.8
0.2	2501	2227	1157	6035	16.8	43.0	8.4
0.2	2560	2235	1154	6207	16.5	44.0	7.9
0.3	2885	2617	1270	6928	16.3	42.8	8.3
0.5	5782	5565	2107	13865	15.1	41.6	7.9
0.6	6321	5892	2254	14865	15.4	40.7	8.0
0.65	6730	6636	2332	16112	15.0	42.4	7.6
0.7	7925	7685	2641	18251	15.6	43.1	7.9
0.7	8099	7745	2760	19097	15.2	41.0	7.9
0.8	8766	8520	2930	20744	15.0	41.6	7.8
0.9	8785	8986	2979	21331	14.6	42.7	7.7
0.95	10612	10448	3483	25239	14.9	41.5	7.8
1.0	10841	11290	3509	26290	14.6	43.2	7.5
1.1	11405	12741	3837	28717	13.9	44.6	7.6
1.2	12734	12475	4202	30230	14.8	41.1	8.7
1.3	13234	13677	4501	32255	14.4	42.2	8.1
1.5	13663	13815	4558	32887	14.6	41.8	8.0
1.6	17123	17197	5587	40758	14.7	41.7	8.1
2.0	22074	23742	7873	55095	14.0	42.4	8.7
3.0	22585	26090	9335	59849	13.1	42.9	9.6
3.7	24627	26004	8551	60761	14.1	42.0	8.6
3.8	25329	26781	8839	62462	14.1	42.1	8.6
4.0	25732	28499	9567	65513	13.7	42.7	8.9
6.0	28715	30978	10596	72078	13.9	42.1	9.1
8.0	31967	34801	11617	80521	13.8	42.3	8.9
8.0	33464	35762	11866	81092	14.0	42.1	8.8
11.0	37583	39415	13129	92391	14.1	41.6	8.7
Background	1170	1012	843	3105			
Bulk Standard	41005	43686	14797	101958	14.0	41.8	9.0

Monte Carlo Electron Trajectory Simulation — An Aid for Particle Analysis

R. L. Myklebust, D. E. Newbury, K. F. J. Heinrich,
J. A. Small and C. E. Fiori

Microanalysis Section
National Bureau of Standards
Washington, D.C. 20234

X-ray intensities emitted from a target can be calculated by algorithms derived from the principles of physics commonly employed in ZAF (atomic number-absorption-fluorescence corrections) quantitative analysis schemes. These calculations can only be rigorously carried out for a flat target which is opaque to the beam[1]. When the sample size approaches the dimensions of the electron/x-ray interaction volume, such as is frequently the case for small particles, the geometrical effects become dominant factors in controlling the intensity of emitted x-radiation[2]. An alternative technique for calculating x-ray intensities which employs basic physics is that of Monte Carlo electron trajectory simulation[3,4]. In the Monte Carlo technique, the trajectory of an electron is calculated in increments corresponding approximately to the mean free path, or a multiple thereof, between scattering events in the solid. Suitable descriptions of the processes of both elastic and inelastic scattering are employed to calculate the mean free path and appropriate scattering angles. Random numbers are used to select values of these parameters in order to distribute the choices over the available range. A sufficient number of trajectories is calculated to yield statistically significant results.

Since the coordinates of the position of the electron are continually calculated along the trajectory, the position can be compared with the function describing the surface of any

object of interest to determine when the electron escapes. Moreover, the production of radiation such as characteristic and continum x-rays can be calculated as a function of electron position in the target. Monte Carlo simulations are thus very useful for the study of electron interactions in particles, even when the shape becomes complicated.

For elastic scattering, a useful model can be chosen among single scattering[5], multiple scattering[6], or a hybrid[7]. The single scattering model gives the most detailed information on a trajectory, since the step length between scattering acts is set equal to the mean free path. Single scattering must be used when the particle volume is a small fraction, less than about 10 percent, of the interaction volume in the bulk material. For intermediate-size particles, from about 10 percent to 90 percent of the bulk interaction volume, a hybrid scattering model can be employed.[7] The hybrid model makes use of single scattering for the initial interactions near the surface and multiple scattering for the balance of the trajectory. In multiple scattering models, 10 to 20 single scattering acts are replaced by one equivalent scattering angle and distance, which gives a significant reduction in calculation time. A Monte Carlo simulation based completely on the multiple scattering approximation can be used for particles which are nearly the same size as the bulk interaction volume. Even for such relatively large particles, the effects of surface curvature can cause significant deviations in the x-ray intenstity from the bulk values.

As an example of the application of the Monte Carlo technique to particle studies, the characteristic x-ray intensity predicted by the calculation for spherical particles is compared with experimental measurements in Figures 1 and 2. The sample is NBS glass K-309 examined at a beam energy of 17.4 keV with normal incidence and a 30° take-off angle above the substrate (equivalent to an angle of 60° between

the beam and spectrometer axis). A good correspondence is observed between the experimental measurements and the calculations. For the relatively soft silicon Kα radiation, the ratio of particle intensity to bulk intensity is observed to exceed unity for a considerable range of particle diameter. This behavior is observed because of the enhanced escape of low energy x-rays from the particle relative to the bulk resulting from the decrease in the length of the absorption path out of the particle due to the curvature of the surface. For the harder barium Lα radiation, this effect is not observed because the absorption is much less significant.

The absorption effects become more significant as the take-off angle is decreased. For the usual arrangement in a scanning electron microscope, the x-ray detector axis is at a right angle to the beam axis, producing a 0° take-off angle for a flat specimen. Flat specimens are normally tilted to yield an acceptable take-off angle. For spherical or cylindrical particles on a substrate, tilting does not change the take-off angle. For such a situation, the Monte Carlo calculation reveals a very strong dependence of the x-ray intensity relative to bulk as a function of particle size, passing through a peak and then decreasing with increasing particle size, Figure 3[8].

The Monte Carlo simulation is also useful for obtaining information on electron scattering from particles, which is frequently difficult to determine experimentally. In addition, with the use of proper cross sections, the continuum emission from a particle can be calculated for the determination of peak-to-background ratios.

The chief value of the Monte Carlo simulation in particle analysis is to provide a reference method against which modifications to the existing physical models can be tested. The cost of the Monte Carlo technique is too high and the calculation time too long to permit direct, on-line reduction

of spectra of unknowns. In simple cases where repetitive
analyses are to be made, the Monte Carlo simulation can be
used to generate working curves for correction of intensity
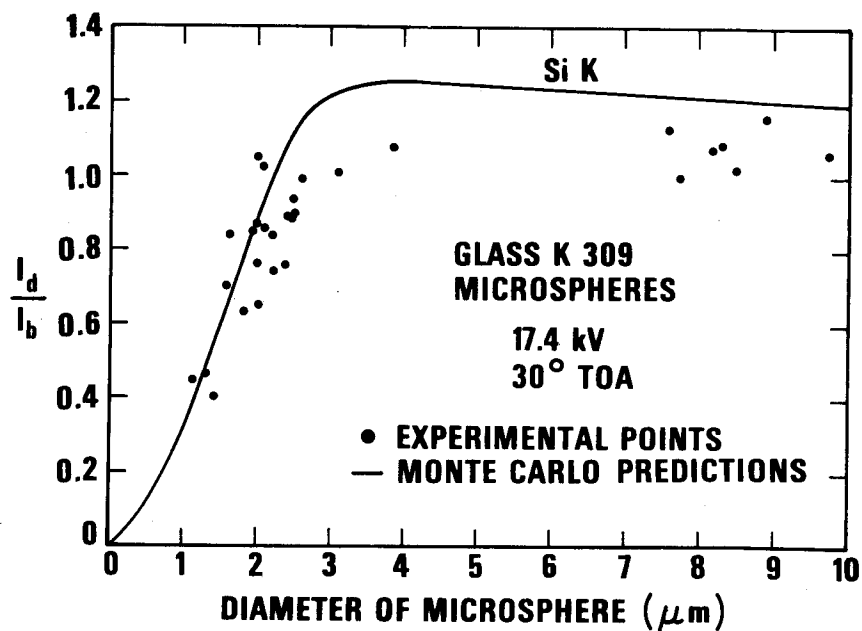ratios if the general composition of the particles is known.

Figure 1. Ratio of intensity from spherical particles to bulk
intensity as a function of particle diameter. Sili-
con Kα radiation. NBS Glass K309 (Nominal composi-
tion by weight percent of the oxide: Al_2O_3 - 15.0;
SiO_2 - 40.0; CaO - 15.0; Fe_2O_3 - 15.0; BaO - 15.0).
Solid curve - Monte Carlo calculations; points-
experimental measurements. Beam energy 17.4 keV;
30° take-off angle.
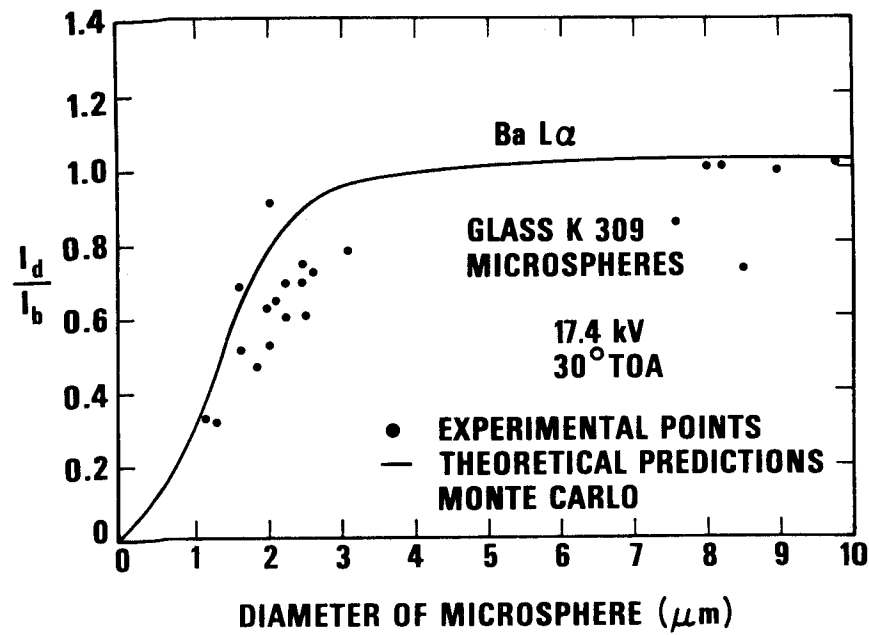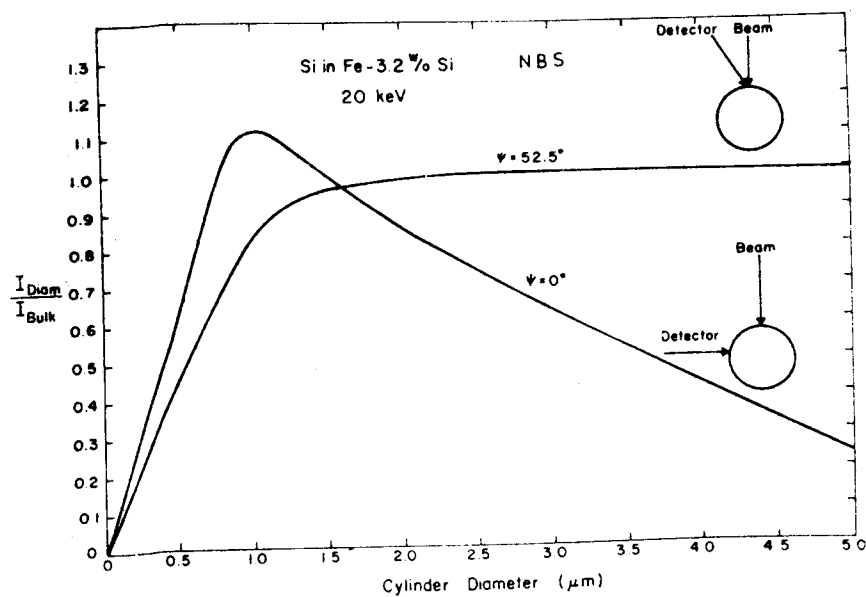
Figure 2. Same conditions as Figure 1; barium Lα radiation.

Figure 3. Ratio of intensity from cylindrical particles to bulk intensity for silicon Kα radiation in Fe - 3.2% Si alloy for two different spectrometer - beam axis arrangements.

References

(1)   Reed, S. J. B., Electron Microprobe Analysis (Cambridge, (1975).

(2)   Goldstein, J. I., Yakowitz, H., Newbury, D. E., Lifshin, E., Colby, J. W., and Coleman, J. R., Practical Scanning Electron Microscopy, (Plenum, New York, 1975) 317.

(3)   Berger, M. J., in Methods in Computational Physics, Vol. 1, Adler, B., Fernbac, S., and Rotenberg, M. eds., (Academic Press, New York, 1963).

(4)   Heinrich, K. F., J., Newbury, D. E., and Yakowitz, H., eds., Use of Monte Carlo Calculations in Electron Probe Microanalysis and Scanning Electron Microscopy, National Bureau of Standards Special Publication 460 (1976).

(5)   Shimizu, R., Kataoka, Y., Ikuta, T., Koshikawa, T., and Hashimoto, H., J. Phys. D: Apl. Phys., 9 (1976) 101.

(6)   Curgenven, L. and Duncumb, P., Simulation of Electron Trajectories in a Solid Target by a Simple Monte Carlo Technique, Tube Investments Research Report No. 303 (1971) Hinxton Hall, Saffron Walden, Essex, England.

(7)   Newbury, D. E., Myklebust, R. L., and Heinrich, K. F. J., "A Monte Carlo Procedure Employing Single and Multiple Scattering", Proc. 8th Intl. Conf. on X-Ray Optics and Microanalysis and 12th Ann. Conf. Microbeam Analysis Society (Boston, 1977) 27.

(8)   Fiori, C. E., Heinrich, K. F. J., Marinenko, R., Darr, M. M., Blackburn, D. H., Newbury, D. E., and Small, J. A., "An Overview of the Glass Standards Program for Micro-analysis at the National Bureau of Standards", Proc. 11th Ann. Conf. Microbeam Analysis Society (Miami Beach, 1976) 27.

(9)   Yakowitz, H., Newbury, D. E., and Myklebust, R. L., "Approaches to Particulate Analysis of the SEM with the Aid of Monte Carlo Program" in Scanning Electron Micro-scopy/1975, O. Johari, ed. (Chicago, IITRI, 1975) 93.

QUANTITATIVE ANALYSIS OF LYOPHILIZED SOLUTIONS :

EXPERIMENTAL AND THEORETICAL EVALUATION OF THE LIMITS OF LINEARITY

OF THE CALIBRATION CURVES

Nicole ROINEL[*], Michel CHAMPIGNY[**], Lucienne MENY[**],

and Jean HENOC [***]

[*] DB/LPPC CEA, C.E.N. Saclay 91190 Gif sur Yvette, France

[**] DTec / SRMA, C.E.N. Saclay

[***] CNET/PEC 92220 Bagneux France.

Quantitative analysis of the elemental content of solutions can be performed with an electron microprobe when the available volumes are too small to allow the use of more conventional and less costly analytical techniques. This case is common in biology. We developed a routine technique to measure element concentrations in 10^{-10}l volumes (1, for review see 2). The aim of the technique is to achieve samples thin enough to avoid electron and X-ray absorption. Known volumes of the solutions are deposited on a beryllium substrate, quickly frozen and lyophilized. The samples are then composed of innumerable crystals distributed more or less homogeneously over a circular surface. As in the case of the particle analysis (3), our samples are irradiated by a defocused beam, and several identical volumes of the same solution are analyzed to average possible effects of the sample geometry. Standards are identical volumes of five solutions of known composition, very close to the composition of the unknown biological samples with regard to the elements Na, Mg, P, Cl, K and Ca, and deposited simultaneously. The measured intensity of an element is related to its concentration in the solution through calibration curves which are linear over the narrow range of concentration characteristic of biological fluids for the $K\alpha$ lines of the elements routinely measured, namely Na, Mg, P, Cl, K and Ca. The unknown concentrations are read directly from the calibration curves without any correction for absorption, fluorescence, or atomic number. The validity of using calibration curves without any correction depends upon the similarity of standards and unknown solutions in terms of main matrix compound, the identity with regard to degree of oxidation when it affects the energy of the elemental line to be analyzed and the stability of the various elements. When these conditions are fulfilled, the accuracy is still dependent upon the linearity of the calibration curves. For each element, the ratio of the slope of its calibration curve to background value depends on various parameters. For example, it increases when the accelerating voltage decreases ; it is thus important to work with the lowest voltage as possible. On the other hand the risk of using lower voltage is that the calibration curves will not be linear.

Experimentally, 10^{-10}l of a NaCl solution (150 mM/1) after lyophilization is a deposit 60 μm in diameter. There are two principal forms in which the deposit could exist, continuous or discontinuous. If continuous, it would consist of identical crystals spread evenly over the surface ; this corresponds to a mean mass thickness of 0.03 mg/cm^2 and a mean cubic crystal size of 0.14 μm. However, at low concentrations the deposits appear discontinuous. The closeness of one particle to the next is a function of the osmolarity of the original solution. When the osmolarity increases, microscopic observations show that the

number of particles per unit of surface increases until the sample appears continuous. Since the measured intensity remains proportional to concentration, we assume that the particles increase in number but keep roughly the same distributi in size. At the limit when they are contiguous, the sample may then be considered a thin continuous film. At this point the sample begins to increase in thickness and may cause the calibration curves to deviate from linearity.

A Monte Carlo procedure (4) is used to calculate the depth distribution functions for increasing sample mass thickness for each element of interest at various electron energies. Biological samples routinely examined are mainly composed of a NaCl matrix (approximately 80 % in weight) so that the electron distribution need be determined only once to calculate the number of ionizations and the emergent intensities for every element of interest in the matrix.

These above considerations will be compared to the experimentally determined limits of linearity obtained by analysis of progressively concentrated solutions of constant composition (Na = 31.1 % ; Cl = 52.8 % ; K = 2.6 % ; P = 2.1 % ; Mg = 1.6 % ; H et O = 9.8 % or Na = 34 % ; Cl = 60.1 % ; K = 2.9 % ; Ca = 3 %). Samples up to 0.7 mg/cm^2 are irradiated with discrete high voltage values (12kV - 15kV - 20kV - 25kV) in a CAMECA MS-46 microprobe with a 18 ° take off angle. For each element the measured intensities are converted to "apparent concentrations" by linear extrapolation of the calibration curves obtained from thinner samples (estimated mass thickness up to 0.06 mg/cm^2). The ratio of the "apparent concentration" to the true one measures the deviation frc linearity, and is related to the sample mass thickness. The deviation of linearity is found to be the same for all the elements at 12kV and increases as a function of the sample mass thickness. At 15kV the deviation from linearity starts below 0.15mg/cm^2 for Na and Mg and later for other elements. At 25kV the measured intensities of Cl, K, Ca and P are still proportional to concentrations for estimated mass thickness of 0.4mg/cm^2 while for this value those of Na and Mg strongly deviate by 30 % from proportionality. This suggests that a 12kV the electron range is the limiting factor while at 25kV absorption becomes predominant.

Bibliography

(1) MOREL F. and ROINEL N. (1969) : J. Chim. Phys. et Phys. Chim., 66, 1084-109)

(2) ROINEL N. (1977) : Proc of "35th Ann. Proc. Electron Microscopy Soc. Amer" Boston, Mass., G.W. Bailey ed., 362-365.

(3) ARMSTRONG J.T. and BUSECK P.R. (1975) : Analyt. Chem., 47, 13, 2178-2192

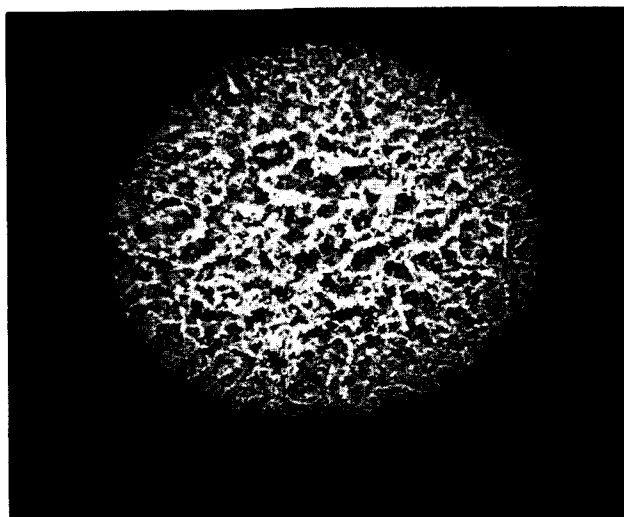(4) BISHOP H.O. (1965) : Doctorate thesis, Cambridge University.

FIGURE 1. SCANNING MICROSCOPE IMAGES OF THE STANDARD SOLUTIONS USED FOR Na, Cl, Mg, AND P CALIBRATION CURVES.
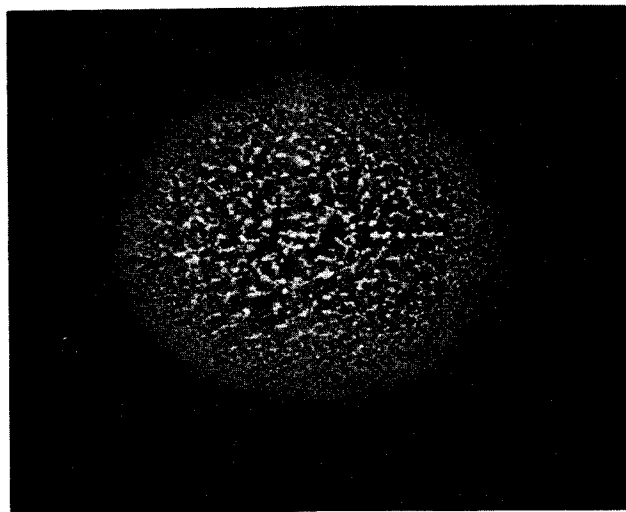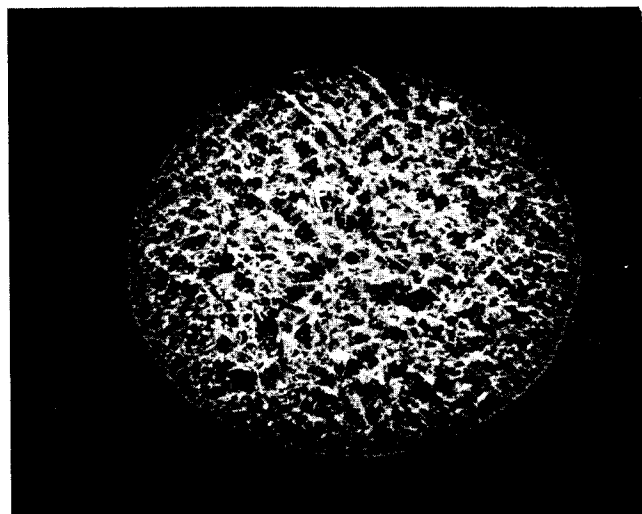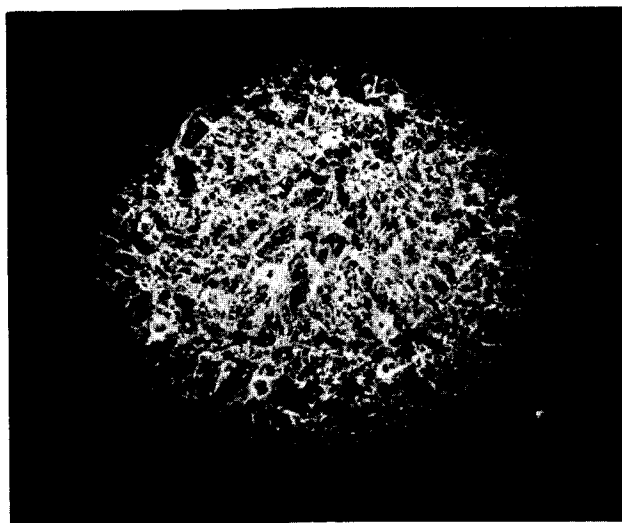

a) dry mass: 1.46 g/l
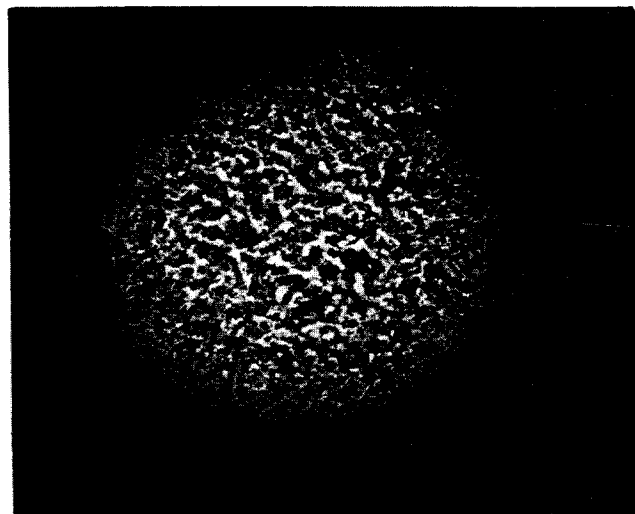
b) dry mass: 3.7 g/l

c) dry mass: 7.4 g/l

d) dry mass: 11.1 g/l

e) dry mass: 14.6 g/l .

⊢——⊣ 10 μm

Composition of solutions (in weight %):

Na= 31.1% ; Cl= 52.8% ; P= 2.1% ;

Mg= 1.6 % ; K= 2.7% ; H and O= 9.8% .

Pipette volume: 0.08 nl .

Magnification: X700 .

E_o = 10 kV ; I= 0.5 x 10^{-11}A ; Θ= 30° .

FIGURE 2. EFFECT OF SAMPLE MASS THICKNESS ON MEASURED INTENSITY FOR

VARIOUS BEAM HIGH VOLTAGES

For each graph, the ordinate is the ratio of measured intensity to primary intensity (primary intensity is the value which would be measured if intensity was proportional to concentration); the abscissa is the sample mass thickness (mg/cm2). The take-off angle is 18°.

Top four graphs: solutions of increasing dry mass and of same composition as the standard solutions used for Na, Cl, Mg and P calibration curves.

Bottom four graphs: solutions of increasing dry mass and of same composition as the standard solutions used for Ca and K calibration curves.
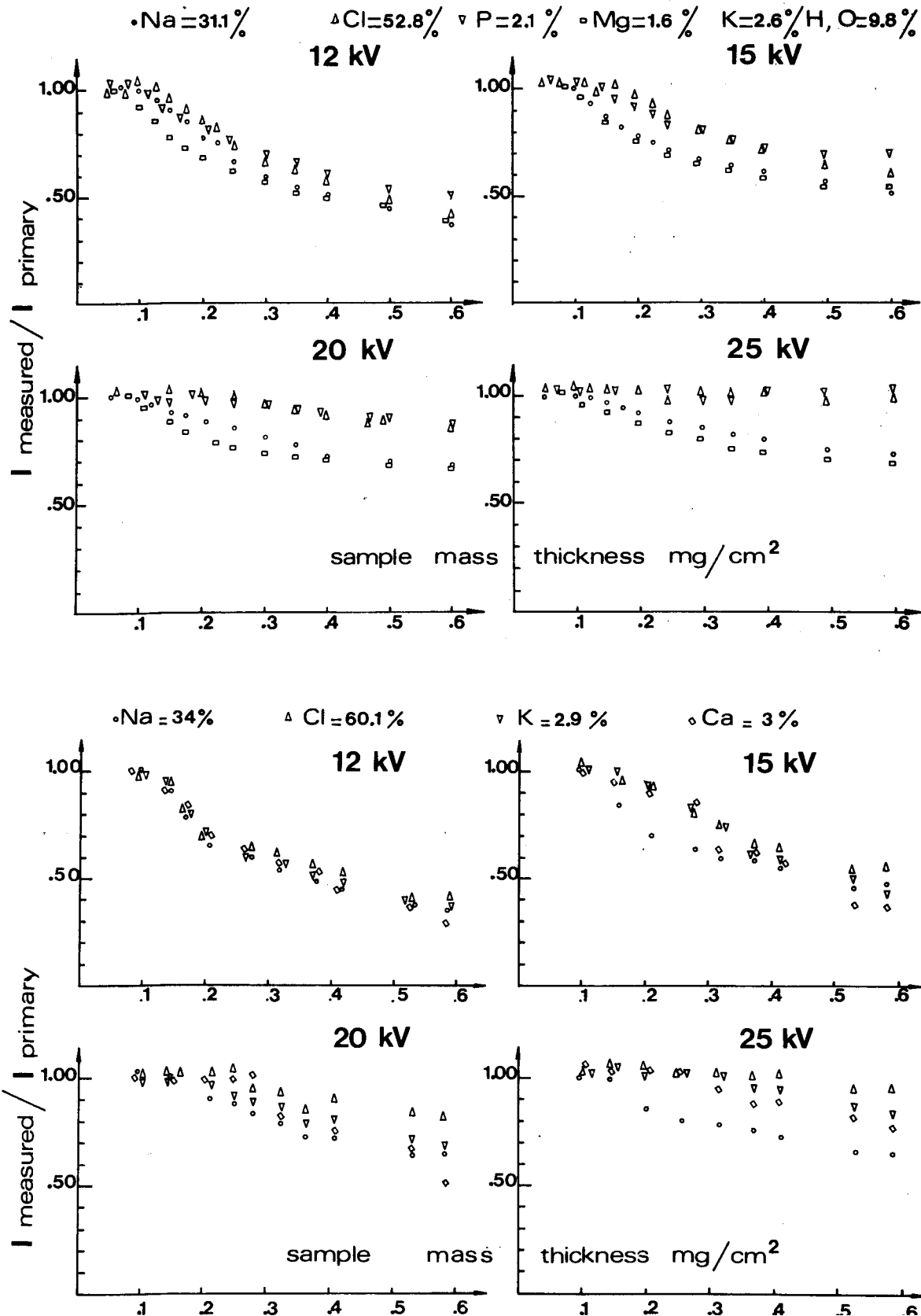
QUANTITATIVE CHARACTERIZATION OF PARTICULATES
BY SCANNING AND HIGH VOLTAGE ELECTRON MICROSCOPY

R.J. Lee and R.M. Fisher

U.S. Steel Corp., Research Laboratory
Monroeville, Pa. 15146

From their inception, the various forms of electron microscopy have been used to observe, measure, count and, by means of ancillary techniques or devices, identify fine particles. The detailed information generated from interactions of an electron beam with matter has made it advantageous to utilize electron optical methods even when the particles of interest are visible in the light microscope. Often the nature of scientific or technological problems requires measurement of subtle differences in the mean values and distribtuion of several characteristics of particulate material, i.e. particle size, shape, aspect ratio, surface area and roughness, chemical composition, crystal structure, concentration and even perhaps internal defects.

The difficulty in quantitative characterization of particulates is apparent from the discrepancies in the number, size, and identity of particles reported by various laboratories, even those participating in controlled round-robin programs. The basic problem is one of statistics. In order to obtain meaningful results, it may be necessary to characterize hundreds, and in some cases, thousands of particles, which is not feasible using manual techniques even if photographic recording can be bypassed. For example, comparison of x-ray spectra obtained from individual particles with standards on a particle-by-particle basis by an electron microscope operator is much too time consuming. Qualitative methods such as multicolor x-ray mapping provide graphic visual displays rather efficiently, but do not provide the basic

quantitative information needed to interpret bulk properties.
New approaches to rapid quantitative characterization are becoming
available as will be described in this review. The methods, al-
though primarily intended for particulates such as flyash, asbestos
fibers, mineral fragments, quarry dusts, comminuted ores, soils,
catalysts, etc., where the matrix is of no interest, are generally
applicable to the analysis inclusions or precipitates in metals,
ceramics or plastics.

Although advances in hardware, such as improved resolution
of energy dispersive analyzing systems continue to be extremely
important, striking gains are resulting from the rapid evolution
of data handling systems. Experience with data processing by large
digital computers, originally used for absorption and fluorescence
corrections in quantitative microanalysis, paved the way for more
general use of dedicated mini-computer control of electron micro-
probes, and now are being used to control the SEM for real-time
analysis of size, shape, and composition.[1]

The information flow in an SEM-based automatic image
analyzer consisting of a computer-driven beam control system
interfaced to a multichannel energy dispersive spectrometer is
illustrated in Figure 1. This system has been used extensively
to characterize the included mineral phases in washed coals. A
typical plot for the illite distribution in such a coal is shown
in Figure 2. Over twenty minerals and mixtures are identified in
coal under the assumption of "characteristic" x-ray spectra.[2]
Similar data is being generated on the included phases in steels,
and the constituents in various powders, and environmental parti-
culate samples.

The transmission electron microscope, which, in the past,
was used primarily for detailed analysis of a very restricted
number of features is experiencing a demand for an increase in the
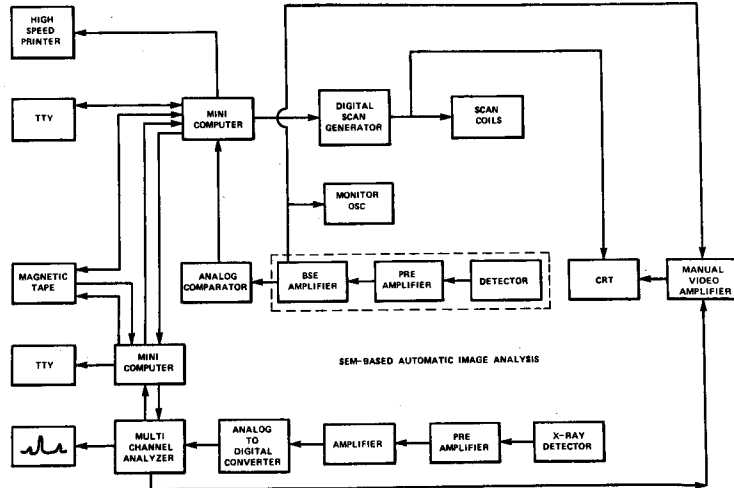number of particles analyzed. The first stage in developing this

Fig. 1. Schematic diagram of the information flow between the mini-computer used to drive the electron beam; the mini-computer used to process x-ray spectra, and the SEM.
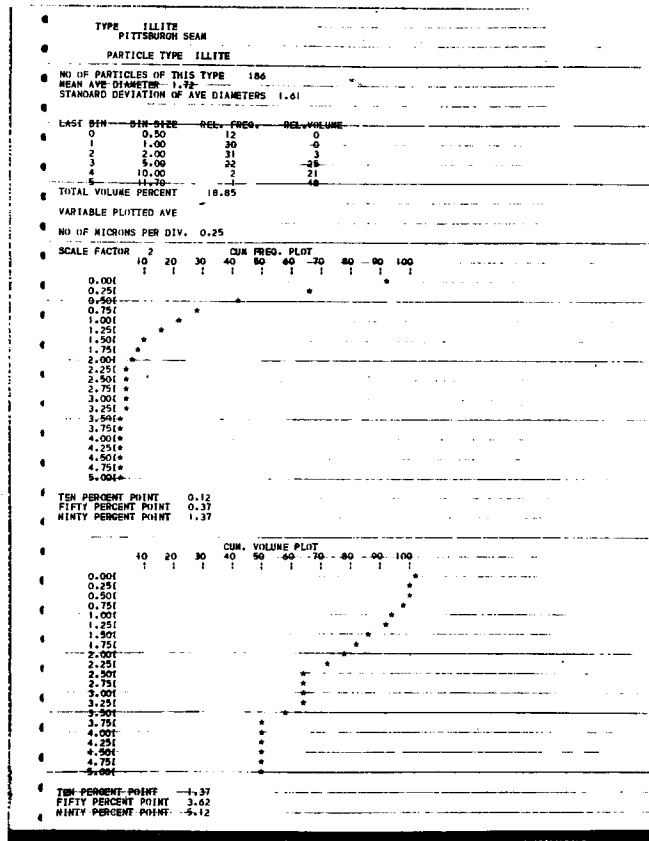

Fig. 2. Cumulative size and volume distribution of illite in sample of washed coal. The other information shown includes the mean diameter, standard deviation and 10,50,90 percent points for each curve.
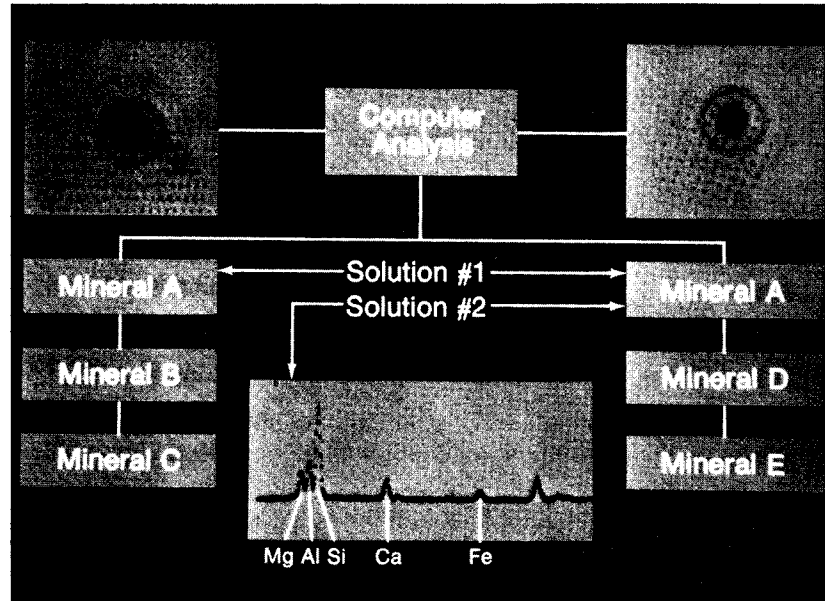
Fig. 3. Quantitative identification of mineral fragments may be obtained by interpreting two selected area diffraction patterns; or by the analysis of an x-ray spectra and one SAD pattern.

capability has been to automate the measurement of selected area diffraction patterns and the interpretation of the pattern in terms of the unit cell parameters of a large number of crystals by means of a suitable library file.[3] Compositional data generated by EDS on the same particle permits the identification of unknown phases using the scheme shown in Figure 3. Thus, complete characterization of the size, shape, composition, and crystal structure of particles is feasible. This procedure, while faster and more accurate than recording EDS spectra, measuring of the size and shape of particles from micrographs, and using stereographic projections to identify phases, still is too time consuming. However, we expect that direct digitizing and computer interpretation of SAD patterns will become possible in the near future.

These advances in characterization technique will continue to have an impact on instrument design and operation, and to improve the ability of the microscopist to describe properties of samples $\sim 10^9$g from the analysis of samples $\sim 10^{-9}$g.

References

1. J. Lebiedzik, "Multiple Electron Detector Method for Quantitative Microtopographic Characterization in the SEM," Doctoral Thesis, Penn State University, University Park, Pa., March 1975.

2. R.J. Lee, F.E. Huggins and G.P. Huffman, "Correlated SEM-Mossbauer Studies of Coal Mineralogy," SEM-1978, O. Johari, Ed., in press.

3. R.J. Lee, J.S. Lally and R.M. Fisher, "Identification and Counting of Mineral Fragments," Proceedings, Workshop on Asbestos: Definitions and Measurement Methods, National Bureau of Standards, Gaithersburg, Md., July 18-20, 1977.

Application of Auger-Electron Spectroscopy
and X-ray Photoelectron Spectroscopy to
the Characterization of Particles

C. J. Powell

National Bureau of Standards, Washington, D.C. 20234

Over the past two decades, there has been considerable public concern over pollution of the atmosphere. Attention was focused initially on gaseous pollutants but it is now established that air pollution by particulate matter is also a serious problem. Particulate pollutants from coal-fired power plants have been shown to have adverse effects on human health, vegetation, and materials. Since this nation and others will depend on energy generated at coal-fired power plants in the next several decades to a greater extent than now, it is clear that the properties of pollutant particles and the nature of reactions of gaseous pollutants on particles need to be better understood.

This talk will review the use of Auger-electron spectroscopy (AES) and X-ray photoelectron spectroscopy (XPS) for the characterization of pollutant particles. These techniques can be used to determine surface composition with a sampling depth of about 1 nm. Such surface sensitivity is necessary as the surface composition determines the nature of pollutant reactions or transformations and the toxicity.

AES and XPS have been used already for studies of particulate pollutants and of various surface reactions. These techniques, XPS in particular, have been used:

(1) to show that finely divided soot particles can play a major role in the catalytic oxidation of sulfur dioxide to sulfate species in polluted atmospheres;[1]

(2) to examine soot-NO and soot-NH_3 reactions that produce ammonium, amine or amide, and nitride species on particulates;[2]

(3) to determine the surface compositon of Pasadena aerosols by particle size and time-of-day to give information on the chemical states of nitrogen and sulfur;[3]

(4) to compare the surface concentrations of lead, sulfur, nitrogen, carbon, silicon, and oxygen on particles collected from urban, suburban, and rural areas during a dry spell and after rain;[4]

(5) to determine the oxidation states of sulfur on the surfaces of fly ash particles and to assess the rates of oxidation of sulfur dioxide on different particulates;[5]

(6) to show the change in the surface concentration of sulfur on fly ash particles after leaching with water;[6] and

(7) to show, together with secondary-ion mass spectroscopy, that the concentrations of certain trace heavy metals were greater in the surface region of fly ash particles than in the bulk.[7]

The recent AES and XPS investigations of particulates will be reviewed and preliminary results from a combined scanning-AES and XPS investigation of selected particles will be presented.

References

1. T. Novakov, S. G. Chang, and A. B. Harker, Science 186, 259 (1974).

2. S. G. Chang and T. Novakov, Atmos. Environ, 9, 495 (1975).

3. T. Novakov, P. K. Mueller, A. E. Alcocer, and J. W. Otvos, J. Colloid Interface Science 39, 225 (1972).

4. G. R. Grieger, American Laboratory 8, No. 4, 77 (April 1976).

5. L. D. Hulett, T. A. Carlson, B. R. Fish and J. L. Durham, in Determination of Air Quality, edited by G. Mamantov and W. D. Shults (Plenum Press, N.Y., 1972), p. 179.

6. L. H. Hulett, H. W. Dunn, J. M. Dale, J. F. Emery, W. S. Lyon, and P. S. Murty, presented at IAEA Conference on Nuclear-Based Techniques for the Measurement, Detection and Control of Environmental Pollutants, Vienna, Austria, 15-19 March 1976.

7. R. W. Linton, A. Loh, D.F.S. Natusch, C. A. Evans, Jr., and P. Williams, Science 191, 852 (1976).

Secondary Ion Mass Spectrometry for Particle Analysis

Dale E. Newbury
Microanalysis Section
National Bureau of Standards
Washington, D.C. 20234

Secondary ion mass spectrometry (SIMS) offers a number of important advantages for the study of particulates, several of which are immediately apparent from the secondary ion spectrum of an individual particle, Figure 1[1,2]:

(1) Signals can be obtained for all the elements, including hydrogen.

(2) Isotopes of an element can be measured, providing the possibility of studying isotopic ratios as a measure of physical and chemical processes.

(3) Molecular signals are observed which can be used to determine speciation in a sample[3].

(4) Peak-to-background ratios of major constituents are high; 10^6: 1 is frequently observed. High sensitivity measurements are therefore possible.

Other advantages include:

(5) Since the primary radiation in SIMS is charged, focusing with a lens system can provide a probe suitable for measurement of individual micrometer-size particles.

(6) The sampling depth of secondary ion emission is shallow, 5 nm or less. Surface microanalysis is possible, at least in principle.

(7) The erosion of the sample by the primary ions provides the option of studying the composition of the target as a function of depth.

(8) Through the use of negative primary ions, both conducting and non-conducting samples can be studied, which is an important attribute in the case of particulates which are frequently oxidized and non-conductive.

(9) Through the use of relative elemental sensitivity factors and standardized instrument operating conditions[4], a useful level of analytical accuracy can be achieved, with about one-half of the analyses falling within 20 percent relative of known values in controlled experiments[5].

(10) The development of images, either by scanning in the ion microprobe or by direct imaging in the ion microscope, allows the analyst to rapidly survey fields of particles.

Disadvantages of SIMS for particulate studies include:

(1) The destructive nature of ion erosion (sputtering) prevents the analyst from studying the same volume of material repeatedly. In instruments equipped with single channel spectrometers, this means that simultaneous data collection from the same volume of material is not possible, leading to difficulties in interpretation. Moreover, it is not possible to subsequently apply other surface analysis techniques such as Auger analysis to the same volume of material.

(2) Strong matrix effects are observed on secondary ion signals, making the interpretation of composition difficult, especially in regions where the oxygen content of the sample varies such as at interfaces.

(3) The presence of polyatomic species, multiply-charged ions, and molecular ions frequently leads to interferences in spectra from targets of complicated compositions.

(4) The current densities necessary for the generation of usable signals from small particles are so high that beam-induced specimen damage effectively eliminates most complicated molecules which may be of interest. The analyst may be forced to examine cracking patterns as characteristics of the complex parent molecules.

(5) The lack of a high spatial resolution (0.1 micro-
meter or finer) imaging technique concurrent with
the analysis technique hinders the correlation of
structural features with chemical analysis.

Limits of detection in particle analysis with the ion
microprobe have been estimated from the signals observed from
multi-element glasses. Table I contains values of the detection
limit (taken as the extrapolated predicted by extrapolation
concentration at a peak-to-background of 3:1) for various
elements in a lead-silicate matrix. Practical analysis
conditions were selected: a 1 nA ion beam and a 1 second
counting time per peak. Detection limits are generally at
the level of 1 ppm, with lower detection limits observed for
alkali elements and poorer detection limits for elements
with lower chemical activity.

Investigation of glass micro-particles of known compo-
sition[4] has revealed an apparent particle effect, Figure
2. The relative elemental sensitivity factors determined
from free standing particles are significantly different and
show a greater range as compared with corresponding measure-
ments on bulk material of the same composition. This
behavior may arise because of irregularities in the emission
and collection of secondary ions due to the curved suface of
the free-standing particles. Measurements of the sectioned
and polished particles showed good correspondence with the
bulk material.

Applications of SIMS to particulates to be described
include studies of environmental particles, particulate
catalysts, and mineral particles.

References

(1) McHugh, J. A., "Secondary Ion Mass Spectrometry" in Methods of Surface Analysis, Czanderna, A. W., ed (Amsterdam, Elsevier, 1975) 223.

(2) Newbury, D. E. "Secondary Ion Mass Spectrometry for Particulate Analysis" to be published in Proc. 10th Ann. Conf. on Environmental Toxicity, Rochester, NY 1977.

(3) Benninghoven, A., Jaspers, D., and Sichtermann, W., Appl. Phys., 11, (1976) 1.

(4) McHugh, J. A., in Secondary Ion Mass Spectrometry, Heinrich, K. F. J. and Newbury, D. E., eds. National Bureau of Standards Special Publication 427 (Washington, 1975) 129.

(5) Newbury, D. E. "Quantitative Analysis of Glasses by Secondary Ion Mass Spectrometry", 8th Intl Conf. on X-Ray Optics and Microanalysis and 12th Ann. Microbeam Analysis Society Conf., (Boston, 1977) 140.

Table I

Detection Limits in Silicon-Lead-Oxygen Glass
(NBS K493 and K523 Glasses)

Element	c/s/nA/Atom Percent[a]	Detection Limit[b] (ppm)
Li	7.22×10^4	0.42
B	4.69×10^3	6.4
Mg	4.66×10^4	0.64
Al	6.32×10^4	0.47
P	1.32×10^3	23.
Ti	5.37×10^4	0.56
Cr	3.01×10^4	1.0
Fe	1.77×10^4	1.7
Ni	1.13×10^4	2.7
Ge	7.45×10^3	4.0
Zr	4.20×10^4	0.71
Ba	7.41×10^4	4.0
Ce	1.85×10^4	1.6
Eu	6.45×10^4	4.6
Ta	2.51×10^3	12.0
Th	1.38×10^4	2.2
U	1.42×10^4	2.1

[a] Corrected for mass abundance.

[b] Concentration expected to produce a signal which is three
times greater than the background (typically 1 c/s) at a
beam current of 1 nA.

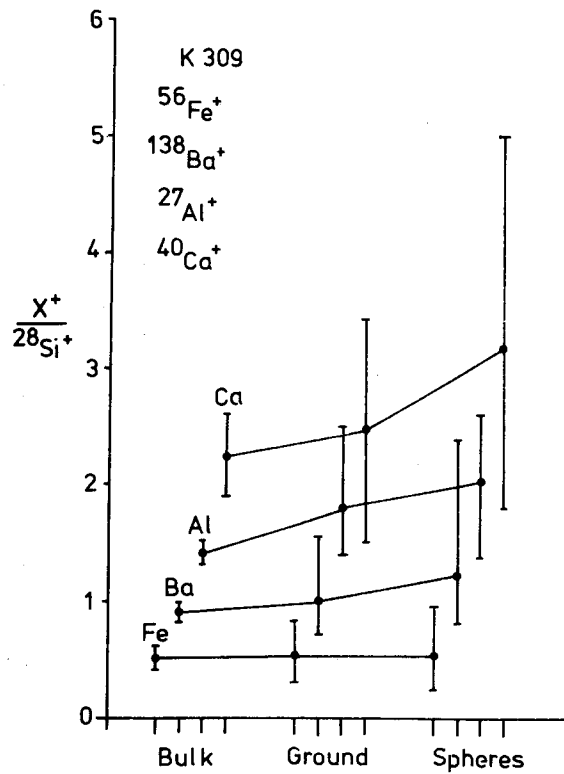Figure 1. Positive secondary ion mass spectrum of a single urban dust particle.

Figure 2. Sensitivity factors observed in bulk glass, sectioned spheres, and free-standing spheres.

Particle Analysis with the Laser-Raman Microprobe

Edgar S. Etz, Gregory J. Rosasco, John J. Blaha,
and Kurt F. J. Heinrich
National Bureau of Standards
and
William C. Cunningham*
Department of Chemistry
University of Maryland

The feasibility of micro-Raman spectroscopy was demonstrated by two laboratories three years ago [1,2]. In the intervening time, laser-Raman microprobes have been developed [3,4] and find routine application to a broad range of problems in microanalysis [5-7]. With these Raman microprobes one can obtain information on the molecular composition of microsamples which heretofore have yielded only to elemental analysis. Raman spectroscopic analysis provides information with respect to the chemical species and the crystalline structure of the sample. When applied to the microscopic domain, it complements the more conventional instrumental microanalytical techniques.

A description and examples are given of the application of micro-Raman spectroscopy to the molecular analysis of microsamples and microparticles in particular. The experiences in Raman microprobe analysis are based on measurements performed with the laser-Raman microprobe developed at the NBS [3]. Some of the earlier results obtained with the new instrument are reviewed and those of current investigations are discussed in greater detail.

Detection and measurement in the Raman microprobe are based on the observation of the normal or spontaneous Raman effect. This effect provides the basis for Raman spectroscopy and has been reviewed in the context of modern chemical analysis [8-10]. In the Raman measurement, a monochromatic beam of visible light, usually from a laser source, is focused on the sample. The scattered radiation contains weak lines, at frequencies both lower and higher than the exciting radiation. The frequency differences, called Raman shifts, are characteristic of the sample

---

* NBS guest worker, 1976-78.

and are independent of the exciting frequency. The spectra
obtained with the Raman microprobe are so-called Stokes-Raman
spectra. These arise from molecules which scatter photons of
lower frequency (Stokes lines) than that of the exciting line.
The Raman pattern they represent provides a molecular fingerprint
for identification and characterization.

Raman scattering is a second order phenomenon (Mie or elastic
scattering is orders of magnitude more intense) and thus Raman
intensities are weak. This places difficult requirements on the
design of a Raman spectrometer for microanalytical applications.
The spectrum is usually excited in a region where the sample does
not absorb. Appreciable absorption of the exciting radiation
generally leads to sample heating, frequently attended by sample
modification or destruction. In microprobe measurements, such
problems can be particularly severe because of the high irradiances
[power/cm^2] that must be employed to excite analytically useful
spectra. A major potential limitation in all Raman work is
sample fluorescence which may totally swamp the Raman effect.
With a choice of laser frequencies, problems of radiation absorp-
tion and sample fluorescence can often be minimized, if not
virtually eliminated. Thus, it is often possible to select such
an excitation frequency that color of a sample is not a limiting
factor.

Identification and characterization of molecular species
present as major components of microsamples are made by qualitative
comparison with reference spectra. If these are not available in
the literature from measurements on bulk samples, the information
is obtained from microprobe measurements of well-characterized
materials.

The measurement of Raman intensities from microparticles for
quantitation is complicated for various reasons [11]. Particle
size, shape, and refractive index influence the intensity of
Raman scattering. Adding to these difficulties are particle
orientation effects, angle of observation and polarization
phenomena that must be considered in conjunction with the optical

design of the instrument and the instrument function itself. Thus, one can, in general, anticipate a complicated relation between Raman intensity and component concentration. Attempts to quantify several of these effects from exact Mie (elastic) and Raman (inelastic) scattering theory have been made by other workers [11,12] and have recently come under investigation in this laboratory [13].

Details on the design and construction of the NBS laser-Raman microprobe have been presented in earlier published work [3,5,6]. The instrument is a monochannel spectrometer of conventional design, arranged so as to permit the acquisition of analytical-quality spectra from microparticles or microscopic regions of micrometer dimensions. A schematic diagram of the instrument is shown in Figure 1. The light from an argon/krypton ion laser is
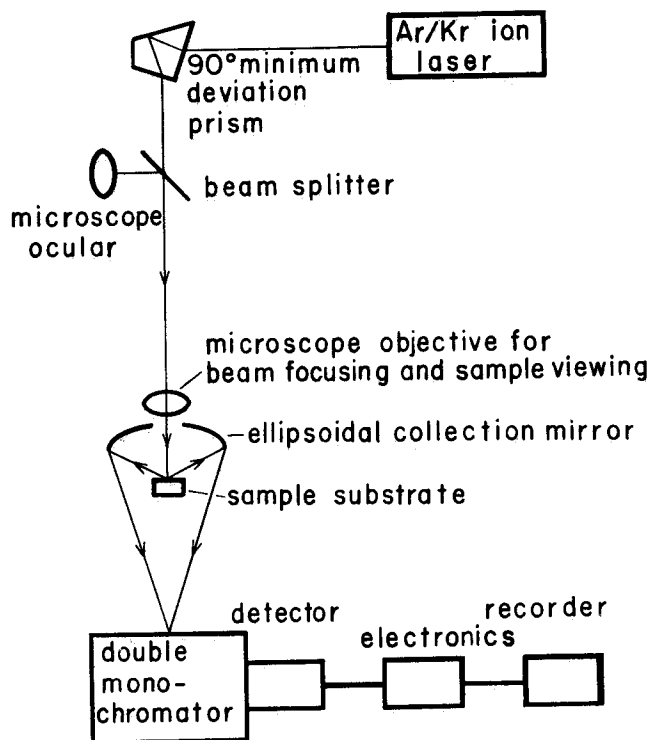
Figure 1. Schematic of the NBS-developed Laser-Raman Microprobe. Typical measurement parameters employed: Excitation, 514.5 nm; laser power, 5-60 mW (at sample); time constant, 0.2-4.0 sec; scan rate, 200-10 cm^{-1}/min; slit width, 3 cm^{-1}.

focused to a small (typically 2-20 µm) spot on the sample. The light scattered by the sample is collected by an ellipsoidal mirror in a 180° back-scattering geometry and transferred into a double monochromator. The signal is detected by a cooled photo-multiplier tube and processed by photon counting electronics.

The sample is supported by a suitable substrate (commonly a disc made of sapphire or lithium fluoride) mounted on a stage driven by remotely-controlled translators. The lateral spatial resolution of a probe measurement is mainly determined by the size of the beam spot placed on the sample and spatial filtering elements placed in the path of the collected scattered light. In addition to being limited by the spatial filtering element, depth resolution is also determined by the optical transparency and surface topography of the sample. For the measurements reported here, the collection volume (in air) is ∿12 µm in depth. Thus, the Raman signal — in most cases — originates from both the surface and the bulk of the sample. Irradiance levels employed in routine probe measurements range from several megawatts/cm^2 to values of several kilowatts/cm^2. Measurement times for single particles of size down to 2 µm may vary from 20 minutes for (fast) survey spectra to scans requiring 3-5 hours for radiation-sensitive microsamples.

The spectrometer system is interfaced to a minicomputer for data logging and total system control. Provisions exist for the storing of standard spectra and for performing computerized spectrum stripping, wherein the spectra of components known to be present in the sample are subtracted, to yield a simplified spectrum. In addition, the computer hook-up of the instrument allows the subtraction of the background spectrum, which often arises from the finite fluorescence emission of the sample under study.

The first studies in analytical micro-Raman spectroscopy dealt with exploring potential application areas to better define the capabilities and limitations of the technique. The measure-ment of microparticles of pure materials was an important aspect of these studies. From the results, estimates of the degree of

specificity of the micro-Raman spectrum with respect to many materials and compounds of interest could be obtained. These measurements served also to establish limits of detectability for common inorganic and organic compounds as well as polymers. Of special interest has been the characterization of environmentally significant species. Among inorganic compounds, the substances studied as microparticles include many of the common minerals (e.g., silicates), as well as inorganic oxides, carbonates, sulfates, sulfites, nitrates, phosphates, and ammonium salts. An example of these measurements on microparticles of pure compounds is given in Figure 2. The upper spectrum illustrates the detection and characterization in the liquid phase of the various sulfate species in a single microdroplet (size, $\sim$30 µm diameter) of sulfuric acid. In concentrated solutions of the acid, all three species — undissociated H_2SO_4, HSO_4^-, and SO_4^{2-} — are present in detectable amounts. The Raman shifts characteristic of the HSO_4^- and SO_4^{2-} ion in solution are indicated. The weak band at 903 cm^{-1} is assigned to the undissociated H_2SO_4 molecule. The middle spectrum was obtained from a microcrystal ($\sim$8 µm in size) of ammonium sulfate. Each of the predicted Raman modes are present. The dominant band is due to the symmetric sulfate stretch with characteristic shift 976 cm^{-1}. The lower spectrum is characteristic of the mineral anhydrite and was obtained from a 5 µm particle. For this sulfate, the symmetric stretch (ν_1) falls at 1018 cm^{-1}. The experimentally observed frequencies of the other fundamental internal vibrational modes (ν_3, ν_4 and ν_2), and which are those predicted from theory, are indicated. The spectra of microparticles are in one-to-one correspondence with those of their bulk sample counterparts, for all the cases investigated to this point.
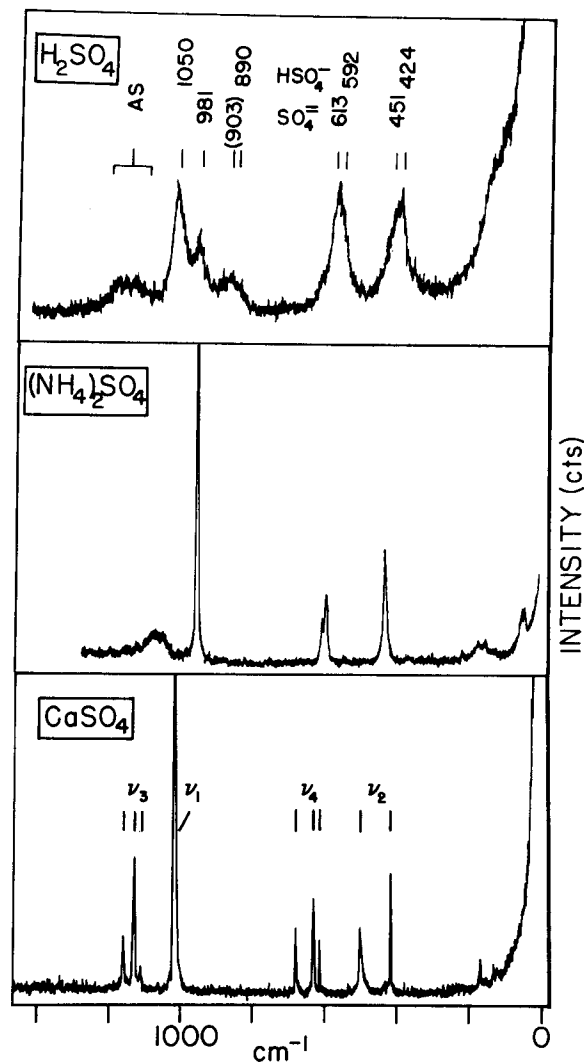
Figure 2. Raman Microprobe Spectra of Sulfate Species in Liquid
and Solid Microparticles. (i) Spectrum of a micro-
droplet (~30 μm diam.) of sulfuric acid. Indicated are
the characteristic Raman shifts (cm^{-1}) of HSO_4^- and SO_4^{2-}
species in the aqueous solution phase. (ii) Spectrum of
a ~8 μm particle of crystalline ammonium sulfate.
(iii) Spectrum of a ~5 μm particle of anhydrite. The ν_i
designations indicate the frequency positions of the
fundamental internal modes of the sulfate ion in $CaSO_4$.

The analysis of single, micrometer-size particles in urban
air particulate samples and in other particulate pollution samples
represent one of the first applications of the instrument to the
study of unknowns. The experimental techniques used in the sampling

and handling of these particles, the spectroscopic measurement conditions employed, and the conclusions drawn from the Raman microprobe analysis, have been discussed [5,6]. Specific examples of this work are the analysis of airborne particles collected by impaction samplers as well as on filters used with conventional high-volume air sampling equipment. Many of the common inorganic and mineral species can be detected and identified in single particles of the primary size fraction (>2 μm) of air particulate dusts. Evidence was presented for particle transformation as a result of bulk sample collection over extended periods of sampling. The spectra showed the conversion of airborne, microparticulate calcite ($CaCO_3$) to insoluble anhydrite ($CaSO_4$) as a consequence of reaction with atmospheric acid aerosol. Observations such as this indicate the importance of unambiguous sampling and point to a useful application of the Raman microprobe to the study of the sampling process itself. These studies were extended to a more detailed spectroscopic investigation of the existence of a form of environmental carbon (e.g., soot) or residual hydrocarbon matter found to be commonly associated with airborne particles. Of interest was the interpretation of two broad bands centered around 1350 and 1600 cm^{-1} frequently observed in these spectra in addition to the spectral features which could be assigned to the host particle. These features arise from the presence of carbon in a form analogous to polycrystalline graphite [14]. The source of the carbon can be either graphitic soot or an organic component which converts to poly-crystalline graphite under high laser irradiance.

Raman microprobe work on airborne particles continues. The results of microprobe measurements performed in the total charac-terization of particles collected at the South Pole are discussed. The samples studied consist of atmospheric aerosol collected by impaction onto micro-Raman substrates. These are concurrently analyzed for elemental composition by SEM microanalysis and instrumental nuclear activation analysis. The bulk of the col-lected particles (on the lower impactor stages) are submicron in size, with few of the impacted particles being larger than 2 μm. They have characteristic morphologies as revealed by SEM examina-

tion. Spectra are discussed for these particle collections for which the x-ray spectrum shows sulfur to be the only major constituent. They show the bands with Raman shifts characteristic of crystalline sulfate. These results support the findings reported by other workers on the existence of sulfuric acid and/or ammonium sulfate in microparticles of the Antarctic atmospheric aerosol [15,16].

Initial results from the investigation of stack particulate emissions from an oil-fired power plant have been reported [6]. The Raman spectra observed from many particles collected in the stack show vanadium pentoxide, V_2O_5, as a major constituent. Other types of particles present in these samples have yielded other types of spectra which are the subject of current studies. Many indicate the presence of crystalline sulfates, and reference spectra from microparticles are being acquired to aid in the identification of these unknowns as to the associated cation species. In many cases, the spectra of these stack particulates also show the "carbon bands" in the 1300-1700 cm^{-1} region. These, we believe, derive either from soot or from residual polycyclic organic matter associated with the particles. These in-stack sample collections have also furnished liquid phase aerosol which is presently being examined for its composition at both ambient and controlled conditions of temperature and relative humidity. Some results have been obtained in the study of coal fly ash particles. The spectra of these particulates confirm a glass-like structure and a lack of long-range crystalline order in the glass. This results in extensive broadening of most spectral features. The vibrational spectrum then indicates the glassy nature of the particle but is less definitive with respect to the composition of the material.

Various types of organic compounds have been examined in the Raman microprobe and initial results on microparticles of non-absorbing and non-fluorescing organics have been reported [6]. Work in progress extends these earlier feasibility studies on pure organic compounds to several classes of hydrocarbons of interest to environmental pollution studies. Examples discussed are the spectroscopic characterization of several types of pesti-cides (e.g., chlorocarbon insecticides) and selected compounds of

the class of polynuclear aromatic hydrocarbons (PAH's). The various PAH's studied in microparticulate form include phenanthrenes, benzophenanthrenes, fluoranthenes, chrysenes, pyrenes, and benzopyrenes. These measurements have aimed to assess the potential measurement difficulties arising from the absorption of the laser radiation and were intended to examine the spectral interferences from the intrinsic fluorescence of the polyaromatic ring systems. To demonstrate the differences in background fluorescence from the sample, the spectra were excited at several laser frequencies (514.5, 568.7, and 647.1 nm). The specificity of the Raman spectrum for several pairs of isomeric condensed ring systems is shown. The results indicate a detectability limit of 10-100 pg for many of these environmentally significant molecules and suggest that the micro-Raman technique may offer an attractive approach to trace organic analysis. Its potential as a sensitive and specific detection system for organic fractions separated by liquid chromatography is currently under experimental study.

In the study of biological samples of macroscopic size, Raman spectroscopy has evolved as an effective method for elucidating the structure and conformation of biomolecules [18,19]. With the advent of Raman microprobe techniques, great possibilities appear to be opening up in biology, pathology, and tissue research. The expection is, therefore, that Raman microprobe analysis can be employed to obtain molecular information at the cellular level. To explore these possibilities, the Raman spectra of microsamples of pure biological molecules have been examined, and these measurements have now been extended to the study of thin sections of biological tissues. The biological compounds studied in pure form are "simple" molecules (e.g., urea, cholesterol, amino acids, sugars), nucleotides (e.g., ADP, ATP) and proteins (e.g., bovine serum albumin, collagen). These biomolecules give a richly detailed "fingerprint" vibrational spectrum with good sensitivity and are amenable to molecular-level interpretation. Tissue studies have been made in two areas of application. The aim was to determine if Raman spectra could be obtained and, if

so, whether or not this information could be correlated with the more conventional morphological and x-ray microanalytical methods. Examples of this work are the examination of thin (5-10 μm thickness) sections of cartilage, bone, and tooth. Of interest are the processes leading to the calcification of tissues and the premineralization of bone. This requires the ability to distinguish between organic and inorganically bound calcium and phosphorus. A result from the microanalysis of mineralized tissue is shown in Figure 3. The bottom spectrum is that of collagen in an air-dried, thin section of rat Achilles tendon. Similar spectra have been
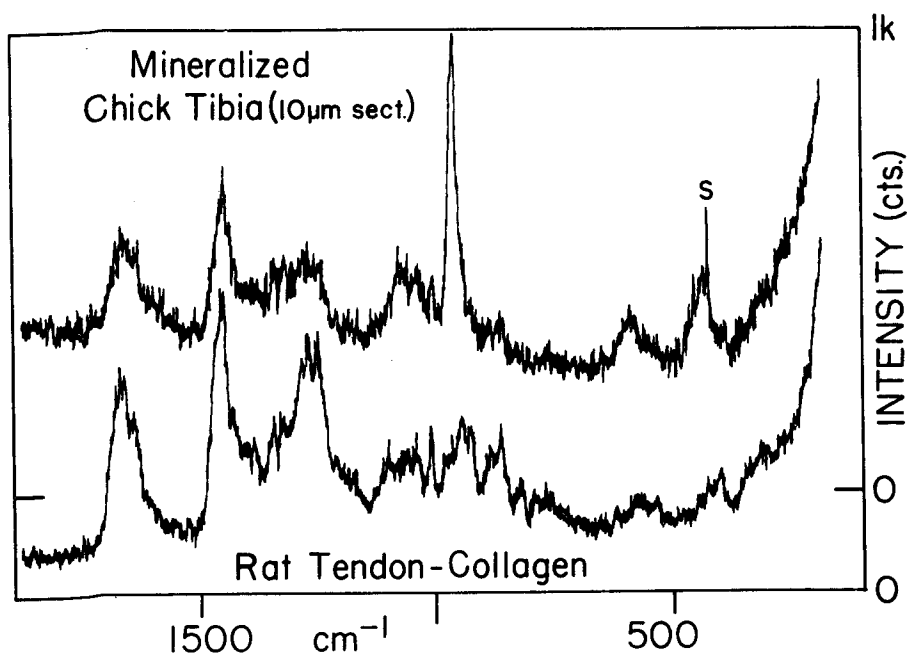

Figure 3. Spectra recorded in the Raman Probe Microanalysis of Thin (10 μm thickness) Sections of Biological Tissue. (i) Spectrum of a microscopic region (∿200 μm²) in the mineralized zone of embryonic chick tibia. Band marked S arises from the Raman scattering by the sapphire substrate. (ii) Collagen spectrum obtained from rat Achilles tendon.

obtained from other types of collagenous tissue, including cartilage in bone. The spectrum shown is consistent with the Raman data for bulk sample collagen reported in the literature [19]. The upper spectrum was obtained from an equally small ($\sim$16 μm beam spot) sample area in the partially mineralized zone of a section of embryonic chick tibia. The spectrum has all the basic features of the collagen spectrum but in addition shows the Raman modes characteristic of hydroxyapatite, $Ca_{10}(PO_4)_6(OH)_2$. Band assignments for the calcium apatites have been given in the literature [20]. The strongest feature is the symmetric stretching mode (ν_1) with Raman shift 963 cm^{-1}.

In a separate area of biological tissue analysis, the microprobe is used to furnish information for pathology studies. Thin sections of human biopsy tissue are under study for the suspected presence of microscopic foreign bodies of silicone polymer. One such case is the detection and identification of microscopic particles of silicone rubber (polydimethylsiloxane) in lymph node tissue away from an implanted silicone elastomer finger joint prosthesis. This study represents the first of its kind in which the molecular composition of a material accidentally intruding in biological tissue has been documented by an instrumental microanalytical technique.

In addition to the examples of application cited above, the Raman microprobe has furnished unique results in several other fields of investigation. Based on past performance and future potential, we confidently anticipate the continued growth and acceptance of Raman microprobe analysis.

References

[1] G. J. Rosasco, E. S. Etz, and W. A. Cassatt, Appl. Spectrosc. 29, 396 (1975).

[2] M. Delhaye and P. Dhamelincourt, J. Raman Spectrosc. 3, 33 (1975).

[3] G. J. Rosasco and E. S. Etz, Res. & Devel. 28, 20 (June 1977).

[4] M. Delhaye, E. DaSilva and G. S. Hayat, Amer. Lab., p. 83 (April 1977).

[5] E. S. Etz, G. J. Rosasco and W. C. Cunningham: The Chemical Identification of Airborne Particles by Laser Raman Spectroscopy, in Environmental Analysis (G. W. Ewing, Ed.), Academic Press, Inc., New York (1977), pp. 295-340.

[6] E. S. Etz, G. J. Rosasco and J. J. Blaha: Observation of the Raman Effect from Small, Single Particles: Its Use in the Chemical Identification of Airborne Particulates, in Environmental Pollutants: Detection and Measurement, Plenum Publishing Corporation, New York (1978), pp. 413-456.

[7] P. Dhamelincourt, F. Wallart, M. Leclercq and D.O. Landon: Some Microanalytical Problems Resolved by the Laser Raman Molecular Microprobe; private communication, to be published.

[8] P. J. Hendra and C. J. Vear, Analyst 95, 321 (1970).

[9] D. E. Irish and H. Chen, Appl. Spectrosc. 25, 1 (1971).

[10] W. M. Tolles and R. D. Turner, Appl. Spectrosc. 31, 96 (1977).

[11] M. Kerker, J. Colloid Interface Sci. 58, 100 (1977).

[12] H. Chew, M. Kerker and P. J. McNulty, J. Opt. Soc. Am. 66, 440 (1976).

[13] G. J. Rosasco and H. S. Bennett: Internal Field Resonance Structure: Implications for Optical Absorption and Scattering by Microscopic Particles, J. Opt. Soc. Am. (to be published).

[14] J. J. Blaha, G. J. Rosasco and E. S. Etz: Raman Microprobe Characterization of Residual Carbonaceous Material Associated with Urban Airborne Particulates, accepted for publication, Appl. Spectrosc. 32 (1978).

[15] R. D. Cadle, W. H. Fisher, E. R. Frank and J. P. Lodge, J. Atmos. Sci. 25, 100 (1968).

[16] M. Kumai, J. Atmos. Sci. 33, 833 (1976).

[17] N. T. Yu, CRC Crit. Revs. Biochem. 4, 229 (1977).

[18] R. C. Lord, Appl. Spectrosc. 31, 187 (1977).

[19] B. G. Frushour and J. L. Koenig, Biopolymers 14, 379 (1975).

[20] W. P. Griffith, J. Chem. Soc. (A), 286 (1970).

PARAMETERS OF QUANTITATIVE X-RAY PHOTOELECTRON SPECTROSCOPY AND AUGER ELECTRON SPECTROSCOPY

W.M. Riggs and L.E. Davis
Physical Electronics Industries, Inc.
6509 Flying Cloud Drive, Eden Prairie, Minnesota, 55344, U.S.A.

Both fundamental and instrumental parameters pertinent to quantitative x-ray photoelectron spectroscopy (ESCA) will be discussed. The analyzer transmission, the theoretical photoelectron cross sections and the mean electron escape depth dependence on energy are evaluated as the primary parameters in determining relative atomic abundance from photoelectron peak heights or peak areas.

Measurements have been made that permit the determination of the double-pass cylindrical mirror analyzer (DCMA) transmission function. For the DCMA, it is advantageous to utilize pre-retardation with spherical grids when measuring photoelectron energy distributions

Theoretical calculations of photoelectron cross sections have been reported by Scofield.[2] These cross sections can be incorporated along with experimental and calculated values for mean electron escape depths. Results from the literature[3,4] suggest that an escape depth dependence of approximately $E^{0.75}$ applies to the kinetic energy range of interest for ESCA. The product of the DCMA transmission function and the approximate escape depth dependence, $E^{-0.25}$, then is applied to relative photoelectron cross sections permitting computer calculation of atomic concentration levels from measurements of photoelectron signals.

Direct measurements of binary compounds and metal alloy standards are compared to theoretical predictions to test the applicability of using the parameters as discussed above. Further, a computer acquisition and reduction system incorporating these quantitative parameters is described. A useful example of this capability which takes advantage of computer control of the instrumentation as well as computer data reduction is the automatic acquisition of quantitative depth profiles by ESCA. The computer is used to accumulate baseline-corrected ESCA peak intensities as a function of time. A differentially pumped ion gun with beam rastered over an area sufficiently large for ESCA measurement is operated under computer control. The ion beam is automatically switched off during ESCA measurement to minimize secondary electron background and to maximize depth resolution. ESCA measurement and sputtering cycles are repeated until the desired depth is reached. The end result is an ESCA compositional depth profile expressed as relative atomic abundance vs. depth.

Quantitation of AES data involves many of the same parameters as XPS since electrons in the same energy range must escape from the sample and be energy analyzed. Additional complications arise, however, since excitation cross sections are dependent upon the incident beam energy as well as upon sample related parameters such as Auger yield. Further, the $dN(E)/dE$ mode of data acquisition is very convenient and frequently used, but introduces effects of modulation voltage and possible uncertainties related to peak shape changes. Thus, quantitation of AES data is normally achieved through use of empirically derived[5] sensitivity factors obtained under standardized operating conditions. Although greater fundamental uncertainties exist for AES quantitation than for XPS, the ability to focus the electron beam excitation source to a small diameter allows quantitative estimation of very small samples. Examples of the utility of this capability in areas such as particle analysis, metallurgy and microelectronics will be described. Comparative data illustrating both AES and XPS quantitation on the same materials will be described.

1. P.W. Palmberg, J. Elect. Spectr. 5, 691(1974).
2. J.H. Scofield, J. Elect. Spectr. 8, 129(1976).
3. C.D. Wagner, Anal. Chem., 49, 1282(1977).
4. D.R. Penn, J. Elec. Spectr. 9, 29(1976).
5. L.E. Davis, N.C. MacDonald, P.W. Palmberg, G.E. Riach, R.E. Weber, Handbook of Auger Electron Spectroscopy 2nd Edition, (1976).

The Role of the Cascade as a Background Effect in Secondary-Electron
Emission Spectroscopy

E. N. Sickafus
Research Staff, Ford Motor Company, Dearborn, Michigan 48121

Abstract

Electron bombardment of a clean, single-crystal surface of a
metal by a monoenergetic beam produces a secondary spectrum whose major
portion is referred to as the cascade. The cascade is the lower energy
part of the spectrum which increases in intensity with decreasing energy
down to the true secondary peak in the range of ca. 5-10 eV. With
increasing energy, the cascade decreases in intensity to a minimum where
further evidence of the cascade is obliterated by the rediffused primaries
which increase in intensity with increasing energy up to the elastic peak.
When primary beam energies of the order of 3 keV are used the cascade can
be evident from 10 eV to 1000 eV; two decades of energy. For metals,
this range of energy covers the range of energies for shortest inelastic
mean free paths of electrons – thus, the region of greatest sensitivity
for electron surface probes.

Atomically clean surfaces and nearly atomically clean surfaces
exhibit rather simple cascade functions. These become evident when the
secondary emission current $j(E)$ is displayed in a log $j(E)$ vs log E mode
where the cascade exhibits a linear property. From this effect the
cascade function can be written as AE^{-m} where A is a constant scaling
factor and m is a constant given by the slope of the log $j(E)$ vs log (E)
display. The cascade, wherever it is evident, is a background for
other spectral features such as Auger electron peaks. By determining
first the functional form of the cascade background of a particular Auger

electron peak it becomes possible to visualize a synthesis of an Auger line. This synthesis consists of a true Auger electron emission line, an associated loss structure, and the cascade background.

It is shown here how an electronic analog of the cascade can be generated and injected at the signal source of a retarding potential analyzer so as to effect a correction for the cascade background. By correcting for the background at the signal source the full dynamic range of the phase-sensitive detector that follows can be utilized for optimum signal to noise recovery. The resulting signal is not the true Auger electron emission line but is a line that has been broadened and bears a low energy step due to inelastic loss processes. It is shown further that these features can be removed by deconvolution of an instrument function so that the resultant line more nearly approaches the true Auger electron emission function. These effects and analytical procedures are demonstrated for the $M_{23}VV$ and $L_{23}VV$ spectra from a Cu(110) surface. The spectra were taken with a 4-grid retarding potential analyzer (LEED optics) using potential modulation and recording the signal at the fundamental frequency of modulation. Background subtraction is done with analog circuitry while deconvolution is done with a digital processor.

THE DIGITAL ACQUISITION AND PROCESSING OF AUGER SPECTRA

Y.E. Strausser, N.J. Taylor, Varian Associates, Inc.,
611 Hansen Way, Palo Alto, California 94303

Analog controls and data streams have been almost exclusively employed in electron beam excited Auger spectrometry to date. The use of digital electronics provides great flexibility in approaches to the acquisition, processing and display of data. We have taken an approach which uses a mini-computer, a micro-processor, a dual floppy disk drive and a graphics terminal to provide digital control functions, a digital signal train, digital data storage and processing with reconversion to analog only in the final data display devices. This permits the acquisition of the EN(E) signal as measured by the CMA with no arbitrarily imposed modulation or time constant effects. This technique provides wide dynamic range in the data storage and enables all data to be immediately stored, unprocessed, there-by precluding the type of information loss which commonly arises from incorrect sensitivity settings in analog systems. After the data are stored, a copy of the data may be digitally processed to provide the smoothing or averaging effect of a time constant, to differentiate the data, to integrate over specific peaks, etc. By converting the signal to digital form immediately after it leaves the CMA, the sensitivity to pickup of stray analog noise is also drastically reduced.

It is inevitable that comparisons be made between analog and digital measurements. These comparisons are usually made in the analog "domain" of differentiated data often, unfortunately, with vague bases for comparison. Factors such as step width, time per datum and smoothing, which influence the comparison are discussed. For a given total acquisition time, the desir-ability of using small step widths followed by smoothing, rather than use the more immediate smoothing offered by wider (and fewer) steps, is graphically illustrated. Since the unsmoothed differentiated signal-to-noise is proportional to the step width to the three halves power, there is a tendency to select large steps, thereby risking loss of resolution unnecessarily. Signal-to-noise and resolution as a function of step width and smoothing are discussed and it is demon-strated that in order to sample without significant loss of features, one should digitize in such a manner as to ensure

that there are at least six data points between the FWHM of
the peaks of interest. For a conventional analyzer in which
the resolution ΔE is proportional to the energy E and with
a minimum $\frac{\Delta E}{E}$ of 0.3%, the step width is determined by the
analyzer resolution at energies above a few hundred eV.
Subsequent smoothing may then be employed to improve S/N at
the expense of resolution. If the loss in resolution cannot
be tolerated, acquisition may be continued for an extended
period.

Since consistency in noise measurement was of utmost importance
in the measurements, the noise voltage amplitude density was
fitted to a Gaussian distribution, a technique commonly em-
ployed in image analysis. This enables an r.m.s. (σ) noise
to be determined. The actual noise amplitude used in a
signal-to-noise measurement is then chosen as some multiple
of this r.m.s. value, usually 4 σ .

The digital approach to data processing facilitates the
separation of interferring spectral features. Examples of
this operation include subtraction of known Auger peaks
from spectra in which these peaks are overlapped by other
peaks, the monitoring of variations in surface elemental
concentrations during processing by subtraction of a sequence
of spectra, and the use of different background models to
subtract the slowly varying true secondary background from
under the Auger peaks. It is well known that the quantitative
accuracy is improved by proper background subtraction and
integration over the Auger peaks. This is particularly
important in depth profiling where Auger peaks frequently
undergo shape changes during the profile. Examples of how
the digital approach facilitates these manipulations are
presented from actual applications.

SCANNING AUGER MICROANALYSIS: PAST, PRESENT AND FUTURE

N. C. MacDonald, R. L. Gerlach, C. T. Hovland

Physical Electronics Industries, Inc.
6509 Flying Cloud Drive
Eden Prairie, MN 55344

As a relative newcomer to the field of microbeam analysis, scanning Auger microbeam analysis has become an accepted analytical technique for the three dimensional chemical analysis of solid surfaces and thin films. Because of the extreme surface sensitivity, thin film analysis and SEM imaging capabilities, the technique has gained widespread acceptance as an analytical tool to compliment analytical results obtained from the electron and ion microprobes and the SEM.

The past nine years of development of scanning Auger microprobe (SAM) instruments has brought the technique from a laboratory curiosity in 1969 to a well accepted analytical technique in 1978. The availability of installed SAM instruments has further demonstrated the necessity to determine the surface chemistry as well as bulk chemistry of solids for the identification and solution of many technological problems.

Like many analytical techniques, the increased use of SAM instruments has exposed some deficiencies with present SAM instrumentation and highlighted more fundamental limitations of microbeam surface analysis. The backscattered electron contribution to the Auger signal sets limits on the applicable chemical spatial resolution of scanning Auger microbeam analysis of thick, solid surfaces. For rough specimens, the chemical spatial resolution of scanning Auger microanalysis is limited by the areal distribution of the backscattered electrons. The ultimate vacuum, electron beam specimen damage, specimen topography and specimen charging represent challenges for the further improvement of the chemical spatial resolution and the applicability of the technique. For small spot sizes, electron beam damage and electron beam desorption sometimes restricts the ultimate quantitative analysis capability of microbeam surface analysis. Techniques and improvements for sample preparation for surface analysis remains an ongoing challenge. Techniques to expose surfaces and record the data before the surface becomes contaminated by the background pressure can degrade the detectability limits on surfaces and interfaces.

At the present, there has been significant advances made in quantitation, automation and control of scanning Auger instruments. Automated instrument control as well as automated data processing, has vastly increased the range of problems that are possible to

attack using scanning Auger microanalysis. Quantitative models are now being used, documented and tested on standards to further improve the quantitative capability of scanning Auger microbeam analysis.

In the future, we can expect further improvements in specimen handling capabilities, vacuum conditions, quantitation, instrument control and automation, as well as reduction in the electron beam spot size. Better specimen handling capabilities, such as fracture in a reactive environment, plasma etching, etc. used to expose the surface of interest and other improvements should further broaden the field of scanning Auger microbeam analysis.

High Spatial Resolution Scanning Auger Electron Spectroscopy:

Individual Grain Boundary Analysis

R. G. Rowe and C. L. Briant
General Electric Company
Corporate Research and Development Center
Schenectady, NY 12301

The study of grain boundary segregation in metals has been advanced considerably by the advent of high spatial resolution scanning Auger microprobe systems. In this paper we will discuss our application of the technique to the analyses of grain-to-grain differences in grain boundary segregation in iron-3% silicon alloys and to low alloy steels such as HY-series and 3330 type steels. Segregation will be examined at grain boundaries produced both by normal grain growth processes, and by rapid solidification from the melt. In the low alloy steels, we will examine the relationship between grain boundary segregation and hydrogen cracking tendencies in weld and heat affected zones of structural weldments.

In the study of grain growth in iron-3% silicon alloys, the question of the effect of grain boundary segregation on grain boundary mobilities is an important one which has received much attention in the past. Recent work on silicon iron alloys containing additions of boron, nitrogen and sulfur has shown a direct relationship between the degree of grain growth inhibition and the segregation of nitrogen to the grain boundaries. These results, which were obtained by analyzing many individual grain boundary surfaces on silicon-iron specimens fractured in-situ have also allowed us to address the question of whether there are significant differences in grain boundary segregation from one grain boundary surface to another.

Grain growth annealing in iron-3% silicon alloys results in the growth, or coarsening of primary recrystallized matrix grains as well as secondary recrystallization or unstable grain growth of a few grains. These secondary recrystallization grains grow much more rapidly than the matrix grains and ultimately consume the entire matrix. Interrupting an anneal by rapidly quenching the sample from the annealing temperature can produce a sample with coexisting coarsened primary grains, nucleating secondary recrystallization grains, and stable matrix grains. Figure 1 shows two areas of the fracture surface of such an alloy. One area shows grains with relatively flat facets maintained by the equilibrium of surface tension forces at grain boundary junctions. The other area shows rounded surfaces which would appear to be due to coarsening of the primary

matrix and not represent equilibrium grain boundary structure. Micrographs (a) and (b) have Auger peak height ratios of Nitrogen/Fe_{651} superimposed and micrographs (c) and (d) the ratios Sulfur/Fe_{651}. As may be seen from this figure, there is not a significant difference from one primary grain boundary surface to another but that coarsened primary grains with rounded surfaces exhibit significant differences in sulfur segregation. The grain to grain variation of the nitrogen/iron Auger ratio is not as significant as the variation for sulfur.

The driving force behind these differences in segregation from one grain boundary shape and another has not been established but the ability to resolve individual grain boundary surfaces is expected to lead to a significant improvement in our understanding of grain growth controlling processes.

Grain boundary Auger analyses of iron-3% silicon alloys solidified rapidly from the melt has indicated a relationship between oxygen exposure and sulfur segregation at grain boundaries. At grain boundary surfaces adjacent to hot cracked boundaries, a strong interaction between oxygen and sulfur segregation has been observed. Regions of the grain boundary high in oxygen were low in sulfur, and conversely regions low in oxygen were high in sulfur. Carbon, nitrogen and boron segregation did not appear to be affected by oxygen adsorption, although some change in the chemical state of boron was suggested.

High spatial resolution scanning Auger microscopy has permitted the analysis of the oxygen/sulfur segregation gradient along the surface of a single grain boundary.

Another area in which grain to grain resolution in Auger electron spectroscopy has been shown to be important is in the analysis of segregation-induced grain boundary embrittlement associated with welding of metals. One of the major problems facing the welding industry today is that of hydrogen-induced cracking in low alloy steel weldments. Cracks can occur in either the weld metal or the heat affected zone and are thought to be due to hydrogen-embrittlement at the grain boundaries. The two most common sources of hydrogen in welds are improperly dried welding electrodes and interaction of weld metal with the environment, e.g., sea water.

It has been shown that hydrogen cracks initiate at either grain boundaries or along particle-matrix interfaces of large inclusions, and based on previous work, one would expect impurity segregation to grain boundaries to be associated with enhanced hydrogen embrittlement. Auger analysis of individual grain boundaries and particle-matrix interfaces has shown impurity segregation to indeed be associated with hydrogen cracking tendencies.

In this paper we will report results from studies of welds in two types of low alloy steels. One, a series of commercial HY-type steels and the other a set of laboratory prepared 3330-type steels. In the HY-series alloys we will show that sulfur, phosphorus, and nitrogen are available to segregate to many inclusion interfaces. In the 3330-type steels we will report Auger results from steels specifically doped with elements such as tin, phosphorus, silicon, and sulfur. In all cases we will compare these Auger results to hydrogen crack initiation measurements.
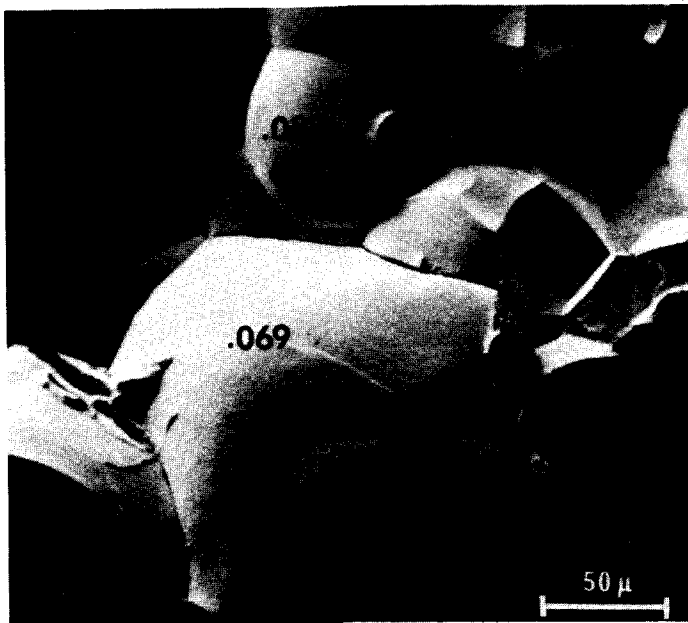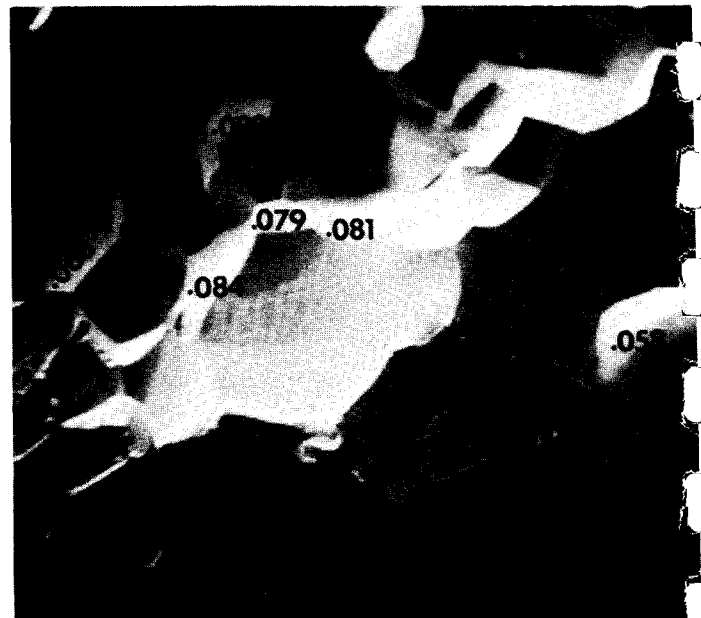
(a)
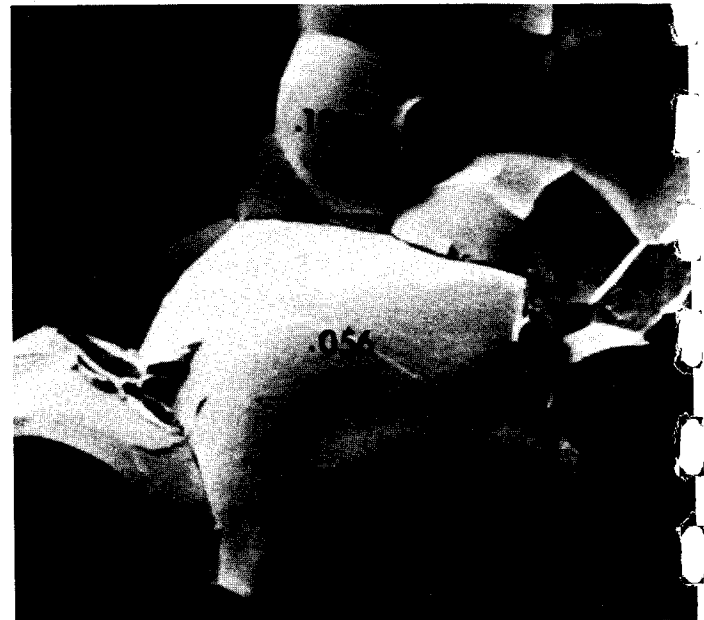
(c)
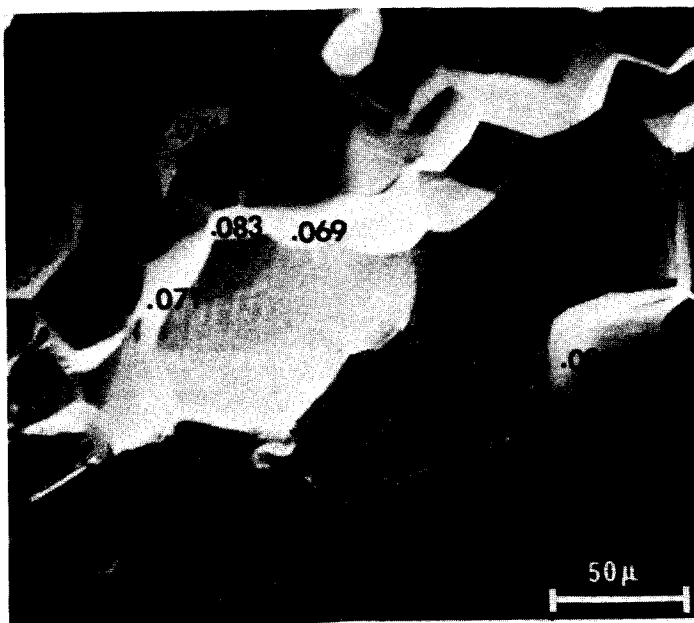
(b)

(d)

N/Fe Auger Ratio

S/Fe Auger Ratio

Figure 1.   Nitrogen/Iron (Micrographs (a) and (b)) and Sulfur/Iron (Micrographs
(c) and (d))   Auger ratios for different grain boundary surfaces
on an in-situ fractured iron-3% silicon specimen.

ANALYSES OF LIFE TESTED DISPENSER CATHODES

B. E. Artz, J. L. Bomback, and M. A. Smith
Technical Services

and

E. Sickafus
Metallurgy Department
Engineering and Research Staff – Research
Ford Motor Company
P.O. Box 2053
Dearborn, Michigan 48121

Dispenser cathodes are used as thermionic electron emitters in several applications including traveling wave tubes in microwave communication systems. When employed in communications satellites, it is essential that they maintain constant emission for over seven years. Laboratory test-stand results show an undesirable slow but steady decay of electron emission from some cathodes. It is important, therefore, to study chemical and metallurgical changes which occur during the life of such cathodes in order to understand and predict their long term behavior. The cathodes investigated* herein consisted of a porous ($\simeq$ 82% theoretical density) tungsten plug impregnated with a mixture of oxides in the molar ratio $BaO:CaO:Al_2O_3::4:1:1$. The plug is brazed into a thin molybdenum cylinder using a molybdenum-nickel-ruthenium braze. A tungsten-rhenium heater, packed in alumina, is also contained in the cylinder. The back of the cathode plug is sealed with a molybdenum-ruthenium layer to prevent loss of Ba impregnate into the heater region. The cathode assembly is shown schematically in Figure 1.

The oxide impregnate is a source of Ba and BaO which lower the work function of the tungsten surface allowing higher electron emission at lower temperatures. Thus, longer life is achieved compared with pure tungsten emitters such as those used in electron microscopes. The exact mechanism by which the Ba/BaO impregnate lowers the work function is currently a subject of study and debate.[1,2,3] There is agreement that elemental and/or oxidized barium forms a thin layer (a fraction to several monolayers) on the tungsten surface which contributes to the lowering of the work function. The layer constituents evaporate from the surface during service and are replenished continusouly by the material in the pore network. The kinetics of barium transport from the plug interior through the pore network and onto the surface are not completely understood.

Cathodes from Life Test Diodes

A series of ten cathodes operated in diodes for 2,000 to 50,000 hours were examined. A diode consists of an assembled cathode in close proximity to a Mo anode enclosed in an evacuated ($\simeq 10^{-10}$ torr) glass tube. Each cathode was operated at 1050°C and was operating satisfactorily when its test was terminated. This series is intended to represent operating cathodes at different stages of life.

Several topological differences were observed among these cathodes and can be seen in Figure 2 which compares the surfaces of the 2,000 hour and 48,000 hour life tested cathodes:

---

*These cathodes were type S manufactured by Semicon Associates, Lexington, Kentucky. There is, however, no reason to believe that the phenomena observed are unique to this type.

1. Spots of as yet unknown chemistry were found in greater frequency and size according to life-test period.

2. Crystallographic faceting was found on the surface manifested as many parallel steps and large planar areas on individual tungsten grains.

3. Crystallographic faceting also was found on the surfaces of the internal pore walls as planar regions but not as parallel steps.

4. The pore openings to the surface were more often found to be empty in the short life tested cathodes and were more often found with a free standing growth-like deposit in the long life tested cathodes.

The formation of crystallographic facets on the emitter surfaces is accompanied, we believe, by evaporative removal of large amounts of tungsten. At the operating temperatures in question, tungsten can leave the surface as a volatile oxide with the oxygen being supplied by the impregnate. Attempts to model long term emission behavior of dispenser cathodes must take faceting into account.

The effect of faceting may be important with respect to the anisotropy of the work function. The exact crystallography of the facets was not determined. Selected area electron channeling was attempted but useful patterns could not be generated due to the small tungsten grain size and the low inherent resolution of channeling patterns in heavy metals. However, right angles between facets were frequently observed which is consistent with the formation of low energy $\{110\}$ or $\{100\}$ types.

Figure 3 shows X-ray spectra from the pore impregnate and a tungsten grain surface respectively. Barium was not detected by this method on the tungsten grain surfaces since it is present in only the top few monolayers. Barium and aluminum were easily detected in the pore impregnate. Calcium was not detected and is assumed to evaporate faster than barium.

Surface Analysis of a New Cathode at Temperature

Ultimately, it is the chemistry of the emitting surface which determines its work function and, therefore, its emission properties at a given temperature. Auger electron spectroscopy has been used to map this chemistry but heretofore only at low spatial resolution due to the choice of beam diameters (e.g., on the order of 500 μm). The SEM results, Figure 2, indicate that such a large diameter incident beam must yield spectra with contributions from pore regions as well as from tungsten grain surfaces. Thermionic emission microscopy studies[4] have shown that emission is extremely heterogeneous and it is important, therefore, to use high resolution surface analysis techniques to relate local chemistry to emission behavior.

A commercial scanning Auger microprobe was used to examine a fresh type S cathode at temperature (1050°C brightness) in the high vacuum system. The pressure in the system was $\simeq 1 \times 10^{-10}$ torr which is comparable to that in an operating traveling wave tube. The incident beam diameter (3 μm) was slightly smaller than the mean tungsten grain size. Typical beam parameters were 4-5 keV electron energy and 10^{-7} Amp probe current. The cathode with the heater leads attached was mounted on a rotary sample manipulator so that it could be rotated between the focal point of the cylindrical mirror analyzer and a viewing port for optical pyrometer temperature measurements. The cathode was taken through a normal thermal activation cycle and then aged for 250 hours at 1050°C while spectra were periodically recorded. No anode was used to extract thermionic emission current so it is not known whether this cathode would operate in a satisfactory manner.

The following observations were made on the cathode surface:

1. At room temperature, prior to activation, the surface was heavily oxidized and contained varying amounts of barium, Figure 4a. After activation, the oxygen intensity was considerably reduced while the intensity of barium and tungsten increased. Small amounts of aluminum, sulfur, and phosphorous, were detected in some regions, Figure 4b.

2. Of the impregnate elements, Ba, Ca, Al, and O, only Ca was not detected on the surface.

3. No appreciable spectral change occurred on the surface through 250 hours at 1050°C following activation.

4. When the probe beam current was increased from a normal operating value of 10^{-7} Amp to 10^{-6} Amp, reversible electron beam induced changes occurred in the surface chemistry. These changes included a decrease in the Ba and O intensities, an increase in the S and P intensities, and the appearance of Mo peaks, Figure 5. These beam-induced changes indicate that impurities and possible poisons S, Mo, and P were present near the surface.

SUMMARY

A heterogeneous and time varying topography of dispenser cathode surfaces is evident in their SEM images. The development of crystallographic facets and stain-like spots on the emitter surfaces are two phenomena which must be better understood before a useful physical model can be developed to predict cathode life. High spatial resolution Auger electron spectroscopy could provide complementary surface chemical information. Long term in-situ studies of active dispenser cathode surfaces would contribute significantly to such a model.

ACKNOWLEDGMENTS

REFERENCES

1. R. Forman, "Surface Studies of Barium and Barium Oxide on Tungsten and Its Application to Understanding the Mechanism of Operation of an Impregnated Tungsten Cathode," JAP 47, 1976, pp. 5272-5279.

2. G. A. Haas, H. F. Gray, R. E. Thomas, "Effects of S, Ba, and C on Impregnated Cathode Surfaces," JAP 46, 1975, pp. 3293-3301.

3. E. S. Rittner, "On the Mechanism of Operation of the Type B Impregnated Cathode," JAP 48, 1977, pp. 4344-4346.

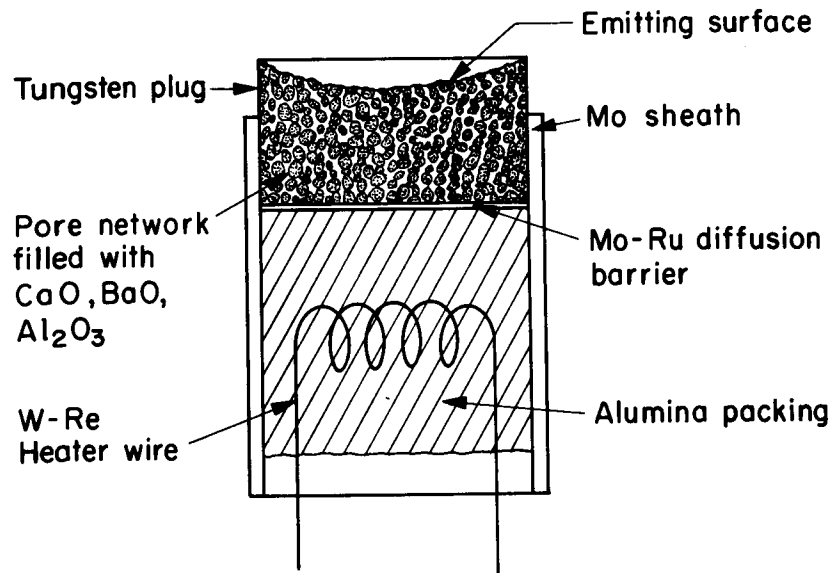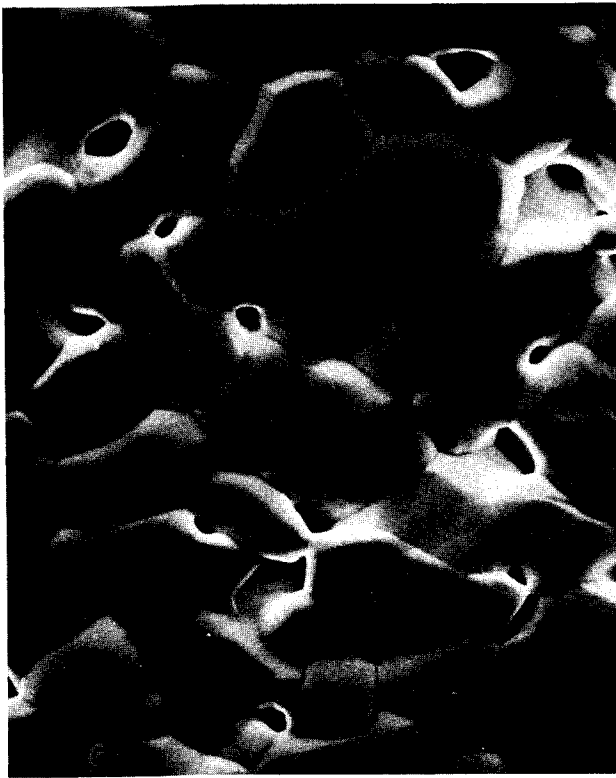4. R. E. Thomas, Naval Research Laboratory, Washington, D.C. Private Communication.

Figure 1. Schematic representation of a dispenser cathode.

a

Figure 2. Surfaces of 2,000 hours (a) and 48,000 hours (b) life tested cathodes.
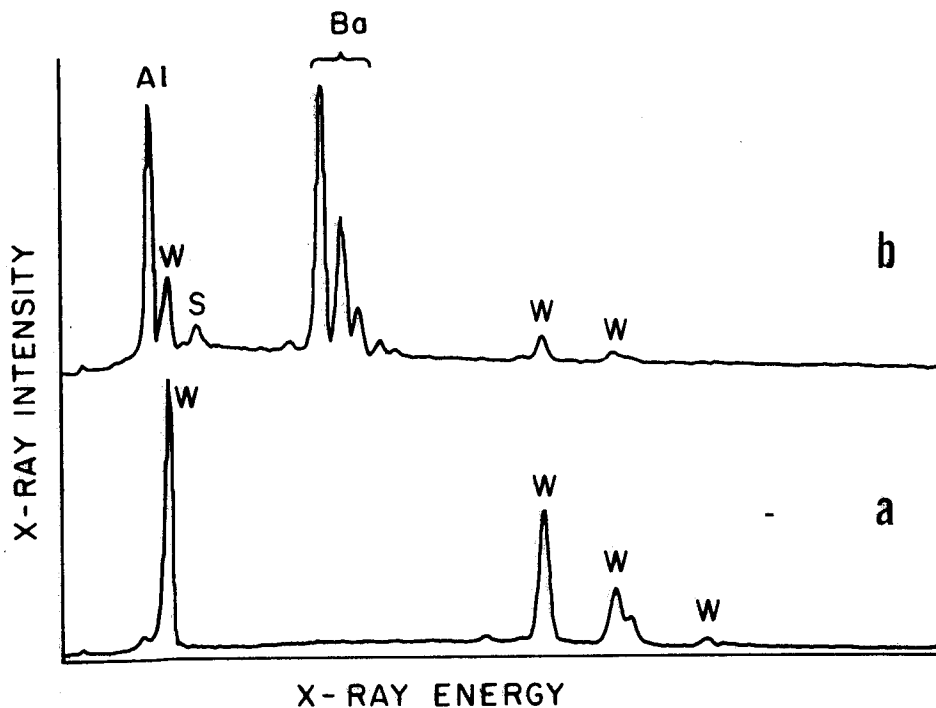
Figure 3. X-ray spectra from a tungsten grain surface (a) and a surface pore impregnate (b).
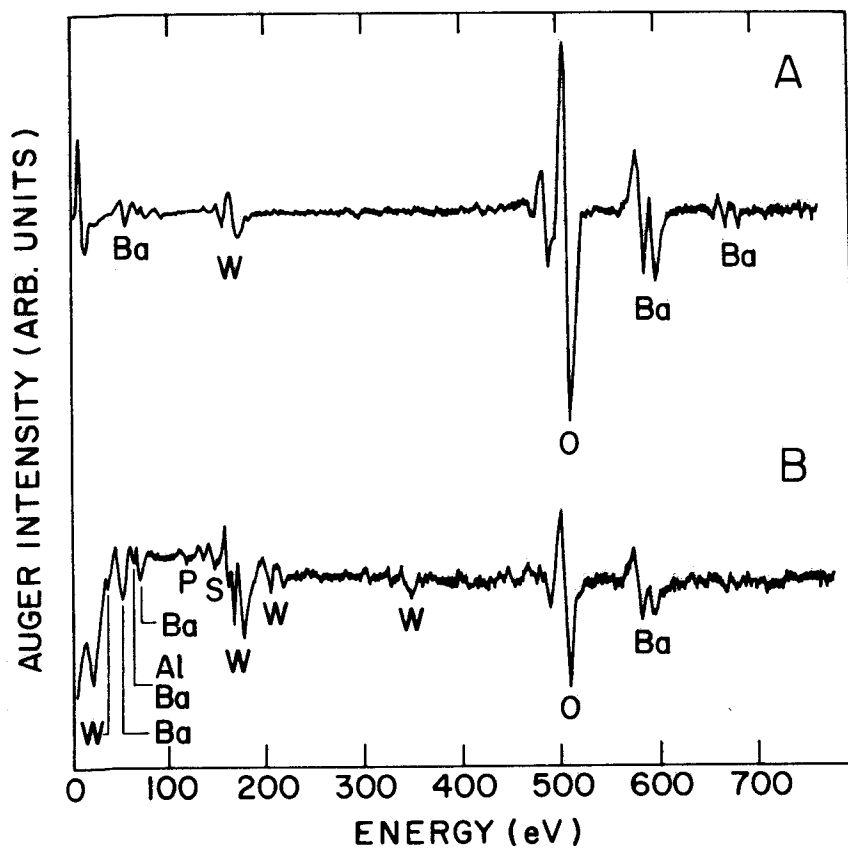

Figure 4. Auger electron spectra of a fresh dispenser cathode prior to thermal activation (a) and after activation at temperature (b).
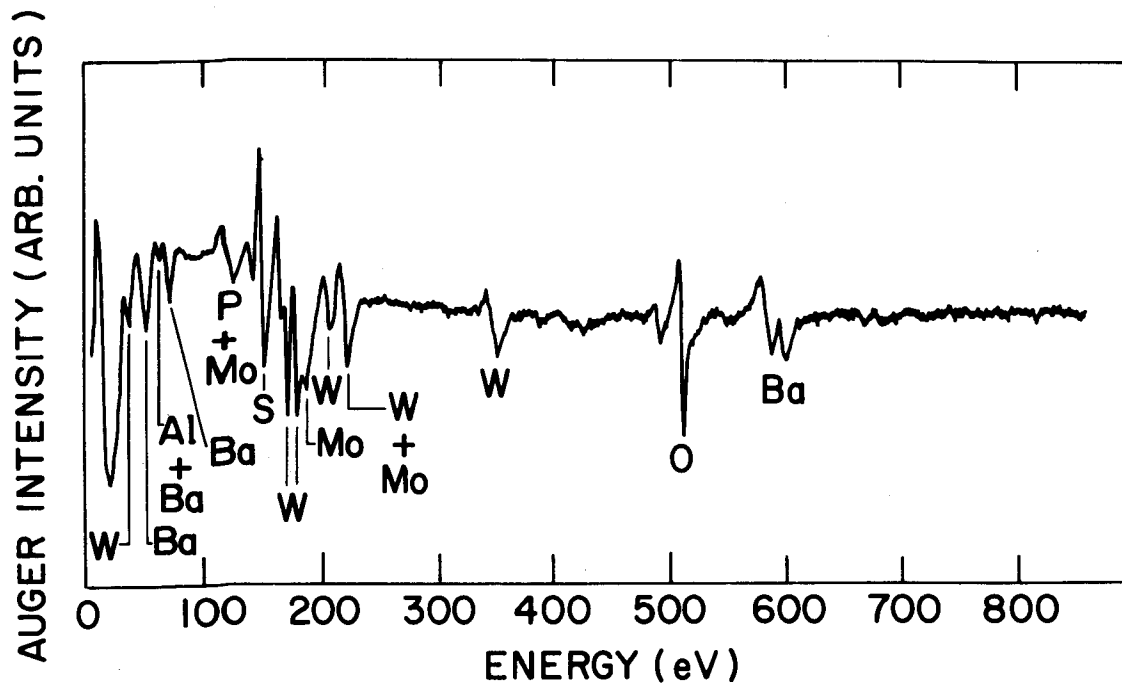
Figure 5. Auger electron spectrum of a cathode at temperature and high incident beam current.

ABSTRACT

Microprobe Analysis Society

N. R. Armstrong, C. Linkous, and C. Sayers
Michigan State University, East Lansing, Michigan
"XPS AND AES STUDIES OF GAS-PHASE AND ELECTROCHEMICAL OXIDATION
OF TITANIUM AND TITANIUM HYDRIDES"

The oxidation of ultrapure titanium and titanium hydride evaporated metal films and bulk metals has been investigated by XPS and AES in combination with ion-beam, depth profiling techniques. Experiments have been conducted in two ways; a) titanium or titanium hydride films with a thin layer of stoichiometric TiO_2, or TiO_2 standard materials, have been sputter etched, and the relative oxygen-to-titanium atomic ratios (N_0/N_{Ti}) and photoelectron and Auger binding energies of all titanium species quantitated as a function of sputtering depth; b) atomically clean titanium surfaces were dosed with oxygen and the N_0/N_{Ti} ratios and photoelectron and Auger binding energies quantitated as a function of oxygen coverage. Previous electrochemical experiments have indicated that the evaporated metal films or bulk metal or metal hydrides have a surface composition which consists mainly of a gradient of TiO_2 and lower oxide stoichiometries, to a depth of 25-30 Å. The above experiments confirm this model of titanium oxidation. Experimental problems in the analysis of the highly complex $Ti(2p_{1/2,3/2})$ XPS spectra will be discussed, including a) assignments of correct binding energy shifts, b) correction for background slope in the Ti(2p) XPS spectra, c) correct assignment of Auger parameters as a function of titanium oxide surface coverage, d) other XPS parameters useful in the quantitation of oxide growth on titanium surfaces.

The Use of Combined Ion- and Electron-Beam
Techniques in Metallurgy Research

by
Paul B. Needham, Jr.

Avondale Metallurgy Research Center
Bureau of Mines, U.S. Department of the Interior
College Park, Maryladd, 20740

EXTENDED ABSTRACT

One of the Bureau of Mines missions is to reduce or minimize the Nation's minerals and metals needs. To support this mission, a surface technology facility was established by the Bureau in 1968 as part of a program to investigate the corrosion and oxidation processes of iron and iron-chromium alloys. A complete characterization of these processes requires analytical techniques to study the preoxidation metal surface, the initially chemisorbed layer of oxygen, the transition to a three-dimensional oxide film, and finally, the growth of thick oxide films or scales. The physical characteristics of importance are: (1) Identification of the elements present, (2) a quantitative measurement of the element coverage or the film thickness, (3) the specific geometrical positions of the elements present with respect to each other as well as to the initial and final surfaces, and (4) the determination of how each of the three previous items is affected by continuing oxidation or corrosion processes. The application of techniques involving combinations of ion- and electron-beam spectroscopies to the study of these physical characteristics will be described in this paper.

The use of proton-excited X-rays (PEX) for surface and thin-film analyses has been described previously ([1-3]). For film analysis or measurement, the range of measurable film thicknesses has been limited by the use of a simple, linear approximation to the more general equation for X-ray excitation ([1]). In this approximation, the energy loss of the incident protons and the target self-absorption of the emitted X-rays are neglected, for example, the counting of oxygen $K\alpha$ X-rays to determine iron-oxide thicknesses less than 400 Å. Recently, we have reported a mathematical method ([4]) for handling the more general equation for X-ray excitation ([1,2]) that allows inclusion of the proton energy loss and target X-ray absorption terms and, therefore, permits accurate determination of film thicknesses up to 2500 Å. The use of this method will be described for oxide films on iron and for evaporated films of iron and carbon on various substrates.

The combined use of PEX and Auger electron spectroscopy (AES) has permitted compensation of the weaknesses of one technique by the strengths of the other. The PEX/AES technique has been used to study segregation, diffusion, and oxidation processes. One example to be described is the high-vacuum annealing of iron at 750° C during which measurements are made of the segregation of sulfur from the metal bulk into the subsurface regions and onto the surface, the diffusion of carbon surface impurities into the bulk of the iron sample, and the desorption of carbon (as oxides) off of the iron surface. The PEX/AES technique has also been used to determine fundamental physical parameters associated with the Auger electron emission process, such as the electron excitation efficiency and the inelastic electron attenuation length (3,5). Examples to be described include determination of the 670-eV iron Auger-electron excitation efficiency and its inelastic attenuation length in iron, carbon, and aluminum.

The use of PEX with low-energy argon-ion sputtering to obtain film composition profiles has been developed and used in various corrosion, oxidation, and ion-implantation studies. The depth profiling technique is described for both evaporated metallic films and the implantation of chromium or nickel into polycrystalline iron. Results will also be described for using this technique to determine the absolute sputtering yields of iron and oxygen from iron oxide, carbon from carbon, and iron from iron.

Finally, the use of proton-excited Auger electrons (PEAS) to make direct determinations of bulk inelastic electron-attenuation lengths has been reported recently (5,6). The results for 670-eV electrons in aluminum and for 100-eV electrons in beryllium are briefly reviewed, and other potential applications for the technique are described.

1. P. B. Needham, Jr., and B. D. Sartwell, Advances in X-ray Analysis, 14, 184, Plenum Press (1971).

2. L. J. Christensen, J. M. Khan, and W. F. Brunner, Rev. Sci. Instr., 38, 20 (1967).

3. P. B. Needham Jr., T. J. Driscoll, and N. G. Rao, Appl. Phys. Lett., 21 502 (1972).

4. B. D. Sartwell and P. B. Needham Jr., Proceedings VIII International Congress on Ion Beam Microanalysis, (In Publication).

5. P. B. Needham Jr., T. J. Driscoll, C. J. Powell, and R. J. Stein, Appl. Phys., Lett., 30, 7 (1977).

6. C. J. Powell, R. J. Stein, P. B. Needham Jr., and T. J. Driscoll, Phys. Rev., A. 16 No. 4, 1370 (1977).

SPATIALLY RESOLVED XPS

C.T. Hovland
Physical Electronics Industries, Inc.
6509 Flying Cloud Drive
Eden Prairie, Minnesota 55344

Preliminary experiments were conducted in 1977 to determine the feasibility of X-ray photoelectron analysis from a small diameter area.[1] Since that time an effort has been made to reduce the photoelectron source area and optimize parameters for maximum photoelectron intensity. Results previously reported[2] showed that 2 micron aluminum foil produced good photoelectron intensity with an acceptable signal to background ratio at 10 keV primary electron beam energy.

Minimization of the photoelectron source area is limited by the dispersion of the X-rays passing through the aluminum foil (Fig. 1). The ratio of the X-ray intensity arriving at the opposite foil surface to the total X-ray intensity created (I/I_G), versus distance from the point of incidence may be plotted (Fig. 2) for 2 micron foil. This curve shows that the X-ray intensity is at half maximum approximately 6 microns from the center.
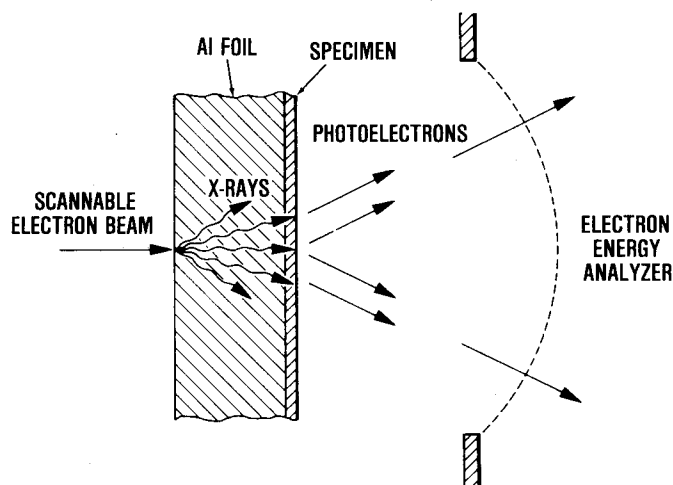

Fig. 1) Dispersion of X-rays within the foil limits photoelectron spatial resolution.
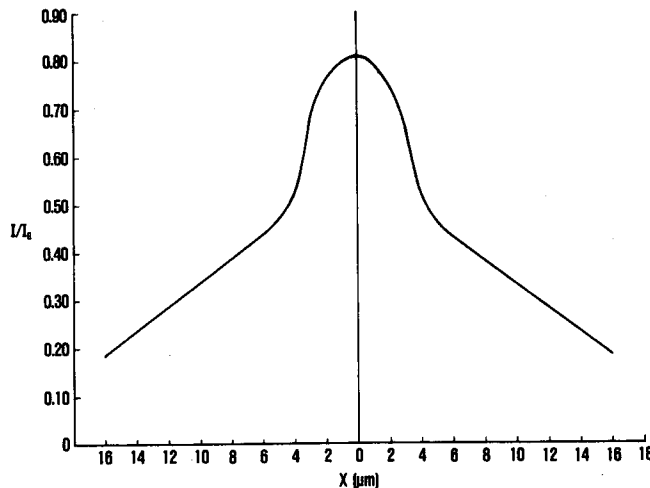
Fig. 2) Relative X-ray intensity (I/I_G) versus distance
       (x) on specimen surface.

An experiment to measure the diameter of the photoelectron
source area with 2 micron aluminum foil was done by sputter
depositing copper on the foil in a 50 micron center to
center grid pattern (Fig. 3). The photoelectron image
generated from this pattern is shown in Fig. 3a and the
photoelectron line deflection is shown in Fig. 3b.
Approximately 12 microns spatial resolution is demonstrated
from the x-distance between the 10 and 90 percent intensity
values. This resolution corresponds to the expected
value from Fig. 2.

Photoelectron spatial resolution in this range allows
study of numerous problems such as surface analysis of
naturally occurring organic particles, many of which have
10 to 100 micron dimensions. For example, surface analysis
of individual 30 micron trachelomonas cells will be
described.

[1] C.T. Hovland, Appl. Phys. Lett. 6, Vol. 30, pp. 274-275 (1977).

[2] C.T. Hovland, 8th Int. Conf. on X-Ray Optics and Micronalysis
and, 12th Annual Proc. Microbeam Analysis Society, Boston,
Mass., 1977, pp. 65 A-D.

3a.
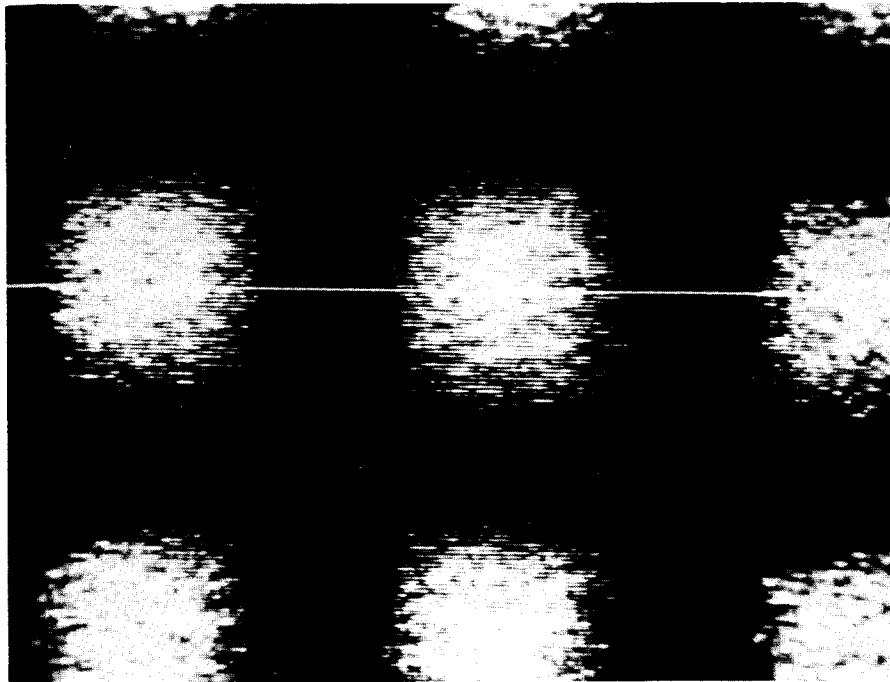
50 μm
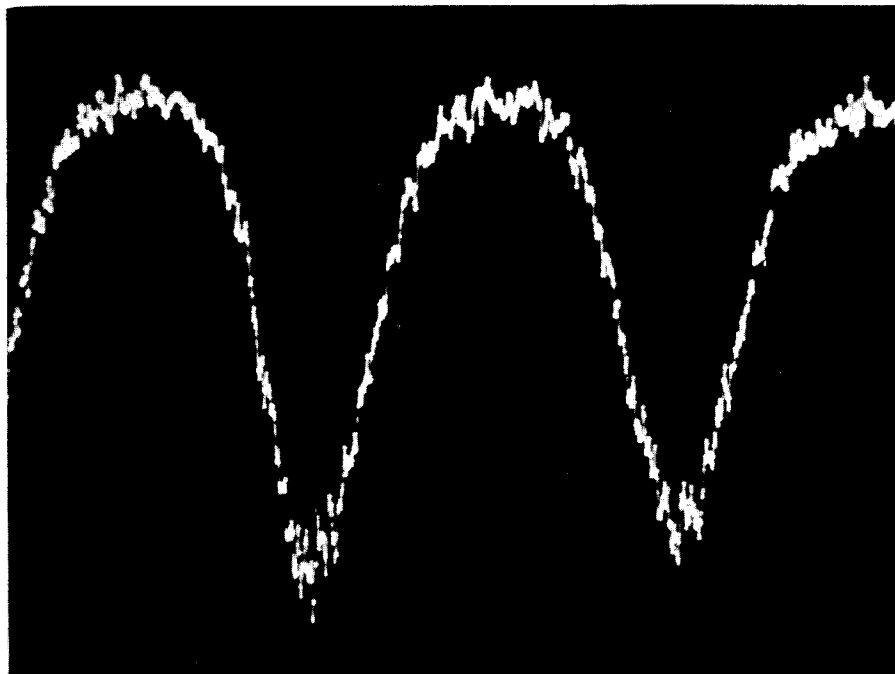
3b.

Fig. 3) Copper deposited on aluminum foil in a grid pattern
yields; a) a photoelectron map and, b) photoelectron
line deflection demonstrating approximately 12 microns
spatial resolution.

X-Ray Photoelectron Spectroscopic

and Photocurrent Studies of Dye-Modified Semiconductor

Electrodes

David D. Hawn and Neal R. Armstrong

Department of Chemistry, Michigan State University

East Lansing, Michigan

Erythrosin (2,4,5,7-tetraiodofluorescein) has been attached to SnO_2 electrode surfaces by either electrochemical adsorption or covalent attachment. Electrodes modified with mercaptopropyltrimethoxysilane, 3-(2-aminoethyl)aminopropyl-trimethoxysilane, or γ-aminopropyltrimethoxysilane showed considerable enhancement of currents passed during erythrosin oxidation, while resulting in the deposition of several monolayers of active chromophore. Erythrosin was covalently attached to silane-modified SnO_2 surfaces by formation of either amide or thiol bonds. Small concentrations of either adsorbed or covalently attached dye could be detected by monitoring the $I(3d_{3/2}-3d_{5/2})$ X-ray photoelectron transitions. Sensitization of semiconductor current/voltage response to visible wavelength light was observed for both adsorbed and covalently modified dye electrodes. Enhanced stability and efficiency was observed for covalently attached versus adsorbed dye-modified electrodes.

A KALEIDOSCOPIC VIEW OF RECENT ADVANCES IN ESCA-ISS-SIMS

by

Gheorghe D. Mateescu

Department of Chemistry
Case Western Reserve University
Cleveland, Ohio 44106

This lecture will begin with a brief description of the principles and
instrumentation of ESCA-ISS-SIMS which will serve as a basis for the com-
parison of the physical and chemical information obtained by these methods.
An instrumental design combining the three techniques will be presented.
Recent applications in organic, organometalic and inorganic chemistry
will be discussed in a kaleidoscopic sequence.

Surface Characterization of Metals, Polymers, and Composites by Combined Techniques: ISS, SIMS, SEM, and EDX

G. Sparrow, 3M Co., St. Paul, MN 55101

The complex nature of problems facing Analytical Chemists today warrants full utilization of all resources available. The Analytical Chemist is challenged with selecting the most suitable instrumental technique available for application to each particular problem. A concerted effort of several different analytical instruments becomes especially necessary for full characterization of surfaces which critically affect device performance.

Proper utilization of combined spectroscopies to exploit the strengths of each can result in excessive savings in time and cost.

Physical characterization of a specimen surface is certainly well accomplished using a Scanning Electron Microscopy. Chemically many specimen surfaces can be perceived as systems in which the usefulness of chemical data decreases exponentially with surface depth. Utilization of UHDR (UltraHigh Depth Resolution) achieved by ISS (Ion Scattering Spectroscopy) provides detailed information about the first 0 to 100Å of a specimen surface. This is readily accomplished by appropriate control of the ion beam sputtering conditions coupled with the high detection sensitivity and monolayer surface sensitivity of ISS. Characterization of the outer monolayer can be accomplished using STATIC ISS.

Trace detection of low Z elements is best accomplished using SIMS for surface detection complemented by EDX for bulk detection. In addition the chemical bonding information obtained from SIMS fingerprint fragmentation patterns can help chemical structural description of surface components. Such extensive specimen analysis is especially applicable to research and development of adhesive bonding systems, passivation or chemical treatments, lubrication, or corrosion of metals or insulators, or to basic studies involving ion physics and chemistry.

Computer Simulations of Ion-Solid Interactions;
H$^+$ and He$^+$ on Au

H. F. Helbig, F. L. Moore and M. Linder
Department of Physics
Clarkson College of Technology
Potsdam, New York   13676

and

B. Popp
Department of Physics
Cornell University
Ithaca, New York   14853

Abstract

When light ions with energies E_o greater than about 1000 eV encounter a solid surface, they find it a minor obstacle to their forward progress (unless they approach it at near-grazing angles). The large majority of them penetrate with only small deflections deeply into the solid until their energy is reduced, primarily through interactions with electrons of the solid, to thermal levels, and they become trapped or diffuse among the atoms of the solid. A small fraction of the incident ions, however, will undergo one or more collisions in such a way that they escape the surface with varying amounts of their original energy. Most of these survivors will have been neutralized during their encounter with the solid; a few will retain their charge.

If the surface is clean and composed of a single atomic species of mass m_1, and if the impinging ions are of a noble gas, e.g. helium, with mass m_o, the tiny fraction which backscatter as ions are found, almost exclusively to have the energy

$$E = \frac{E_o}{(1 + \mu)^2} [\cos\theta + (\mu^2 - \sin^2\theta)^{\frac{1}{2}}]^2$$

where $\mu = m_1/m_O > 1$ and θ is the angle between the initial direction of the ion

beam and the direction to the detector. In other words, the energy spectrum

of such scattered ions consists of a single peak at the energy to be expected

for single binary elastic collisions (SBEC) between the incident ions and

surface atoms. If the surface contains several atomic species then the scattered

ion energy spectrum is found to contain peaks at the several corresponding

SBEC energies. Smith [1] was first to point out this remarkable fact and to

demonstrate that it amounts to an ion scattering spectrometry (ISS) which is

a reliable method for identifying the atomic species composing the outer

monolayer of solid surfaces.

As indicated above, the fact that single binary elastic collisions

account for virtually all of the scattered noble gas ions is rather surprising.

Without the benefit of hindsight, one might suppose the spectrum of back-

scattered ions to consist of a broad distribution peaking below the energy for

SBEC as is the case, for example, when protons are used instead of noble gas

ions. There would seem to be, after all, many more ways for multiple rather

than single collisions to occur. A resolution of this problem is important for

at least two extensions of ISS beyond a surface atom identification method.

First, it would be desireable to infer quantitative information regarding

fractional coverage of the surface species from the relative intensities of

their ISS peaks. Second, since the ion beam can remove successive layers

of the surface in a controlled fashion, ISS can provide a compostion-versus-

depth profile of the sample. Satisfactory interpretations of peak intensities

and of depth profile data require a more complete understanding of the interaction

of ions with solids than is currently available.

The inquiry into ion solid interactions at the energies under

consideration breaks conveniently into two parts; the classical motion of the

ions through the solid and the quantum mechanics of the electrons which control

the charge state of the scattered particles. It is toward the first of these processes that this report is directed. While progress on both fronts has been made, it has become clear that meaningful treatments of the neutralization processes will require involved calculations which must be based on a knowledge about what sorts of ion motion in fact produce the flux of back-scattered particles. The ion motion, on the other hand, does not depend strongly on the electronic processes which control the final charge states of the probe ions.

The utility of computer simulations of ion-solid interactions is well documented [2]. The present simulation, ARGUS, was constructed to obtain an estimate of the energy distribution of gold atoms ejected (sputtered) by neon ion bombardment. Its current application is to the scattering of helium ions from gold.

The solid is modeled by a perfect face centered cubic array of gold atoms with the (111) face exposed. Ions are launched toward random locations on this surface along lines of fixed polar but random azimuthal angles (the latter to simulate a polycrystaline solid) and their courses followed through the crystal until they penetrate below some predetermined depth, lose sufficient energy to become trapped, or emerge from the surface. Of the later, those which would enter a detector in the direction for specular reflection are retraced and their history documented in detail. The ion-gold atom interaction is represented by a screened coulomb potential. In addition to the energy losses due to gold atom recoil, the ions are assumed to lose energy to the electons of the solid in amount proportional to their path length between collisions and proportional to their speed. No account is taken of those few gold atoms which receive enough energy to be displaced from their lattice sites. It is chiefly in this latter approximation that ARGUS differs from

other simulations currently in use.

The impetus for this work is the measurement which Buck [3] has made of the yields of He and He^+ at the angle for specular reflection when He^+ is incident upon polycrystalline gold at 45° from the surface normal. The energy spectrum of scattered helium (neutrals plus ions) was measured using a time-of-flight spectrometer. The spectra for 32, 16 and 8 keV incident helium ion energies show peaks which move progressively toward the energy for SBEC as the incident energy decreases. The 16 and 8 keV spectra also show a shoulder at energies somewhat less than half that for SBEC. The simulation reproduces these features reasonably well, and their origin may be inferred from the detailed histories of the particles which emerge in the specular direction. The high energy peak is populated by particles whose histories include single large deflection while the shoulder arises from particles which undergo several large deflections before leaving the crystal.

A detailed comparison of the measured and simulated helium spectra will be presented along with results on the energy and particle reflection coefficients for both He^+ and H^+ scattered from gold.

References

[1] D.P. Smith, Surface Sci. 25, 171 (1971).

[2] See for examples Inelastic Ion-Surface Collisions, edited by N.H. Tolk, J.C. Tully, W. Heiland and C.W. White (Academic Press, Inc., New York, 1977).

[3] T.M. Buck, Y. -S. Chen, G.H. Wheatley and W.F. Van der Weg, Surface Sci. 47, 244 (1975).

NON-DESTRUCTIVE, QUANTITATIVE ANALYSIS OF THIN FILMS

R. G. Musket
Kevex Corporation
Foster City, CA. 94404

ABSTRACT

Alpha-particle-induced X-ray emission has been used to obtain, non-destructively, quantitative analysis of surface layers and thin films. This technique consists of the spectrometry of characteristic X-rays emanating from a specimen irradiated with $\sim$ 5 MeV alpha particles. The ALPHA-X version of the technique employs a radioactive alpha source closely coupled to a windowless Si(Li) detector via a unique source holder and collimator assembly, which permits analysis of a 6 mm diameter spot and minimizes the detection of extraneous background radiation.

The main advantages of this technique over electron-excited X-ray techniques are (a) improved limits of detectability resulting from greatly reduced bremsstrahlung background radiation and (b) direct correlation of the X-ray data with elemental surface densities (e.g., film thicknesses). Compared to X-ray fluorescence techniques, ALPHA-X has considerably higher cross-sections for low atomic number elements. Quantitative analysis for all elements with atomic numbers $Z \geq 6$ on conducting and non-conducting substrates has been demonstrated using the ALPHA-X approach. Several applications to oxide layers, aerosol samples, and thin films serve as examples of the usefulness of this technique for the analysis of thin layers with thicknesses between about 20 Å and several micrometers.

Although ALPHA-X does not have the very high surface sensitivity and micro-imaging capabilities of many of the surface and thin film analysis techniques, it has been shown to be a means for quantitative, non-destructive analyses. In fact ALPHA-X can be used to complement the sputter profile data obtained with other techniques by determining the integral amounts of elements under each segment of the sputter profile.

THERMAL BATTERY REACTION PRODUCTS*

Paul F. Hlava
Sandia Laboratories
Albuquerque, New Mexico 87115

Thermal batteries, more properly termed thermally activated batteries, are special purpose batteries which fulfill unique applications in military and aerospace systems. They serve as reserve power sources in which the electrolyte is solid and nonconducting at normal temperature (-54° to 75°C). At high temperatures (> 350°C), the electrolyte melts and becomes highly conductive thus activating the battery. The advantages of thermal batteries include compactness, mechanical ruggedness, operability in any position, and lack of maintenance during storage times of as long as 20 years.[1]

Although these batteries have been used for over two decades, the reactions by which they operate have not been fully characterized. Knowledge of the pertinent reaction(s) is required before further improvements in battery design can proceed. Reaction characterization has been hampered by a lack of information about the compositions of the reaction products formed upon discharge. The reactive and hygroscopic nature of the battery reactants and products, and their small size, preclude their characterization by most conventional techniques. The electron microprobe is essentially an ideal tool for characterizing thermal battery materials because it can provide quantitative chemical information on the small crystals present while the materials are maintained in a vacuum.[2]

A single thermal battery cell contains:

1. A Ca-metal anode $\sim$ 250 μm thick which has been vapor deposited onto an $\sim$ 125 μm thick Fe or stainless steel back, and

2. A DEB pellet $\sim$ 1800 μm thick containing $CaCrO_4$ Depolarizer, LiCl-KCl eutectic Electrolyte, and SiO_2 Binder.

Flat, highly polished specimen surfaces are essential for good quantitative microprobe analyses or truly representative elemental distribution photomicrographs (EDPMs). Unfortunately, thermal battery materials are not amenable to polishing. Several of the materials are highly reactive and/or hygroscopic, thus requiring all handling to be done in a clean and very dry environment (usually ∿ 100 ppm H_2O, 300 ppm maximum).[†] The specimens were potted in epoxy, machined to expose a suitable cross section, and ground, dry, with increasingly finer grades of SiC coated paper but no true polishing was performed. This processing resulted in a flat, rather scratched surface contaminated by a few obvious particles of SiC . Considering the nature of the material, the surface finish is remarkably good but it does account for some analytical uncertainty.

The initial steps in characterizing the thermal battery materials were determining all the important elements in the system, including contaminants, and obtaining a set of identical area EDPMs for each of the samples. Most of the known elements in the system showed up quite well on an energy dispersive analysis (Si, Cl, K, Ca, Cr, and Fe). Oxygen could be detected only by wavelength dispersive analysis, and lithium could not be detected. All identical area EDPMs were taken at a magnification of 500X (20 μm/cm) and, for most of the elements (Si, Cl, K, Ca, Cr, and Fe), the exposure conditions were kept constant to allow rough correlation between intensity and elemental concentrations. EDPMs for oxygen require long exposure so these were made for only a few specimens. The EDPMs allowed excellent and rapid correlation between zones visible as color bands on the specimens and zones distinguished by chemical differences. They also were used to great advantage in guiding the direction of quantitative analyses.

Several problems were encountered during quantitative correction procedures. The poor surface finish of the specimens has already been described. Since the correction procedures assume that the sample is homogeneous, only selected point (or very small area) quantitative analyses were possible; however, a majority of the DEB pellet consists of volatile chlorides. The two other main problems, the changing valence of Cr and the non-analyzability of Li are interactive. Since Cr changes valence during discharge of the cell, there is uncertainty about the correct stoichiometry to be used. It was decided to treat all Cr as having the

---

†Sample preparation was performed by personnel from the Thermal Battery Group, Sandia Laboratories, Albuquerque, NM.

same valence as the starting material (Cr^{+6}) and interpret analyses of over 100% as due to Cr reduction. Indeed this gave a reasonable understanding of such reduction. To incorporate Li into the corrections, the difference from 100% in low analyses was calculated as being due to the presence of Li_2O. Weight percent oxygen equivalent to the Cl present in each analysis was subtracted from the corrected total and any deficiency calculated as Li in the form of Li_2O. The good quality of the quantitative data in the light of these problems was due, to a large extent, to the problems not all being concentrated in any one material.

An undischarged cell was examined in cross section to determine the extent of the inhomogeneity of the pellet material, the locations of the various phases, and the presence of any obvious contaminants or low temperature reactions. The DEB is obviously inhomogeneous with large spots of white material in a host that is yellow with small white spots.

EDPMs of this cell show quite clearly (and quantitative spot checks confirm) that the materials are those that were expected. The yellow host material is $CaCrO_4$ and the white spots consist of KCl/LiCl. Not only are these materials not thoroughly mixed on a gross scale, but the chlorides themselves show a minor amount of inhomogeneity. The bulk of the chloride appears K-rich with small scale inhomogeneity showing up as 5-10 μm K-rich or Cl-rich spots within the grossly uniform K and Cl areas. Scattered throughout these regions are rare areas a few ten's of micrometers across that exhibit Li enrichment. (Because Li x-rays cannot be detected it was assumed that the Li is present in those areas that show very high Cl concentrati i, a small amount of K, and no other elements. Subsequent Auger analyses confirmed the presence of Li in these areas.) The SiO_2 binder is surprisingly nonuniform in distribution, being concentrated almost exclusively in KCl. There is also a thin oxide layer on the Ca anode.

Discharged cells develop a complicated sequence of layers within the DEB pellet. These layers exhibit various colors and textures and are composed of several different phases. These layers have been numbered 1 through 6, in order, from the Ca-anode through the prior DEB pellet. The layers are described below for a cell discharged approximately 15 minutes (3/4 of life).

1. A uniform, gray crystalline layer $\sim$ 100 μm thick consisting of $KCaCl_3$. Small spots of $CaCl_2$ are present directly adjacent to the anode.

2. A fine-grained, bluish layer $\sim$ 40 μm thick consisting of crystals of Ca_2CrO_4Cl in a matrix of $KCaCl_3$, KCl, and LiCl.

3. A coarse-grained, greenish layer $\sim$ 60 μm thick consisting of crystals of Ca_2CrO_4Cl in a matrix of $KCaCl_3$, KCl, and LiCl.

4. A layer of mottled white on yellow $\sim$ 100 μm thick which is unused DEB material ($CaCrO_4$, LiCl-KCl, SiO_2).

5. A very thick layer ($\sim$ 500 μm) consisting of long and narrow ($\sim$ 500 μm x 75 μm max), black crystals ($\sim$ $Ca_6Cr_4O_xSiCl_2$) in a white to gray matrix of KCl, LiCl, and minor $KCaCl_3$.

6. A thick layer ($\sim$ 320 μm) of moderately large, equant, black crystals ($\sim$ 100 μm across, $\sim$ $Ca_6Cr_4O_xSiCl_2$) in a gray to greenish gray matrix of KCl, LiCl, minor $KCaCl_3$, and a few small crystals of a Ca-Si-O+Cr material.

The examination of a series of cells which were discharged for varying amounts of time shows that the sequence outlined above is representative. As a cell is discharged, Layer 5 grows rapidly at the expense of Layer 4; however, the other layers show no drastic size changes.

This study provided a challenging set of problems. It illustrates that it is possible to work around many problems and provide the research and development personnel with abundant, meaningful data on a very complex system.

References:

1. B. H. Van Domelen, R. D. Wehrle, "A Review of Thermal Battery Technology," 9th Intersociety Energy Conversion Engineering Conference, Aug. 1974.

2. Paul F. Hlava, Thomas J. Headley, "Thermal Battery Reaction Products: Characterization by Electron Microprobe, X-ray Analyzer and Transmission Electron Microscope," SAND77-1317, Oct. 1977.

Abstract

Analysis of Primary Deposition Sites for Silica ($SiO_2 \cdot nH_2O$) in Panicoid and Festucoid Grasses and in Scouring Rushes (<u>Equisetum</u>) By Scanning Electron Microscopy and Energy-Dispersive Microanalysis

by

Peter B. Kaufman, P. Dayanandan, Marcia Goldoftas, Elizabeth Lau, Jyotsna Srinivasan, John M. Clark, Peggie Hollingsworth, John Mardinly, and Wilbur C. Bigelow, University of Michigan, Ann Arbor, MI

Our primary objective in this study has been to determine the primary deposition sites for silica in leaves, stems, and inflorescence parts of rice (<u>Oryza</u> <u>sativa</u>), sugarcane (<u>Saccharum</u> <u>officinarum</u>), oats (<u>Avena</u> <u>sativa</u>), bamboo (<u>Bambusa</u> sp.), and reed grass (<u>Phragmites</u> <u>australis</u>) and in stems of annual and perennial scouring rushes (<u>Equisetum</u> spp.). Silica is important in these plants in (1) preventing attack by predators, (2) preventing attack by pathogenic fungi, (3) strengthening and helping to support the leaves and stems (as an alternative to lignin deposition), (4) increasing grain yield in the cereals, and (5) increasing photosynthetic efficiency. It is also <u>hypothesized</u> to provide a means of conserving water in scouring rushes, sedges, and grasses during periods of drought, and in grasses, of allowing more light to be transmitted through the epidermal system, via silica cells, to photosynthetic mesophyll tissue below the epidermis in stems, leaves, and inflorescence parts. In the absence of silica, it has been shown by Chen and Lewis (1969) that shoots of <u>Equisetum</u> <u>arvense</u> (an annual scouring rush) collapse. Furthermore, in Japan, applications of silica as slag can cause substantial increases in grain yield.

Our specimens were prepared for scanning electron microscopy and analysis for distribution of silicon in tissue samples by energy-dispersive microanalysis as follows:

(1) Fresh or dry plant material (leaves, stems, inflorescence parts) were mounted on aluminum stubs with "Tube-kote" and coated with

gold for scanning electron microscopy (SEM) or carbon for energy-dispersive microanalysis.

(2) Plant material high in water content was first critical-point dried before either type of analysis in (1) above.

(3) For SEM analysis, we operated at 15 to 20 KeV, using a Japan Electron Optics, model JSM-U3. For energy-dispersive microanalysis, we used the SEM coupled to an X-ray detector and amplifier system (KEVEX) and a multichannel analyzer (Northern Scientific, Model 710). Selected areas were first photographed in the secondary emission mode followed by X-ray mapping for silicon. This order is necessary because beam or vacuum damage to the specimen is increased with longer exposure times that are used for X-ray analysis. For X-ray analysis, we routinely used 200 second counts.

Our results show that silica is excluded from 2 sites in grasses: the geo-sensitive leaf and internode pulvini and basal intercalary meristem tissue in internodes of grasses. The epidermal system of leaves, stems, and inflorescences in grasses is the primary deposition site for $SiO_2 \cdot nH_2O$. Here, it can become localized in stomatal cells, hairs, silica cells, and in the tangential and radial walls of long epidermal cells (Kaufman et al., 1969). The latter site (long epidermal cell walls) is especially significant inasmuch as these highly silicified cells provide significant support for the internodes of the grass culms (shoots). Silicified hairs would repel predators, and silica cells may function as "windows" in the epidermal system, allowing more light to reach photosynthetic mesophyll tissue below the epidermis than if they were absent. Absence of silica in geo-sensitive pulvini (as well as lignin) allow these basal portions of leaves and/or internodes to function in negative geotropic response when grass shoots fall over due to action of wind or rain (lodging). The greatest amount of silica in grasses was detected in the bottom (abaxial) sides of bamboo leaves and in the protective bracts (glumes, lemmas, paleas) surrounding the grains of rice and oats. SEM photos and X-ray maps will be shown together with point counts for Si to substantiate these results.

In _Equisetum_ spp., the scouring rushes,we showed (Kaufman _et al._, 1973) that silica deposition in the epidermis of developing shoots of the perennial scouring rush (_Equisetum hyemale_ var. _affine_) starts in the stomatal apparatuses beginning with internode 3 below the shoot apex, followed by epidermal papillae (internode 8) and finally in radial walls of long epidermal cells (internode 10). The last-mentioned process starts after internodal elongation has almost ceased. An X-ray image of silica distribution in a mature stomata shows that entire outer walls of the uppermost cells (subsidiary cells) of the stomatal apparatus, and the ridge-like thickenings on the bottom (inner) sides of these cells are highly silicified (Dayanandan, 1977); silicification at these two sites effectively prevents mature stomata in this plant from opening and closing in response to light and dark. In the annual scouring rush (_Equisetum arvense_), the silica is deposited only in localized papillae on the surfaces of stomata and surrounding epidermal cells. This difference probably explains why shoots of _E. arvense_ are annual or seasonal, whereas those of _E. hyemale_ var. _affine_ are perennial, persisting in the field for several years. Supporting SEM photographs and X-ray maps will be presented to illustrate these differences.

References Cited

(1) Chen, C.-H. and J. Lewis. 1969. Silicon as a nutrient element for _Equisetum arvense_. Canad. J. Botany _47_, 125-131.

(2) Dayanandan, P. 1977. Stomata in _Equisetum_: A structural and functional study. Ph.D. Dissertation, University of Michigan, Ann Arbor, Michigan.

(3) Kaufman, P. B., W. C. ʾigelow, L. B. Petering, and F. B. Drogosz. 1969. Silica in developing epidermal cells of _Avena_ internodes: electron microprobe analysis. Science _166_, 1015-1017.

(4) Kaufman, P. B., J. D. LaCroix, P. Dayanandan, L. F. Allard, J.J. Rosen, and W. C.Bigelow. 1973. Silicification of developing internodes in the perennial scouring rush (_Equisetum hyemale_ var. _affine_). Develop. Biol. _31_,, 124-135.

MICROPROBE AND X-RAY ANALYSIS OF GAS TURBINE MATERIALS AFTER HOT CORROSION

H. van Amerongen[1] D.J.Gras[2] A.P. von Rosenstiel[2] J.D. Brown[3] J.W. Visser[4]

1) Central Technical Laboratory TNO, Apeldoorn, The Netherlands
2) Metal Research Institute TNO, Apeldoorn, The Netherlands
3) The University of Western Ontario London/Canada
4) Techn. Physical Services TNO-T.H. Delft, The Netherlands

INTRODUCTION

To protect industrial gas turbines against high temperature corrosion a silicide based conversion type coating with good mechanical properties was developed. Such a development requires an insight into the corrosion mechanisms and the role of the protective layer.

Uncoated and coated specimens of IN738LC alloy were subjected to the corrosive attack of an eutectic 40-53-7 Na-Ca-Mg sulfate melt at 850°C with additional O_2 bubbling containing 5×10^{-2} vol.% $SO_2 + SO_3$. The phenomena occuring during the initial stages (incubation period) and in later stages up to 4000 hours were studied. Test pieces along with a melt sample were removed at set intervals, to investigate the formation of sulfides in the metal, the nature of the oxides formed, the diffusion of elements in the alloy and dissolution into the melt.

X-ray diffraction analysis of the surface of each specimen was made after which the test pieces were sectioned, polished and examined metallographically using an interference technique (Pepperhoff). A number of specimens were then selected for electron microprobe analysis of the phases formed and measurement of diffusion patterns for several elements. After isolation by dissolution of the substrate in a 10 wt.% CrO_3 solution the phases present in the coating were identified by X-ray powder diffraction analysis. Melt samples were analysed for dissolved alloy components by emission spectrography.

RESULTS

a) Uncoated IN738LC

X-ray diffraction patterns showed that on the nickel matrix (γ') spinel phases, $Ni(Cr,AL)_2O_4$ appear after a short time (48 hrs), followed by $NiCrO_3$ (after 150 hrs). After 1000 hrs a phase resembling ilmenite ($NiTiO_3$) could be detected. Metallography and microprobe analysis of cross sections revealed that after immersion for only 24 hrs, internal sulfidation, followed by oxidation had occured. These phenomena gradually increased with time, with preferential corrosion along the grain boundaries. A typical detail of an uncoated IN738LC sample after 3800 hrs is shown in fig. 1. The areas of lightest gray are Cr depleted , the darks specks are sulfides.

Quantitative microprobe analysis showed that the composition of the small sulfide particles is $(Ni,Cr,Ti)_3S_4$ with a Ti content varying from 6 to 20 at.% and the highest Ti content at the tip of the corroded grain boundary.

The large sulfide particles and some of the smaller ones near the surface were determined to be Cr_5S_8. In the oxide layer Ni_3S_2 was found.

b) Ti/Si coated IN738LC

X-ray diffraction showed a spinel phase (A=8.26) formed only after long exposure and some $NiCrO_3$ and $NiCrO_4$.

Studies of the cross sections of the samples showed that only oxidation at the surface occurred, without sulfidation. The phase composition of the coating changes because of preferential oxidation of Ti forming a rather thick unprotective TiO_2 layer at the outside. After 24 hrs the coating consists of a homogeneous ternary Ni, Si, Ti phase or mixture of phases with an overall chemical composition of about $Ni_{16}Ti_6Si_{12}$. The thickness of the coating is 60 μm. After 500 hrs the outside of the coating is totally depleted of Ti with an overall chemical composition of about Ni_5Si_3.

The ternary phase in the rest of the coating is about the same as after 24 hrs. The tickness of the coating has become 150 μm. From microprobe analysis of the 3000 hrs specimen, see fig. 2, not only has Ti depletion at the outside of the coating taken place but also locally in the rest of the coating.
The silicon content of the ternary phases is also lowered. Diffusion of Al and Cr from the substrate into the coating has occured, the Al going into the binary Ni, Si phases and the Cr going into the ternary Ni, Ti, Si phases forming $Ni_5(Si,Al)_3$ and $Ni_{16}(Ti,Cr)_6Si_7$, respectively. The thickness of the coating is still 150 μm.

Analysis of the oxide layer showed a rather thick non protective TiO_2 at the outside. Under this layer and directly on the metal surface a thin protective SiO_2 layer is formed which also contains Cr_2O_3 and Al_2O_3.

CONCLUSIONS

Accelerated corrosion of IN738LC in a sulfate melt appeared to be caused by internal sulfidation followed by reaction of the protective oxide layer with oxide ions in the melt. The product of the reaction is non protective with respect to the alloy substrate. Ti/Si coated IN738LC forms an outer TiO_2 layer which reacts with and reduces the oxide ion content of Na_2SO_4. Furthermore, the stable silicide present in the coating did not show any signs of sulfidation. The same corrosion behaviour was found on test blades which were rig tested (at Sulzer).

The coating consists of a mixture of ternary Ni, Ti, Si phases ($Ni_{49}Ti_{14}Si_{37}Ni_{16}$, Ti_6Si_7 and NiTiSi) which change after prolonged heating in an oxidizing atmosphere (3000 hrs at 850°C) to a mixture of binary nickel silicide phases in which Si is partly displaced by Al (composition $Ni_5(Si,Al)_3$), and the G phase in which Ti is partly displaced by Cr ($Ni_{16}(Ti,Cr)_6Si_7$).
This binary nickel-silicon and ternary nickel-silicon-titanium phase coating has an excellent thermal stability. Its X-ray diffraction pattern did not change after heating to temperatures of up to 1000°C. The distribution of Si remained unaltered after haeting to 850°C for peroids from 500 to 3000 hrs.

ACKNOWLEDGEMENTS

REFERENCES

1. H. van Amerongen, "Study of properties of silicide based coatings for IN738LC"
   Final Report NL-2 Programme,
   European concerted action Materials for Gas Turbines (COST-50) 1976

2. H. van Amerongen, "Study of the hot corrosion of uncoated and Ti/Si coated
   IN-738LC in a sulfate melt".
   Final Report NL-3 Programme
   European concerted action Materials for Gas Turbines (COST-50) 1977

3. J. Stringer, "Hot Corrosion in Gas Turbines", MCIC Report 7208 June 1972

4. J.A. Goebel and F.S. Pettit, Met. Trans. 1970 1, 1943

5. P.C. Felix, "Comparion of Different Corrosion Tests for the Evaluation of
   Gas Turbine Materials". Turboforum 1974 4, 205

6. V.Ya. Markiv, E.I. Gladyshevskii, P.I. Kripyakevich and T.I. Fedoruk,
   "The system Titanium-Nickel-Silicon"
   Izvestiya Akademii Nauk. SSSR, Neorganicheskie Materialy 1966, 2, 7, 1317.
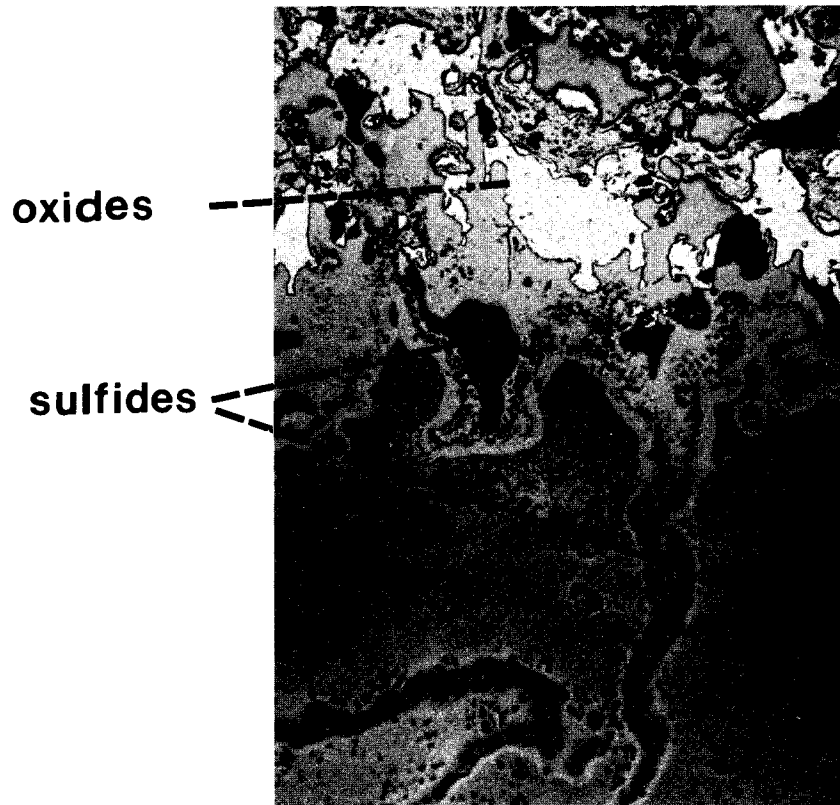
oxides

sulfides

Fig.1   **175X**
Uncoated IN 738 LC
after 3800 hrs. in sulfate melt

oxide
layer

Ni/Si phase

Ni/Ti/Si phase
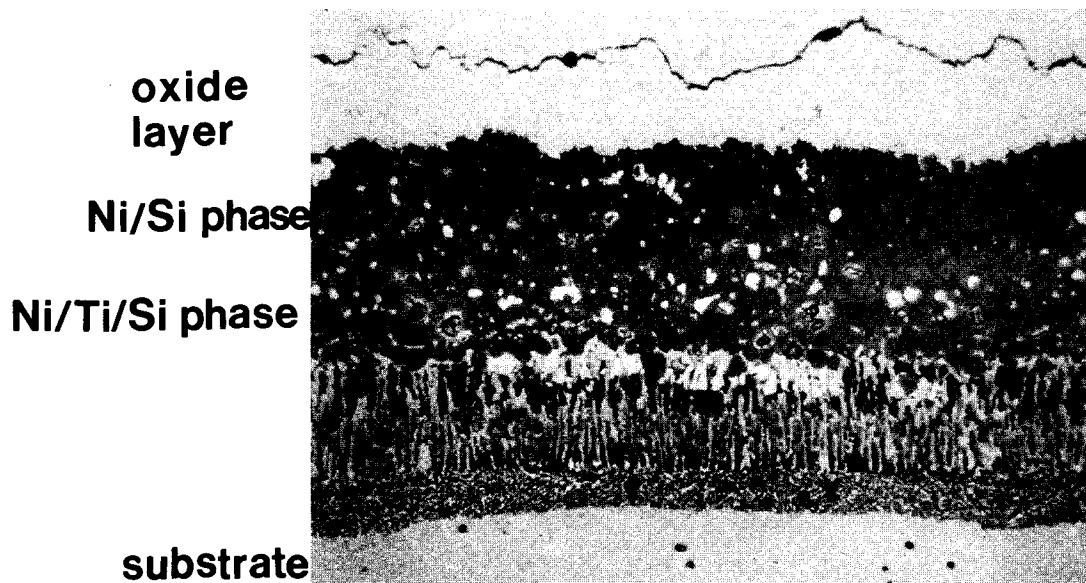
substrate

Fig.2   **500X**
Ti/Si coated IN 738 LC
after 3000 hrs. in sulfate melt

Microprobe Automation Using A
General Purpose Microcomputer System

W. T. Hatfield and M. D. McConnell

General Electric Company
Corporate Research and Development
Schenectady, New York

Over the past two years, a number of low cost microcomputer systems have become available. These systems can generally be programmed in a high level language such as BASIC and can support a variety of peripherals. At the same time, a number of large scale integrated (LSI) circuits have been developed which can be used to provide various functions necessary for instrument automation such as stepper motor controllers, timer/scalars and parallel and serial input/output. The availability of such hardware suggests that the microcomputer can replace existing electronics in addition to providing instrument automation and data processing capabilities.

This paper describes the practical aspects of using a Laboratory Automation Module (LAM) to replace the semi-automated data logging electronics on a Cameca electron microprobe. The LAM consists of an Intel single board computer (SBC 80/20), 16K bytes of read only memory (ROM) used for the system monitor and BASIC interpreter, 16K of random access memory (RAM) for program and data storage, a cassette tape unit and two parallel and serial ports. Programmable interval timers (Inter 8253) are used to provide timer/scalar and stepper motor controller functions. Quantitative analysis for up to four elements is carried out using National Bureau of Standards FRAME[2] written in BASIC. Routines were added to read the timer/scalars, compute K ratios, drive stepping motors and print concentrations in an acceptable format. In addition, it was necessary to modify the program to some extent to reduce processing time.

The basic philosophy used in designing the system as well as hardware and software considerations used and the level of expertise required to use a microcomputer to automate the microprobe, will be discussed.

REFERENCES

1. "Future Trends in Microprobe Automation," W.T. Hatfield, Proc. 8th International Conference on X-ray Optics and Microanalysis,, Boston, Mass. (1977).

2. FRAME, NBS Technical Note 796, H. Yakowitz, R.L. Myklebust and K.F.J. Heinrich, U.S. Department of Commerce, Oct. (1973).

ELECTRON PROBE ANALYSIS USING
COMPUTER AUTOMATED ELECTRON BEAM POSITIONING

W. J. Hamilton, J. R. Hinthorne & H. K. Gille

Applied Research Laboratories
9545 Wentworth Street
Sunland, California 91040

Computer automation has provided numerous benefits to the electron
microprobe analyst. The accuracy, reproducibility, and speed of
computer positioning of wavelength scanning spectrometers; the
convenience of mass storage and retrieval of often used data
such as x-ray wavelength values, constants, correction factors;
and the speed and convenience of "on-line" data reduction are but
a few of the advantages of computer control.[1] Computer control
of the electron microprobe sample stage has also provided
additional advantages. Automatic positioning of the stage
to reference standards and to analysis points preselected by the
operator has increased the efficiency and throughput of samples.

For some specimens it is necessary or desirable to select analysis
points which are more closely spaced or require greater accuracy
of positioning than that provided by the mechanical precision of
stepper motors. Examples of such analytical problems occur in
the study of large scale integrated circuits, in complexly zoned
phases of mineral samples, in analysis of small inclusions in
metallurgical specimens, and in eutectic studies, etc.

In such cases the needed precise positioning of the analysis point
may be accomplished by utilizing the scanning coils to place the
electron beam accurately on the desired location on the specimen.
This operation typically has been performed by imaging the
specimen on a storage oscilloscope or long persistence phosphor
cathode ray tube, manually switching to a static spot mode, moving
the beam to the desired location in the image by manually changing

potentiometers controlling the electron beam position with the scanning coils and proceeding with the analysis. Although this technique is effective, it is very inefficient, particularly where large numbers of analyses are required.

In order to overcome the deficiencies of these tedious procedures, an automation system, utilizing existing hardware and modifications of programs for stage automation, has been assembled to enable rapid and efficient analysis of points using electron beam positioning.

SYSTEM HARDWARE AND OPERATION

The basic hardware components of the automated beam positioning system are a joystick, a frequency counter, the beam position indicator, a data interface to the computer, two digital to analog convertors (DAC's), and a digitally controlled scan generator. These components are interconnected as shown in Figure 1.

In the manual mode of operation the beam position indicator appears as a bright cross on the viewing screen while the area is being scanned at viewing rates. The cross may be positioned anywhere on the screen by manually adjusting the X and Y position controls. These control voltages are sent to the beam position indicating circuitry when relay K_1 is de-energized. If the scan generator is switched into the point mode, the beam will shift to the previously indicated location on the sample.

Under program control the computer can activate relay K_1. This transfers beam position indicator control from the front panel to the computer programmed DACs. The indicator may now be positioned by the joystick. The joystick consists of potentiometers coupled to a linkage such that X or Y motion of the linkage produces a corresponding voltage change. These voltage analogs of X or Y joystick position determine the output frequencies of two voltage to frequency (V to F) converters. By measuring the frequencies of the two V to F converters, two data words can be

generated which correspond to the X-Y coordinates of the beam
position indicator. These data words are looped through the
interface and sent to DACs where they are converted to voltages
which position the indicator.

At any time the operator may push the "store" button on the
joystick. This generates an interrupt which causes the computer
to store the X and Y data words in memory for future analysis.
The sequence is repeated until all the desired analysis points
are selected. During each iteration the operator has the option
of displaying all the selected points, to change one or all of
the points, or to terminate the input of points. After all the
desired analysis points have been located and stored, the system
is ready to begin analysis under computer control.

The program causes the computer to activate relay K_2 which
switches the scan generator into the point mode. The program
steps through the previously stored analysis points and completes
data acquisition and data reduction for each. All points are
analyzed in sequence without further operator intervention.

A number of options are available to the operator in the method
of selection of points for analysis. As well as the choice of
groups of individual points, the operator may set up step scans
along a line and area scans (rectangular lattices of points).
The beam coordinates are chosen for step scans by pressing the
"store" button at each end of the line and typing the number of
steps. The positions of each point are computed by linear inter-
polation and stored. The image coordinates of a lattice of points
similarly may be stored by pushbutton entry of three corners
and specification of the number of steps for the base and for
the side of the area.

COMBINED AUTOMATED STAGE & BEAM POSITIONING

A modification of the above program has also been constructed for
special applications in semiconductor studies. This program
combines automated positioning of the stage with automated

electron beam positioning. It should provide rapid testing and analysis of large scale integrated circuit devices where there are numerous small unit "cells" repeating over distances of several centimeters. Because of the small dimensions within each cell, accurate beam positioning is essential for reliable analysis.

SUMMARY

A novel design for automation of electron beam positioning for microprobe analysis has been constructed. Using standard hardware, this system enables the probe operator to select analysis points with joystick control of a beam position indicator and pushbutton entry. The approach should be useful in areas such as studies of semiconductor devices, complexly zoned minerals, small inclusions in materials, and eutectics. For study of large-scale semiconductor circuitry the use of combined stage and beam automation should be particularly useful.

REFERENCES

[1] Hamilton, W. J.; Hinthorne, J. R.; Ray, L. A.; Whatley, T. A., 12th Annual Conference of the Microbeam Analysis Society, Paper Number 52 (1977).
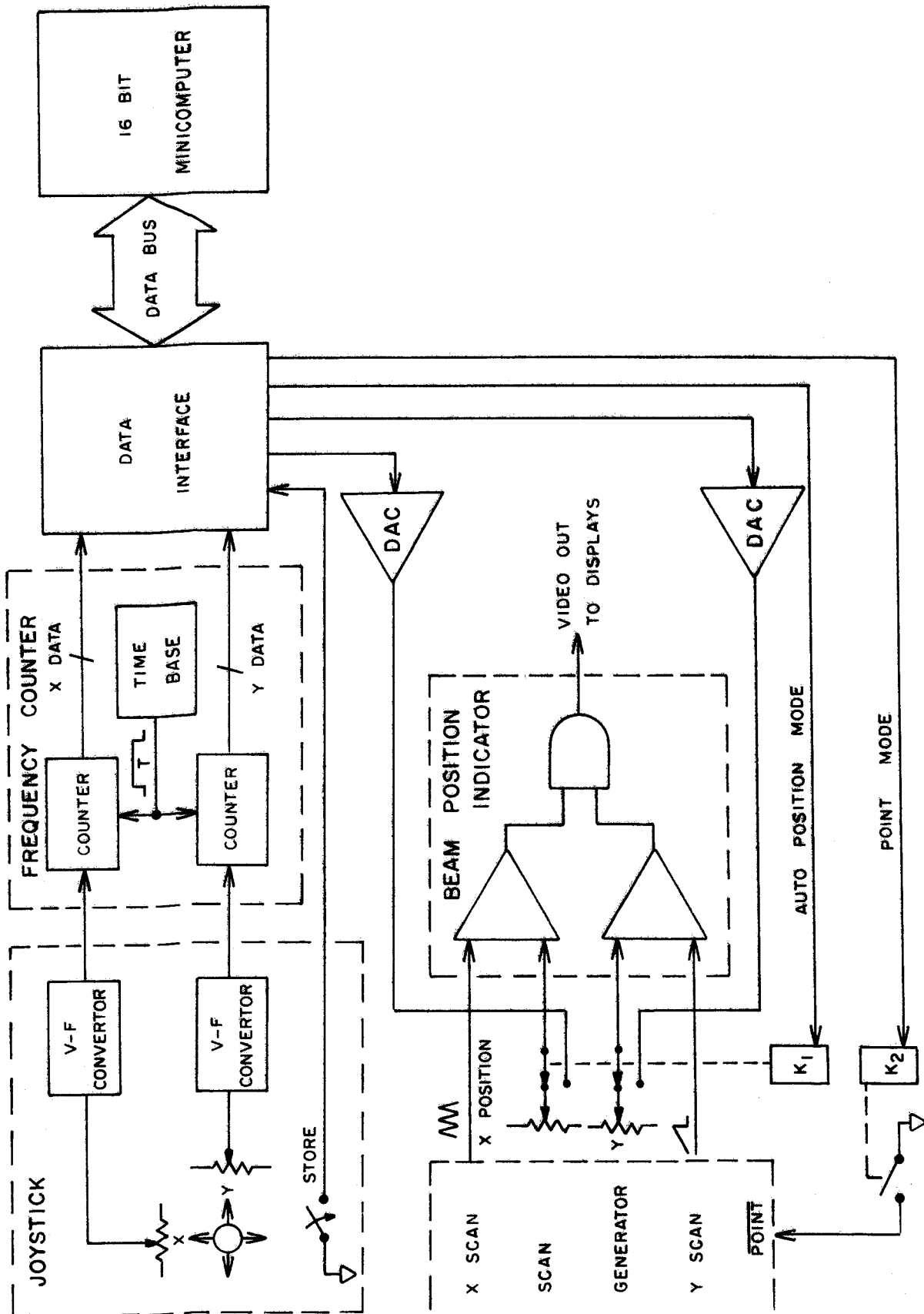
AUTOMATED BEAM POSITIONING SYSTEM

FIGURE 1

An Efficient Combined ED/WD X-Ray Analysis System

J.C. Russ and R.B. Shen
EDAX Laboratories
103 Schelter Road
Prairie View, IL 60069

A number of systems have become available for automated control of motorized crystal spectrometers, sometimes using the same computer provided in an energy-dispersive system. The one described here is unique in that not only are the computer (equipped with dual floppy disks) and the display capability of the ED system used both for spectral readouts (ED and WD) as well as setting of pulse height discriminators, but also both data collection systems can function at full efficiency simultaneously. This is accomplished by using a dedicated multichannel analyzer as a buffer to acquire the ED spectrum while the counts from up to three crystal spectrometers are counted in buffered scalars. The ED or WD intensity data are transferred to computer memory under program control.

Figure 1 shows a block diagram of the system. Note that the pulses from the proportional counter can be routed to the MCA to observe the setting of the upper and lower discriminators in the pulse height selector. The baseline of the PHS is computer controlled so that the energy window scans as a sin function of the Bragg angle. The system can control the angle (or wavelength) setting, slit selection and alignment, selection of counter and/or gas pressure, and crystal changer for three spectrometers and five axes (eg. x, y, z, tilt, rotation) of the SEM stage, provided these various controls are stepping motor or actuator equipped. Interfaces to spectrometers for Cambridge, JEOL, AMR, Philips, and other SEM's using Microspec spectrometers are available now.

Modes of operation provided in the software include qualitative, quantitative, and specimen scanning routines. The user can specify wavelength scans either at a constant rate over a range of angle or lambda (for instance, an area seen in an initially acquired ED spectrum to have possible hidden peaks) or a peak-seeking dual rate scan (for instance to search for trace peaks not visible above background in the ED spectrum). Peak-search uses first a high rate scan to acquire a spectrum which is then searched in the computer to detect statistically significant possible peaks, each of which is then scanned more slowly with the crystal slewing at high speed in between them. The total net intensity in each detected peak, its wavelength, and possible identification from a disk file of elements and lines is presented in a compact table.

For quantitative analysis the user can specify a list of elements and lines (by symbol - the system recognizes twenty lines for each element), and the system refers to a master file of user-established analysis conditions for choice of spectrometer crystal, detector, slit, order, and time or required precision. For each element the location of the standard and its composition can be entered, or "learned" by moving the stage to it and pressing a button. If a Faraday cage is provided, the beam current can also be digitized and read by the computer to normalize any long term drift. The stage will move the Faraday cage into position as often as requested, and express all intensities as counts per second per nanoampere. If a shift in current is observed the measurements since the last beam current reading can be repeated.

A hill-climbing algorithm to center the crystal on each element peak can be applied to standards (and the readings used for the unknowns) or on both standards and unknowns. Background measurements on one or both sides of the peak can be specified. Intensity measurements can be taken singly, or with 3 or 5 separate measurements with specified steps of a few microns on the specimen, with the statistical spread in the results used to

estimate final accuracy (or to reject doubtful measurements). A list of points to be analyzed can either be entered or "learned" as the specimen is examined. The file of measured net intensities on both standards and unknowns with their statistical precision, corrected for long term drift in beam current, dead time, etc. is then passed to a ZAF calculation (either FRAME or COR-2) or a more specialized correction program (eg. calibration curves or Bence Albee). Data from the ED spectrum can be combined with this file. The concentrations in atomic and weight percent, with propagated errors, are calculated. Such a series of automated measurements can run unattended, overnight.

Element variations across the specimen can be studied by scanning along any line between two points entered as coordinates or "learned". As many elements can be measured simultaneously as there are crystal spectrometers, plus those measured with the ED system. The user can select the number of points to be measured along each line, up to 4000. The resulting line scans and any algebraic combinations (eg. element sums or ratios) can be displayed or plotted. Area rasters can also be measured in the same way.

The combined system with its comprehensive software (written in FORTRAN-IV and fully supported by a real time disc-operating system) is supplemented by an extended Basic interpreter which can also control the various hardware functions (albeit less efficiently - one at a time). The user can program special experiments, turn routine work over to inexperienced personnel, or run lengthy series of measurements unattended, to obtain significantly increased analytical power from his SEM/probe.
FIGURE 1: Block diagram of combined ED/WD System.

References

1. H. Yakowitz, R.L. Myklebust, K.F.J. Heinrich, "FRAME: An On-Line Correction Procedure for Quantitative Electron Probe Microanalysis", U.S. Natl. Bur. Stds. Technical Note 796, U.S. Government Printing Office Washington, D.C. (1973).

2. J. Henoc, K.F.J. Heinrich, a d R.L. Myklebust, "A Rigorous Correction Procedure for Quantitative Electron Probe Microanalysis (COR 2), " U.S. Natl. Bur. Stds. Technical Note 769, U.S. Government Printing Office Washington, D.C. (1973).

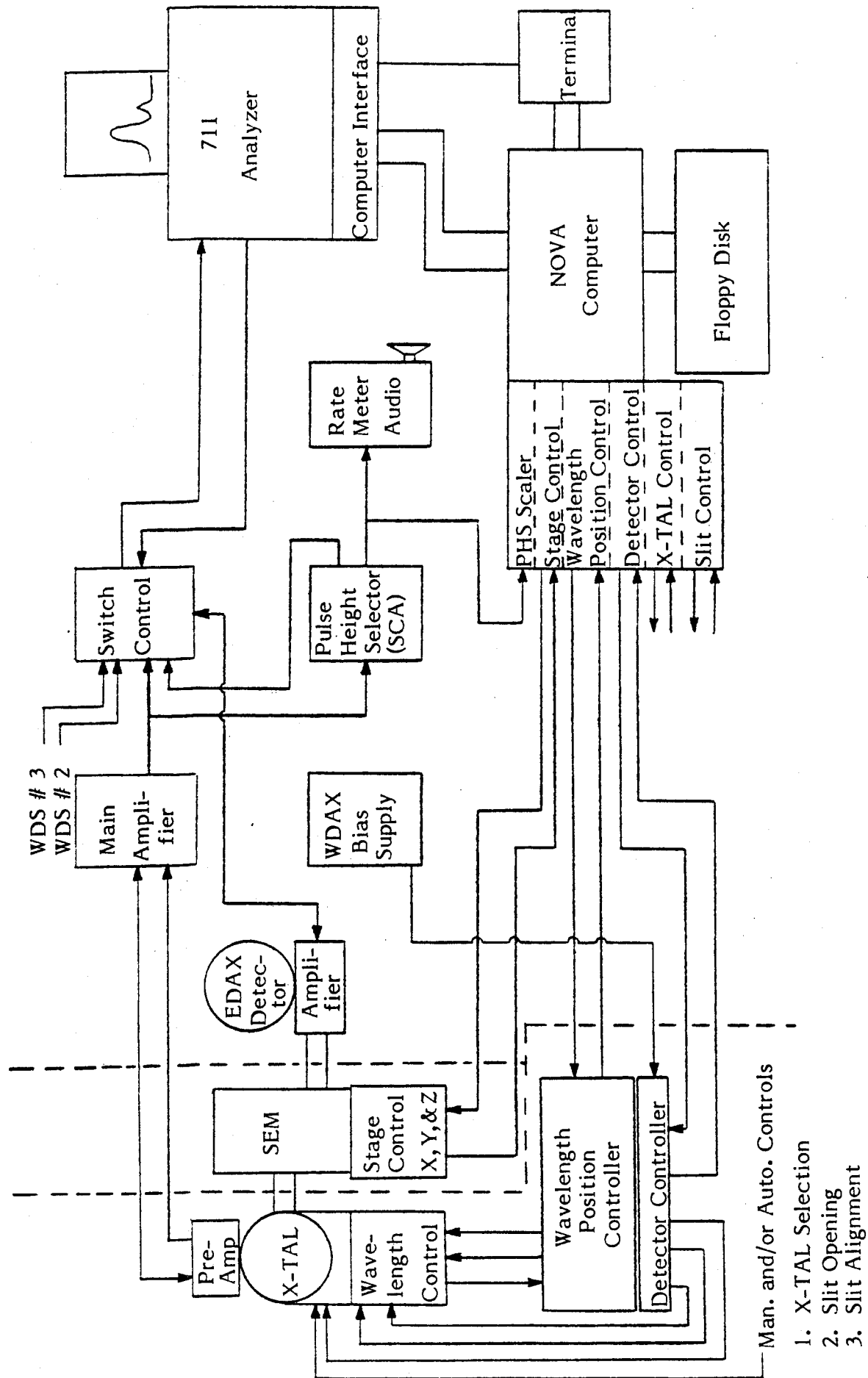3. A.E. Bence and A.L. Albee, Journal of Geology 76, 382 (1968).

FIGURE 1: Block diagram of combined ED/WD System.

COMPUTER CONTROLLED PHOTOGRAPHY ON
AN ELECTRON MICROPROBE[†]

William F. Chambers
Sandia Laboratories
Albuquerque, New Mexico 87115

A Cameca MBX electron microprobe has been modified to permit computer control of its beam-scanning and camera circuits. Several advantages accrue as a result of such control: First, low magnification (100X) x-ray Elemental Distribution PhotoMicrographs (EDPMs) are possible by aligning the fast (X) scan direction of the beam with an insensitive axis of the x-ray spectrometer and synchronously scanning the spectrometer with the slow (Y) scan direction of the beam. Second, a series of EDPMs can be scheduled so that a complete set of EDPMs can be taken from each of several areas while the instrument is operating in an unattended mode. This makes possible greater instrument utilization through overnight and weekend operation. Third, by utilizing 70 mm roll film the film cost drops substantially.

Low magnification EDPMs can be partially realized via a hardware module available from Cameca instruments. This module, however, provides accurate synchronization at only three magnifications (100X, 200X, 400X) and a limited set of scan speeds, whereas computer control not only permits any magnification and scan speed but also permits multiple scans.

The software for the system has been written in Flextran and incorporated in the operating program, TASK.* In use, a TASK command of the form: PHOTO ELEMENT MAGNIFICATION, SCAN TIME is given. For example, consider the command: PHOTO CU1 100, 260. Stored tabular data indicate that CU1 corresponds to the CU-Kα line on spectromer 1 and that this line, which is found at 0.38272 sin θ on the LIF crystal, should be analyzed with a detector bias of 1188 volts and a 2-volt pulse height analyzer window. The computer computes an offset from the relationships:

$$\Delta\theta = YA/L \quad ,$$

and

$$L = 2R \sin\theta \quad ,$$

where

θ = Bragg angle

R = spectrometer radius

L = distance from x-ray source to crystal

Y = offset of x-ray source from focused position in mm

  = (50/magnification)

A = 1 for an inclined spectrometer

  = $\sin\beta$ for a vertical spectrometer

β = x-ray take-off angle

which can be combined to yield:

$$\Delta L = 2R \cos\theta \; \Delta\theta = YA \frac{\cos\theta}{\sin\theta} \quad .$$

Since we are dealing with a constant take-off angle instrument, ΔL can be related to the number of steps offset through the pitch of the lead screw by:

$$\text{Offset} = 200 \; \frac{\text{steps}}{\text{revolution}} \; \text{x} \; 3.125 \; \frac{\text{revolution}}{\text{mm}} \; \text{x} \; \Delta L \; \text{mm} \quad .$$

Thus,

$$\text{Offset} = 31{,}250 \; \frac{A\sqrt{1-Q^2}}{MQ} \; \text{steps} \quad ,$$

where

M = magnification

Q = $\sin\theta$ which, for the MBX, is the spectrometer dial reading

After the computer verifies that an LIF crystal is in spectrometer 1, or changes to an LIF if necessary, it sets the window and detector voltages, positions the spectrometer, starts the sweep, opens the camera shutter, and scans the spectrometer. Film is advanced by providing a switch closure signal to a bulk load film transport which uses 70 mm film in 45.7 meter (150 ft) rolls. A partially exposed roll can be removed by sacrificing about three frames. A subprogram schedule can be written which will cause a series of EDPMs to be taken at a given spot and then the sample trans-lated in either an incremental or a table-driven manner and another set of EDPMs taken.

Although the modifications described were made to a Cameca instrument and the software written in Flextran, similar modifications could be made to any instrument that utilizes an electron beam scanning system which incorporates electronic beam rotation. If beam rotation is unavailable, the low magnification EDPM capability will be lost; however, camera control can still offer the advantages of unattended operation.

A GRAPHICAL METHOD OF RESOLVING X-RAY INTER-

FERENCES ON THE ELECTRON MICROPROBE

John W. Geissman and Eric J. Essene

Department of Geology and Mineralogy
The University of Michigan
Ann Arbor, Michigan   48109

Many characteristic X-ray lines overlap within $\pm$ 0.02 $\overset{\circ}{A}$ with $E_o \lesssim$ 1 kv, providing interferences of considerable annoyance in quantitative analysis with the electron microprobe. Common examples are K_α-K_β overlap in adjacent first row transition metals (i.e., TiK_β/VK_α), L_α-L_β-L_γ overlap in rare earth elements, and specific interferences such as BaL_α/TiK_α, PbM_α/SK_α, etc. A graphical method has been found to evaluate possible overlaps allowing an estimation of and correction for each interference. An example is given for TiK_β interference with VK_α X-rays (the difference in wavelength, Δ , being 0.009 $\overset{\circ}{A}$) using an ARL-EMX electron microprobe with an LiF crystal spectrometer. The TiK_β intensities of several titanium-bearing, vanadium-free standards are measured at the wavelength of VK_α. An approximately linear relationship exists between the "vanadium" count rate recorded and the titanium weight percent of each phase (Figure 1). ⌐his is not affected by secondary slit settings between 0.032 and 0.064 mm or by the bonding of the interferant (metallic, sulfide, or oxide). If analyzed under the identical set of conditions as those used to determine the titanium "interference" curve, the vanadium-bearing phase will yield a count rate above the curve at its particular titanium composition. The true vanadium count rate can be obtained by measuring the titanium content of the sample and then subtracting the interpolated value for titanium interference. At 15 kv, analysis of vanadium using titanium metal and ilmenite ($FeTiO_3$) gives 1.42 and 0.79 weight percent "vanadium" respectively. Analysis of vanadium in magnetite from the Butte Quartz Monzonite, Montana, when corrected for 0.17 weight percent "vanadium" yields an actual vanadium content of 0.50 weight percent and has been confirmed by atomic absorption methods.
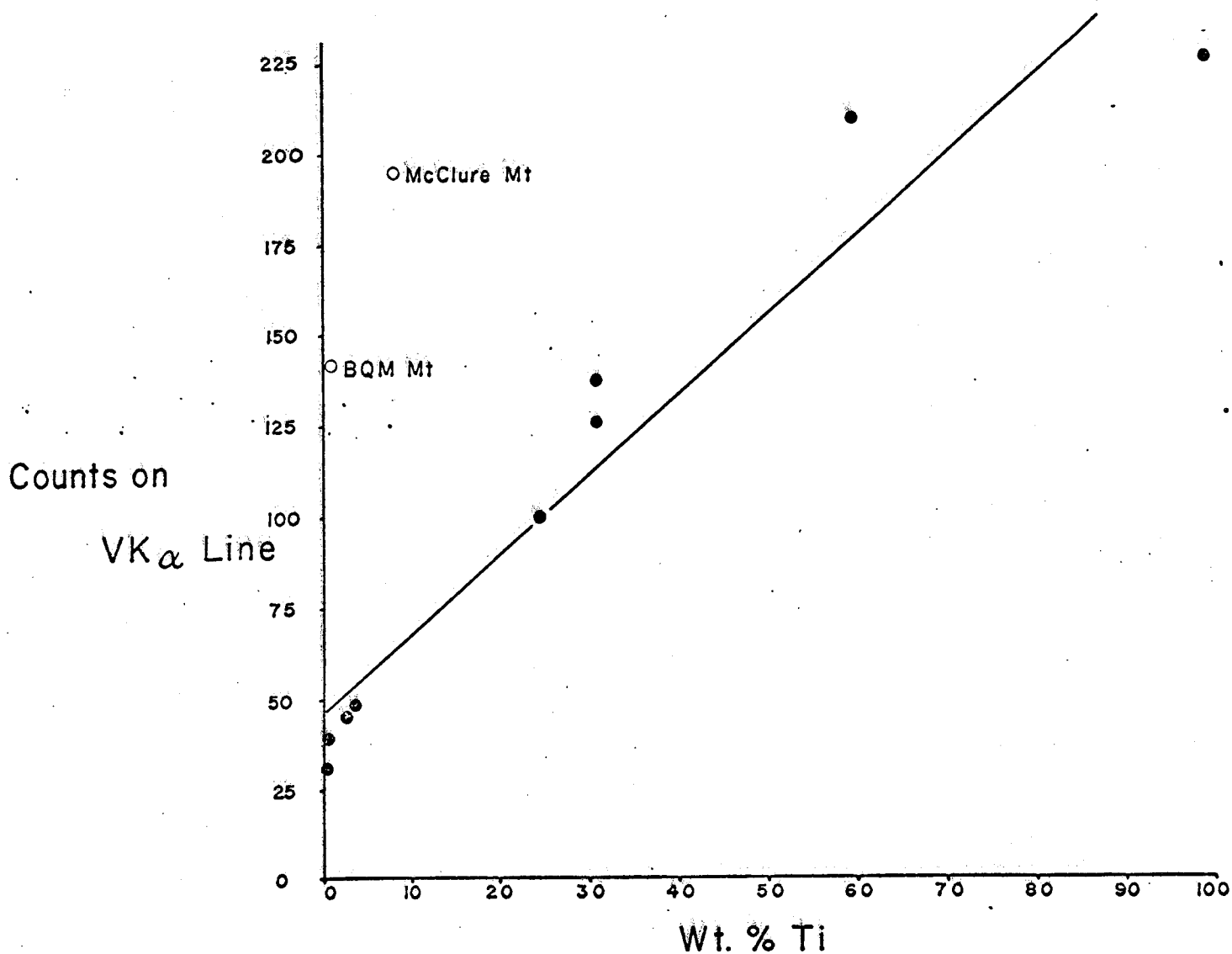
Figure 1. Apparent vanadium counts recorded vs. titanium weight percent of each standard.

Other apparent transition metal interferences detectable on an LiF crystal include VK_β on CrK_α (Δ equals 0.006 Å), CrK_β on MnK_α (Δ equals 0.018 Å), and MnK_β on FeK_α (Δ equals 0.027 Å). The effect of the delta value on the amount of interference is dramatic (Figure 2); the greater the interference, the larger the slope of the curve. The relative positions and the small positive slopes of the Cr-Mn and Mn-Fe interference lines may be explained by continuous background radiation. On a TAP crystal, the MnK_α (4th order) on AlK_α interference (Δ being 0.011 TAP units, or 0.072 Å) is negligible. Using a PET crystal, the only significant interference found is MoL_α on SK_α (Δ equals 0.015 PET units, or 0.034 Å). MoL_α-PbM_α and PbM_α-SK_α interferences are absent. Use of this simple, graphical

procedure allows resolution of potential X-ray interferences on the electron microprobe. Where possible interferences exist, workers should use the above technique to demonstrate the absence of or approximate correction for overlap.
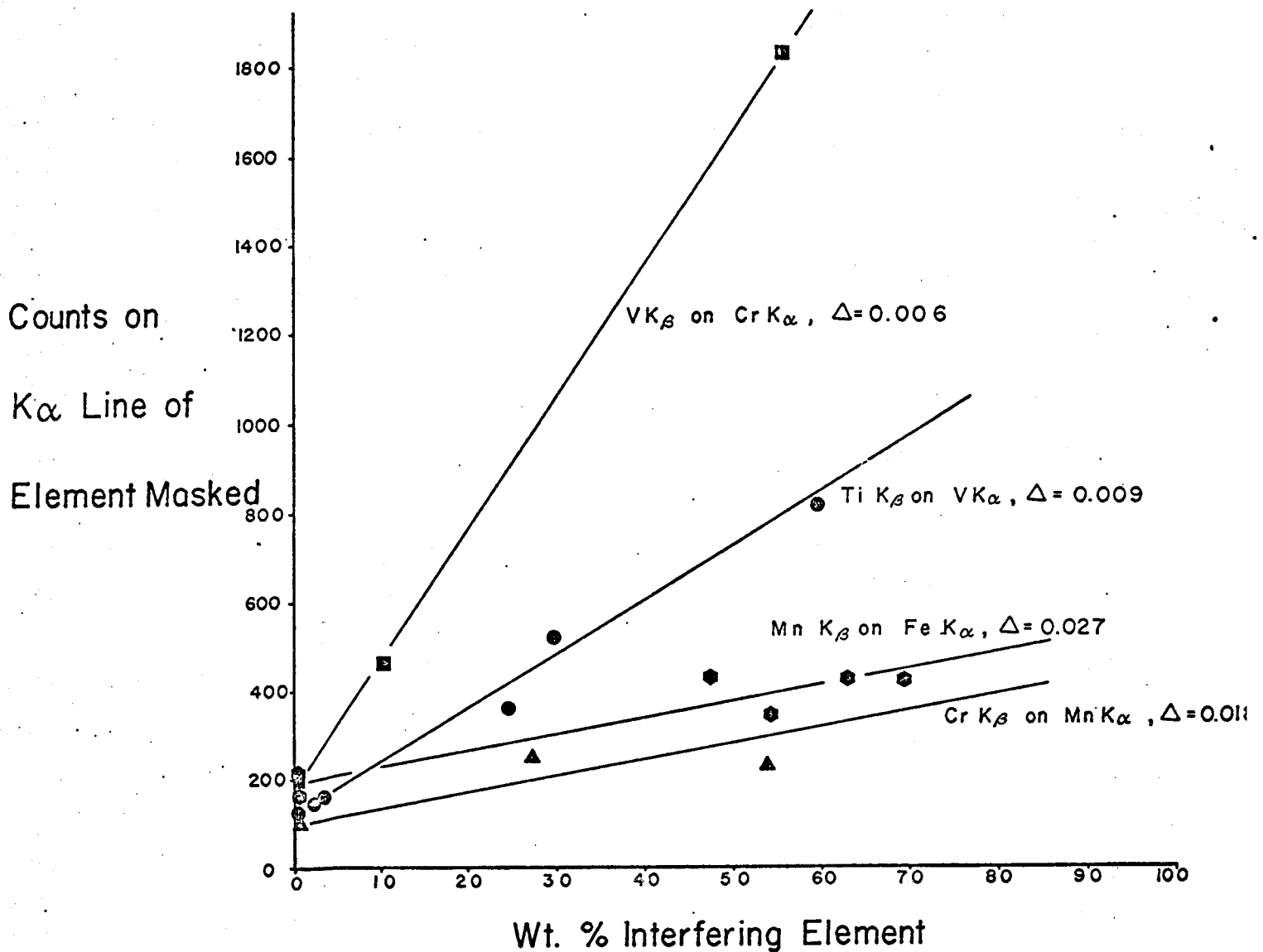

Figure 2. Apparent K_α counts vs. weight percent interfering element for four K_β-K_α transition metal overlaps.

Microanalysis of Small Particles on Complex Surfaces
by
D. G. Brandon and M. B. Hornstein
Technion, Israel Institute of Technology

The use of the SEM in the failure analysis of microcircuits is today almost routine for qualitative detection of flawed and contaminated surfaces. However, difficulties still remain in the quantitative determination of particulate matter which is often found on the surface. The difficulties arise from two aspects of the surface which become obvious from looking at a diagrammatic crossection of a typical microcircuit surface as the one shown in Figure 1. First, there is the
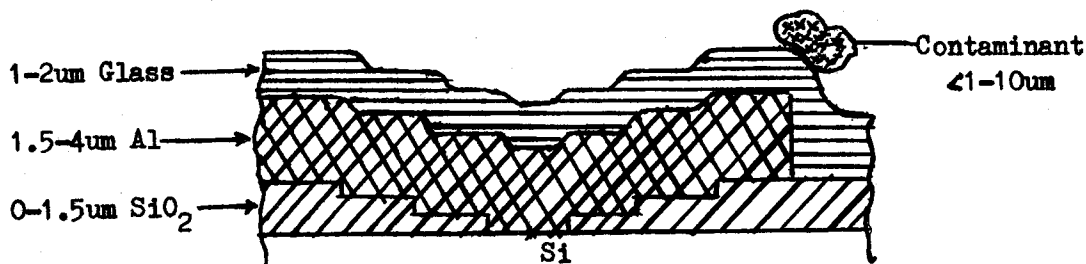

Figure 1. Crossection of microcircuit
surface, with contaminant

overall thinness of the surface layers (including the contaminant). In the worst case it is less than 3um. Second, is the fact that it is a composite, and therefore, all of the effects of this composite must be eliminated in order to determine the composition of the contaminants on the surface. Al and Si cannot simply be eliminated from the spectral analysis, since the particle often contains them.

The use of a 30 kV beam in the spectrographic analysis usually penetrates the surface to about 5 um. At least 80% of the time, this takes us past the region of interest and into the background material. On the other hand, lowering the beam energy to less than 10 kV causes loss of information about the higher activation energy elements. Comparison of the spectra taken at various energy levels is one method of minimizing the effects of the spectral lines arising from the microcircuit itself. Preliminary results indicate that this technique is at least qualitatively effective, but the data has not yet been completely quantized.

A second approach is based on geometrical considerations. Looking at the set-up in Figure 2, it can be seen that for any position of the collector relative to
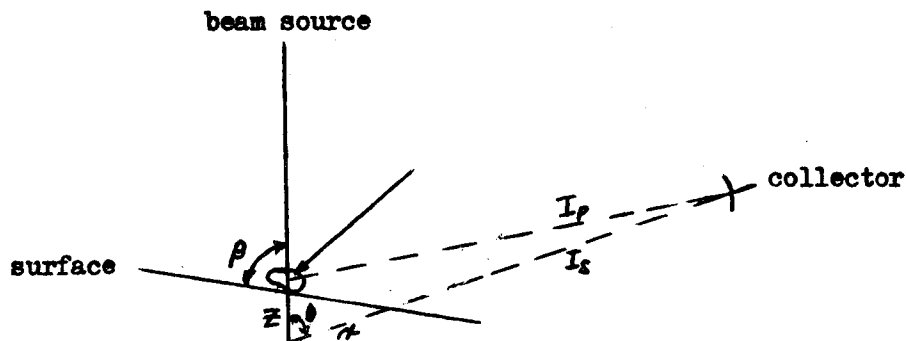

Figure 2. Geometrical set-up for angular analysis

the substrate surface, the intensity of the collected beam, I_m, will be equal to $I_p + I_s$ (where I_p is the beam intensity due to electrons scattered from the particle and I_s is the beam intensity due to electrons scattered from the substrate). Consideration of the geometry shows that:

$$x = \frac{Z \sin\beta}{\sin(\beta+\theta)}$$

where: x=distance from scattering point to surface of microcircuit

Z=penetration depth

β=angle betwee initial beam and surface

θ=angle between initial beam and I_s

Therefore, since I_s decreases with increasing x according to the absorption equation, when $x \rightarrow \infty$ at $\beta = 90^\circ + \theta$, I_s will drop to 0. Since Z is in the order of microns and the distance between the scattering point and the collector is of the order of centimeters, can be considered constant, regardless of the depth of penetration. Practical considerations generally preclude the tilting of the surface to an angle of $(90 + \theta)^\circ$, it is therefore necessary to make two or more measurements at different angles and calculate the effects of the substrate.

Figure 3 is a microphotograph of a piece of on the surface of an LM111, monolithic voltage comparator. The particle was analyzed at $\beta = 105^\circ$, 90° and 77°.
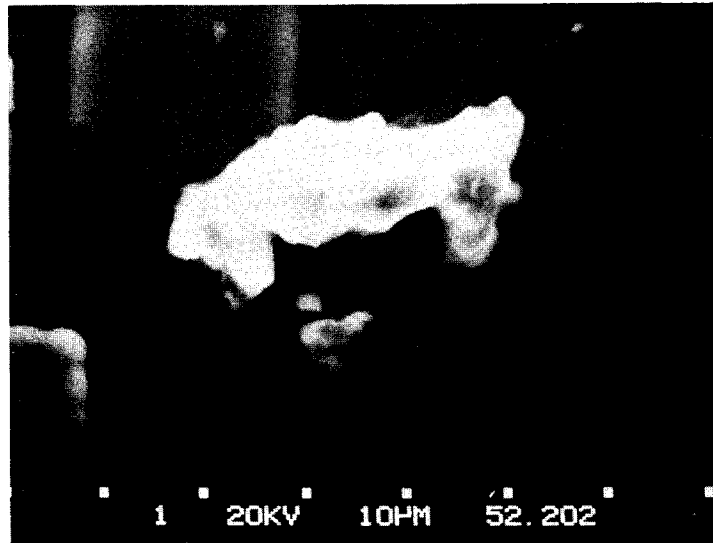

Figure 3. Sample dirt particle   1300X
($\beta =105^\circ$)

The percentage of Si was found to be 39.8%, 48.3% and 51.2%, respectively. Since in this case, it is known that Si is the underlying material, the basic validity of the technique is demonstrated.

A KOSSEL CAMERA DESIGNED FOR THE CAMECA MBX-INSTRUMENT

By:

C. CONTY   CAMECA - 92400 COURBEVOIE, France
F. MAURICE CEA SACLAY - BP N° 2 - 91190 SACLAY, France
R. TIXIER   IRSID - 78104 SAINT GERMAIN EN LAYE, France

1 - INTRODUCTION

In the early days of electron probe microanalysis, CASTAING and GUINIER |1| showed that an electron probe instrument, in which a very small X-ray source is obtained and accurately localized on a selected area, is ideally suited for the production of divergent beam X-ray patterns or KOSSEL patterns.

As electron probe microanalyzers or scanning electron microscopes are now frequently available in laboratories where X-ray crystallographic techniques are also used, there is a real opportunity for using these instruments as very high performance microdiffractometers.

As a matter of fact there has long been interest in this X-ray crystallographic technique and it has been illustrated by some remarkable applications. However, development to full potential has been hampered by difficulties related to the calculation involved in making proper use of the patterns and by technological problems especially in the back reflection mode (use of punched film, films outgassing in vacuum, camera complexity, and so on.)

To overcome these problems and make the recording and use of these patterns very simple, even for people not thoroughly trained in crystallography, a new concept of KOSSEL camera has been presented in several earlier papers |2, 3|. A prototype |4| has been built and intensively used in several labs.

For the experience gained in using this prototype, two cameras has been developed for the CAMECA MBX-instrument: one for transmission and one for back reflection.

The purpose of this paper is to describe these cameras and to emphasize that such an attachment in conjunction with related computer programs makes the use of KOSSEL lines easy and fast.

2 - DESIGN CONSIDERATIONS

General

The requirements considered for this instrument were of two different kinds. First, the patterns should be easily obtainable in both modes, transmission and back-reflection. Second, fully computerized analytical analysis of the pattern should be possible.

Electron source

As said previously, electron probe or SEM are ideally suited to provide a microsource of X-rays, but as it has to be used for many other purposes, the change-over from the usual techniques to KOSSEL microdiffraction has to be completed within a few minutes.

Cameras have been built as an attachment ot the MBX but they can also be fitted on the former MS 46 CAMECA electron probe micro-analyzer by using a special adaptator.

In all cases, cameras are simply interchangeable with the standard specimen stage drawer without any modifications on the instrument column.

Specimen holder

We need to examine reasonably large specimens. The orthogonal XY motions enable 20 mm to be traversed in the specimen plane, with coordinates shown on external micrometers.

The analytical computerized technique we use |5| is valid for any crystal orientation. It gives the most accurate results when the specimen surface is exactly parallel to the film plane. This can be machined usually to an accuracy of better than a few tenths of a degree.

The knowledge of the centre of the pattern and the specimen film distance is not needed. A goniometer stage is not necessary in these conditions specimen handling is very simple.

In both cameras, transmission and back-reflection, the specimen can be observed by using scanning images obtained with secondary electrons or with the specimen current. One also needs to have an optical microscope in order to recognize microscopic features which might not give contrast in electron images.

Film chamber

The source-to-film distance should be as large as possible as it is the major parameters by which the contrast of the patterns can be improved. On the other hand, it is desirable to make the X-ray divergent angle intercepted by the film as large as possible, in order to record enough conic sections for interpretation and analysis. If the film is large enough, prints and enlargement are not needed. This saves time and avoids problems related to uneven shrinkage of photographic prints.

Film of standard format 13 x 18 cm is used.

A major design characteristic of the film chamber is the use of a window to separate the specimen and the film, this allows the specimen to be kept in a vacuum while the film is in air. This has been done both for the transmission and for the back reflection modes. An air film chamber offers many advantages, as discussed by VIETH & YAKOWITZ (1966). It allows multi-exposures without disturbing either the vacuum, the specimen or the alignment and it permits immediate processing. Films are wrapped in black polyethylene foil and need not to be shielded against back-scattered electrons. The vacuum is not disturbed by films out-gassing. With direct access to the film there is no need for any shutter. Filters can be easily inserted in the X-ray paths.

These conditions have been obtained in the back-reflection mode by tilting the specimen against the beam axis, as the angle of incidence of electrons on the specimen has no effect on the patterns. With such a geometry there is no need to punch a hole in the film near the centre of the pattern for the primary beam to pass through. Thus our film is undamaged, and an important part of the pattern is not cut off.

With the X-ray wavelengths involved, an air path increases exposure times by less than 20 or 30 %. On the other hand, soft bremsstrahlung radiations are absorbed before reaching the film, and this does, in fact, improve the contrast. Air scattering along the distances involved is negligible.

The window material is mylar, 200 um thick. Such windows are very reliable; they have been used on the prototype for more than eighteen months without remplacement.

Geometrical limits

All these requirements had to be met both in the transmission and in the back-reflection modes of recording the patterns. In our design, we decided to build two cameras with two separate specimen holders, one for each mode. This was found to be the most economical way of realization, compatible with mechanical accuracy, and the easiest configuration to fit in the space available in a specimen holder drawer.

3 - DESCRIPTION

Transmission stage (Fig. 1)

The specimen is held in a metal frame which can be machined with various openings. The holder carries a polished thorium oxide standard for electron-beam alignment.

The specimen can traverse X and Y up to 20 mm. It lies in a horizontal plane, adjustable with a Z movement to the focal plane of the standard optical microscope of the microanalyzer (magnification 400 X).

Semi-aperture angles are 22° and 30° and the specimen film distance may be varied between 100 and 152 mm.

Back reflection stage (Fig. 2)

The specimen is inserted in a holder. It can be 20 mm x 30 mm and 7 mm thick. The holder carries a fluorescent screen for electron-beam alignment and is connected to the specimen current amplifier.

The specimen lies in the lower part of the camera and its plane is titled by 30° to the beam axis. The mylar window, which separates the air film chamber from the vacuum is transparent. Thus, an optical microscope can be inserted in this air chamber, in front of the specimen, and adjusted so that the point bombardes by the electrons can be looked at. Because of the long focal distance, magnification is only 200 X. Thus any point on the specimen can be selected by either scanning or optical microscopy. The microscope includes a metal shield to protect the operator. But it is important to point out that, because of the low probe currents, X-ray emission is very low as compared to standard X-ray tubes.

The specimen lies at a relatively long distance from the focusing lens of the microanalyzer (WD = 148 mm), but with the low beam currents needed, the probe diameter is less than one micron in these conditions.
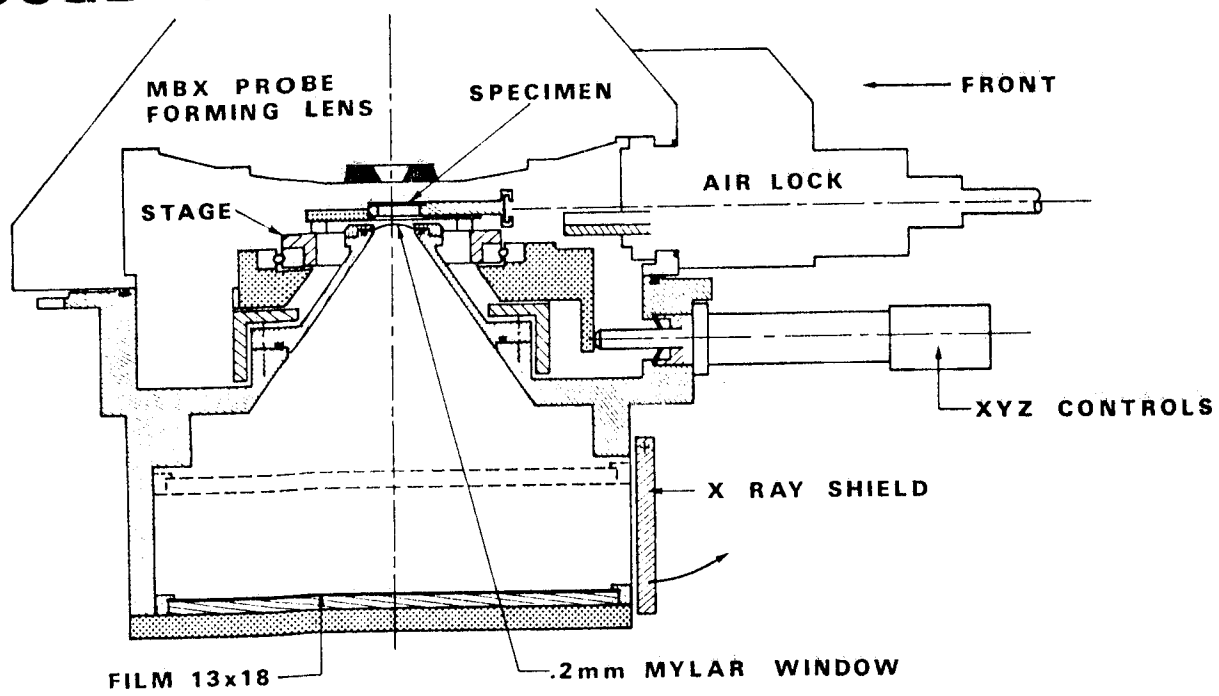
KOSSEL CAMERAS

MBX PROBE FORMING LENS
SPECIMEN
FRONT
STAGE
AIR LOCK
XYZ CONTROLS
X RAY SHIELD
FILM 13x18
.2mm MYLAR WINDOW

Fig:1 — TRANSMISSION STAGE

RETRACTABLE LIGHT MICROSCOPE
MBX PROBE FORMING LENS
FRONT
ILLUMINATOR
BACK PORT
30°
X RAY SHIELD
FILM 13x18
.2mm MYLAR WINDOW
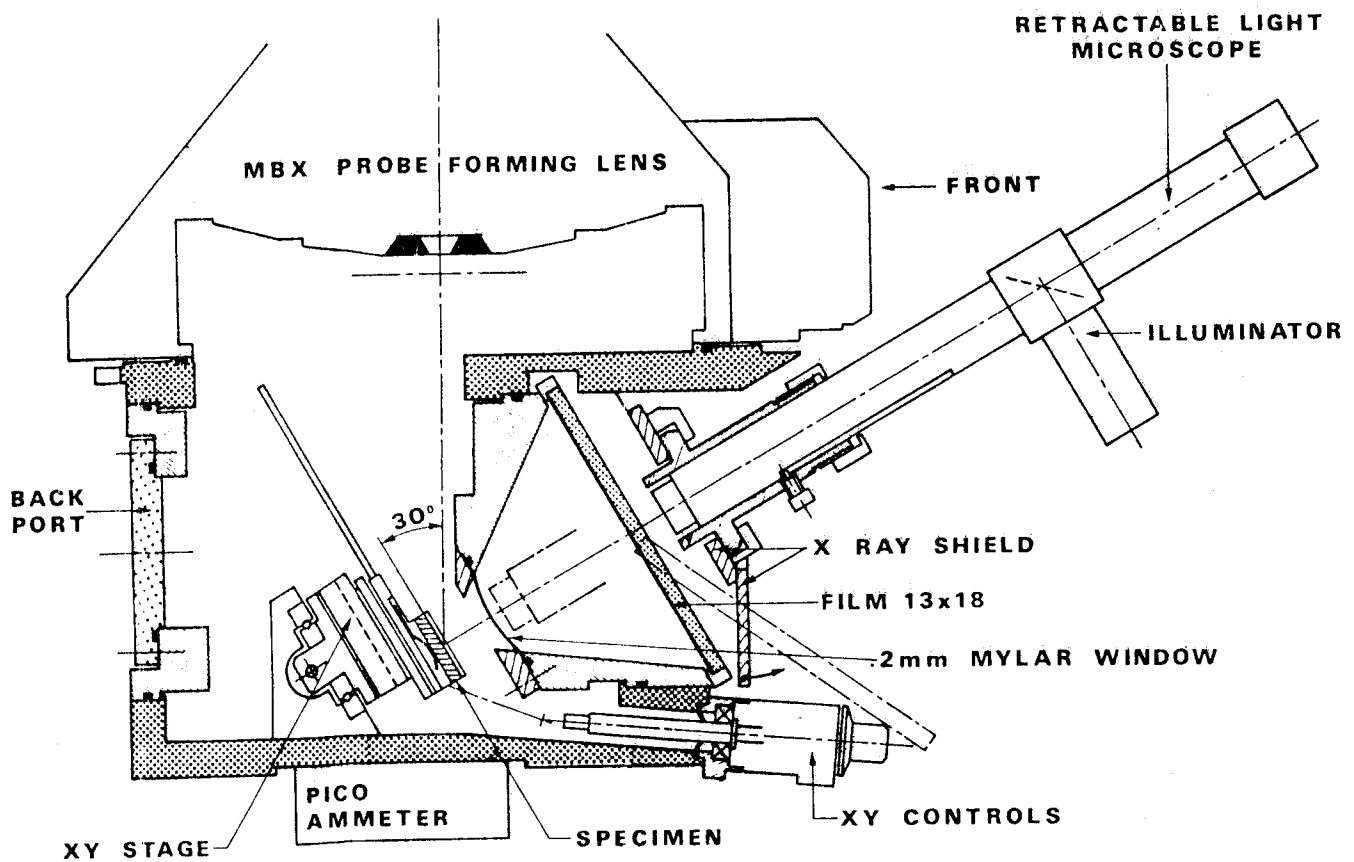PICO AMMETER
XY STAGE
SPECIMEN
XY CONTROLS

Fig:2 — BACK REFLECTION STAGE

Semi-aperture angles are 36° and 45° and the specimen film distance is 85 mm.

A large port located in the back of the camera chamber will provide access to the sample for the installation of devices to control sample parameters, such as temperature, strain, etc.

Operating conditions

The table gives examples of operating conditions :

Examples of operating conditions using KODIREX film

	Target	Beam	Film distance	Exposure
Transmission	Fe 30 μm	30 kV 60 nA	100 mm	15 min.
Back reflection	Fe massive	35 kV 8 nA	90 mm	5 min.

4 - SOFTWARE

A comprehensive set of programs has been developed to make full use of the KOSSEL technique and to free the operator from difficult and tedious cryostallographic computations. In fact, by using a simple standard procedure, a pattern can be indexed and interpreted in less than 5 minutes.

The software library which supports the KOSSEL camera hardware contains more than thirty subroutines corresponding to the general cristallographic operations for any crystal having any orientation. These are for instance, calculation of the metric tensor transformation, calculations of lattice constants and diffraction angles, calculations of inverse lattices, vector operations and so on...

General programs make use of these subroutines for KOSSEL pattern interpretation and other related crystallographic calculations. They are:

A program for plotting stereographic projections of the KOSSEL sphere, a program which computes the orientation using the analitical method of RYDER and al |5|, a program which computes a lattice constant using the method described by TIXIER and WACHE |6|, a program which lists the points in the patterns, defined by conic intersections in ascending order of sensitivity to lattice constant changes. Other programs are ancillary programs of general crystallographic interest: a program for plotting pole stereographic projections, a program for calculating tables giving lattice constants and angles between planes, a program

for calculating the indexes of the planes orthogonal to a given axis and a program for plotting reciprocal lattice cross section.

All these programs can be operated on any crystal (even on tri-clinic). They have been written in FORTRAN conforming to the specifications of the American National standard which can be run on any computer with 16 K memory (or 8 K in an overlay mode).

The library structure makes it an easy and simple job to build new programs, like for instance, perspective views of crystal structures, direct and inverse pole figures, etc.

A users group is open to any user of the attachment.

5 - APPLICATIONS

The KOSSEL pattern technique can be compared to other crystallo-graphic techniques in the same way as microprobe analysis com-pares to the usual analytical methods. In this respect, all ap-plications to be found in crystallography are possible, but the results can be localized on a microstructural scale. Many appli-cations have been published and are reviewed, for instance, in YAKOWITZ |7| or in TIXIER and WACHE |6| . Recent works using the prototype of the camera include studies in the mechanisms of texture formation for which, due to the statistical aspect of the problem, hundreds of patterns were easily and quickly recor-ded in the back reflection mode |8|. This made it possible to obtain new results in recrystallization and grain growth studies.

Other applications include accurate lattice constant determina-tion on aluminium all νs, studies of disorientation during poly-gonization creeps and studies of crystal deformation.

Many other applications are also possible as it has been shown by various scientists. They are for instance : small phase iden-tification in mineralogy |9|, lattice constant variations asso-ciated with dopent concentrations in semi-conductors, dynamic effects studies |10, 11|, phase orientation relationships |12, 13| deformation studies |14|, and so on...

6 - CONCLUSION

All these new and exciting fields are now fully opened to micro-probers. On the other hand, crystallographers in your institution will be delighted to know that this new and efficient technique is now available to them.

REFERENCES

|1| - CASTAING R., GUINIER A. (1951) C.R. Académie Sciences - PARIS - 232, 1948

|2| - GIRAUD A., GRATON G., QUENNEVAT A and TIXIER R. (1973) Journal de Microscopie 18, 128.

|3| - MAURICE F., PHILIBERT J., SEGUIN R. and TIXIER R. (1975) J. Appl. Cryst. 8, 287

|4| - French Patent n° 2 185 190 - May 19th (1972)

|5| - RYDER P.L., HALBIG H. and PITSCH W. (1969) - Proc. V Cong. X-ray optics and microanalysis, p 388 - BERLIN SPRINGER.

|6| - TIXIER R. and WACHE C. (1970) - J. of Appl. Cryst. 3, 466.

|7| - YAKOWITZ H. (1969) - Advances in Electronics and Electron Physics, Supplement 6, p. 361.

|8| - BENOIT-BRYCKAERT D., MEYZAUD Y., PARNIERE P. and TIXIER R. (1975) - 4th International Conference on texture, Cambridge.

|9| - ULLRICH H.J. und SCHFEIBER H. (1974) - Mikrochimica Acta (Vienna) - Suppl. 5 - 209 SPRINGER VERLAG.

|10| - KALMAN Z.H., SUGA H. and WEISSMANN (1977) - 8th Int. Conf. on X-ray optics and microanalysis - Boston August 18-24, 197 .

|11| - BRUMMER O., BEIER W. and NIEBER H. - Phys. stat. Sol. (a) (1973) 20 K 119

|12| - KING A.D. and BELL T. (1976) - Metallography 9, 397

|13| - SWINDELLS N., AVERY J.D. and HARRIS N. (1974) - Proc. 2nd Int Conf. Metallurgy of Cast Iron, Geneva.

|14| - ARISTOV V.V., SHMYTKO I.M., and SHULAKOV E. (1974) - J. Appl Cryst. 7, 413

Contrast Mechanism of Electron Channeling Patterns

T. Yamamoto
JEOL Ltd., Nakagami Akishima, Tokyo 196.
and
M. Mori, Y. Ishida
Institute of Industrial Science, University of Tokyo, Roppongi Tokyo 106.

General aspects of electron channeling patterns (ECP) has been elucidated from the anomalous transmission and diffraction effect of primary electrons incident upon a solid specimen[1,2]. However, quantitative description of ECP has been still unsatisfactory, since in theories[3,4] it is difficult to take into account both inelastic and multiple scatterings. One of the authors has proposed a theory of ECP in which both the scattering processes could be taken into account with the aid of a Monte Carlo simulation, and a preliminary result has been given[5]. In this report, a more detailed calculation is made and some features of ECP are discussed.

Let us denote the intensity of a jth Bloch wave at a depth of z as $I^j(z)$ and the probability of the initial inelastic scattering as $u_j(\theta_n)$ where θ_n is the scattering angle (see Fig. 1). This scattering angle is related to the momentum transfer hq as follows:

$$q^2 = 4k^2[\sin^2(\theta_n/2) + (\Delta E/E)^2] \equiv q_o^2 + q_t^2, \quad (q_t^2 = k^2(\Delta E/E)^2) \tag{1}$$

where k and E are the wave number and energy of the incident electron, ΔE is the mean energy loss due to the inelastic scattering. Here, we introduce $F(q_o,z,T)$ for a fraction at which an electron scattered initially at z and by θ_n emerges from the specimen surface, where T represents the arrangement of the detector and specimen. By summing up all the scattering processes, the back-scattering yield $I_B(T)$ of a solid specimen can be expressed as

$$I_B(T) = \int dz \int d\omega_{q_o} F(q_o,z,T) \Sigma_j u_j(q_o)I^j(z) \tag{2}$$

$u_j(q_o)$ has been well studied in theories of inelastic scattering[6-8] and it can be reduced to a general form

$$u_j(q_o) = \Sigma_g \Sigma_h S_{gh}(q_o) C_g^j C_h^j \tag{3}$$

where C_g^j is the gth amplitude of the jth Bloch wave. Inelastic scatterings considered are due to the excitation of phonon and core electrons. For the phonon excitation[7],

$$S_{gh}^{ph} = f(q_g)f(q_h) [\exp(-\alpha(g-h)^2) - \exp(-\alpha(q_g^2+q_h^2))]/\Omega \tag{4}$$

where Ω and f are the atomic volume and scattering amplitude, α is a constant for the Debye-Waller factor, and $q_g = q_o - g$. For the core electron excitation,

$$S_{gh}^c = (\frac{me^2}{2\pi^2h^2})^2\frac{Z}{\Omega(q_g^2+q_t^2)(q_h^2+q_t^2)}[\frac{1}{(g-h)^2+q_s^2} - \frac{q_s^2}{(q_g^2+q_s^2)(q_h^2+q_s^2)}] \tag{5}$$

where Z is the atomic number and $q_s^2 = me^2/2\pi^2h^2f(0)$. In eq. 5, S_{gg}^c is approximately determined[8] so that the charge density derived by Lenz[9] is

given in the atomic scattering amplitude, and for $g \neq h$, S^c_{gh} is determined from inspection by taking into account the order of magnitude in the scattering matrix elements[10] and the dependence of S^c on $g-h$[6].

The fraction F is evaluated by a Monte Carlo simulation[11] and it is expanded in a power series of z

$$F(q_0, z, T) = \Sigma_m a^{(m)}(q_0, T) z^m \tag{6}$$

Here we define the following quantities:

$$M^m_{gh}(T) = \int d\omega_{q_0} S_{gh}(q_0) a^{(m)}(q_0, T) \tag{7}$$

Now we apply the two-beam approximation to eqs. 2,3,6 and 7 in the order up to $m = 1$, and neglect some terms giving a minor contribution. Then, we can obtain

$$I_B(T) = I_0(T) + \frac{Aw + B}{\mu_0^2(1+w^2) - \mu_g^2} \tag{8}$$

where $I_0(T)$ is the background, i.e.,

$$I_0(T) = M^0_{oo}/\mu_0 + M^1_{oo}/\mu_0^2$$

and

$$A = \mu_g M^0_{oo} - \mu_0 M^0_{go} + 2\mu_g M^1_{oo}/\mu_0 - M^1_{go}$$

$$B = B_r + B_d$$

$$B_r = (\mu_g/\mu_0)(A + \mu_g M^1_{oo}/\mu_0 - M^1_{go})$$

$$B_d = \mu_0(M^0_{gg} - M^0_{oo})/2 + (M^1_{gg} - M^1_{oo})/2$$

$$\tag{9}$$

In these equations, μ_0 and μ_g are the mean and anomalous absorption coefficients, respectively.

It can be shown that $a^{(0)}(q_0)$ for all backscattered electrons tends to the backscattering yield of amorphous material at a specimen tilt angle of $\theta_s = \theta_n$ when $\theta_n < 90°$ and tends to 1 when $\theta_n > 90°$. These were first shown by Baines et al[12]. The contribution of the integral of eq. 7 becomes significant for S^{ph} at $\theta_n < 25°$ and for S^c at $\theta_n < 1°$. Therefore M_{gh} is mostly determined by S_{gh} and $a^{(m)}$ at such small angles of the initial scattering. Moreover, $F(q_0, z)$ shows almost linear decrease at such angles. A majority of ECP contrast is therefore expressed by eq. 8 within the order of $m = 1$. It should be noted further that if in eq. 7 $a^{(0)} = 1$ for all q_0's, M^0_{oo} and M^0_{go} become μ_0 and μ_g, respectively.

Core electron excitation gives rise to inelastic scatterings at a very small angle. The waves scattered at such small angles are subject to a strong diffraction effect[13], i.e., some of them can be regarded approximately as the initial Bloch waves. We define a critical wave number transfer q_0^c as follows: The scattered waves preserve the initial Bloch wave at $q_0 < q_0^c$ whereas they become diffuse-scattered waves apart from the Bloch state at $q_0 > q_0^c$. ECP contrast for all backscattered electrons at $\theta_s = 0°$ is calculated under various conditions. The results are compared in Table I. It is shown that the neglect of S^c induces a somewhat large estimate of the contrast whereas no significant

a weak initial peak, when the sign of α is reversed, This is due to the contribution of the first term in the square bracket of eq. 10 and B_d^o, and also due to similar contributions in the order of $m = 1$.

One of the authors (T.Y) is grateful to Dr. A. Howie for his valuable comments regarding the present theory.

References

1. G. R. Booker, A. M. B. Shaw, M. J. Whelan and P. B. Hirsch, Phil. Mag., 16, 1185(1967).
2. P. B. Hirsch and C. J. Humphreys, Proc. 3rd Ann. Symp. on Scanning Electron Microscopy, Chicago 1970 (p. 449).
3. J. P. Spencer and C. J. Humphreys, Electron Microscopy and Analysis, Inst. of Phys., 1971 (p. 310).
4. R. Sandström, J. P. Spencer and C. J. Humphreys, J. Phys, D, 7, 1030(1974).
5. T. Yamamoto, Read at Int. Conf. to mark the 50th Anniversary of the Discovery of Electron Diffraction, Inst. of Phys., London 1977.
6. H. Yoshioka, J. Phys. Soc. Japan, 12, 618(1957).
7. C. R. Hall and P. B. Hirsch, Proc. Roy. Soc., A232, 158(1965).
8. M. J. Whelan, J. Appl. Phys., 36, 2099(1965).
9. F. Lenz, Z. Naturf., a9, 185(1954).
10. C. J. Humphreys and M. J. Whelan, Phil. Mag., 20, 165(1969),
11. K. Murata, T. Matsukawa and R. Shimizu, Jap. J. Appl. Phys., 10, 678(1971).
12. M. Baines, D. R. Clarke and A. Howie, Scanning Electron Microscopy (Systems and Applications), Inst. of Phys., 1973.
13. A. Howie, Proc. Roy. Soc., A271, 268(1963).
14. T. Yamamoto, Phys. Stat. Sol., (a) 44, 137(1977).
15. J. P. Spencer, C. J. Humphreys and P. B. Hirsch, Phil. Mag., 26, 193(1973).
16. M. Pitaval, P. Morin, J. Baudry and G. Fontaine, Journ. de Phys. (Lett.), 37, L309(1976).
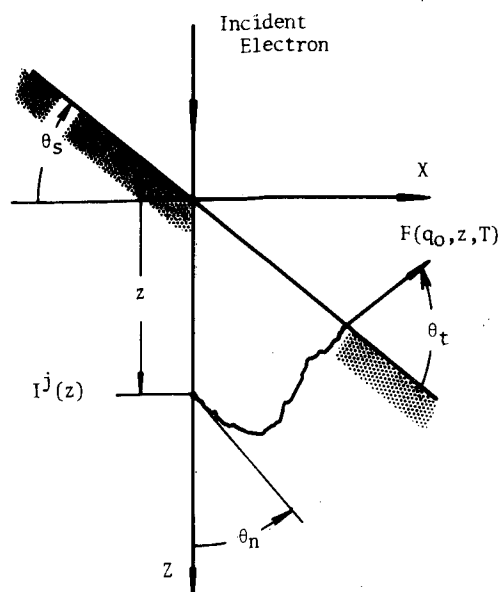
Fig. 1 Schematic illustration of electron trajectory and definition of symbols.

alteration is found by changing w from 1 to 2 while the contrast is much smaller than the observed one[14]. Although there is some ambiguity in the used value of f(0) in Lenz's approximation[8], the underestimate of the contrast may be due to the diffraction effect in the waves caused by the subsequent small angle scatterings. In view of this result, we calculate M_{gh} and μ_g resulting from the core electron excitation by dividing eq.7 by 5.

The dependence of the backscattering yield on the incident beam direction can be characterized by two factors in the last term of eq. 8. The factor A gives rise to an asymmetric change in the yield with respect to w, whereas the factor B gives rise to a symmetric one. As a result, the former and latter changes in the yield cause the ECP band and ECP line, respectively. For the sake of simplicity, we consider the reflecting plane being parallel to the un-deflected incident beam direction and examine the following two cases: (c,1) the direction of the reflecting vector is parallel to the specimen tilt axis, and (c,2) the direction is perpendicular to the axis.

For normal incidence in (c,1) (see Fig. 2), when all backscattered electrons are collected, $F(q_M^A,z) = F(q_M^B,z)$ where q_0 is transformed into $q_M = q_0 - g/2$ and thus $B_d = 0$. In addition, $B_r < A$ and so the ECP displayed is of the band contrast type. On the other hand, if the detection is restricted by a detector as in Fig. 2, $F(q_M^A,z) < F(q_M^B,z)$, thus $M_{gg}^0 - M_{oo}^0 > 0$. This results in a dissymmetric ECP, in particular, the dissymmetry becomes more prominence for high index reflections. Generally, the magnitude of B_d indicates a difference between the emerging fractions of electrons scattered diffusely around the 0 and g directions. When B_d is large, an ECP line appears. From Table II, B_d for oblique incidence is mostly determined in the order of m = 0. This fact suggests that Baines et al's interpretation within this order[12] is satisfactory. For oblique incidence in (c,1), $F(q_M^A,z) < F(q_M^B,z)$ even with the detection of collecting all backscattered electrons, and B_d greatly increases with the specimen tilt angle, thus exhibiting a strong dissymmetric ECP line. In the case of (c,2), when the detector is set in the x direction or for all backscattered electrons, a complete cancellation of M_{gg} and M_{oo} is achieved for symmetry. Therefore, $B_d = 0$. Moreover, the numerical calculation shows that $B_r < A$ and thus ECP's displayed are of the band contrast type. Calculated A, B_r and B_d in a restricted detection for $\theta_s = 45°$ are given in Table II, and the intensity profiles are shown in Fig. 3. It is of interest that this type contrast decreases with the specimen tilt angle as shown in a previous report[14] (see also Fig. 4).

Spencer et al[15] have discussed the imaging of lattice defects in the case of the band contrast and suggested a difficulty in observing the defects of bulk specimens because of a small contrast. Pitaval et al[16] reported a success of observing the defects in the backscattering mode. In the present theory, the oscillating part in the intensity change due to an inclined stacking fault can be expressed in the order of m = 0 as

$$\Delta I = \frac{\exp(-\mu_0 t_0)}{(\mu_0^2(1+w^2) - \mu_g^2)}\left[\frac{w(1-\cos\alpha)\cos\beta + \sqrt{1+w^2}\sin\alpha\sin\beta}{(1 + w^2)}\right] (D - B_d^0 w) \qquad (10)$$

where t_0 is the depth at the fault, $D = A^0 + \mu_0 B_d^0/\mu_g$ (the upper suffix 0 means the order m = 0), α is the phase change due to the fault and $\beta = 2\pi t_0\sqrt{1+w^2}/\xi_g$ (ξ_g, extinction distance). In the case of (c,1) for oblique incidence, the maximum intensity change in the depth oscillation appears at $w \neq 0$ (see Fig. 5). Furthermore, a small variation is found in the intensity profile, aside from

Table I   Absorption coefficients and ECP contrast of silicon in various treatments of core electron excitation (at 20 kV and $\theta_S = 0°$).

Conditions		μ_O	μ_g	Contrast	
w_C	s^c	$(\times 10^{-4}$ Å$^{-1})$		(220)	(%)
1	x 1/3	22.9	7.3	3.1	
2	x 0	9.1	6.7	9.7	
2	x 1	42.1	8.2	1.7	
1	x 1	50.3	8.2	1.4	
1	x 1/5	17.4	7.1	5.1	

Note: $w_C = \xi_g \ g \ q_o{}^c/k$

Table II   Contrast parameters of silicon in restricted detection for $\theta_S = 45°$ (20 kV).

Parameter	(220)	($\bar{2}$20)	(2$\bar{2}$0)
A^O	12.25	-21.03	-4.90
B_r^O	4.97	-8.53	-1.99
B_d^O	-41.02	41.02	0.0
D^O	-4.39	4.39	-4.90
A^1	-10.16	-8.06	-10.22
B_r^1	-4.53	-3.25	-4.55
B_d^1	1.29	-1.29	0.0

The unit of numerical values is 10^{-9} Å^{-1} and the tilt axis is parallel to (2$\bar{2}$0).

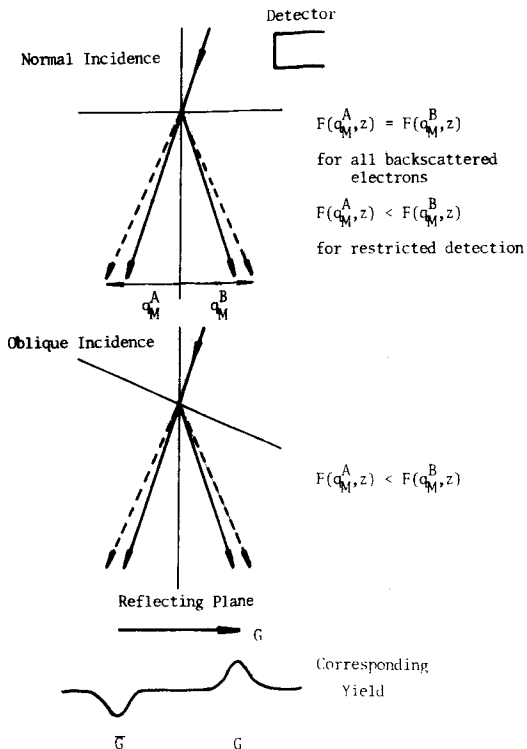Fig.2   Illustration elucidating the difference in the fraction of emerging primary electrons in the 0 and g directions.
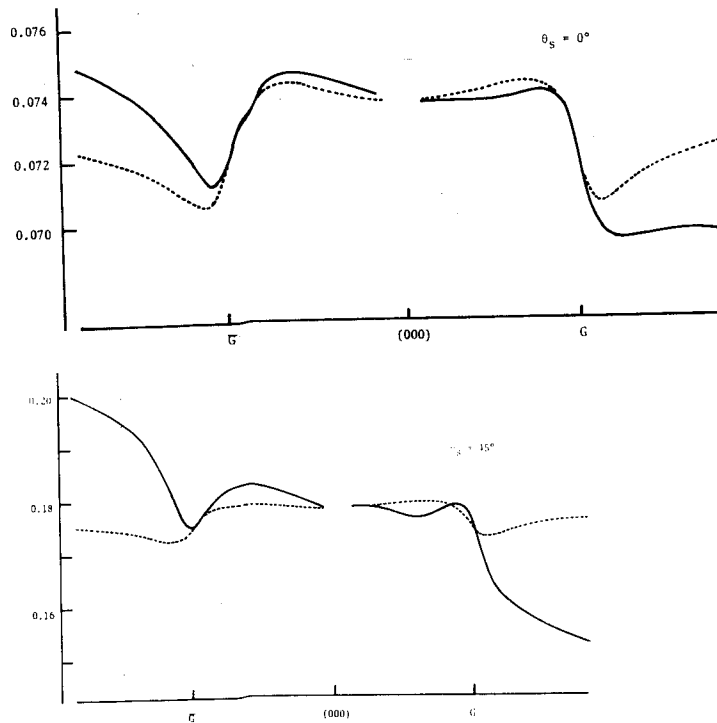
——————————, Bloch electron

············, diffuse-scattered electron.

Fig. 3 Calculated rocking curves of Si (220) reflection. The range of detection is $0 < \theta_t < 90°$ and $-90° < \phi < 90°$ for both $\theta_s = 0°$ (upper) and $45°$ (lower). The reflecting plane is parallel to the incident direction. The dotted and solid lines show g being parallel and perpendicular to the y axis, respectively.
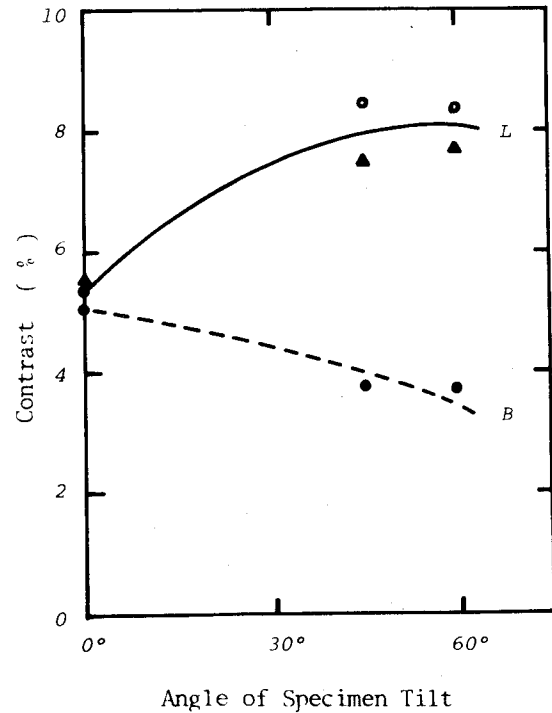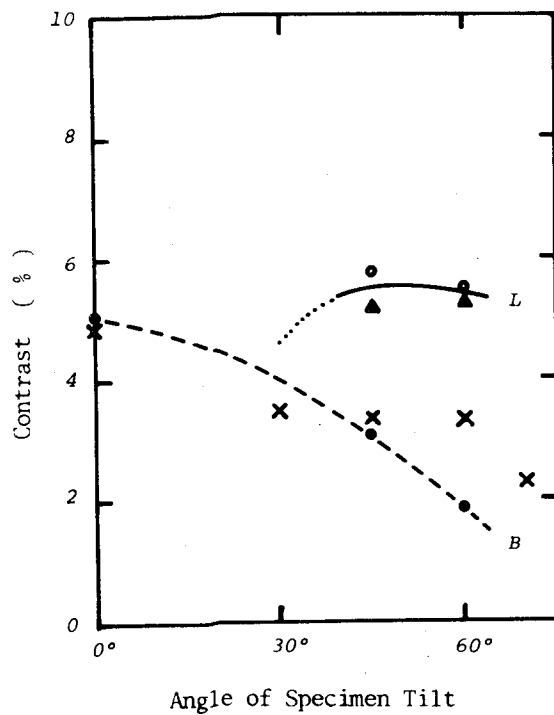

Fig. 4 Line and band ECP contrast of Si {220} reflections plotted against the angle of specimen tilt.
Left: all backscattered electrons are collected. Right: the detection is restricted. For $\theta_s = 0°$ and $45°$, the range of detection is the same as that in Fig. 3, whereas for $\theta_s = 60°$, $0° < \theta_t < 60°$ and $-90° < \phi < 90°$. L: line contrast, g is perpendicular to the tilt axis. B: band contrast, g is parallel to the axis. x indicates the mean experimental value of the band contrast[14].
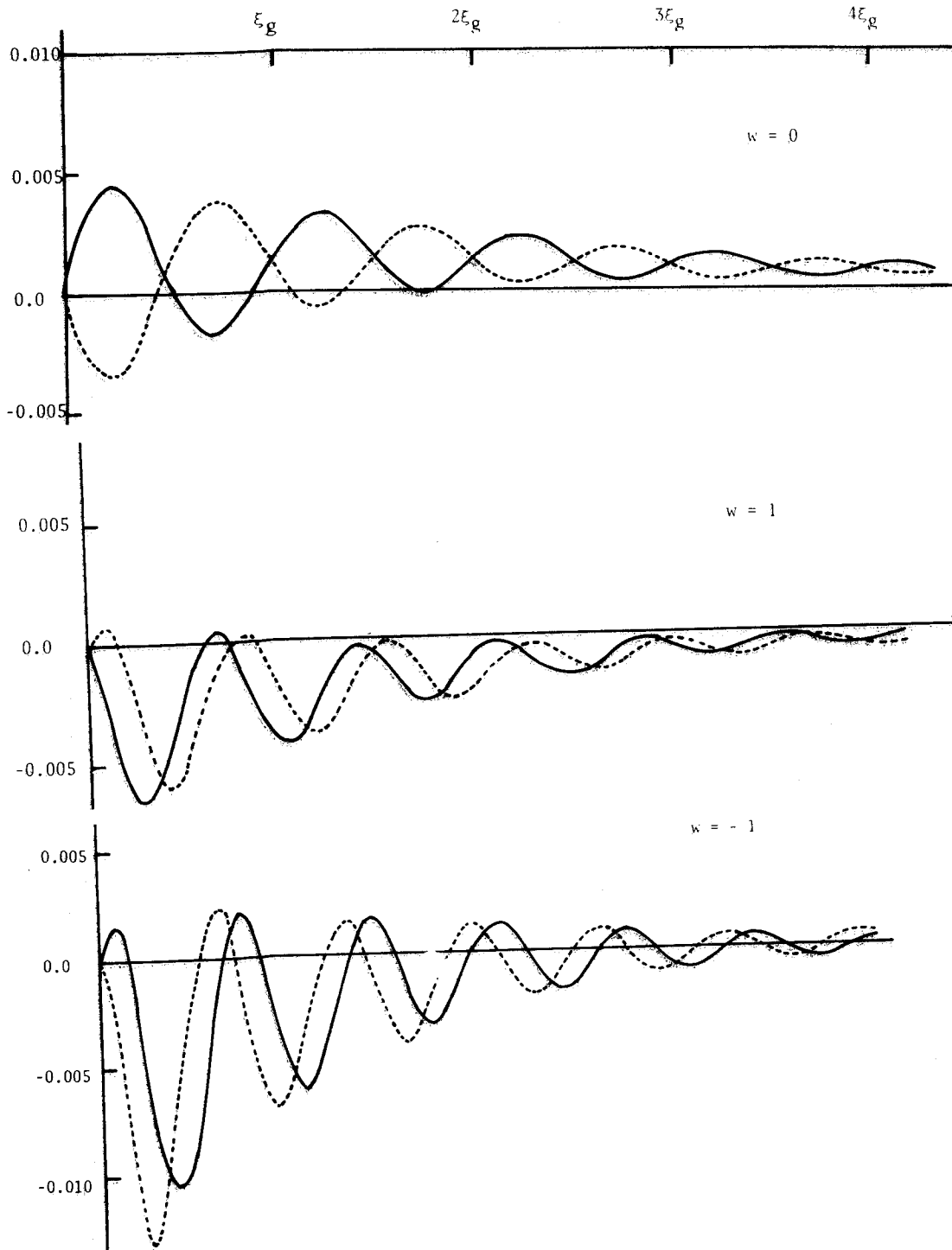
Fig. 5 Intensity profile of an inclined stacking fault in silicon.
$\theta_s = 45°$, g = (220) which is in the plus direction of the x axis.
·········, $\alpha = 2\pi/3$, ─────────, $\alpha = -2\pi/3$.

THE SCANNING ELECTRON MICROSCOPY TECHNIQUE FOR MEASURING THE LOCAL NITROGEN CONCENTRATION IN GaP

Ya.A.Golubev*, V.V.Evstropov**, B.N.Kalinin**, V.P.Lejnin*,
V.I.Petrov* and G.V.Spivak*

* Electron Optics Laboratory, Department of Physics, Moscow
  State University, Moscow, 117234, USSR
**A.F.Ioffe Physico-Technical Institute, USSR Academy of
  Sciences, Leningrad, 194021, USSR

The nuclear reaction and optical absorption techniques have been developed to determine the absolute nitrogen doping concentration in GaP crystals [1].In both cases the data measured are averaged over the doped layer and these methods do not permit to obtain the nitrogen doping profile across the layer. In this work the measurement of local nitrogen concentration in GaP LED structures is carried out by using the local CL (cathodoluminescence) data obtained in the SEM (scanning electron microscope).The method is based on determining the degree of the A-line self-absorption by substitutional nitrogen.

It has been shown [2] that in the temperature range of 77°K--130°K without self-absorption the peak intensities ratio of A-line and its phonon replication side bands A-LO and A-2LO in luminescence spectra of GaP should correspond to 1,00 : : 0,36 : 0,065.In the real case the A-line peak intensity is less due to its self-absorption in bulk material and the ratio changes (Fig.1).The degree of the A-line self-absorption or the value of the A-line relative yeild $f = I_A/I_{Ao}$ where I_A and I_{Ao} are the A-line intensities with and without the self--absorption can be defined from the experiment. I_{Ao} – from the measured peak intensities of A-LO and A-2LO lines using the known peaks ratio, I_A is the real intensity of A-line in the experiment.For the particular carrier-pair source function, particular diffusion length L and surface recombination velocity S this known value of f can be used to obtain the value of the peak absorption coefficient for A-line – α .

Such curves for the source with Gaussian distribution are shown
in Fig.2.The peak absorption coefficient is proportional to the
nitrogen concentration.For the known temperature under the beam
in the SEM that is determined from the position of the A-line
the value of this coefficient of proportionality and thus the
nitrogen concentration can be obtained [1].In this method the
shape of the crystal and the local change of nonradiative recom-
bination channel do not influence the measured value of nitrogen
concentration.The spatial resolution is limited by the volume of
diffusion and can be improved if the SEM operates in the pulse
mode [3].

Further improvement of spatial resolution can be achieved
with the help of special mathematical treatment.Under several
assumptions it is possible to represent the profile of the
nonabsorbed A-LO line intensity across the specimen in the form
of

$$I_{A-LO} = C \cdot \int \varphi(x-\xi) N(\xi) d\xi$$

where C is a constant, $\varphi(x)$ is the excess carrier density
obtained by solution of continuity equation and $N(x)$ is the
distribution of nitrogen in the specimen.Now using deconvolution
one can determine from this equation nitrogen concentration
profile across the specimen.In order to obtain the absolute
value of concentration in this case the concentration from the
CL spectra at one poi t of the specimen should be measured.The
use of this method is limited since the absolute value of the
A-LO line intensity depends not only on the local nitrogen
concentration but also on the contributions of other recombina-
tion channels.The example of application of these methods is
given in Fig.3.

References

1.E.C.Lightowlers, J.C.North and O.G.Lorimor, J.Appl.Phys.,
   45, 2191 (1974).

2.V.V.Evstropov, B.N.Kalinin and B.V.Tsarenkov, Sov.Phys.Sem.,
   (in russ.), 10, 1898 (1976).

3.G.V.Spivak, G.V.Saparin and L.F.Komolova, in SEM/77,
   Proceedings of the 10th Annual SEM Symposium, ed. O.Johari,
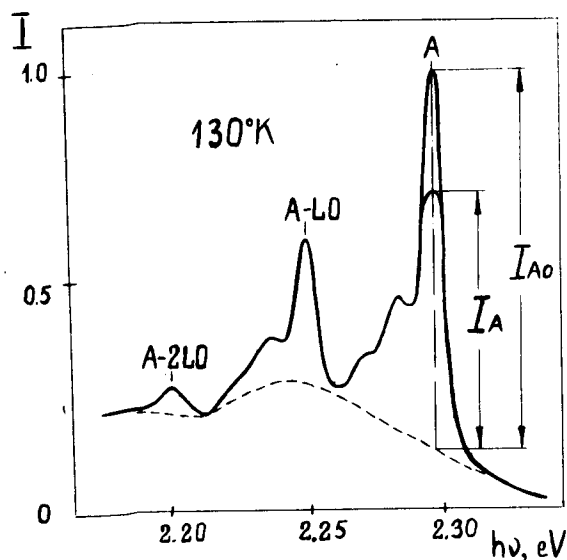   IITRI, Chicago, Ill., v.1, p.191 (1977).

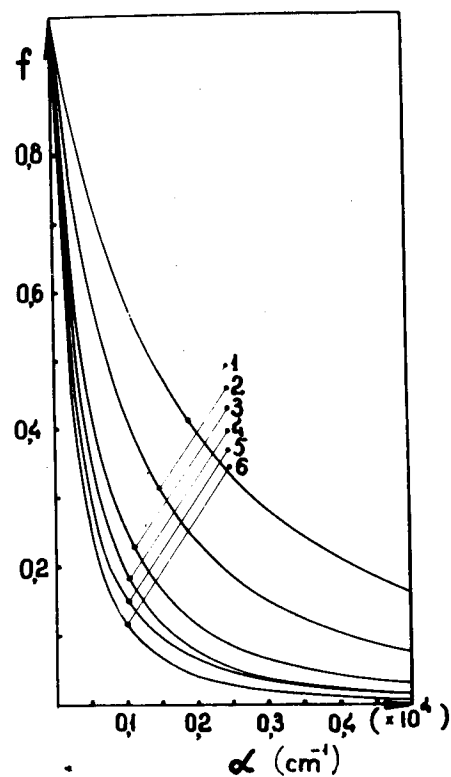Fig.1.The A-lines group in the luminescence spectra of GaP.

Fig.2.The relative yield of A-line as a function of absorption coefficient.U=10kV (1,2), 30kV(3,4), 50kV(5,6); L=1μm(1,3,5), 3μm(2,4,6); S=∞.
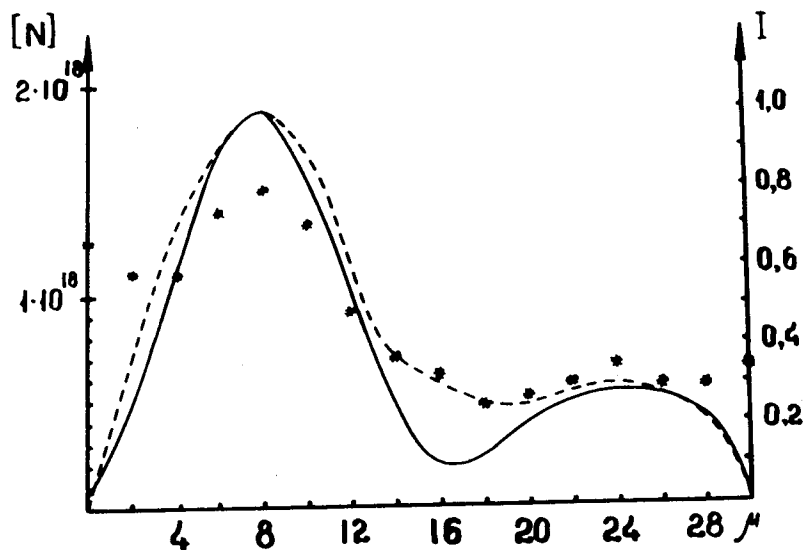

Fig.3.The nitrogen concentration profile (solid line) and the A-LO line intensity (broken line) across GaP layer.Points show the nitrogen concentration measured from CL spectra.

Color and Video Enhancement of SEM Backscattered Electron Images

by

Phillip B. DeNee[1,2,3] and Richard G. Frederickson[2]

[1]Appalachian Laboratory for Occupational Safety and Health
National Institute for Occupational Safety and Health
Morgantown, West Virginia

and

[2]Department of Anatomy
West Virginia University School of Medicine

[3]Present Address: Inhalation Toxicology Research Institute
Lovelace Foundation, Albuquerque, NM

Backscattered Electron Imaging (BSI) in the SEM has been used for the past several years to image heavy metal stained (HMS) biological tissue,[1-4] and to reveal respirable dust particles in biological tissue[4-7] and on air sampling filters.[7] A recent innovation using BSI has been a quantitative method for measuring the mass and thickness of single respirable dust particles (usually less than 5 μm in diameter)[8,9] and for measuring the amount of heavy metal stains in biological tissue preparations.[9] It was shown that for thin films, small particles or heavy metal stained biological tissue, the backscattering coefficient increases with increasing thickness and mass density, i.e., with increasing mass thickness as long as the material qualifies as a thin film.[8,9] The backscattering coefficient also increases with increasing atomic number (Z) (except for several slight fluctuations relating to a change in the A/Z ratio, where A = atomic weight).[10]   Thus, the brightness of a BSI of a thin film material is a measure of its mass thickness and atomic number.

The thickness (brightness) information can be obtained from the backscattered electron (BSE) signal by measuring (A) the brightness of the photographic image with a densitometer, (B) the height of a Y modulation curve or (C) the output current from the BSE detector. The information from any of the above techniques is in the form of a continuum of grey levels or thicknesses which is not easy to visually interpret. If the data can be digitized or put into discrete steps, grey levels or contours, it is much easier to assimilate. The device described in this report changes the grey level continuum into discrete grey levels or discrete contours as shown in Fig. 1. The input signal can range continuously from 0 to 100% (Fig. 1A) while the output will be either 1, 2, 4 or 8 selectable levels of contour mapping (Fig. 1B) or grey levels (Fig. 1C). Thus, if correctly adjusted, the output photograph will represent either thickness contours or thickness levels.

Color enhancement of the SEM image is done by (A) making a double exposure of a SEI and either a video enhanced or unenhanced BSI (using a color filter) or (B) making a multiple color exposure of selected grey level obtained by using an image analyses system.[9] Color photos will be shown in the presentation.

The equipment used in this work was a standard ETEC* Autoscan SEM equipped with a special 6 chip BSE detector[3] and a standard video signal enhancement module. The video signal enhancer was apparently designed for Secondary Electron Imaging (SEI) but was purchased for use with BSI.

The application of the technique to respirable dust particles is illustrated in the next figure. Fig. 2 shows a SEI, BSI grey scale map and contour map of an iron particle on a membrane filter.[8,9] The SEI (Fig. 2A) shows not only the particle but the background as well. The background (filter) is not seen in the BSI (Fig. 2B) since it is much lower Z than the particle except that a portion of the filter lies over the right side of the particle diffusing the image somewhat. Figs. 2C, 2D and 2E show 1, 2 and 4 grey level maps while Figs. 2F, 2G and 2H show 1, 2 and 4 level contour maps. The grey levels and contours can be easily varied by adjusting the brightness and contrast of the BSE signal before it is fed into the video signal enhancer. The resultant images are thickness or contour maps for the particle which give a three dimensional quality to the enhanced image as compared to the unenhanced image.

The application of the technique to heavy stained biological tissue is shown in the next figure. The tissue used was liver from Guinea pig. The tissue had been embedded in butoxyethanol-glycol methacrylate, thin sectioned and stained with lead citrate 30 min. and uranyl acetate 60 min.[3] Images of the same field were obtained using (-) BSI and different degrees of grey-level enhancement. Fig. 3A is an unenhanced (-) BSI which shows three different types of cells; sinusoidal lining cells; and light and dark staining liver parenchymal cells. In Fig. 3B one grey level was chosen to enhance the appearance of the more heavily stained parenchymal cells and the sinusoidal lining cells. Thus better visual discrimination can be made between two of the three cell types. In Fig. 3C the detection threshold was lowered and a different grey level was used. This enhanced the stained appearance of the sinusoidal lining cells and diminished the visualization of the parenchymal cells. In this manner a specific cell type can be brought out of a field of other cells and a more rapid differentiation can be made. Fig. 3D illustrates the appearance of the liver cells using two grey levels. The three cell types are more distinct than seen with standard (-) BSI (Fig. 3A). Each cell type possesses a readily distinguishable contrast level.

Plans are currently underway to use the individual grey levels to modulate a color T.V. monitor, thus, resulting in a real time color backscattered image. The color coding should represent real usable information such as the thickness, density and atomic number of the object and not the less practical topographic information such as is available in the color SEI, which was introduced several years ago but quickly discarded.

In conclusion, this paper introduces the technique of video and color enhancement of backscattered electron images. This technique provides visual information to the observer such as thickness, density and atomic number, which is easier to interpret than information from ordinary backscattered electron images.

---

*Mention of specific brand names is for information only and does not imply endorsement by the National Institute for Occupational Safety and Health

REFERENCES

1. P.B. DeNee, J.L. Abraham and P.A. Willard, "Histochemical Stains for the Scanning Electron Microscope--Qualitative and Semi-Quantitative Aspects of Specific Silver Stains", IITRI/SEM/1974[#], 259-266.

2. J.L. Abraham and P.B. DeNee, "Biomedical Applications of Backscattered Electron Imaging--One Year's Experience with SEM Histochemistry", IITRI/SEM/1974, 251-258.

3. P.B. DeNee, R.G. Frederickson and R.S. Pope, "Heavy Metal Staining of Paraffin, Epoxy and Glycol Methacrylate Embedded Biological Tissue for Scanning Electron Microscope Histology", IITRI/SEM/1977, Vol.II, 83-92.

4. P.B. DeNee and J.L. Abraham, "Backscattered Electron Imaging (Application of Atomic Number Contrast)", in Principles and Techniques of Scanning Electron Microscopy-Biological Applications - Vol. 5, M.A. Hayat (ed.). Van Nostrand Reinhold Co., New York, N.Y., U.S.A. 1976, 144-180.

5. P.B. DeNee, J.L. Abraham, A.H. Gelderman and G. Boyd Shaw, "SEM Identification of Biogenic Silica in Jute: Silica in Human Lung Following Exposure to Burning Jute", Proc. Microbeam Analysis Soc., Ottawa, Canada, July 1974, Abstract No. 10.

6. P. B. DeNee, "Identification and Analysis of Particles in Biological Tissue Using SEM and Related Techniques", IITRI/SEM/1976 (Part III), 461-468.

7. P.B. DeNee, "The Use of Backscattered Electron Imaging (BSI) in the Scanning Electron Microscope for the Detection of Microfibers in Airborn Dust Sample and Biological Tissue" in Symposium on Electron Microscopy of Microfibers, Proceedings of the First FDA Office of Science Summer Symposium, Penn State University, Aug., 1976, HEW Publication No. (FDA) 77-1033, U.S. Govt. Printing Office, Washington, D.C., U.S.A., 68-72.

8. P.B. DeNee, "Measurement of Mass and Thickness of Respirable Size Dust Particles by SEM Backscattered Electron Imaging", SEM/1978[##] (in press).

9. P.B. DeNee, "Semi-Quantitative Mass Measurement with SEM Backscattered Electron Imaging", in Transactions of the Eight International Conference in X-Ray Optics and Microanalysis, Summer 1978 (in press).

10. K.F.J. Heinrich, "Quantitative Electron Probe Microanalysis: A Progress Report", National Bureau of Standards Special Publication 298, U.S. Govt. Printing Office, Washington, D.C., 1968, 5-12.

[#]IITRI/SEM/1974 is used to designate Proceedings of the SEM Symposium (Om Johari, ed.), IIT Research Institute, Chicago, IL 1974.

[##]SEM/1978 is used to designate Proceedings of the SEM Symposium (Om Johari, ed.), SEM Inc. AMF O'Hare, IL, 1978
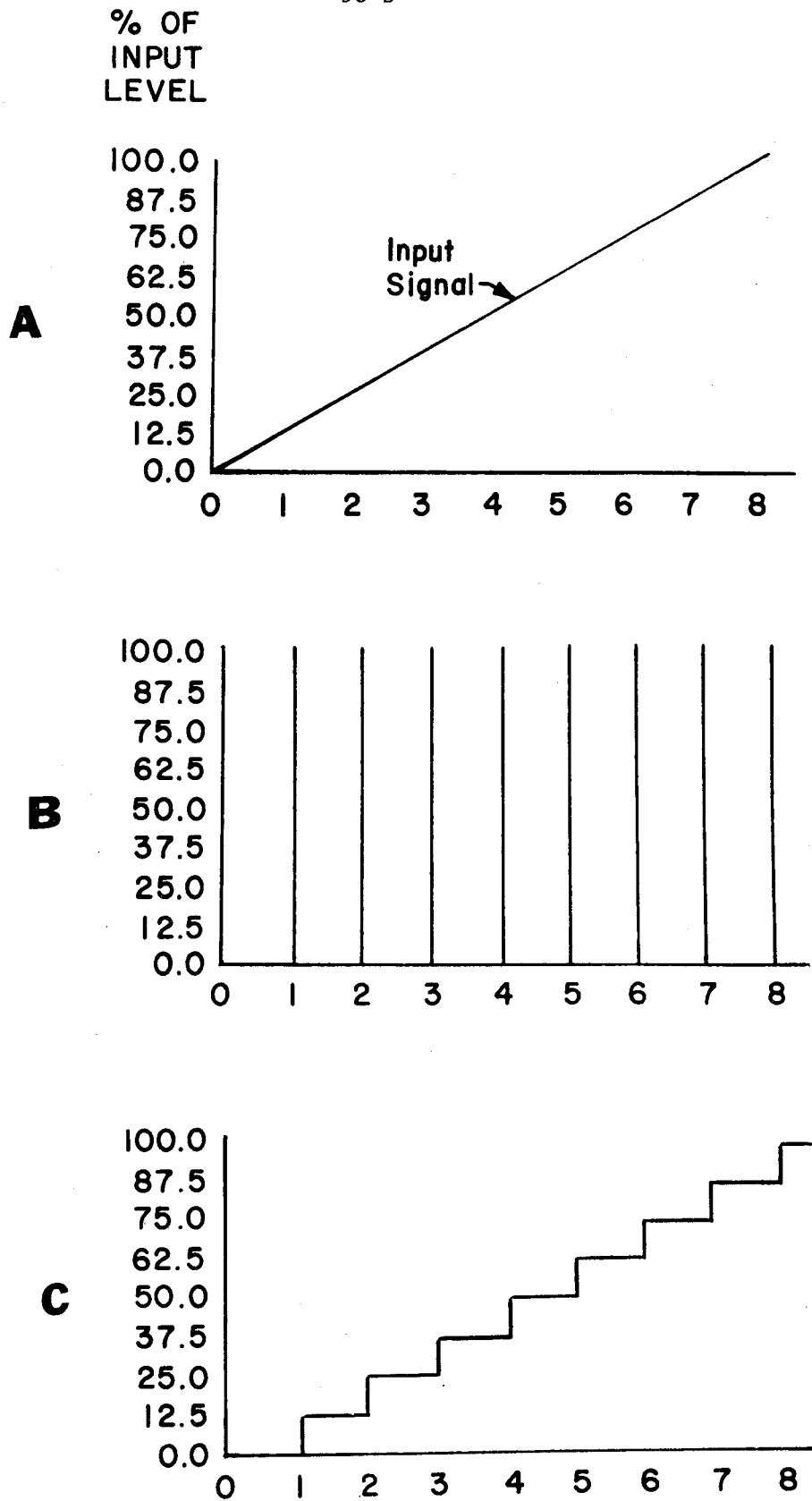
Fig. 1. This figure shows the variation in output of the video signal enhancement module as a function of (A) input when operating in either (B) the contour mapping mode or (C) the grey level mapping mode.
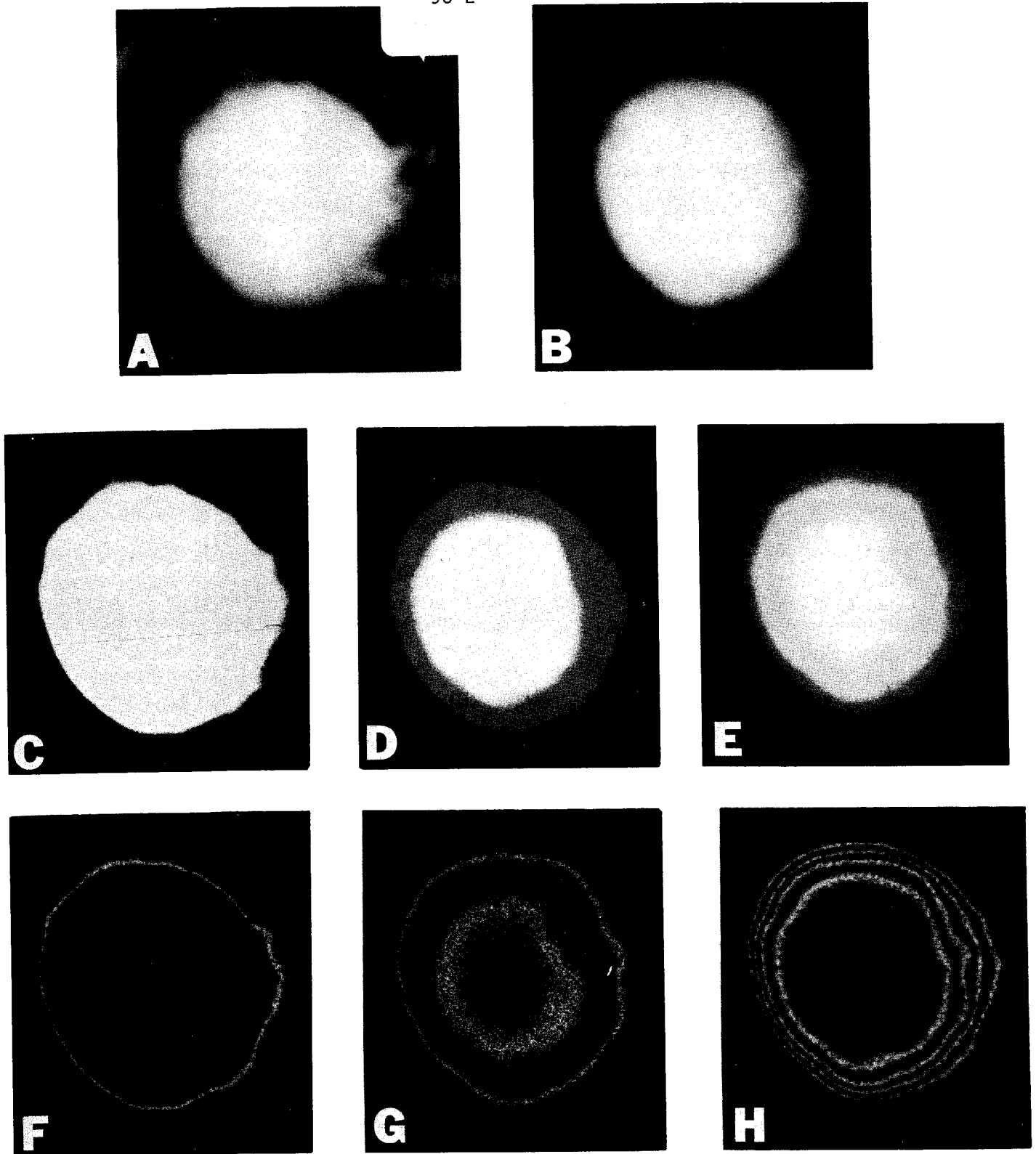
Fig. 2. Shows the secondary electron image (SEI) and the unenhanced and enhanced backscattered electron images (BSI) of an iron sphere on a membrane filter. Width of particle is 10μm in SEI and BSI. (A) SEI, (B) BSI, BSI grey level maps (C) 1 level (D) 2 levels (E) 4 levels, BSI contour maps (F) 1 level (G) 2 levels and (H) 4 levels. Note that there is a slight difference in the size of the enhanced images which resulted from a slight shift in output from the BSE detector.
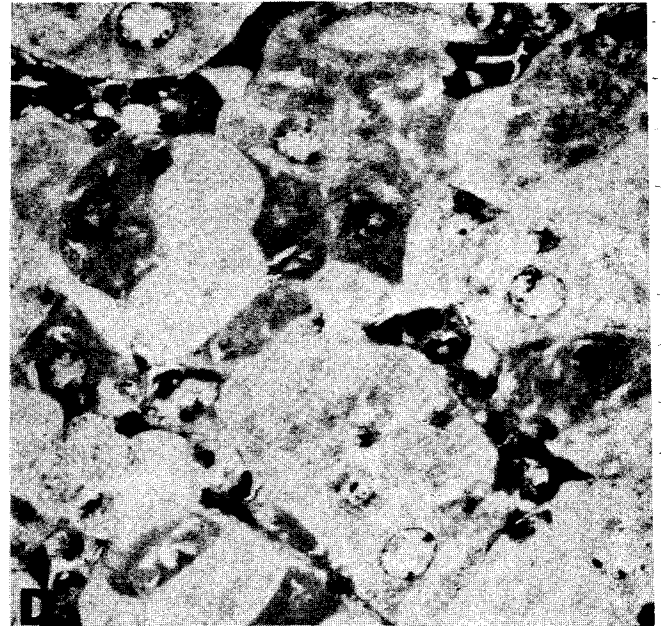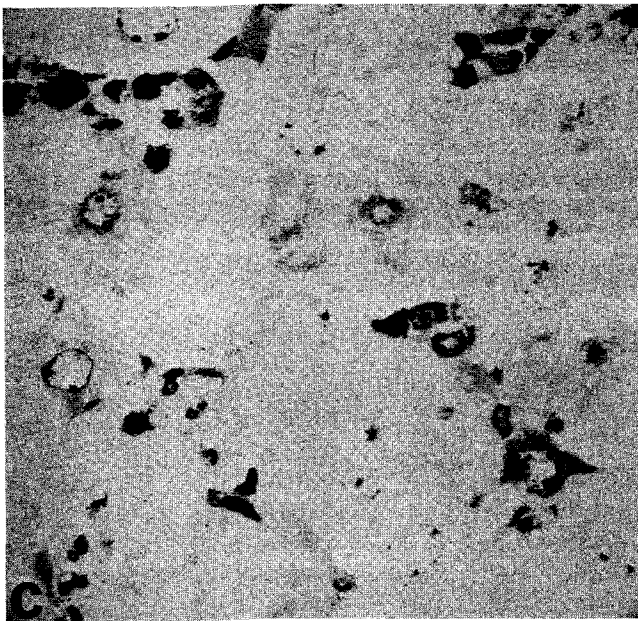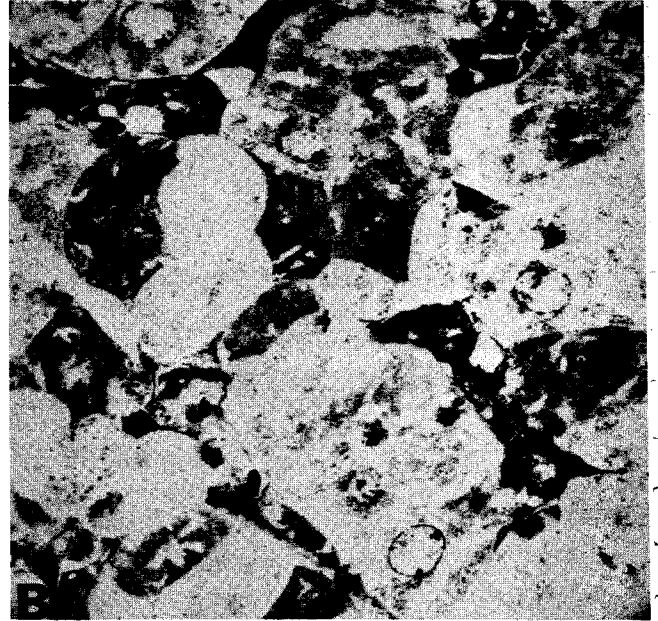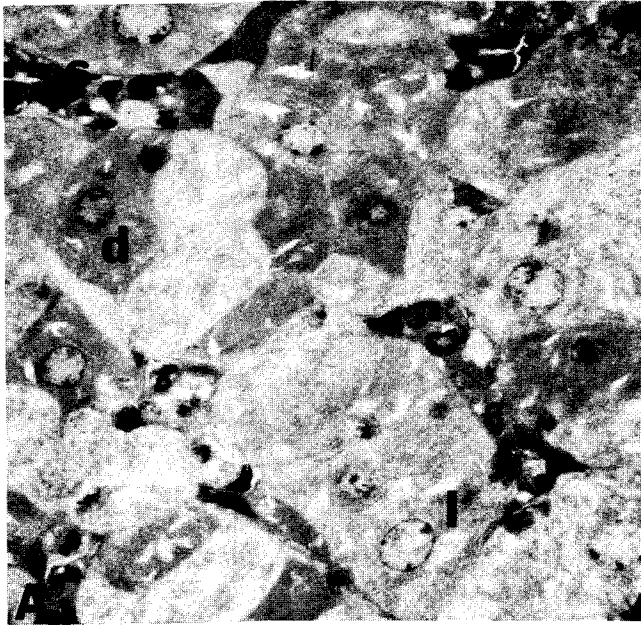
Fig. 3. Guinea pig liver embedded in butoxyethanol-glycol methacrylate (0.5 μm section) and stained with uranyl acetate (60 min) and lead citrate (30 min.).
(A) unenhanced (-) BSI, light(l) and dark (d) parenchymal cells and sinusoidal lining cells (s) are present; (B) (-) BSI, 1 grey level with threshold increased;
(C) (-) BSI, 1 grey level with threshold decreased; (D) (-) BSI, 2 grey levels. The enhanced images with grey level mapping (B, C and D) provide improved visualization of the different cells. Bar = 0.1 mm. ⟵⟶

SCANNING ELECTRON MICROSCOPY OF ANCIENT GEOLOGICAL FLUIDS AND THEIR CRYSTALLIZATION PRODUCTS

William C. Kelly
Bruce E. Nesbitt
Frederick W. Metzger
Eric J. Essene

Department of Geology and Mineralogy
The University of Michigan
Ann Arbor, Michigan, 48109

Any mineral crystallized from or in the presence of a fluid phase normally retains microscopic samples of that phase in the form of fluid inclusions that are typically 5-100 μm in size. Trapped globules of igneous melts either crystallize or quench to beads of glass upon cooling of their crystal host. Trapped inclusions of hot aqueous solutions (Figure 1) contract upon cooling, normally nucleating a vapor phase and precipitating salts (daughter minerals). Optical methods are well established for heating and freezing tests of such inclusions and are being routinely applied to determine fluid salinities and original pressure-temperature ⌐onditions during crystallization of the host mineral, but heretofore it has been extremely difficult to identify the daughter minerals in these inclusions by optical microscopy. Such information is potentially of great value in setting compositional limits on the original, mineral-forming fluid.

The scanning electron microscope provides a powerful tool for rapid identification of these daughter minerals in fluid inclusions. Conventional optical methods are first used to establish the abundance and general character of inclusions

present in polished plates of the host crystal. These plates are then chipped or cleaved and the freshly broken surfaces surveyed under the SEM. The inclusions appear as pits and, upon enlargement, superb views of the contained daughter minerals are obtained (Figure 2). The cleavage and morphology of the daughter minerals can be studied at various angles. Using the SEM in a spot mode, the electron beam is positioned on individual daughter crystals and their characteristic X-ray spectra obtained using the EDA system. Spectra of known compounds are compared with those of the unknowns under constant operating conditions. The resulting morphological and chemical informations, coupled with previous optical observations, is usually sufficient to specify or at least limit the daughter mineral identity.

The new procedure is illustrated with daughter minerals in samples from three different localities. Using scanning electron microscopy nine previously unidentified daughter minerals were recognized in complex inclusions from a fluorite mine in Colorado. The identification of a fibrous daughter mineral from a California gold mine as dawsonite ($NaAl(CO_3)(OH_2)$) by scanning electron microscopy was confirmed by X-ray diffraction studies. In the companion paper (Nesbitt and Kelly), the value of the method is demonstrated by an in-depth study of inclusions in the famous "carbonatite" locality of Magnet Cove, Arkansas.

Fig. 1 - Optical view of supersaline fluid inclusions in polished plate of
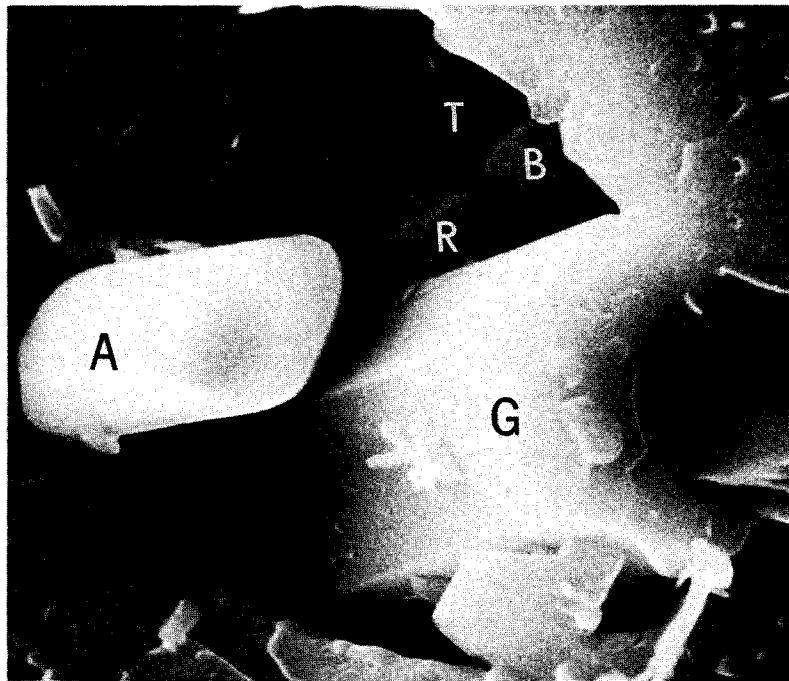Emmett mine fluorite.   200X.

Fig. 2 - SEM view of opened fluid inclusion in Emmett mine fluorite.   Exposed
daughter crystals include gypsum (G), anorthite (A), barite (B),
rhodochrosite (R) and thenardite (T).   6000X.

APPLICATION OF SCANNING ELECTRON MICROSCOPY
TO INCLUSIONS IN CARBONATITES

Bruce E. Nesbitt and William C. Kelly

Department of Geology and Mineralogy
The University of Michigan
Ann Arbor, Michigan, 48109

"Carbonatites" are calcite-rich rocks of worldwide occur-
rence that are mined for their rare earth, base metal and other
mineral content. Their origin is controversial. Early workers
believed they are metamorphosed limestones whereas it is generally
accepted today that these rocks form by crystallization of igneous
melts (magmas) of unusually high carbonate content. However,
little is known of the quantitative composition of such metls,
of their progressive changes during crystallization and of vola-
tile phases associated with carbonatite magmas. The minerals in
carbonatites commonly contain traces of the original melt as
microscopic fluid inclusions which could potentially provide the
needed information, but these are typically less than 50 μm in
size and difficult to study by optical methods.

The scanning electron microscope (SEM) methods developed for
fluid inclusion study (see companion abstract by Kelly and
others) offers a breakthough in terms of carbonatite investiga-
tion. The classical carbonatite locality at Magnet Cove, Arkansas
was selected as a test case for in-depth application of these new
techniques.

A variety of fluid inclusions occur in minerals of the
Magnet Cove carbonatite, some requiring refinements of the SEM

methods. Inclusions in calcite could be easily exposed by cleaving the mineral while other minerals, such as apatite and monticellite ($CaMgSiO_4$), lack cleavage and could only be fractured. Many of the crystalline daughter phases within magmatic inclusions (Figure 1) do not display good crystal form and this necessitated heavier reliance on semi-quantitative energy dispersive analysis for identifications. For example, a calcium silicate was recognized in many inclusions by qualitative study, but only after careful semi-quantitative work could it be specified as Ca_2SiO_4 (probably the polymorph larnite).

Excellent primary melt inclusions occur in apatite and monticellite and these offer the first direct information on the composition of a carbonatite magma. These inclusions represent minute samples of the original melt trapped during crystallization of their host minerals. As originally trapped, the molten carbonatite was homogeneous but, upon cooling, crystallized to form several discrete daughter phases including calcite, magnetite, larnite and other minor silicates. In addition, each inclusion contains a small amount of H_2O liquid and CO_2 vapor which occupy the space created by contraction of the melt during its crystallization.

Based upon the determined compositions of the daughter phases and estimates of their relative volumes in the inclusions, the bulk composition of the carbonatite magma was approximately 49.7 wt% CaO, 16.7% CO_2, 15.7 SiO_2, 11.4% H_2O, 4.4% FeO + Fe_2O_3, 1.1% P_2O_5 and 1.0% MgO. These same data reveal, for the first time, that a carbonatite melt has a bulk density of about

2.3-2.3 g/cc, and this is geologically significant. Such a light melt would separate rapidly from any denser parent material and be driven into overlying materials by buoyant forces alone, and this may explain frequent observations of forceful intrusion reported in the literature. Furthermore, the Magnet Cove carbonatite as a whole is somewhat depleted in heavier minerals like magnetite when compared with their abundance in the inclusions and this is compatible with gravitative settling of these heavier phases in the low density melt once the magma was emplaced.

Inclusions in the mineral apatite indicate that a separate, immiscible fluid composed of supercritical CO_2 coexisted with the carbonatite magma. From the measured density of this CO_2, maximum total pressures at the time of its initial entrapment are calculated as 450 bars. This sets a maximum geological depth of 1.5 Km on the apatite crystallization, supporting earlier proposals of a shallow, subvolcanic setting for carbonatite emplacement.

Numerous secondary inclusions (Figure 2) in the Magnet Cove calcite contain an intriguing variety of daughter minerals including some 19 alkali, alkaline earth and rare earth carbonates, sulfates and chlorides few of which are known as macroscopic phases in the complex. These inclusions, formed by the filling of fractures by post-crystallization fluids, reveal a complex history of cooling and dilution of post-crystallization hydrothermal fluids. Chemically the fluids shift from a high temperature Ca, K, Na, S, Cl, Fe, and Mg brine to a much simpler,

low temperature solution with Ca, Sr, Ce and La. This shift in
the character of the hydrothermal brine probably reflects
gradual mixing of meteoric water with the original hydrothermal
fluid.

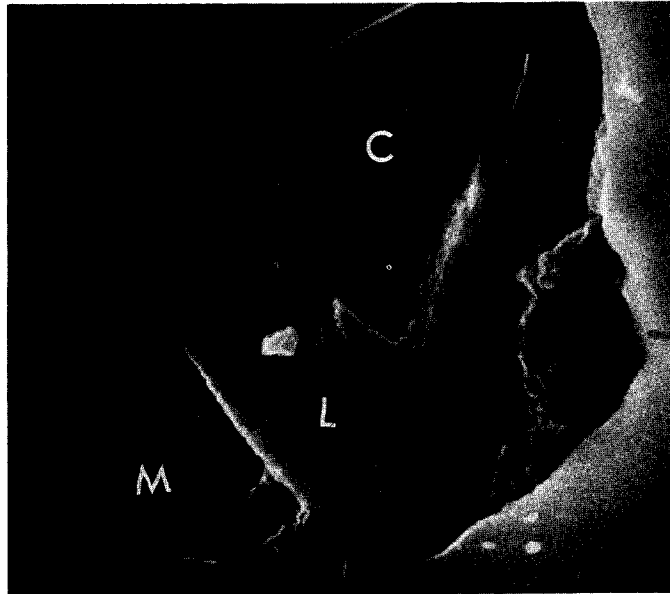Fig. 1 - SEM view of solidified melt inclusion in polished surface of monticellite from Magnet Cove. Daughter minerals include calcite (C), larnite (L) and magnetite (M). 7000X.
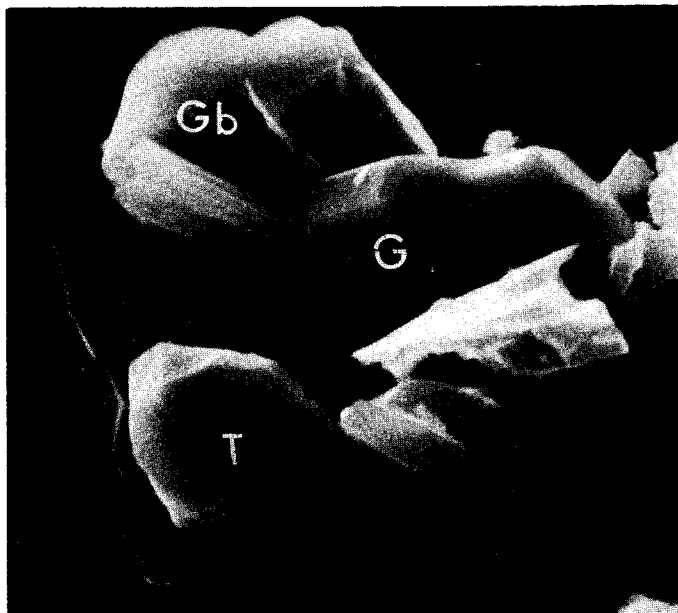

Fig. 2 - SEM view of opened fluid inclusion in calcite from Nagnet Cove. Daughter crystals include gypsum (G), glauberite (Gb) and thenardite (T). Void space was occupied by aqueous solution lost on cleaving the calcite. 5000X.

TYPE II MAGNETIC DOMAIN CONTRAST

For

PERMALLOY AND AMORPHOUS MAGNETIC FILMS

H. C. Tong

IBM Corporation
General Products Division
San Jose, California

ABSTRACT

The observations of type II magnetic domain contrast for magnetic bulk crystalline solids by using the SEM technique have been reported since 1969[1]. The systematic research was not published until 1973[2,3,4]. Recently, this technique has been applied to observe type II magnetic domain contrast of amorphous solids[5]. This paper will report a further application of the techniques to observe domain contrasts of magnetic films.

Type II magnetic contrast in the SEM observation results from the interaction of the Lorentz force and the incident electrons inside the magnetic domains. Therefore, this technique is sensitive to the angle between the incident electron beam and the surface normal, the magnetization and directions of the component $\bar{B}$ parallel to the sample surface. Type II magnetic domain contrast exists whenever the following condition holds:

$$(\vec{e} \times \vec{n}) \cdot (\vec{b}_i - \vec{b}_j) \neq 0$$

where $\vec{e}$, $\vec{n}$, $\vec{b}_i$ and $\vec{b}_j$ are unit vectors parallel to directions of the incident electron beam, the surface normal, and the magnetization of the domains i and j.

Both Permalloy films and $(Co_{94}Fe_6)_{80}B_{20}$ amorphous magnetic films were studied. In contrast to bulk samples, the observation of the domain contrast was found much easier for polycrystalline or amorphous film samples since there are no other contrast mechanisms such as surface roughness, scratches, grain orientation, and the contrast from crystal twin faults. Both permalloy and $(Co_{94}Fe_6)_{80}B_{20}$ films have

magnetization much less than that of Fe-3% Si samples, but their domain contrast could be observed easily and clearly. Evidence of magnetic anisotropy was found for these films. The domain walls were 180°C walls. They were parallel to their easy axis, which is a natural consequence of minimizing the magnetostatic energy.

The pair ordering mechanism was used to explain the origin of the magnetic anisotropy for strain-free crystalline materials[6]. The anisotropy origin for the amorphous films is not clearly understood yet. It is not unreasonable to consider the origin of the amorphous film to be pair ordering also, since the $(Co_{94}Fe_6)_{80}B_{20}$ has been reported to have a zero magnetostriction coefficient[7].

References:

1. J. Philibert and R. Tixier, Micron 1, 174 (1969)

2. D. J. Fathers, J. P. Jakubovics, and D. C. Joy, Phil. Mag. 27, 765 (1973)

3. D. E. Newbury, H. Yakowitz, and R. L. Myklebust, Appl. Phys. Letters 23, 488 (1973).

4. D. J. Fathers, J. P. Jakubovics, D. C. Joy, D. E. Newbury, and H. Yakowitz, Phys. Stat. Sol. (a) 20, 535 (1973)

5. H. L. Leamy, S. D. Ferris, G. Norman, D. C. Joy, R. C. Sherwood, E. M. Byorgy, and H. S. Chen, Appl. Phys. Letters 26, 259 (1975)

6. L. Neel, J. Phys. Radium 15, 225 (1954)

7. R. C. O'Handley, L. I. Mendelsohn and E. A. Nesbitt, IEEE Transactions on Magnetics, 12, 942 (1976)

AMR CORPORATION

160 Middlesex Turnpike
Bedford, Massachusetts 01730

Contact: K. A. Lindberg, (616) 275-1400

Product Line: Manufacturer and distributor of scanning electron microscopes and a complete line of accessories.

Sales Offices:
Mid Atlantic--George Russell and Ken Benoit
Mid Eastern--Parker Brinkman
Southeast--Floyd Hunsaker

APPLIED RESEARCH LABORATORIES

9545 Wentworth Street
P. O. Box 129
Sunland, California 91040

Contact: Bryce I. Hanna, (213) 352-6011

Product Line: Electron microprobes, ion microprobes, optical emission spectrometers, x-ray fluorescence instrumentation.

Sales Offices:
239 Newburyport Turnpike, Topsfield, MA 01983, (617) 887-8995
20200 W. Outer Drive, Dearborn, MI 48124, (313) 565-6633
842 Hamilton Mall, Allentown, PA 18101, (215) 434-7441

BABCOCK AND WILCOX RESEARCH CENTER

Alliance Research Center
P. O. Box 835
Alliance, Ohio 44601

Contact: Alex S. Miller, (216) 821-9110 Ext. 360

CAMECA INSTRUMENTS, INC.

37 Brownhouse Road
Stamford, Connecticut   06902

Contact: Robert J. Hessler, (203) 348-5252

Product Line: Electron probe analyzers, scanning electron micro-
   scopes, combination SEM/EMP instruments and ion mass analyzers.
   The IMS-800, a new SIMS instrument, has the features of improved
   performance at a lower price. The new IMS is the only direct
   imaging instrument available. The CAMECA MBX is a flexible
   combination SEM/EMP with an extensive array of accessories.

Sales Office:
   Robert D. Boies, P. O. Box 262, Reedley, CA   93654

EDAX INTERNATIONAL, INC.

P. O. Box 135
Prairie View, Illinois   60069

Contact: Luis F. Lopez, (312) 634-0600

Product Line: Manufactures Energy Dispersive X-Ray Analysis Systems
   for X-ray microanalysis in SEMs, TEMs, electron probes, as well as
   Energy Dispersive X-ray fluorescence Spectrometers. System
   configurations from basic qualitative to fully automated quantita-
   tive (with computer control and data processing) are available,
   including an automated W.D./E.D. system with stage and spectrometer
   controls.

Sales Offices:
   F. Martin, P. O. Box 547, New Rochelle, NY   10802 (914) 576-3117
   V. Balmer, 637 Sunnyside Rd., Vermilion, Ohio   44089 (216)967-4148
   D. Epley, P. O. Box 397, Orinda, CA   94563 (415) 254-8685
   J. Moore, P. O. Box 2253, Boulder, CO   80306   (303) 443-3610

EG and G/ORTEC - MATERIALS ANALYSIS DIVISION

100 Midland Road
Oak Ridge, Tennessee   37830

Contact: Michael J. Kirchoff, (615) 482-4411 Ext. 500

Product Line: Energy dispersive systems for electron optical
   microscopes of all types. Wavelength Dispersive System electronics.
   Backscattered Electron Detection Systems.

Sales Offices:
   Val Johnson, P. O. Box 1678, Boulder, CO   80306 (303) 449-5933
   Gene Embry, P. O. Box 631, Cary, NC   27511 (919) 467-8028
   Charles Thomas, 24222 Via Luisa, Mission Viejo, CA 92675 (800)251-9732
   Nick Alen, 5257 Arquilla Dr., Richton Park, IL 60471 (800)251-9732
   Bob Bardorf, P. O. Box 3355, Oak Ridge, TN 37830 (615) 482-9072
   Tim Bates and Jacqueline Rams, Suite 311, 11800 Sunrise Valley Dr.,

ETEC CORPORATION

3392 Investment Boulevard
Hayward, CA   94545

Contact: Mrs. P. J. Breton, (415) 783-9210

Product Line: High performance electron microprobes and scanning
  electron microscopes. Modular design allows alternative configura-
  tions to be offered with a wide range of retrofittable accessories.
  Instruments are available for manual operation, with automated
  control through dedicated minicomputers, with shielding for
  imaging and analysis of radioactive materials, and for laboratory
  and manufacturing electron beam lithography. Microbeam products
  include: Autoscan, Omniscan, Autoprobe, LEBES, Vistascan,
  Viewpoint, Biosea, and ADRES.

Sales Offices:
  Midland Park, NJ, (201) 444-4446
  Des Plaines, IL, (312) 297-0114
  Alexandria, VA, (703) 549-1660
  Atlanta, GA   (404) 962-0402
  Houston, TX, (713) 488-3562

INTERNATIONAL SCIENTIFIC INSTRUMENTS, INC.

3255-6C Scott Blvd.
Santa Clara, California   95050

Contact: Wim Derksen, (408) 249-9840

Product Line: Scanning Electron Microscopes with a full complement
  of accessories including WDX spectrometers. The ISI SEMs include:
  Alpha-9, Super II, Super IIIA, ISI-60, and System-100. A complete
  line of scanning electron microscopes suited for any application
  and budget.

Sales Offices:
  Bill Maguire, 795 N. Mountain Rd., Newington, CT (203) 246-5639
  Mike McCarthy, 415 W. Golf Rd., Suite 37, Arlington Heights, IL
     (312) 437-7790
  Dana Kelley, 6655 Hillcroft/ Suite 100, Houston, TX (713)777-0321
  Rob Bromelow, Santa Clara
  Robert Turcotte, 4633 Seminary Rd. #301, Alexandria, VA (703)751-7761

JEOL U.S.A. INC.

477 Riverside Avenue
Medford, Massachusetts 02155

Contact: Robert T. Santorelli, (617) 391-7240

Product Line: Manufacturer of scanning electron microscopes,
   transmission electron microscopes, scanning electron microprobes,
   and electron energy loss spectrometers.

Sales Offices:
   R. Steiner, Chicago, IL (312) 825-7164
   Jack Francis, Cincinnati
   Jeff Wolfe, Pittsburgh
   James Sealey, Ridge Instruments, Tucker, GA
   Jean-Pierre Slakmon, Sequelec Ltd., 5925 Monkland Avenue, Montreal,
      Quebec, Canada
   Thomas Gildea, Boston
   Ray Gundersdorff, Washington, D.C.
   Roland Marti, Los Angeles
   Thayer Brickman, SFO

KEVEX CORPORATION

1101 Chess Drive
Foster City, CA 94404

Contact: Henry S. Culver, (415) 573-5866

Product Line: Analytical systems for X-ray energy spectrometry,
   wavelength dispersive X-ray spectrometry and electron energy
   spectrometry. Kevex detector/cryostats and analytical spectrometer
   systems are compatible with all electron microprobe, scanning
   electron microscopes and transmission electron microscopes in
   current production. Systems are available for both qualitative
   and quantitative analysis.

Sales Offices:
   Fred Luehrs, 9410 Island Road, North Ridgeville, OH 44039
   David Janson, Toktela, Inc., Box 41 Upperville, VA 22176
   John Scott, 16 Higate Rd., Chelmsford, MA 01824 (617) 256-4961
   APTEC Engineering, Ltd., 4251 Steeles Avenue West, Downsview,
      Ontario, Canada M3N 1V7 (416) 661-9722
   George Kladnik, Foster City

WALTER C. McCRONE ASSOCIATES, INC.

2820 South Michigan Avenue
Chicago, Illinois 60616

Contact: Ian M. Stewart, (312) 842-7100

Product Line: Analytical services in desciplines such as:
pharmaceuticals, forensic sciences, contamination control,
metallography, air and water pollution, painting and document
authentication, and corrosion. Analytical tools available:
electron and ion microprobes, TEM, SEM, EMMA, ESCA, XRD, XRF,
GC-MS, IR-UV, and optical microscopy.

MICRON INC.

P. O. Box 3536
Wilmington, Deleware 19807

Contact: James F. Ficca, Jr., (302) 998-1184

Product Line: Analytical services, Scanning Electron Microscopy,
Electron Probe X-Ray Microanalysis, Electron Spectroscopy (ESCA),
X-ray Diffraction, etc.

MICROSPEC CORPORATION

265-G Sobrante Way
Sunnyvale, California 94086

Contact: Richard C. Wolf or William D. Donnelly, (408) 733-3540

Product Line: WDX-210 wavelength dispersive x-ray spectrometer
systems. X-ray microanalysis systems for use as accessories on
scanning electron microscopes and other electron beam instruments.
Capable of quantitative x-ray analysis of all elements down to
beryllium, atomic number 4. Unique design permits attachment to
most SEM electron columns without interference to other detectors
or operational modes.

3M COMPANY, ANALYTICAL SYSTEMS

Building 209-B
3M Center
St. Paul, Minnesota 55101

Contact: Thomas W. Kenny, (612) 733-0606

Product Line: Ion Scattering Spectrometer (ISS) and Secondary Ion
  Mass Spectrometer (SIMS) are separate or combined spectrometers
  used for chemical analysis of surfaces. Offered in full systems
  with vacuum or as complete systems for attachment to customer's
  existing vacuum. MiniBeam Ion Gun Systems also offered.

Sales Offices:
  Gerald H. Rosenthal, 15 Henderson Dr., P. O. Box 76, West Caldwell,
    NJ 07006, (201) 575-2123
  Robert W. Geiger, P. O. Box 460, Noblesville, IN 46060
  Paul B. Clark, 346 Drexel Avenue, Ventura, CA 93003, (213) 726-6417

THE PERKIN-ELMER CORPORATION

411 Clyde Avenue
Mountain View, California 94043

Contact: Ned Shikashio, (415) 961-0461

Product Line: Transmission and scanning electron microscopes and a
  complete line of accessories.

Sales Offices:
  15 Firstfield Road, Gaithersburg, MD, (301) 840-1650
  328 Eisenhower Lane, Lombard, IL (312) 495-9440
  1110 Los Alamitos Boulevard, Los Alamitos, CA (213) 596-2512
  Montreal, Canada, (514) 735-1121

PHILIPS ELECTRONIC INSTRUMENTS, INC.

85 McKee Drive
Mahwah, New Jersey 07430

Contact: J. D. Rodgers, (201) 529-3800

Product Line: Electron optical instrumentation, electron energy
  analyzers, and x-ray analytical instrumentation.

Sales Offices:
  Main Line Professional Building, Suite A 1104, Rt. 130, Cinnaminson,
    NJ, (609) 829-4454
  7525 Long Avenue, Skokie, IL 60076, (312) 676-1714
  11141 Georgia Avenue, Suite 210, Silver Spring, MD (301) 933-3002
  3000 Scott Boulevard, Suite 113, Santa Clara, CA 95050 (408)247-5333
  3760 Cahvenga Boulevard W., Suite 101, North Hollywood, CA 91604
    (213) 980-2884

PHYSICAL ELECTRONICS INDUSTRIES, INC.

6509 Flying Cloud Drive
Eden Prairie, Minnesota 55344

Contact: Thomas J. Swanson, (612) 941-5540 Ext. 513

Product Line: ESCA/Auger electron spectrometers, scanning auger
  microprobes, thin film analy ers, secondary ion mass spectrometers,
  specialized combination systems, and a broad range of components
  including electron energy analyzers, sputter-etching systems, specimen
  manipulators, x-ray generators, UV sources, and sample introduction
  stages. Also operates an analytical service laboratory for custom
  surface analysis.

Sales Offices:
  960 S. Springfield Avenue, Springfield, NJ 07081 (201) 376-3650
  1550 Northwest Hwy., Suite 108-E, Park Ridge, IL 60068 (312)297-7730
  324 N. Central Expy., Richardson, TX 75080 (214) 231-8661
  1922 The Alameda, San Jose, CA 95126 (408) 247-7767
  570 Kelley Boulevard, North Attleboro, MA 02760 (617) 695-7504
  7300 Ritchie Hwy., Glen Burnie, MD 21061 (301) 761-3053
  655 Deep Valley Drive, Rolling Hills Estates, CA 90274 (213) 377-7750

PRINCETON GAMMA-TECH

Box 641
Princeton, New Jersey 08540

Contact: Chellie Goldberg, (609) 924-7310

Product Line: X-ray energy dispersive and x-ray fluorescence
  microanalysis systems. An application laboratory and extensive
  program library.

Sales Offices:
  Richard Stancher, Princeton, NJ
  Tom Griffin, 701 Morewood Pkwy., Rocky River, OH 44116 (216)331-0120
  Fred Feeley, Box 4319, Thousand Oaks, CA 91359 (805) 497-2427
  Joe Piersante, (404) 992-3207

QBI INTERNATIONAL

2034 Golden Gate Avenue
San Francisco, California 94115

Contact: Quentin A. Brown, (415) 929-1622

Product Line: Signal processors for the scanning electron microscope
  and STEM. Video systems for the electron microprobe. X-ray systems
  for the electron microprobe. Crystals and detectors. Stage and
  goniometer drive systems. Computer control of the SEM or electron
  microprobe. Computerised data acquisition systems.

Sales Office:
  Box 6A, Russell Road, Bloomington, IN, (812) 336-6244

CHARLES M. TAYLOR CO.

P. O. Box 7087
Stanford, California 94305

Contact: Dr. Charles M. Taylor, (415) 497-3479 or (408) 245-4229

Product Line: Different types of multi-element standards for micro-
    beam analysis by SEM, microprobe, and ion probe using energy,
    wavelength, and mass spectrometers. The standards available exceed
    135 different metals, alloys, or compounds. Bence-Albee standards
    are available. Also supply sample holders for ARL-EMX and ARL-
    EMX-SM stages and many types of sample holders and polishing jigs
    for sample preparation. Offer analytical services to customers
    desiring electron beam microprobe analysis, MAC-5 instrument.

TRACOR NORTHERN

2551 West Beltline Highway
Middleton, Wisconsin 53562

Contact: Tyler North, (608) 831-6511

Product Line: Wide range of data processing instrumentation for
    qualitative and quantitative X-ray analysis. Products include
    data acquisition, reduction and automation instruments for electron
    microprobe, SEM, TEM and STEM. Featuring simultaneous EDS/WDS
    acquisition/reduction; beam control allowing for digital mapping,
    line scans and other digital image processing. Other products are
    used in nuclear, optical, signal averaging and medical applications.

Sales Offices:
    1430 Danzig Plaza #110, Concord, CA 94520
    Technical Instrument Co., Suite 333, 13612 Midway Road, Dallas, TX
        75240
    Scientific Systems Sales Corp., 6901 Jericho Tpk., Syosset, NY
        11791, (516) 921-3737
    Contemporary Science, Inc., P. O. Box 205, Mt. Prospect, IL 60056,
        (312) 255-3793
    Pulcir, Inc., P. O. Box 357, Oak Ridge, TN 37830, (615) 483-6358
    Buhrke Company, 2180 Sand Hill Road, Suite 160, Menlo Park, CA
        94025, (415) 854-5689
    Tracor Europa, Schiphol Airport Amsterdam, Bldg. 106, P. O. Box
        7553, Amsterdam, The Netherlands, (020) 41-1865

UNITED SCIENTIFIC CORPORATION
ANALYTICAL INSTRUMENT DIVISION

1400 D Stierlin Road
P. O. Box 1389
Mountain View, California 94042

Contact: William D. Stewart, (415) 969-9400

Product Line: Automated x-ray analysis systems, including x-ray tube
   and isotopes, Si(Li) x-ray detector, and computer-based x-ray analyzer;
   Si(Li) x-ray detection systems for use on scanning electron micro-
   scopes, transmission electron microscopes and electron microprobes;
   Si(Li) x-ray detectors for basic research; and portable x-ray
   spectrometers.

Sales Offices:
   The Buhrke Company, 2180 Sand Hill Road, Menlo Park, CA (415)854-5689
   International Instrument Corp., 64 E. Main St., Marlon, NJ,
      (609) 983-6550
   Instruments and Technology, 220 E. 14th St., Naperville, IL,
      (312) 355-7748
   Overall Engineering Inc., 15755 Daleport, Dallas, TX (214)233-2311
   North Eastern Analytical Corp., 17 Sherman Rd., Millis, MA,
      (617) 376-4132

VARIAN ASSOCIATES

Vacuum Division
611 Hansen Way, MS G017
Palo Alto, California 94303

Contact: Douglas R. Hillier, (415) 493-4000 Ext. 2815

Product Line: Analytical surface analysis equipment including Auger
   spectrometers, low energy electron diffraction system, UHV vacuum
   systems and components. A new automated Auger microprobe features
   spatial resolution capability of 0.2 microns, permanent storage of
   direct energy data, digital processing of Auger data and clean
   pumping UHV equipment.

Sales Offices:
   25 Route 22, Springfield, NJ 07081, (201) 376-6610
   Ste 306, 25000 Euclid Avenue, Euclid, OH 44117, (216) 261-2115
   4940 El Camino Real, Los Altos, CA 94022, (415) 968-4936